EFFECTS OF INTRAMOLECULAR SPIN POLARIZATION ON THE PHYSICAL AND PHOTOPHYSICAL PROPERTIES OF EXCHANGE-COUPLED SYSTEMS

By

Shuxuan Li

A DISSERTATION

Submitted to
Michigan State University
in partial fulfillment of the requirements
for the degree of

Chemistry - Doctor of Philosophy

2019

ABSTRACT

EFFECTS OF INTROMOLECULAR SPIN POLARIZATION ON THE PHYSICAL AND PHOTOPHYSCIAL PROPERTIES OF EXCHANGE-COUPLED SYSTEMS

By

Shuxuan Li

Heisenberg spin exchange takes place when two or more unpaired spins in close proximity interact, so that their relative orientations are no longer independent of one another. Previous studies on dimeric complexes of $[MM'(tren)_2(CA^{n-})]^{m+}$ (M, M' = Cr^{III} or Ga^{III}, CA) is the bisdentate chloranilate ligand, tren is tris(2-aminoethyl)amine) provided experimental evidence that the presence of spin exchange can affect optical and magnetic properties. The bridging ligand is redox active, which can be changed to yield various redox states via redox reactions, e.g. semiquinone, catecholate, or quinone. These simple systems provide a convenient platform for the studies of both spectroscopic and magnetic behaviors. In semiquinone form, the unpaired electrons on Cr^{III} can interact with the unpaired electron on the bridging ligand. The different forms of ligand can turn "on" or "off" the exchange coupling interactions within the dimeric complex.

The Heisenberg model of these systems predicts that the introduction of spin exchange results in a net thermodynamic stabilization of the system. The results seen in cyclic voltammetry (CV) experiments suggest that the larger potential peak separation (ΔE_{echem}) of $[Cr_2(tren)_2(CA)]^{m+}$ may be a thermodynamic consequence of spin exchange compared to $[Ga_2(tren)_2(CA)]^{m+}$. This may be the first time that the thermodynamic stabilization energy of spin exchange is possibly quantified by other physical measurements.

In order to examine the effects of the thermodynamic stabilization by the spin exchange interaction and establish the thermodynamic correlation seen in both electrochemical and magnetic behaviors, Cr^{III} and Ga^{III} analogues with various substituents on the tetraoxolene bridge are synthesized and characterized. R = H, F, Cl, Br, I, cyano, phenyl, and piperidino make excellent choices of substituents. Additionally, horizontally-elongated bridging ligands, anthracene and naphthalene tetraoxo-derivatives, were synthesized and coordinated to Cr^{III} for the studies, because the electron mobility within these conjugated ligands can delocalize the spin density further away from the metal ions. In addition, the effects of intraligand electron delocalization can be examined by incorporating N,N-dimethylaminophenyl and cyanophenyl substituents on an anilate-bridging ligand to change the directionality of spin polarization. Density Functional Theory (DFT) calculations were employed to validate synthetic viability and provide some in-depth insight of the experimental data.

The cyclic voltammetry and variable-temperature magnetic susceptibility data of these $[Cr_2(tren)_2(L)]^{n+}$ and $[Ga_2(tren)_2(L)]^{n+}$ systems were collected and compared. Among all, the thermodynamic stabilization observed in the $[Cr_2(tren)_2(Me_2\text{-}AnT)]^{n+}$ complex is the weakest. This result matches the prediction of both our hypothesis and our DFT calculations. Both electrochemical and magnetic measurements are employed to provide experimental evidence, which will become advantageous tools for the further study of spin polarization, photophysics and photoelectronic properties of spin-coupled systems.

Copyright by
SHUXUAN LI
2019

This is dedicated to my mother, Lanhuan Tang (汤兰欢), my husband, and Felix Zhai (翟文轩) and my parents-in-law, Yuxia Qiu (邱玉霞) and Guang Zhai (翟广), who are being extremely understanding and supportive for my Ph.D. career.

ACKNOWLEDGEMENTS

I would like to thank my Ph. D. advisor, Jim K. McCusker, for all the support and guidance he has provided me throughout the years, for opening the gateway to the spintronic world, and for all the opportunities for me to see my potential and capabilities. The McCusker group is a huge support group scientifically and socially. Their help and synthetic advice are priceless during group meetings, literature seminar preparation, second-year oral exam practice, especially my final defense practice, and for all the fun moments in the lab. I would like to specially thank Monica Carey to be my best friend by not only discussing science but also talking about cats, music, movies, and makeup, listening to my complaints, and hanging out with me outside of school, and Sara Adelman to be my glovebox buddy by spending all the late-nights in lab, educating me with Jewish culture and customs, motivating me to exercise, and especially fixing the gloveboxes with me. Although I never enjoy those moments when they happen, I do appreciate these two ladies' efforts of trying to persuade me to rest, yelling at me when I was sick, sleep-deprived, or over-work, and calling me stubborn when I refused to listen. In addition, Shannon Kraemer and Olivia Chesniak have been amazing friends for physical exercises and coffee break.

I have enjoyed my x-ray crystallography time with Dr. Richard Staples tremendously, because he has been an extremely helpful and patient mentor. He has taught me all the amazing techniques about crystallography, listened to me and advised me my break-through of the bottle neck in science, and been providing me as much scientific assistance as he can. Without the constant assistance of Dr. Reza Loloee with the SQUID magnetometers, I would not be able to collect all of my variable-temperature magnetic susceptibility data, so I would like to thank him too. To Glenn Wesley, Bob Rasico, Dan Holmes, and other staffs in the MSU chemistry

department, for their generosity of sharing their knowledge and support. Research would be million times harder without their help. I would also love to express my gratitude to my undergraduate advisor, Dr. Kathleen Murphy, and chemistry professors, Dr. Sally Smesko and Dr. Joe Ward at Daemen College.

Even though my gratitude toward my family cannot be solely expressed in words, I would like to let them know my deep appreciation for their endless support and understanding so I can pursue my dream free from inhibitions. To my beloved husband, Felix Zhai, I am tremendously thankful to have you in my life. Your high tolerance of my grumpy temperament spoils me, your workout advice strengthens my health, your unconditional love enables me, and your approval of getting a corgi after my graduation fulfill my life. To my super-heroin mom, your mental and physical support allows me excel and help me fly higher, and your open mind gives me huge space to roam and explore my interest. I am fully aware of how much a pain I was as a child, and you did a wonderful job of raising me alone. I am your proud daughter, and hopefully I will become a daughter you are proud of.

TABLE OF CONTENTS

LIST OF TABLES xi

LIST OF FIGURES xii

LIST OF SCHEMES xxiv

KEY TO SYMBOLS AND ABBREVIATIONS xxv

Chapter 1. Introduction of Heisenberg Exchange Coupling and the Impact on Spin Density Polarization and Delocalization 1
1.1 Introduction on Heisenberg Exchange Interactions 1
1.1.1 Introduction of Spin Exchange Coupling 2
1.1.2 Determination of Exchange Coupling Constant, *J*, with Heisenberg-Dirac-van-Vleck Hamiltonian 3
1.1.3 Direct Exchange and Superexchange Interactions 4
1.2 Effects of Spin Density Polarization 8
1.3 Thermodynamic Effects of Spin Coupling 11
1.4 Previous Work on $[M_2(tren)_2(CA)]^{n+}$ 13
1.5 Comproportionation Free Energy 15
1.6 Contents of Dissertation 17
REFERENCES 20

Chapter 2. Substituent Effects on Spin Density and Charge Density of Tetraoxo-Semiquinoidal Radical Ligands 27
2.1 Introduction 27
2.2 DFT Calculation on Spin and Charge Polarization in Substituted Phenoxy, *o*-Semiquinone, and *o*-Phenanthrenesemiquinone Radicals 27
2.3 Substituent Effects on Spin Density and Charge Density of Tetraoxo-Semiquinoidal Radicals 29
2.4 Computational Details of DFT Calculations 31
2.4.1 Geometry Optimizations and Single-Point Energy Calculations 31
2.5 Results and Discussion 32
2.5.1 Spin and Charge Density of Substituted Tetraoxo-Semiquinoidal Trianionic Radicals 33
2.5.1.1 Charge Density Polarization in 3,6-R-tetraoxosemiquinones 36
2.5.1.2 Spin Density Polarization in 3,6-R-tetraoxosemiquinones 39
2.6 Concluding Comments 41
APPENDIX 43
REFERENCES 60

Chapter 3. Magnetic Properties and Substituent Effect on the Modulation of Heisenberg Exchange Coupling Interactions in Chromium (III) Tetraoxo-Dimeric Complexes 65
3.1 Introduction 65

3.2 Experimental Section 67
3.2.1 Synthetic Procedures of Substituted Tetraoxoanilate, Naphthalene, and Anthracene Ligands 68
3.2.2 Synthetic Procedures and Schemes of Chromium (III) Dimeric Analogues 76
3.2.3 Physical Measurements 84
3.3 SQUID Variable-Tempearture Magnetic Susceptibility Measurements 87
3.3.1 Sample Preparation for Powders 88
3.3.2 Temperature Sequence for Variable-Temperature Magnetic Data Collection 90
3.4 Results and Discussion 91
3.4.1 Synthesis and Characterization 91
3.4.2 Single Crystal X-Ray Structures 98
3.5 Magnetic Susceptibility Measurements 106
3.5.1 Previous Studies on Similar Systems: Experimental and Theoretical Examination of Cr (III) Phenanthrenesemiquinone 106
3.5.2 Magnetic Susceptibility Measurement and Extrapolation of *J*-coupling on $[Cr_2(tren)_2(L^{cat,cat})]^{2+}$ 107
3.5.3 Magnetic Susceptibility Measurement and Extrapolation of *J*-coupling on $[Cr_2(tren)_2(L^{sq,cat})]^{3+}$ 113
3.6 Concluding Comments 127
APPENDIX 129
REFERENCES 178

Chapter 4. Magnetic Properties and Substituent Effects of Gallium (III) Tetraoxo-Dimeric Complexes 184
4.1 Introduction 184
4.1.1 Previous Studies on Similar Systems: An EPR, ENDOR, and Density Functional Study on Ga (III) Phenanthrenesemiquinone Complexes, $[Ga_2(tren)_2(CA^{sq,cat})]^{3+}$ and $[Ga_2(tren)_2(DHBQ^{sq,cat})]^{3+}$ 185
4.2 Computational Details of DFT Calculations 186
4.2.1 Geometry Optimization and Single Point Energy Calculations 187
4.3 Experimental Section 188
4.3.1 Synthetic Procedures of Substituted Tetraohydroxy-Ligands 189
4.3.2 Synthetic Procedures of Gallium(III) Dimeric Complexes 190
4.3.3 Physical Measurements 194
4.4 SQUID Variable-Temperature Magnetic Susceptibility Measurement on $[Ga_2(tren)_2(L^{sq,cat})]^{3+}$ 196
4.5 Results and Discussion 196
4.5.1 Synthesis and Characterization 196
4.5.2 Single Crystal X-Ray Structures 200
4.5.3 DFT Calculations 206
4.5.4 Magnetic Properties of $[Ga_2(tren)_2(L^{sq,cat})](BPh_4)_2(BF_4)$ 211
4.6 Concluding Comments 213
APPENDIX 215
REFERENCES 232

Chapter 5. Thermodynamics of Heisenberg Spin Exchange Coupling Reflected on Electrochemical Properties: Comparison of Chromium(III) and Gallium(III) Dimeric Complexes 236
5.1 Introduction.....236
5.2 Electronic Absorption Spectroscopy of Chromium(III) and Gallium(III) Dimeric Complexes.....237
5.3 Electrochemistry Studies of Chromium(III) and Gallium(III) Dimeric Complexes 237
5.3.1 Experimental Sections 237
5.3.2 Electrochemical Properties of $[M_2(tren)_2(L)]^{n+}$ ($M = Ga^{3+}$ or Cr^{3+}) 239
5.3.3 Thermodynamic Stabilization of Spin Exchange Interactions.....250
5.3.3.1 Comproportionation Free Energy 251
5.4 Extrapolation of Thermodynamic Stabilization Energies of Cr(III) Dimers from Magnetic Susceptibility Data by Referencing Ga(III) Analogues 254
5.5 Concluding Comments 258
APPENDIX.....260
REFERENCES 267

Chapter 6. Conclusion and Future Directions 270
6.1 Future Works 270
6.1.1 DFT Calculations.....270
6.1.1.1 Geometry Optimization and Single Point Energy Calculations 271
6.1.2 Finish the Other Derivatives of the Substituted Anilate and Anthracene Bridging Systems 271
6.1.2.1 Synthesis 272
6.1.2.2 Discussion.....273
6.1.3 Expand the Conjugation of Tetraoxo-Bridging Ligands with 9,10-Diphenylanthracene, Terrylene, and Pyrene 275
6.1.3.1 Synthesis 278
6.1.3.2 Discussion.....279
6.1.4 Fast-Scan Cyclic Voltammetry Measurements 279
6.1.5 Electron Paramagnetic Resonance and DFT Studies of the Electronic Structures of the Semiquinoidal Gallium(III) Dimeric Systems.....280
6.1.6 A Broken Symmetry DFT Study for the Spin Exchange Coupling Constants of the Semiquinoidal Cr(III) Dimeric Systems 281
6.1.7 Solution-Phase SQUID Magnetic Susceptibility Measurements.....282
6.2 Concluding Comments.....283
APPENDIX.....285
REFERENCES 292

LIST OF TABLES

Table 2.1. Net spin density, charge density, and σ-HOMO- σ-LUMO gap (eV) of 3,6-R-semiquinone 41

Table 3.1. Crystallographic data for Complex **1**, **2**, **4** and **5** 85

Table 3.2. Crystallographic data for Complex **6**, **7** and **10** 86

Table 3.3. Selected Bond Length (Å) and Angle (˚) for Complex **1**, **2**, **4**, and **5** 99

Table 3.4. Selected Bond Length (Å) and Angle (˚) for Complex **6**, **7**, and **10** 102

Table 3.5. Magnetic Properties and J-Couping Constants of $[Cr_2(tren)_2(L^{cat,cat})](BPh_4)_2$ 112

Table 3.6. Magnetic Properties and *J*-Couping Constants of $[Cr_2(tren)_2(L^{sq,cat})](BPh_4)_2(BF_4)$ 122

Table 3.7. Crystal data and structural refinement for 2,7-dimethoxy-3,6-di(N,N-dimethylaminophenyl)benzoquinone) 143

Table 3.8. Bond lengths for 2,7-dimethoxy-3,6-di(N,N-dimethylaminophenyl)benzoquinone) 143

Table 3.9. Bond angles for 2,7-dimethoxy-3,6-di(N,N-dimethylaminophenyl)benzoquinone) 143

Table 3.10. Crystal data and structural refinement for $[Cr(II)(tren)Cl](BPh_4)$ 168

Table 4.1. Crystallographic data for Complex **20**, **21**, **23**, and **24** 195

Table 4.2. Selected Bond Length (Å) and Angle (˚) for Complex **20**, **21**, **23**, and **24** 202

Table 5.1. Electrochemical Properties of $[M_2(tren)_2(L)]^{n+}$ (M = Ga^{3+} or Cr^{3+}) 248

Table 5.2. Electrochemical and Magnetic Data for $[M_2(tren)_2(L)]^{n+}$ (M = Ga^{3+} or Cr^{3+}) 254

LIST OF FIGURES

Figure 1.1. Spin ladders of a system with antiferromagnetic interaction ($J < 0$) between two **S** = ½ spins resulting in a singlet ground spin state 5

Figure 1.2. Spin ladders of a system with ferromagnetic interaction ($J > 0$) between two **S** = ½ spins resulting in a triplet ground spin state 5

Figure 1.3. Molecular orbital diagram with *d-p* orbital mixing of superexchange interaction between two metals and one intervening O^{2-} via σ-bonding.....6

Figure 1.4. 180˚ orbital overlap configuration of superexchange interaction between two metals and one intervening O^{2-} via σ-bonding (a), or π-bonding (b) 6

Figure 1.5. The 90˚ configurations of metal *d* orbitals and diamagnetic ligand *p* orbitals overlap. Antiferromagnetic interaction is shown in (a), whereas ferromagnetic interaction is shown in (b).....7

Figure 1.6. A quinoidal ligand undergoing one-electron redox reactions 9

Figure 1.7. Multiple possible chelating forms tetraoxolene quinone undergoing one-electron redox reactions.....10

Figure 1.8. The structural representation of protein cluster rubredoxin (a) and ferredoxin (b) active sites 12

Figure 1.9. Cyclic voltammograms of $[Ga_2(tren)_2(CA^{cat,cat})](BPh_4)_2$ (blue), and $[Cr_2(tren)_2(CA^{cat,cat})](BPh_4)_2$ (red). All data were recollected in degassed acetonitrile containing 0.1 M NBu_4PF_6 at a scan rate of 100 mV/s 12

Figure 1.10. Cr(III) and Ga(III) -tetraoxolene quinodal complexes 13

Figure 1.11. Indication of spin exchange couplings for $[Cr_2(tren)_2(CA^{sq,cat})]^{3+}$, see text for details on notation 14

Figure 2.1. Resonance structure of a ketyl radical.....29

Figure 2.2. A quinoidal ligand undergoing one-electron redox reactions 29

Figure 2.3. Substituted 2,3,5,6-tetraoxoanilate (left), 2,3,6,7-tetraoxonaphthalene (middle), and 2,3,6,7-tetraoxoanthracene (right) 31

Figure 2.4. Resonance structure of substituted anilate.....33

Figure 2.5. Shift in spin (red) and charge (blue) density at the oxygen atom for a series of substituted-anilate, naphthalene, and anthracene bridging radicals 35

Figure 2.6. Resonance effects of amino-π-donors 36

Figure 2.7. Percent change charge density vs. additive Hammett parameters for 3,6-R-tetraoxosemiquinones 37

Figure 2.8. Percent change charge density vs. *meta* Hammett parameters for 3,6-R-tetraoxosemiquinones 38

Figure 2.9. Percent Change charge density vs. *ortho* Hammett parameters for 3,6-R-tetraoxosemiquinones 38

Figure 2.10. Total spin density plots of $DHBQ^{sq,cat}$ (left), $CA^{sq,cat}$ (middle), and $NMe_2A^{sq,cat}$ (right) 40

Figure 2.11. Total spin density plots of $CN^{sq,cat}$ 40

Figure 2.12. Percent Change spin density vs σ-HOMO- σ-LUMO gap (eV) parameters for 3,6-R-tetraoxosemiquinones 41

Figure 2.13. Cr^{3+} or Ga^{3+} -tetraoxolene quinodal complexes with combination of diamagnetic or paramagnetic substituted-bridging ligands, where R_1 are the substituents on tetraoxoanilate, and R_2 are the substituents on 2,3,6,7-tetraoxoanthracene 42

Figure 2.14. Total spin density plots of $FA^{sq,cat}$ (left), $BA^{sq,cat}$ (middle), and $IA^{sq,cat}$ (right) 57

Figure 2.15. Total spin density plots of $CF_3An^{sq,cat}$ (left), $OMeAn^{sq,cat}$ (middle), and $PipAn^{sq,cat}$ (right) 58

Figure 2.16. Total spin density plots of $PhAn^{sq,cat}$ (left), $NMe_2PhAn^{sq,cat}$ (middle), and $CNPhAn^{sq,cat}$ (right) 58

Figure 2.17. Total spin density plots of $CF_3PhAn^{sq,cat}$ (left), $NAT^{sq,cat}$ (middle), and $AnT^{sq,cat}$ (right) 58

Figure 2.18. Total spin density plots of $MeAnT^{sq,cat}$ (left), $PhAnT^{sq,cat}$ (middle), and $CNPhAnT^{sq,cat}$ (right) 58

Figure 2.19. Total spin density plots of $pyrene^{sq,cat}$ (left) and $terrylene^{sq,cat}$ (right) 59

Figure 3.1. Cr^{III}-tetraoxolene quinodal complexes with combination of diamagnetic or paramagnetic substituted-bridging ligands, where R_1 are the substituents on tetraoxoanilate, and R_2 are the substituents on 2,3,6,7-tetraoxoanthracene 65

Figure 3.2. Quantum Design Delrin® liquid sample holder.....89

Figure 3.3. (a) Quantum Design Delrin® powder sample holder; (b) Brass half-tube; (c) a Delrin® powder sample holder snapped into a brass half-tube.....90

Figure 3.4. Resonance structure of substituted 3,6-R-tetraoxoquinone 94

Figure 3.5. Oxidation of naphthalene and anthracene to their quinone derivatives.....95

Figure 3.6. ORTEP drawing of Complex **1** (a), **2** (b), **4** (c), and **5** (d) obtain from single crystal x-ray structure determination 100

Figure 3.7. ORTEP drawing of Complex **6** (a), **7** (b), and **10** (c) obtain from single crystal x-ray structure determination.....101

Figure 3.8. Plots of the effective magnetic moment versus temperature for Complex **1**, **2**, **3**, **4**, **5**, **6**, **7**, **8**, **9** and **10** acquired in solid states.....108

Figure 3.9. Spin latters of $[Cr_2(tren)_2(L^{cat,cat})^{2+}$ due to the Heisenberg Hamiltonian 109

Figure 3.10. The effective magnetic moment of Complex **1** (blue square), and the solid line represents a fit to the data using parameters described in the text.....111

Figure 3.11. Indication of spin exchange coupling interactions for $[Cr_2(tren)_2(L^{sq,cat})]^{3+}$, see text for details on notation 113

Figure 3.12. The DSC plots of Complex **13**, **14** and **16**.....115

Figure 3.13. Plots of the effective magnetic moment versus temperature for all samples in solid states, Complex **11**, **12**, **13**, **14**, **15**, **16**, **17**, **18** and **19** 116

Figure 3.14. Plot of the eigenvalues of various spin states for $[Cr_2(tren)_2(L^{sq,cat})]^{2+}$. J <0 and J^* *<0* with both superexchange and direct exchange interactions considered as antiferromagnetic were used to generate this plot. Each state is labeled as $|S_T, S_A>$..... 117

Figure 3.15. Plot of the eigenvalues of various spin states for $[Cr_2(tren)_2(L^{sq,cat})]^{2+}$. J <0 and J^* *>0* with direct exchange and superexchange interactions considered as antiferromagnetic and ferromagnetic respectively were used to generate this plot. Each state is labeled as $|S_T, S_A>$ 118

Figure 3.16. A spin ladder diagram for of $[Cr_2(tren)_2(L^{sq,cat})](BPh_4)_2(BF_4)$.....119

Figure 3.17. Molecular orbital diagram with *d-p* orbital mixing of superexchange interaction between two metals and one intervening O^{2-} via σ-bonding.....120

Figure 3.18. The effective magnetic moment of Complex **12** (blue square), and the solid line represents a fit to the data using parameters described in the text.....121

Figure 3.19. Excess spin density associated with the highest energy, singly-occupied molecular orbital of $(BA^{sq,cat})^{3-}$ (a) and $(IA^{sq,cat})^{3-}$ (b).....123

Figure 3.20. The inter-ring torsion angle (ϑ) of phenyl-substituted complexes.....124

Figure 3.21. Multiple possible chelating forms of deprotonated 2,3,6,7-tetraoxoanthracene undergoing one-electron redox reactions.....126

Figure 3.22. ^{1}H NMR of 2,5-dimethoxy-1,4-benzoquinone in $CDCl_3$.....130

Figure 3.23. ^{13}C NMR of 2,5-dimethoxy-1,4-benzoquinone in $CDCl_3$.....130

Figure 3.24. ^{1}H NMR of 2,5-dibromo-3,6-dimethoxy-1,4-benzoquinone in $CDCl_3$.....131

Figure 3.25. ^{13}C NMR of 2,5-dibromo-3,6-dimethoxy-1,4-benzoquinone in $CDCl_3$.....131

Figure 3.26. ESI-MS of H_2BA. Top: calculated isotope pattern for $[M-H]^-$ ($C_6H_1O_4Br_2$). Bottom: experimental result. 132

Figure 3.27. ESI-MS of H_2FA. Top: calculated isotope pattern for $[M-H]^-$ ($C_6H_1O_4F_2$). Bottom: experimental result.....132

Figure 3.28. ^{13}C NMR of bromanil (left) and iodanil (right) in benzene-d_6.....133

Figure 3.29. ESI-MS of H_2IA. Top: calculated isotope pattern for $[M-H]^-$ ($C_6H_1O_4I_2$). Bottom: experimental result.....133

Figure 3.30. ^{1}H NMR of 2,5-dimethoxy-3,6-diphenyl-1,4-benzoquinone in $CDCl_3$.....134

Figure 3.31. ^{13}C NMR of 2,5-dimethoxy-3,6-diphenyl-1,4-benzoquinone in $CDCl_3$ 134

Figure 3.32. ESI-MS of 2,5-dimethoxy-3,6-diphenyl-1,4-benzoquinone. Top: calculated isotope pattern for $[M+H]^+$ ($C_{10}H_{15}O_4$). Bottom: experimental result. 135

Figure 3.33. ^{1}H NMR of H_2PhA in acetone-d_6 135

Figure 3.34. ^{13}C NMR of H_2PhA in acetone-d_6.....136

Figure 3.35. ESI-MS of H_2PhA. Top: calculated isotope pattern for $[M-H]^-$ ($C_{18}H_{11}O_4$). Bottom: experimental result.....136

Figure 3.36. ^{1}H NMR of 2,3,6,7-tetramethoxy-9,10-dimethylanthracene in $CDCl_3$.....137

Figure 3.37. ^{13}C NMR of 2,3,6,7-tetramethoxy-9,10-dimethylanthracene in $CDCl_3$.....137

Figure 3.38. ESI-MS of 2,3,6,7-tetramethoxy-9,10-dimethylanthracene. Experimental result for $[M+H]^+$ ($C_{20}H_{23}O_4$). 138

Figure 3.39. ^1H NMR of H_4(Me-AnT) in dmso-d_6 138

Figure 3.40. ESI-MS of H_4(Me-AnT). Experimental result for $[M-H]^-$ ($C_{12}H_{15}O_4$).....139

Figure 3.41. ^1H NMR of 4-(N,N-Dimethylamino)phenylboronic acid in dmso-d_6 139

Figure 3.42. ^{11}B NMR of 4-(N,N-Dimethylamino)phenylboronic acid in dmso-d_6.....140

Figure 3.43. ^1H NMR of 2,7-dimethoxy-3,6-di(N,N-dimethylaminophenyl)benzoquinone in $CDCl_3$ 140

Figure 3.44. ^{13}C NMR of 2,7-dimethoxy-3,6-di(N,N-dimethylaminophenyl)benzoquinone in $CDCl_3$ 141

Figure 3.45. ESI-MS of 2,7-dimethoxy-3,6-di(N,N-dimethylaminophenyl)benzoquinone. Top: calculated isotope pattern for $[M+H]^+$ ($C_{24}H_{27}O_4N_2$). Bottom: experimental result 141

Figure 3.46. ORTEP drawing of 2,7-dimethoxy-3-bromo-6-(N,N-dimethylaminophenyl)benzoquinone from single-crystal x-ray structure determination 142

Figure 3.47. ORTEP drawing of 2,7-dimethoxy-3,6-di(N,N-dimethylaminophenyl)benzoquinone from single-crystal x-ray structure determination.....142

Figure 3.48. ^1H NMR of H_2NMe_2-PhA in dmso-d_6.....144

Figure 3.49. ESI-MS of H_2NMe_2-PhA. Left: top, calculated isotope pattern for $[M-H]^-$ ($C_{22}H_{21}O_4N_2$); bottom: experimental result. Right: top, calculated isotope pattern for $[M+H]^+$ ($C_{22}H_{23}O_4N_2$); bottom: experimental result 144

Figure 3.50. ^1H NMR of 3,6-dibromo-2,7-dihydroxynaphthalene in DMSO-d_6.....145

Figure 3.51. ^1H NMR of 3,6-dibromo-2,7-dimethoxynaphthalene in $CDCl_3$.....145

Figure 3.52. ^{13}C NMR of 3,6-dibromo-2,7-dimethoxynaphthalene in $CDCl_3$.....146

Figure 3.53. ^1H NMR of 2,3,6,7-tetramethoxynaphthalene in $CDCl_3$.....146

Figure 3.54. ^{13}C NMR of 2,3,6,7-tetramethoxynaphthalene in $CDCl_3$.....147

Figure 3.55. ^{1}H NMR of H_4NAT in dmso-d_6.....147

Figure 3.56. ^{13}C NMR of H_4NAT in dmso-d_6 148

Figure 3.57. ^{1}H NMR of 2,3,6,7-Tetramethoxyanthraquinone in $CDCl_3$.....148

Figure 3.58. ^{13}C NMR of 2,3,6,7-Tetramethoxyanthraquinone in $CDCl_3$.....149

Figure 3.59. ^{1}H NMR of 2,3,6,7-tetramethoxyanthracene in $CDCl_3$.....149

Figure 3.60. ^{13}C NMR of 2,3,6,7-tetramethoxyanthracene in $CDCl_3$.....150

Figure 3.61. ^{1}H NMR of H_4AnT in acetone-d_6.....150

Figure 3.62. ^{13}C NMR of H_4AnT in acetone-d_6.....151

Figure 3.63. ESI-MS of H_4AnT. Top: calculated isotope pattern for $[M-H]^-$ ($C_{14}H_9O_4$). Bottom: experimental result.....151

Figure 3.64. ESI-MS of $[FeCp^*_2](BF_4)$. Top: calculated isotope pattern for $[M]^+$ ($C_{20}H_{30}Fe_2$). Bottom: experimental result 152

Figure 3.65. ESI-MS of Complex **11**. Top: calculated isotope pattern for $[M]^{3+}$ ($Cr_2C_{18}H_{38}O_4N_8$). Bottom: experimental result.....152

Figure 3.66. ESI-MS of Complex **13**. Left: top, calculated isotope pattern for $[M]^{3+}$ ($Cr_2C_{18}Cl_2H_{36}O_4N_8$); bottom, experimental result. Right: top, calculated isotope pattern for $[Cr(tren)(C_6Cl_2O_4)]^+$ ($CrC_{12}H_{18}O_4N_4Cl_2$); bottom, experimental result 153

Figure 3.67. ESI-MS of Complex **4**. Upper left: top, calculated isotope pattern for $[M]^{2+}$ ($Cr_2C_{18}O_4Br_2H_{35}N_8$); bottom: experimental result. Upper right: top, calculated isotope pattern for $[M]^{3+}$ ($Cr_2C_{18}O_4Br_2H_{36}N_8$); bottom: experimental result. Lower: top, calculated isotope pattern for $[Cr(tren)(C_6O_4Br_2)]^+$ ($CrC_{12}H_{18}O_4N_4Br_2$); bottom, experimental result.....154

Figure 3.68. ESI-MS of Complex **14**. Left: top, calculated isotope pattern for $[M]^{3+}$ ($Cr_2C_{18}H_{36}O_4N_8Br_2$); bottom, experimental result. Right: top, calculated isotope pattern for $[Cr(tren)(C_6O_4Br_2)]^+$ ($CrC_{12}H_{18}O_4N_4Br_2$); bottom, experimental result 155

Figure 3.69. ESI-MS of Complex **2**. Upper left: top, calculated isotope pattern for $[M]^{2+}$ ($Cr_2C_{18}H_{36}O_4N_8F_2$); bottom, experimental result. Upper right: top, calculated isotope pattern for $[M]^{3+}$ ($Cr_2C_{18}H_{36}O_4N_8F_2$); bottom, experimental result. Lower: top, calculated isotope pattern for $[Cr(tren)(C_6F_2O_4)]^+$ ($CrC_{12}H_{18}O_4N_4F_2$); bottom, experimental result.....156

Figure 3.70. ESI-MS of Complex **12**. Top: calculated isotope pattern for $[M]^{3+}$ ($Cr_2C_{18}H_{36}O_4N_8F_2$). Bottom: experimental result. $[Cr(tren)(C_6O_4F_2)]^+$ ($CrC_{12}H_{18}O_4N_4F_2$).....157

Figure 3.71. ESI-MS of Complex **5**. Upper left: top, calculated isotope pattern for $[M]^{2+}$ ($Cr_2C_{18}H_{36}O_4N_8I_2$); bottom, experimental result. Upper right: top, calculated isotope pattern for $[M]^{3+}$ ($Cr_2C_{18}H_{36}O_4N_8I_2$); bottom, experimental result. Lower: top, calculated isotope pattern for $[Cr(tren)(C_6O_4I_2)]^+$ ($CrC_{12}H_{18}O_4N_4I_2$); bottom, experimental result.....158

Figure 3.72. ESI-MS of Complex **15**. Left: top, calculated isotope pattern for $[M]^{3+}$ ($Cr_2C_{18}H_{36}O_4N_8I_2$); bottom, experimental result. Right: top, calculated isotope pattern for $[Cr(tren)(C_6O_4I_2)]^+$ ($CrC_{12}H_{18}O_4N_4I_2$); bottom, experimental result....159

Figure 3.73. ESI-MS of Complex **6**. Top: calculated isotope pattern for $[M]^{2+}$ ($Cr_2C_{30}H_{46}O_4N_8$). Bottom: experimental result 160

Figure 3.74. ESI-MS of Complex **16**. Left: top, calculated isotope pattern for $[M]^{3+}$ ($Cr_2C_{30}H_{46}O_4N_8$); bottom, experimental result. Right: top, calculated isotope pattern for $[Cr(tren)(C_{18}O_4H_{10})]^+$ ($CrC_{24}H_{28}O_4N_4$); bottom, experimental result.....160

Figure 3.75. ESI-MS of Complex **7**. Left: top, calculated isotope pattern for $[M]^{2+}$ ($Cr_2C_{18}O_4Br_2H_{36}N_8$); bottom, experimental result. Right: top, calculated isotope pattern for $[M]^+$ ($Cr_2C_{18}O_4Br_2H_{36}N_8$); bottom, experimental result.....161

Figure 3.76. ESI-MS of Complex **17**. Left: top, calculated isotope pattern for $[M]^{3+}$ ($Cr_2C_{34}H_{54}O_4N_{10}$); bottom, experimental result. Right: top, calculated isotope pattern for $[Cr(tren)(C_{22}H_{20}O_4N_2)]^+$ ($CrC_{28}H_{38}O_4N_6$); bottom, experimental result 162

Figure 3.77. ESI-MS of Complex **10**. Left: top, calculated isotope pattern for $[M]^{2+}$ ($Cr_2C_{18}H_{14}O_4N_8$); bottom, experimental result. Right: top, calculated isotope pattern for $[Cr(tren)(C_{14}H_8O_4)]^+$ ($CrC_{22}H_{30}O_4N_4$); bottom, experimental result.....163

Figure 3.78. ESI-MS of Complex **19.** Left: top, calculated isotope pattern for $[M]^{3+}$ ($Cr_2C_{18}H_{14}O_4N_8$); bottom, experimental result. Right: top, calculated isotope pattern for $[Cr(tren)(C_{14}H_8O_4)]^+$ ($CrC_{22}H_{30}O_4N_4$); bottom, experimental result.....163

Figure 3.79. ESI-MS of Complex **8**. Upper left: top, calculated isotope pattern for $[M]^{2+}$ ($Cr_2C_{22}H_{40}O_4N_8$); bottom, experimental result. Upper right: top, calculated isotope pattern for $[M]^{3+}$ ($Cr_2C_{22}H_{40}O_4N_8$); bottom, experimental result. Bottom: top, calculated isotope pattern for $[Cr(tren)(C_{10}H_6O_4)]^+$ ($CrC_{16}H_{24}O_4N_4$); bottom, experimental result.....164

Figure 3.80. ESI-MS of Complex **18**. Left: top, calculated isotope pattern for $[M]^{3+}$ ($Cr_2C_{22}H_{40}O_4N_8$); bottom: experimental result. Right: top, calculated isotope pattern for $[Cr(tren)(C_{10}H_6O_4)]^+$ ($CrC_{16}H_{24}O_4N_4$); bottom: experimental result 165

Figure 3.81. ESI-MS of Complex **9**. Left: top, calculated isotope pattern for $[M]^{2+}$ ($Cr_2C_{18}H_{14}O_4N_8$); bottom, experimental result. Right: top, calculated isotope pattern for $[M]^{3+}$ ($Cr_2C_{18}H_{14}O_4N_8$); bottom, experimental result 166

Figure 3.82. ESI-MS of Complex **9**. Top, calculated isotope pattern for $[Cr(tren)(C_{14}H_8O_4)]^+$ ($CrC_{20}H_{26}O_4N_4$); bottom, experimental result 167

Figure 3.83. ORTEP drawing of $[Cr(tren)Cl](BPh_4)$ from single-crystal x-ray structure determination. Atoms are represented as 50% thermal ellipsoids 168

Figure 3.84. The effective magnetic moment of Complex **2** (blue square), and the solid line represents a fit to the data using MagFit 169

Figure 3.85. The effective magnetic moment of Complex **3** (blue square), and the solid line represents a fit to the data using MagFit 169

Figure 3.86. The effective magnetic moment of Complex **4** (blue square), and the solid line represents a fit to the data using MagFit 170

Figure 3.87. The effective magnetic moment of Complex **5** (blue square), and the solid line represents a fit to the data using MagFit 170

Figure 3.88. The effective magnetic moment of Complex **6** (blue square), and the solid line represents a fit to the data using MagFit 171

Figure 3.89. The effective magnetic moment of Complex **7** (blue square), and the solid line represents a fit to the data using MagFit 171

Figure 3.90. The effective magnetic moment of Complex **8** (blue square), and the solid line represents a fit to the data using MagFit 172

Figure 3.91. The effective magnetic moment of Complex **9** (blue square), and the solid line represents a fit to the data using MagFit 172

Figure 3.92. The effective magnetic moment of Complex **10** (blue square), and the solid line represents a fit to the data using MagFit 173

Figure 3.93. The effective magnetic moment of Complex **11** (blue square), and the solid line represents a fit to the data using MagFit 173

Figure 3.94. The effective magnetic moment of Complex **13** (blue square), and the solid line represents a fit to the data using MagFit 174

Figure 3.95. The effective magnetic moment of Complex **14** (blue square), and the solid line represents a fit to the data using MagFit.....174

Figure 3.96. The effective magnetic moment of Complex **15** (blue square), and the solid line represents a fit to the data using MagFit 175

Figure 3.97. The effective magnetic moment of Complex **16** (blue square), and the solid line represents a fit to the data using MagFit 175

Figure 3.98. The effective magnetic moment of Complex **17** (blue square), and the solid line represents a fit to the data using MagFit 176

Figure 3.99. The effective magnetic moment of Complex **18** (blue square), and the solid line represents a fit to the data using MagFit 176

Figure 3.100. The effective magnetic moment of Complex **19** (blue square), and the solid line represents a fit to the data using MagFit 177

Figure 4.1. Chemical structures of $[Ga_2(tren)_2(DHBQ^{sq,cat})]^{3+}$ (left) and $[Ga_2(tren)_2(CA^{sq,cat})]^{3+}$ (right) 185

Figure 4.2. 3,6-diphenyl-tetraoxoanilate undergoing one-electron redox reactions.....199

Figure 4.3. ORTEP drawing of Complex **20** (a), **21** (b), **23** (c), and **24** (d) obtain from single crystal x-ray structure determination.....201

Figure 4.4. Shift in spin (red) and charge (blue) density at the oxygen atom for a series of substituted-anilate, naphthalene, and anthracene bridging radicals. The % change is referenced to the parameters obtained for $[Ga_2(tren)_2(DHBQ^{sq,cat})]^{3+}$ (i.e. R = H, where spin = 0.102 σ-electron and charge = -0.558 electron) 205

Figure 4.5. Excess spin density associated with the highest energy, singly-occupied molecular orbital of Complex **25** (a), **26** (b), **28** (c) and **29** (d).....207

Figure 4.6. Weak bonding interaction between the Ga(III) *3d*, *4s*, *4p* orbitals and two energetically different SQ-SOMO orbitals, where the α-HOMO-α-LUMO gap is labeled in red 208

Figure 4.7. % Change spin density vs. σ-HOMO- σ-LUMO gap (eV) parameters for digallium (III)-tetraoxosemiquinones complexes.....208

Figure 4.8. The SOMO (a) orbital picture and total spin density (b) distribution plot of $[Ga_2(tren)_2(NMe_2\text{-}PhA^{sq,cat})]^{3+}$ based on NPA of single point energy calculations .210

Figure 4.9. Plots of the effective magnetic moment versus temperature for all samples in solid states, Complex **25**, **26**, **27** and **28**.....212

Figure 4.10. ^{1}H NMR of THB in CD_3CN.....216

Figure 4.11. ^{13}C NMR of THB in CD_3CN.....216

Figure 4.12. ESI-MS of H_4CA. Top: calculated isotope pattern for $[M-H]^-$ ($C_6O_4H_3Cl_2$). Bottom: experimental result.....217

Figure 4.13. ESI-MS of H_4BA. Top: calculated isotope pattern for $[M-H]^-$ ($C_6O_4H_3Br_2$). Bottom: experimental result.....217

Figure 4.14. ESI-MS of H_4FA. Top: calculated isotope pattern for $[M-H]^-$ ($C_6O_4H_3F_2$). Bottom: experimental result.....218

Figure 4.15. ESI-MS of H_4IA. Top: calculated isotope pattern for $[M-H]^-$ ($C_6O_4H_3I_2$). Bottom: experimental result.....218

Figure 4.16. ESI-MS of Complex **20**. Upper left: top, calculated isotope pattern for $[M]^{2+}$ ($Ga_2C_{18}O_4H_{38}N_8$); bottom, experimental result. Upper right: top, calculated isotope pattern for $[M]^{3+}$ ($Ga_2C_{18}O_4H_{38}N_8$); bottom, experimental result. Lower: top, calculated isotope pattern for $[Ga(tren)(C_6H_2O_4)]^+$ ($GaC_{12}H_{20}O_4N_4$); bottom, experimental result.....219

Figure 4.17. ESI-MS of Complex **25**. Left: top, calculated isotope pattern for $[M]^{3+}$ ($Ga_2C_{18}O_4H_{38}N_8$); bottom, experimental result. Right: top, calculated isotope pattern for $[Ga(tren)(C_6H_2O_4)]^+$ ($GaC_{12}H_{20}O_4N_4$); bottom, experimental result.....220

Figure 4.18. ESI-MS of Complex **22**. Left: top, calculated isotope pattern for $[M]^{2+}$ ($Ga_2C_{18}H_{36}O_4N_8Cl_2$); bottom, experimental result. Right: top, calculated isotope pattern for $[Ga(tren)(C_6Cl_2O_4)]^+$ ($GaC_{12}H_{18}O_4N_4Cl_2$); bottom, experimental result..... 221

Figure 4.19. ESI-MS of Complex **21**. Left: top, calculated isotope pattern for $[M]^{2+}$ ($Ga_2C_{18}H_{36}O_4N_8F_2$); bottom, experimental result. Right: top, calculated isotope pattern for $[Ga(tren)(C_6F_2O_4)]^+$ ($GaC_{12}H_{18}O_4N_4F_2$); bottom, experimental result..... 222

Figure 4.20. ESI-MS of Complex **26**. Left: top, calculated isotope pattern for $[M]^{3+}$ ($Ga_2C_{18}H_{36}O_4N_8F_2$); bottom, experimental result. Right: top, calculated isotope pattern for $[Ga(tren)(C_6F_2O_4)]^+$ ($GaC_{12}H_{18}O_4N_4F_2$); bottom, experimental result..... 223

Figure 4.21. ESI-MS of Complex **23**. Upper left: top, calculated isotope pattern for $[M]^{2+}$ ($Ga_2C_{18}H_{36}O_4N_8Br_2$); bottom, experimental result. Upper right: top, calculated isotope pattern for $[M]^{3+}$ ($Ga_2C_{18}H_{36}O_4N_8Br_2$); bottom, experimental result. Lower: top, calculated isotope pattern for $[Ga(tren)(C_6Br_2O_4)]^+$ ($GaC_{12}H_{18}O_4N_4Br_2$); bottom, experimental result.....224

Figure 4.22. ESI-MS of Complex **28**. Left: top, calculated isotope pattern for $[M]^{3+}$ ($Ga_2C_{18}H_{36}O_4N_8Br_2$); bottom, experimental result. Right: top, calculated isotope pattern for $[Ga(tren)(C_6Br_2O_4)]^+$ ($GaC_{12}H_{18}O_4N_4Br_2$); bottom, experimental result 225

Figure 4.23. ESI-MS of Complex **24**. Left: top, calculated isotope pattern for $[M]^{3+}$ ($Ga_2C_{18}H_{36}O_4N_8I_2$); bottom, experimental result. Right: top, calculated isotope pattern for $[Ga(tren)(C_6Br_2O_4)]^+$ ($GaC_{12}H_{18}O_4N_4I_2$); bottom, experimental result..... 226

Figure 4.24. ESI-MS of $[Ga_2(tren)_2(PhA^{cat,cat})](BPh_4)_2$. Left: top, calculated isotope pattern for $[M]^{2+}$ ($Ga_2C_{30}H_{46}O_4N_8$); bottom, experimental result. Right: top, calculated isotope pattern for $[Ga(tren)(C_{18}H_{10}O_4)]^+$ ($GaC_{24}H_{28}O_4N_4$); bottom, experimental result..... 227

Figure 4.25. Total spin density associated with the highest energy, singly-occupied molecular orbital of $[Cr_2(tren)_2(CA^{sq,cat})]^{3+}$ (left), and $[Cr_2(tren)_2(CNA^{sq,cat})]^{3+}$ (right) 227

Figure 4.26. Total spin density associated with the highest energy, singly-occupied molecular orbital of $[Cr_2(tren)_2(CF_3A^{sq,cat})]^{3+}$ (left), and $[Cr_2(tren)_2(OMeA^{sq,cat})]^{3+}$ (right).....228

Figure 4.27. Total spin density associated with the highest energy, singly-occupied molecular orbital of $[Cr_2(tren)_2(NMe_2A^{sq,cat})]^{3+}$ (left), and $[Cr_2(tren)_2(PipA^{sq,cat})]^{3+}$ (right) 228

Figure 4.28. Total spin density associated with the highest energy, singly-occupied molecular orbital of $[Cr_2(tren)_2(PhA^{sq,cat})]^{3+}$ (left), and $[Cr_2(tren)_2(NMe_2\text{-}PhA^{sq,cat})]^{3+}$ 229

Figure 4.29. Total spin density associated with the highest energy, singly-occupied molecular orbital of $[Ga_2(tren)_2(NH_2\text{-}PhA^{sq,cat})]^{3+}$ (left), and $[Ga_2(tren)_2(CN\text{-}PhA^{sq,cat})]^{3+}$ (right) 229

Figure 4.30. Total spin density associated with the highest energy, singly-occupied molecular orbital of $[Ga_2(tren)_2(CF_3\text{-}PhA^{sq,cat})]^{3+}$ (left), and $[Ga_2(tren)_2(NAT^{sq,cat})]^{3+}$ (right) .230

Figure 4.31. Total spin density associated with the highest energy, singly-occupied molecular orbital $[Ga_2(tren)_2(AnT^{sq,cat})]^{3+}$ (left), and of $[Ga_2(tren)_2(Me\text{-}AnT^{sq,cat})]^{3+}$ (right)....230

Figure 4.32. Total spin density associated with the highest energy, singly-occupied molecular orbital of $[Ga_2(tren)_2(Ph\text{-}AnT^{sq,cat})]^{3+}$ (left), and $[Ga_2(tren)_2(CNPh\text{-}AnT^{sq,cat})]^{3+}$ (right).....231

Figure 4.33. Total spin density associated with the highest energy, singly-occupied molecular orbital of $[Ga_2(tren)_2(Pyrene^{sq,cat})]^{3+}$ (left) and $[Ga_2(tren)_2(Terrylene^{sq,cat})]^{3+}$ (right) 231

Figure 5.1. The structural representation of protein cluster rubredoxin (left) and ferredoxin (right) active sites 236

Figure 5.2. The cyclic voltammogram of $[Cr_2(tren)_2(DHBQ^{cat,cat})](BPh_4)_2$ in MeCN with 1.0 M $TBAPF_6$ as supporting electrolyte. All potentials are referenced to the $DmFc^{+/0}$ couple ($E_{1/2}$ =0 V in MeCN), and the inserts show the DPV traces 238

Figure 5.3. The cyclic voltammogram of $[Ga_2(tren)_2(PhA)]^{n+}$ in MeCN with 1.0 M $TBAPF_6$ as supporting electrolyte. The redox potential of ferrocene is at 0.324V 240

Figure 5.4. The cyclic voltammogram of $[Cr_2(tren)_2(NMe_2\text{-}PhA)]^{n+}$ in MeCN with 1.0 M $TBAPF_6$ as supporting electrolyte and Pt working electrode 241

Figure 5.5. The cyclic voltammogram of $[Cr_2(tren)_2(NMe_2\text{-}PhA)]^{n+}$ in MeCN with 1.0 M $TBAPF_6$ as supporting electrolyte and glassy carbon working electrode.....241

Figure 5.6. Possible reaction of $[Cr_2(tren)_2(NMe_2\text{-}PhA)]^{n+}$ with MeCN to produce HCN and an acetonitrilo-coordinated complex.....242

Figure 5.7. Resonance structures of dianionic anilate bridging ligand.....243

Figure 5.8. The cyclic voltammogram of $[Cr_2(tren)_2(NAT)]^{n+}$ in MeCN with 1.0 M $TBAPF_6$ as supporting electrolyte with $Fc^{+/0}$ as internal reference 244

Figure 5.9. Multiple possible chelating forms of deprotonated 2,3,6,7-tetraoxonaphthalene undergoing one-electron redox reactions 244

Figure 5.10. The cyclic voltammogram of $[Cr_2(tren)_2(NAT)]^{n+}$ in MeCN with 1.0 M $TBAPF_6$ as supporting electrolyte with $Fc^{+/0}$ as internal reference. The reported potential is referenced to DmFc couple at 0V vs $DmFc^{+/0}$. DPV shows in the inserts collected at the 1st sweep (a), and 2nd sweep (b) 245

Figure 5.11. Cyclic voltammograms of the $[Cr_2(tren)_2(CA)]^{n+}$ in MeCN with 1.0 M $TBAPF_6$ collected at 20 mV/s (red dash), 50 mV/s (green dash), and 100 mV/s (blue solid) 247

Figure 5.12. Cyclic voltammograms of $[Cr_2(tren)_2(IA)]^{n+}$ (red) and $[Ga_2(tren)_2(IA)]^{n+}$ (blue) in MeCN with 1.0 M $TBAPF_6$ as supporting electrolyte.....248

Figure 5.13. Energy level diagram for $[Cr_2(tren)_2(L^{sq,cat})]^{3+}$ with (left) stronger spin exchange interaction, larger *J*; (right) weaker spin exchange interaction, smaller *J*.....250

Figure 5.14. The spin ladder of a molecule with $\mathbf{S}_1 = \mathbf{S}_2 = ½$ based on the Heisenberg exchange Hamitonian. The red arrow indicates a net thermodynamic stabilization resulted from spin exchange coupling 251

Figure 5.15. CV of $[Cr_2(tren)_2(FA)](BPh_4)_2$ in MeCN with 1.0 M $TBAPF_6$ as supporting electrolyte. All potentials are referenced to the $DmFc^{+/0}$ couple 261

Figure 5.16. CV of $[Cr_2(tren)_2(CA)](BPh_4)_2$ in MeCN with 1.0 M $TBAPF_6$ as supporting electrolyte. All potentials are referenced to the $DmFc^{+/0}$ couple 261

Figure 5.17. CV of $[Cr_2(tren)_2(BA)](BPh_4)_2$ in MeCN with 1.0 M $TBAPF_6$ as supporting electrolyte. All potentials are referenced to the $DmFc^{+/0}$ couple 262

Figure 5.18. CV of $[Cr_2(tren)_2(PhA)](BPh_4)_2$ in MeCN with 1.0 M $TBAPF_6$ as supporting electrolyte. All potentials are referenced to the $DmFc^{+/0}$ couple 262

Figure 5.19. CV of $[Cr_2(tren)_2(Me_2\text{-}AnT)](BPh_4)_2$ in MeCN with 1.0 M $TBAPF_6$ as supporting electrolyte. All potentials are referenced to the $DmFc^{+/0}$ couple 263

Figure 5.20. CV of $[Ga_2(tren)_2(DHBQ)](BPh_4)_2$ in MeCN with 1.0 M $TBAPF_6$ as supporting electrolyte. All potentials are referenced to the $DmFc^{+/0}$ couple 263

Figure 5.21. CV of $[Ga_2(tren)_2(CA)](BPh_4)_2$ in MeCN with 1.0 M $TBAPF_6$ as supporting electrolyte. All potentials are referenced to the $DmFc^{+/0}$ couple 264

Figure 5.22. CV of $[Ga_2(tren)_2(BA)](BPh_4)_2$ in MeCN with 1.0 M $TBAPF_6$ as supporting electrolyte. All potentials are referenced to the $DmFc^{+/0}$ couple 264

Figure 5.23. CV of $[Ga_2(tren)_2(PhA)](BPh_4)_2$ in MeCN with 1.0 M $TBAPF_6$ as supporting electrolyte. All potentials are referenced to the $DmFc^{+/0}$ couple 265

Figure 5.24. CV of ferrocene (at 0.569V) and decamethylferrocene (at 0.06V) in MeCN with 1.0 M $TBAPF_6$ as supporting electrolyte.....265

Figure 5.25. Cyclic voltammograms of the $[Cr_2(tren)_2(CA^{cat,cat})](BPh_4)_2$ in MeCN with 1.0 M $TBAPF_6$ collected from 50 mV/s to 400 mV/s.....266

Figure 6.1. The calculated structures of 4,5,9,10-tetraoxopyrene (left), and 4,5,12,13-tetraoxoterrylene (right) 277

Figure 6.2. Shift in spin (red) and charge (blue) density at the oxygen atom for a series of deprotonated trianionic tetraoxo-substituted phenylanilate, naphthalene, anthracene, pyrene (PAH), and terrylene bridging radicals 277

Figure 6.3. Shift in spin (red) and charge (blue) density at the oxygen atom for a series of tetraoxo-substituted phenylanilate, naphthalene, anthracene, pyrene (PAH), and terrylene Ga (III) complexes 281

LIST OF SCHEMES

Scheme 3.1. General synthetic routes of $[Cr_2(tren)_2(Anilate^{cat,cat})](BPh_4)_2$ and $[Cr_2(tren)_2(Anilate^{sq,cat})](BPh_4)_2(BF_4)$, where anilate represents substituted anilate bridging ligands, DHBQ, FA, CA, BA, IA, PhA, or NMe_2-PhA 95

Scheme 3.2. General synthetic routes of $[Cr_2(tren)_2(L^{cat,cat})](BPh_4)_2$ and $[Cr_2(tren)_2(L^{sq,cat})](BPh_4)_2(BF_4)$, where L represents naphthalene or anthracene bridging ligands, NAT, AnT, or Me-AnT.....96

KEYS TO SYMBOLS AND ABBREVIATIONS

BA: Bromanilate

BF_4^-: tetrafluoroborate

BPh_4^-: tetraphenylborate

CA: Chloranilate

CV: Cyclic Voltammetry

DCM: Dichloromethane

DFT: Density Functional Theory

DHBQ: 2,5-Dihydroxy-3,6-benzoquinone

DMF: Dimethylformamide

DMSO: Dimethyl Sulfoxide

DPV: Differential-Pulse Voltammetry

DSC: Differential Scanning Calorimetry

EDG: Electron Donating Group

ENDOR: Electron Nuclear Double Resonance

EPR: Electron Paramagnetic Resonance

ES: Excited State

ESI-MS: Electrospray Ionization Mass Spectrometry

EtOH: Ethanol

EWG: Electron Withdrawing Group

FA: Fluoranilate

GS: Ground State

H_2BA: Bromanilic acid

H_2CA: Chloranilic acid

HDVV: Heisenberg-Dirac-van-Vleck

H_2FA: Fluoranilic acid

H_2IA: Iodanilic acid

HOMO: Highest Occupied Molecular Orbital

IA: Iodanilate

LMCT: Ligand-to-Metal Charge Transfer

LUMO: Lowest Unoccupied Molecular Orbital

MeCN: Acetonitrile

MeOH: Methanol

MLCT: Metal-to-Ligand Charge Transfer

SOMO: Singly Occupied Molecular Orbital

SQUID: Superconducting Quantum Interference Device

$TBAPF_6$: Tetrabutylammonium hexafluorophosphate

TGA: Thermogravimetry Analysis

THB: 2,3,5,6-tetrahydroxybenzene

tren: Tris(2-aminoethyl)amine

Chapter 1. Introduction of Heisenberg Exchange Coupling and the Impact on Spin Density Polarization and Delocalization

1.1 Introduction on Heisenberg Exchange Interactions

In quantum mechanics, spin is an intrinsic form of angular momentum carried by particles,[1] and it refers to unpaired electrons possessing magnetically induced dipole moment in magnetism.[2,3] The spin has direct impact on the physical or photophysical properties of molecular system. For example, a spin-allowed transition process, fluorescence, and a spin-forbidden process, phosphorescence, present various emission lifetime when a molecule stays in its excited state before emitting a photon.[4,5] Understanding the physical nature of how spin affecting a molecular system allows us to learn and interpret its optical property.

In addition, it plays an important role in biological systems, molecular structures and practical applications to assist in interpreting the nature of metalloproteins, advancing the computing technology, and improving data reading, storage, and transfer. The study of spin and magnetism in various chemical systems has been ongoing for decades in many different areas,[2] including single-molecule magnets,[6-9] bioinorganic chemistry,[10-12] material science,[13,14] and more recently, quantum computing,[15,16] giant magnetoresistance[17] and spintronics.[18-23]

Spin polarization is an important parameter in understanding the perturbation of spins in nature, and it is generally defined as specific spin locations and alignments inside a molecule. Recently, there has been increased interest in studying the influence of exchange coupling in areas that range from fundamental research of a system's electronic structure to more complicated systems with application in biology and materials science.[2,24-27] A rising number of research papers prove that spin exchange interactions have direct impact on the photophysical properties and photo-induced reactivity of magnetic systems.[28-30] Furthermore, intramolecular

spin polarization appears to have some effects on the strength of exchange coupling interaction.[31-34] Metalloprotein is a type of protein that contains a metal cofactor, and most of these metal cofactors are paramagnetic because of the presence of unpaired electrons.[35,36] These transition metal ions within the cofactors play an important role in both the magnetic property and the redox chemistry.[11,35,36] The study of Bertrand and Gayda[97] suggested spin exchange coupling interactions relate to the shift in the reduction potentials, which is potentially a thermodynamic consequence of the spin exchange effect. The goal of this project is to design and synthesize molecular systems to tune the spin exchange interaction in order to perceive the cause-and-effect of the thermodynamics of spin-exchanged systems. However, the syntheses and characterization of metalloproteins can be quite complicated. Instead, simple inorganic molecular systems are designed and synthesized in this project to facilitate my study. Previous work by our group members has been conducted to discern this relationship.[37-39]

1.1.1 Introduction of Spin Exchange Coupling

When two or more paramagnetic spin centers are located far away from one another, they do not interact with each other. In this case, their relative spin orientations have no effect on the energy in the system. As this distance diminishes,[40] the parallel (ferromagnetic) or antiparallel (antiferromagnetic) orientation between the magnetic orbitals on the paramagnetic centers will change the energy of the system, which is known as an exchange coupling interaction.[41] Spin exchange interaction is described as an quantum electrostatic interaction arising from Pauli's exclusion principle between two spin operators mathematically,[2,42] and spin coupling is a zero-field effect in the absence of external magnetic field. Exchange interactions can take place between two directly bound spin centers (direct exchange) or through a diamagnetic bridge (superexchange). Direct exchange requires direct orbital overlap through a bonding interaction

and has been widely observed in metal nitroxide,[43-46] pyrazine,[47] verdazyl,[48] thiazyl,[49,50] carbene[51] and semiquinone compounds.[41,52,53] Superexchange is a relatively weak coupling interaction, because the exchange coupling pathway needs to be mediated by a diamagnetic bridging ligand. This indirect coupling interaction has been observed generally in transition metal dimers.[37,54,55] Intermolecular or through-space exchange interactions between paramagnetic molecules are another commonly seen exchange coupling, but they are very weak, even weaker than superexchange intramolecular exchange coupling in magnitude.[56] Both intermolecular and intramolecular exchange interactions play important roles in determining the ground state magnetic properties,[2] but the focus of my project is intramolecular exchange.

1.1.2 Determination of Exchange Coupling Constant, *J*, with Heisenberg-Dirac-van-Vleck Hamiltonian

The Heisenberg-Dirac-van Vleck (HDVV) Hamiltonian ($\widehat{H}$), shown in Eq. 1.1, can be used to describe spin exchange interactions between two spin operators, $\widehat{S_1}$and $\widehat{S_2}$. The strength of the exchange coupling interaction is reflected in the magnitude of the exchange coupling constant, *J*. In general, the HDVV Hamiltonian is the simplest formalism for molecular magnetism,[56] and works well with systems in which each paramagnetic site contains only one unpaired electron with well-defined and localized magnetic orbitals.[57] There are examples of well-predicted spin ladders of Cr(III) (**S** = 3/2) spin-exchanged complexes by the HDVV Hamiltonian reported in literature.[58] In addition, the HDVV Hamiltonian can also be applied to systems with multiple paramagnetic centers, and this will be discussed later in this chapter.

$$\widehat{H} = -2J\widehat{S_1} \cdot \widehat{S_2} \tag{1.1}$$

The HDVV Hamiltonian only applies for spin-only ions, and *S* is not a good quantum number and its associated operator cannot commute with the Hamiltonian when spin-orbit

coupling arises from orbital moments.[42] Therefore, the value of Landé g-factor derived from the Hamiltonian is very close to 2.0, in which L, the orbital angular momentum, is considered zero (Eq. 1.2). This project focuses on systems of dichromium(III) and digallium(III) compounds with C_{2v} or C_i symmetry, where spin-orbit coupling will not be a concern since orbit angular momentum is quenched either partially (with a negligible L value) or completely ($L = 0$).[60] When the symmetry of a system is lower than octahedral, orbital angular momentum is quenched due to the fact that an electron in an orbital of a degenerate set cannot rotate into the other orbital.[60]

$$g = \frac{J(J+1)+S(S+1)-L(L+1)}{2J(J+1)} \tag{1.2}$$

Using Kambe's method[61] to find the eigenvalues of a spin Hamiltonian, the total spin operator is defined as $\widehat{\boldsymbol{S}}_T = \widehat{\boldsymbol{S}}_1 + \widehat{\boldsymbol{S}}_2$, where $S_T = |S_1 - S_2|, |S_1 - S_2| + 1, \ldots, |S_1 + S_2|$. When this is substituted into Eq. 1.1, the expression in Eq. 1.3 is obtained. From that expression, the eigenvalue for the system can be calculated (Eq. 1.4).

$$\widehat{\boldsymbol{H}} = -J\,[\,\widehat{\boldsymbol{S}}_T^2 - \widehat{\boldsymbol{S}}_1^2 - \widehat{\boldsymbol{S}}_2^2] \tag{1.3}$$

$$E\,(S_T) = -J\,[S_T\,(S_T+1) - S_1\,(S_1+1) - S_2\,(S_2+1)] \tag{1.4}$$

1.1.3 Direct Exchange and Superexchange Interactions

Direct exchange interaction requires direct orbital overlap between two paramagnetic centers since it is a through-bond intramolecular exchange, and the Pauli exclusion principle keeps spins away to reduce the coulombic repulsion.[42]An energy diagram for a simple case of two spin centers with $\mathbf{S_1} = \mathbf{S_2} = ½$ undergoing an exchange coupling interaction is shown in Fig. 1.1. Two spin orientations are possible, and the energy difference between them depends on J. When antiparallel is the preferred orientation between two spins, antiferromagnetic interaction is observed with a total spin of 0 according to Hund's rule (Fig. 1.1) and the singlet spin state will

be lower in energy. When two spins orient parallel, ferromagnetic interaction arises with a total spin of 1, and a triplet ground state was stabilized to have lower energy (see Fig. 1.2). The magnetic orbitals of these two spin centers are orthogonal to each other. The form used in eq. 1.1 indicates that antiferromagnetic coupled system if $J < 0$, and ferromagnetic coupled system if $J > 0$. The case of two **S** = ½ with the Cu(II) dimers was studied by Bleaney and Bower.[62]

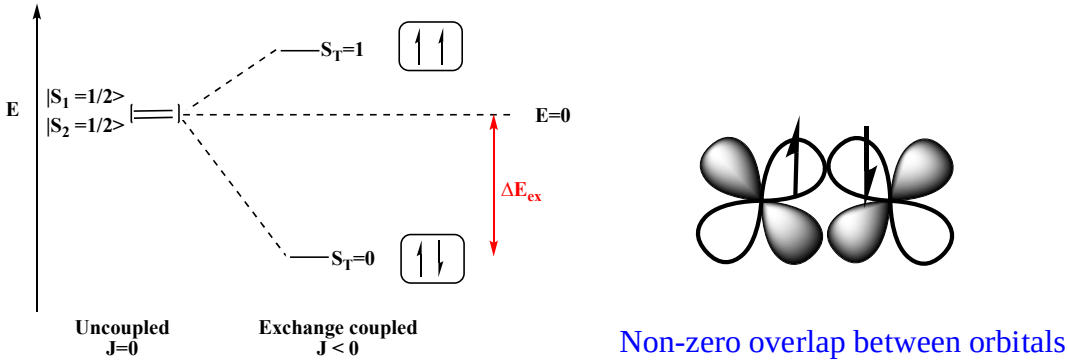

Figure 1.1. Spin ladders of a system with antiferromagnetic interaction ($J < 0$) between two **S** = ½ spins resulting in a singlet ground spin state.

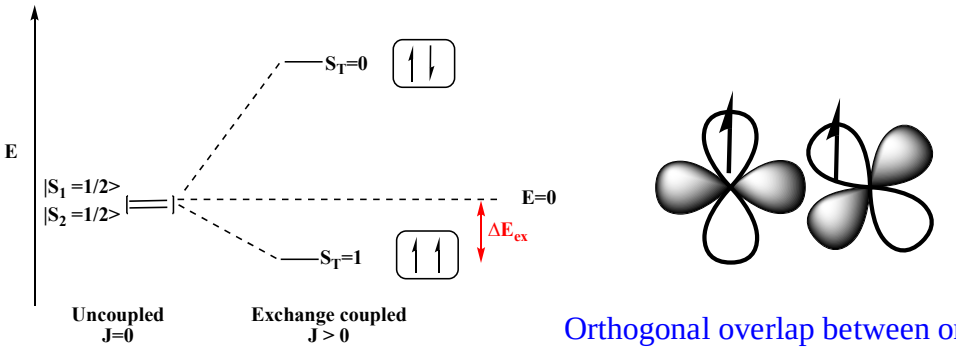

Figure 1.2. Spin ladders of a system with ferromagnetic interaction ($J > 0$) between two **S** = ½ spins resulting in a triplet ground spin state.

Superexchange coupling describes the exchange coupling interaction between two paramagnetic centers through intermediate a diamagnetic ionic ligand with *d-p* orbital mixing, which results in two orbitals: one bonding orbital and one antibonding orbital.[61] A spin transferred from one magnetic metal *d* orbital to the other magnetic *d* orbital by extending its orbital overlap via the antibonding orbital on this intervening bridging ligand (Fig. 1.3).[63] Kramers first noticed

this coupling interaction in crystalline MnO.[64] Due to the overlap of wavefunction between O^{2-} *pz* and two Mn^{2+} dz^2 orbitals aligned 180˚ along z-axis, one electron from O^{2-} extends to couple with the unpaired spin in Mn^{2+}. The remaining *p* electron will then exchange-couple with the spin in the other Mn^{2+} (left in Fig. 1.4).[77] The strength of the exchange coupling, *J*, can also be described by Eq. 1.1, where $\mathbf{S}_1 = \mathbf{S}_2 = 5/2$ are the spins of the two Mn^{2+} sites. The example of MnO superexchange is via σ-bonding. Superexchange can also occur via π-bonding (right Fig. 1.4),[59] where the overlap of wavefunction is between O^{2-} p_x and two metal *dxz* orbitals aligned 180˚ along z-axis. This 180˚ configuration is strongly antiferromagnetic and occurs mostly in octahedral systems according to the Goodenough-Kanamori-Anderson rules.[67-69]

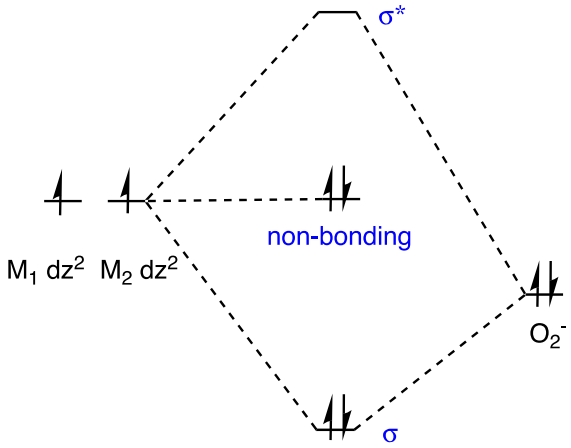

Figure 1.3. Molecular orbital diagram with *d-p* orbital mixing of superexchange interaction between two metals and one intervening O^{2-} via σ-bonding.

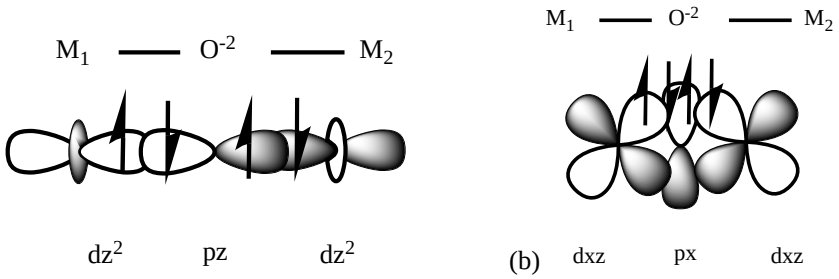

Figure 1.4. 180˚ orbital overlap configuration of superexchange interaction between two metals and one intervening O^{2-} via σ-bonding (a), or π-bonding (b).

Superexchange coupling can occur in 90˚ configuration: the interaction is antiferromagnetic if one metal occupying the dz^2 overlaps with the other metal occupying the *dxz* through $p\pi$ and $p\sigma$ orbitals of the diamagnetic ligand; the interaction is weakly ferromagnetic if two dz^2 magnetic orbitals overlap through the *px* and *pz* orbitals of the diamagnetic ligand (Fig. 1.5).[67-69]

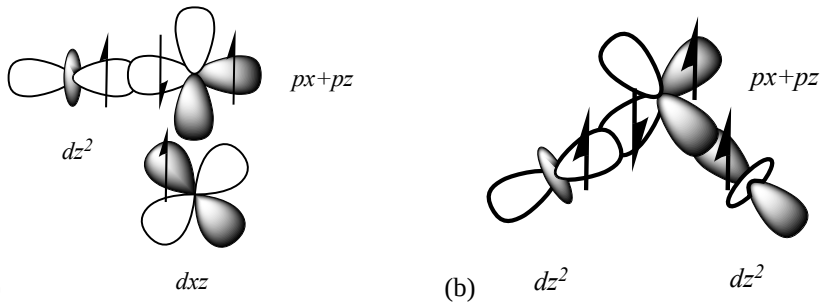

Figure 1.5. The 90˚ configurations of metal *d* orbitals and diamagnetic ligand *p* orbitals overlap. Antiferromagnetic interaction is shown in (a), whereas ferromagnetic interaction is shown in (b).

Variable-temperature magnetic susceptibility measurement is generally used to experimentally determine the strength of coupling between paramagnetic spin centers, in which the macroscopic magnetization (M) is evaluated as a function of temperature (usually ranging from 2-350K) reflecting the Boltzmann distribution (Eq. 1.5).[42] The macroscopic magnetization is a sum of microscopic magnetization of all spin states. At low temperature, more spins locate at the lower energy level (N_+), and energy embodied as temperature (T) is applied to populate spins into the higher energy level (N_-).

$$\frac{N^+}{N^-} = e^{-\Delta E/kT} \tag{1.5}$$

The magnetization has a relationship with magnetic susceptibility shown in Eq. 1.6, where χ is the molar magnetic susceptibility and H is the applied magnetic field.

$$\chi = \frac{M}{H} \tag{1.6}$$

The magnetic susceptibility can also be expressed by the van Vleck equation in Eq. 1.7,

$$\chi = \frac{N_A \sum_n (\frac{E_n^{(1)2}}{kT} - 2E_n^{(2)}) \exp(\frac{-E_n^{(0)}}{kT})}{\sum_n \exp(\frac{-E_n^{(0)}}{kT})} \quad (1.7)$$

where N_A is Avogadro's number, k is Boltzmann's constant, $E_n^{(0)}$ is energy of level n in zero field (H = 0), $E_n^{(1)}$ and $E_n^{(2)}$ is the first and second order Zeeman coefficients, which are energies dependent upon applied magnetic field (Eq. 1.7). Magnetic data obtained from variable-temperature magnetic susceptibility measurement can be fitted in Eq. 1.7, and the exchange coupling constant, J, can be determined by a least-square fitting. This method will be used to extrapolate J for exchange-coupling systems in this thesis.[70]

1.2 Effects of Spin Density Polarization

This dissertation focuses on transition metal complexes directly coordinate to organic radicals, so spin density can be manipulated via spin delocalization or localization by synthetic substitution on these organic radicals. Transition metal-quinone complexes have been widely studied over the last two decades with regard to their synthetic, physical, and optical properties.[41,71-73] *o*-Semiquinone is known to be able to bind to metal ions to create a wide range of different couplings, including both ferromagnetic and antiferromagnetic couplings.[74] Quinone is a redox-active ligand with various oxidation states, each of which has a different spin. A quinone (q, with **S** = 0) can be reduced into a seqmiquinone radical (sq, with **S** = ½) and also to a catechol (cat, with **S** = 0) as illustrated in Fig. 1.6.[41] These electrochemical processes are reversible, which is another reason why quinones have been widely studied and used as chelating ligands. [41,65-67] The radical nature of semiquinone produces compounds with unusual magnetic and optical properties arising when bound to a metal.[73,75,76]

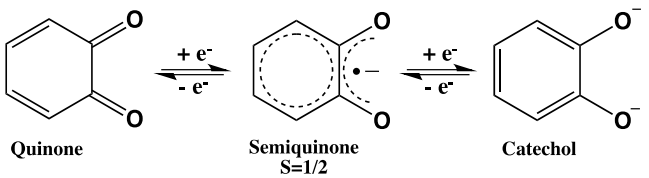

Figure 1.6. A quinoidal ligand undergoing one-electron redox reactions.

A simple *o*-semiquinone does not possess an appropriate binding geometry to act as a bridging ligand between two metal ions to form a symmetric system, so tetraoxolene was proposed for the construction of extended magnetic systems. The advantages of associating tetraoxolene-quinoidal ligand are: (1) the four redox reactions are accessible to this compound as a free ligand and also when coordinated to metals;[37] (2) it has four oxygen donor atoms to coordinate with two metal ions;[74] (3) it possesses multiple chelating modes (Fig. 1.7).[77] 1,4,5,8-Tetraoxonaphthalene was first employed by Dei and co-workers for a study of $[Ru_2(bpy)_4(tetraoxo)]^{n+}$, but no radical species was observed after redox reactions had occurred.[78] 2,5-Dihydroxy-1,4-benzoquinone (DHBQ) was then used into their study of radical species because of the $(sq, cat)^{3-}$ and $(q, sq)^{-}$.[74] Incorporating quinone with a paramagnetic metal ion, exchange coupling can be turned "on" with catechol being oxidized to semiquinone, and "off" with semiquinone being reduced to catechol or oxidized to quinone.

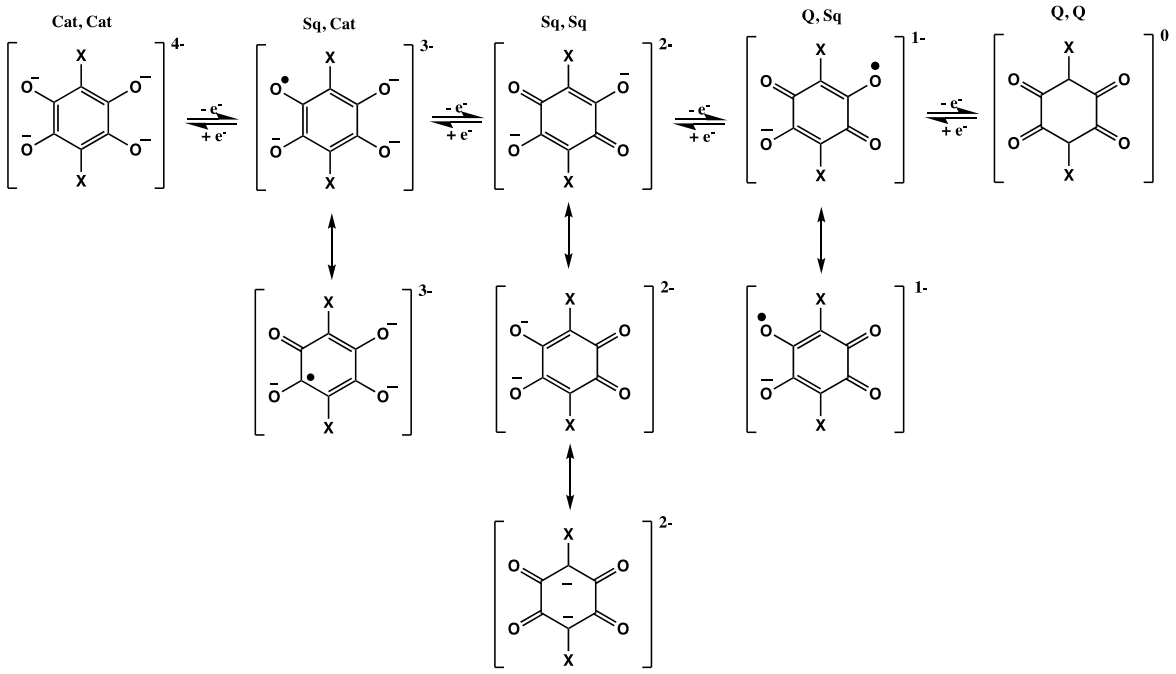

Figure 1.7. Multiple possible chelating forms tetraoxolene quinone undergoing one-electron redox reactions.

The π symmetry orbitals of tetraoxolene-based ligand are closer in energy to the metal-based *d* orbitals to introduce more orbital mixing, and metal tetraoxolene complexes thus exhibit vast variety of intramolecular electrochemical and spectroscopic properties.[79] More detail about orbital information supported by computational results will be discussed in Chap. 2 and 4. First-row transition metal (Cu^{2+}, Ni^{2+}, Fe^{3+}, and Cr^{3+})[74,80-83] tetraoxolene complexes present localized charge distribution with various substituted (X = H, Cl, or NO_2)[84] tetraoxolene dianionic (sq, sq) form. Spin distribution within the tetraoxolene ligand can be possibly manipulated by switching to electron donating (EDG) or electron withdrawing groups (EWG). Associating paramagnetic metal centers with the substituted tetraoxolene ligands provides a platform for spin polarization effects on spin exchange coupling.

1.3 Thermodynamic Effects of Spin Coupling

One of the biggest forces driving the interest in exchange coupling is to understand the polynuclear metal clusters at the active site of metalloprotein.[10,85-90] The research of metalloprotein has concentrated on the spectroscopic and magnetic properties related to how exchange coupling affects the electronic structures, chemical reactivity, and biological functions.[91-96]

The studies by Bertrand and Gayda[97] on rubredoxin and ferredoxin extracted from plant and algae extracts show the redox potential of $Fe^{2+/3+}$ in ferredoxin [2Fe-2S] is generally more negative than that of rubredoxin (Fig. 1.8). The active site of ferredoxin consists of two [$Fe^{III}S_4$] centers with an antiferromagnetic coupling interaction induced by the two Fe(III) paramagnetic centers, while rubredoxin only contain one [$Fe^{III}S_4$] center without any exchange coupling interaction. In DMF solution, rubredoxin [$Fe^{III}S_4$] is reduced to [$Fe^{II}S_4$] at -1.02V,[98] whereas [2Fe-2S] is reduced at -1.49V.[99] Bertrand and Gayda[97] collected electrochemical data of desulforedoxin - one Fe(III) coordinating to four cysteine groups - and [2Fe-2Se], and compared their redox potentials with those of rubredoxin and ferredoxin. Previous studies reported significant structural difference between all four of the moieties based on Mössbauer, UV-vis, and infrared (IR) spectroscopy. [99] However, desulforedoxin and rubredoxin exhibited redox potentials relatively close in values,[100] while [2Fe-2Se] and [2Fe-2S] presented similar redox behaviors to each other.[101] These results indicated exchange coupling interaction stabilized the oxidation states of [2Fe-2Se] and [2Fe-2S] by lowering c.a. 100 mV in their redox potentials.[97] Bertrand and Gayda's studies[97,101] are the first experimental evidence proposing the hypothesis of Heisenberg spin exchange affecting the electrochemical properties of a system.

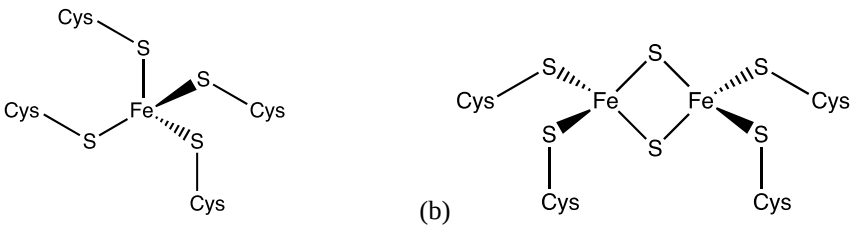

Figure 1.8. The structural representation of protein cluster rubredoxin (a) and ferredoxin (b) active sites.

Density Functional Theory (DFT) calculations were later conducted on similar systems, Fe clusters with one, two, and four Fe metal centers, by Mouesca et al.[102] The information obtained on effects of electron exchange, electron delocalization, charge distribution, and solvation energies agrees with the finding of one and two [$Fe^{III}S_4$] centers, as reported by Bertrand and Gayda.[97]

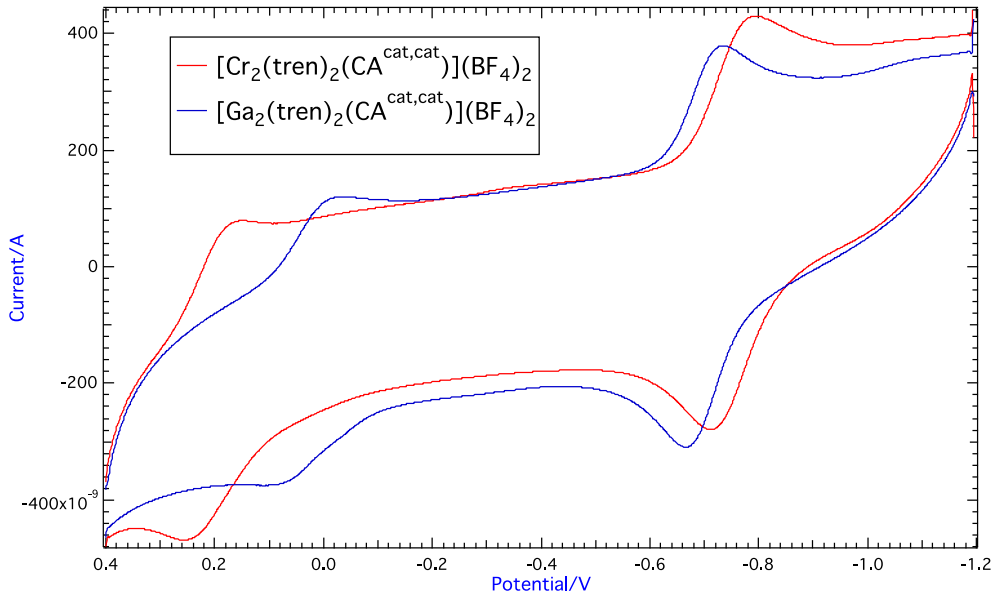

Figure 1.9. Cyclic voltammograms of $[Ga_2(tren)_2(CA^{cat,cat})](BPh_4)_2$ (blue), and $[Cr_2(tren)_2(CA^{cat,cat})](BPh_4)_2$ (red). All data were recollected in degassed acetonitrile containing 0.1 M NBu_4PF_6 at a scan rate of 100 mV/s.

Similar thermodynamic stabilization was observed from the electrochemical data collected for $[Cr_2(tren)_2(CA)]^{n+}$, where CA is the chloranilate and tren is tris(2-aminoethyl)amine, reported by Dr. Guo in our group (Fig. 1.9).[37] The goal of this project is to

further examine the effect of the thermodynamic stabilization through spin exchange interactions and establish the thermodynamic correlation seen in both electrochemical and magnetic behaviors.

1.4 Previous Work on $[M_2(tren)_2(CA)]^{n+}$

Tetraoxolene complexes provide a good avenue to study the correlation between the photophysical properties of molecules and the spin exchange interactions that define their electronic structures. Previously, our group has studied several different chloranilate-bridge (CA) bimetallic complexes, shown in Fig. 1.10, with R = Cl. Cr(III) ion (S = 3/2) was chosen because it is redox-inert and not easily reduced to Cr(II). Incorporating Ga^{III} into the binuclear motif provides a spectroscopically silent d^{10} ion (S = 0) with a similar charge-to-radius ratio as Cr(III).[41] The chloranilate bridge was chosen as a free radical ligand for the molecular assemblies because of its accessibility to its multiple oxidation states.[37] Only the semiquinone-catechol (sq, cat; S = ½), catechol-catechol (cat, cat; S = 0) and semiquinone-semiquinone (sq, sq; S = 0) forms will be discussed in detail, because the quinone-semiquinone (q, sq) and quinone-quinone (q, q) forms only coordinate to one metal, which then rapidly degrades upon further oxidation.

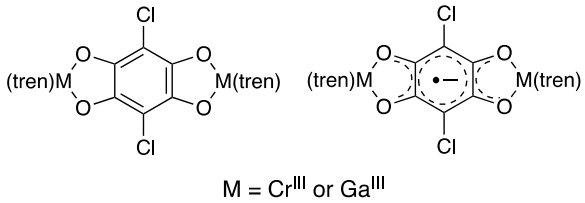

Figure 1.10. Cr(III) and Ga(III) -tetraoxolene quinodal complexes.

A variety of magnetic behaviors are exhibited among these systems. $[Ga_2(tren)_2(CA^{cat,cat})]^{2+}$ is a diamagnetic compound, while $[Ga_2(tren)_2(CA^{sq,cat})]^{3+}$ is paramagnetic with the $[CA^{sq,cat}]^{3-}$ radical ligand. $[Cr_2(tren)_2(CA^{cat,cat})]^{2+}$ is a superexchange coupling system

with two paramagnetic Cr(III) centers linked by a diamagnetic $[CA^{cat,cat}]^{4-}$ intermediate. $[Cr_2(tren)_2(CA^{sq,cat})]^{3+}$ possesses both superexchange and direct exchange coupling interactions, and exhibit rich magnetic charac,ter: it is composed of three paramagnetic centers, two Cr(III) (**S** = 3/2), Center 1 and 3, and a $[CA^{sq,cat}]^{3-}$ radical bridge, Center 2. There is superexchange coupling between the two Cr(III) ions, while direct exchange interactions, J_{12} and J_{23}, take place between the Cr(III) centers and $CA^{sq,cat}$ (Fig. 1.10).

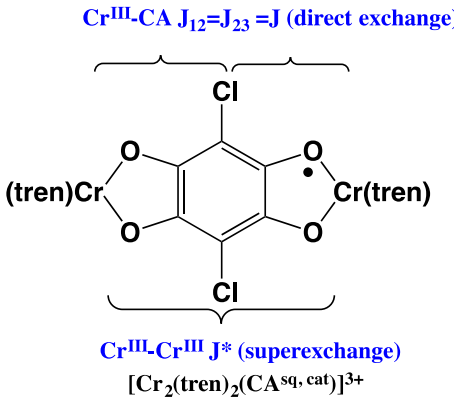

Figure 1.11. Indication of spin exchange couplings for $[Cr_2(tren)_2(CA^{sq,cat})]^{3+}$, see text for details on notation.

In order to better explain the complicated magnetic behavior of this system, the HDVV Hamiltonian is employed again. With three paramagnetic centers, the total spin operator of the system is defined as $\widehat{\boldsymbol{S}_T} = \widehat{\boldsymbol{S}_A} + \widehat{\boldsymbol{S}_2}$ (where $\widehat{\boldsymbol{S}_A} = \widehat{\boldsymbol{S}_1} + \widehat{\boldsymbol{S}_3}$) here, $\mathbf{S}_1 = \mathbf{S}_3 = 3/2$ correspond the two Cr(III) ions and $\mathbf{S}_2$ to the $CA^{sq,cat}$ bridge. In this way, the Hamiltonian operator can be derived from Eq. 1.12 using two coupling constants, where J quantifies the Cr^{III}-$CA^{sq,cat}$ direct exchange, and J^* is the superexchange coupling for Cr^{III}-Cr^{III} (this coupling scheme is shown in Fig. 1.10). Eq.1.13 is the eigenvalue equation for this system.

$$\hat{H} = -2J(\hat{S}_1 \cdot \hat{S}_2 + \hat{S}_2 \cdot \hat{S}_3) - 2J^*\hat{S}_1 \cdot \hat{S}_3 \qquad (1.12)$$

$$E = -J\,[S_T(S_T+1) - S_A(S_A+1) - S_2(S_2+1)] - J^*\,[S_A(S_A+1) - S_1(S_1+1) - S_3(S_3+1)] \qquad (1.13)$$

It is known that the HDVV Hamiltonian is used to best describe systems with two spin centers contributing only one unpaired electron;[106] thus, it will be necessary to actually compare the magnetic experimental results of systems with more than one unpaired electrons modelled by the HDVV Hamiltonian for multiple-spin systems with $\mathbf{S} > ½$ to determine the effectiveness of this spin-only Hamiltonian.

1.5 Comproportionation Free Energy

Comproportionation is a chemical reaction between one oxidized reactant and one reduced reactant with the same composition of elements with different oxidation states to form a product of an intermediate oxidation state (Eq. 1.8). The comproportionation constant, K_C, is the equilibrium constant as illustrated in Eq. 1.9.

$$M^{II}M^{II} + M^{III}M^{III} \overset{K_C}{\rightleftharpoons} 2M^{II}M^{III} \tag{1.8}$$

$$K_C = \frac{[M^{II}M^{III}]^2}{[M^{II}M^{II}][M^{III}M^{III}]} \tag{1.9}$$

The comproportionation constant can provide insight into the thermodynamics of the system. Cyclic voltammetry has been developed and widely employed to evaluate the thermodynamic stability and metal-metal coupling of mixed-valence complexes.[103-105] The potential difference, ΔE, between the electrodes of a cell is a measure of the tendency for a reaction to occur. According to the Gibb's free energy, ΔE correlates to the free energy of comproportionation (Eq. 1.10), ΔG_C, which also evaluates the strength of the exchange coupling between redox centers through the ligand bridge.[103] Therefore, ΔG_C can be considered equivalent to the thermodynamic stabilization energy induced by spin exchange. In this regard, an electrochemical measurement for ΔE offers a way of experimentally determining the thermodynamic stabilization of a system.

$$\Delta G_C = -nF\Delta E = -2.303RT \log (K_C) \quad (1.10)$$

A proof-of-concept experiment has already been performed to verify the hypothesis. Between the two electrochemical waves in Fig. 1.8, the potential difference of $[Cr_2(tren)_2(CA^{cat,cat})](BPh_4)_2$ is larger than $[Ga_2(tren)_2(CA^{cat,cat})](BPh_4)_2$. The observation reveals that there should be an intrinsic factor causing the $CA^{sq,cat}$ form of the Cr^{III}-Cr^{III} dimer to be more stable than the Ga^{III}-Ga^{III} dimer. This intrinsic factor is thought to be the spin exchange interaction suggested by the finding of Betrand and Gayda.[97]

Based on the electrochemical data for $[Cr_2(tren)_2(CA^{cat,cat})]^{2+}$, a net thermodynamic stabilization larger in magnitude is suggested to be induced by the direct exchange interaction between Cr(III) and the $CA^{sq,cat}$ ligand. As mentioned above, ΔG_C can be calculated from the redox potential difference (Eq. 1.10),[106] and it corresponds to the comproportionation constant, K_C, in accordance to the Gibbs free energy (Eq. 1.10) and the Nernst equation (Eq. 1.11).[104]

$$K_C = 10^{(E_1 - E_2)/59mV} \quad (1.11)$$

$K_C > 1$ reflects the stability of the semiquinone form of the system relative to the other two states illustrated in Eq. 1.9. Exchange coupling inherent in $[Cr_2(tren)_2(CA^{sq,cat})]^{3+}$ is thought to be the contribution of the thermodynamic stabilization,[107] since the $CA^{sq,cat}$ species is subject to significant direct exchange interaction rather than the $CA^{sq,sq}$ and $CA^{cat,cat}$ forms of the diamagnetic bridge.

The redox potential shift shown on $[Cr_2(tren)_2(CA)]^{n+}$ compared with $[Ga_2(tren)_2(CA^{sq,cat})]^{n+}$ indicate a thermodynamic stabilization possibly induced by the spin exchange interaction; however, it is unknown if this phenomenon exclusively exhibits in these systems. In this project, similar Cr(III) and Ga(III) assemblies with various substituents on the bridging ligands will be synthesized and characterized magnetically and electrochemically, so we

can further examine the relationship between the redox chemistry and spin exchange interaction. By varying the electron withdrawing and donating substituents on the targeted systems in this project, the connection between the spin density on a molecular system and the strength of spin exchange will be perceived, and the strength of the spin coupling can be systematically and synthetically manipulated.

1.6 Contents of Dissertation

This research can be divided into four main components: (1) computational studies of spin polarization in tetraoxo-semiquinone ligand radicals and Ga(III) tetraoxo-semiquinoidal compounds; (2) the synthesis and magnetic characterization of Cr(III) and Ga(III) dimeric semiquinoidal complexes; (3) the electrochemical behavior of Cr(III) and Ga(III) dimeric moieties; (4) the thermodynamics of spin exchange interaction, and the correlation between electrochemical and magnetic properties. The literature reports stabilization of an oxidation state as induced by the exchange interaction;[94] however, it is lacking a quantitative method to directly measure the Heisenberg stabilization energy. The *J* coupling constant measured from variable-temperature magnetic susceptibility experiment only shows the relative energy levels of each spin state induced by the spin exchange interaction. The thermodynamic consequence extrapolated from electrochemical data can provide some insights by measuring absolute stabilization energy of a spin-coupled system.

Chapter 2 begins with the Density Functional Theory (DFT) calculation of a series of substituted tetraoxo-semiquinoidal radicals to understand the factors influencing spin and charge density distribution in systems. These calculations facilitate the assessment of synthetic viability of a series of proposed substituted ligands. In addition, they reveal inductive and resonance

effects are the major factors in charge polarization within a molecule. The mixing between the HOMO of the substituent and the SOMO of the semiquinone moiety explains the spin localization on the oxygen binding sites.

Chapter 3 shows the synthesis and physical characterization of both substituted ligands and Cr(III) quinoidal dimeric complexes. Meanwhile, magnetic data collection and sample preparation are discussed in an attempt to contribute to the systematic procedures reported, which are sadly lacking in the literature. The variable-temperature magnetic susceptibility data of various substituted Cr(III) dimers show a trend of fluctuation in the exchange coupling constants. The implication of how spin polarization affects the exchange coupling interactions will be discussed.

In Chapter 4, the DFT calculations examining spin and charge density distribution in open-shell digallium(III) systems are compared with those of the free ligands. The synthesis and physical characterizations of substituted tetrahydroxy ligands and Ga(III) quinoidal compounds are presented. Variable-temperature magnetic data collected for $[Ga_2(tren)_2(L^{sq,cat})]^{3+}$ are discussed in term of their magnetic behaviors.

In Chapter 5, the electrochemical data are presented for both Cr(III) and Ga(III) dimeric analogues, as well as the thermodynamic stabilization observed for their various oxidation states. It correlates the relationship between the electrochemical and magnetic properties, and proposes a hypothesis of how electrochemical data will be able to quantify the thermodynamic stabilization induced by the Heisenberg exchange interaction.

Chapter 6 details some ongoing synthetic routes for more substituted ligands, including EWG and EDG substituents, intraligand electron delocalizing ligands, and horizontal aromatic extension ligands, and possible modifications and improvements to existing procedures.

Polycyclic aromatic hydrocarbons (PAHs) are proposed to be the next series of bridging ligands to further examine the spin polarization on spin exchange. Liquid variable-temperature magnetic susceptibility measurement will be proposed to characterize magnetic behaviors of the systems involving solvation properties.

In this project, we exploit the connection between intramolecular spin polarization and the strength of exchange coupling interaction to manipulate spin polarization and synthetically tune exchange interactions using simple inorganic molecular systems, so the cause-and-effect of how spin affecting the thermodynamics, electronic structures, and magnetic properties will be perceived.

REFERENCES

REFERENCES

(1) Merzbacher, E. *Quantum Mechanics*, 3rd ed.; John Wiley & Sons: New York, 1998; pp 372.

(2) Kahn, O. *Molecular Magnetism*; VCH Publishers: New York, 1993.

(3) Carlin, R. L. *Magnetochemistry*, 1st ed.; Springer-Verlag: Berlin, 1986.

(4) Drago, R. S. *Physical Methods for Chemists*; Saunders College Pub: Philadelphia, 1992.

(5) Lakowicz, J. R. *Principles of Fluorescence Spectroscopy*, 3rd ed.; Springer US: Boston, 2006.

(6) Gatteschi, D.; Sessoli, R. *Angew. Chem. Int. Ed.* **2003**, *42*, 268.

(7) Ferrando-Soria, J.; Vallejo, J.; Castellano, M.; Martínez-Lillo, J.; Pardo, E.; Cano, J.; Castro, I.; Lloret, F.; Ruiz-García, R.; Julve, M. *Coord. Chem. Rev.* **2017**, *339*, 17-103.

(8) Demir, S.; Jeon, I.; Long, J. R.; Harris, T. D. *Coord. Chem. Rev.* **2015**, *289-290*, 149-176.

(9) Craig, G. A.; Murrie, M. *Chem. Soc. Rev.* **2015**, *44*, 2135.

(10) Brunold, T. C.; Solomon, E. I. *J. Am. Chem. Soc.* **1999**, *121*, 8277-8295.

(11) Lippard, S. J.; Berg, J. M. *Principles of Bioinorganic Chemistry*, University Science Books, Mill Valley, CA, 1994.

(12) Itoh, S.; Taki, M.; Fukuzumi, S. *Coord. Chem. Rev.* **2000**, *198*, 3.

(13) Weisheit, M.; Fähler, S.; Marty, A.; Souche, Y.; Poinsignon, C.; Givord, D. *Science*, **2007**, *315*, 349-351.

(14) Klein, D. R.; MacNeill, D.; Lado, J. L.; Soriano, D.; Navarro-Moratalla, E.; Watanabe, K.; Taniguchi, T.; Manni, S.; Canfield, B.; Fernández-Rossier, J.; Jarillo-Herrero, P. *Science*, **2018**, *360*, 1218-1222.

(15) Mannini, M.; Pineider, F.; Sainctavit, P.; Danieli, Otero, E.; Sciancalepore, C.; Talarico, A. M.; Arrio, M.; Cornia, A.; Gatteschi, D.; Sessoli, R. *Nat. Mater.* **2009**, *8*, 194.

(16) Ardavan, A.; Blundell, S. J. *J. Mater. Chem.* **2009**, *19*, 1754.

(17) Reig, C.; Cardoso, S.; Mukhopadhyay, S. C. *Giant Magnetoresistance (GMR) Sensors*: *From Basic to State-of-Art Applications*; Springer-Verlag Berlin Heidelberg: Berlin, Germany, 2013.

(18) Bogani, L.; Wernsdorfer, W. *Nat. Mater.* **2008**, *7*, 179-186.

(19) Liang, W.; Shores, M. P.; Bockrath, M.; Long, J. R.; Park, P. *Nature*. **2002**, *417*, 725-729.

(20) Jo, M.; Grose, J. E.; Baheti, K.; Deshmukh, M. M.; Sokol, J. J.; Rumberger, E. M.; Hendrickson, D. N.; Long, J. R.; Park, H.; Ralph, D. C. *Nano. Lett.* **2006**, *6*, 2014-2020.

(21) Heersche, H. B.; de Groot, Z.; Folk, J. A.; van der Zant, H. S. J.; Romeike, C.; Wegewijs, M. R.; Zobbi, L.; Barreca, D.; Tondello, E.; Cornia, A. *Phys, Rev. Lett.* **2006**, *96*, 206801.

(22) Urdampilleta, M.; Nguyen, N.; Cleuziou, J.; Klyatskaya, S.; Ruben, M.; Wernsdorfer, W. *Int. J. Mol. Sci.* **2011**, *12*, 6656-6667.

(23) Thiele, S.; Vincent, R.; Holzmann, M.; Klyatskaya, S.; Ruben, M.; Balestro, F.; Wernsdorfer, W. *Phys. Rev. Lett.* **2013**, *111*, 037203.

(24) Hendrickson, D. N.; O'Connor, C. J. *Research Frontiers in Magnetochemistry*. World Scientific: Singapore, 1993.

(25) Sloop, J. C.; Shultz, D. A.; Beikmohamadi, M. *J. Phys. Org. Chem.* **2011**, *25*, 101-109.

(26) Kahn, O. *Acc. Chem. Res.* **2000**, *33*, 647.

(27) Wang, J.; Hou, L.; Browne, W. R.; Feringa, B. L. *J. Am. Chem. Soc.* **2011**, *133*, 8162.

(28) Guo, D.; Knight, T. E.; McCusker, J. K. *Science.* **2011**, *334*, 1684.

(29) Theil, H.; von Richthofen, C. F.; Stammler, A.; Bögge, H.; Glaser, T. *Inorg. Chim. Acta.* **2008**, *361*, 916-924.

(30) Habib, H. A.; Sanchiz, J.; Janiak, C. *Inorg. Chim. Acta.* **2009**, *362*, 2452.

(31) Awaga, K.; Sugano, T.; Kinoshita, M. *Chem. Phys. Lett.* **1987**, *141*, 540.

(32) Oshio, H.; Ichida, H. *J. Phys. Chem.* **1995**, *99*, 3294-3302.

(33) Matsuda, K.; Irie, M. *J. Am. Chem. Soc.* **2000**, *122*, 7195-7201.

(34) Sugawara, T.; Komatsu, H.; Suzuki, K. *Chem. Soc. Rev.* **2011**, *40*, 3105-3118.

(35) Bertini, I.; Sigel, A.; Sigel, H., Eds. *Handbook on Metalloproteins.* Marcel Dekker: New York, 2001.

(36) Messerschmidt, A.; Huber, R.; Wieghardt, K.; Poulos, T., Eds. *Handbook on Metalloproteins.* Wiley: Chichester, U.K., 2001.

(37) Guo, D.; McCusker, J. K. *Inorg. Chem.* **2007**, *46*, 3257-3274.

(38) Schrauben, J. N.; Guo, D.; McCracken, J. L.; McCusker, J. K. *Inorganica Chimica Acta*, **2008**, *361*, 3539-3547.

(39) Fehir, Jr., R. J.; McCusker, J. K. *J. Phys. Chem. A.* **2009**, *113*, 9249.

(40) Ginsberg, A. P. *Inorg. Chim. Acta. Rev.* **1971**, *5*, 45.

(41) Wheeler, D. E.; McCusker, J. K. *Inorg. Chem.* **1998**, *37*, 2296-2307.

(42) McCarthy, P. J.; Güdel, H. U. *Coord. Chem. Rev.* **1988**, *88*, 69-131.

(43) Cogne, A.; Laugier, J.; Luneau, D.; Rey, P. *Inorg. Chem.* **2000**, *39*, 5510.

(44) Okazawa, A.; Nagaichi, Y.; Nogami, T.; Ishida, T. *Inorg. Chem.* **2008**, *47*, 8859.

(45) Gass, I. A.; Tewary, S.; Nafady, A.; Chilton, N. F.; Gartshore, C. J.; Asadi, M.; Lupton, D. W.; Moubaraki, B.; Bond, A. M.; Boas, J. F.; Guo, S.; Rajaraman, G.; Murray, K. S. *Inorg. Chem.* **2013**, *52*, 7557-7572.

(46) Luneau, D.; Romero, F. M.; Ziessel, R. *Inorg. Chem.* **1998**, *37*, 5078-5087.

(47) Pedersen, K. S.; Perlepe, P.; Aubery, M. L.; Woodruff, D. N.; Reyes-Lillo, S. E.; Reinholdt, A.; Voigt, L.; Li, Z.; Borup, K.; Rouzières, M.; Samohvalov, D.; Wilhelm, F.; Rogalev, A.; Neaton, J. B.; Long, J. R.; Clérac, R. *Nat. Chem.* **2018**, *10*, 1056.

(48) Hicks, R. G.; Lemaire, M. T.; Thompson, L. K.; Barclay, T. M. *J. Am. Chem. Soc.* **2000**, *122*, 8077-8078.

(49) Brook, D. J. R.; Richardson, C. J.; Haller, B. C.; Hundley, M.; Yee, G. T.; *Chem. Commun.* **2010**, *46*, 6590-6592.

(50) Preuss, K. E. *Coord. Chem. Rev.* **2015**, *289-290*, 49-61.

(51) Karasawa, S.; Yoshihara, D.; Watanabe, N.; Nakano, M.; Koga, N. *Dalton. Trans.* 2008, 1418-1420.

(52) Caneschi, A.; Dei, A.; Gatteschi, Tangoulis, V. *Inorg. Chem.* **2002**, *41*, 3508-3512.

(53) Pierpont, C. G.; Attia, A. S. *Collect. Czech. Chem. Commun.* **2001**, *66*, 33.

(54) Holyńska, M.; Frank, N.; Pichon, C.; Jeon, I.; Clérac, R.; Dehnen, S. *Inorg. Chem.* **2013**, *52*, 7317-7319.

(55) Jeon, I.; Park, J. G.; Xiao, D. J.; Harris, T. D. *J. Am. Chem. Soc.* **2013**, *135*, 16845-16848.

(56) Schultz, D.; Weyhermüller, T.; Wieghardt, K.; Butzlaff, C.; Trautwein, A. X. *Inorg. Chim. Acta.* **1996**, *246*, 387.

(57) Herring, C. *Magnetism*, edited by Rado, G. T.; Suhl, H. Academic: New York, Vol. 2B, 1965.

(58) de P. R. Moreira, I.; Suaud, N.; Guihéry, N.; Malrieu, J.P.; Caballol, R.; Bofill, J. M.; Illas, F. *Phys. Rev. B* **2002**, *66*, 134430.

(59) Mabbs, F. E.; Machin, D. J. *Magnetism and Transition Metal Complexes.* Dover Publication: Mineola, NY, 2008.

(60) Figgis, B. N.; Lewis, J. *The Magnetic Properties of Transition Metal Complexes.*; John Wiley & Sons: New York, NY, 1964.

(61) Kambe, K. *J. Phys. Soc. Japan* **1950**, *5*, 48-51.

(62) Bleaney, B.; Bower, K. D. *Proc. R. Soc. A Math. Phys. Eng. Sci.* **1952**, *214*, 451-465.

(63) Anderson, P. W. *Phys. Rev.* **1950**, *79*, 350-356.

(64) Kramers, H. A. *Physica*, **1934**, *1*, 182.

(65) White, R. M. *Quantum Theory of Magnetism.* Springer-Verlag: Berlin, Germany, 1996.

(66) Anderson, P. W. *Phys. Rev.* **1959**, *115*, 2.

(67) Goodenough, J. B. *Phys. Rev.* **1955**, *100*, 564.

(68) Kanamori, J. *J. Phys. Chem. Solid.* **1959**, *10*, 87.

(69) Goodenough, J. B. *Magnetism and the Chemical Bond.* Interscience Publisher: New York, NY, 1963.

(70) Schmitt, E. Ph.D Dissertation. Department of Chemistry, University of Illinois, Urbana-Champaign, IL, 1996.

(71) Pierpont, C. G.; Larsen, S. K.; Boone, S. R. *Pure Appl. Chem.* **1998,** *60*, 1331.

(72) Pierpont, C. G.; Lange, C. *Prog. Inorg. Chem.* **1994,** *41*, 331.

(73) Sloop, J. C.; Shultz, D. A.; Beikmohamadi, M. *J. Phys. Org. Chem.* **2011**, *25*, 101-109.

(74) Dei, A.; Gatteschi, D.; Pardi, L.; Russo, U. *Inorg. Chem.* **1991**, *30*, 2589-2594.

(75) Ohtsu, H.; Tanaka, K. *Angew. Chem., Int. Ed.* **2004**, *43*, 6301.

(76) Bin-Salamon, S.; Brewer, S.; Franzen, S.; Feldheim, D. L.; Lappi, S.; Shultz, D. A. *J. Am. Chem. Soc.* **2005**, *127*, 5328.

(77) Kitagawa, S.; Kawata, S. *Coord. Chem. Rev.* **2002**, *224*, 11.

(78) Dei, A.; Gatteschi, D.; Pardi, L. *Inorg. Chem.* **1990**, *29*, 1442.

(79) Ward, M. D. *Inorg. Chem.* **1996**, *35*, 1712-1714.

(80) Heinze, K; Huttner, G.; Zsolnai, L.; Jacobi, A.; Schober, P. *Chem. Eur. J.* **1997**, *3*, 732.

(81) Tinti, F.; Verdaguer, M.; Kahn, O.; Savariault, J. -M. *Inorg. Chem.* **1987**, *26*, 2380.

(82) Pierpont, C. G.; Francesconi, L. C.; Hendrickson, D. N. *Inorg. Chem.* **1977**, *16*, 2367.

(83) Lloret, F.; Julve, M.; Faus, J.; Solans, X.; Journaux, Y.; Morgenstern-Badarau, I. *Inorg. Chem.* **1990**, *29*, 2232.

(84) Cotton, F. A.; Murillo, C. A.; Villagrán, D.; Yu, R. *J. Am. Chem. Soc.* **2006**, *128*, 3281.

(85) Que, L., Ed. *Metal Clusters in Protein*; ACS Symposium Series; American Chemical Society: Washington, DC, 1988; Vol. 372.

(86) Yoon, J.; Mirica, L. M.; Stack, T.D.P.; Solomon, E. I. *J. Am. Chem. Soc.* **2004**, *126*, 12586.

(87) Yoon, S.; Lippard, S. J. *J. Am. Chem. Soc.* **2005**, *127*, 8386.

(88) Moragues-Cánovas, M.; Rivière, É.; Richard, L.; Paulsen, C.; Wernsdorfer, W.; Rajaraman, G.; Brechin, E. K.; Mallah, T. *Adv. Mater.* **2004**, *16*, 1101.

(89) Stamatatos, T. C.; Foguet-Albiol, D.; Stoumpos, C. C.; Raptopoulou, C. P.; Terzis, A.; Wernsdorfer, W.; Perlepes, S. P.; Christou, G. *J. Am. Chem. Soc.* **2005**, *127*, 15380.

(90) Weldon, B. T.; Wheeler, D. E.; Kirby, J. P.; McCuerks, J. K. *Inogr. Chem.* **2001**, *40*, 6802.

(91) Picraux, L. B.; Smeigh, A. L.; Guo, D.; McCusker, J. K. *Inorg. Chem.* **2005**, *44*, 7846.

(92) Picraux, L. B.; Weldon, B. T.; McCusker, J. K. *Inorg. Chem.* **2003**, *42*, 273.

(93) Blondin, G.; Girerd, J.-J. *Chem. Rev.* **1990**, *90*, 1359.

(94) Wei, P. P.; Skulan, A. J.; Wade, H.; DeGrado, W. F.; Solomon, E. I. *J. Am. Chem. Soc.* **2005**, *127*, 16098.

(95) Chen, P.; Solomon, E. I. *J. Am. Chem. Soc.* **2004**, *126*, 4991.

(96) Holm, R. H.; Kennepohl, P.; Solomon, E. I. *Chem. Rev.* **1996**, *96*, 2239–2314.

(97) Bertrand, P.; Gayda, J. *Biochim. Biophys. Acta*. **1982**, *680*, 331-335.

(98) Lane, R. W.; Ibers, J. A.; Frankel, B. B.; Papefthymiou, G. C.; Holm, R. H. *J. Am. Chem. Soc.* **1977**, *99*, 84-98.

(99) Mayerle, J. J.; Denmark, S. E.; Depamphilis, G. C.; Holm, R. H. *J. Am. Chem. Soc.* **1975**, *97*, 1032-1045.

(100) Xavier, A. V.; Moura, J. J. G.; Mousra, I. *Struct. Bonding* **1981**, *43*, 187-213.

(101) Bertrand, P.; Gayda, J. *Biochim. Biophys. Acta*. **1980**, *625*, 337-342.

(102) Mouesca, J. -M.; Chen, J. L.; Noodleman, L.; Bashford, D.; Case, D. A. *J. Am. Chem. Soc.* **1994**, *116*, 11898–11914.

(103) Gagné, R. R.; Spiro, C. L.; Smith, T. J.; Hamann, C. A.; Thies, W. R.; Shiemke, A. K. *J. Am. Chem. Soc.* **1981**,*103*, 4073.

(104) Aquino, M. A. S.; Lee, F. L.; Gabe, E. J.; Bensimon, C.; Greedan, J. E.; Crutchley, R. J. *J. Am. Chem. Soc.* **1992**, *114*, 5130.

(105) Astruc, D. *Electron Transfer and Radical Processes in Transition-Metal Chemistry*, VCH, New York, 1995.

(106) Kaim, W.; Klein, A.; Glöckle, M. *Acc. Chem. Res.* **2000,** *33*, 755.

(107) Palaniappan, V.; Singru, R. M.; Agarwala, U. C. *Inorg. Chem.* **1988,** *27*, 181.

Chapter 2. Substituent Effects on Spin Density and Charge Density of Tetraoxo-Semiquinoidal Radical Ligands

2.1 Introduction

Spin and charge are closely correlative fundamental parameters in nature. Charge distribution is more commonly discussed across various scientific fields, while spin is only intensely studied in magnetism. Both of these two parameters play important roles in defining the electronic structures of a molecule. The deep understanding of the interplay between spin and charge density in radicals is still lacking, and the need to develop more in-depth knowledge about them arises in spintronics.[1-3] Spin refers to spin angular momentum, and it generally manifests as unpaired electrons in a system.[4] Spin density measures the probability of an electron to be present at a certain location. Charge density quantifies the amount of electric charge per unit area, length, surface area, or volume, and is considered to relate to electronegativity in molecular systems.

Density Functional Theory (DFT) calculations have been employed to provide energy mapping analysis of spin states along with spin Hamiltonian parameters, spin and electron delocalization.[5-7] The spin-unrestricted formalism is a powerful computational tool to give important insight that explain experimental spectra, reactivity trend, and electronic structures of molecular systems directly[8,9] or indirectly.[10-12]

2.2 DFT Calculations on Spin and Charge Polarization in Substituted Phenoxy, *o*-Semiquinone, and *o*-Phenanthrenesemiquinone Radicals.

The general assumption about spin and charge density is that they should track each other accordingly, since the intrinsic nature of both spin and charge is from the electron. However, they illustrate significantly different properties in magnetism. The strength of exchange

interaction reflects the spatial distribution of unpaired spin, whereas charge density indicates the stability of metal complex formation.[13] Previous studies conducted in our group examined the intimate movement between spin and charge density distribution, and *para*-substituent effects of phenoxy radicals,[13] *o*-semiquinone, *o*-phenanthrenesemiquinone with DFT calculations.[14]

Fehir in our group discovered that spin and charge distribution are not correlated in *para*-substituted phenoxy radicals.[13] Within the phenoxy radicals with various electron withdrawing groups (EWG) and electron donating groups (EDG), charge density distribution is induced by the resonance effect and shows a Hammett-type relationship.[13] The Hammett equation describes the change in free energy of activation corresponding to the change in Gibbs free energy when *meta*- or *para*- substituted aromatic reactants differ in substituents.[15] Nevertheless, spin density plots generated from the DFT calculations match the SOMO orbital pictures, and show a trend consistent with the σ-HOMO-σ-LUMO gap.[13] Fehir concluded that spin polarization is governed by the nature of the unpaired electron in a system, whereas charge polarization reflects the overall electron distribution over the entire molecule.[13]

Similar density functional studies were carried out by Fehir on *o*-semiquinone and *o*-phenanthrenesemiquinone. These systems also exhibit the spatial characteristics of spin density consistent with the σ-HOMO-σ-LUMO gap.[13,14] However, due to the different arene substitution pattern, *ortho*-substituted, from the phenoxy radicals, the calculations indicate very different spin and charge polarization of these systems, and the spin density induced by charge-dipole is mostly concentrated on the oxygen atoms in both types of radicals,[14] unlike the typical resonance structure of ketyl radicals (Fig. 2.1), where spin and charge density oscillates between the carbonyl carbon and oxygens.[16] Substituent effects are more profound in these systems: EWG stabilize the negative charge on the rings to decrease spin density on the oxygens, while EDG

destabilize the charge to increase spin density.[14] More details will be discussed for the DFT results obtained for the tetraoxo-semiquinoidal radicals in my project, and similar phenomena were observed.

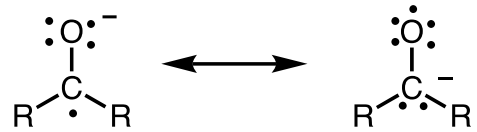

Figure 2.1. Resonance structure of a ketyl radical.

2.3 Substituent Effects on Spin Density and Charge Density of Tetraoxo-Semiquinoidal Radicals

The significant amount of charge density localized on the oxygen atoms in *o*-catechol makes them strong Lewis acids (Fig. 2.2).[17] After binding to a metal ion, the Heisenberg exchange interaction can be turned on when the complex is oxidized to metal-semiquinone. Magneto researchers have extensively studied these kinds of the metal quinoidal complexes over decades.[18-24]

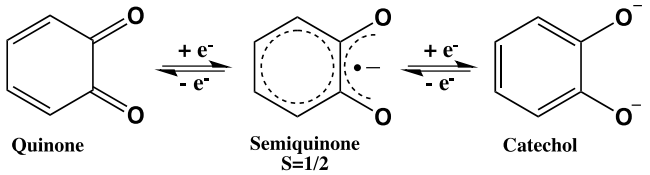

Figure 2.2. A quinoidal ligand undergoing one-electron redox reactions.

Instead of using *o*-semiquinone as ligands, tetradentate tetraoxo-semiquinone ligands were chosen to be the bridging ligands in our binuclear metal systems. The benefit of employing the tetraoxo-quinoidal ligands is their ability to coordinate with two metal ions to yield metal complexes with higher symmetry orientations. By combining these quinoidal ligands with relatively redox-inert metal ions, Cr(III) and Ga(III), it allowed us to systematically study the effect of spin exchange on the physical and magnetic properties without changing their overall composition, connectivity of elements, or geometry. Previously in our group, DFT calculations

were performed on deprotonated trianionic forms of chloranilate and 2,5-dihydroxy-3,6-benzoquinone radicals to characterize their electronic structures and provide insightful information to help interpret and simulate electron paramagnetic resonance (EPR) spectra.[25]

In the project outlined in this chapter, similar DFT calculations with natural population analysis (NPA) were carried out on substituted-tetraoxoanilate, tetraoxonaphthalene, and tetraoxoanthracene. Various EWG and EDG were incorporated into the substituents to facilitate the study of the spin density delocalization effects on the spin exchange properties, including π-donor/ σ-acceptors: F (FA), Cl (CA), Br (BA), I (IA), and phenyl (Ph); π-donors: OMe, NMe_2, and piperidino; a π-acceptor, CN; and a σ-acceptor, CF_3. Other derivatives are also included to investigate the effect of the intraligand electron delocalization, CN-phenyl (CNPh), NMe_2-phenyl (NMe2Ph), and CF_3-phenyl (CF3Ph). Bridging ligands with extended horizontal conjugation extension, naphthalene (NAT) and anthracene (AnT), are good candidates for our systems to decrease *J* for determination of the strength of the spin exchange due to their extended conjugated systems. Literature studies show a very strong direct exchange interaction on Cr(III) – semiquinoidal complexes,[55-57] and their magnetic data show temperature independence and *J* cannot be extrapolated accurately due to the lack of thermal population of more spin states. However, if the substituents destabilize the negative charge on the aromatic rings to an extreme level, it will largely decrease the formation constants, resulting in instability of the desired metal-semiquinone compounds or even prevent their formation.

DFT has been proved to be a useful tool for spin and charge density calculations, so it can examine the charge distribution of certain substituted tetraoxo-quinoidal ligands (Fig. 2.3) to glean their synthetic viability. Secondly, it was used to map out the spin distribution in these

radicals for their magnetic behaviors, since the strength of spin exchange coupling is suggested to be proportional to the spin density of paramagnetic centers in magnetism.[26-29]

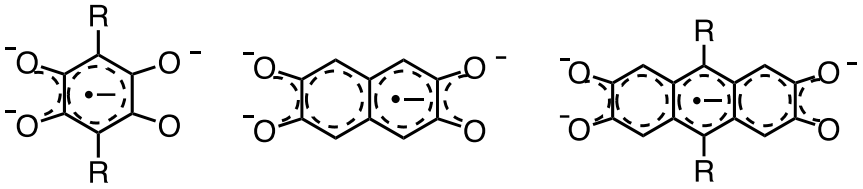

Figure 2.3. Substituted 2,3,5,6-tetraoxoanilate (left), 2,3,6,7-tetraoxonaphthalene (middle), and 2,3,6,7-tetraoxoanthracene (right).

2.4 Computational Details of DFT Calculations

General Methods. All electronic structure calculations of semiquinodal anions were carried out using density functional theory implemented in Gaussian 09[30] on HPCC at Institute for Cyber-Enabled Research at Michigan State University. The B3LYP functional with open shell was used in the calculations.[31-34] The calculations were performed using the default tight convergence criteria with a fine grid.[35] Analysis of atomic charge and spin densities were performed using natural population analysis (NPA) framework developed by Weinhold et al.[36]

2.4.1 Geometry Optimizations and Single-Point Energy Calculations

The initial geometries of all semiquinoidal ligands were generated using GaussView[37] and subsequently optimized using the UB3LYP functional and a 6-31G basis set with imposed symmetries of D_{2h}, and default fine grid in Gaussian09. Final geometries were checked with frequency calculations at the UB3LYP/6-31G level, and the absence of negative imaginary frequencies indicated that the final structures had reached their global minima. Single-point energy calculations were performed using the unrestricted open shell density function UB3LYP with the 6-311G basis set assuming a doublet ground state and a molecular charge of 3-.

2.5 Results and Discussion

Geometry. The electron spin resonance spectrum of chloranilic trianionic radical has been reported in aqueous NaOH along with $Na_2S_2O_4$;[38] nevertheless, there are no literature reports of the successful isolation of the protonated or deprotonated $DHBQ^{sq,cat}$ and $CA^{sq,cat}$ as free ligands as far as we know. Thus, it is difficult to predict if the optimized structures of the free ligands can accurately represent their true geometries. It has been widely observed that the C-C and C-O bond lengths within the ring of *o*-semiquinone can indicate the oxidation state of the quinoidal ligand when binding to first-row transition metals,[39-41] so the C-C and C-O bond lengths from the calculated trianionic structures can be used as reasonable parameters to gauge the validity of these geometry by comparing them with the corresponding x-ray crystal structures. Alternating short and long C-C bonds should be observed in semiquinone radicals due to the localization of electrons in the C=C bonds. In all calculated structures, the C-C bond distances range from 1.35 to 1.55 Å (See Appendix for detail), and this suggests that the structures obtained are in their semiquinone form. The C-O bonds within a semiquinone radical should be shorter and show a larger difference compared with the catechol form,[17,39] and the optimized structures indicated a similar trend.

In addition, the crystal structures of various protonated anilic acid, the dianionic form, have been intensively studied and characterized,[42-51] and the bond lengths and bond angles in these structures can be treated as references for the legitimacy of the calculated geometries calculated. The x-ray crystal structural analysis showed that these substituted dianionic anilates generally contain four C-C bonds with similar bond lengths (1.404 – 1.435 Å), and two longer C-C bonds whose bond lengths vary as a function of substituents.[52]

2.5.1 Spin and Charge Density of Substituted Tetraoxo-Semiquinoidal Trianionic Radicals

The results of DFT calculations on *ortho*-1,2-semiquinone radicals previously reported by our group revealed that the interaction between EDG or EWD substituents with the delocalized negative charge density in the semiquinoidal aromatic ring impacted the spin delocalizing ability of these substituents.[14] In this project, 3,6-R-tetraoxo-semiquinone bridging ligands served to examine the spin polarization effect instead of the *o*-1,2-semiquinones, and it will be unreasonable to predict the substituents exert similar effects with four electron-donating oxygens. Due to the strong resonance effects within a quinoidal ring along O-C-C(-R)-O bonds (Fig. 2.4), parallel offseting π-stacking interactions are dominate between bromanilic alkali salt to minimize electron-electron repulsion.[54] The strong π-stacking interactions present in anilic molecules allow electrons to move more freely. Polycyclic aromatic hydrocarbons (PAHs), e.g. naphthalene (NAT), and anthracene (AnT), are also considered good candidates for bridging ligands in our systems due to the presence of lighter elements (i.e. C, H, O) for low spin-orbit coupling and π-stacking for good electron mobility by spin delocalization.[53]

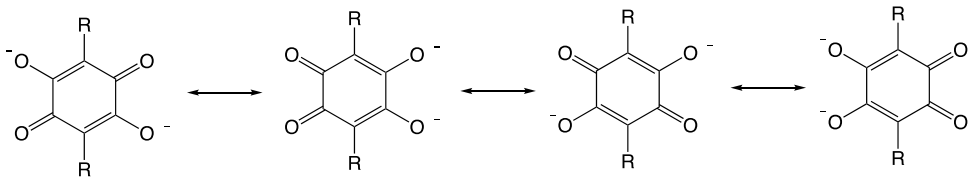

Figure 2.4. Resonance structure of substituted anilate.

As mentioned above, a wide range of substituents were chosen in these calculations to examine their interactions with the anilate and anthracene rings, and the unsubstituted anilate (R=H) radical was used as a reference point for comparisons. Fig. 2.5 shows the computational results of spin and charge density at the oxygens for substituted ligand radicals. The percent change is referenced to the parameters obtained for the tetrahydroxyanilate radical (i.e. R = H, where spin = 0.146 σ-electron and charge = - 0.648 electron). A positive change shows an

increase in the magnitude of either parameter, and a negative change indicates a decrease in that parameter. Most of the substituents exhibit spin and charge density percent change tracking to each other, except the halogenated, OMe, CN, CF_3, phenyl-anthracene (Ph-AnT), and cyanophenylanthracene. Concerns were raised about the low Lewis basicity of these anilates and PAHs, due to their strong electron delocalization, potentially negatively affecting the information constant of the transition metal complexes. Computational results indicated a general decrease in charge density (Fig. 2.5), so all complexes studies proved to be weaker Lewis bases. The most considerable decrease was shown in trianionic IA, CnPh, CF_3Ph, and CNPh-AnT.

Synthetic evidence is needed to provide supporting information about how low the level of Lewis basicity would be needed to prevent the formation of their corresponding metal complexes. The successful syntheses of both $[Cr_2(tren)_2(IA^{cat,cat})](BPh_4)_2$ and $[Cr_2(tren)_2(IA^{sq,cat})](BPh_4)_2(BF_4)$ are reported in Chapter 3, so iodanilic acid can stably coordinates with Cr(III) ions. However, the reaction between Ga(III) and the iodanilate ligand is thermodynamically unfavorable with Ga(III). Both $[Ga_2(tren)_2(IA^{cat,cat})](BPh_4)_2$ and $[Ga_2(tren)_2(IA^{sq,cat})](BPh_4)_2(BF_4)$ are synthesizable (reported in Chapter 4), but they are both unstable even being stored in the dark under inert atmosphere. Therefore, we can predict that either the coordination between Ga (III) and CNPh or CF_3Ph will be synthetically infeasible, or their products will be unstable in accordance to the degree of charge density.

The attenuation of charge density is quite pronounced in trianionic Me-AnT, Ph-AnT, and CNPh-AnT. Successful syntheis of $[Cr_2(tren)_2(Me\text{-}AnT^{cat,cat})](BPh_4)_2$ and $[Cr_2(tren)_2(Me\text{-}AnT^{cat,cat})](BPh_4)_2(BF_4)$ are reported in Chapter 3. However, the synthesis of Ga (III)-Me-AnT adduct has failed after multiple attempts, which will be further discussed in Chapter 4. Thus, we can anticipate the similar difficulties will be encountered for the coordination between Ga(III)

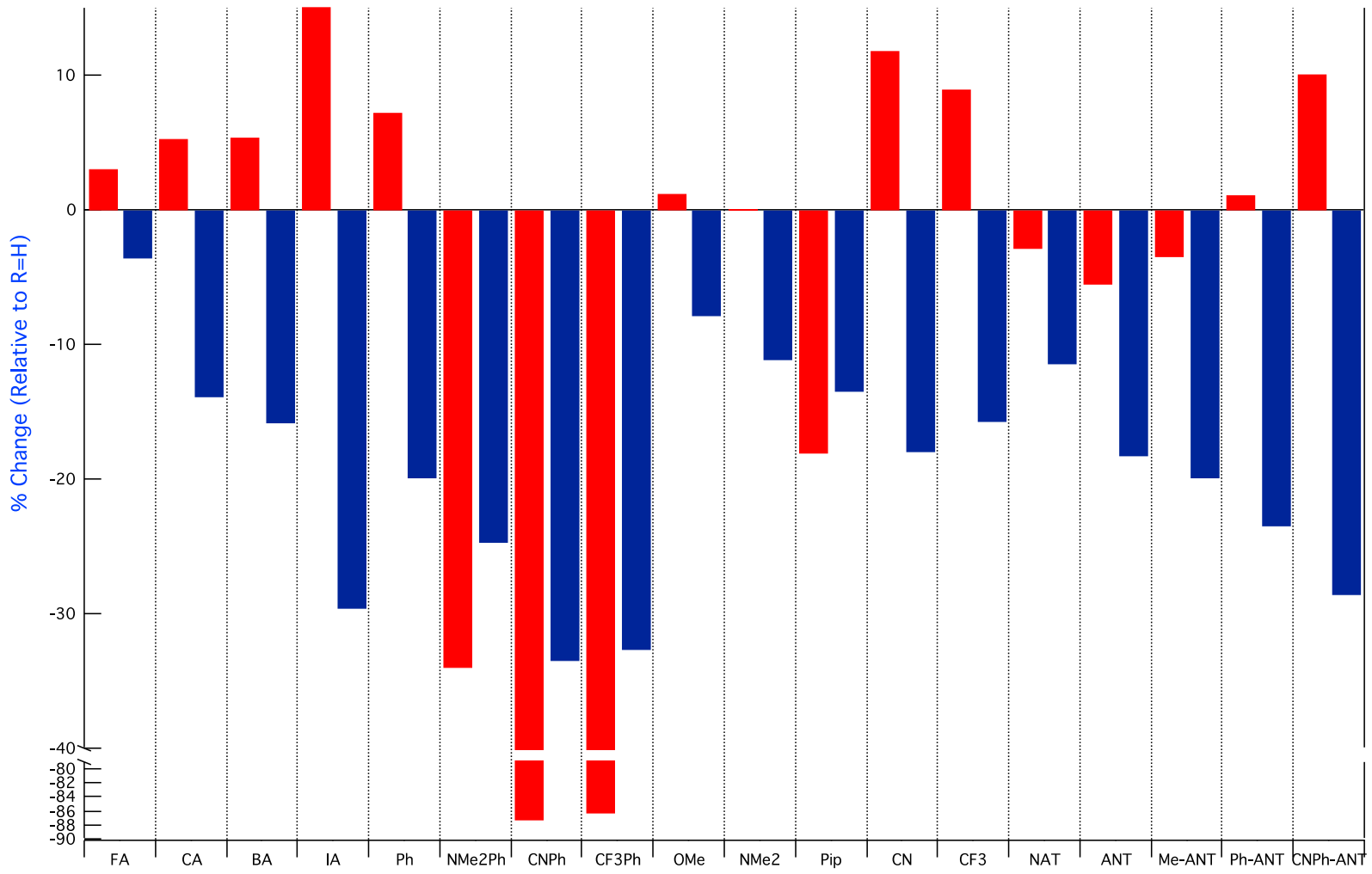

Figure 2.5. Shift in spin (red) and charge (blue) density at the oxygen atom for a series of substituted-anilate, naphthalene, and anthracene bridging radicals.

and Ph-AnT or CNPh-AnT.

Among the π-donors, piperidino exhibits a decrease in both spin and charge density, while OMe and NMe_2 show slight increases of spin density. Piperidino possesses a strong inductive effect due to the long electron-donating alkyl chain attached to the nitrogen, so the nitrogen is even more electron donating/basic than the one in NMe_2 (Fig. 2.6). However, higher electrostatic repulsion will occur within the semiquinone ring to destabilize the radical system, and possibly resulting in a decrease in both spin and charge densities in order to reduce the unfavorable electron-electron repulsion.

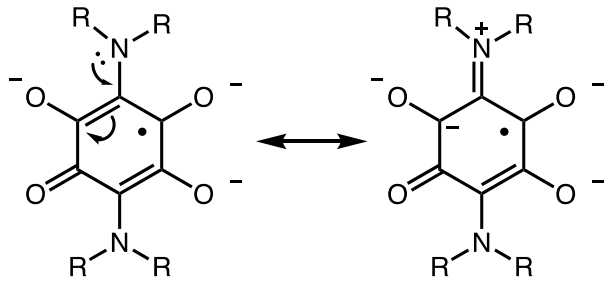

Figure 2.6. Resonance effects of amino-π-donors.

2.5.1.1 Charge Density Polarization in 3,6-R-tetraoxosemiquinones

The Hammett equation has been widely used for the study and interpretation of organic reactions and their mechanisms,[58] and has shown success in describing a linear free-energy relationship between reaction rates and equilibrium constants for reactions involving *meta*- and *para*- substituted benzoic acid.[59] According to arene substitution patterns, the installation of the substituents in the tetraoxo-ligands is located on *meta*- and *ortho*-positions to the oxygen atoms. Therefore, an additive Hammett parameter, i.e. $\sigma = \sigma_m + \sigma_o$, was used to consider both the *meta* and *ortho* effects.[60] The plot generated does not show a strong enough correlation ($R^2 = 0.68$) to

indicate either inductive effects (σ_I) or resonance/π-effects (σ_R) as the dominating effect on charge polarization (Fig. 2.7).

Both the *meta*-Hammett plot ($R^2 = 0.73$, Fig. 2.8) and the *ortho*-Hammett plot (R= 0.62, Fig. 2.9) shows some correlation with the change of charge density, but not well enough to suggest either are the dominant effect of charge polarization. σ_m is indicative of stronger inductive effects (σ_I) than resonance/π-effects (σ_R), where $\sigma_m = \sigma_I + 0.33\ \sigma_R$;[60,61] while σ_o indicates π-effect dominates, where $\sigma_o = \sigma_I + \sigma_R$.[61]

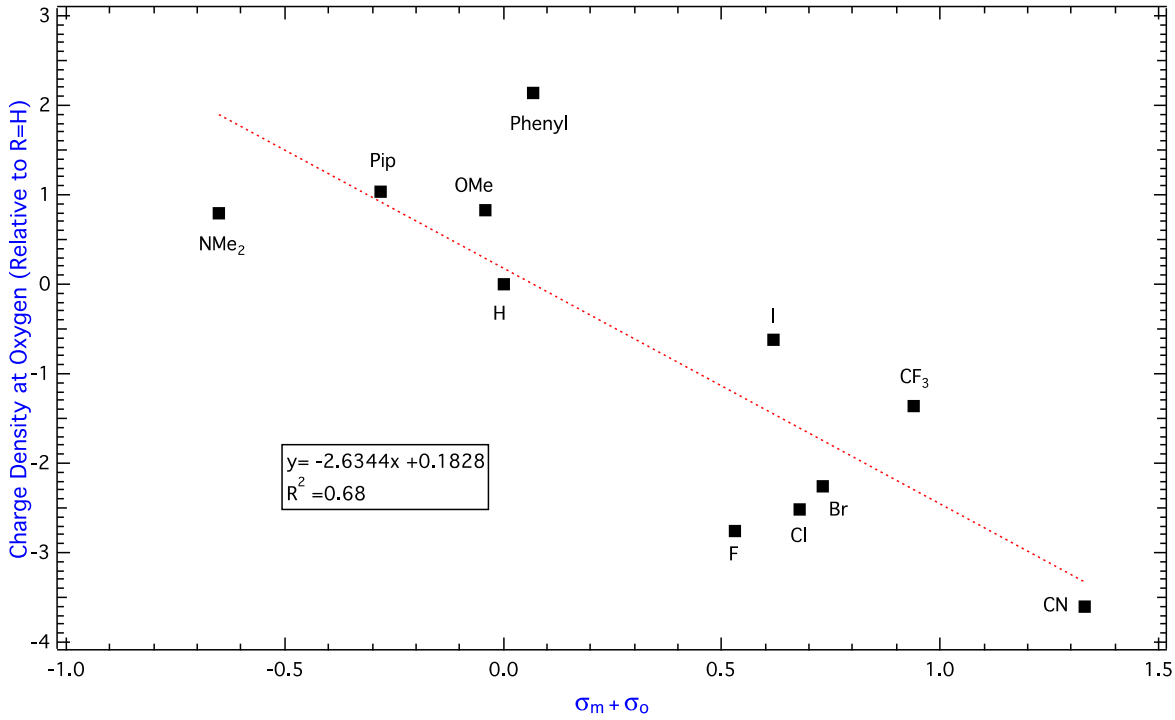

Figure 2.7. Percent change charge density vs. additive Hammett parameters for 3,6-R-tetraoxosemiquinones.

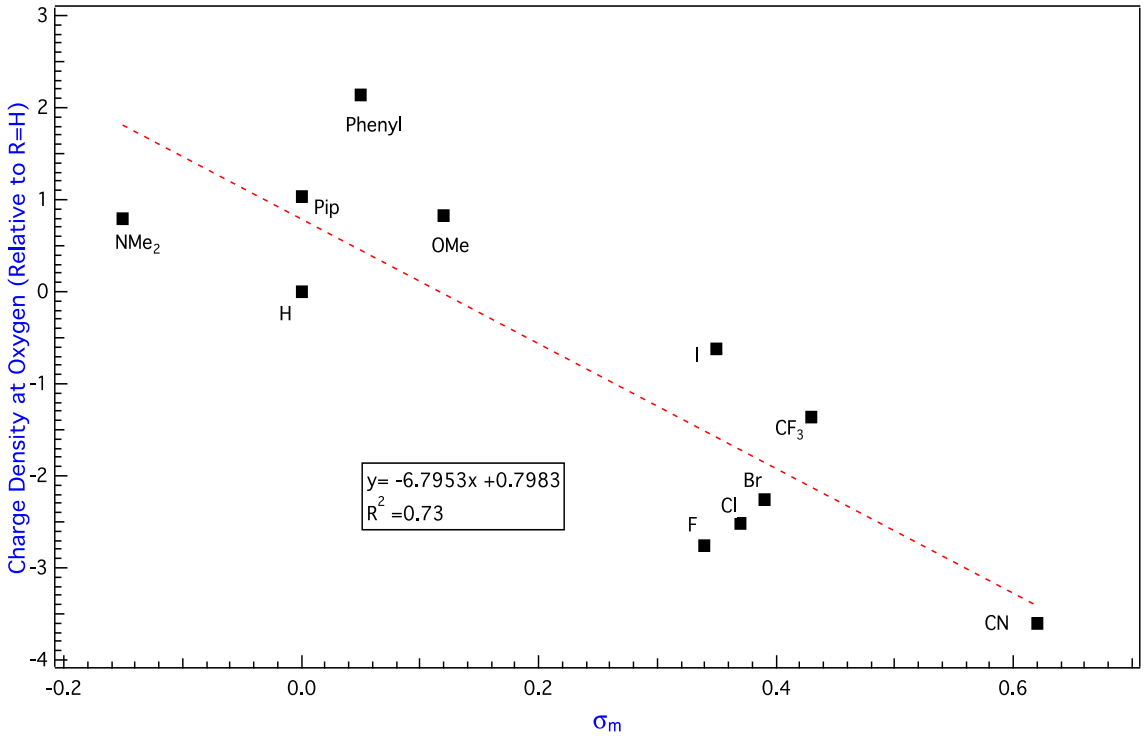

Figure 2.8. Percent change charge density vs. *meta* Hammett parameters for 3,6-R-tetraoxosemiquinones.

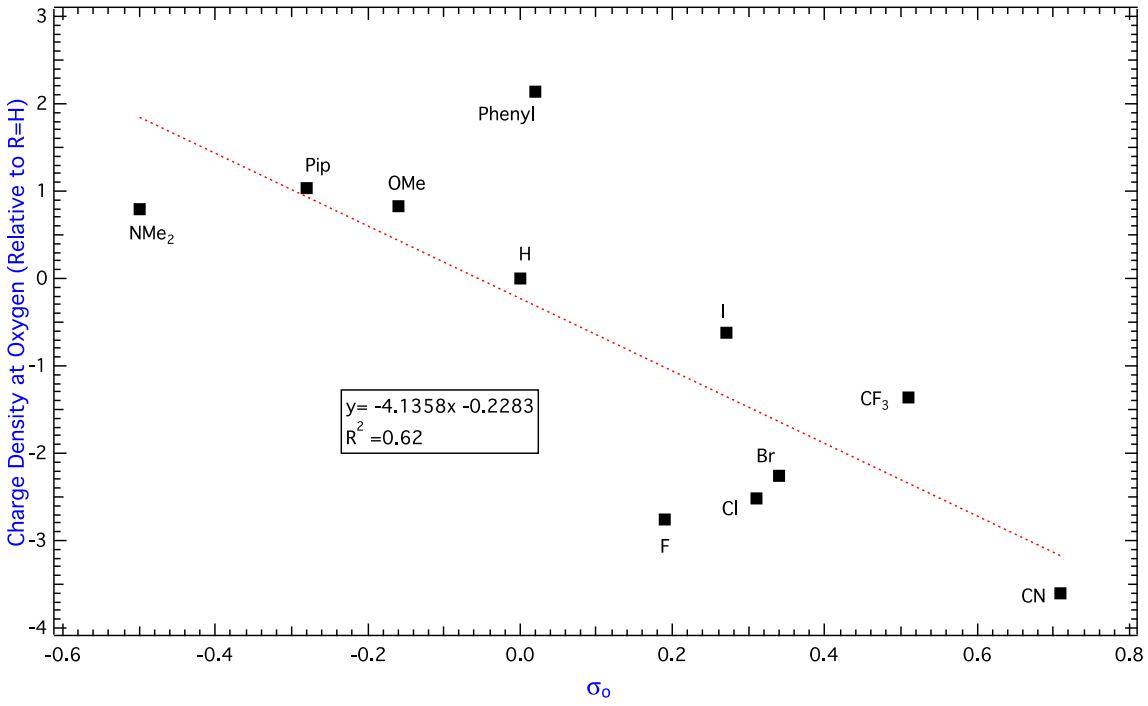

Figure 2.9. Percent Change charge density vs. *ortho* Hammett parameters for 3,6-R-tetraoxosemiquinones.

There may not be a clear picture about how charge is polarized by the substituents studied, but the Lewis basicity, as related to the change of charge density calculated by DFT, seemed to reflect well on the experimental reactivity of the corresponding ligands. This matches the synthetic observations of the series of dichromium(III) and digallium(III)-tetraoxo bridging complexes described in later chapters.

2.5.1.2 Spin Density Polarization in 3,6-R-tetraoxosemiquinones

As shown in Fig. 2.5, the change in spin density and charge density inflicted by various substituents mostly track each other, except in the case of π-donor/ σ-acceptors, π-acceptor, and a σ-acceptor. This trend does not agree with the spin density calculated for 3,6-R-*o*-semiquinones.[14] The extra two *ortho*-oxygens may exert extra donating effects on the aromatic ring, altering the substituent effects. Total spin density plots of these deprotonated trianionic free ligands can provide some useful information. Previous study with EPR spectroscopy on $[Ga_2(tren)_2(DHBQ^{sq,cat})](BPh_4)_2(BF_4)$ and $[Ga_2(tren)_2(CA^{sq,cat})](BPh_4)_2(BF_4)$ by our group[25] reported Cl induced spin delocalization, and its total spin density picture reinforced the experimental results with β-spin density on the chlorine. Fig. 2.9 shows β-spin density on the $CA^{sq,cat}$ trianionic ligand, and the heavier β-spin density is seen on the $[Ga_2(tren)_2(CA^{sq,cat})]^{3+}$ and the $[Ga_2(tren)_2(NMe_2\text{-}PhA^{sq,cat})]^{3+}$ (see figures in Chapter 4 Appendix). π-donors are β-spin donors with α-spin delocalized onto the substituents,[62] which is reflected on the total spin orbital picture shown in Fig. 2.10 for $NMe_2A^{sq,cat}$ with increasing spin density on the oxygen atoms. This may be caused by the dominating resonance effect from NMe_2 to induce charge separation with stronger charge-dipole repulsion.[63]

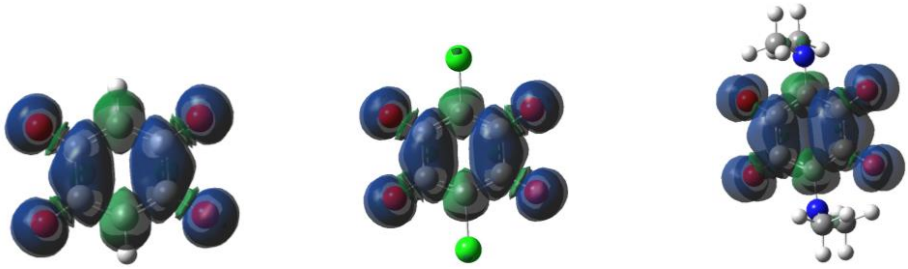

Figure 2.10. Total spin density plots of $DHBQ^{sq,cat}$ (left), $CA^{sq,cat}$ (middle), and $NMe_2A^{sq,cat}$ (right).

As opposed to π-donors, π-acceptors are α-acceptors and can stabilize charge density on oxygen by reducing electrostatic repulsion within the aromatic ring.[62] This effect only impacts on the charge density in 3,6-R-tetraoxosemiquinones, and an increase of spin density was observed. The spin density picture (Fig. 2.11) also has both α spin and β spin density spread onto the CN group. It is likely that the four oxygen atoms exert more electron density on the ring; therefore, the effect of α-acceptors is not sufficient enough to reduce the unfavorable charge-dipole repulsion.

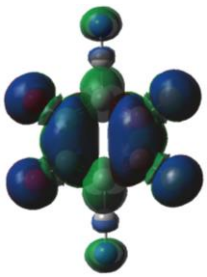

Figure 2.11. Total spin density plots of $CN^{sq,cat}$.

The change in spin density does not correlate to σ-HOMO- σ-LUMO gap (Fig. 2.12), which also disagrees with the DFT calculations done previously on phenoxy and 3,6-R-semiquinones.[14] In addition to that, spin density calculated for deprotonated trianioanic 3,6-R-semiquinone exhibits discrepancies with the ones calculated for digallium-semiquinone complexes, which will be discussed in Chapter 4. The spin density information about free ligands may not be relevant to spin polarization when coordinating to a metal ion.

Table 2.1. Net spin density, charge density, and σ-HOMO- σ-LUMO gap (eV) of 3,6-R-semiquinone

R	Spin Density[a]	Charge Density[b]	σ-HOMO- σ-LUMO gap (eV) [c]
H	0.145636	-0.648431	3.81
F	0.150166	-0.625116	4.64
Cl	0.153349	-0.558264	2.70
Br	0.153577	-0.545560	2.09
I	0.167597	-0.456596	1.58
Ph	0.156225	-0.519430	1.01
OMe	0.147429	-0.597403	1.42
NMe_2	0.145744	-0.576497	1.23
Pip	0.119366	-0.560983	0.48
CN	0.162844	-0.532202	2.19
CF_3	0.158722	-0.546376	2.64

[a]Spin density = $\frac{(O_1+O_2+O_3+O_4)}{4}$ [b]Charge density = $\frac{(O_1+O_2+O_3+O_4)}{4}$

[c] σ-HOMO- σ-LUMO gap = [energy level (σ-LUMO) – energy level (σ-HOMO)] in a.u.

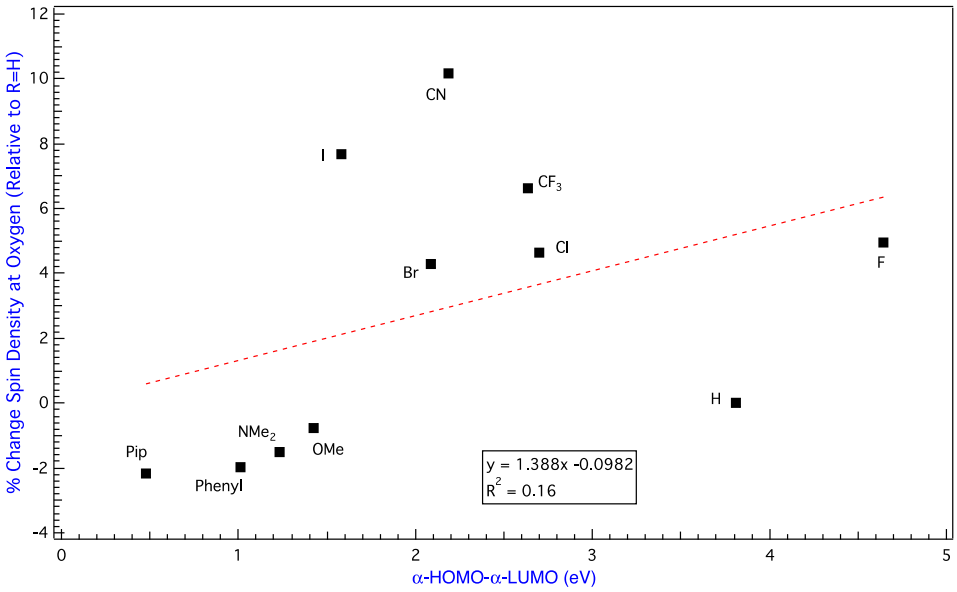

Figure 2.12. Percent Change spin density vs σ-HOMO- σ-LUMO gap (eV) parameters for 3,6-R-tetraoxosemiquinones.

2.6 Concluding Comments

The goal of this chapter was to utilize density functional calculations to examine spin and charge distribution and understand their underlying mechanisms. In addition, the information provided for charge density can validate the synthetic viability of the substituents proposed. The Lewis basicity predicted by the trend in charge density matches the synthetic characteristics of

the corresponding bimetallic complexes, which will be further discussed in Chapters 3 and 4. Although no absolute Hammett-typed relationship was established to explain if the substituents effects are dominated by inductive or resonance/π-effects, the information provided about Lewis basicity is very handy for synthetic proposal before proceeding to the reactions. Based on this information, a series of bimetallic tetraoxolene-quinodal complexes were proposed as our synthetic targets (Fig. 2.13), and the synthetic design for spin exchange-coupled systems focuses on these substituents.

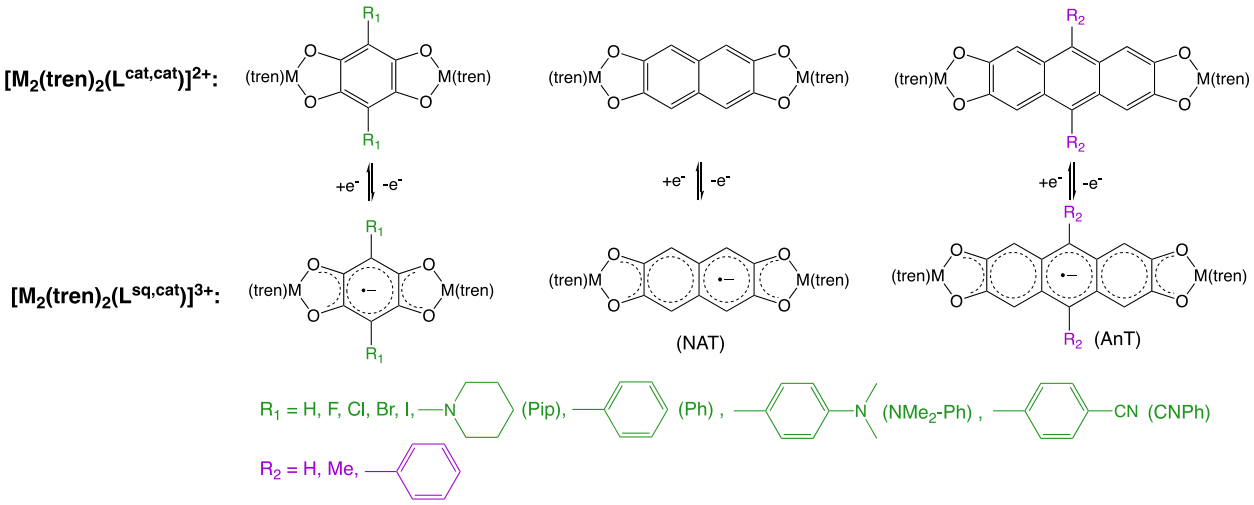

Figure 2.13. Cr^{3+} or Ga^{3+} tetraoxolene-quinodal complexes with a combination of diamagnetic or paramagnetic substituted-bridging ligands, where R_1 are the substituents on tetraoxoanilate, and R_2 are the substituents on 2,3,6,7-tetraoxoanthracene.

Spin polarization resulted from NPA analysis showed inconsistent trends with the DFT results of 3,6-R-*o*-1,2-semiquinones.[14] Again, no correlation can be established with the trend of spin density, and the electronic structure of the tetraoxo-quinoidal ligands may be altered from 3,6-R-*o*-1,2-semiquinone because of the four chelating oxygens. In the future, EPR studies can be performed on trianionic free ligands in aqueous NaOH solution in the presence of $Na_2S_2O_4$ to experimentally validate if the DFT calculations are legitimate benchmarks for spin polarization.

APPENDIX

APPENDIX

Cartesian Coordinates and Bonding Information Used in the Single-Point Energy Calculations

1. $[THB^{sq,cat}]^{3-}$

Element	Bond Length	Bond Angle	X	Y	Z
O1			-0.2544210	-2.2096230	1.7004450
O2	2.8782385		-0.0659190	-2.5512650	-1.1512220
C3	2.4024056	88.4994841	-0.0901600	0.1633600	1.3635140
C4	1.3018761	30.1935377	-0.1357600	-1.1928360	0.8961160
C5	1.3018711	58.3061691	-0.0368140	-1.3721070	-0.6002160
O6	3.7005098	131.9656342	0.2544210	2.2096230	-1.7004450
O7	2.4023986	176.9995151	0.0659190	2.5512650	1.1512220
C8	1.4352057	122.6637102	0.0901600	-0.1633600	-1.3635140
C9	1.3018761	17.8408281	0.1357600	1.1928360	-0.8961160
C10	1.3018711	30.1938622	0.0368140	1.3721070	0.6002160
H11	1.1033722	88.5011709	-0.1624100	0.2943600	2.4566970
H12	1.1033722	115.6407720	0.1624100	-0.2943600	-2.4566970

2. $[FA^{sq,cat}]^{3-}$

Element	Bond Length	Bond Angle	X	Y	Z
O1			-0.2492820	-2.2073370	1.6958030
O2	2.8687275		-0.0700450	-2.5473140	-1.1470630
C3	2.3996327	88.2059208	-0.0865180	0.1612240	1.3470000
C4	1.2952874	29.7776638	-0.1342250	-1.1937980	0.8975110
C5	1.2952584	58.4280626	-0.0395580	-1.3730720	-0.6012420
O6	3.6821176	132.4385159	0.2492820	2.2073370	-1.6958030
O7	2.3995650	176.4172903	0.0700450	2.5473140	1.1470630
C8	1.4285047	123.4464186	0.0865180	-0.1612240	-1.3470000
C9	1.2952874	17.7838734	0.1342250	1.1937980	-0.8975110
C10	1.2952584	29.7841880	0.0395580	1.3730720	0.6012420
F11	1.4267483	88.2132747	-0.1756230	0.3304900	2.7608670
F12	1.4267483	114.9741541	0.1756230	-0.3304900	-2.7608670

3. $[CA^{sq,cat}]^{3-}$

Element	Bond Length	Bond Angle	X	Y	Z
Cl1			-0.1925700	0.3839140	3.2139340
O2	3.0382799		-0.2438260	-2.2261730	1.6595970
O3	2.7916885	127.4310024	-0.0779870	-2.5567720	-1.1074820
C4	2.4130483	38.3704779	-0.0805510	0.1606100	1.3443030
C5	1.2789978	67.0749334	-0.1321060	-1.1992830	0.9053750
C6	1.2789989	60.3557610	-0.0414370	-1.3800540	-0.6076450

Element	Bond Length	Bond Angle	X	Y	Z
Cl7	2.7999637	88.0478582	0.1925700	-0.3839140	-3.2139340
O8	3.6599435	132.1802437	0.2438260	2.2261730	-1.6595970
O9	2.4130501	178.1200129	0.0779870	2.5567720	1.1074820
C10	1.4298915	125.8542314	0.0805510	-0.1606100	-1.3443030
C11	1.2789978	19.1153007	0.1321060	1.1992830	-0.9053750
C12	1.2789989	28.7037276	0.0414370	1.3800540	0.6076450

4. $[BA^{sq,cat}]^{3-}$

Element	Bond Length	Bond Angle	X	Y	Z
O1			-0.2420170	-2.2266010	1.6585800
O2	2.7893483		-0.0798100	-2.5567100	-1.1064120
C3	2.4133491	88.9076789	-0.0783690	0.1596060	1.3368820
C4	1.2761865	28.4399103	-0.1313780	-1.2004460	0.9079690
C5	1.2761877	60.4674447	-0.0423570	-1.3816640	-0.6099050
O6	3.6534789	132.4258537	0.2420170	2.2266010	-1.6585800
O7	2.4133472	177.8147481	0.0798100	2.5567100	1.1064120
C8	1.4270585	126.3537159	0.0783690	-0.1596060	-1.3368820
C9	1.2761865	19.1342360	0.1313780	1.2004460	-0.9079690
C10	1.2761877	28.4396263	0.0423570	1.3816640	0.6099050
Br11	2.0529546	114.1144733	0.1976860	-0.4025350	-3.3719180
Br12	2.0529546	88.9069346	-0.1976860	0.4025350	3.3719180

5. $[IA^{sq,cat}]^{3-}$

Element	Bond Length	Bond Angle	X	Y	Z
O1			-0.2441640	-2.2586950	1.6809260
O2	2.8262540		-0.0821910	-2.5929630	-1.1208130
C3	2.4479835	88.7548796	-0.0765930	0.1607880	1.3482920
C4	1.3092510	28.2395506	-0.1304110	-1.2053090	0.9117860
C5	1.3092774	60.5129668	-0.0439200	-1.3870470	-0.6123750
O6	3.6986836	132.6737299	0.2441640	2.2586950	-1.6809260
O7	2.4479449	177.5122225	0.0821910	2.5929630	1.1208130
C8	1.4352032	126.1778812	0.0765930	-0.1607880	-1.3482920
C9	1.3092510	19.0867737	0.1304110	1.2053090	-0.9117860
C10	1.3092774	28.2451836	0.0439200	1.3870470	0.6123750
I11	2.2715344	88.7556259	-0.2060890	0.4294360	3.6001640
I12	2.2715344	114.3343536	0.2060890	-0.4294360	-3.6001640

6. $[CF_3A^{sq,cat}]^{3-}$

Element	Bond Length	Bond Angle	X	Y	Z
O1			-1.4996370	2.3225230	0.0000010
O2	2.7441211		1.2390000	2.4959240	-0.0000250
C3	2.3974024	91.8264303	-1.4244790	-0.0737010	0.0000030

Element	Bond Length	Bond Angle	X	Y	Z
C4	1.2799636	30.9593169	-0.8071000	1.2460940	-0.0000040
C5	1.2785370	61.2732390	0.6965680	1.3381570	-0.0000140
O6	3.6888557	129.3590205	1.4996350	-2.3225260	-0.0000070
O7	2.4293173	177.4176001	-1.2389960	-2.4959270	-0.0000170
C8	1.4590116	124.9684190	1.4244800	0.0736970	-0.0000070
C9	1.2799621	19.6819369	0.8071040	-1.2460950	-0.0000060
C10	1.2785368	29.4823894	-0.6965710	-1.3381570	-0.0000090
C11	1.4705222	87.2369764	-2.8947920	-0.0488960	0.0000040
C12	1.4705221	120.8940401	2.8947930	0.0488980	0.0000020
F13	1.3727628	116.9324586	-3.5371270	-1.2621080	0.0000170
F14	1.4062044	115.8691195	-3.4973980	0.6050720	-1.0893090
F15	1.4062107	115.8687605	-3.4973910	0.6050920	1.0893170
F16	1.4062138	115.8686728	3.4973890	-0.6050360	1.0893530
F17	1.3727612	116.9323018	3.5371190	1.2621130	-0.0000400
F18	1.4062043	115.8690039	3.4974040	-0.6051250	-1.0892750

7. [OMeA^{sq,cat}]$^{3-}$

Element	Bond Length	Bond Angle	X	Y	Z
O1			-1.7858720	2.1246410	-0.2827190
O2	2.8314301		0.9704730	2.6096660	0.1465940
C3	2.4011586	89.1811938	-1.3437400	-0.2348580	-0.2293690
C4	1.3018743	30.0483459	-0.9454970	1.1381180	-0.1585460
C5	1.2890101	59.3843300	0.5185310	1.4042930	0.0804770
O6	3.6916031	131.4689861	1.7858610	-2.1246380	0.2827470
O7	2.4053789	178.1802706	-0.9704780	-2.6096570	-0.1465880
C8	1.4389917	123.6123390	1.3437430	0.2348660	0.2293490
C9	1.3018753	18.4892136	0.9454910	-1.1381100	0.1585690
C10	1.2890104	29.8818875	-0.5185350	-1.4042840	-0.0804730
O11	1.4485209	89.8550771	-2.7414230	-0.4992170	-0.5028820
O12	1.4485216	115.1222759	2.7414280	0.4992370	0.5028440
C13	1.3958182	111.7148571	3.5672620	0.0123260	-0.5116630
H14	1.1161057	108.2147314	4.6282880	0.1763060	-0.2066610
H15	1.1020178	109.9856829	3.3892360	-1.0653870	-0.6575560
H16	1.1147781	112.8748570	3.4245850	0.5457980	-1.4800540
C17	1.3958174	111.7142607	-3.5672480	-0.0123660	0.5116600
H18	1.1020189	109.9858844	-3.3892420	1.0653450	0.6576000
H19	1.1161065	108.2148868	-4.6282780	-0.1763460	0.2066690
H20	1.1147751	112.8747157	-3.4245440	-0.5458790	1.4800210

8. [PipA^{sq,cat}]$^{3-}$

Element	Bond Length	Bond Angle	X	Y	Z
O1			-1.5706160	2.2651810	-0.3344560

Element	Bond Length	Bond Angle	X	Y	Z
N2	4.9249259		2.8640030	0.1346390	-0.1112070
C3	1.2992675	29.9292638	-0.8385180	1.2002060	-0.2004530
C4	1.4992567	119.9621465	0.6542790	1.3008340	-0.2963790
C5	1.4373292	116.8351415	1.4016960	0.0937240	-0.0723960
C6	1.4333101	97.1560662	3.6089750	1.3089010	0.2359290
H7	1.0896846	108.9920317	2.9773800	1.9658340	0.8333730
H8	1.1179864	113.1825880	3.9045500	1.9209840	-0.6516990
C9	1.5479535	109.8260299	4.9119140	0.9065680	0.9684850
H10	1.1098191	111.0156676	5.5267380	1.7993860	1.2063210
H11	1.0996445	108.8619872	4.6495560	0.4196120	1.9188850
C12	1.5383701	110.1204264	5.7288040	-0.0654690	0.0999130
H13	1.1062212	108.0231355	6.0936870	0.4898060	-0.7845390
H14	1.1073608	111.3968835	6.6311730	-0.4228850	0.6330470
C15	1.5368804	111.0779781	4.8605500	-1.2377560	-0.3836980
H16	1.1077229	109.7945609	5.4365640	-1.8633320	-1.0935660
H17	1.0976321	110.5790596	4.5579230	-1.8683840	0.4621870
C18	1.4361307	131.6366403	3.5504260	-0.7377310	-1.0223960
H19	1.1272872	113.3441850	3.8001200	-0.2484320	-2.0067820
H20	1.0934237	106.5624266	2.8967780	-1.5998630	-1.1806620
O21	2.3995159	152.6948248	1.5705880	-2.2650910	0.3339830
N22	2.4455602	89.6437714	-2.8639980	-0.1344670	0.1107440
C23	1.2992689	30.3522375	0.8385770	-1.2000430	0.2000710
C24	1.4993714	119.9569452	-0.6543220	-1.3006670	0.2962070
C25	1.4370988	122.4592312	-1.4016440	-0.0936010	0.0719540
C26	1.4333272	147.8640719	-3.6088630	-1.3088940	-0.2361340
H27	1.0896633	108.9927521	-2.9774350	-1.9656010	-0.8339640
H28	1.1179598	113.1846683	-3.9038600	-1.9211420	0.6515390
C29	1.5479442	109.8256266	-4.9122060	-0.9068100	-0.9680880
H30	1.1099782	111.0155030	-5.5270410	-1.7998770	-1.2057030
H31	1.0995630	108.8718650	-4.6505780	-0.4197350	-1.9185340
C32	1.5383609	110.1216915	-5.7289760	0.0649450	-0.0991040
H33	1.1061906	108.0315160	-6.0933750	-0.4903320	0.7855080
H34	1.1073806	111.3967084	-6.6316150	0.4222640	-0.6318870
C35	1.5369965	111.0750874	-4.8607070	1.2375050	0.3841870
H36	1.1077247	109.7958940	-5.4365440	1.8629770	1.0942930
H37	1.0976454	110.5775823	-4.5585660	1.8681840	-0.4618510
C38	1.4361561	98.3424727	-3.5502310	0.7376910	1.0223190
H39	1.1272744	113.3442628	-3.7993850	0.2482630	2.0067630
H40	1.0934226	106.5599530	-2.8966180	1.5998740	1.1804440
O41	1.2949128	120.0930878	1.2131150	2.4406780	-0.5518340
O42	1.2945424	120.0872694	-1.2128370	-2.4401710	0.5520030

9. [PhA^{sq,cat}]$^{3-}$

Element	Bond Length	Bond Angle	X	Y	Z
O1			-1.4943450	0.0000000	-0.0000050
C2	1.4684744		-0.7519820	-1.2670100	-0.0000160
C3	1.5039640	120.3668108	0.7519820	-1.2670110	0.0000170
C4	1.4684753	120.3667149	1.4943450	0.0000000	0.0000030
C5	1.4684758	119.2664603	0.7519810	1.2670110	-0.0000100
C6	1.4684758	119.2664405	-0.7519810	1.2670110	0.0000050
C7	1.4664640	120.3667530	2.9608090	0.0000000	0.0000020
C8	1.4397667	123.2226260	3.7496480	1.2044340	-0.0000280
C9	1.4397681	123.2226375	3.7496490	-1.2044350	0.0000310
C10	1.3919874	122.7915825	5.1415960	1.1939620	-0.0000310
H11	1.0847265	115.4486969	3.1856480	2.1310060	-0.0000490
C12	1.3919864	122.7915525	5.1415960	-1.1939620	0.0000280
H13	1.0847257	115.4486579	3.1856490	-2.1310060	0.0000540
C14	1.4040872	122.1815603	5.8804570	0.0000000	-0.0000030
H15	1.0966372	118.4639777	5.6714980	2.1540750	-0.0000560
H16	1.0966377	118.4639819	5.6714990	-2.1540750	0.0000510
H17	1.0942180	121.7505169	6.9746750	0.0000000	-0.0000040
C18	1.4664640	120.3667728	-2.9608090	0.0000000	-0.0000040
C19	1.4397667	123.2226260	-3.7496480	1.2044340	0.0000350
C20	1.4397676	123.2226042	-3.7496480	-1.2044350	-0.0000370
C21	1.3919874	122.7915825	-5.1415960	1.1939620	0.0000400
H22	1.0847265	115.4486969	-3.1856480	2.1310060	0.0000590
C23	1.3919874	122.7915195	-5.1415960	-1.1939620	-0.0000320
H24	1.0847257	115.4486912	-3.1856480	-2.1310060	-0.0000660
C25	1.4040867	122.1815256	-5.8804560	0.0000000	0.0000070
H26	1.0966377	118.4640234	-5.6714990	2.1540750	0.0000710
H27	1.0966377	118.4639822	-5.6714990	-2.1540750	-0.0000590
H28	1.0942190	121.7504822	6.9746750	0.0000000	0.0000090
O29	1.2811311	115.7410342	1.3083820	-2.4210110	0.0000490
O30	1.2811311	123.8922311	-1.3083820	-2.4210100	-0.0000440
O31	1.2811316	123.8921769	1.3083820	2.4210110	-0.0000260
O32	1.2811307	123.8921575	-1.3083820	2.4210100	0.0000190

10. [NMe$_2$PhA^{sq,cat}]$^{3-}$

Element	Bond Length	Bond Angle	X	Y	Z
O1			-1.2211130	2.4652000	-0.0002120
O2	2.6169188		1.3941550	2.3722640	-0.0001320
N3	6.4795882	158.4429104	-7.3282150	0.2999360	-0.0000280
C4	2.4268932	94.3894525	-1.4926740	0.0535480	-0.0000930
C5	1.4623803	94.3341056	-2.9540810	0.1068940	-0.0000740

Element	Bond Length	Bond Angle	X	Y	Z
C6	1.2794654	30.1954772	-0.7053870	1.2942780	-0.0001650
C7	1.4408114	123.1303192	-3.7850400	-1.0701550	0.0003500
H8	1.0846785	115.4525123	-3.2537780	-2.0158230	0.0005980
C9	1.2798365	64.1934748	0.7964320	1.2405800	-0.0001210
C10	1.4613198	23.0577732	-5.8696770	0.2098110	-0.0000310
C11	1.3900124	122.8825734	-5.1738950	-1.0134430	0.0003920
H12	1.0952854	118.5676035	-5.7364660	-1.9532110	0.0007490
C13	1.4034556	120.1501030	-5.0912630	1.3776120	-0.0004730
H14	1.0937246	118.1117743	-5.6081410	2.3414950	-0.0008200
C15	1.3904600	122.0714760	-3.7013550	1.3384360	-0.0004760
H16	1.0844356	121.5836513	-3.1075870	2.2458720	-0.0007730
C17	1.4523879	121.6665625	-7.9457680	-0.2400610	-1.1985530
H18	1.0944355	108.9280624	-7.4698400	0.2085020	-2.0760910
H19	1.1059259	110.4093683	-9.0241610	0.0042080	-1.2203080
H20	1.1110945	114.2829550	-7.8591180	-1.3431230	-1.2999280
C21	1.4523874	121.6476865	-7.9456980	-0.2388350	1.1990840
H22	1.1110936	114.2835270	-7.8590900	-1.3417970	1.3015670
H23	1.1059260	110.4092563	-9.0240780	0.0055060	1.2206780
H24	1.0944367	108.9276532	-7.4696850	0.2105980	2.0761320
O25	3.7025135	126.4406418	1.2211020	-2.4651870	-0.0001930
O26	2.4278003	171.2493628	-1.3941420	-2.3722520	-0.0000600
N27	6.4795961	117.6129906	7.3282180	-0.2999390	0.0003190
C28	1.4695236	123.8777465	1.4926760	-0.0535390	-0.0000760
C29	1.4623808	120.3715451	2.9540830	-0.1068970	-0.0000060
C30	1.2794597	23.3647957	0.7053970	-1.2942620	-0.0001110
C31	1.4408114	123.1299936	3.7850450	1.0701500	-0.0001270
H32	1.0846805	115.4515210	3.2537680	2.0158120	-0.0002830
C33	1.2798307	30.1668343	-0.7964390	-1.2405640	-0.0000620
C34	1.4613202	23.0572048	5.8696790	-0.2098240	0.0002580
C35	1.3900106	122.8825078	5.1738980	1.0134330	-0.0000180
H36	1.0952852	118.5675827	5.7364720	1.9531990	-0.0001520
C37	1.4034539	120.1506906	5.0912620	-1.3776210	0.0003570
H38	1.0937240	118.1117419	5.6081370	-2.3415050	0.0005800
C39	1.3904611	122.0715059	3.7013530	-1.3384410	0.0002240
H40	1.0844342	121.5832828	3.1075890	-2.2458780	0.0002700
C41	1.4523785	121.6740670	7.9457640	0.2401650	1.1987880
H42	1.0944383	108.9285031	7.4698570	-0.2083350	2.0763730
H43	1.1059253	110.4092470	9.0241600	-0.0040870	1.2205570
H44	1.1110930	114.2834520	7.8591070	1.3432330	1.3000760
C45	1.4523954	121.6393335	7.9456930	0.2387160	-1.1988590
H46	1.1110967	114.2821189	7.8589940	1.3416620	-1.3014710
H47	1.1059255	110.4105932	9.0240920	-0.0055420	-1.2204200
H48	1.0944337	108.9273368	7.4697120	-0.2108530	-2.0758510

11. [CNPhA^{sq,cat}]$^{3-}$

Element	Bond Length	Bond Angle	X	Y	Z
O1			1.2064550	-2.3207790	0.5413500
O2	2.6442863		-1.2063100	-2.3208940	-0.5406920
C3	2.4059253	91.9131798	1.5370390	0.0000830	0.0002490
C4	1.4545130	97.8982957	2.9915520	0.0000520	0.0000450
C5	1.2498681	29.4166312	0.7551460	-1.2106860	0.1861260
C6	1.4422212	123.0582005	3.7782520	1.1690560	-0.3074200
H7	1.0823137	116.9030065	3.2364650	2.0735060	-0.5520420
C8	1.2498755	63.5296203	-0.7550870	-1.2107510	-0.1854890
C9	2.4632489	93.6707771	5.9245520	0.0000160	-0.0002770
C10	1.3777257	123.1556727	5.1559750	1.1716900	-0.3067030
H11	1.0912852	119.2073798	5.6868580	2.0932860	-0.5510950
C12	1.4343916	86.9884173	5.1560060	-1.1716610	0.3063000
H13	1.0912837	118.4896049	5.6869360	-2.0932700	0.5505340
C14	1.3777190	122.3016804	3.7782900	-1.1689930	0.3073370
H15	1.0823003	119.9413630	3.2365310	-2.0734110	0.5520800
O16	3.6337656	151.0722129	-1.2064580	2.3208700	0.5412640
O17	2.4059284	164.2019230	1.2063400	2.3209990	-0.5405640
C18	1.4532241	125.5960749	-1.5370400	0.0000020	0.0002180
C19	1.4545160	122.5510890	-2.9915560	-0.0000290	0.0000780
C20	1.2498628	15.2239333	-0.7551750	1.2107520	0.1861040
C21	1.4422366	123.0580541	-3.7782250	-1.1690760	-0.3073750
H22	1.0823098	116.9024297	-3.2364000	-2.0735040	-0.5519770
C23	1.2498675	29.4151573	0.7551140	1.2108250	-0.1854900
C24	2.4632481	93.6701761	-5.9245510	-0.0000760	-0.0002680
C25	1.3777218	123.1551020	-5.1559440	-1.1717430	-0.3066550
H26	1.0912847	119.2077897	-5.6868120	-2.0933550	-0.5510170
C27	1.4343835	86.9889319	-5.1560470	1.1716170	0.3063150
H28	1.0912840	118.4896470	-5.6870060	2.0932020	0.5505780
C29	1.3777219	122.3015328	-3.7783280	1.1689880	0.3073580
H30	1.0823016	119.9425847	-3.2365750	2.0734150	0.5520870
C31	1.4039230	150.6134235	7.3284750	-0.0000170	-0.0004040
N32	1.1844500	179.9927690	8.5129250	-0.0001930	-0.0005310
C33	1.4039260	150.6131303	-7.3284770	-0.0000670	-0.0004540
N34	1.1844520	179.9958813	-8.5129290	0.0000030	-0.0005530

12. [CF$_3$PhA^{sq,cat}]$^{3-}$

Element	Bond Length	Bond Angle	X	Y	Z
O1			1.2110170	2.3263940	0.5288050
O2	2.6429266		-1.2110280	2.3263800	-0.5289090
C3	2.4065358	92.0267027	1.5393070	0.0040980	-0.0102510
C4	1.2513435	29.4564356	0.7564520	1.2141630	0.1792720

Element	Bond Length	Bond Angle	X	Y	Z
C5	1.2513425	63.5961145	-0.7564560	1.2141580	-0.1793600
O6	3.6341139	150.9883293	-1.2063370	-2.3199940	0.5376900
O7	2.4063468	164.2036758	1.2063480	-2.3199800	-0.5377970
C8	1.4536317	125.4985590	-1.5393070	0.0040910	0.0101850
C9	1.2514248	15.2059206	-0.7545370	-1.2068540	0.1871760
C10	1.2514252	29.4792407	0.7545410	-1.2068480	-0.1872650
C11	1.4541348	97.9028178	2.9933790	0.0055830	-0.0236800
C12	1.4447335	123.1445685	3.7817350	-1.1668450	-0.3256110
C13	1.4447485	123.1368974	3.7845870	1.1807940	0.2594580
C14	1.3783228	123.1245538	5.1599570	-1.1640160	-0.3420380
H15	1.0822704	116.8491312	3.2392970	-2.0746660	-0.5556790
C16	1.3782961	123.1267434	5.1627480	1.1835370	0.2403540
H17	1.0822897	116.8583772	3.2446380	2.0881460	0.4971940
C18	1.4288318	122.1865991	5.9218730	0.0150710	-0.0758370
H19	1.0910153	118.9895562	5.6877500	-2.0873160	-0.5854840
H20	1.0910092	118.9884341	5.6927780	2.1108190	0.4628790
C21	1.4541351	122.6075176	-2.9933790	0.0055770	0.0236450
C22	1.4447332	123.1445599	-3.7817290	-1.1668500	0.3255940
C23	1.4447483	123.1368920	-3.7845920	1.1807890	-0.2594740
C24	1.3783222	123.1245796	-5.1599500	-1.1640190	0.3420580
H25	1.0822701	116.8490868	-3.2392860	-2.0746720	0.5556450
C26	1.3782957	123.1267442	-5.1627520	1.1835350	-0.2403330
H27	1.0822901	116.8584227	-3.2446480	2.0881400	-0.4972270
C28	1.4288327	122.1866196	-5.9218720	0.0150700	0.0758780
H29	1.0910149	118.9895778	-5.6877380	-2.0873180	0.5855170
H30	1.0910092	118.9884953	-5.6927870	2.1108170	-0.4628460
C31	1.4420742	122.0524497	-7.3621270	-0.0039750	0.0060160
C32	1.4420751	122.0523807	7.3621270	-0.0039760	-0.0059360
F33	1.4287295	117.5149208	-7.9577260	-0.3193860	-1.2537640
F34	1.3819196	114.4308080	-7.9644450	1.2055880	0.2956230
F35	1.3821708	114.4313941	-7.9621740	-0.9370250	0.8304900
F36	1.3821707	114.4313766	7.9621940	-0.9370360	-0.8303840
F37	1.3819203	114.4308362	7.9644560	1.2055830	-0.2955400
F38	1.4287275	117.5148913	7.9576900	-0.3193740	1.2538620

13. [NAT^{sq,cat}]$^{3-}$

Element	Bond Length	Bond Angle	X	Y	Z
C1			-2.5356630	-0.7650380	0.0000020
C2	1.4241907		-1.2579070	-1.3940520	0.0000010
C3	1.4213172	126.0449867	0.0000000	-0.7323780	0.0000000
C4	1.4647560	117.7449024	0.0000000	0.7323780	0.0000020
C5	1.4213172	117.7449024	-1.2579070	1.3940520	0.0000000

Element	Bond Length	Bond Angle	X	Y	Z
C6	1.4241907	126.0449867	-2.5356630	0.7650380	-0.0000030
H7	2.1685599	98.0161215	1.2673190	-2.4920810	-0.0000010
H8	1.0980693	115.7189472	-1.2673200	-2.4920810	0.0000000
C9	1.4213172	124.5101952	1.2579070	-1.3940520	0.0000000
C10	1.4213172	117.7449024	1.2579070	1.3940520	0.0000010
H11	1.0980693	118.2360661	-1.2673200	2.4920810	0.0000000
C12	1.4241898	126.0449690	2.5356620	0.7650380	0.0000020
C13	1.4241907	126.0449867	2.5356630	-0.7650380	0.0000020
H14	1.0980693	118.2360139	1.2673190	2.4920810	0.0000000
O15	1.2828617	123.2019129	-3.6400130	1.4178360	0.0000000
O16	1.2828617	123.2019129	-3.6400130	-1.4178360	-0.0000010
O17	1.2828626	123.2019179	3.6400130	1.4178360	-0.0000010
O18	1.2828612	123.2019513	3.6400130	-1.4178350	-0.0000020

14. [AnT^{sq,cat}]$^{3-}$

Element	Bond Length	Bond Angle	X	Y	Z
C1			-0.7691250	3.7724360	-0.0000250
C2	1.4226812		-1.4034070	2.4989730	-0.0000330
C3	1.4163938	125.3948525	-0.7356510	1.2498640	-0.0003770
C4	1.4713030	118.1276279	0.7356520	1.2498820	-0.0003930
C5	1.4164233	118.1283461	1.4034070	2.4990250	-0.0002010
C6	1.4226418	125.3947463	0.7691250	3.7724440	-0.0003210
C7	1.4124184	124.1145416	-1.3934490	-0.0000270	-0.0003530
C8	1.4123861	117.7570706	1.3934490	0.0000270	-0.0003530
C9	1.4124184	124.4851009	0.7356510	-1.2498640	-0.0003770
C10	1.4123861	124.4851009	-0.7356520	-1.2498820	-0.0003930
C11	1.4164233	124.1145822	-1.4034070	-2.4990250	-0.0002010
H12	1.0955513	118.5396057	-2.4989300	-2.5069020	-0.0000250
C13	1.4226418	125.3947463	-0.7691250	-3.7724440	-0.0003210
C14	1.5382500	116.4773072	0.7691250	-3.7724360	-0.0000250
C15	1.4163938	124.1145416	1.4034070	-2.4989730	-0.0000330
H16	1.0955418	116.0618199	-2.4989200	2.5069080	0.0001540
H17	1.0955513	118.5396057	2.4989300	2.5069020	-0.0000250
H18	1.0955418	118.5433274	2.4989200	-2.5069080	0.0001540
O19	1.2723320	123.4142545	1.4073690	4.8731130	0.0006520
O20	1.2723340	123.4124587	-1.4074200	4.8730780	0.0006300
O21	1.2723340	120.1104232	1.4074200	-4.8730780	0.0006300
O22	1.2723320	123.4142545	-1.4073690	-4.8731130	0.0006520
H23	1.0949120	117.7585564	2.4883610	0.0000120	-0.0001680
H24	1.0949120	117.7563422	-2.4883610	-0.0000120	-0.0001680

15. [MeAnT^{sq,cat}]$^{3-}$

Element	Bond Length	Bond Angle	X	Y	Z
C1			-3.7790180	-0.7633690	0.0668410
C2	1.4236161		-2.5030950	-1.3934520	0.0256250
C3	1.4197233	126.1738947	-1.2456940	-0.7367650	-0.0319860
C4	1.4735590	117.5520286	-1.2456860	0.7367940	-0.0321060
C5	1.4196705	117.5507719	-2.5030620	1.3934520	0.0250800
C6	1.4236528	126.1739380	-3.7790180	0.7633450	0.0661750
C7	1.4237644	123.6269593	-0.0000280	-1.4231080	-0.0979760
C8	1.4237860	118.8189206	0.0000270	1.4231080	-0.0979760
C9	1.4237699	122.0712972	1.2457010	0.7367670	-0.0319980
C10	1.4237915	122.0712972	1.2456930	-0.7367960	-0.0321180
C11	1.4196724	123.6292852	2.5030720	-1.3934510	0.0250840
H12	1.0902412	119.6367945	2.5411070	-2.4819260	0.0740880
C13	1.4236529	126.1741100	3.7790280	-0.7633440	0.0661830
C14	1.5267131	116.2706099	3.7790280	0.7633690	0.0668480
C15	1.4197251	123.6273568	2.5031050	1.3934510	0.0256280
H16	1.0902354	114.1668283	-2.5410020	-2.4819060	0.0750640
H17	1.0902431	119.6365443	-2.5410900	2.4819300	0.0740640
H18	1.0902336	119.6320482	2.5410190	2.4819020	0.0750870
O19	1.2716324	123.1618307	-4.8728190	1.4099570	0.1165870
O20	1.2716386	123.1661115	-4.8728490	-1.4099040	0.1177420
O21	1.2716382	120.5602054	4.8728580	1.4099030	0.1177730
O22	1.2716325	123.1618217	4.8728280	-1.4099560	0.1166190
C23	1.5141367	118.9605802	0.0000090	2.9318680	-0.2254640
H24	1.0977509	110.9798658	-0.8859470	3.2801020	-0.7721560
H25	1.1079179	114.2534549	-0.0001970	3.4704070	0.7427600
H26	1.0977690	110.9799861	0.8862050	3.2801650	-0.7717630
C27	1.5141377	118.9624385	-0.0000570	-2.9318690	-0.2254640
H28	1.0977492	110.9802775	0.8857770	-3.2801220	-0.7723380
H29	1.1079166	114.2534364	0.0003250	-3.4704070	0.7427590
H30	1.0977699	110.9794211	-0.8863750	-3.2801440	-0.7715810

16. [PhAnT^{sq,cat}]$^{3-}$

Element	Bond Length	Bond Angle	X	Y	Z
C1			0.7600170	-3.7881570	-0.1338160
C2	1.4259003		1.3894720	-2.5092170	-0.0978900
C3	1.4132598	126.2800162	0.7372930	-1.2582110	-0.0145250
C4	1.4747220	117.4854175	-0.7374290	-1.2581120	-0.0147250
C5	1.4132580	117.4857632	-1.3897600	-2.5090030	-0.0985940
C6	1.4259083	126.2799801	-0.7604830	-3.7880440	-0.1343560
C7	1.4362072	123.6086371	1.4298110	-0.0000770	-0.0000710
C8	1.4362194	118.8272500	-1.4298490	0.0000880	-0.0001140

Element	Bond Length	Bond Angle	X	Y	Z
C9	1.4362228	122.3468013	-0.7372910	1.2582170	0.0144030
C10	1.4361915	122.3493982	0.7374290	1.2581150	0.0142800
C11	1.4132743	123.6064062	1.3897890	2.5090470	0.0975860
H12	1.0871224	119.5498381	2.4742320	2.5447490	0.1649940
C13	1.4258870	126.2802341	0.7605280	3.7880730	0.1333180
C14	1.5204981	116.1912514	-0.7599700	3.7881530	0.1339070
C15	1.4132450	123.6076638	-1.3894360	2.5091990	0.0981430
H16	1.0871204	114.1533760	2.4739110	-2.5451100	-0.1652290
H17	1.0871229	119.5514086	-2.4741740	-2.5447070	-0.1664740
H18	1.0871205	119.5527859	-2.4738450	2.5450940	0.1659640
O19	1.2667202	123.0134315	-1.4087880	-4.8748310	-0.1907010
O20	1.2667277	123.0129362	1.4081980	-4.8750600	-0.1895140
O21	1.2667207	120.7806057	-1.4081380	4.8750230	0.1902380
O22	1.2667302	123.0142152	1.4088410	4.8748970	0.1890790
C23	1.4840380	118.8258406	-2.9138870	0.0001470	0.0000390
C24	1.4145690	122.0887771	-3.6654260	0.6884300	-0.9810120
C25	1.4145692	122.0825844	-3.6651490	-0.6881110	0.9813200
C26	1.3939545	122.2143262	-5.0593770	0.6893560	-0.9839890
H27	1.0858771	117.9879586	-3.1238350	1.2356620	-1.7467440
C28	1.3939556	122.2150151	-5.0591000	-0.6889290	0.9847870
H29	1.0858744	117.9871700	-3.1233310	-1.2354080	1.7468410
C30	1.3996353	120.7187102	-5.7769060	0.0002470	0.0005210
H31	1.0912797	119.3842019	-5.5927980	1.2315060	-1.7665660
H32	1.0912789	119.3839898	-5.5922840	-1.2310450	1.7675480
H33	1.0905830	120.8468505	-6.8674890	0.0003230	0.0007150
C34	1.4840650	118.8242950	2.9138760	-0.0001800	0.0000360
C35	1.4145462	122.0863573	3.6653970	0.6877650	-0.9812330
C36	1.4145579	122.0823786	3.6650830	-0.6881440	0.9815490
C37	1.3939635	122.2135435	5.0593570	0.6886080	-0.9842530
H38	1.0858764	117.9879540	3.1238020	1.2347760	-1.7471190
C39	1.3939575	122.2134615	5.0590360	-0.6890560	0.9849730
H40	1.0858761	117.9873942	3.1232290	-1.2351570	1.7472500
C41	1.3996310	120.7174050	5.7768460	-0.0002380	0.0004640
H42	1.0912779	119.3854600	5.5928060	1.2304930	-1.7669920
H43	1.0912774	119.3850989	5.5922250	-1.2309430	1.7678870
H44	1.0905840	120.8460364	6.8674300	-0.0002590	0.0006130

17. [CNPh-AnT^{sq,cat}]$^{3-}$

Element	Bond Length	Bond Angle	X	Y	Z
C1			-0.7570440	3.7883960	-0.1397280
C2	1.4303917		-1.3853500	2.5037820	-0.1078100
C3	1.4059423	126.3784644	-0.7372500	1.2610220	0.0025880
C4	1.4745660	117.4515974	0.7373160	1.2609920	0.0027600

Element	Bond Length	Bond Angle	X	Y	Z
C5	1.4059726	117.4511267	1.3854960	2.5037780	-0.1072610
C6	1.4303506	126.3795658	0.7572610	3.7883750	-0.1394210
C7	1.4456395	123.0619408	-1.4440680	-0.0000390	-0.0000770
C8	1.4455900	119.2659635	1.4439880	-0.0000940	0.0000940
C9	1.4455460	121.4678093	0.7372810	-1.2611100	-0.0025740
C10	1.4455921	121.4640280	-0.7373770	-1.2611170	-0.0026600
C11	1.4059368	123.0683060	-1.3854550	-2.5038930	0.1076170
H12	1.0853041	119.9233421	-2.4651140	-2.5442150	0.2105520
C13	1.4303831	126.3806846	-0.7571600	-3.7884970	0.1397680
C14	1.5143390	116.0558430	0.7571790	-3.7884950	0.1396780
C15	1.4059573	123.0641786	1.3854120	-2.5038800	0.1077210
H16	1.0852965	113.6717808	-2.4649830	2.5440780	-0.2109470
H17	1.0853069	119.9215567	2.4651820	2.5440220	-0.2099720
H18	1.0853041	119.9207908	2.4650730	-2.5441140	0.2106690
O19	1.2606352	122.7741356	1.4091910	4.8654450	-0.2035190
O20	1.2606199	122.7720457	-1.4089460	4.8654490	-0.2040950
O21	1.2606183	121.1394670	1.4090790	-4.8655620	0.2038000
O22	1.2606116	122.7732196	-1.4090480	-4.8655490	0.2041320
C23	1.4653260	119.2654405	2.9093140	-0.0001100	0.0000600
C24	1.4254250	122.3979399	3.6730220	-0.7935250	-0.9049700
C25	1.4254063	122.3959270	3.6730290	0.7933490	0.9050160
C26	1.3816567	122.7386361	5.0545890	-0.7889280	-0.9200260
H27	1.0847106	118.0886318	3.1386870	-1.4080440	-1.6215240
C28	1.3816781	122.7387871	5.0546200	0.7889380	0.9198870
H29	1.0847127	118.0907364	3.1387430	1.4077720	1.6216920
C30	1.4187930	120.9799158	5.7923560	0.0000600	-0.0001080
H31	1.0881617	119.8862350	5.5908640	-1.3903110	-1.6513560
H32	1.0881627	119.8846580	5.5908860	1.3903660	1.6511880
C33	1.4652590	119.2676452	-2.9093270	0.0000300	-0.0000620
C34	1.4254517	122.3983399	-3.6731340	-0.7936330	-0.9048330
C35	1.4254457	122.3997437	-3.6730670	0.7937980	0.9046640
C36	1.3816495	122.7407671	-5.0546950	-0.7890810	-0.9197930
H37	1.0847119	118.0885976	-3.1388660	-1.4082440	-1.6213600
C38	1.3816525	122.7401659	-5.0546310	0.7893160	0.9196420
H39	1.0847099	118.0904743	-3.1387810	1.4084540	1.6211360
C40	1.4188219	120.9816726	-5.7924590	0.0001200	-0.0000530
H41	1.0881660	119.8840983	-5.5909700	-1.3906590	-1.6509690
H42	1.0881665	119.8839361	-5.5908640	1.3909590	1.6507960
C43	1.4175910	121.3304251	7.2099470	0.0001480	-0.0001800
N44	1.1734380	179.9985842	8.3833850	0.0002150	-0.0002680
C45	1.4175720	121.3336969	-7.2100310	0.0001540	0.0000010
N46	1.1734440	179.9958599	-8.3834750	0.0001460	-0.0000310

18. [pyrene]$^{3-}$

Element	Bond Length	Bond Angle	X	Y	Z
C1			-0.0000010	3.5211880	-0.0003670
C2	1.4032882		-1.2182940	2.8247830	-0.0003070
C3	1.4060200	121.5287941	-1.2618570	1.4194380	-0.0001610
C4	1.4542966	118.0348379	0.0000010	0.6964630	-0.0000720
C5	1.4542953	120.3792694	1.2618570	1.4194390	-0.0001350
C6	1.4032894	120.4934693	1.2182940	2.8247840	-0.0002820
C7	1.4728133	119.1838874	-2.5693440	0.7414580	-0.0001050
C8	1.3929260	119.8103287	0.0000010	-0.6964630	0.0000730
C9	1.4542966	119.8103286	-1.2618570	-1.4194380	0.0001350
C10	1.4728133	122.7812746	-2.5693440	-0.7414580	0.0000500
C11	1.4060200	118.0348378	-1.2182940	-2.8247830	0.0002820
H12	1.0899604	116.6433026	-2.1769060	-3.3435090	0.0003260
C13	1.4032882	121.5287942	-0.0000010	-3.5211880	0.0003680
C14	1.4032894	120.4934693	1.2182940	-2.8247840	0.0003080
C15	1.4060200	121.5287181	1.2618570	-1.4194390	0.0001620
C16	1.4728138	119.1839220	2.5693440	-0.7414580	0.0001050
C17	1.4728138	122.7811667	2.5693440	0.7414580	-0.0000500
H18	1.0974370	119.7533033	-0.0000010	4.6186250	-0.0004820
H19	1.0899604	121.8279033	-2.1769060	3.3435090	-0.0003720
H20	1.0899613	121.8278868	2.1769060	3.3435120	-0.0003260
H21	1.0974370	119.7533034	-0.0000010	-4.6186250	0.0004820
H22	1.0899613	121.8278868	2.1769060	-3.3435120	0.0003720
O23	1.2801697	121.3229526	-3.6635600	1.4059320	-0.0001860
O24	1.2801697	121.3229526	-3.6635600	-1.4059320	0.0001070
O25	1.2801691	121.3229564	3.6635600	-1.4059310	0.0001850
O26	1.2801691	121.3229563	3.6635600	1.4059310	-0.0001090

19. [terrylene]$^{3-}$

Element	Bond Length	Bond Angle	X	Y	Z
C1			-1.4523900	1.2362110	0.1590140
C2	1.4392563		-0.7326700	-0.0000070	0.0001840
C3	1.4392603	119.9941306	-1.4523360	-1.2362590	-0.1586620
C4	1.4570781	119.9101781	-2.9061450	-1.2233910	-0.2553600
C5	1.4520151	119.8224196	-0.7272880	2.4934570	0.2026890
C6	1.4653420	120.0034071	0.7326720	0.0000140	0.0001840
C7	1.4392618	120.0024274	1.4523380	1.2362670	-0.1586680
C8	1.4520097	119.8231067	0.7272300	2.4935170	-0.2019470
C9	1.4570797	119.9098592	2.9061490	1.2233920	-0.2553580
C10	1.4417606	119.5581000	3.6251170	0.0000270	-0.0001390
C11	1.4417630	120.1789189	2.9062240	-1.2233340	0.2553240
C12	1.4392566	120.0032170	1.4523880	-1.2362060	0.1590190

Element	Bond Length	Bond Angle	X	Y	Z
C13	1.4520160	119.8225060	0.7272810	-2.4934490	0.2027270
C14	1.4520093	119.8231332	-0.7272300	-2.4935100	-0.2019300
O15	1.2610144	125.5986512	-1.2221150	3.6165310	0.4925310
O16	1.2610203	125.5994048	1.2220340	3.6166960	-0.4914470
O17	1.2610150	125.5991239	1.2220960	-3.6165230	0.4925920
O18	1.2610190	125.5992622	-1.2220320	-3.6166840	-0.4914470
C19	1.4417599	119.5578852	-3.6251160	-0.0000300	-0.0001340
C20	1.4481290	119.9104952	-5.0732450	-0.0000320	-0.0003650
C21	1.4192233	119.6145630	-5.7746210	1.1982410	0.2935880
H22	1.0923789	118.8496928	-6.8668900	1.1828170	0.2951050
C23	1.3845019	119.5841533	-5.0657170	2.3533940	0.5762930
H24	1.0942465	119.6181268	-5.6058530	3.2746460	0.8148790
C25	1.4417618	120.1788288	-2.9062250	1.2233290	0.2553370
C26	1.3964044	121.7159173	-3.6696370	2.3799540	0.5621320
C27	1.4192235	119.6145650	-5.7745240	-1.1983070	-0.2945420
C28	1.3845014	119.5842520	-5.0655290	-2.3534650	-0.5769960
C29	1.3964053	121.7158778	-3.6694530	-2.3800280	-0.5623670
C30	1.4194016	122.9370674	3.6694640	2.3800300	-0.5623430
C31	1.4481280	119.9105380	5.0732450	0.0000250	-0.0003650
C32	1.4192235	119.6145959	5.7745290	1.1983020	-0.2945220
H33	1.0923795	118.8496238	6.8667980	1.1828760	-0.2963840
C34	1.3845001	119.5842762	5.0655400	2.3534650	-0.5769640
H35	1.0942465	119.6181943	5.6056020	3.2747210	-0.8157020
C36	1.4192242	119.6146985	5.7746200	-1.1982530	0.2935740
C37	1.3845004	119.5841339	5.0657150	-2.3534090	0.5762570
C38	1.3964054	121.7159473	3.6696340	-2.3799670	0.5620970
H39	1.0795639	121.2079926	-3.1253500	3.2893190	0.7677170
H40	1.0923795	118.8496113	-6.8667930	-1.1828840	-0.2964090
H41	1.0942462	119.6181053	-5.6055880	-3.2747180	-0.8157510
H42	1.0795614	121.2082371	-3.1250970	-3.2894000	-0.7677250
H43	1.0795621	121.2081726	3.1253440	-3.2893310	0.7676690
H44	1.0942467	119.6181085	5.6058500	-3.2746660	0.8148270
H45	1.0923790	118.8496612	6.8668890	-1.1828290	0.2950940
H46	1.0795626	117.1547971	3.1251140	3.2894100	-0.7676880

Figure 2.14. Total spin density plots of $FA^{sq,cat}$ (left), $BA^{sq,cat}$ (middle), and $IA^{sq,cat}$ (right).

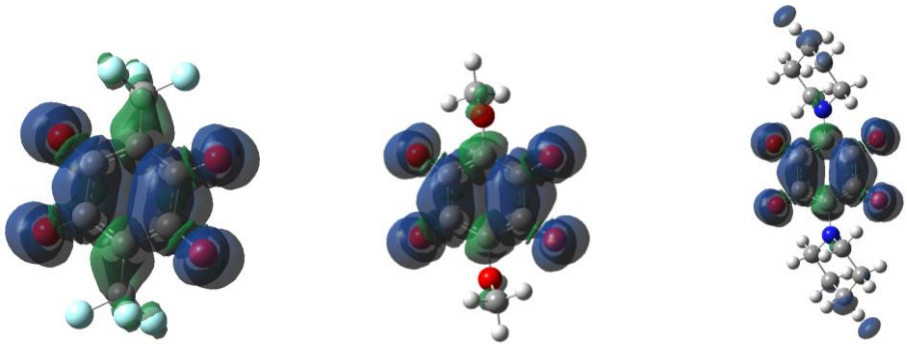

Figure 2.15. Total spin density plots of $CF_3An^{sq,cat}$ (left), $OMeAn^{sq,cat}$ (middle), and $PipAn^{sq,cat}$ (right).

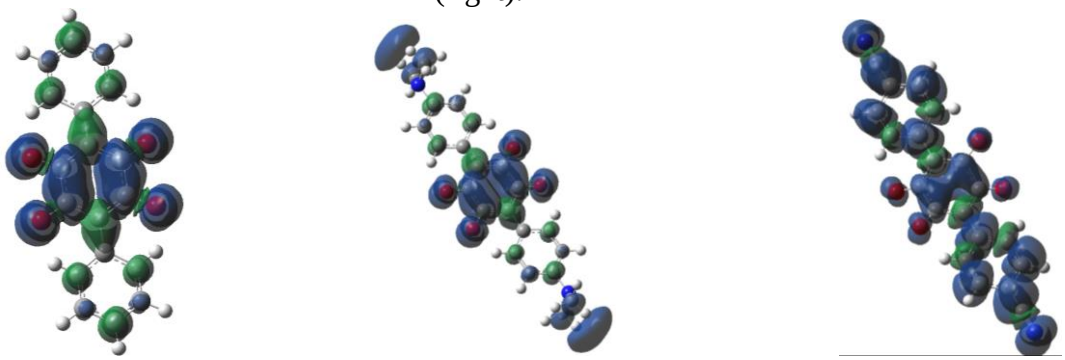

Figure 2.16. Total spin density plots of $PhAn^{sq,cat}$ (left), $NMe_2PhAn^{sq,cat}$ (middle), and $CNPhAn^{sq,cat}$ (right).

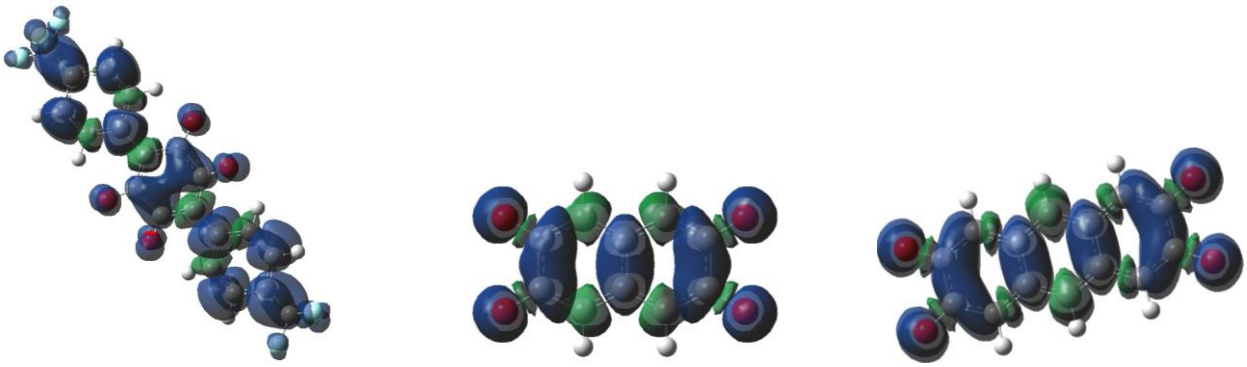

Figure 2.17. Total spin density plots of $CF_3PhAn^{sq,cat}$ (left), $NAT^{sq,cat}$ (middle), and $AnT^{sq,cat}$ (right).

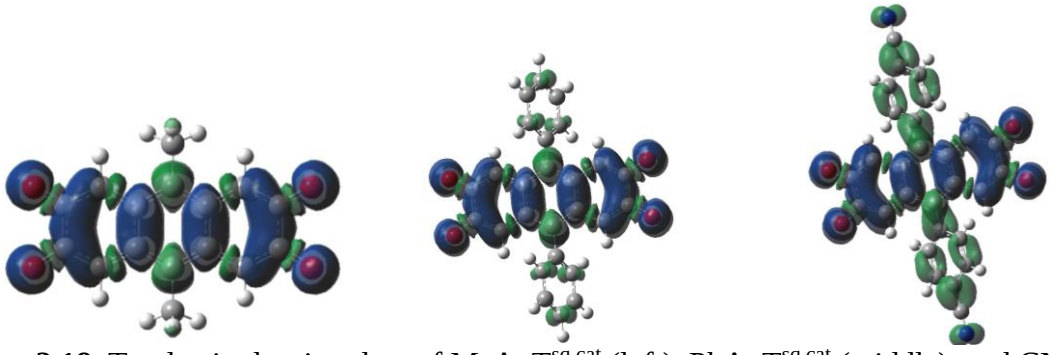

Figure 2.18. Total spin density plots of $MeAnT^{sq,cat}$ (left), $PhAnT^{sq,cat}$ (middle), and $CNPh\text{-}AnT^{sq,cat}$ (right).

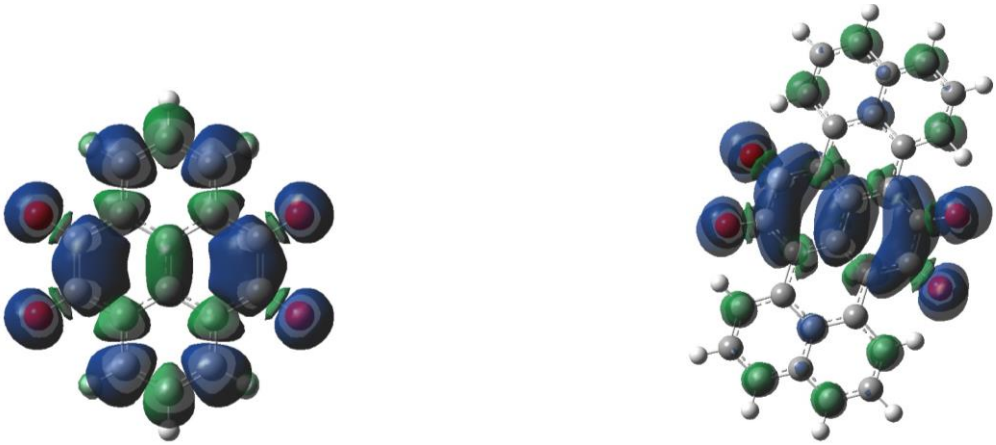

Figure 2.19. Total spin density plots of pyrene^{sq,cat} (left) and terrylene^{sq,cat} (right).

REFERENCES

REFERENCES

(1) Wolf, S. A.; Awschalom, D. D.; Buhrman, R. A.; Daughton, J. M.; von Molnár, S.; Roukes, M. L.; Chtchelkanova, A. Y.; Treger, D. M. *Science* **2001**, *294*, 1488.

(2) Fert, A. *Rev. Mod. Phys.* **2008**, *80*, 1517.

(3) Bogani, L.; Wernsdorfer, W. *Nat. Mater.* **2008**, *7*, 179.

(4) Kahn, O. *Molecular Magnetism*; VCH Publishers: New York, 1993.

(5) Mouesca, J. -M.; Chen, J. L.; Noodleman, L.; Bashford, D.; Case, D. A. *J. Am. Chem. Soc.* **1994**, *116*, 11898–11914.

(6) Koo, H. -J. *Bull. Korean Chem. Soc.* **2012**, *33*, 2338.

(7) Visser, S. P.; Stillman, M. J. *Int. J. Mol. Sci.* **2016**, *17*, 519.

(8) Claiser, N.; Souhassou, M.; Lecomte, C.; Gillon, B.; Carbonera, C.; Caneschi, A.; Dei, A.; Gatteschi, D.; Bencini, A.; Pontillon, Y.; Lelièvre-Berna, *J. Phys. Chem. B* **2005**, *109*, 2723.

(9) Zheludev, A.; Barone, V.; Bonnet, M.; Delley, B.; Grand, A.; Ressouche, E.; Rey, P.; Subra, R.; Schweizer, J. *J. Am. Chem. Soc.* **1994**, *116*, 2019.

(10) McConnell, H. M. *J. Chem. Phys.* **1956**, *24*, 764.

(11) Remenyi, C.; Reviakine, R.; Kaupp, M. *J. Phys. Chem. B* **2007**, *111*, 8290.

(12) Nguyen, M. T.; Creve, S.; Vanquickenborne, L. G. *J. Phys. Chem. A* **1997**, *101*, 3174.

(13) Fehir, Jr., R. J.; McCusker, J. K. *J. Phys. Chem. A.* **2009**, *113*, 9249.

(14) Fehir, Jr., R. J. Ph. D. Dissertation. Department of Chemistry, Michigan State University, East Lansing, MI, 2009.

(15) Carey, F. A.; Sundberg, R. J. *Advanced Organic Chemistry Part A: Structure and Mechanisms.* 5th Ed.; Springer: New York, NY, 2008.

(16) Kawai, A.; Hirakawa, M.; Abe, T.; Obi, K.; Shibuya, K. *J. Phys. Chem. A* **2001**,*105*, 9628.

(17) Rodriguez, J. H.; Wheeler, D. E.; McCusker, J. K. *J. Am. Chem. Soc.* **1998**, *120*, 12051-12068.

(18) Pierpont, C. G.; Buchanan, R. M. *Coord. Chem. Rev.* **1981**, *38*, 45.

(19) Pierpont, C. G.; Lange, C. W. *Prog. Inorg. Chem.* **1994**, *41*, 331.

(20) Pierpont, C. G. *Coord. Chem. Rev.* **2001**, *216-217*, 99.

(21) Kaim, W. *Coord. Chem. Rev.* **1987**, *76*, 187.

(22) Zanello, P.; Corsini, M. *Coord. Chem. Rev.* **2006**, *250*, 2000.

(23) Poddel'ski, A.; Cherkasov, V. K.; Abakumov, G. A. *Coord. Chem. Rev.* **2009**, *253*, 291.

(24) Sugiura, K.-I.; Arif, A. M.; Rittenberg, D. K.; Schweizer, J.; Öhrstrom, L.; Epstein, A. J.; Miller, J. S. *Chem. Eur. J.* **1997**, *3*, 138.

(25) Schrauben, J. N.; Guo, D.; McCracken, J. L.; McCusker, J. K. *Inorganica Chimica Acta*, **2008**, *361*, 3539-3547.

(26) Osanai, K.; Okazawa, A.; Nogami, T.; Ishida, T. *J. Am. Chem. Soc.* **2006**, *128*, 14008.

(27) McConnell, H., M, *J. Chem. Phys.* **1963**, *39*, 1910.

(28) Hicks, R. G.; Lemaire, M. T.; Thompson, L. K.; Barclay, T. M. *J. Am. Chem. Soc.* **2000**, *122*, 8077.

(29) Shultz, D. A.; Sloop, J. C.; Washington, G. *J. Org. Chem.* **2006**, *71*, 9104.

(30) Gaussian 09, Revision A.02, M. J. Frisch, G. W. Trucks, H. B. Schlegel, G. E. Scuseria, M. A. Robb, J. R. Cheeseman, G. Scalmani, V. Barone, G. A. Petersson, H. Nakatsuji, X. Li, M. Caricato, A. Marenich, J. Bloino, B. G. Janesko, R. Gomperts, B. Mennucci, H. P. Hratchian, J. V. Ortiz, A. F. Izmaylov, J. L. Sonnenberg, D. Williams-Young, F. Ding, F. Lipparini, F. Egidi, J. Goings, B. Peng, A. Petrone, T. Henderson, D. Ranasinghe, V. G. Zakrzewski, J. Gao, N. Rega, G. Zheng, W. Liang, M. Hada, M. Ehara, K. Toyota, R. Fukuda, J. Hasegawa, M. Ishida, T. Nakajima, Y. Honda, O. Kitao, H. Nakai, T. Vreven, K. Throssell, J. A. Montgomery, Jr., J. E. Peralta, F. Ogliaro, M. Bearpark, J. J. Heyd, E. Brothers, K. N. Kudin, V. N. Staroverov, T. Keith, R. Kobayashi, J. Normand, K. Raghavachari, A. Rendell, J. C. Burant, S. S. Iyengar, J. Tomasi, M. Cossi, J. M. Millam, M. Klene, C. Adamo, R. Cammi, J. W. Ochterski, R. L. Martin, K. Morokuma, O. Farkas, J. B. Foresman, and D. J. Fox, Gaussian, Inc., Wallingford CT, 2009.

(31) Vosko, S. H.; Wilk, L.; Nusair, M. *Can. J. Phys.* **1980**, *58*, 1200-1211.

(32) Lee, C.; Yang, W.; Parr, R.G. *Phys. Rev. B* **1988**, *37*, 785-789.

(33) Becke, A. D. *J. Chem. Phys.* **1993**, *98*, 5648-5652.

(34) Stephens, P. J.; Devlin, F. J.; Chabalowski, C. F.; Frisch, M. J. *J. Phys. Chem.* **1994**, *98*, 11623-11629.

(35) Tirado-Rives, J.; Jorgensen, W. *J. Chem. Theory Comput.* **2008**, *4*, 297-306.

(36) Glendening, E. D.; Reed, A. E.; Carpenter, J. E.; Weinhold, F. NBO 3.1; Theoretical Chemistry Institute, University of Wisconsin: Madison, WI, 1994.

(37) GaussView, Version 5, Dennington, R.; Keith, T. A.; Millam, J. M. Semichem Inc., Shawnee Mission, KS, 2009.

(38) Broze, M.; Luz, Z. *J. Phys. Chem.* **1967**, *71*, 3690.

(39) Wheeler, D. E.; McCusker, J. K. *Inorg. Chem.* **1998**, *37*, 2296-2307.

(40) Pierpont, C. G.; Attia, A. S. *Collect. Czech. Chem. Commun.* **2001**, *66*, 33.

(41) Pierpont, C. G.; Lange, C. W. *Prog. Inorg. Chem.* **1994**, *41*, 331.

(42) Akutagawa, T.; Nakamura, T. *Cryst. Growth Des.* **2006**, *6*, 70–74.

(43) Munakata, M.; Wu, L.P.; Kuroda-Sowa, T.; Yamamoto, M.; Maekawa, M.; Moriwaki, K. *Inorg. Chim. Acta* **1998**, *268*, 317–321.

(44) Semmingsen, D. *Acta Chem. Scand. B* **1977**, *31*, 11–14.

(45) Klug, A. *Acta Crystallogr.* **1965**, *19*, 983–992.

(46) Robl, C. *Z. Krist. Cryst. Mater.* **1988**, *184*, 289–293.

(47) Andersen, E.K.; Andersen, I.G.K. *Acta Crystallogra. Sect. B* **1975**, *31*, 379–383.

(48) Andersen, E.K.; Andersen, I.G.K. *Acta Crystallogr. Sect. B* **1975**, *31*, 384–387.

(49) Andersen, E. *Acta Crystallogr.* **1967**, *22*, 188–191.

(50) Andersen, E. *Acta Crystallogr.* **1967**, *22*, 191–196.

(51) Andersen, E. *Acta Crystallogr.* **1967**, *22*, 204–208.

(52) Mercuri, M. L.; Congiu, F.; Concas, G.; Sahadevan, S. A. *Magnetochemistry* **2017**, *3*, 17.

(53) Molcanov, K.; Kojic-Prodic, B. *Acta Crystallogr. Section B* **2012**, *68*, 57–65.

(54) Hellberg, J.; Dahlstedt, E.; Pelcman, M. E. *Tetrahedron*, **2004**, *60*, 8899-8912.

(55) Guo, D.; McCusker, J. K. *Inorg. Chem.* **2007**, *46*, 3257-3274.

(56) Dei, A.; Gatteschi, D.; Pardi, L.; Russo, U. *Inorg. Chem.* **1991**, *30*, 2589-2594.

(57) Wheeler, D. E.; McCusker, J. K. *Inorg. Chem.* **1998**, *37*, 2296-2307.

(58) Hansch, C.; Leo, A.; Taft, R. W. *Chem. Rev.* **1991**, *91*, 165-195.

(59) Keenan, S. L.; Peterson, K. P.; Peterson, K.; Jacobson, K. *J. Chem. Educ.* **2008**, *85*, 558.

(60) Exner, O. *Correlation Analysis of Chemical Data.* Plenum Publishing Corporation: New York, NY, 1988.

(61) Shorter, J. *Correlation analysis in organic chemistry: an introduction to linear free-energy relationships.* Oxford University Press: Oxford, 1973.

(62) Wayner, D. D. M.; Arnold, D. R. *Can. J. Chem.* **1985**, *63*, 2378.

(63) Clark, K. B.; Wayner, D. D. M. *J. Am. Chem. Soc.* **1991**, *113*, 9363.

Chapter 3. Magnetic Properties and Substituent Effect on the Modulation of Heisenberg Exchange Coupling Interactions in Chromium (III) Tetraoxo-Dimeric Complexes

3.1 Introduction

The application of spin exchange interaction in biology usually involve complicated metalloprotein molecules or their active site synthetic analogues.[1-7] These systems are synthetically more challenging for the manipulation of spin exchange. It will be more beneficial if a simpler system can be designed to tune 'on' or 'off' the spin exchange interaction without composition change, the fundamentals for spin polarization can be determined more easily with experimental tools, e.g. x-ray crystallography. The design of more advanced metalloprotein analogues then can be accomplished for similar purposes.

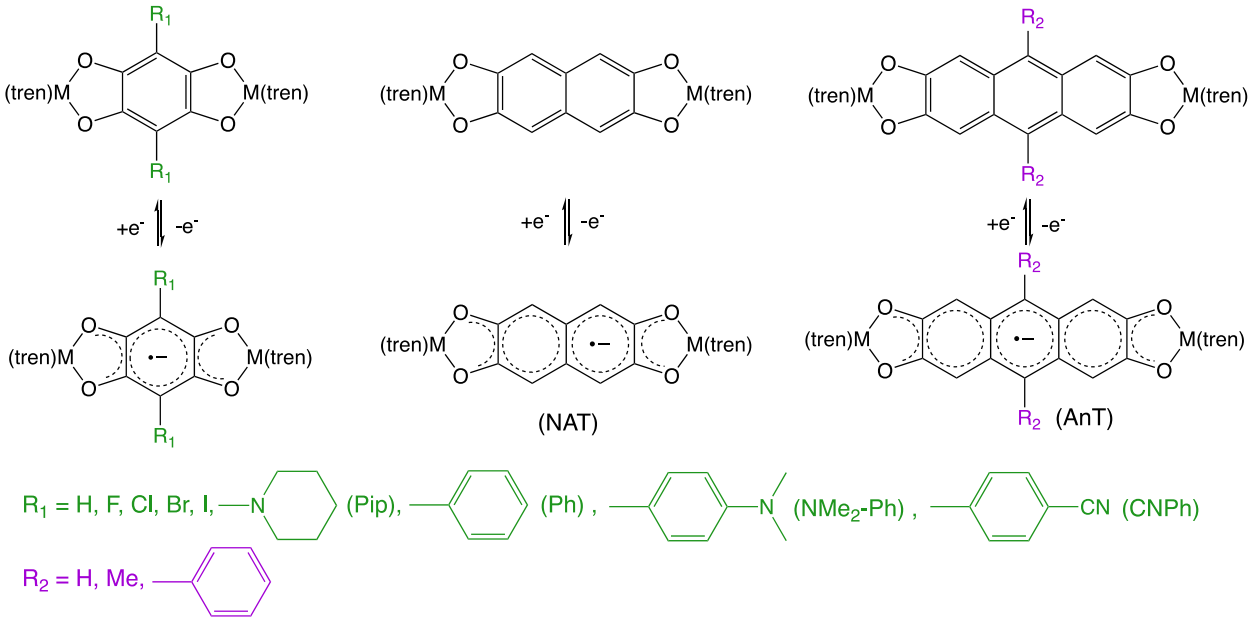

Figure 3.1. Cr^{III}-tetraoxolene quinodal complexes with a combination of diamagnetic or paramagnetic substituted-bridging ligands, where R_1 are the substituents on tetraoxoanilate, and R_2 are the substituents on 2,3,6,7-tetraoxoanthracene.

Cr (III) -tetraoxoquinoidal systems are chosen to be the system, since Cr^{III} ion (**S** = 3/2) is redox-inert and not easily reduced to Cr^{II},[8] and it is well-studied spectroscopically in the absence

of spin exchange.[9,10] When coordinating to metal center, catecholate bridging ligands can be oxidized to semiquinone (**S** = ½) to turn 'on' spin exchange. The computational results obtained in Chapter 2 can facilitate the synthetic design of the substituted analogues. The charge density of the trianionic and tetraanionic radicals can provide the information about their Lewis basicity, since increasing the negative charge density at the chelating oxygen atoms will increase the formation constant for better stability, and vice versa.[11] A series of dichromium (III) tetraoxo-quinoidal complexes are proposed as experimental targets in our studies (Fig. 3.1).

The strength of spin exchange in transitional metal complexes is proportional to the spin density of the atom in one paramagnetic center, which is directly binding to the metal center.[12-15] Thus, the control of spin density distribution can cause stronger or weaker exchange interaction. Several studies present the modulation of spin coupling constants by substituents effects in Mn(II) and Cu(II) 5-aryl-substituted semiquinones,[16] and Co (III) iminosemiquinone.[17] Cr (III) is a d^3 ion with three unpaired electrons sitting in *dxz, dyz, dxy* orbitals of π-symmetry, and they overlap with the π-symmetric unpaired electron of semiquinone ligand to have antiferromagnetic interactions. The antiferromagnetic interaction of Cr (III)-semiquinone has been observed experimentally in $[Cr_2(CTH)_2(DHBQ)Y_3$ (Y = ClO_4^-, PF_6^-),[18] [Cr(tren)(3,6-DTBSQ)](PF_6),[19] and $[Cr_2(tren)_2(CA^{sq,cat})](BPh_4)_2$.[8] No temperature dependence was observed in the variable-temperature magnetic susceptibility data for all three Cr (III) complexes because the direct exchange *J* coupling is too strong. The thermal energy applied during the SQUID measurement is not enough to overcome the spin energy gap (>>kT) to populate spins into the second excited spin states. In order to accurately fit *J* coupling constant with MagFit,[46] thermal population to access more higher energy spin states is required. Thus, the *J* constants of these Cr (III) - semiquinone systems are only estimations, > 400 cm^{-1}. Although the exchange coupling

interactions are predicted to be strong, the trend of *J* constants can provide some insight about the substituent effects on the strength.

3.2 Experimental Section

General. All chemicals were of reagent grade, purchased from Alfa Aesar, Sigma-Aldrich, Acros Organics, TCI Chemicals, Oakwood Chemicals, Strem Chemicals, or Matrix Chemicals, and used as received unless otherwise noted. Solvents were purchased from Sigma-Aldrich, Jade Scientific, Alfa Aesar, Fisher Scientific, EMD Chemicals, Mallinckrodt, or CCI and were purified using standard purification techniques. All air-sensitive and water-sensitive reactions were carried out under inert atmosphere either by standard Schlenk techniques or in dryboxes. The solvents used for these air-sensitive reactions were thoroughly dried by being stored over 4 Å molecular sieve and deoxygenated by the freeze-pump-thaw method. The ligand tris(2-aminoethyl)amine (tren) was purchased from either Sigma-Aldrich or Alfa Aesar, vacuum-distilled from NaOH with activated carbon, then degassed by the freeze-pump-thaw method, and stored in the glovebox prior to use. ^{1}H NMR and ^{13}C NMR were collected on Agilent DDR2 500 MHz NMR spectrometers equipped with 7600AS 96-sample autosamplers. Electrospray mass spectra (ESI-MS) were obtained on Waters Xevo G2-XS QTof Quadruple UPLC/MS/MS at Michigan State University Mass Spectrometry and Metabolomics Core. CHN elemental analyses were obtained on a Perkin-Elmer 2400 Series II CHNS/O Analyzer through the analytical facilities in the Chemistry department of Michigan State University.

3.2.1 Synthetic Procedures of Substituted Tetraoxoanilate, Naphthalene, and Anthracene Ligands

2,5-Dimethoxy-1,4-benzoquinone (DHBQ).[8] $BF_3 \cdot OEt_2$ (≥46.5% BF_3 basis, 9 mL, 33.8 mmol) was added to a solution of 2,5-dihydroxy-1,4-benzoquinone (1.67 g, 12 mmol) in MeOH (50 mL). The reaction mixture was stirred at 70 ˚C for 2 hours. As the mixture was heated, orange brown precipitate formed. The orange brown product was filtered, washed by cold MeOH (3 x 30 mL), and dried under vacuum overnight. Yield: 1.72 g (95%). ^{1}H NMR ($CDCl_3$, 500 MHz) δ (ppm): 3.83 (s, 6H, CH_3), 5.85 (s, 2H, Aromatic CH). ^{13}C NMR ($CDCl_3$, 500 MHz) δ (ppm): 56.84, 105.68, 159.75, 181.88.

2,5-Dibromo-3,6-dimethoxy-1,4-benzoquinone.[21] N-Bromosuccinimide (NBS) was recrystallized from boiling water before use (10 g of NBS for 100 mL of water). NBS is incompatible in contact with iron or iron salts, and plastic spatula should be used to handle it. NBS (7.2g, 40.4 mmol) was added slowly to a solution of 2,5-dimethoxy-1,4-benzoquinone (3.4g, 20.0 mmol) in DMF (100 mL), and it was stirred at room temperature (RT) for 15 hours. 50 mL of H_2O was added to quench the reaction, and the aqueous layer was extracted with EtOAc (3 x 10 mL) and followed by Et_2O (3 x 200 mL). Both EtOAc and Et_2O extracted organic layers were combined, and washed by H_2O (2 x 20 mL), brine (2 x 20 mL), and dried over Na_2SO_4. The crude product was purified by silica gel plug with hexane/$CHCl_3$ (1:1) - (0:1), and orange red product was collected. Yield: 4.58 g (70%). ^{1}H NMR ($CDCl_3$, 500 MHz) δ (ppm): 4.24 (s, CH_3). ^{13}C NMR ($CDCl_3$, 500 MHz) δ (ppm): 20.09, 62.49, 110.21, 174.93.

Bromanilic acid (H_2BA).

Route 1. A solution of 2,5-dibromo-3,6-dimethoxy-1,4-benzoquinone (1.4 g, 4.3 mmol) in anhydrous CH_2Cl_2 (100 mL) was degassed by freeze-pump-thaw method. To this solution, BBr_3 (1.6 mL, 17.3 mmol) was added slowly by a syringe at -78˚C under N_2. The reaction

mixture was stirred overnight until room temperature was attained gradually. The reaction was quenched by 10 mL of MeOH, and the solvent was evaporated under vacuum. The orange solids were washed by H_2O, and recrystallized from AcOH. Yield: 1.1 g (86%).

Route 2.[23] DHBQ (7.8 g, 5.6 mmol) was suspended in EtOH (100 mL). Br_2 (5.7 mL, 111.2 mmol) was added dropwise to the EtOH suspension above, and it was stirred at RT for 12h. The solvent was evaporated down in volume. The orange product was filtered, washed with $CHCl_3$ (3 x 20 mL), and dried under vacuum. Yield: 16.2 g (97%). Anal. Calcd $C_6H_2O_4Br_2$: C, 24.2; H, 0.7; N, 0. Found: C, 24.6; H, 0.6; N, 0. HRMS [ESI-TOF, *m/z* (rel. int.)]: $[M-H]^-$ Calcd for $[C_6H_1O_4Br_2]^-$, 296.8221; Found, 296.8231.

Fluoranilic acid (H_2FA).[24,25] Tetrafluoro-1,4-benzoquinone (1.0 g, 5.6 mmol) was dissolved in 1,4-dioxane (8 mL) and cooled at 20˚C. 4M NaOH aqueous solution (20 mL) was added dropwise into the solution above at 20˚C. The reaction mixture was vigorously shaken by hand for 30 min with intermittent cooling at 20˚C. Some brown purple product formed, and they were filtered and recrystallized from 30 mL of hot H_2O resulting in the brown purple sodium salt. The brown purple product was filtered and re-dissolved in hot H_2O (20 mL). While the solution is hot, 37% concentrated HCl was added dropwise into the sodium salt solution until the solution turned red with the formation of red precipitates. The red solids were filtered, washed with H_2O (3 x 10 mL), and dried under vacuum. Yield: 0.36 g (37%). HRMS [ESI-TOF, *m/z* (rel. int.)]: $[M-H]^-$ Calcd for $[C_6HO_4F_2]^-$, 174.9843; Found, 174.9918.

Tetraiodo-1,4-benzoquinone. [24,25] KI (4.0 g, 24 mmol) and tetrabromo-1,4-benzoquinone (2.0 g, 4.5 mmol) were mixed in EtOH (40 mL), and this suspension was refluxed for 2h. After being cooled to RT, brown red product was filtered, and washed with H_2O (3 x 10 mL), EtOH (2 x 10 mL). The brown red solids and KI (1.6 g, 9.6 mmol) were refluxed for

additional 2h. The resulted brown solids were filtered and recrystallized from EtOAc to obtain dark grey crystals. Yield: 1.55 g (56%). M. P. 270 – 274 ˚C and decompose upon melting. ^{13}C NMR (benzene-d_6, 500 MHz) δ (ppm): 130.22, 170.02. Anal. Calcd $C_6O_2I_4$: C, 72.1; H, 0; N, 0. Found: C, 24.6; H, 0.6; N, 0.

Iodanilic acid (H_2IA). [24,25] Tetraiodo-1,4-benzoquinone (1.0 g, 1.6 mmol) was suspended in EtOH/H_2O (1:2, 4.5 mL). 1.5 mL of 50% (w/v) NaOH aqueous solution was added dropwise into the suspension, and they were stirred overnight. The resulted brown purple solids were filtered, and washed with EtOH (1 x 10 mL). The solids were dissolved in H_2O (20 mL), and acidified by dropwise addition of diluted H_2SO_4 aqueous solution. Orange precipitates formed slowly during the addition, and the product was filtered and re-dissolved in H_2O (40 mL) while heating. The solution was acidified with diluted H_2SO_4 solution again, and the red product was obtained by filtration and washed with H_2O (3 x 10 mL). Yield: 0.43 g (68%). HRMS [ESI-TOF, *m/z* (rel. int.)]: $[M-H]^-$ Calcd for $[C_6HO_4I_2]^-$, 390.7964; Found, 390.8028.

2,5-Dimethoxy-3,6-diphenyl-1,4-benzoquinone.[25] A mixture of K_2CO_3 (0.69 g, 5.0 mmol), phenylboronic acid (0.533 g, 4.0 mmol), and $Pd(PPh_3)_2Cl_2$ (0.07 g, 10 mol%) in 1,4-dioxane/H_2O (20 mL/ 2 mL) was stirred at 90˚C for 30 min under N_2. H_2O was added to facilitate the dissolution of K_2CO_3, due to the low solubility of K_2CO_3 in dioxane. 2,5-Dibromo-3,6-dimethoxy-1,4-benzoquinone (0.326 g, 1.0 mmol) was added into the mixture, and the reaction was stirred at 110 ˚C for 24 h. After the reaction was cooled to RT, the reaction was diluted with 50 mL of DCM, and dried over Mg_2SO_4. The mixture was filtered through a pad of Celite and concentrated under vacuum. Red product was obtained after purification by silica flash column chromatography (n-pentane/DCM, 3:7). Yield: 0.24 g (75%). ^1H NMR ($CDCl_3$, 500 MHz) δ (ppm): 3.81 (s, 6 H, OCH_3), 7.30-7.50 (m, 10 H, ArH). ^{13}C NMR ($CDCl_3$, 500

MHz) δ (ppm): 61.3, 126.1, 127.5, 128.6, 129.8, 130.5, 154.0, 184.9. HRMS [ESI-TOF, *m/z* (rel. int.)]: $[M+H]^+$ Calcd for $[C_{20}H_{15}O_4]^-$, 321.1136; Found, 321.1127.

2,5-Dihydroxy-3,6-diphenyl-1,4-benzoquinone (H_2PhA). The synthetic procedure is similar with the demethylation to obtain H_2BA in Route 1. 2,5-Dimethoxy-3,6-diphenyl-1,4-benzoquinone (0.24 g, 0.75 mmol) reacted with BBr_3 (0.34 mL, 3.6 mmol) under N_2. Brown product was obtained after recrystallization from dioxane. Yield: 0.16 g (73%). ^{1}H NMR (acetone-d_6, 500 MHz) δ (ppm): 7.33 (t, 2 H, ArH), 7.41 (t, 4 H, ArH), 7.54 (d, 4H, ArH), 10.3 (br. s, 2H, OH). ^{13}C NMR (acetone-d_6, 500 MHz) δ (ppm): 128.4, 128.5, 131.4, 131.5, 131.8. HRMS [ESI-TOF, *m/z* (rel. int.)]: $[M-H]^-$ Calcd for $[C_{18}H_{11}O_4]^-$, 291.0657; Found, 291.0658.

2,3,6,7-Tetramethoxy-9,10-dimethylanthracene.[25,26] Acetaldehyde (7 mL, 125 mmol) in MeOH (10 mL) was added dropwise in a stirring solution of veratrole (9 mL, 72.4mmol) in AcOH (40 mL) at 0˚C for 1 h. 90% aq. H_2SO_4 (35 mL) solution was added over 1-hour period into the solution above at 0˚C for 24 h, and the mixture was vigorously stirred. As more H_2SO_4 solution was added, the reaction mixture became viscous. The dark purple mixture was poured into 500 mL of ice H_2O, and precipitation happen over time. The solvent was decanted, and the viscous tacky product was triturated and washed with EtOH. Beige product was obtained after recrystallization in $CHCl_3$. Yield: 4.4 g (37%). ^{1}H NMR ($CDCl_3$, 500 MHz) δ (ppm): 2.93 (s, 6 H, CH_3), 4.06 (s, 12 H, OCH_3), 7.38 (s, 4H, ArH). HRMS [ESI-TOF, *m/z* (rel. int.)]: $[M+H]^+$ Calcd for $[C_{20}H_{23}O_4]^+$, 327.1597; Found, 327.1595.

2,3,6,7-Tetrahydroxy-9,10-dimethylanthracene (H_4(Me-AnT)). [25,26] 1 M BBr_3 in DCM (8.6 mL, 8.6 mmol) was injected into a suspension of 2,3,6,7-tetramethoxy-9,10-dimethylanthracene (1.0 g, 3.06 mmol) in DCM (50 mL) at -78˚C under N_2, and the mixture was stirred for 1 h until the temperature slowly retained to RT. The reaction mixture was reflux for 24

h until the it turned from purple red to orange. The yellow brown product was filtered, washed by 0.2 M aq. HCl (3 x 100 mL), and H_2O (3 x 100 mL). Black product was obtained after recrystallization in AcOH. Yield: 0.68 g (82%). ^{1}H NMR (DMSO-d_6, 500 MHz) δ (ppm): 2.69 (s, 6 H, CH_3), 7.33 (s, 4 H, ArH), 9.44 (br. s, 4H, OH). HRMS [ESI-TOF, *m/z* (rel. int.)]: $[M-H]^-$ Calcd for $[C_{12}H_{15}O_4]^-$, 269.0814; Found, 269.0815.

4-(N,N-Dimethylamino)phenylboronic acid.[27,28] Mg turnings (1.22 g, 50 mmol) were added into the solution of 0.5 M LiCl in THF (50 mL) under N_2.1.0 M diisobutylaluminum hydride (DIBAL-H) in THF (0.2 mL, 0.2 mmol) was added by a syringe into the reaction mixture, and they were stirred for 5 min. 4-Bromo-N,N-dimethylaniline (4.0 g, 20 mmol) was added in, and the mixture was stirred for 15 h at RT. $B(OMe)_3$ was injected into the mixture, and stirred for an addition of 3 h at -78˚C under N_2. The reaction was quenched with 0.1 M HCl (100 mL), and extracted with EtOAc (3 x 200 mL), and dried over Na_2SO_4. The solution was concentrated under vacuum, washed by MeCN, and Et_2O. Yield: 2.0 g (61%). ^{1}H NMR (DMSO-d_6, 500 MHz) δ (ppm): 2.89 (s, 6 H, NCH_3), 6.64 (d, 2 H, ArH), 7.60 (d, 2H, ArH), 7.64 (s, 2H, OH). ^{11}B NMR (DMSO-d_6, 500 MHz) δ (ppm): 26.67.

2,7-Dimethoxy-3,6-di-(N,N-dimetylaminophenyl)benzoquinone.[30] A mixture of K_2CO_3 (0.5 g, 3.6 mmol), 4-(N,N-dimethylamino)phenylboronic acid (0.62 g, 4.0 mmol), and $Pd(PPh_3)_4$ (0.06 g, 5 mol%) in 1,4-dioxane/H_2O (20 mL/ 1 mL) was stirred at 90˚C for 30 min under N_2. H_2O was added to facilitate the dissolution of K_2CO_3, due to the low solubility of K_2CO_3 in dioxane. 2,5-Dibromo-3,6-dimethoxy-1,4-benzoquinone (0.326 g, 1.0 mmol) and Ag_2O (0.25 g, 1.0 mmol) were added into the mixture, and the reaction was stirred at 110 ˚C for 24 h. After the reaction was cooled to RT, the reaction was diluted with 50 mL of DCM, and dried over Mg_2SO_4. The mixture was filtered through a pad of Celite and concentrated under

vacuum. Purple product was obtained after purification by silica flash column chromatography (first eluent: n-pentane/DCM, 3:7, 2nd eluent: hexane/DCM/EtOAc, 8:1:1). Purple crystals were formed in hexane/DCM (8:1), which is suitable for x-ray diffraction. Yield: 0.147 g (36%). ^{1}H NMR ($CDCl_3$, 500 MHz) δ (ppm): 2.99 (s, 12 H, NCH_3), 3.78 (s, 6 H, OCH_3), 6.72 (d, 4H, ArH), 7.28 (d, 4 H, ArH). ^{13}C NMR ($CDCl_3$, 500 MHz) δ (ppm): 40.49, 61.39, 111.61, 117.54, 127.78, 131.99, 150.65, 154.06, 184.59. HRMS [ESI-TOF, *m/z* (rel. int.)]: $[M+H]^+$ Calcd for $[C_{24}H_{27}O_4N_2]^+$, 407.1987; Found, 407.1971.

2,7-Dihydroxy-3,6-di-(N,N-dimetylaminophenyl)benzoquinone (H_2NMe_2-PhA) . The synthetic procedure is similar with the demethylation to obtain H_2BA in Route 1. 2,7-Dimethoxy-3,6-di-(N,N-dimetylaminophenyl)benzoquinone (0.26 g, 0.64 mmol) reacted with BBr_3 (0.3 mL, 3.1 mmol) under N_2. Purple grey product was obtained after recrystallization from AcOH. Yield: 0.20 g (83%). ^{1}H NMR (dmso-d_6, 500 MHz) δ (ppm): 2.96 (s, 12 H, NCH_3), 6.80 (br. s, 2 H, OH), 7.29 (d, 4 H, ArH), 7.54 (d, 4H, ArH). ^{13}C NMR (dmso-d_6, 500 MHz) δ (ppm): 128.4, 128.5, 131.4, 131.5, 131.8. HRMS [ESI-TOF, *m/z* (rel. int.)]: $[M-H]^-$ Calcd for $[C_{22}H_{21}O_4N_2]^-$, 377.1505; Found, 377.1501. $[M+H]^+$ Calcd for $[C_{22}H_{23}O_4N_2]^+$, 379.1658; Found, 179.1598.

3,6-Dibromo-2,7-dihydroxynaphthalene.[29] A solution of Br_2 (1.7 mL, 32.4 mmol) in AcOH (10 mL) was added dropwise over a 20-min period to a stirring solution of 2,7-dihydroxynaphthalene (1.3 g, 9.2 mmol) in AcOH (30 mL). The reaction mixture was refluxed for 12 h. After 4 mL of H_2O was added into the mixture, yellow fluffy precipitates formed. Sn (1.0 g, 8.4 mmol) was added into the reaction portionwise, and the reaction mixture was continuously refluxed until all the yellow precipitate re-dissolved and the solution turned yellow. If that does not happen, 0.1 g of Sn should be added with sufficient reaction time until the

solution turned yellow. After additional 3 h reflux, white precipitates formed. The white product was collected through filtration, and was recrystallized from AcOH. Yield: 2.3 g (78%). ^{1}H NMR (DMSO-d_6, 500 MHz) δ (ppm): 7.05 (s, 2 H, ArH-OH), 8.02 (s, 2 H, ArH-Br), 10.52 (s, 2H, OH).

3,6-Dibromo-2,7-dimethoxynaphthalene.[30] KOH (0.42 g, 7.5 mmol) was mixed with DMSO (10 mL) and stirred for 5 min at RT under N_2. To the suspension above, 3,6-Dibromo-2,7-dihydroxynaphthalene (0.3 g, 0.94 mmol) and methyl iodide (0.23 mL, 3.76 mmol) were added, and the mixture was stirred at RT overnight. The mixture was diluted with H_2O (10 mL) with white precipitate crashed out. The product was filtered, washed by H_2O (3 x 20 mL), MeOH (1 x 10 mL), and dried under vacuum. Beige product was obtained from recrystallization in EtOH. Yield: 0.27 g (83%). ^{1}H NMR ($CDCl_3$, 500 MHz) δ (ppm): 3.97 (s, 6 H, OCH_3), 7.04 (s, 2 H, ArH-OCH_3), 7.86 (s, 2H, ArH-Br). ^{13}C NMR ($CDCl_3$, 500 MHz) δ (ppm): 56.44, 105.92, 111.60, 125.48, 131.22, 134.10, 154.50.

2,3,6,7-Tetramethoxynaphthalene.[29,31] Na metal (0.16 g, 3.2 mmol) was added portionwise to anhydrous MeOH (22 mL) under N_2. Upon complete dissolution, CuI (1.23 g, 6.4 mmol) and DMF (3.7 mL) were added. 3,6-Dibromo-2,7-dimethoxynaphthalene (1.12 g, 3.2 mmol) was added to result in an orange suspension. After the reaction was refluxed for 24 h, additional CuI (0.62 g, 3.26 mmol) and saturated $NaOCH_3$ (1.58 g Na in 15 mL MeOH, 15 mL) MeOH solution were added in order to regenerate the catalyst. The reaction was refluxed for an additional 12 h. After cooling down to RT, the reaction mixture was quenched by 11 mL of 2 M aq. HCl. It was diluted with H_2O (44 mL), and extracted with DCM (3 x 50 mL). The organic layer was washed by H_2O (3 x 30 mL), dried over $MgSO_4$, and concentrated in vacuum. Beige product was recrystallized from EtOH. Yield: 0.57g (71%). ^{1}H NMR ($CDCl_3$, 500 MHz) δ

(ppm): 3.95 (s, 12 H, OCH_3), 7.02 (s, 4 H, ArH). ^{13}C NMR ($CDCl_3$, 500 MHz) δ (ppm): 56.04, 106.07, 124.47, 148.31.

2,3,6,7-Tetrahydroxynaphthalene (H_4NAT). The synthetic procedure is similar with the demethylation to obtain H_2BA in Route 1. 2,3,6,7-Tetramethoxynaphthalene (0.57 g, 2.3 mmol) reacted with BBr_3 (1.8 mL, 18.4 mmol). The product was washed by H_2O, and dried under vacuum over P_2O_5. Yield: 0.2 g (45%). ^1H NMR (DMSO-d_6, 500 MHz) δ (ppm): 6.80 (s, 4 H, ArH), 8.94 (br. s, 4 H, OH). ^{13}C NMR (DMSO-d_6, 500 MHz) δ (ppm): 108.44, 123.82, 144.41.

2,3,6,7-Tetramethoxyanthraquinone.[27,32,33] 2,3,6,7-Tetramethoxy-9,10-dimethylanthracene (4.0 g, 12.3 mmol) and $Na_2Cr_2O_7$ (20.0 g, 76.6 mmol) were mixed in AcOH (200 mL), and refluxed for 1 h. After the mixture was cooled to RT, it was filtered to obtain bright yellow product. The product was washed by H_2O and Et_2O. Yield: 3.2 g (79%). 1H NMR ($CDCl_3$, 500 MHz) δ (ppm): 4.05 (s, 12 H, OCH_3), 7.67 (s, 4 H, ArH). ^{13}C NMR ($CDCl_3$, 500 MHz) δ (ppm): 56.77, 108.60, 128.65, 153.64, 182.20.

2,3,6,7-Tetramethoxyanthracene.[33] In order to activate Zn powders, they were washed by 3% (w/v) HCl aqueous solution twice, and H_2O, EtOH, and Et_2O once respectively. 2,3,6,7-Tetramethoxyanthraquinone (2.0 g, 8.26 mmol) and Zn (33.5 g, 510 mmol) were added to a stirring aqueous solution of 2 M NaOH (130 mL) under N_2. The mixture was heated at 100˚C for 48 h. After the reaction was cooled to RT, solids were obtained through filtration. The solids were washed by 37% HCl until no more Zn powder left. White crystals were obtained after purification by silica flash column chromatography (DCM). Yield: 1.06 g (43%). ^1H NMR ($CDCl_3$, 500 MHz) δ (ppm): 4.01(s, 12 H, OCH_3), 7.12 (s, 4 H, ArH), 8.01 (s, 2 H, ArH). ^{13}C

NMR ($CDCl_3$, 500 MHz) δ (ppm): 56.04, 104.96, 122.23, 127.60, 149.60. HRMS [ESI-TOF, *m/z* (rel. int.)]: $[M+H]^-$ Calcd for $[C_{20}H_{23}O_4]^+$, 327.1597; Found, 327.1595.

2,3,6,7-Tetrahydroxyanthracene (H_4AnT).[34,35] BBr_3 (1.4 mL, 14.4 mmol) was added by syringes into the suspension of 2,3,6,7-Tetramethoxyanthracene (0.534 g, 1.8 mmol) in DCM (50 mL) at -78˚C under N_2. The reaction mixture was stirred overnight until its temperature slowly rose back to RT. The suspension was poured to 0.1 M aq. HCl (300 mL) with white precipitate crashed out. The product was extracted with Et_2O (3 x 200 mL), and washed by H_2O (1 x 50 mL), brine (1 x 50 mL), and dried over $MgSO_4$. Beige powders were obtained after the reduction of solvent. Yield: 0.38 g (87%). ^{1}H NMR (acetone-d_6, 500 MHz) δ (ppm): 7.18(s, 4 H, ArH), 7.86 (s, 2 H, ArH), 8.49 (s, 4 H, OH). ^{13}C NMR (acetone-d_6, 500 MHz) δ (ppm): 108.47, 121.62, 128.66, 146.99. HRMS [ESI-TOF, *m/z* (rel. int.)]: $[M-H]^-$ Calcd for $[C_{14}H_9O_4]^-$, 241.0501; Found, 241.0489.

3.2.2 Synthetic Procedures of Chromium (III) Dimeric Analogues

$(Et_3NH)_2$(DHBQ) (where DHBQ is the deprotonated dianionic form of 2,5-dihydroxy-1,4-benzoquinone). To an orange solution of DHBQ (2.8 g, 20 mmol) in EtOH, Et_3N (6.4 mL, 46 mmol) was added slowly. Upon addition, the solution turned pink and precipitate formed. The dark red solids were filtered, washed with Et_2O, and dried under vacuum overnight. Yield: 5.5 g (80%).

(1) $[Cr_2(tren)_2(DHBQ^{cat,cat})](BPh_4)_2$.[8] Under N_2, tren (0.07 mL, 0.44 mmol) was added dropwise to a rapidly stirring solution of $CrCl_2$ (0.05 g, 0.4 mmol) in MeOH (40mL). A solution of $(Et_3NH)_2$(DHBQ) in 20 mL MeOH was added dropwise to the above solution, resulting in an emerald green solution. Following by additional 30 min stirring of the solution, $NaBPh_4$ (0.68g,

2 mmol) in 80 mL of MeOH was layered carefully on top. The solution was allowed to stand overnight without disturbing, and brown red crystals, suitable for X-ray diffraction, were formed slowly over time. (Do not use excess $CrCl_2$ for recrystallization, because it would form crystals of $Cr(tren)Cl_2$, which requires extra purification steps.) The product was filtered, and washed with MeOH (3 x 40 mL). Yield: 0.15 g (65%). Anal. Calcd $Cr_2C_{66}H_{78}O_4N_8B_2 \cdot CH_3OH$: C, 66.8; H, 6.9; N, 9.3. Found: C, 66.3; H, 6.8; N, 9.3.

$[FeCp^*_2](BF_4)$.[35,36] 1,4-benzoquinone (0.07 g, 0.65 mmol) was dissolved in 20 mL of Et_2O, and it was filtered to yield yellow filtrate. 48% concentrated HBF_4 (0.5 mL, 3.8 mmol) was added into the yellow filtrate while stirring. After 10 min of reaction time, a solution of decamethylferrocene, $FeCp^*_2$, (0.423 g, 1.3 mmol) in Et_2O (20 mL) was added dropwise into the reaction. Green precipitates formed after the addition, and the product was washed by Et_2O and dried under vacuum. Yield: 0.45 g (84%). HRMS [ESI-TOF, *m/z* (rel. int.)]: $[M]^+$ Calcd for $[C_{20}H_{30}Fe]^+$, 362.1697; Found, 362.1704.

(11) $[Cr_2(tren)_2(DHBQ^{sq,cat})](BPh_4)_2(BF_4)$.[8,37] Under N_2, a solution of $(FeCp^*_2)(BF_4)$ (0.14 g, 0.34 mmol) in MeCN (20 mL) was added dropwise into a stirring solution of $[Cr_2(tren)_2(DHBQ^{cat,cat})](BPh_4)_2$ (0.2 g, 0.17 mmol) in MeCN (10 mL). The solution was stirred for 6 h, which turned yellow-green. After filtration, the solvent volume of the filtrate was reduced under vacuum to 10 mL. 30 mL of DCM was added, and the mixture was filtered to eliminate excess $[FeCp^*_2](BF_4)$ salt. The filtrate was reduced in volume under vacuum again to 10 mL, and 30 mL of Et_2O was added to yield yellow brown solids. The product was filtered, washed by DCM (3 x 10 mL), and Et_2O (3 x 10 mL). Yield: 0.12 g (56%). HRMS [ESI-TOF, *m/z* (rel. int.)]: $[M]^{3+}$ Calcd for $[Cr_2C_{18}H_{38}O_4N_8]^{3+}$, 178.0609; Found, 178.0618. Anal. Calcd $Cr_2C_{66}H_{78}O_4N_8B_3F_4 \cdot CH_3OH \cdot CH_3CN$: C, 62.2; H, 6.4; N, 9.5. Found: C, 62.0; H, 6.8; N, 9.1.

$(Et_3NH)_2(CA)$. The synthesis of this compound was similar to that for $(Et_3NH)_2(DHBQ)$. H_2CA (2.1 g, 10 mmol) was used to react with Et_3N (3.0 mL, 22 mmol), and pink product was obtained. Yield: 3.1 g (76%).

(2) $[Cr_2(tren)_2(CA^{cat,cat})](BPh_4)_2$.[8] The synthesis of this complex was similar to that for $[Cr_2(tren)_2(DHBQ^{cat,cat})](BPh_4)_2$. $(Et_3NH)_2(CA)$ (0.07 g, 0.2 mmol) was used. Yellow green crystals, suitable for x-ray diffraction, were obtained by layering a solution of $NaBPh_4$ in MeOH. Yield: 0.20 g (86%). Anal. Calcd $Cr_2C_{66}H_{76}Cl_2O_4N_8B_2 \cdot CH_3OH$: C, 63.2; H, 6.3; N, 8.8. Found: C, 63.0; H, 6.4; N, 8.8.

(12) $[Cr_2(tren)_2(CA^{sq,cat})](BPh_4)_2(BF_4)$. Under N_2, a solution of $(CPh_3)(BF_4)$ (0.09 g, 0.27 mmol) in MeCN (10 mL) was added dropwise into a stirring solution of $[Cr_2(tren)_2(CA^{cat,cat})](BPh_4)_2$ (0.17 g, 0.137 mmol) in MeCN (20 mL). The solution was stirred for 6 h, which turned yellow-green. After filtration, the solvent volume of the filtrate was reduced under vacuum to 10 mL. 30 mL of DCM was added, and the mixture was filtered to eliminate excess $(CPh_3)(BF_4)$ salt. The filtrate was reduced in volume under vacuum again to 10 mL, and 30 mL of Et_2O was added to yield yellow brown solids. The product was filtered, washed by DCM (3 x 10 mL), and Et_2O (3 x 10 mL). Yield: 0.117 g (64%). HRMS [ESI-TOF, *m/z* (rel. int.)]: $[M]^{3+}$ Calcd for $[Cr_2C_{18}H_{36}O_4N_8Cl_2]^{3+}$, 200.7016; Found, 200.7025. $[Cr(tren)(C_6O_4Cl_2)]^+$ Calcd for $[CrC_{12}H_{18}O_4N_4Cl_2]^+$, 404.0111; Found, 404.0117. Anal. Calcd $Cr_2C_{66}H_{76}Cl_2O_4N_8B_3F_4 \cdot CH_3OH \cdot CH_3CN$: C, 59.1; H, 6.0; N, 9.0. Found: C, 59.0; H, 6.4; N, 8.6.

$(Et_3NH)_2(BA)$. The synthesis of this compound was similar to that for $(Et_3NH)_2(DHBQ)$. H_2BA (0.12 g, 0.4 mmol) was used to react with Et_3N (0.14 mL, 1 mmol), and pink product was obtained. Yield: 0.16 g (80%).

(3) $[Cr_2(tren)_2(BA^{cat,cat})](BPh_4)_2$. The synthesis of this complex was similar to that for $[Cr_2(tren)_2(DHBQ^{cat,cat})](BPh_4)_2$. $(Et_3NH)_2(BA)$ (0.07 g, 0.2 mmol) was used. Brown crystals, suitable for x-ray diffraction, were obtained by layering a solution of $NaBPh_4$ in MeOH. Yield: 0.20 g (86%). Anal. Calcd $Cr_2C_{66}H_{76}Br_2O_4N_8B_2 \cdot CH_3OH$: C, 59.1; H, 5.9; N, 8.2. Found: C, 59.5; H, 6.2; N, 8.2. HRMS [ESI-TOF, *m/z* (rel. int.)]: $[M]^{2+}$ Calcd for $[Cr_2C_{18}H_{36}O_4N_8Br_2]^{2+}$, 345.4971; Found, 345.4992. $[M]^{3+}$ Calcd for $[Cr_2C_{18}H_{35}O_4N_8Br_2]^{3+}$, 230.6674; Found, 230.6693. $[Cr(tren)(C_6O_4Br_2)]^+$ Calcd for $[CrC_{12}H_{18}O_4N_4Br_2]^+$, 493.9081; Found, 493.9102.

(13) $[Cr_2(tren)_2(BA^{sq,cat})](BPh_4)_2(BF_4)$. The synthetic procedure of this compound was similar to that of $[Cr_2(tren)_2(CA^{sq,cat})](BPh_4)_2(BF_4)$. Instead, $(CPh_3)(BF_4)$ (0.04 g, 0.12 mmol) was used to react with $[Cr_2(tren)_2(BA^{cat,cat})](BPh_4)_2$ (0.11 g, 0.08 mmol). Yield: 0.08 g (68%). HRMS [ESI-TOF, *m/z* (rel. int.)]: $[M]^{3+}$ Calcd for $[Cr_2C_{18}H_{36}O_4N_8Br_2]^{3+}$, 230.6674; Found, 230.6680. $[Cr(tren)(C_6O_4Br_2)]^+$ Calcd for $[CrC_{12}H_{18}O_4N_4Br_2]^+$, 493.9081; Found, 493.9088. Anal. Calcd $Cr_2C_{66}H_{76}Br_2O_4N_8B_3F_4 \cdot CH_3OH \cdot CH_3CN$: C, 55.6; H, 5.6; N, 8.5. Found: C, 55.5; H, 6.0; N, 8.2.

$(Et_3NH)_2(FA)$. The synthesis of this compound was similar to that for $(Et_3NH)_2(DHBQ)$. H_2FA (0.11 g, 0.6 mmol) was used to react with Et_3N (0.2 mL, 1.3 mmol), and violet product was obtained. Yield: 0.2 g (87%).

(4) $[Cr_2(tren)_2(FA^{cat,cat})](BPh_4)_2$. The synthesis of this complex was similar to that for $[Cr_2(tren)_2(DHBQ^{cat,cat})](BPh_4)_2$. $(Et_3NH)_2(FA)$ (0.076 g, 0.2 mmol) was used. Red purple crystals, suitable for x-ray diffraction, were obtained by layering a solution of $NaBPh_4$ in MeOH. Yield: 0.22 g (80%). Anal. Calcd $Cr_2C_{66}H_{76}F_2O_4N_8B_2 \cdot CH_3OH$: C, 64.8; H, 6.5; N, 9.0. Found: C, 64.6; H, 6.4; N, 9.3. HRMS [ESI-TOF, *m/z* (rel. int.)]: $[M]^{2+}$ Calcd for $[Cr_2C_{18}H_{36}O_4N_8F_2]^{2+}$,

285.0819; Found, 285.0822. $[M]^{3+}$ Calcd for $[Cr_2C_{18}H_{36}O_4N_8F_2]^{3+}$, 190.0546; Found, 190.0597. $[Cr(tren)(C_6O_4F_2)]^+$ Calcd for $[CrC_{12}H_{18}O_4N_4F_2]^+$, 372.0701; Found, 372.0719.

(14) $[Cr_2(tren)_2(FA^{sq,cat})](BPh_4)_2(BF_4)$. The synthetic procedure of this compound was similar to that of $[Cr_2(tren)_2(CA^{sq,cat})](BPh_4)_2(BF_4)$. Instead, $(CPh_3)(BF_4)$ (0.1 g, 0.33 mmol) was used to react with $[Cr_2(tren)_2(FA^{cat,cat})](BPh_4)_2$ (0.2 g, 0.17 mmol). Light yellow brown product was obtained after filtration and washing with DCM and Et_2O. Yield: 0.09 g (42%). HRMS [ESI-TOF, *m/z* (rel. int.)]: $[M]^{3+}$ Calcd for $[Cr_2C_{18}H_{34}O_4N_8F_2]^{3+}$, 190.0546; Found, 190.0556. $[Cr(tren)(C_6O_4F_2)]^+$ Calcd for $[CrC_{12}H_{18}O_4N_4F_2]^+$, 372.0701; Found, 372.0706. Anal. Calcd $Cr_2C_{66}H_{76}F_6O_4N_8B_3{\cdot}CH_3OH{\cdot}CH_3CN$: C, 60.5; H, 6.1; N, 9.2. Found: C, 60.6; H, 6.4; N, 8.9.

$(Et_3NH)_2(IA)$. The synthesis of this compound was similar to that for $(Et_3NH)_2(DHBQ)$. H_2IA (0.2 g, 0.6 mmol) was used to react with Et_3N (0.2 mL, 1.32 mmol), and magenta product was obtained. Yield: 0.29 g (81%).

(5) $[Cr_2(tren)_2(IA^{cat,cat})](BPh_4)_2$. The synthesis of this complex was similar to that for $[Cr_2(tren)_2(DHBQ^{cat,cat})](BPh_4)_2$. A solution of $(Et_3NH)_2(IA)$ (0.12 g, 0.2 mmol) in MeOH (40 mL) was added to a mixture of $CrCl_2$ (0.05 g, 0.4 mmol) and tren (0.07 mL, 0.44 mmol) in MeOH (40 mL). Brown crystals, suitable for x-ray diffraction, were obtained by layering a solution of $NaBPh_4$ (0.68 g, 2.0 mmol) in MeOH (40 mL). Yield: 0.16 g (57%). Anal. Calcd $Cr_2C_{66}H_{76}I_2O_4N_8B_2{\cdot}CH_3OH$: C, 55.2; H, 5.5; N, 7.7. Found: C, 55.3; H, 5.8; N, 7.9. HRMS [ESI-TOF, *m/z* (rel. int.)]: $[M]^{2+}$ Calcd for $[Cr_2C_{18}H_{35}O_4N_8I_2]^{2+}$, 392.4841; Found, 392.4861. $[M]^{3+}$ Calcd for $[Cr_2C_{18}H_{36}O_4N_8I_2]^{3+}$, 261.9920; Found, 261.9950. $[Cr(tren)(C_6O_4I_2)]^+$ Calcd for $[CrC_{12}H_{18}O_4I_2]^+$, 587.8823; Found, 587.8848.

(15) $[Cr_2(tren)_2(IA^{sq,cat})](BPh_4)_2(BF_4)$. The synthetic procedure of this compound was similar to that of $[Cr_2(tren)_2(CA^{sq,cat})](BPh_4)_2(BF_4)$. Instead, $(CPh_3)(BF_4)$ (0.06 g, 0.17 mmol)

was used to react with $[Cr_2(tren)_2(IA^{cat,cat})](BPh_4)_2$ (0.152 g, 0.11 mmol). Brown product was obtained. Yield: 0.12 g (72%). HRMS [ESI-TOF, *m/z* (rel. int.)]: $[M]^{3+}$ Calcd for $[Cr_2C_{18}H_{34}O_4N_8I_2]^{3+}$, 261.9920; Found, 261.9937. $[Cr(tren)(C_6O_4I_2)]^+$ Calcd for $[CrC_{12}H_{18}O_4N_4I_2]^+$, 587.8823; Found, 587.8843. Anal. Calcd $Cr_2C_{66}H_{76}I_2O_4N_8B_3F_4 \cdot CH_3OH \cdot CH_3CN$: C, 52.3; H, 5.3; N, 8.0. Found: C, 52.3; H, 5.7; N, 7.9.

$(Et_3NH)_2$(PhA). The synthesis of this compound was similar to that for $(Et_3NH)_2$(DHBQ). H_2PhA (0.14 g, 0.5 mmol) was used to react with Et_3N (0.17 mL, 1.3 mmol), and pink purple product was obtained. Yield: 0.16 g (67%).

(6) $[Cr_2(tren)_2(PhA^{cat,cat})](BPh_4)_2$. The synthesis of this complex was similar to that for $[Cr_2(tren)_2(DHBQ^{cat,cat})](BPh_4)_2$. $(Et_3NH)_2$(PhA) (0.07 g, 0.2 mmol) was used. Yellow brown crystals, suitable for x-ray diffraction, were obtained by layering a solution of $NaBPh_4$ in MeOH. Yield: 0.26 g (93%). Anal. Calcd $Cr_2C_{78}H_{86}O_4N_8B_2 \cdot CH_3OH$: C, 69.9; H, 6.7; N, 8.3. Found: C, 69.8; H, 7.1; N, 8.5. HRMS [ESI-TOF, *m/z* (rel. int.)]: $[M]^{2+}$ Calcd for $[Cr_2C_{30}H_{46}O_4N_8]^{2+}$, 343.1227; Found, 343.1237.

(16) $[Cr_2(tren)_2(PhA^{sq,cat})](BPh_4)_2(BF_4)$. The synthetic procedure of this compound was similar to that of $[Cr_2(tren)_2(DHBQ^{sq,cat})](BPh_4)_2(BF_4)$. Instead, $(FeCp^*_2)(BF_4)$ (0.15 g, 0.36 mmol) was used to react with $[Cr_2(tren)_2(PhA^{cat,cat})](BPh_4)_2$ (0.2 g, 0.15 mmol). The product was filtered, washed by DCM (3 x 10 mL), and Et_2O (3 x 10 mL). Yield: 0.06 g (26%). HRMS [ESI-TOF, *m/z* (rel. int.)]: $[M]^{3+}$ Calcd for $[Cr_2C_{30}H_{46}O_4N_8]^{3+}$, 228.7484; Found, 228.7494. $[Cr(tren)(C_{18}O_4H_{10})]^+$ Calcd for $[CrC_{24}H_{28}O_4N_4]^+$, 488.1516; Found, 488.1519. Anal. Calcd $Cr_2C_{78}H_{86}O_4N_8B_3F_4 \cdot CH_3OH \cdot CH_3CN$: C, 65.5; H, 6.3; N, 8.5. Found: C, 65.8; H, 6.1; N, 8.5.

$(Et_3NH)_2$(NMe$_2$-PhA). The synthesis of this compound was similar to that for $(Et_3NH)_2$(DHBQ). H_2NMe_2PhA (0.53 g, 1.41 mmol) was used to react with Et_3N (0.8 mL, 5.6

mmol), and purple product was obtained. Yield: 0.5 g (74%). HRMS [ESI-TOF, *m/z* (rel. int.)]: $[M+H]^+$ Calcd for $[C_{22}H_{23}O_4N_2]^+$, 379.1658; Found, 379.1598. $[M+2H]^{2+}$ Calcd for $[C_{22}H_{24}O_4N_2]^{2+}$, 190.0868; Found, 190.0761. $[Et_3NH]^+$ Calcd for $[C_6H_{16}N]^+$, 102.1283; Found, 102.1238. $[M-H]^-$ Calcd for $[C_{22}H_{21}O_4N_2]^-$, 377.1501; Found, 377.1551.

(7) $[Cr_2(tren)_2(NMe_2\text{-}PhA^{cat,cat})](BPh_4)_2$. The synthesis of this complex was similar to that for $[Cr_2(tren)_2(DHBQ^{cat,cat})](BPh_4)_2$. $(Et_3NH)_2(NMe_2PhA)$ (0.12 g, 0.2 mmol) was used. Red crystals, suitable for x-ray diffraction, were obtained by layering a solution of $NaBPh_4$ in MeOH. Yield: 0.25 g (87%). Anal. Calcd $Cr_2C_{82}H_{96}O_4N_{10}B_2\cdot 3CH_3OH$: C, 67.7; H, 7.2; N, 9.3. Found: C, 67.3; H, 7.8; N, 9.3. HRMS [ESI-TOF, *m/z* (rel. int.)]: $[M]^{2+}$ Calcd for $[Cr_2C_{34}H_{54}O_4N_{10}]^{2+}$, 385.6610; Found, 385.6565. $[M]^{3+}$ Calcd for $[Cr_2C_{34}H_{54}O_4N_{10}]^{3+}$, 257.4433; Found, 257.4416.

(17) $[Cr_2(tren)_2(NMe_2\text{-}PhA^{sq,cat})](BPh_4)_2(BF_4)$. The synthetic procedure of this compound was similar to that of $[Cr_2(tren)_2(DHBQ^{sq,cat})](BPh_4)_2(BF_4)$. Instead, $(FeCp^*_2)(BF_4)$ (0.2 g, 0.13 mmol) was used to react with $[Cr_2(tren)_2(NMe_2\text{-}PhA^{cat,cat})](BPh_4)_2$ (0.11 g, 0.26 mmol). Yield: 0.09 g (45%). HRMS [ESI-TOF, *m/z* (rel. int.)]: $[M]^{3+}$ Calcd for $[Cr_2C_{34}H_{54}O_4N_{10}]^{3+}$, 257.4433; Found, 257.4450. $[Cr(tren)(C_{22}H_{20}O_4N_2)]^+$ Calcd for $[CrC_{28}H_{38}O_4N_6]^+$, 274.2360; Found, 274.2355. Anal. Calcd $Cr_2C_{82}H_{96}O_4N_{10}B_3F_4\cdot 3CH_3OH\cdot CH_3CN$: C, 63.9; H, 6.8; N, 9.4. Found: C, 63.7; H, 6.8; N, 9.3.

(10) $[Cr_2(tren)_2(Me\text{-}AnT^{cat,cat})](BPh_4)_2$. $[Cr(tren)Cl_2]Cl$ (0.12 g, 0.4 mmol) in $MeOH/H_2O$ (1:1, 40 mL) was degassed by the freeze-pump-thaw method. In a drybox, Et_3N (0.2 mL, 1.0 mmol) was added dropwise to a rapidly stirring suspension of Me-AnT (0.05 g, 0.2 mmol) in MeOH (20 mL). Under N_2, the above solution was cannula-transferred to the $[Cr(tren)Cl_2]Cl$ solution. The reaction mixture was stirred under reflux (c.a. 70˚C) for 2 days. After the reaction was cooled to RT, the solvents were evaporated under vacuum, and the

reaction was pumped into the drybox for workup. In the drybox, the product was dissolved in MeCN, and filtered. $NaBPh_4$ (0.68g, 2 mmol) in 80 mL of MeCN was layered carefully on top the filtrate for metathesis and recrystallization. Dark green crystals, suitable for x-ray diffraction, were obtained. Yield: 0.09 g (59%). Anal. Calcd $Cr_2C_{76}H_{86}O_4N_8B_2 \cdot CH_3OH$: C, 69.4; H, 6.8; N, 8.4. Found: C, 69.8; H, 6.6; N, 8.6. HRMS [ESI-TOF, *m/z* (rel. int.)]: $[M]^{2+}$ Calcd for $[Cr_2C_{18}H_{14}O_4N_8]^{2+}$, 317.1070; Found, 317.1066. $[Cr(tren)(C_{14}H_8O_4)]^+$ Calcd for $[Cr_2C_{34}H_{54}O_4N_8]^+$, 438.1359; Found, 438.1385.

(18) $[Cr_2(tren)_2(Me\text{-}AnT^{sq,cat})](BPh_4)_2(BF_4)$. The synthetic procedure of this compound was similar to that of $[Cr_2(tren)_2(CA^{sq,cat})](BPh_4)_2(BF_4)$. Instead, $(CPh_3)(BF_4)$ (0.04 g, 0.12 mmol) was used to react with $[Cr_2(tren)_2(Me\text{-}AnT^{cat,cat})](BPh_4)_2$ (0.1 g, 0.08 mmol). Yield: 0.06 g (58%). HRMS [ESI-TOF, *m/z* (rel. int.)]: $[M]^{3+}$ Calcd for $[Cr_2C_{18}H_{14}O_4N_8]^{3+}$, 220.7484; Found, 220.7482. $[Cr(tren)C_{16}H_{12}O_4]^+$ Calcd for $[CrC_{22}H_{30}O_4N_4]^+$, 446.1672; Found, 446.1670. Anal. Calcd $Cr_2C_{76}H_{86}O_4N_8B_3F_4 \cdot CH_3OH \cdot CH_3CN$: C, 64.9; H, 6.4; N, 8.6. Found: C, 64.8; H, 6.6; N, 8.6.

(8) $[Cr_2(tren)_2(NAT^{cat,cat})](BPh_4)_2$. The synthesis of this complex was similar to that for $[Cr_2(tren)_2(Me\text{-}AnT^{cat,cat})](BPh_4)_2$.Green crystals were obtained by layering a solution of $NaBPh_4$ in MeOH; however, the crystals were too small for x-ray diffraction. Yield: 0.12 g (51%). Anal. Calcd $Cr_2C_{70}H_{80}O_4N_8B_2 \cdot 2CH_3OH \cdot CH_3CN$: C, 66.9; H, 6.9; N, 9.5. Found: C, 66.5; H, 6.6; N, 9.1. HRMS [ESI-TOF, *m/z* (rel. int.)]: $[M]^{2+}$ Calcd for $[Cr_2C_{22}H_{40}O_4N_8]^{2+}$, 292.0992; Found, 292.1009. $[M]^{3+}$ Calcd for $[Cr_2C_{22}H_{40}O_4N_8]^{3+}$, 194.7328; Found, 194.7341. $[Cr(tren)(C_{10}H_6O_4)]^+$ Calcd for $[CrC_{16}H_{24}O_4N_4]^{3+}$, 388.1203; Found, 388.1195.

(18) $[Cr_2(tren)_2(NAT^{sq,cat})](BPh_4)_2(BF_4)$. The synthetic procedure of this compound was similar to that of $[Cr_2(tren)_2(DHBQ^{sq,cat})](BPh_4)_2(BF_4)$. Instead, $(CPh_3)(BF_4)$ (0.05 g, 1.4 mmol)

was used to react with $[Cr_2(tren)_2(NAT^{cat,cat})](BPh_4)_2$ (0.12 g, 0.096 mmol). Yield: 0.048 g (38%). HRMS [ESI-TOF, *m/z* (rel. int.)]: $[M]^{3+}$ Calcd for $[Cr_2C_{22}H_{40}O_4N_8]^{3+}$, 194.7328; Found, 194.7334. $[Cr(tren)(C_{10}H_6O_4)]^+$ Calcd for $[CrC_{16}H_{24}O_4N_4]^+$, 388.1203; Found, 388.1248.

(9) $[Cr_2(tren)_2(AnT^{cat,cat})](BPh_4)_2$. The synthesis of this complex was similar to that for $[Cr_2(tren)_2(Me\text{-}AnT^{cat,cat})](BPh_4)_2$. Recrystallization was unsuccessful, so no crystal structure for x-ray diffraction was obtained. Yield: 0.14 g (55%). Anal. Calcd $Cr_2C_{74}H_{82}O_4N_8B_2\cdot 2CH_3OH\cdot 2CH_3CN$: C, 67.7; H, 6.8; N, 9.9. Found: C, 68.1; H, 7.2; N, 9.6. HRMS [ESI-TOF, *m/z* (rel. int.)]: $[M]^{2+}$ Calcd for $[Cr_2C_{18}H_{14}O_4N_8]^{2+}$, 317.1070; Found, 317.1066. $[Cr(tren)(C_{14}H_8O_4)]^+$ Calcd for $[Cr_2C_{34}H_{54}O_4N_{10}]^{3+}$, 438.1359; Found, 438.1385.

3.2.3 Physical Measurements

X-Ray Single-Crystal Structure Determinations. Single-crystal structure measurement for all Cr (III) dimeric complexes was acquired at the center for crystallographic research of Michigan State University. The crystals were mounted on nylon loops using small amount of paratone oil. X-ray diffraction data were collected at 173 K on Bruker SMART APEX II CCDs (charge coupled device) either with Mo Kα radiation (λ = 0.71073 Å) using a 3-axis goniometer with Oxford 600 low-temperature device or with Cu Kα radiation (λ = 1.54178 Å) using a 3-axis goniometer APEX II diffraction system with Oxford Cyrosystream 700 low-temperature device. Each system is equipped with a camera for viewing the crystals and a Pentium PC to control the diffractometer. The total number of runs and images was based on results from the program **COSMO**,[38] of which redundancy was expected to be 4.0 and completeness of 100% out to 0.83 Å for the Mo Kα radiation diffractometer or 0.81 Å for the Cu Kα radiation diffractometer. Cell parameters were retrieved and refined using the **SAINT** software.[39] Scaling and absorption

corrections were applied by the **SAINT**[39] for Lorentz and polarization factors. A multi-scan absorption correction was performed by **SADABS**-2014/5.[40] The structures were solved by intrinsic phasing using **ShelXT**[41] structure solution program. The structures were refined by least squares using **XL**-2014/6[42] with **Olex2**[43] incorporated.

All non-hydrogen atoms were refined anisotropically. The positions of hydrogen atom were calculated geometrically and refined using the riding model, except for the hydrogen atoms on the non-carbon atoms, which was found by difference Fourier methods and refined isotropically.

Table 3.1. Crystallographic data for Complex **1**, **2**, **4** and **5**.

	1	**2**	**4**	**5**
Empirical Formula	$C_{68}H_{86}B_2Cr_2N_8O_6$	$C_{72}H_{100}B_2Cr_2F_2N_8O_{10}$	$C_{68}H_{84}B_2Cr_2Br_2N_8O_6$	$C_{68}H_{76}B_2Cr_2I_2N_8O_6$
Formula Weight (g/mol)	1237.07	1401.22	1394.87	1488.85
Temperature (K)	173(2)	173(2)	173(2)	173(2)
Crystal System	Monoclinic	monoclinic	Monoclinic	monoclinic
Space Group	$P2_1/c$	$P2_1/n$	$P2_1/n$	$P2_1/n$
a (Å)	9.6548(12)	9.9610(9)	13.5437(16)	13.4573(3)
b (Å)	14.919(2)	29.248(3)	9.7886(12)	9.9351(2)
c (Å)	22.171(3)	12.8274(12)	25.008(3)	25.0568(5)
β (˚)	98.059(2)	104.313(6)	96.2718(15)	96.674(2)
Volume (Å^3)	3162.0(8)	3621.1(6)	3295.5(7)	3327.38(12)
Z	2	2	2	2
D_{calc} (g/cm^3)	1.299	1.278	1.406	1.486
Radiation	MoKσ	CuKσ	MoKσ	CuKσ
Goodness of Fit (F^2)	1.050	1.053	1.029	1.036
R_1 ($I \geq 2\sigma(I)$)[a]	0.0403	0.0691	0.0414	0.0455
wR_2 ($I \geq 2\sigma(I)$)[b]	0.1052	0.1913	0.0995	0.1230

[a] $R_1 = \sum \frac{||F_o| - |F_c||}{\sum |F_o|}$. [b] $wR_2 = [\sum w(F_o^2 - F_c^2)^2 / \sum w(F_o^2)^2]^{1/2}$, $w = 1/[\alpha^2(F_o^2) + (aP)^2 + bP]$, where $P = [F_o^2 + F_c^2]/3$.

Table 3.2. Crystallographic data for Complex **6**, **7** and **10**.

	6	**7**	**10**
Empirical Formula	$C_{80}H_{94}B_2Cr_2N_8O_6$	$C_{44.5}H_{62}BCrN_5O_{5.5}$	$C_{76}H_{86}B_2Cr_2N_8O_6$
Formula Weight (g/mol)	1389.25	817.8	1301.14
Temperature (K)	173(2)	173(2)	173(2)
Crystal System	Monoclinic	monoclinic	Triclinic
Space Group	$P2_1/c$	$P2_1/c$	$P\overline{1}$
a (Å)	19.4630(6)	14.0445(7)	9.6955(2)
b (Å)	16.0465(5)	10.1824(5)	10.3278(2)
c (Å)	23.1461(7)	31.2970(13)	18.9856(4)
α (˚)	90.00	90.00	102.6000(10)
β (˚)	101.534(2)	95.492(3)	91.614(2)
γ (˚)	90.00	90.00	96.949 (2)
Volume ($Å^3$)	7082.9(4)	4455.1(4)	1838.75(7)
Z	4	4	1
D_{calc} (g/cm^3)	1.303	1.219	1.175
Radiation	CuKσ	CuKσ	CuKσ
Goodness of Fit (F^2)	1.022	1.044	1.043
R_1 ($I \geq 2\sigma(I)$)[a]	0.0631	0.0782	0.0690
wR_2 ($I \geq 2\sigma(I)$)[b]	0.1539	0.2092	0.1905

[a] $R_1 = \sum \frac{||F_o| - |F_c||}{\sum |F_o|}$. [b] $wR_2 = [\sum w(F_o^2 - F_c^2)^2 / \sum w(F_o^2)^2]^{1/2}$, $w = 1/[\alpha^2(F_o^2) + (aP)^2 + bP]$, where $P = [F_o^2 + F_c^2]/3$.

Electronic Absorption Measurement. Electronic absorption spectra were measured using a Varian Cary 50 UV-vis spectrophotometer for all $[Cr_2(tren)_2(L^{cat,cat})](BPh_4)_2$ at a spectral resolution of ≤ 1.5 nm, due to the extreme air-sensitivity of the samples and the spectra were corrected and normalized based on the spectra of $[Cr_2(tren)_2(L^{sq,cat})](BPh_4)(BF_4)$. The high-resolution spectra of $[Cr_2(tren)_2(L^{sq,cat})](BPh_4)(BF_4)$ were recorded on a Perkin-Elmer Lambda 1050 UV-vis/NIR spectrophotometer at a spectral resolution of 0.2 nm. Data were obtained on samples dissolved in MeCN, which had been degassed, dried over neutral alumina, and stored under an inert atmosphere. All solutions were prepared in a N_2-flushed drybox in 1 cm pathlength air-tight optical cells.

Differential Scanning Calorimetry. Differential scanning calorimetry (DSC) measurement were conducted for thermal characterization of solid samples, including melting behavior, degree of crystallinity, sample morphology, and possible purity. The DSC reactor is

locating in Dr. Donald Morelli's lab in the department of Chemical Engineering and Material Science at Michigan State University. The data were collected by Dr. Jared Williams on a Netzsch DSC 200-F3 Maia with aluminum crucibles. This instrument has a temperature range of 50 – 600 ˚C, and is calibrated by 100 mg of a Al_2O_3 single crystal standard for the calculation of heat capacity before measurement. All measurements were performed under constant flow of argon to ensure sample stability from oxidation, and sample masses are c.a. 50 to 200 mg.

3.3 SQUID Variable-Temperature Magnetic Susceptibility Measurements

General. Magnetic susceptibility measurement was collected in direct-current (DC) scan mode using a Quantum Desgien MPMS® 3 SQUID magnetometer Cryogen Free with EverCool® He gas regulator interfaced to a Dell PC. Data were collected in an applied field of 1 T. $[TMENH_2](CuCl_4)$ (TMEN = $(CH_3)_2N(CH_2)_2N(CH_3)_2$) was used as a calibration standard and temperature error check.[44] Temperature was ramped up with small temperature increments to ensure the samples were thermally equilibrated. Data were corrected for diamagnetism of the sample using Pascals' constants,[45] and the measured susceptibility of the sample holder, including a plastic straw and a plastic sealed bag. Magnetic data for all measured complexes were fitted to an operator-equivalent form of the Heisenberg-Dirac-van-Vleck Hamiltonian given in Eq. 3.1 using MAGFIT,[46] and were reported as effective magnetic moment (μ_{eff}). Paramagnetic impurity (5 mol % of an S = ½ compound) and temperature-independent paramagnetism (200 x 10^{-6} cgsu for each Cr (III) center) were included in fitting.

3.3.1 Sample Preparation for Powders

SQUID measurement is widely used for measurement the magnetic properties of materials or tightly packed and pressed solid both in academia and industry. The sample packing and mounting techniques have been maturely developed by Quantum Design, and various sample holders for materials are commercially available by the company. However, magnetic measurement done for powder samples is not as common. As far as I know, it is not very commonly done in industry, and materialists and physicists usually conduct their magnetic experiments on materials in academia. Magnetochemists, who conduct powder measurement, each develop their own SOPs, which are not widely accessible for other users.

The way we prepared powder samples is to pack them in a 1.5 x 1.5 cm plastic bag, and roll the packed sample into a 5 x 5 mm square so that it can be fit into a plastic straw holder. Before packing the sample, it needs to be ground into fine powder. The packing of powder samples was performed in a N_2-flushed drybox due to the air sensitivity of the Cr(III) complexes. Another way to pack air-sensitive samples done by Professor Aaron L. Odom's group is to use a food vacuum sealer, and it can vacuum seal the powder sample in a drybox to prevent it from exposing to air. After that, similar technique was used to roll and fit the sealed sample into a straw holder. One problem arise from both preparations is that the shapes of these rolled 5 x 5 mm samples are not identical. Since SQUID measurement is a very sensitive measurement, the slight shape change can cause c.a. 1-5% deviation in sample data. Gelatin capsules are recommended by Quantum Design as sample holders with cotton filler to prevent powder from moving while performing DC scan measurement.[47] Two issues can be caused by these capsules: one is that the background contribution of the capsule and cotton is too large to convolute the

sample signal if the sample is a magnetically diluted sample; anther one is that the size of this capsule exceeds 5 x 5 mm.

The sample is moved linearly over several centimeters up and down through second-order gradiometer superconducting detection coils during the DC scan. The single turn-wound clockwise upper coil (-1), the two turn-wound counter-clockwise center coils (+1), and another single turn-wound clockwise bottom coil (+1) in the detection coils within the MPMS® 3 SQUID magnetometer are each about 2 cm apart.[30] If the sample size exceeds 5 x 5 mm, the sample moved through the coils can be detected by both the upper and center coils at a time, and the signal will be partly cancelled. Therefore, the data collected will all be resulted in smaller magnetic moment. The sample need to be centered in the plastic straw at 66 $\pm$ 3 mm. If the height of the sample exceeds greater than 10 mm, reduced magnetization will be obtained due to the sample position outside of the second-order gradiometer superconducting detection coils.

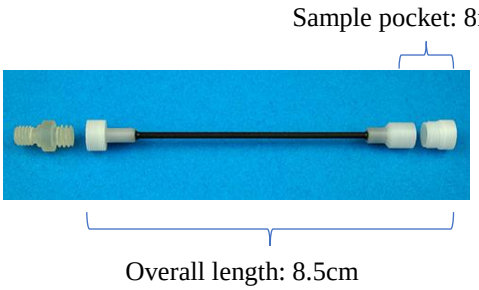

Figure 3.2. Quantum Design Delrin® liquid sample holder.

Quantum Design provides a Delrin® liquid sample holder (Fig. 3.2.). This sample holder can be used as a powder holder in the future. There are two major advantages of employing this sample holder: one is that the size of the sample socket is consistent, so we will not have the concern about size change between sample measurements; another one is its heat resistance for higher temperature measurement, > 350 K. However, the cost of this holder is $220, which is much more expensive than using plastic bags to pack samples. Quantum Design provides another

alternative sample holder, including a Delrin® liquid sample holder and a brass half-tube. This Delrin® liquid sample holder will be snapped into the center of a brass tube for the measurement. However, this setup is not recommended, because the sample socket of this Delrin® liquid sample holder is very small, which cannot hold a lot less sample (Fig. 3.3.), and the background contribution of brass material is too intense magnetic signal to convolute magnetic diluted sample signal.

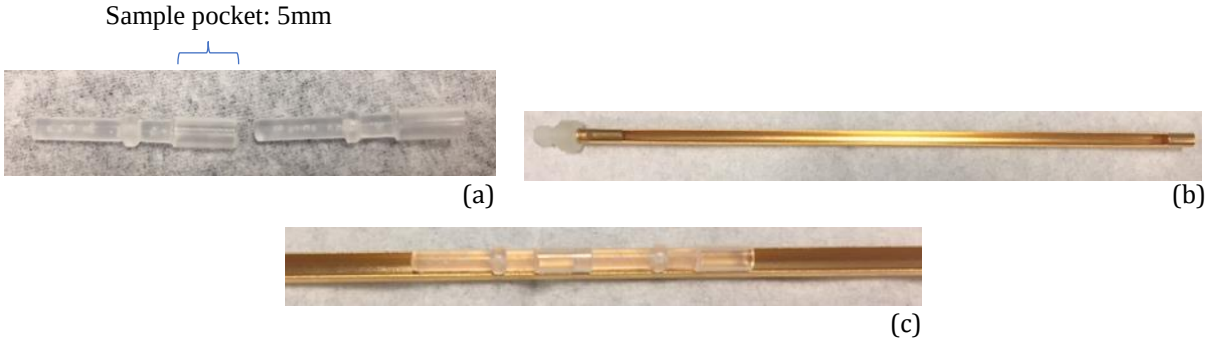

Figure 3.3. (a) Quantum Design Delrin® powder sample holder; (b) Brass half-tube; (c) a Delrin® powder sample holder snapped into a brass half-tube.

3.3.2 Temperature Sequence for Variable-Temperature Magnetic Data Collection

For variable-temperature magnetic measurement, the system is generally kept at each temperature point for additional 5 to 10 min before data collection to ensure thermal equilibrium of the sample and the sample chamber (see Sequence 3.1 in Appendix). Instead, the sequence (Sequence 3.2 in Appendix) employed for my samples is to ramp up temperature with small increments to ensure thermally equilibrium. Data were collected using both sequences for the same sample, and they are the same within error, <1%.

Temperature independence of the $[Cr_2(tren)_2(CA^{sq,cat})]^{3+}$ data[1] at 2 – 350 K fails to populate higher-energy spin states to accurately determine *J*. The energy applied at 350K is not high enough to overcome ΔE and thermally populate higher spin states. MPMS® 3 SQUID has a temperature range of 1.8 – 400 K, and it provides an option to use an external oven heater stick

for higher temperature measurement, 300 – 1000 K. Magnetic data of all $[Cr_2(tren)_2(L^{sq,cat})]^{3+}$ were obtained from 2 to 400 K, because specially tailored sample holder is required for the use of an external oven.

However, the plastic bag holding the sample starts to melt at above 350 K. When holding sample at above 350 K for 5 or more minutes, the plastic bag will be broken eventually and cause sample spilling inside the sample to cause contamination of the instrument and inaccurate data. The same problem will not be encountered when change the temperature point with small increments, and this is another reason that Sequence 3.2 was used for data collection.

3.4 Results and Discussions

3.4.1 Synthesis and Characterization.

The benefit of employing the quinoidal ligands is their reversible redox properties. By combining these quinoidal ligands with relatively redox-inert metal ions, Cr(III), it allows us to systematically study the effect of spin exchange on the physical and photophysical properties without changing their overall composition of elements and drastically altering their structures. Complexes prepared for this study are based off the previous work of Dr. Dong Guo[8], a former group member in the McCusker group.

The dianionic solid forms of THB, H_2FA, H_2CA, H_2BA, H_2IA, H_2PhA, and H_2NMe_2-PhA are stable in air, and their dianionic forms are used as starting materials for synthesis of dichromium (III) complexes. The synthetic procedures of these quinoidal organic compounds are vastly different even though they are the derivatives of one another. Both THB and H_2CA are commercially available, which are used without further purification. The synthesis of H_2IA starts with bromanil, and it is a two-step synthetic procedure. After obtaining iodanil, which cannot be

purchased commercially, it was reacted with NaOH at c.a. 19˚C. In order to boost the reaction, it needs to be hand shaken. Both H_2PhA, and H_2NMe_2-PhA are synthesized through Suzuki coupling. These reactions proceed at c.a. 110˚C to increase the solubility of all starting materials in 1,4-dioxane and allow fully coupling to the 1,4-positions of 2,5-Dibromo-3,6-dimethoxy-1,4-benzoquinone. Mono-coupling benzoquinone will be formed as the primary product at ≤ 70˚C. However, the products can be reduced fully into their benzene forms under high heat. Ag_2O therefore was added to prevent the reduction of benzoquinone. Both compounds have to be purified by running through a silica gel flash column. For H_2PhA, the product will be eluted out from the first orange band due to its low polarity. However, one eluent cannot fully purify H_2NMe_2-PhA. With the first eluent, DCM/n-pentane (6:4), the first yellow-orange impurity band can be eliminated, and the product was stuck on top of the stationary phase due to its high polarity. With the second eluent, hexane/EtOAc/DCM (8:1:1), the product was collected as the first magenta band. When mono-coupling benzoquinone product was formed, the band was violet. DCM was added into the eluent to increase the solubility of the mixture, since H_2NMe_2-PhA is insoluble in hexane. Alumina can be used as the stationary phase for H_2NMe_2-PhA for its weakly acidity. But the impurity eluted out in DCM/n-pentane is weakly basic, silica gel is chosen as the stationary phase instead. Sands are not recommended to be used during the packing of these silica gel column, because the compound mixtures will bleach on sands.

The synthesis of other derivatives, including 2,7-dihydroxy-3,6-di(4-cyano phenyl)benzoquinone (H_2(CN-PhA)), 2,7-dihydroxy-3,6-dicyanobenzoquinone (H_2CNA), 2,7-dihydroxy-3,6-dipiperidinobenzoquinone (H_2PipA), and 2,3,6,7-tetrahydroxy-9,10-diphenylanthracene (H_4(Ph-AnT)), was attempted. The synthetic procedures involve multiple

steps, and some of them have been established. Future students, who follow up this project, can attempt the synthesis based on my suggestions, which will be further discussed in Chap. 6.

The synthetic procedures for the halogen series and phenyl derivatives metal complexes are very similar. However, due to the ligand nature of the naphthalene and anthracene quinoidal ligands, the synthesis was modified. The choice of metals was determined by the desire of limiting redox activity only to the quinoidal ligands. As discussed previous in our introduction, tren is widely used as a capping ligand in many transition metal complexes due to its formation of a single isomer when bound to metal, and it will not directly affect the absorption spectra of the compounds.

The dianionic forms of THB, H_2FA, H_2CA, H_2BA, H_2IA, H_2PhA, and H_2NMe_2-PhA are used as starting materials to react with Cr (II), and these dianionic forms are very air stability. Deprotonated anilates appear to have four resonance structure (Fig. 3.4). These ligands are chosen for their redox properties and multiple chelating/binding modes. Upon one electron reduction, the dianionic version (L^{2-}) is converted into their radical form $[L^{sq,cat}]^{3-}$. We believe that neither any of the protonated or deprotonated isolated form of $[L^{sq,cat}]^{3-}$ has been reported in literature. The only report about the detection of $CA^{sq,cat}$ formation was in aqueous NaOH with a reductant $Na_2S_2O_4$ added.[31] The fully reduced form, $[L^{cat,cat}]^{4-}$, is extremely air sensitive, and its deprotonated form is only stable in solution in the presence of a strong reductant, i.e. Na metal or $Na_2S_2O_4$. Some of the protonated form, H_4L, can be prepared and isolated, when stored dry under inert atmosphere. However, not all derivatives were able to prepared and isolated, and more information will be discussed in Chapter 4.

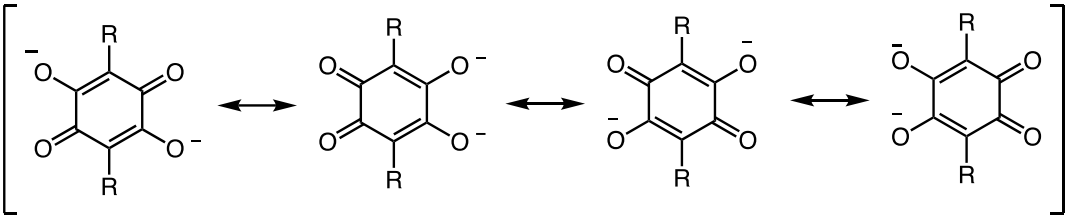

Figure 3.4. Resonance structure of substituted 3,6-R-tetraoxoquinone.

The choice of chromium was not only motivated by its relatively redox-inert property, but also its well-studied and well-documented physical and photophysical properties.[9,10,49] These properties simplify the characterization features contributed by Cr (III), and allow us to focus on the effect of spin exchange across the series of complexes. Our initial synthetic approach of the anilate bridging Cr (III) dimers is inspired by the route of a similar system, $[Cr_2(CTH)_2(DHBQ)](PF_6)_2$, reported by Dei and co-workers.[18] Cr (II) is a much more labile form, and two Cr (II) react with the dianionic ligands, the (sq, sq) form, via redox reactions. $[Cr^{II}(tren)Cl]Cl$ was generated in situ because of its extreme air-sensitivity. When binding to [Cr(tren)Cl]Cl, the ligand got fully reduced to its (cat, cat) form; meanwhile, Cr (II) was oxidized to Cr (III) formed. The summary of synthetic routes is shown in Scheme 3.1. Only 2 equivalents (eq.) or slight over amount of [Cr(tren)Cl]Cl should be used to react with anilate bridging ligands. When 3 or more eq. of [Cr(tren)Cl]Cl were added to the reaction, the crystal form of $[Cr(tren)Cl](BPh_4)$ was grown (Appendix Figure 3.82) and mixed with the desired Cr (III) dimers, which increases the difficulty of product isolation. If starting from two Cr (III) with the (cat, cat), fully reduced, form of the ligands, the coordination reaction require heat to be applied, and the (cat, cat) form is extremely air-sensitive as mentioned above. This will increase the difficulty of preserving the reaction from oxidation under inert atmosphere, since $[Cr_2(tren)_2(Anilate^{cat,cat})]^{2+}$ complexes are also extremely air-sensitive in both solid and solution states. The paramagnetism of these complexes make NMR spectroscopy inaccessible for

characterization, and these products were characterized by ESI mass spectrometry and x-ray crystallography. $[Cr(tren)(Anilate^{cat,q})]^{+}$ was detected by ESI+; however, it is not known that whether this product was formed during the reaction or via the ionization and fragmentation while passing through instrument under high voltage.

Scheme 3.1. General synthetic routes of $[Cr_2(tren)_2(Anilate^{cat,cat})](BPh_4)_2$ and $[Cr_2(tren)_2(Anilate^{sq,cat})](BPh_4)_2(BF_4)$, where anilate represents substituted anilate bridging ligands, DHBQ, FA, CA, BA, IA, PhA, or NMe_2-PhA.

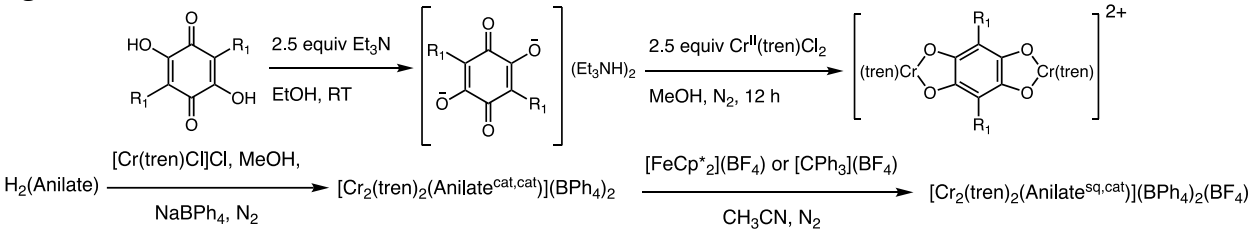

Due to the binding nature of anthracene (AnT) and naphthalene (NAT), the reaction of Cr (III) dimers have to start with H_4NAT, H_4AnT, and H_4(Me-AnT). Direct oxidation of these kind of polycyclic aromatic hydrocarbons (PAHs), such as naphthalene, anthracene, phenanthrene, terrylene, and pyrene, happen readily and are reported in literature (Figure 3.5).[51-53] However, these quinone derivatives alter the binding motives between these PAHs ligand with metal ion.

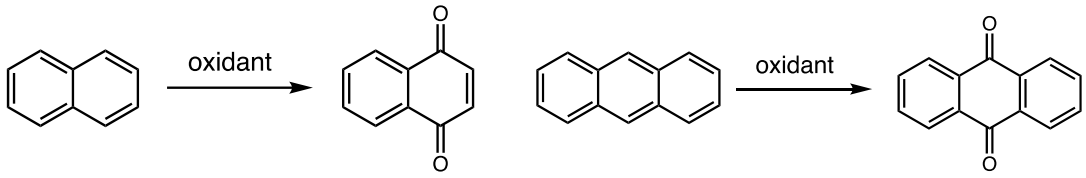

Figure 3.5. Oxidation of naphthalene and anthracene to their quinone derivatives.

Instead of using our original approach with $[Cr^{II}(tren)Cl]Cl$ and quinones, $[Cr^{III}(tren)Cl_2]Cl$ was added to react with H_4NAT, H_4AnT, or H_4(Me-AnT) for our systems. The synthetic routes of these AnT/NAT bridging Cr (III) dimeric systems are summarized and shown in Scheme 3.2. However, the reaction needed to be transferred out from the drybox and refluxed using Schlenk line technique in order to maximize the formation of product due to the unlability

of Cr (III). The maximum reaction time is 48 h for the highest yield of products, and it needs to be heated at c.a. 60˚C. When refluxing for longer time or at higher temperature, the product started to decompose into the monomeric form, $[Cr(tren)(L^{q,cat})]^+$ for the halogen series and phenyl derivatives, and $[Cr(tren)(L^{cat,cat})]^+$ for the naphthalene and anthracene analogues (Figure 3.1), which was detected by ESI+ mass spectrometry. Two types of Cr (III) monomers can be produced during the reaction of these Cr (III) dimeric systems: for anilate bridging dimers, $[Cr(tren)(L^{cat,q})]^+$ was produced with the bridging ligand in (cat, q) form; for the horizontally extended aromatic bridging dimers, e.g. NAT, Me-AnT, and AnT, $[Cr(tren)(L^{cat,cat})]^+$ was produced with the bridging ligand in (cat, cat) form.

Scheme 3.2. General synthetic routes of $[Cr_2(tren)_2(L^{cat,cat})](BPh_4)_2$ and $[Cr_2(tren)_2(L^{sq,cat})](BPh_4)_2(BF_4)$, where L represents naphthalene or anthracene bridging ligands, NAT, AnT, or Me-AnT.

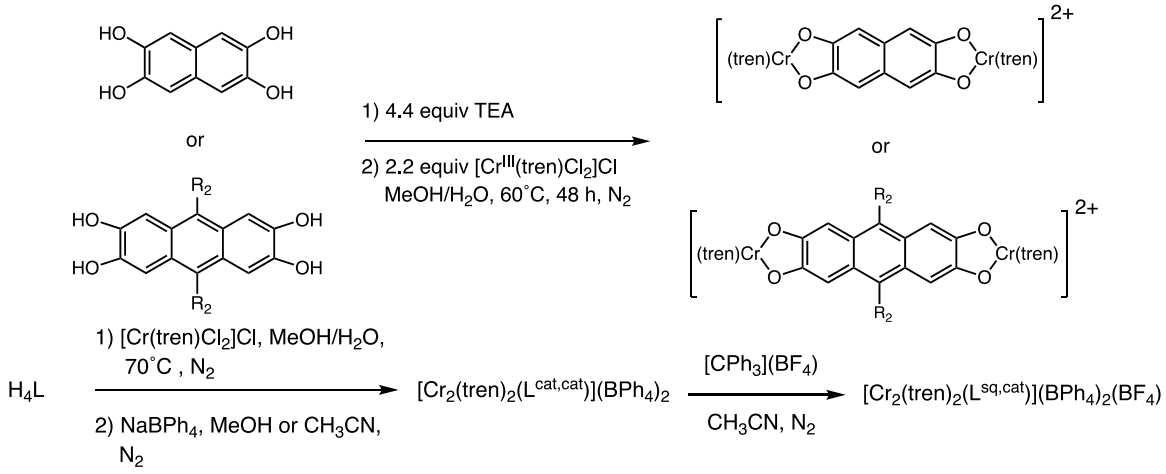

The crystallines of $[Cr_2(tren)_2(L^{cat,cat})](BPh_4)_2$ (L: NAT, AnT, or Me-AnT) were obtained by metathesis from solution prior oxidation. Both anthracene and naphthalene have an extended conjugated system, which can reduce electron-electron repulsion within a system. Our initial thought of employing them into our bridging system is their ability to delocalize the spin density away from the binding oxygen. However, the planar π-system of PAHs cause them to be less soluble. Both H_4AnT and H_4(Me-AnT) are insoluble in MeOH. The resulting product of

$Cr_2(tren)_2(Me\text{-}AnT^{cat,cat})Cl_2$ is also insoluble in MeOH; therefore, it needed to be recrystallized and metathesized in MeCN. The solubility of $Cr_2(tren)_2(AnT^{cat,cat})Cl_2$ is even poorer, and it is only very slightly soluble in MeCN, which makes its recrystallization extremely difficult. Growing x-ray diffraction suitable crystals require the modulation of solvents and solution concentration, and the method will be further discussed below.

$$[Cr_2(tren)(L^{cat,cat})]^{2+} \underset{+e^-}{\overset{-e^-}{\rightleftharpoons}} [Cr_2(tren)(L^{sq,cat})]^{3+} \quad (3.1)$$

$$[Cr_2(tren)(L^{sq,cat})]^{3+} \underset{+e^-}{\overset{-e^-}{\rightleftharpoons}} [Cr_2(tren)(L^{sq,sq})]^{4+} \quad (3.2)$$

$[Cr_2(tren)_2(L^{cat,cat})]^{2+}$ can be oxidized to $[Cr_2(tren)_2(L^{sq,cat})]^{3+}$ by mild chemical oxidants (eq. 1a). The choice of oxidants is determined from comparing the redox potentials, which will be further discussed in Chapter 5, measured by cyclic voltammetry with the redox potentials of some common chemical oxidants.[54] $[FeCp^*_2](BF_4)$ with a redox potential of -0.535 V (vs Fc/Fc^+) was chosen as the oxidizing agent for $[Cr_2(tren)_2(DHBQ^{cat,cat})]^{2+}$, $[Cr_2(tren)_2(PhA^{cat,cat})]^{2+}$, and $[Cr_2(tren)_2(NMe_2\text{-}PhA^{cat,cat})]^{2+}$ to prevent over-oxidizing the starting materials into their monomer derivatives, because its redox potential is more negative than the ones of $[Cr_2(tren)_2(L)]^{3+/4+}$ (eq. 1b). $[CPh_3](BF_4)$, -0.11 V vs Fc/Fc^+, a slightly stronger oxidant than $[FeCp^*_2](BF_4)$, was the choice of oxidant for the other $[Cr_2(tren)_2(L^{cat,cat})]^{2+}$ for the similar reason. The reaction time of these oxidations should be limited to 4 to 8 h. Long reaction time can result in over-oxidation, and the only product detected by ESI+ was Cr (III) monomeric systems after 12 h oxidation. It is likely that the oxidation equilibrium gets shifted as more $[Cr_2(tren)_2(L^{sq,cat})]^{3+}$ formed, so it potentially stimulates the production of $[Cr_2(tren)_2(L^{sq,sq})]^{4+}$ even with the two mild oxidants (Scheme 3.2). $[Cr_2(tren)_2(L^{sq,sq})]^{4+}$ is unstable, because the preferred binding motif of the bridging ligand is $(L^{cat,\,q})$. When the meta-unstable form of

$[Cr_2(tren)_2(L^{sq,sq})]^{4+}$ produced, it potentially rearranges into $[Cr(tren)(L^{cat,q})]^{+}$ for better stability. This can potentially explain the detection of Cr (III) monomer by ESI+ with long reaction, and the quasi-reversibility of $[Cr_2(tren)_2(L)]^{3+/4+}$ observed during electrochemistry.

The CV of $Cr_2(tren)_2(AnT)^{2+/3+}$ is irreversible, which will be further discussed in Chap. 5. The irreversibility of $Cr_2(tren)_2(AnT)^{2+/3+}$ indicate that the formation of $Cr_2(tren)_2(AnT^{cat,cat})^{3+}$ is likely to be thermodynamically unfavorable. The oxidation of $Cr_2(tren)_2(AnT^{cat,cat})^{2+}$ to $Cr_2(tren)_2(AnT^{sq,cat})^{3+}$ with $[FeCp^*_2](BF_4)$ was unsuccessful. No $[M]^{3+}$ species was detected by ESI+ after the similar synthetic procedure as $[Cr_2(tren)_2(DHBQ^{sq,cat})](BPh_4)_2(BF_4)$. These experimental evidence supports my hypothesis.

3.4.2 Single Crystal X-Ray Structures

X-ray diffraction quality crystal structures were collected for $[Cr_2(tren)_2(DHBQ^{cat,cat})](BPh_4)_2$ (**1**), $[Cr_2(tren)_2(FA^{cat,cat})](BPh_4)_2$ (**2**), $[Cr_2(tren)_2(BA^{cat,cat})](BPh_4)_2$ (**4**), $[Cr_2(tren)_2(IA^{cat,cat})](BPh_4)_2$ (**5**), $[Cr_2(tren)_2(PhA^{cat,cat})](BPh_4)_2$ (**6**), $[Cr_2(tren)_2(NMe_2\text{-}PhA^{cat,cat})](BPh_4)_2$ (**7**), and $[Cr_2(tren)_2(Me\text{-}AnT^{cat,cat})](BPh_4)_2$ (**10**). The crystal structure of $[Cr_2(tren)_2(CA^{cat,cat})](BPh_4)_2$ (**3**) has been reported by Dr. Guo in our group.[1]

The crystals of Complex **1**, **2**, **4**, **5**, **6**, and **7** were grown via metathesis by carefully layering $NaBPh_4$ MeOH solution on top of its product MeOH solution in a N_2-filled drybox. The crystals were grown in dark after 2 weeks. The most challenging part of growing crystals is the modulation of solution concentration. If the mother solution is too concentrated, the product would either be too small or powder out. Chromium complexes naturally do not diffract well under x-ray, so the size of the crystal for x-ray analysis is crucial. The recrystallization of $[Cr_2(tren)_2(NAT^{cat,cat})](BPh_4)_2$ was attempted a few times. Small crystal was grown; however, the

diffraction rate of these crystals was too weak. Future students should consider adding aromatic solvent for π-stacking or viscous alcohol for hydrogen bonding to facilitate bigger crystal grown.

All of the compounds mentioned above are extremely air-sensitive; thus, mounting the crystal is also challenging. These crystals were confined in their lattices with solvent molecules. The crystal needs to be picked out, mounted on a goniometer, and placed under a stream of liquid He quickly. Exposing the product too long in air will result in product decomposition and solvent lost. Color change of the crystal indicates the decomposition, and structural disorder implies the loss of solvent.

Table 3.3. Selected Bond Length (Å) and Angle (˚) for Complex **1**, **2**, **4**, and **5**.

	1	**2**	**4**	**5**
	Bond Length (Å)			
Cr(1) – O(1)	1.9422(15)	1.947(3)	1.949(2)	1.952(3)
Cr(1) – O(2)	1.9136(15)	1.936(3)	1.920(2)	1.914(3)
Cr(1) – N(1)	2.1031(18)	2.102(3)	2.084(2)	2.091(3)
Cr(1) – N(2)	2.0974(19)	2.095(4)	2.076(3)	2.117(4)
Cr(1) – N(3)	2.092(2)	2.077(4)	2.113(3)	2.082(3)
Cr(1) – N(4)	2.0692(19)	2.075(3)	2.075(3)	2.080(3)
O(1) – C(8)	1.388(2)	1.368(4)	1.364(3)	1.360(5)
O(2) – C(9)	1.357(3)	1.356(4)	1.348(3)	1.342(5)
C(7) – C(8)	1.384(3)	1.386(5)	1.392(4)	1.394(5)
C(8) – C(9)	1.395(3)	1.396(5)	1.407(4)	1.417(5)
C(7) – C(9)	1.395(3)	1.384(5)	1.394(4)	1.391(5)
Cr ··· Cr[a]	7.628	7.644	7.667	7.657
	Bond Angles (˚)			
O(1) – Cr(1) – N(1)	97.31(7)	95.98(12)	93.95(9)	94.78(12)
O(1) – Cr(1) – N(2)	99.34(7)	98.96(14)	100.02(10)	94.56(14)
O(1) – Cr(1) – N(3)	93.03(7)	95.14(13)	94.82(11)	100.20(12)
O(1) – Cr(1) – N(4)	177.05(7)	178.29(14)	175.64(10)	175.99(13)
O(2) – Cr(1) – O(1)	86.42(6)	86.06(11)	86.21(8)	86.23(11)
O(2) – Cr(1) – N(1)	175.72(7)	177.08(13)	178.97(10)	178.91(13)
O(2) – Cr(1) – N(2)	86.58(7)	87.46(14)	86.54(12)	86.51(14)
O(2) – Cr(1) – N(3)	86.55(8)	86.37(14)	86.32(12)	86.18(13)
O(2) – Cr(1) – N(4)	92.59(7)	94.36(13)	96.02(9)	95.51(12)
N(1) – Cr(1) – N(2)	94.82(8)	94.28(15)	94.43(12)	92.99(15)
N(1) – Cr(1) – N(3)	91.17(8)	91.35(15)	92.66(13)	94.06(14)
N(1) – Cr(1) – N(4)	83.57(7)	83.54(14)	83.76(10)	83.46(13)
N(2) – Cr(1) – N(3)	165.43(8)	164.17(16)	163.06(13)	163.04(14)
N(2) – Cr(1) – N(4)	83.36(8)	82.72(15)	83.89(11)	81.96(15)
N(3) – Cr(1) – N(4)	84.14(8)	83.23(15)	81.61(11)	83.55(13)

[a]Nonbonding metal-to-metal distance.

Complex **1**, **4** and **5** contains two MeOH solvent molecules in their crystal lattice. The molecular formula of Complex **2** shows that the crystal lattice contained six MeOH solvent molecules. All of these crystal structures do not show structural disorder.

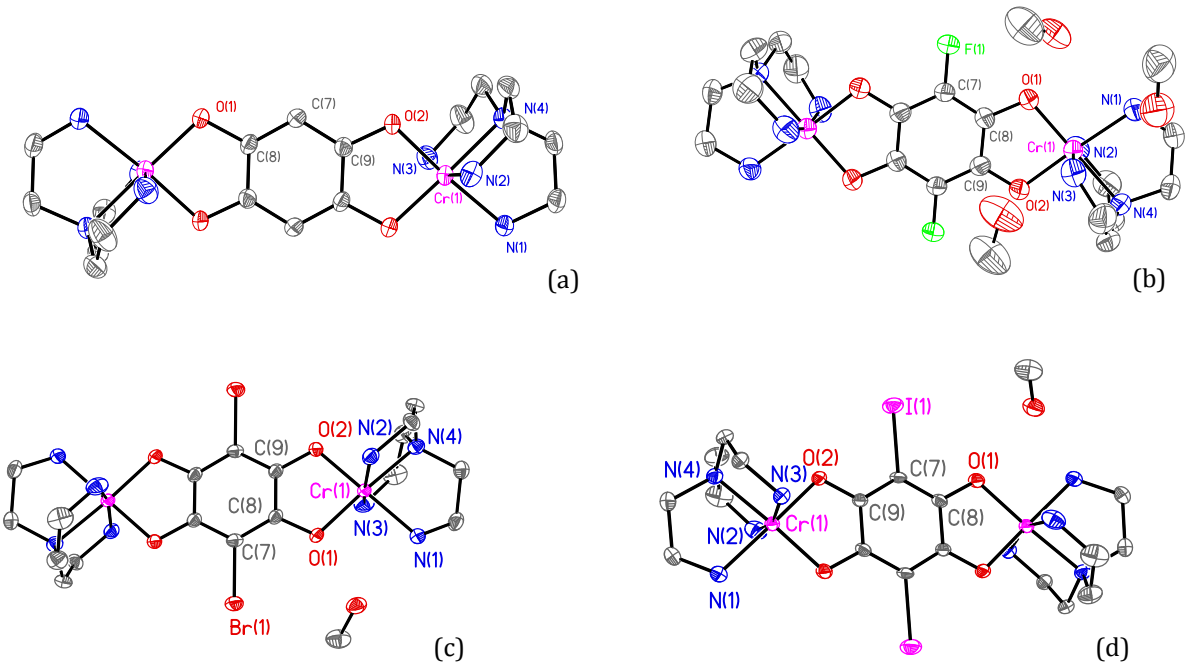

Figure 3.6. ORTEP drawing of Complex **1** (a), **2** (b), **4** (c), and **5** (d) obtain from single crystal x-ray structure determination. Atoms are represented as 50% probability thermal ellipsoids. Hydrogen atoms are omitted for clarity.

The molecular formula of Complex **7** shows that the crystal lattice contained six MeOH solvate molecules with solvent disorder. Due to the solubility issue of Complex **10**, its crystal was grown by layering $NaBPh_4$ MeCN solution on top of its MeCN/MeOH solution. The crystal collected show solvent disorder, which does not affect the body structure of the product. However, modelling the various solvent disorder was unsuccessful. The crystal has a R_1 of 6.90% with solvent mask, which indicate a high-quality crystal structure with omitted structural disorder. The bond lengths and bond angles are still useful for our discussion here. A few approaches were attempted, including adding a few drops of octanol into the crystallization chamber. The reasoning behind is that the hydrogen bonding between alcohol and the complex

will potentially help confine solvate molecules in the crystal lattice. An aliphatic alcohol is more viscous with higher boiling point, so it will not easily evaporate and leave crystal lattice resulting in structural disorder. However, no crystal was grown. Better quality crystal with no structural disorder or analyzable disorder should be grown in the future with other alternative approach.

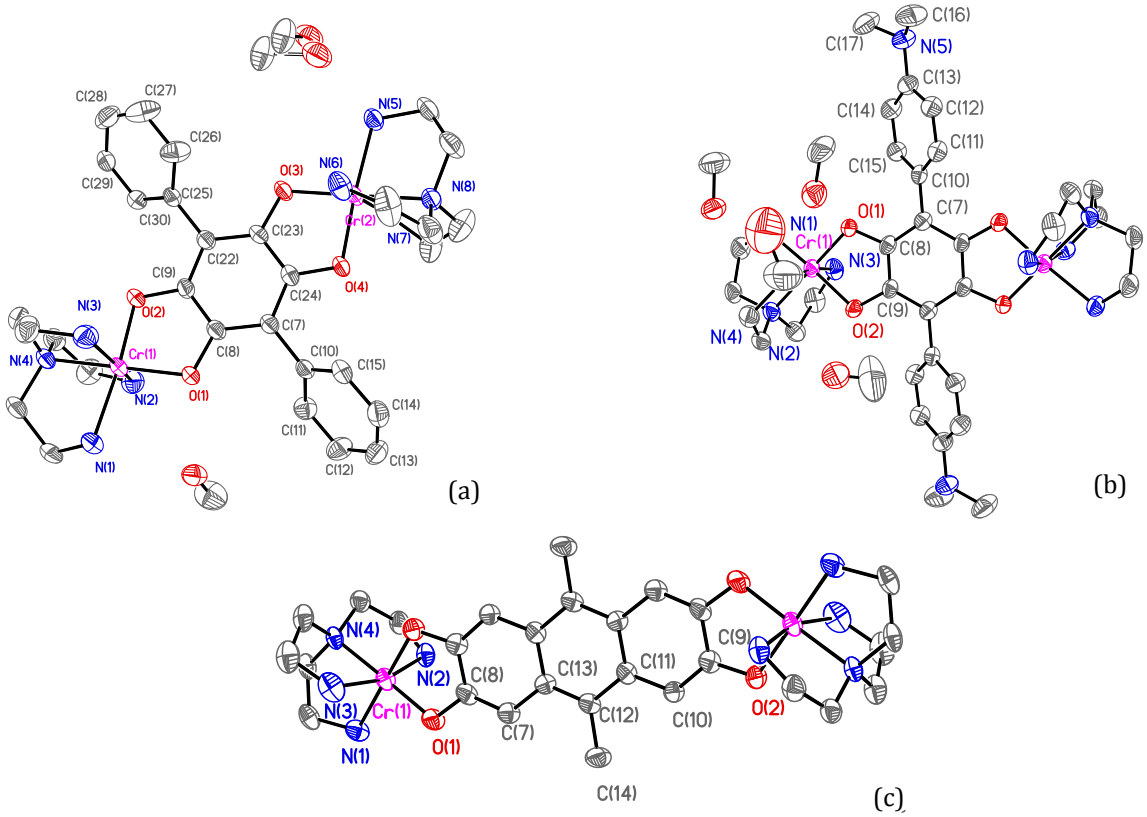

Figure 3.7. ORTEP drawing of Complex **6** (a), **7** (b), and **10** (c) obtain from single crystal x-ray structure determination. Atoms are represented as 50% probability thermal ellipsoids. Hydrogen atoms are omitted for clarity.

Due to the solubility issue, the crystals of Complex **10** were grown by layering $NaBPh_4$ MeCN solution on top of its MeCN/MeOH solution. The crystal collected show solvent disorder, which does not affect the body structure of the product. However, modelling the disorder was unsuccessful. The crystal has a R_1 of with solvent mask, which indicates a high qualitystructure without the solvent disorder. The bond lengths and bond angles are used for our discussion here.

Better quality crystal with no solvent disorder or analyzable disorder should be grown in the future.

Table 3.4. Selected Bond Length (Å) and Angle (˚) for Complex **6**, **7**, and **10**.

	6	**7**	**10**	
	Bond Length (Å)		Bond Length (Å)	
Cr(1) – O(1)	1.935(2)	1.913(3)	Cr(1) – O(1)	1.916(3)
Cr(1) – O(2)	1.906(2)	1.939(3)	Cr(1) – O(2)	1.946(3)
Cr(2) – O(3)	1.943(2)			
Cr(2) – O(4)	1.910(2)			
Cr(1) – N(1)	2.107(3)	2.099(3)	Cr(1) – N(1)	2.077(4)
Cr(1) – N(2)	2.121(3)	2.087(4)	Cr(1) – N(2)	2.085(4)
Cr(1) – N(3)	2.083(3)	2.093(4)	Cr(1) – N(3)	2.113(4)
Cr(1) – N(4)	2.074(3)	2.091(4)	Cr(1) – N(4)	2.078(4)
Cr(2) – N(5)	2.093(3)			
Cr(2) – N(6)	2.097(3)			
Cr(2) – N(7)	2.087(3)			
Cr(2) – N(8)	2.085(3)			
O(1) – C(8)	1.376(4)	1.377(5)	O(1) – C(8)	1.355(3)
O(2) – C(9)	1.361(4)	1.364(5)	O(2) – C(9)	1.357(3)
O(3) – C(23)	1.379(4)		C(11) – C(13)	1.450(6)
O(3) – C(24)	1.361(4)		C(12) – C(13)	1.401(6)
C(7) – C(8)	1.401(4)	1.395(6)	C(7) – C(8)	1.356(6)
C(8) – C(9)	1.404(5)	1.408(6)	C(8) – C(9)	1.432(6)
C(9) – C(22)	1.404(4)	1.418(6)	C(9) – C(10)	1.365(6)
C(22) – C(23)	1.405(4)		C(7) – C(13)	1.439(5)
C(23) – C(24)	1.404(5)		C(10) – C(11)	1.429(6)
C(7) – C(24)	1.401(4)		C(11) – C(12)	1.420(5)
Cr ··· Cr[a]	7.646	7.652	Cr ··· Cr[a]	12.545
	Bond Angles (˚)		Bond Angles (˚)	
O(1) – Cr(1) – N(1)	98.59(11)	97.67(14)	O(1) – Cr(1) – N(1)	94.71(14)
O(1) – Cr(1) – N(2)	92.50(12)	95.14(15)	O(1) – Cr(1) – N(2)	97.00(14)
O(1) – Cr(1) – N(3)	101.94(11)	98.40(15)	O(1) – Cr(1) – N(3)	98.31(16)
O(1) – Cr(1) – N(4)	173.95(12)	178.57(14)	O(1) – Cr(1) – N(4)	178.25(13)
O(2) – Cr(1) – O(1)	85.87(10)	85.74(11)	O(2) – Cr(1) – O(1)	85.20(12)
O(2) – Cr(1) – N(1)	174.90(11)	176.55(16)	O(2) – Cr(1) – N(1)	179.41(15)
O(2) – Cr(1) – N(2)	88.19(13)	88.58(15)	O(2) – Cr(1) – N(2)	87.14(14)
O(2) – Cr(1) – N(3)	84.23(12)	87.44(16)	O(2) – Cr(1) – N(3)	88.60(16)
O(2) – Cr(1) – N(4)	92.99(11)	94.04(13)	O(2) – Cr(1) – N(4)	96.50(13)
N(1) – Cr(1) – N(2)	94.06(12)	91.65(17)	N(1) – Cr(1) – N(2)	92.30(15)
N(1) – Cr(1) – N(3)	92.39(12)	91.51(18)	N(1) – Cr(1) – N(3)	91.99(17)
N(1) – Cr(1) – N(4)	82.83(11)	82.56(15)	N(1) – Cr(1) – N(4)	83.59(15)
N(2) – Cr(1) – N(3)	163.12(13)	165.56(18)	N(2) – Cr(1) – N(3)	163.70(17)
N(2) – Cr(1) – N(4)	81.52(12)	83.44(16)	N(2) – Cr(1) – N(4)	82.69(13)
N(3) – Cr(1) – N(4)	83.84(12)	83.01(16)	N(3) – Cr(1) – N(4)	82.18(15)

[a]Nonbonding metal-to-metal distance.

The halogenated Cr (III) complexes are isostructural in monoclinic space group $P2_1/n$ (a more orthogonal cell), and crystallographic details are shown in Table 3.4. with selected bond lengths and angle given in Table 3.4. Complexes **1**, **6**, and **7** are isostructural in monoclinic space group $P2_1/c$, a more oblique cell compared with $P2_1/n$. These complexes are all structurally similar with centrosymmetric monoclinic space groups, and complexes **1**, **2**, **3**,[1] **4**, **5**, and **7** are situated on inversion centers making only half of a dimer unique in a cell. The entire dimeric system of complex Ph is unique due to the inter-ring torsions within the phenylanilate bridging ligand. The ORTEP drawings of the cations are shown in Fig. 3.6 and Fig. 3.7, respectively.

The chromium center is coordinated with four aliphatic nitrogens from the tren capping ligand and two oxygens from the catecholate bridging ligand to form a distorted octahedral environment. This kind of distorted octahedral coordination is typically observed in other chromium-catecholate complexes, e.g. [Cr(tren)(3,6-DTBCat)](ClO_4).[55] The bite angles around the chromium coordination site for a given complex are c.a. 90˚ and 180˚, which is expected to be seen for tetradentate tripodal tren ligand. The Cr-N bond lengths are ranging from 2.087 to 2.096 Å, which are similar to those observed in [Cr(tren)(3,6-DTBCat)](ClO_4) (average 2.098 Å)[40] and slightly longer than those in [Cr(tren)(3,6-DTBSQ)](PF_6) (average 2.07 Å).[19] The Cr-O bond distances are ranging between 1.906 and 1.952 Å (Table 3.3 and 3.4); for example, the bond distances are 1.942 Å and 1.913 Å respectively in complex H. It was believed that the discrepancy in Cr-O bond distances was due to one positioning shoulder-by-shoulder to the NH_2 in tren, and the other one locating in between two NH_2. This phenomenon was observed in complexes **1**, **2**, **3**,[1] **4**, **5**, and **6**. However, the opposite situation was observed for complexes NMe_2Ph and MeAnT. Similar situations were seen in [Cr(tren)(3,6-DTBCat)](ClO_4)[55] with larger difference and [Cr(tren)(3,6-DTBSQ)](PF_6)[19] with smaller difference.

It has been widely observed that the C-C bond length within the ring can indicate the oxidation state of the quinoidal ligand when binding to first-row transition metals.[56-58] For the fully reduced catecholate form, the C-C bond distances are nearly identical indicating the aromatic nature of the ligand. For the semiquinoidal radical form, the ring shows alternating single and double C-C bond feature, because the electrons are more localized in the C=C bond. This reflects on the short and long C-C bond lengths seen in x-ray crystal structure. The C-C bond lengths within the bridging ring show a narrow range for some complexes: 1.384 – 1.395 Å in complex H; 1.386 – 1.396 Å in complex F; 1.393 – 1.402 Å in complex Cl^1; 1.392 – 1.407 Å in complex Br; 1.401 – 1.405 Å in complex Ph. However, C-C bond distances in complexes Br (1.391 – 1.417 Å) and NMe_2Ph (1.395 – 1.418 Å) show a much wider range. Based on this evidence, Complex **5** and **7** are potentially less stable and easier to be oxidized into their semiquinone forms. More physical evidence will be discussed in Chapter 5 to support this hypothesis.

The C-O bonds in quinoidal ligands can also provide information about the oxidation state of the ligands. [56-58] The C-O bond lengths are generally different in semiquinodal complexes, e.g. 1.293 Å and 1.312 Å in [Cr(tren)(3,6-DTBSQ)](PF_6),[19] which is consistent with the pseudo single and double C-C character. The C-O bond distances are nearly identical in catecholate complexes, e.g. 1.372 and 1.378 Å in [Cr(tren)(3,6-DTBCat)](ClO_4).[55] However, C-O bond distances cannot be a valid indication for the oxidation state in the chromium complexes reported here, since their differences are not negligible (Table 3.3 and 3.4) except for Complex **8**. Even though the C-O bond lengths are not identical, they are all much longer than the reported C-O bond length in chromium-semiquinoidal complexes.[19]

Tetraoxoanthracene ligand was incorporated in our systems to greatly increase the spin delocalization and steel electron density away from the oxygens coordinating to the chromium

centers. The structure in this system is more planar compared with other Cr analogues. Although Complex **10** contains a horizontally extended conjugated ligand, it does not make a huge impact on its Cr-N and Cr-O bond distances and the coordination environment around its Cr centers. The C-C bond lengths within the rings show slightly larger discrepancies, but it does not have the alternating long and short bond character. Two C-C bonds are significantly shorter, 1.356 and 1.365 Å, compared with the rest of the bonds with an average of 1.429 Å. These C-C bond distances are consistent with the reported anthracene bond lengths with an average value of 1.395 Å.[59] Kalescky et al. reported that the middle ring contained the shortest C-C distance of 1.246 Å,[60] which indicates the middle ring of anthracene exhibit double or even triple bond character with more electron localized in the center. However, the C-C bond distance in the middle ring of Complex **10** presents an opposite phenomenon, because it contains the longest bond length of 1.450 Å. As suggested in the computational results, spin density localizes more on the chelating oxygens, and this is likely to cause spin move away from the middle ring. The difference of C-O bonds is statistically negligible, 1.355 and 1.357 Å. It is still unknown what is the directly cause of these kinds of discrepancy in bond lengths observed for Complex **10**.

It will be highly desirable to structurally compare $[Cr_2(tren)_2(L^{cat,cat})]^{2+}$ and $[Cr_2(tren)_2(L^{sq,cat})]^{3+}$ so that more evidence of how the oxidation state impact the various bond distance can be discussed. Unfortunately, the recrystallization of x-ray quality crystal for $[Cr_2(tren)_2(L^{sq,cat})]^{3+}$ has thus far unsuccessful. Future students who follow this project can attempt to grow them to extend the discussion.

The phenylanilate bridging ligands are incorporate to change the directionality of the spin delocalization vertically and examine the steric effect on electron delocalization.[61,62] The dihedral angles between two rings have found to provide information of the relative oxidation

state, and reduced ligand generally prefer a more planar geometry.[44] One important information is the inter-ring torsion between the anilate ring and the phenyl ring. The inter-ring torsional angles, ϑ, in Complex **6** are 60.08˚ and 51.74˚; ϑ in Complex **7** is 45.54˚. These dihedral angles are all twisted, and do not exhibit coplanar geometry as predicted in other findings in our group. Given the fact that they were confined in solid lattice, these torsional angles may be affected by the coordination and packing environment around.

3.5 Magnetic Susceptibility Measurements

3.5.1 Previous Studies on Similar Systems: Experimental and Theoretical Examination of Cr (III) Phenanthrenesemiquinone

Previous work done by Dr. Fehir in our group of substituted Cr(III) phenanthrenesemiquinone provide some insight about the magnetic behavior of Cr(III) semiquinone, and these systems were studied experimentally and computationally.[63] Broken symmetry formalism was perfomed to calculate *J* on substituted $[Cr(tren)(PSQ)]^{2+}$ systems. This calculation formalism is not conducted in this project, so the underlying principle will not be discussed here. It shows that EWG increase *J* by increasing the spin localization on the interacting oxygens, whereas EDG decrease *J* by increasing the spin delocalization.[63] It suggests that the unpaired spin in EDG sitting in an orbital has a closer energy level with the spins in Cr(III), so β-HOMO-β-LUMO gap is smaller to allow mixing between two orbitals to induce spin delicalization.[63] Inversely, the orbital of the unpaired electron in EWG is lower in energy than the one in Cr(III) to cause a larger β-HOMO-β-LUMO gap and prevent orbital mixing.[63] The magnetic susceptibility data collected on $[Cr(tren)(PSQ)](BPh_4)$ and $[Cr(tren)(3,6\text{-}NO_2\text{-}PSQ)](BF_4)_2$ show temperature independence and indicate a very strong exchange coupling interaction between Cr(III) and PSQ^- radical,[63]

which agree with both the computational results and literature finding of Cr(III) semiquinoidal compounds.[8,18,19]

Variable-temperature magnetic susceptibility measurement is generally used to experimentally determine the strength of coupling between paramagnetic spin centers, in which the magnetization of a sample is evaluated as a function of temperature (usually ranging from 2-350K) reflecting the Boltzmann distribution (Eq. 3.3). At low temperature, more spins locate at the lower energy level (N_+), and energy embodied as temperature will be applied to populate spins into the higher energy level (N_-).

$$\frac{N^+}{N^-} = e^{-E/kT} \tag{3.3}$$

3.5.2 Magnetic Susceptibility Measurement and Extrapolation of *J*-coupling on $[Cr_2(tren)_2(L^{cat,cat})]^{2+}$

Variable-temperature magnetic susceptibility data were collected for $[Cr_2(tren)_2(L^{cat,cat})](BPh_4)_2$ in solid state in a temperature range of 2 – 350 K at applied field of 0.50 T, 1.00 T, and 2.50 T. The results at all three field were the same within error.

The magnetic data collected were plotted as effective magnetic moment, μ_{eff}, versus temperature, T, and paramagnetic susceptibility, χ_{para}, versus T. Sample magnetic moment, m_{exp}, is corrected with the magnetic moment of the sample holder, m_{bag} (Eq. 3.4). The experimental magnetic susceptibility, χ_{exp}, is then calculated following Eq. 3.5, where M is molar mass in g/mol, m is the mass of the sample in g, and *H* is the applied field in Gauss. χ_{para} is obtained using Pascal's constants[45] for diamagnetic correction in the sample (Eq. 3.6). Effective magnetic moment, μ_{eff}, is calculated for data analysis (Eq. 3.7), where *k* is Boltzmann's constant,

$$m_{sample} = m_{exp} - m_{bag} \tag{3.4}$$

$$\chi_{exp} = \frac{m_{sample} \cdot M}{m \cdot H} \tag{3.5}$$

$$\chi_{para} = \chi_{exp} - \chi_{dia} \tag{3.6}$$

$$\mu_{eff} = \sqrt{\frac{3k}{N_A \mu_B^2}} \sqrt{\chi_{para} \cdot T} \tag{3.7}$$

N_A is Avogadro's number, and μ_B is Bohr Magneton, and $\sqrt{\frac{3k}{N_A \mu_B^2}}$ is called Curie's constant.

$$\mu_{eff} = \sqrt{4S(S+1)} \tag{3.8}$$

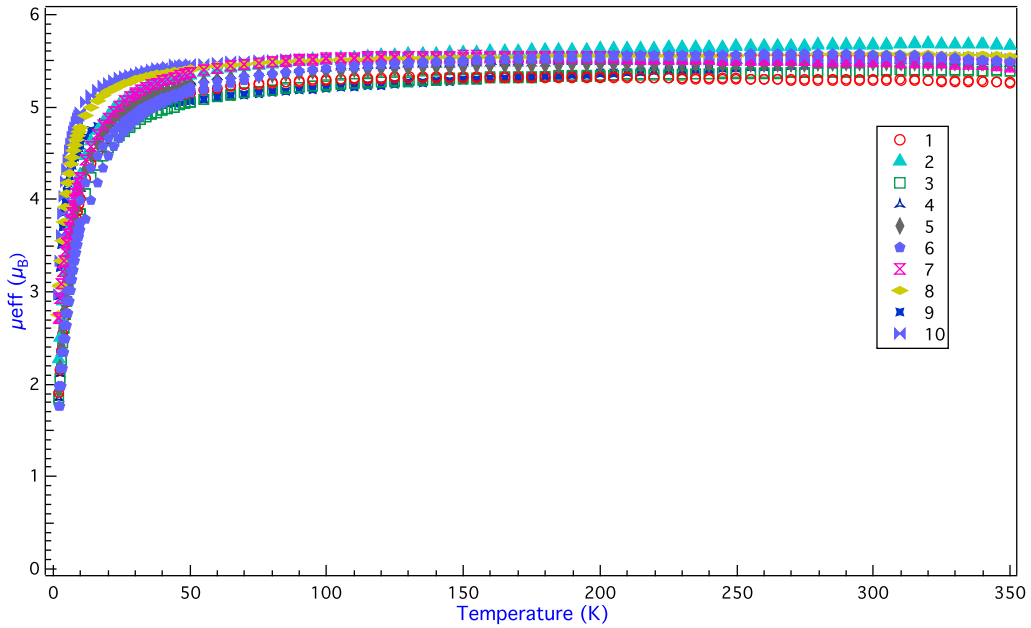

Figure 3.8. Plots of the effective magnetic moment versus temperature for Complex **1**, **2**, **3**, **4**, **5**, **6**, **7**, **8**, **9** and **10** acquired in solid states.

For $[Cr_2(tren)_2(L^{cat,cat})]^{2+}$, the presence of the two paramagnetic Cr (III) (**S**=3/2) centers gives rise to superexchange interaction since they are bridged by a diamagnetic catecholate ligand. The obtained experimental values of μ_{eff} at room temperature are 5.33 μ_B for Complex **1**, 5.68 μ_B for Complex **2**, 5.40 μ_B for Complex **3**, 5.51 μ_B for Complex **4**, 5.49 μ_B for Complex **5**, 5.57 μ_B for Complex **6**, 5.56 μ_B for Complex **7**, 5.57 μ_B for Complex **8**, 5.51 μ_B for Complex **9**, 5.54 μ_B for Complex **10**. Except Complex **2**, all the other experimental μ_{eff} values are close to the

spin-only value of 5.48 μ_B for two Cr (III) ions (Eq. 3.8). The magnetic moment drops below 100 K until μ_{eff} =1.8 μ_B at 2 K indicating S_T=0. A general spin ladder is generated for $[Cr_2(tren)_2(L^{cat,cat})]^{2+}$ based on the HDVV Hamiltonian (Fig. 3.9), and the experimental results are consistent with our predicted magnetic properties.

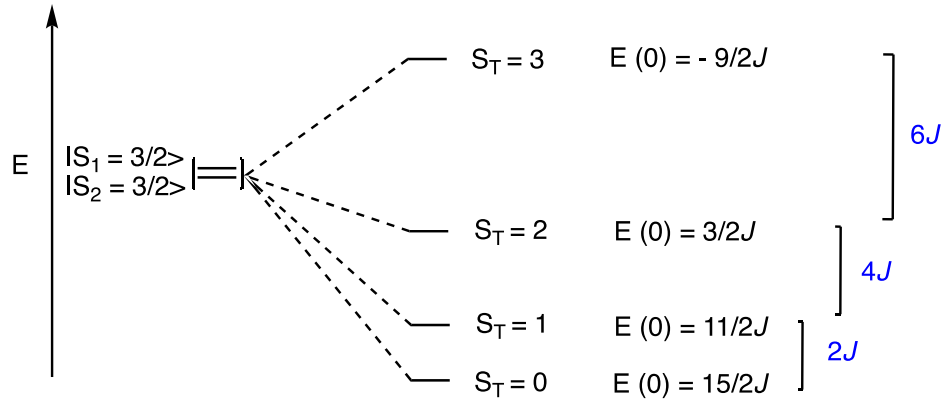

Figure 3.9. Spin latters of $[Cr_2(tren)_2(L^{cat,cat})^{2+}$ due to the Heisenberg Hamiltonian.

The outliner among this series shown in Fig. 3.8 is Complex **2** with F as the substituent on the anilate bridging ligand, and it shows an elevation of magnetic moment. F has a large gyromagnetic ratio, and it generally shows a higher magnetic moment. This agrees with our experimental result of Complex **2** showing a slightly higher of μ_{eff}.

The temperatures were fitted with MagFit[46] by using a form of van Vleck equation[64] shown in Eq. 3.7, where N_A is Avogadro's number, *k* is Boltzmann's constant, *g* is the Landé g factor of an electron,

$$\chi = \frac{N_A g^2 \mu_B^2 \sum_S S(S+1)(2S+1)e^{-E(S)/kT}}{3kT \quad \sum_S (2s+1)e^{-E(S)/kT}} \tag{3.9}$$

μ_B is Bohr Magneton, T is the temperature, S is the total spin quantum number of given spin states, and E(S) (Eq. 3.9) is the eigenvalue from the Heisenberg exchange Hamiltonian (Eq. 3.10).

$$\hat{H} = -2J\hat{S}_1 \cdot \hat{S}_2 \tag{3.10}$$

Using Kambe's method[65] to find the eigenvalues of a spin Hamiltonian, the total spin operator is defined as $S_T = S_1 + S_2$, where $S_T = |S_1 - S_2|, |S_1 - S_2| + 1, \ldots, |S_1 + S_2|$, i.e. S_T = 0, 1, 2, 3. When this is substituted into Eq. 3.10, the expression in Eq. 3.11 is obtained. From that expression, the eigenvalues for the system can be calculated (Eq. 3.12).

$$\widehat{\boldsymbol{H}} = -J\,[\,\widehat{\boldsymbol{S}}_T^2 - \widehat{\boldsymbol{S}}_1^2 - \widehat{\boldsymbol{S}}_2^2] \tag{3.11}$$

$$E\,(S_T) = -J\,[S_T\,(S_T+1) - S_1\,(S_1+1) - S_2\,(S_2+1)] \tag{3.12}$$

The experimental data of χ_{para} was compared with data calculated from the fit in Eq. 3.7 and *J* can be determined by the least-squares fitting. The *J* and g-factor values are variables allowed to vary (see Appendix for input file detail). g-factor obtained from the fit should be equal or close to 2.0, since Cr(III) is a metal ion with minimum spin-orbit coupling. The temperature independent paramagnetism (χ_{TIP}) is fixed at 400 x 10^{-6} cm^3mol^{-1} analogous to Cr (II) dimers[66] and $Cr^{III}(H_2O)_6(NO_3)_3 \cdot 3H_2O$.[67] The plot of the fit for Complex **1** is shown in Fig. 3.10 (see Appendix for the fit plots of other complexes). The fit to the experimental data gave *J* shown in Table 3.5. The MagFit program utilizes the HDVV Hamiltonian formalism as in Eq. 3.11. for the data analysis, where the energy difference between the first and second spin states is 2*J*, the second and third spin states is 4*J*, and third and fourth spin states is 6*J* (Eq. 3.12).

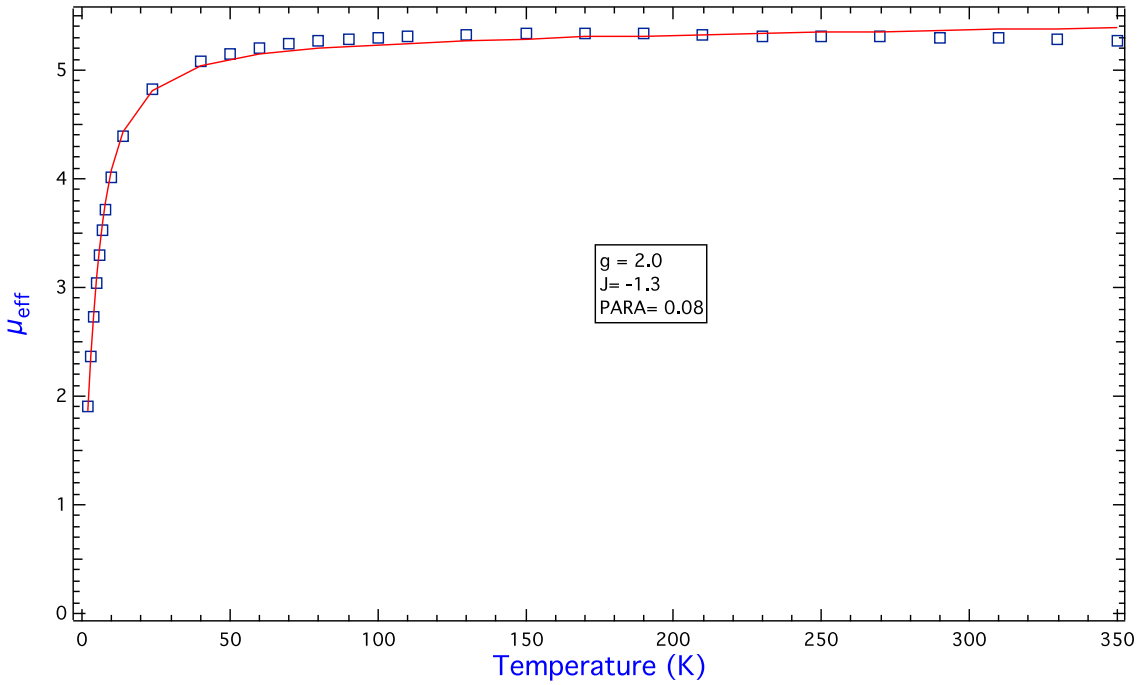

Figure 3.10. The effective magnetic moment of Complex **1** (blue square), and the solid line represents a fit to the data using parameters described in the text.

The variable-temperature magnetic susceptibility data were collected at 2 – 350 K, and the thermal energy applied during the experiment is large enough to overcome the energy barrier (>>kT) to populate the spin fully to its $\mathbf{S}_T = 3$ spin state, and even to their uncoupled situation to indicate a very weak antiferromagnetic interaction between two Cr(III) centers.

J coupling constants (Table 3.5) are very small, and the extrapolation of *J* constants with the HDVV Hamiltonian by MagFit[46] may not be accurate when the strength of the spin exchange interaction is close to the first-order Zeeman splitting. First-order Zeeman effect is a magnetic field induced phenomenon, and it gives rise to the splitting of energy levels as the electron spins can only be oriented parallel or antiparallel in the presence of static magnetic field.[63] The magnitude of the Zeeman splitting (Eq. 3.13) is small with respect to the coulomb energy even in the presence of very strong magnetic field.

$$\Delta E = \frac{|e|\hbar}{2m_e c}(m_l + 2m_s)B \tag{3.13}$$

where m_l is the magnetic quantum number, m_s is the electron spin quantum number, B is an external applied magnetic field, and Bohr's magneton, μ_B

$$\mu_B = \frac{|e|\hbar}{2m_e c} = 5788 \times 10^{-5} eV/T$$

When *J* is small and relatively close to the energy of the Zeeman splitting, the HDVV Hamiltonian is not able to distinguish if the splitting is soley caused by the spin exchange interaction or a mixing of the spin exchange and the Zeeman splitting. In this case, a full matrix diagnolization will be the analytical method for the fitting and extrapolation of small *J* values. Unfortunately, we do not have an access of a software/program equipped with the full matrix diagnolization at the moment. Therefore, the results shown in Table 3.5 are not able to conclude if the substituents have any effect on the strength of the spin exchange interaction.

Table 3.5. Magnetic Properties and J-Couping Constants of $[Cr_2(tren)_2(L^{cat,cat})](BPh_4)_2$.

Complex	*J*-Coupling (cm^{-1})
1	-1.3
2	-1.1
3	-1.4
4	-1.3
5	-1.3
6	-1.6
7	-1.0
8	-0.6
9	-0.6
10	-0.5

If we treat these results as reference to provide some information about the substituent effect regardless the accuracy of the data, these values are considered the same within analytical error. Complex **8**, **9** and **10** with naphthalene and anthracene briding ligands exhibit a slight deviation compared with the other systems.

2,3,6,7-tetraoxonaphthalene and 2,3,6,7-tetraoxoanthracene are introduced as bridging ligands to weaken the strength of spin exchange due to the extended aromatic conjugation along

the orbital x-axis. Their extension of π-symmetry mobilizes electrons and strengthens the spin delocalization horizontally within the systems. Both Complex **8-10** show sight decrease of *J* among all Cr(III) catecholate analogues (Table 3.5). Overall, the magnetic results collected and analyzed on Complex **1-10** are inconclusive, and the magnetic data of $[Cr_2(tren)_2(L^{sq,cat})]^{3+}$ are more detrimental for the analysis in this project.

3.5.3 Magnetic Susceptibility Measurement and Extrapolation of *J*-coupling on $[Cr_2(tren)_2(L^{sq,cat})]^{3+}$

As discussed in Chapter 1, $[Cr_2(tren)_2(L^{sq,cat})]^{3+}$ contains three paramagnetic centers, so there is a direct exchange interaction between the Cr(III) ion and the semiquinone ligand, and a superexchange interaction between the two Cr(III) centers (Fig. 3.11). The magnetic data collected previously on Complex **13**[8] show a very strong direct exchange interaction within the system, and the magnetic susceptibility measured at 2 – 350 K exhibits no significant temperature dependence. Several research papers show that the direct exchange interaction between Cr(III) and semiquinone is very strong with *J* over 400 cm^{-1}.[8,18,19,63]

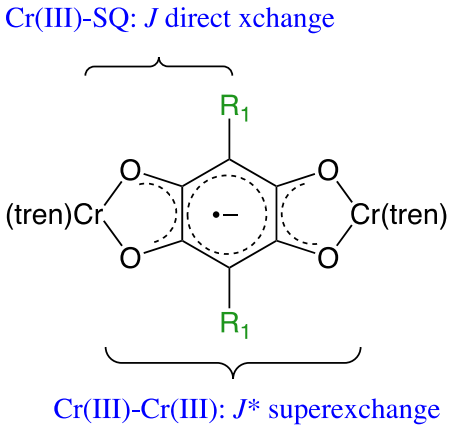

Figure 3.11. Indication of spin exchange coupling interactions for $[Cr_2(tren)_2(L^{sq,cat})]^{3+}$, see text for details on notation.

In order to fit data with HDVV Hamiltonian (Eq. 3.7) to extrapolate two variables, *J* and *J**, thermal population of more spin states are required. The lack of temperature dependence

prevents the accurate determination of J^*. In the case of $[Cr_2(tren)_2(L^{sq,cat})]^{3+}$ measurement, temperature yielding higher thermal energy is required to overcome the energy difference between spin states, but the temperature cannot be too high to decompose the samples. Differential scanning calorimetry (DSC) analysis were performed to test the thermal stability of the molecules. DSC is a thermoanalytical technique measure the heat flow of a sample at constant temperature, and this sample may undergo one or more phase change during the measurement. In a DSC experiment, the heat flow measured for a sample is relative to the heat flow to a reference material.

The DSC plots for Complex **13**, **14** and **16** are presented in Fig. 3.12. The negative heat flow indicates an endothermic consequence and implies a melting of a sample. The sharp negative peak of Complex **13** represent a melting point of 290 ˚C (563 K), and the little shoulder next to the sharp peak is possibly indicative of amorphous sample. According to the DSC, the melting point of Complex **14** is around 300 ˚C (573 K). The data trace of Complex **16** is more complicated without an obvious indication of melting. A second run of this sample should be performed after slow cool. However, the information provided by DSC measurement is inconclusive about thermal degradation of samples. It will be more ideal if we can have access to thermalgravimetric analysis (TGA), because it is a simpler thermoanalytical technique, which measure sample weight loss as a function of temperature in a defined atmosphere. This is a more intuitive analysis for thermal stability.

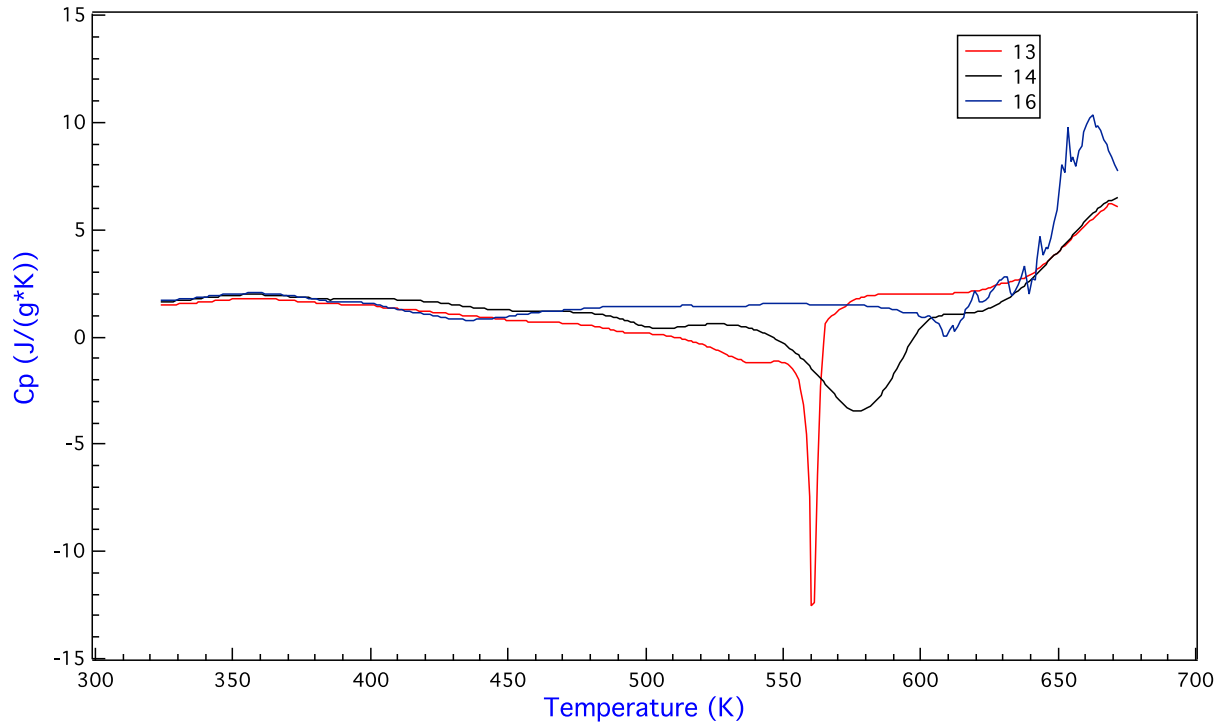

Figure 3.12. The DSC plots of Complex **13**, **14** and **16**.

Since the temperature range of MPMS® 3 SQUID magnetometer is 1.8 – 400 K without an external oven heater stick, the data were collected in solid state from 2 to 400 K at applied field of 1.00 T. The use of an external oven requires a new design of sample holder, so higher temperature measurement was not performed here.

$[Cr_2(tren)_2(L^{sq,cat})]^{3+}$ is a more complicated magnetic system**,** with three paramagnetic centers (both Cr (III) ions and the bridge). In order to better explain the magnetic data, the Heisenberg model is employed again. With three paramagnetic centers, the total spin operator of the system is defined as $\widehat{\boldsymbol{S_T}} = \widehat{\boldsymbol{S_A}} + \widehat{\boldsymbol{S_2}}$ (where $\widehat{\boldsymbol{S_A}} = \widehat{\boldsymbol{S_1}} + \widehat{\boldsymbol{S_3}}$) here, $S_1 = S_3 = 3/2$ correspond the two Cr (III) ions and $S_2 = ½$ corresponds to the $L^{sq,cat}$ bridge. In this way, the Hamiltonian operator can be derived from Eq. 3.14 using two coupling constants, where *J* quantifies the Cr^{III}-$L^{sq,cat}$ direct exchange, and *J** is the superexchange coupling for Cr^{III}-Cr^{III}. Eq.3.15 is the eigenvalue equation for this system.

$$\hat{H} = -2J(\hat{S_1} \cdot \hat{S_2} + \hat{S_2} \cdot \hat{S_3}) - 2J^{*}\hat{S_1} \cdot \hat{S_3} \quad (3.14)$$

$$E = -J\,[S_T\,(S_T+1) - S_A\,(S_A+1) - S_2\,(S_2+1)] - J^{*}\,[S_A\,(S_A+1) - S_1\,(S_1+1) - S_3\,(S_3+1)] \quad (3.15)$$

The effective magnetic moment data (Fig. 3.13) of $[Cr_2(tren)_2(L^{sq,cat})](BPh_4)_2(BF_4)$ collected experimentally show temperature dependence above 100 K. The highest μ_{eff} observed from the sets of data is c.a. 5.64 μ_B for Complex **11**, 5.52 μ_B for Complex **12**, 5.53 μ_B for Complex **13**, 5.50 μ_B for Complex **14**, 5.55 μ_B Complex **15**, 5.62 μ_B for Complex **16**, 6.02 μ_B for Complex **17**, 5.67 μ_B for Complex **18**, and 5.54 μ_B for Complex **19**. The $\mu_{S.O.}$ value for a S =5/2 ground state is 5.916 μ_B (Eq. 3.6), so $|S_T = 5/2, S_A = 3\rangle$ is predicted to be the ground spin state according to the HDVV Hamiltonian (Eq. 3.11).

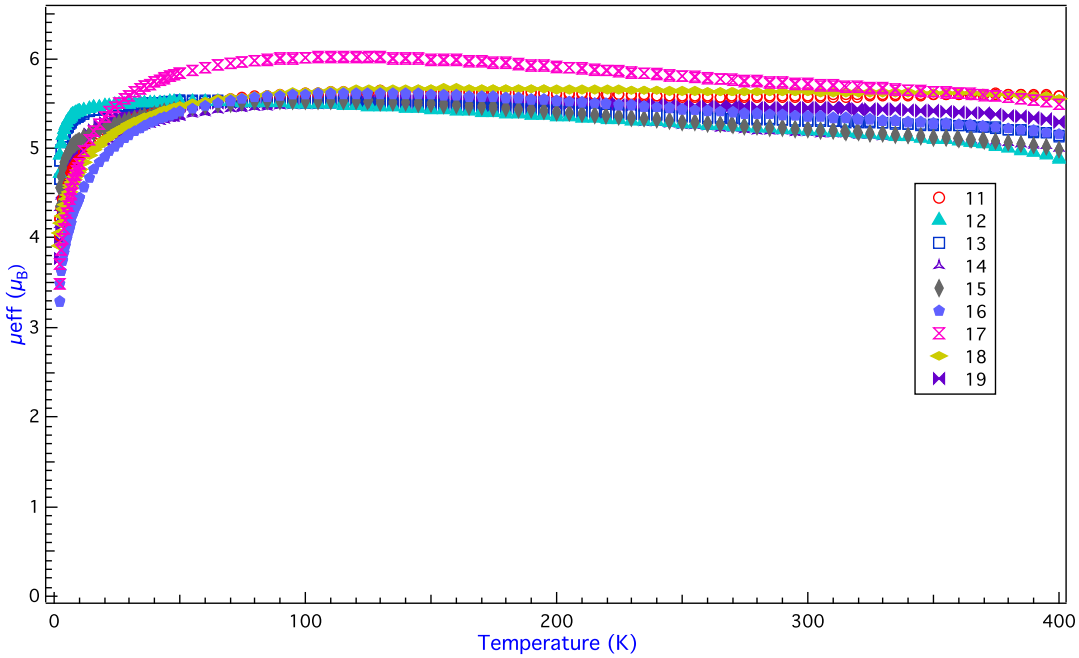

Figure 3.13. Plots of the effective magnetic moment versus temperature for all samples in solid states, Complex **11**, **12**, **13**, **14**, **15**, **16**, **17**, **18** and **19**.

Based on the information obtained for ground states on $[Cr_2(tren)_2(CA^{cat,cat})](BPh_4)_2$ and $[CrGa(tren)_2(CA^{sq,cat})](BPh_4)_2(BF_4)$,[8] the coupling interaction for both Cr^{III} -$L^{sq,cat}$ and Cr^{III}-Cr^{III} is expected to both be antiferromagnetic. This indicates that both *J* and *J** are negative. A plot of

eigenvalues can be generated (Fig. 3.14) to show the correlation between J and J^*. From this plot, the energy splitting of each spin state is governed by J, the direct exchange coupling. The energy levels of |5/2, 3> and |3/2, 2> (the second spin state predicted by the Hamiltonian) intersect at $J/J^* = 6$ (Fig. 3.15), and |5/2, 3> will be raised as the second spin state if $J/J^* > 6$. Thus, the magnitude of J should be more than 6 times larger than J^* for the predicted ground state, |5/2, 3>, in accordance to the Heisenberg exchange Hamiltonian (Eq. 3.12). If both direct exchange and superexchange interactions in this system are antiferromagnetic, these magnetic interactions are frustrated, because it is impossible to orient the configuration of the third set of spin to be both antiferromagnetic to the first two sets of spin.

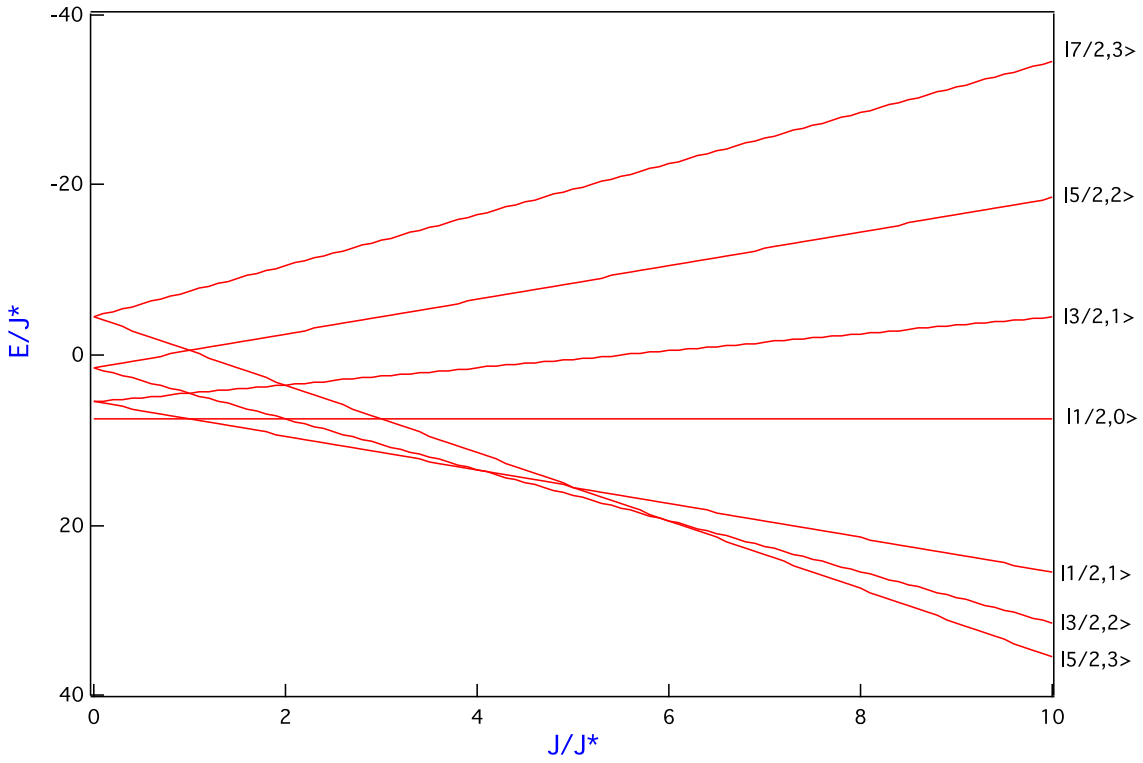

Figure 3.14. Plot of the eigenvalues of various spin states for $[Cr_2(tren)_2(L^{sq,cat})]^{2+}$. $J < 0$ and $J^* < 0$ with both superexchange and direct exchange interactions considered as antiferromagnetic were used to generate this plot. Each state is labeled as $|S_T, S_A>$.[71]

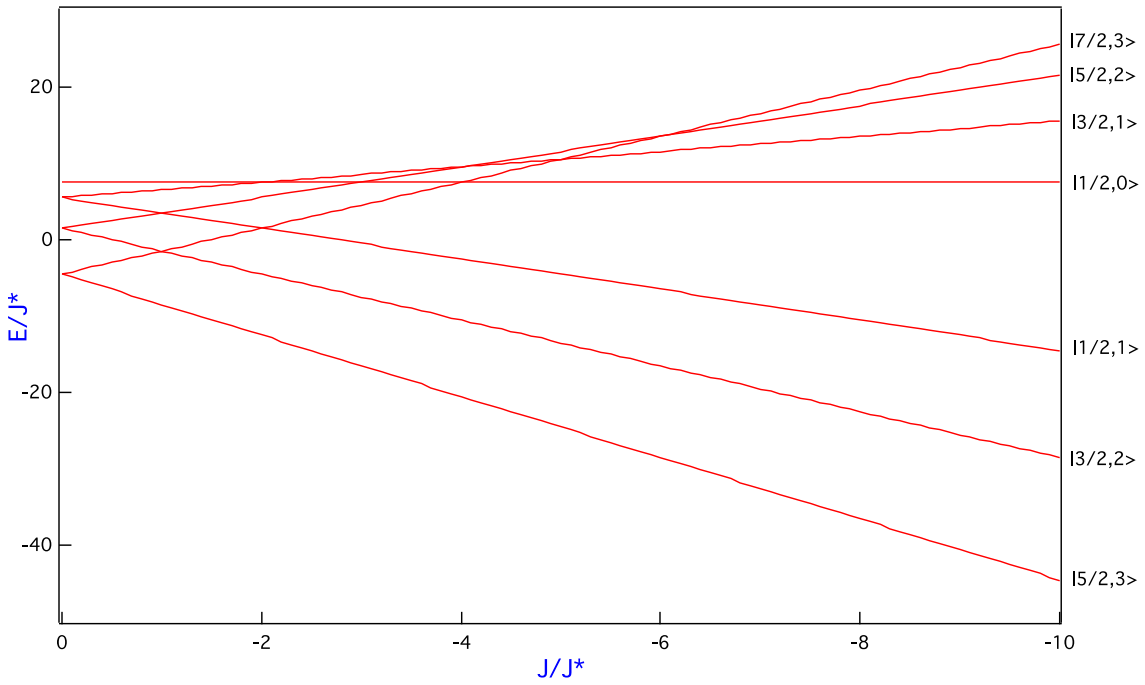

Figure 3.15. Plot of the eigenvalues of various spin states for $[Cr_2(tren)_2(L^{sq,cat})]^{2+}$. J <0 and J^* >0 with direct exchange and superexchange interactions considered as antiferromagnetic and ferromagnetic respectively were used to generate this plot. Each state is labeled as $|S_T, S_A>$.

Since the direct exchange interaction is the dominant effect within the system, and it was experimentally proved to be antiferromagnetic on $[CrGa(tren)_2(CA^{sq,cat})](BPh_4)_2(BF_4)$.[8] The superexchange interaction between two Cr(III) ions is ferromagnetic, i.e. $J^* > 0$, to prevent spin frustration. Another plot of eigenvalues is generated (Fig. 3.15). With |5/2, 3> as the first spin state, |3/2, 2> is predicted as the second spin state again. Unlike in Fig. 3.13, this plot does not provide information about the relative magnitudes of J^* and J. A generic spin ladder (Fig. 3.16) of $[Cr_2(tren)_2(L^{sq,cat})](BPh_4)_2(BF_4)$ with |5/2, 3> as the ground state is generated based on the models (Fig. 3.14 and 3.15) and the Heisenberg exchange Hamiltonian (Eq. 3.11). The energy difference between the first and second spin states is $(1J - 6J^*)$ with this Hamiltonian (Eq. 3.12), and this could be the reason why temperature dependence is shown in the magnetic data

for Cr(III) semiquinone dimers compared with Cr(III) semiquinone monomers reported in literature.[8,18,19]

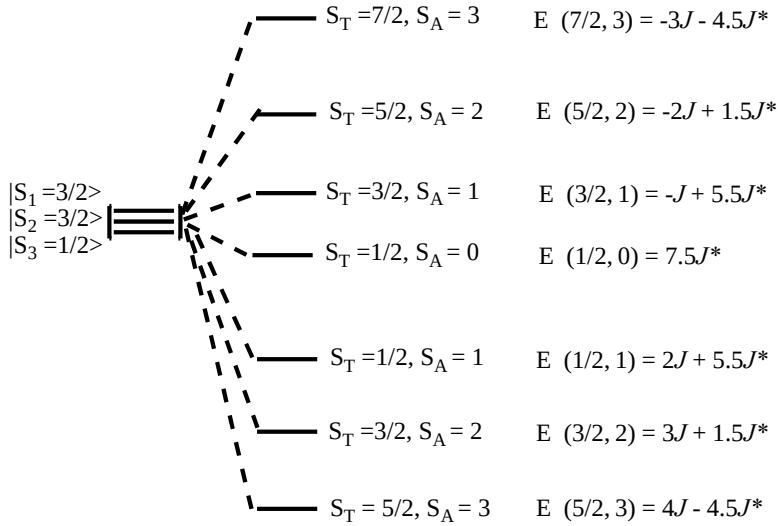

Figure 3.16. A spin ladder diagram for of $[Cr_2(tren)_2(L^{sq,cat})](BPh_4)_2(BF_4)$.

The variable-temperature magnetic susceptibility measurement reflects the Boltzmann distribution across the spin ladder and provides information on the energy separation between spin-coupled states. In order to extrapolate two coupling constants accurately with the HDVV Hamiltonian, thermal population of three or more spin state is required. Therefore, thermal population to the third spin state, |1/2, 1> (S = ½, $\mu_{s.o.}$ = 1.87 μ_B), need to be observed experimentally. The temperature dependence of the data (Fig. 3.13) shows thermal population beyond the first spin state, |5/2, 3>, but the thermal energy applied up to 400K is still not high enough to overcome energy gap and thermally populate up to the spin state of |1/2, 1> for accurate determination of *J**. Based on the magnetic data collected, *J* is believed to be very large in magnitude. The magnetic data collected on $[Cr_2(tren)_2(L^{cat,cat})](BPh_4)_2$ indicate very weak superexchange interactions with small *J**. Therefore, the superexchange interaction is considered too small to perturb the overall spin exchange interaction, and the determination of *J** may not be as meaningful.

The existence of superexchange along with strong direct exchange interaction is questionable. If superexchange interaction actually exists in these complicated exchange coupling systems, temperature dependence of the data has to be obtained and fitted in order to extrapolate two variables, both J and J^*. If not, a higher temperature range for magnetic susceptibility measurement is not necessary. In order to explore the existence of this interaction, a better understanding of superexchange interaction and its coupling pathway is required.

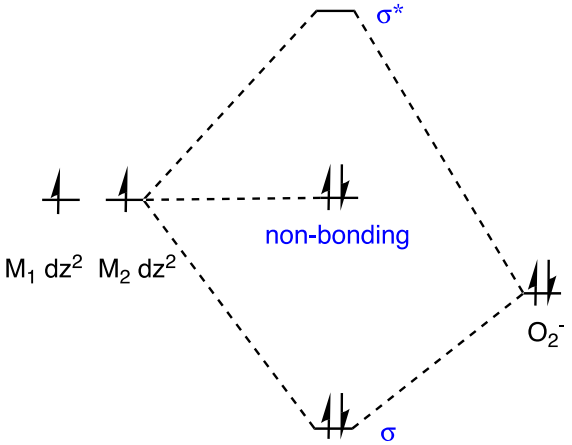

Figure 3.17. Molecular orbital diagram with *d-p* orbital mixing of superexchange interaction between two metals and one intervening O^{2-} via σ-bonding.

Superexchange coupling describes the exchange coupling interaction between two paramagnetic centers through intermediate a diamagnetic ionic ligand with *d-p* orbital mixing, which results in two orbitals: one bonding orbital and one antibonding orbital.[72] The superexchange pathway requires the antibonding orbital to be energetically accessible. However, the strong direct exchange in $[Cr_2(tren)_2(L^{sq,cat})](BPh_4)_2(BF_4)$ stabilizes the bonding orbital between the paramagnetic centers; meanwhile, it destabilizes the antibonding orbital and cause it to be much higher in energy (Fig. 3.17). This either prevents or greatly weakens the *d-p* orbital mixing for superexchange from happening. In this case, J^* is considered to be either zero or negligibly small. Based on both hypotheses described above, the determination of J^* does not

seem to be detrimental for our understanding and analysis of the magnetic properties of $[Cr_2(tren)_2(L^{sq,cat})](BPh_4)_2(BF_4)$.

The experimental data of χ_{para} was compared with data calculated from the fit in Eq. 3.9, and *J* and *J** constants were determined by the least-squares fitting. The *J* and *J** were allowed to vary. The g-factor was fixed at 2.0, and χ_{TIP} was fixed at 400 x 10^{-6} cm^3mol^{-1} analogous to Cr(III) dimers[66] and $Cr^{III}(H_2O)_6(NO_3)_3 \cdot 3H_2O$.[67] The plot of the fit for Complex **12** is shown in Fig. 3.18. Only the *J* constants extrapolated by MagFit[46] is reported in Table 3.6, and the *J** constants were not reported here because of the inaccurate determination described above.

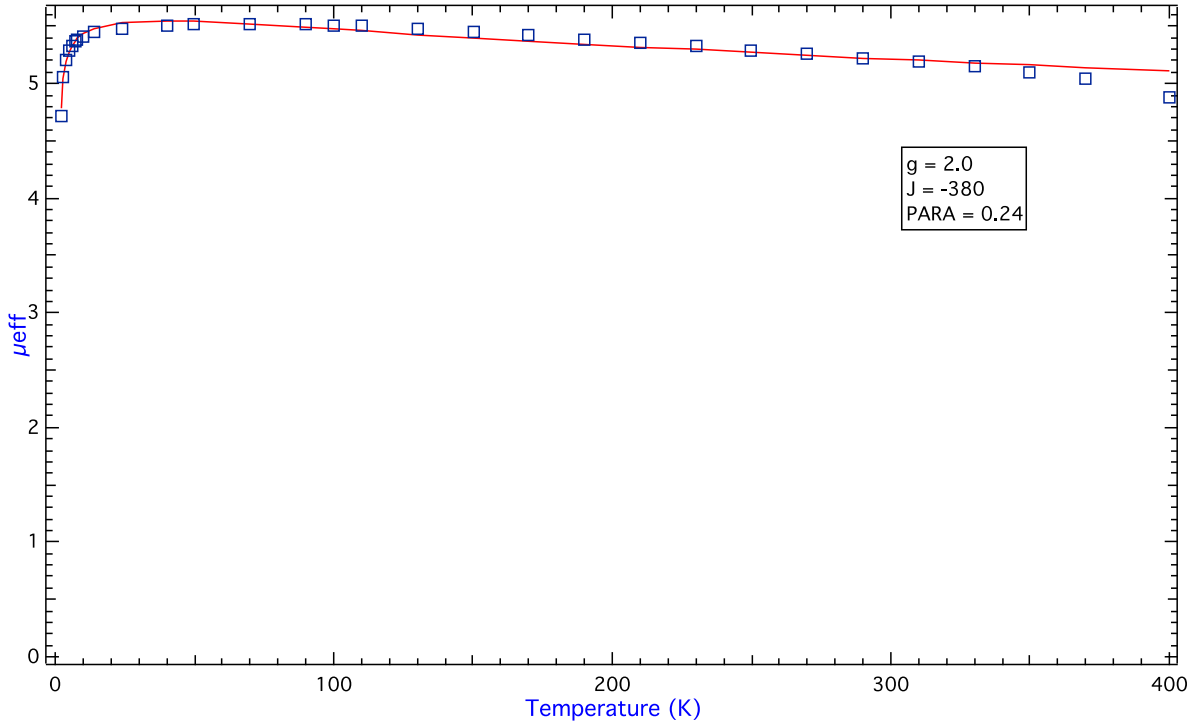

Figure 3.18. The effective magnetic moment of Complex **12** (blue square), and the solid line represents a fit to the data using parameters described in the text.

Table 3.6. Magnetic Properties and *J*-Couping Constants of $[Cr_2(tren)_2(L^{sq,cat})](BPh_4)_2(BF_4)$.

Complex	*J*-Coupling (cm^{-1})
11	-380
12	-380
13	-390
14	-380
15	-380
16	-380
17	-350
18	-340
19	-340

Halogen is π-donor and σ-acceptor due to their relatively high electronegativity. Since halogen is binding to the tetraoxolene ligand via a sigma bond, they are considered more σ-electron withdrawing. The spin polarization effect should be different among the halogen series due to their various electronegativity and the size of the electron cloud. However, the *J* values of Complex **12**, **14** and **15** are the same with Complex **11**, while Complex **13** shows a slightly larger *J* (Table 3.6).

In general, electron withdrawing groups (EWG) increase the double bond character in an aromatic ring by rearranging electrons in the *p* orbitals. F is the most electronegative element in the periodic table with strong coulombic attraction due to the distance factor, and it has very strong electronegativity dipole. In addition, F possesses strong resonance effect because of its sufficient 2*p*-2*p* overlap with the aromatic carbon because of their same relative sizes, and it is more donating than other halides. The electronegativity dipole and the resonance dipole cancel out each other resulting in a zero-net dipole in F so that F presents no inductive effect when substituting aromatic rings.[68] The Hammett parameter for fluorine in para position is +0.15, which also prove that F is only very weakly electron withdrawing.[69]

Unlike F, chlorine has insufficient 3*p*-2*p* overlap with the aromatic C, its resonance dipole is much weaker that the electronegativity dipole dominates, which makes it more electron

withdrawing. The empty σ* orbital of Cl is high in energy to prevent spin delocalization, so Complex **13** presents a higher *J* value compared with Complex **11**.

Similar with Cl, electron withdrawing properties should dominate in Br and I. However, their huge electron clouds shield their nuclei to weaken the withdrawing effects. The long C-Br and C-I bond distances agree with this hypothesis. The spin density plots of $(BA^{sq,cat})^{3-}$ and $(IA^{sq,cat})^{3-}$ generated from DFT calculations show sparse β spin density on the oxygen atoms (Fig. 3.19), and this also support our hypothesis about the experimental trend (see detail explanation of the computational results on spin polarization in Chapter 2).

(a) (b)

Figure 3.19. Excess spin density associated with the highest energy, singly-occupied molecular orbital of $(BA^{sq,cat})^{3-}$ (a) and $(IA^{sq,cat})^{3-}$ (b).

The six sp^2 hybridized carbons in phenyl group show the conjugation of the C-C bonds within the ring, and the patial-double bond characters are equally distributed. Phenyl is considered both an inductively withdrawing group (-*I*) and a resonance donating group (+*M*) because of its higher electronegative sp^2 carbons and electron-donating ability of a π conjugated system, respectively.[78] James and Williams's study[79] on Cu-bipyridine (bpy) systems shows that the phenyl group is very weakly withdrawing when substituting on a bpy ligand. Therefore, the substituent effect of phenyl is possibly similar to F with -*I* and +*M* cancelling out each other, which presents no intraligand delicalization. The *J* constant extrapolated by experimental data agrees with this theory. Computational and photophysical experimental results previously conducted on Ru (II)-bpy complexes in our group[61,80] show that both steric effect and the inter-

ring torsional angle are detrimental for intraligand delocalization. Coplanar orientation between the aromatic ring substituent and the ligand in a system facilitates spin delocalization, while orthogonal configuration will prevent delocalization by reducing both steric hindrance and electron-electron repulsion.[61,80] Orthogonal twist angle between two rings therefore is indicative of thermodynamic stabilization. The inter-ring torsion can be used to evaluate the spin polarization in the system (Fig. 3.20). Unfortunately, the growth of $[Cr_2(tren)_2(L^{sq,cat})](BPh_4)_2(BF_4)$ crystals was unsuccessful to provide structural information.

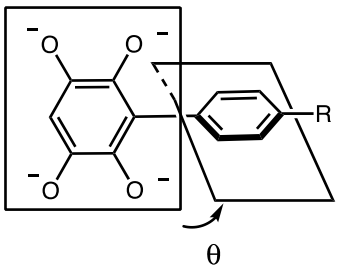

Figure 3.20. The inter-ring torsion angle (ϑ) of phenyl-substituted complexes.

NMe_2-Ph is chosen to change the directionality, i.e. vertical extension, of spin polarization within the system. As a π-donor, NMe_2 will delocalize spins by introducing more orbital mixing and decrease HOMO-LUMO gap; thus, *J* determined from the fit of Complex 1**7** should be smaller compared with Complex 1**6**. However, the difference in *J* coupling constants between the two complexes are insignificant. Computational studies of substituent effects on Fe(II) chromophore reported by Jakubikova and coworkers[70] suggest that an aromatic linker group between the ligand and EDG or EWG will attenuate the substituent effect of spin delocalization. Since the magnitude of *J* is small, and it will be hard to gauge the significance of the effect.

Both anthracene and naphthalene were introduced to delocalize spin from the interacting oxygens because of their extended conjugated system. The *J* values of both Complex **18** and **19**

are greatly reduced (Table 3.6) to prove that polyaromatic hydrocarbon ligands are the most sufficient to decrease the strength of the spin exchange interaction.

No magnetic data was collected for $[Cr_2(tren)_2(AnT^{sq,cat})](BPh_4)_2(BF_4)$ since the synthesis of this complex is unsuccessful. Upon oxidation of $[Cr_2(tren)_2(AnT^{cat,cat})](BPh_4)_2$, ESI-MS spectrum shows no detection of $[Cr_2(tren)_2(AnT^{sq,cat})]^{3+}$ species. The electrochemical data of $[Cr_2(tren)_2(AnT^{cat,cat})](BPh_4)_2$ exhibits an irreversible redox wave beyond one-electron oxidation, and the electrochemical properties will be further discussed in Chapter 5. These experimental evidences suggest that $[Cr_2(tren)_2(AnT^{sq,cat})]^{3+}$ is unstable, and the chelating mode of (Me-$AnT^{sq,cat})^{3-}$ with Cr (III) ions is likely to be form (3) (Fig. 3.21), where the spin is more delocalized within the inner aromatic ring. This causes the decomposition of the dimer.

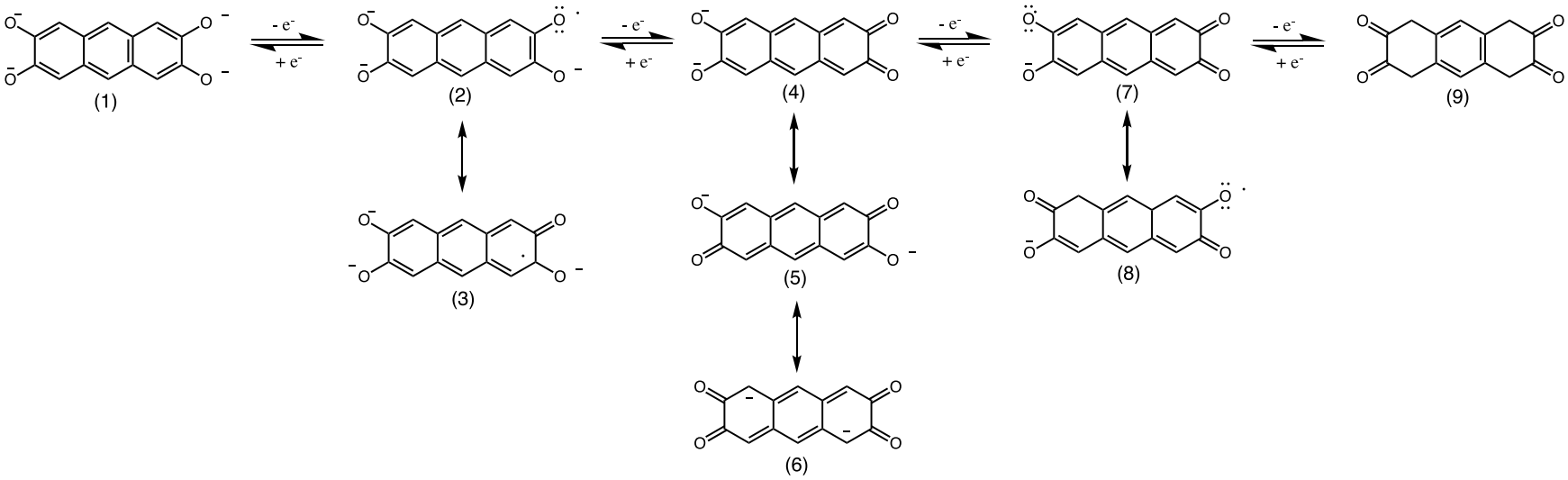

Figure 3.21. Multiple possible chelating forms of deprotonated 2,3,6,7-tetraoxoanthracene undergoing one-electron redox reactions.

Electrons are highly delocalized within the anthracene rings, and the resonance effect (Fig. 3.17) reduces the basicity of $(AnT^{sq,cat})^{3-}$ and makes it very weakly chelating to one Cr(III) ion. It may be surprising that $[Cr_2(tren)_2(AnT^{sq,cat})]^{3+}$ is highly unstable, and $[Cr_2(tren)_2(Me\text{-}AnT^{sq,cat})](BPh_4)_2(BF_4)$ (**19**) is stable. The stability of complex **19** may be a cause of substituent effect. The inductive effect of σ-donor methyl group on Me-AnT stabilizes the ring and attenuates spin delocalization to increase the stability of $[Cr_2(tren)_2(AnT^{sq,cat})](BPh_4)_2(BF_4)$.

3.6 Concluding Comments

Our goal in this chapter was to establish the relationship of how substituent affects spin delocalization/polarization, and how it manifests on magnetic properties. The variable-temperature magnetic data collected for the Cr(III) dimeric series provide some experimental evidence to support the correlation, because the strength of the spin exchange interaction decreases when Cr(III) ions are coordinated to naphthalene and anthracene bridging ligands (Complex **18** and **19**). However, there is no trend can be established among the halogenated Cr(III) dimers. No significant substituent effect is observed with a phenyl linker. The result obtained from the vertical spin polarization is preliminary, and more substituents, CN-phenyl and CF_3-phenyl, should be developed for magnetic studies in order to further rationalize our hypothesis. To modulate the *J* value, the proper substituents need to be chosen, and our series developed is still lacking a π-donor and π-acceptor to show all possible variations. The syntheses of these substituents are still under development, and some of them will be discussed in Chapter 6.

The syntheses of all substituted ligands are quite challenging because they do not follow similar synthetic schemes. It will be problematic to randomly choose a few substituents and start

the syntheses. Computational calculations prove to be a useful tool to provide insight about the synthetic viability. DFT calculations collected on the free ligands (Chapter 2) are informative, which should be used continuously in the future.

MagFit[46] employs the HDVV Hamiltonian to extrapolate *J* by comparing the experimental data and then fitted them with the least-square fit. When the magnitude of *J* is very small and relatively close to the Zeeman splitting, the HDVV Hamiltonian fails. In this case, a suitable software with full matrix diagonalization will need to be used for accurate determination of the superexchange coupling constants among the $[Cr_2(tren)_2(L^{cat,cat})](BPh_4)_2$ complexes. However, the appropriate software with full matrix diagonalizations is not available during my graduate career. Unfortunately, the experimental data collected for this series fail to provide insightful information about the substituent effect without the proper software.

One of the biggest obstacles is to accurately determine *J** superexchange constants for the $[Cr_2(tren)_2(L^{sq,cat})](BPh_4)_2(BF_4)$ series. The magnetic data collected up to 400 K do not show enough thermal population to higher spin-coupled state. We propose that the superexchange interaction is too weak to perturb the overall exchange interaction within these systems, so the determination of *J** might not be detrimental for our analysis in this project. It is not impossible to collect magnetic data to accurately extrapolate *J** by MagFit.[46] The magnetic data will need to be collected over higher range of temperature, > 400 K, to thermally populate more spins into the third spin state. Therefore, a heat resistant sample holder with minimal magnetic background should be developed to be compatible with the MPMS® 3 SQUID external oven. TGA analysis should be acquired before conducting high temperature magnetic susceptibility measurement for the thermal stability of samples.

APPENDIX

APPENDIX

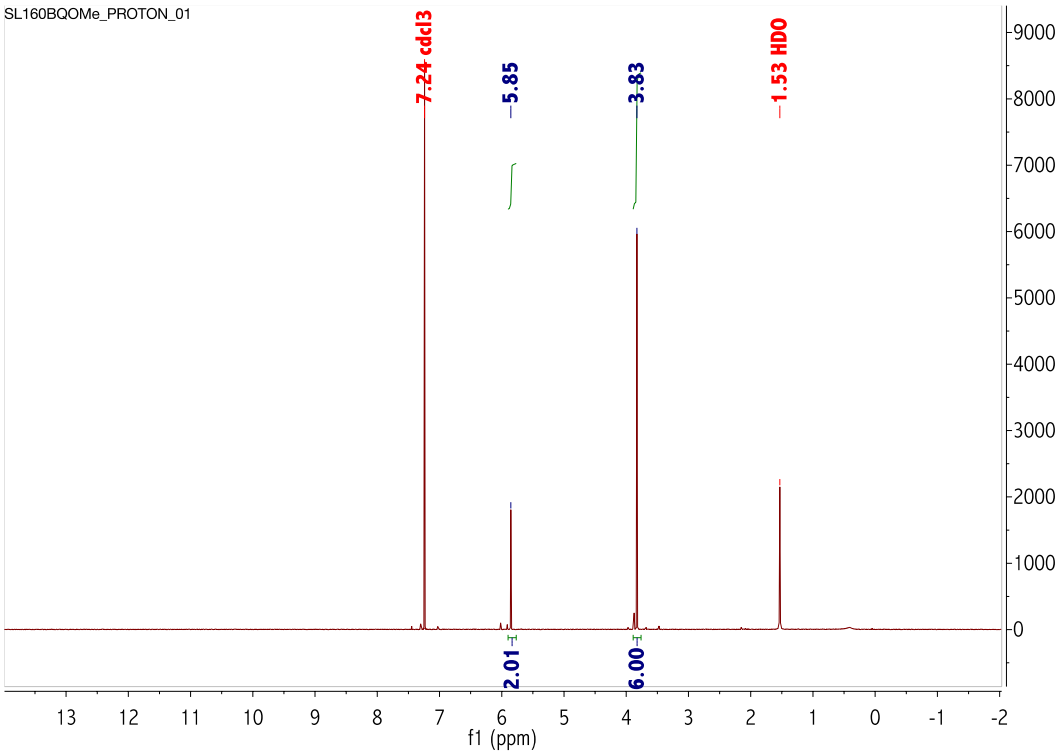

Figure 3.22. ^{1}H NMR of 2,5-dimethoxy-1,4-benzoquinone in $CDCl_3$.

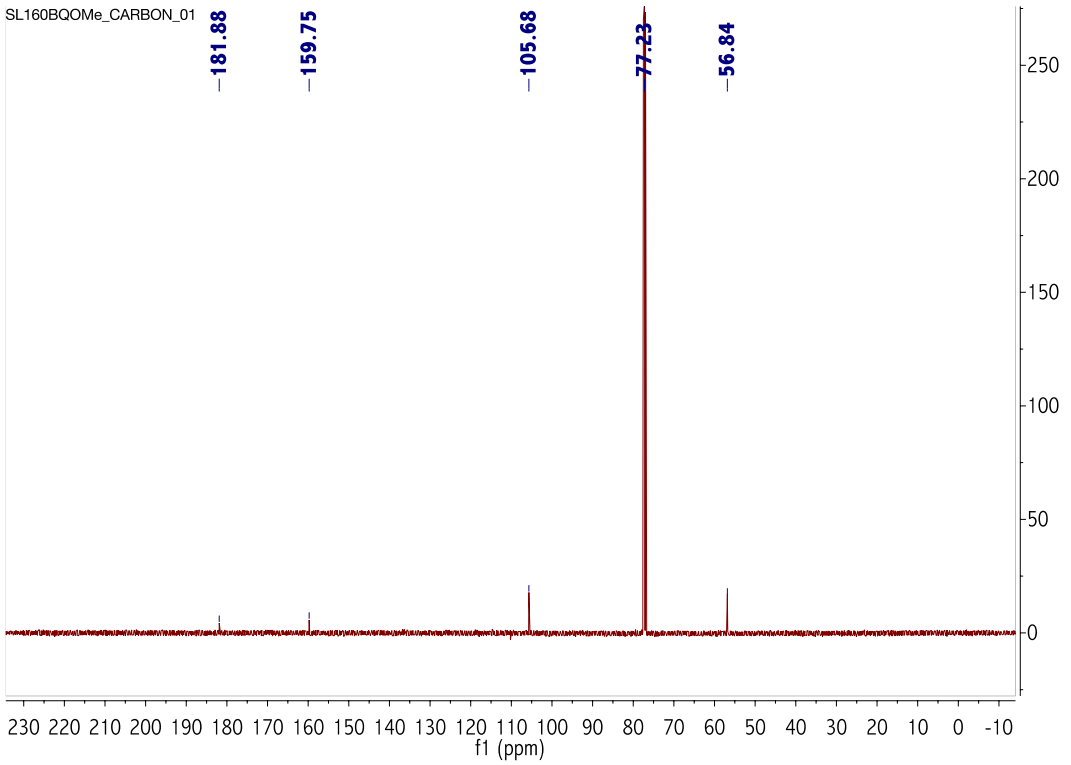

Figure 3.23. ^{13}C NMR of 2,5-dimethoxy-1,4-benzoquinone in $CDCl_3$.

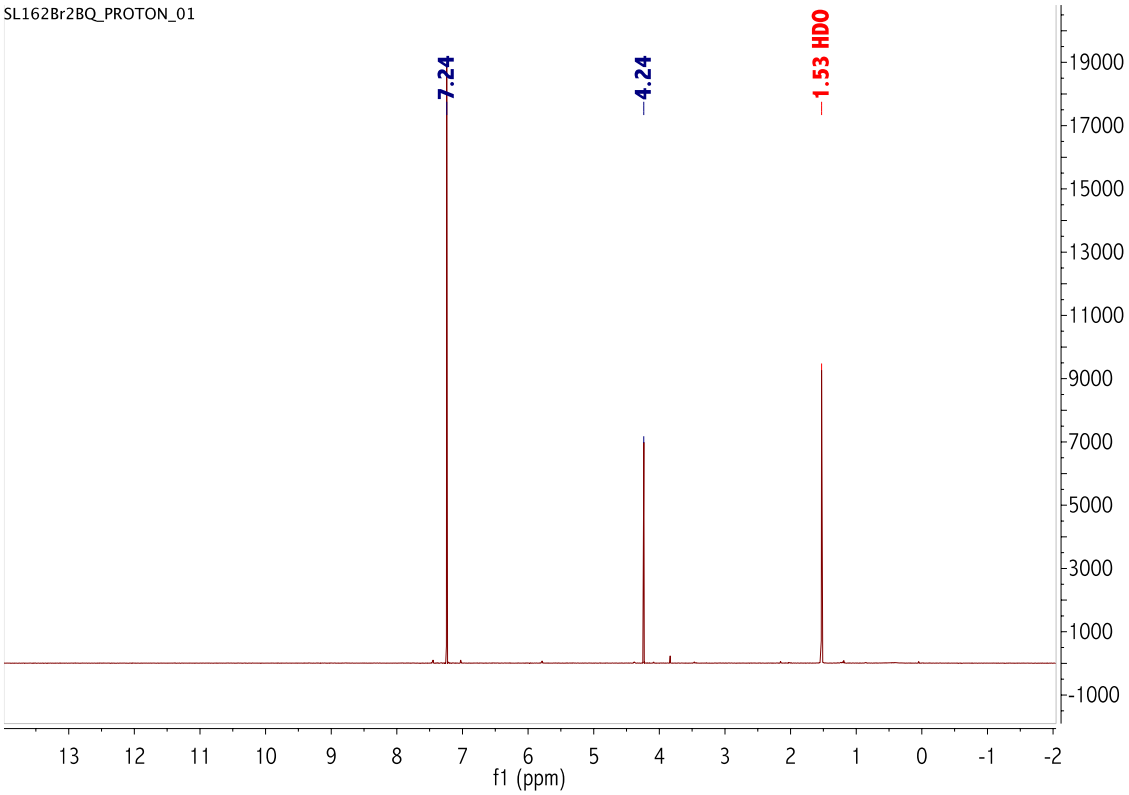

Figure 3.24. ^{1}H NMR of 2,5-dibromo-3,6-dimethoxy-1,4-benzoquinone in $CDCl_3$.

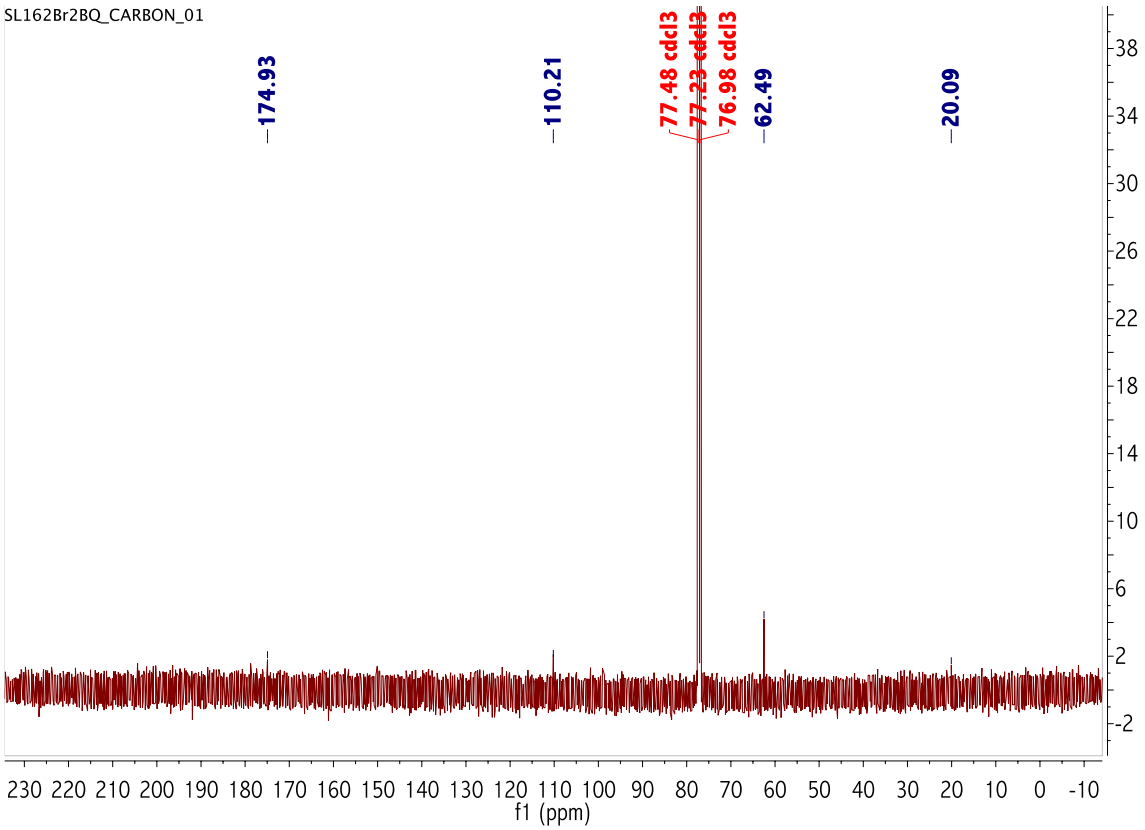

Figure 3.25. ^{13}C NMR of 2,5-dibromo-3,6-dimethoxy-1,4-benzoquinone in $CDCl_3$.

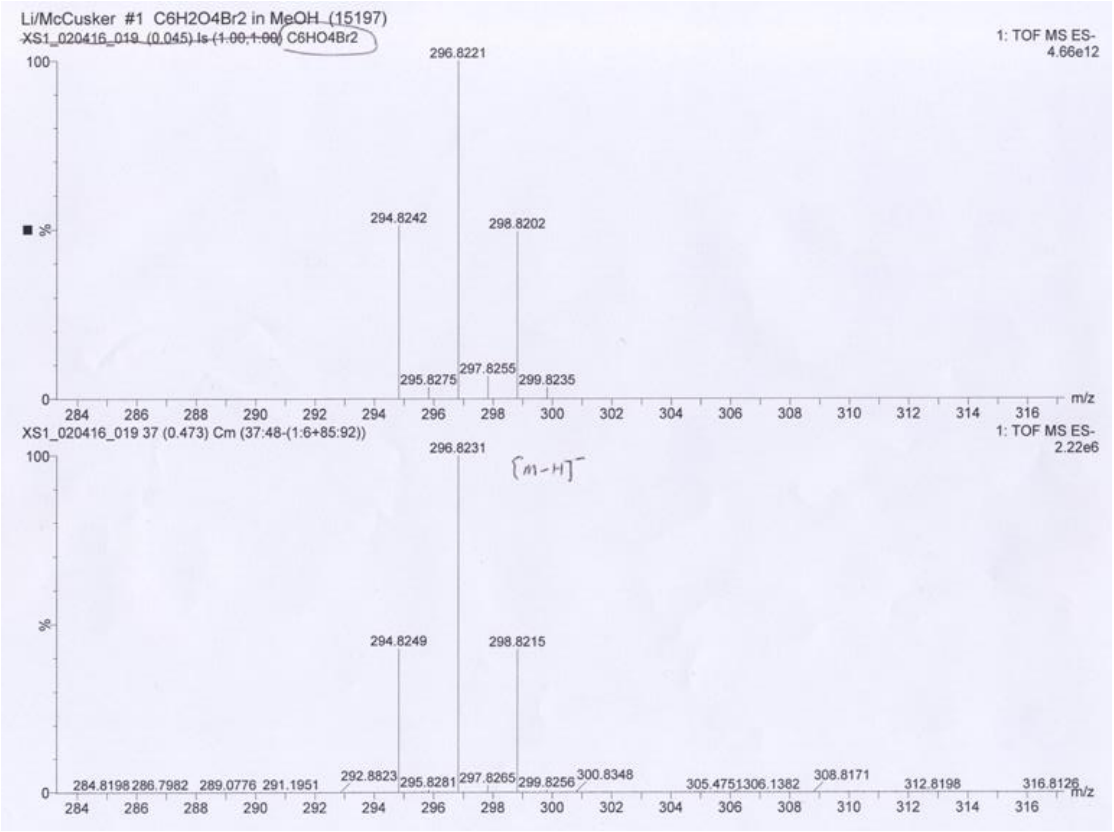

Figure 3.26. ESI-MS of H_2BA. Top: calculated isotope pattern for $[M-H]^-$ ($C_6H_1O_4Br_2$). Bottom: experimental result.

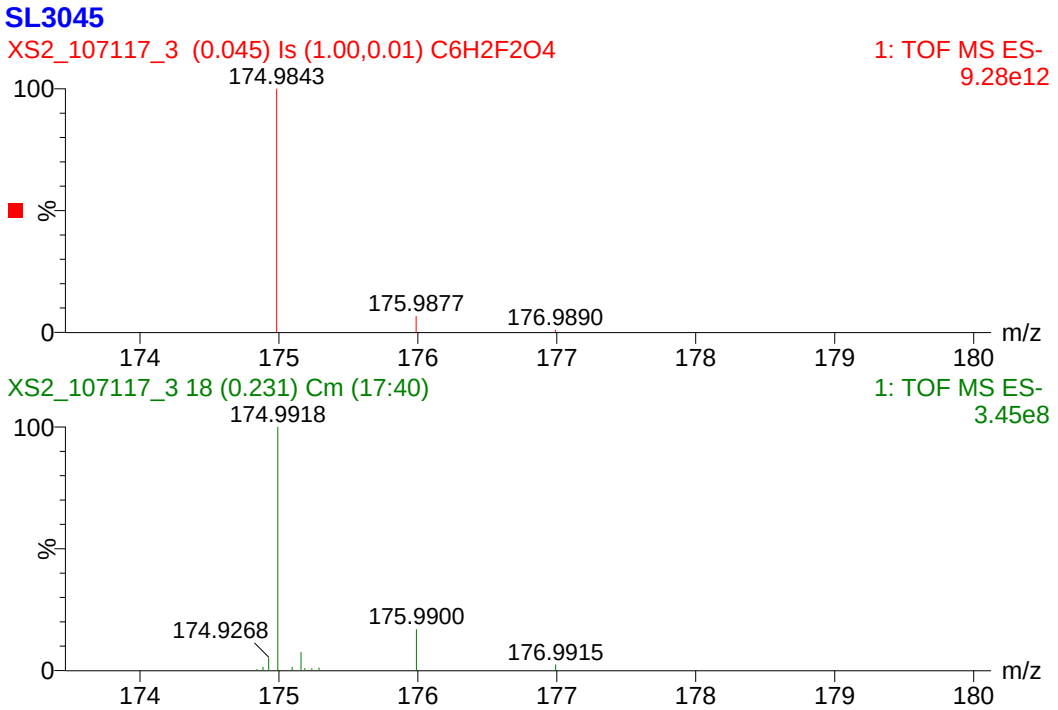

Figure 3.27. ESI-MS of H_2FA. Top: calculated isotope pattern for $[M-H]^-$ ($C_6H_1O_4F_2$). Bottom: experimental result.

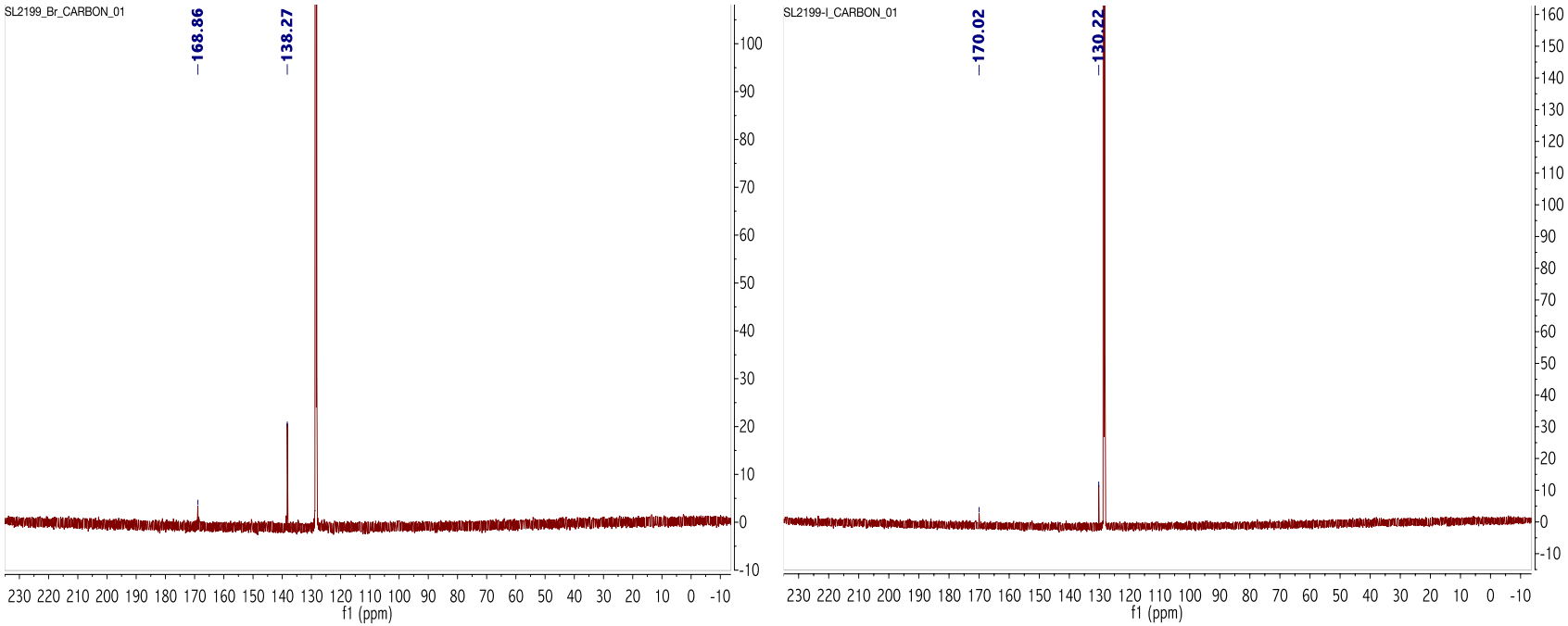

Figure 3.28. ^{13}C NMR of bromanil (left) and iodanil (right) in benzene-d_6.

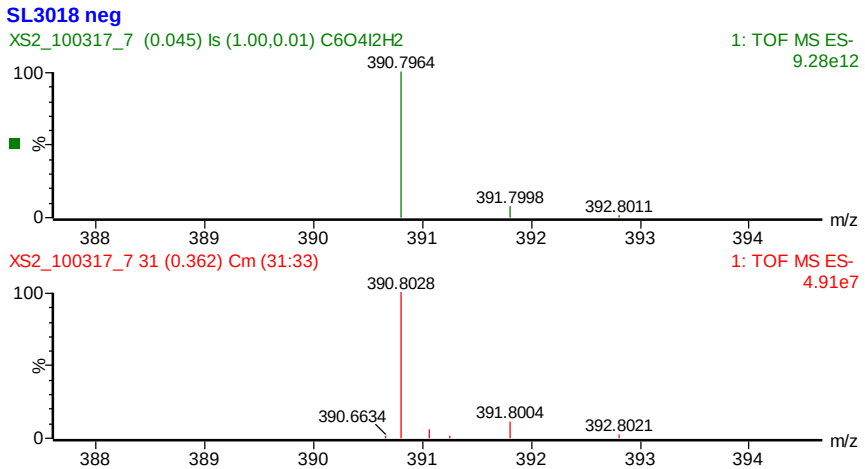

Figure 3.29. ESI-MS of H_2IA. Top: calculated isotope pattern for $[M-H]^-$ ($C_6H_1O_4I_2$). Bottom: experimental result.

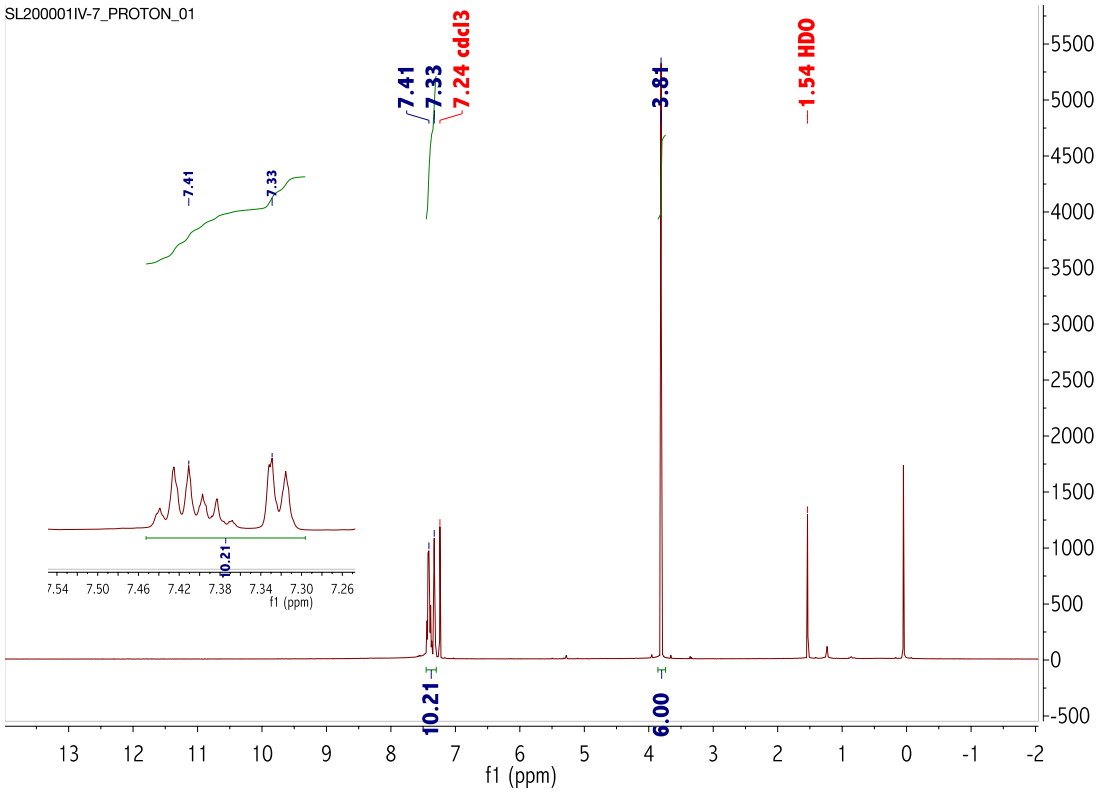

Figure 3.30. ^{1}H NMR of 2,5-dimethoxy-3,6-diphenyl-1,4-benzoquinone in $CDCl_3$.

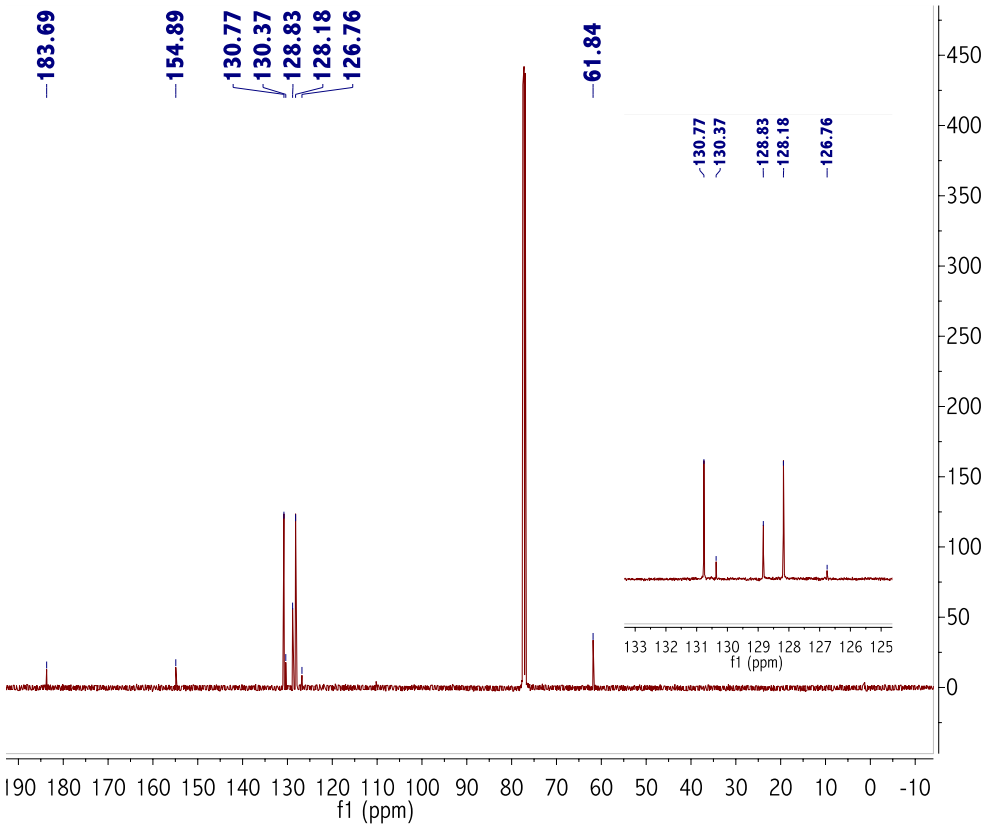

Figure 3.31. ^{13}C NMR of 2,5-dimethoxy-3,6-diphenyl-1,4-benzoquinone in $CDCl_3$.

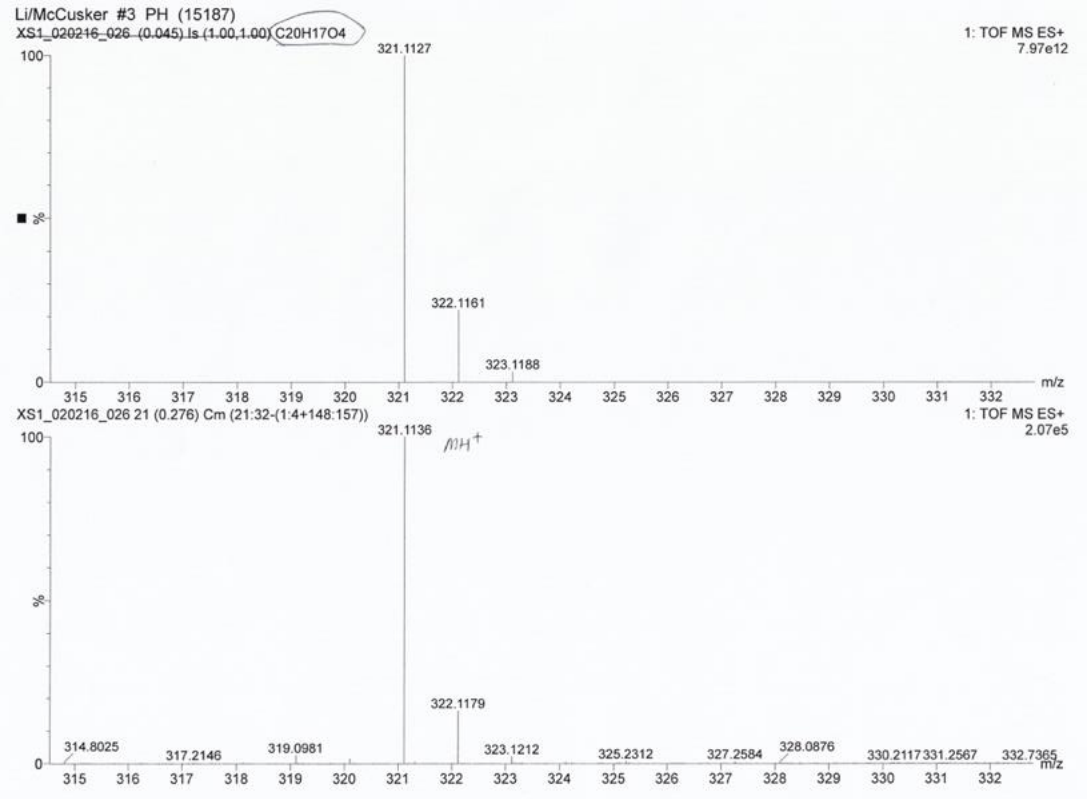

Figure 3.32. ESI-MS of 2,5-dimethoxy-3,6-diphenyl-1,4-benzoquinone. Top: calculated isotope pattern for $[M+H]^+$ ($C_{10}H_{15}O_4$). Bottom: experimental result.

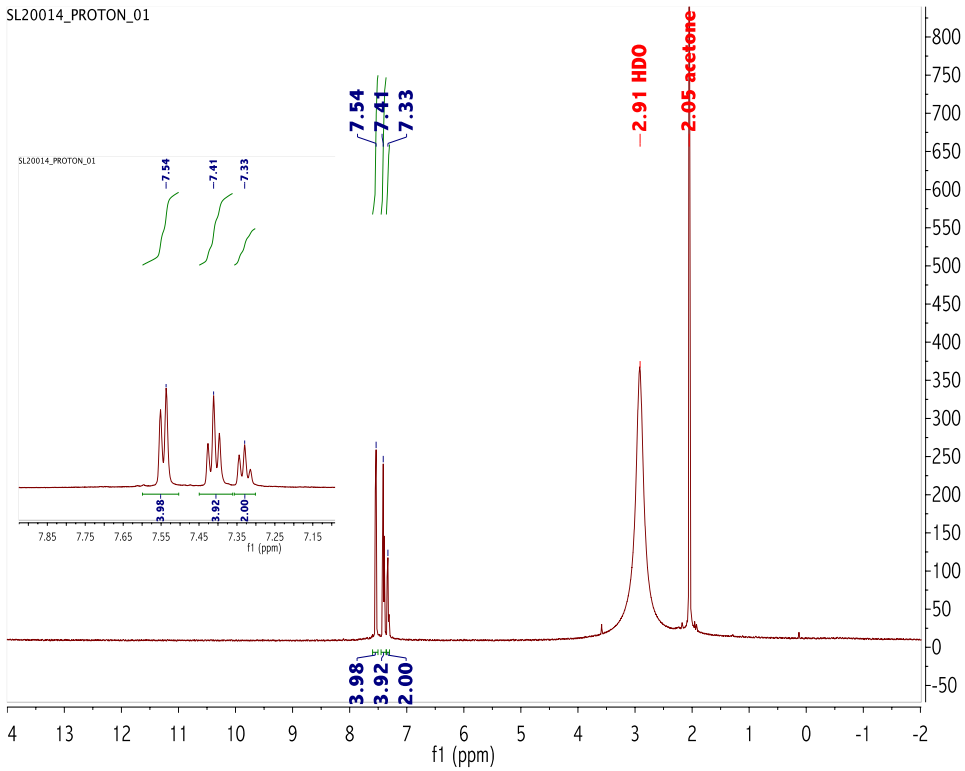

Figure 3.33. ^{1}H NMR of H_2PhA in acetone-d_6.

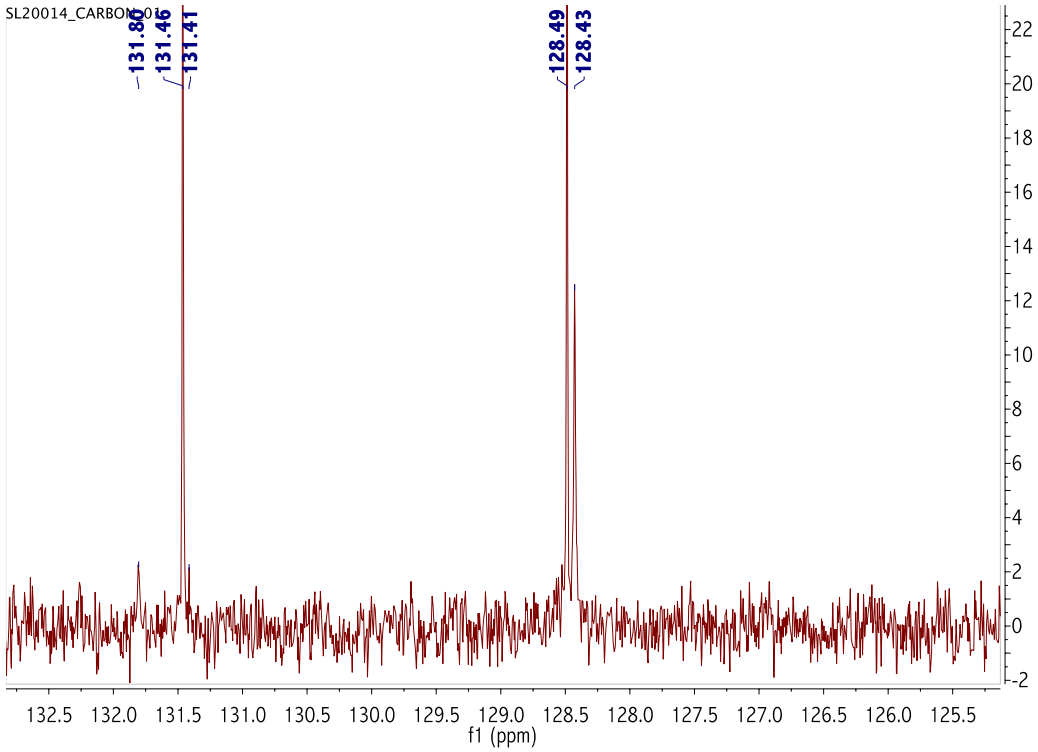

Figure 3.34. ^{13}C NMR of H_2PhA in acetone-d_6.

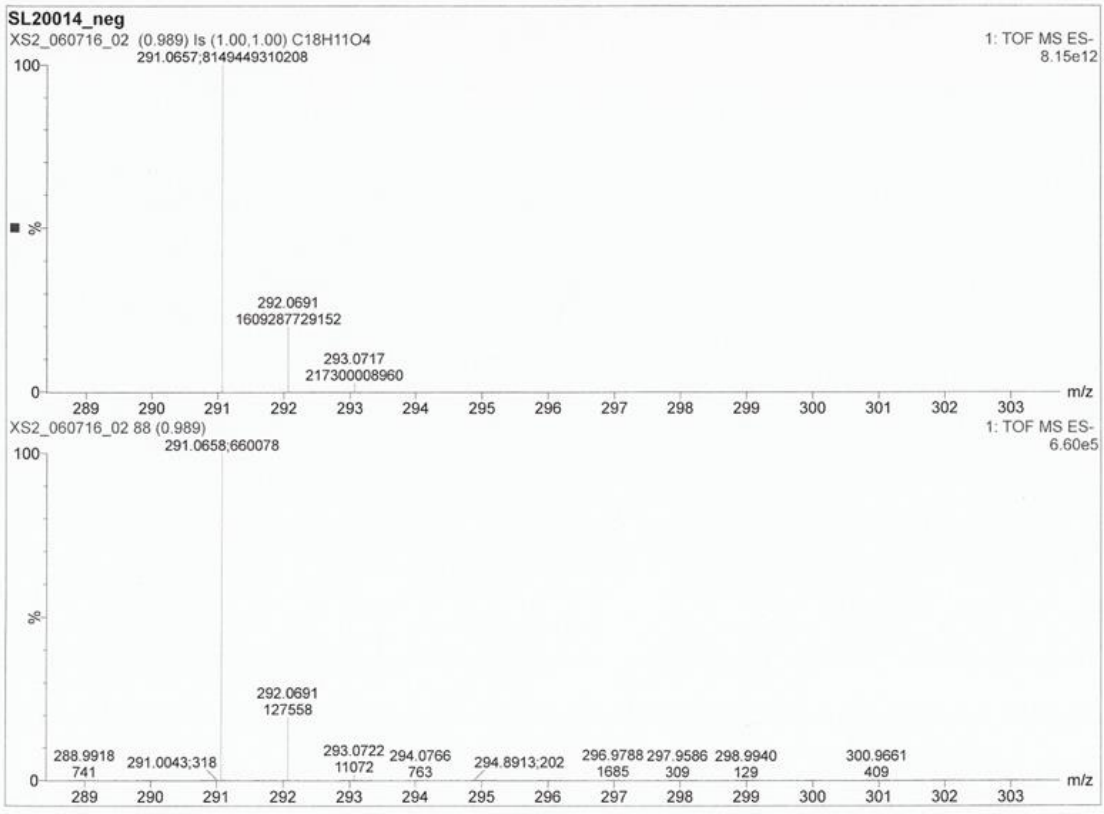

Figure 3.35. ESI-MS of H_2PhA. Top: calculated isotope pattern for $[M-H]^-$ ($C_{18}H_{11}O_4$). Bottom: experimental result.

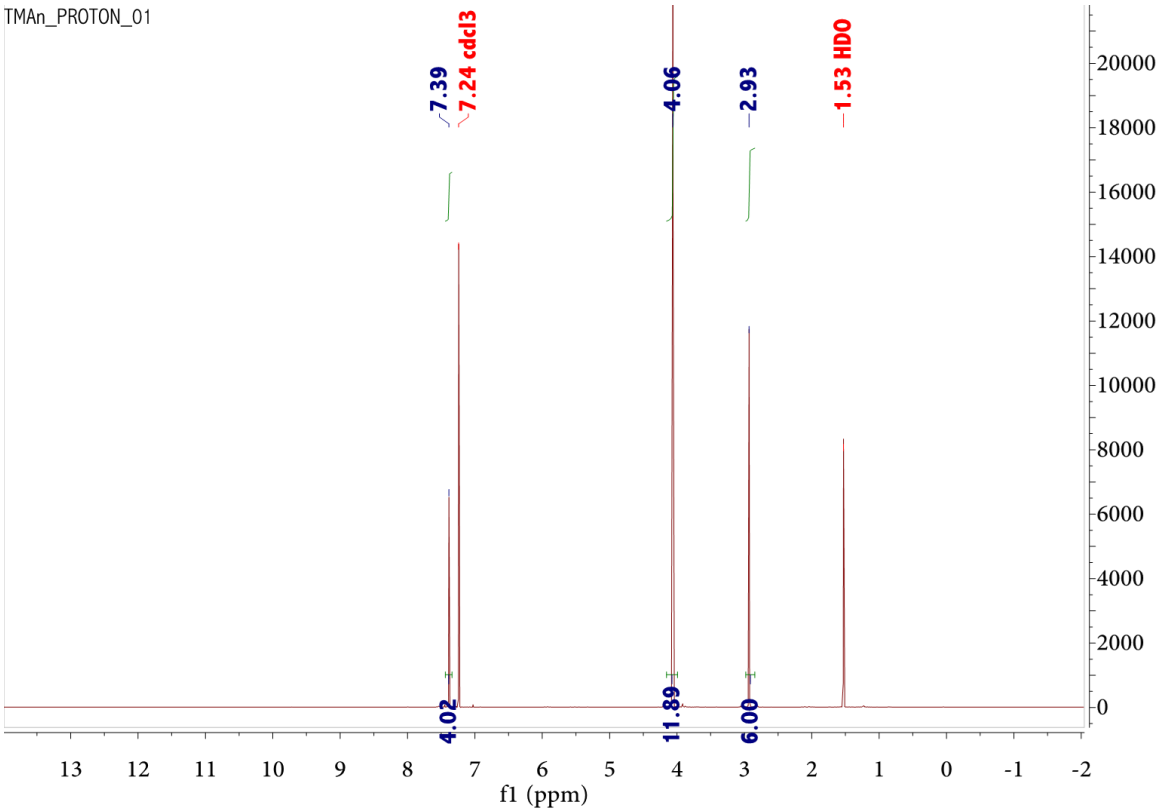

Figure 3.36. ^{1}H NMR of 2,3,6,7-tetramethoxy-9,10-dimethylanthracene in $CDCl_3$.

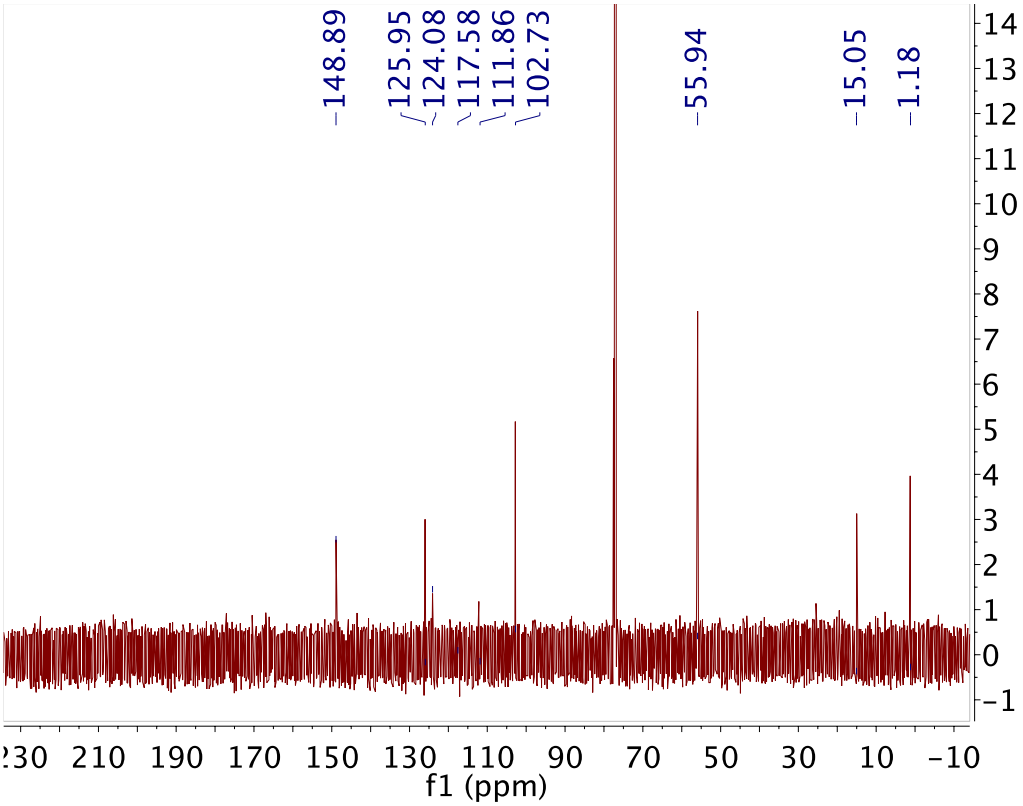

Figure 3.37. ^{13}C NMR of 2,3,6,7-tetramethoxy-9,10-dimethylanthracene in $CDCl_3$.

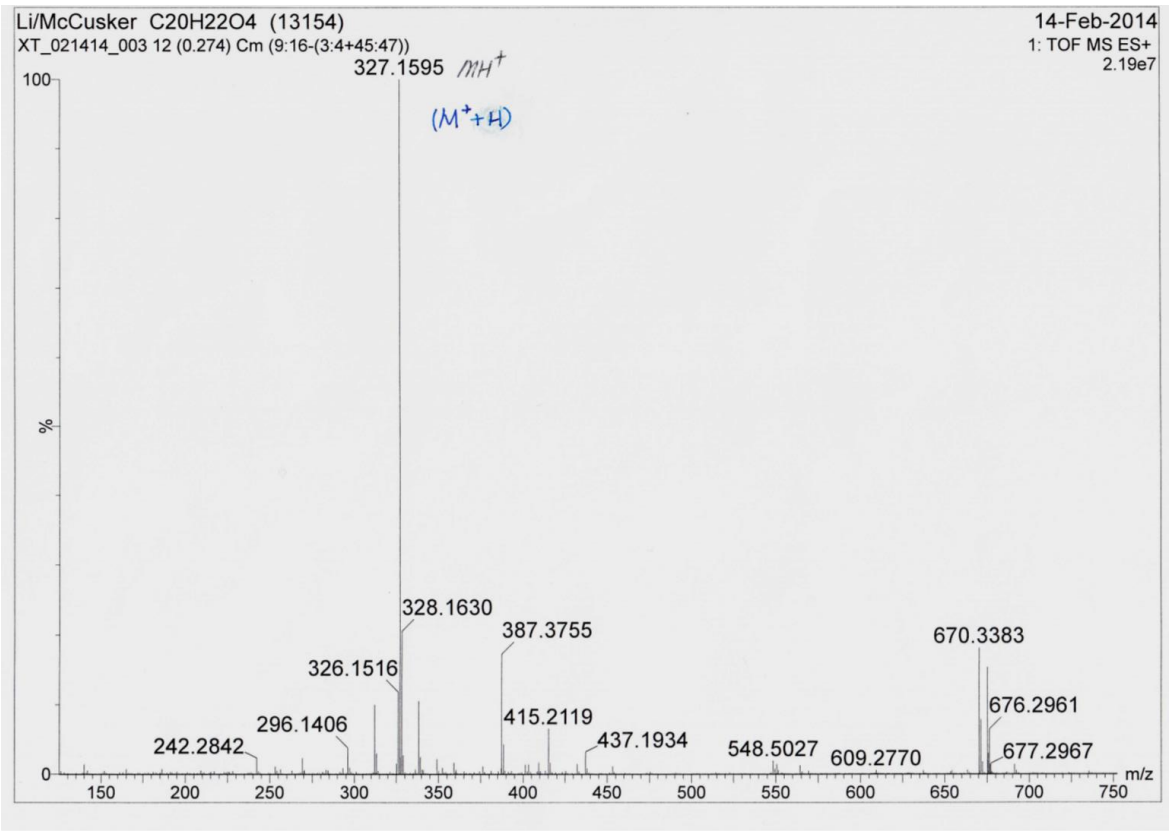

Figure 3.38. ESI-MS of 2,3,6,7-tetramethoxy-9,10-dimethylanthracene. Experimental result for $[M+H]^+$ ($C_{20}H_{23}O_4$).

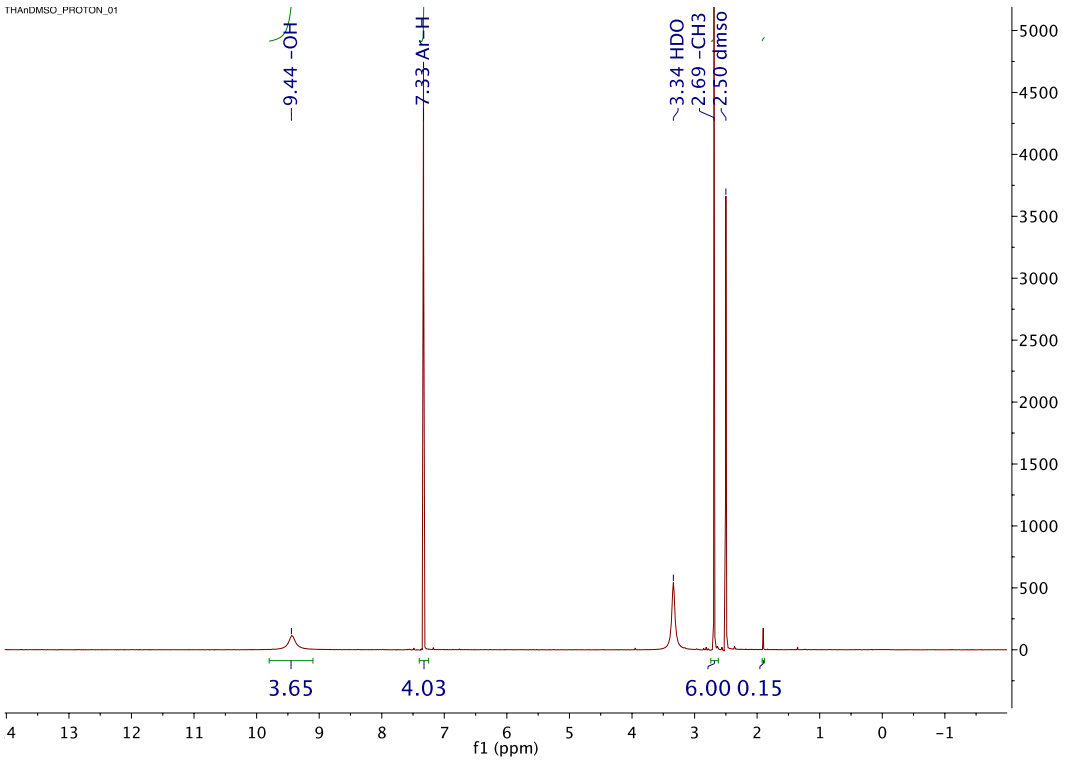

Figure 3.39. ^{1}H NMR of H_4(Me-AnT) in dmso-d_6.

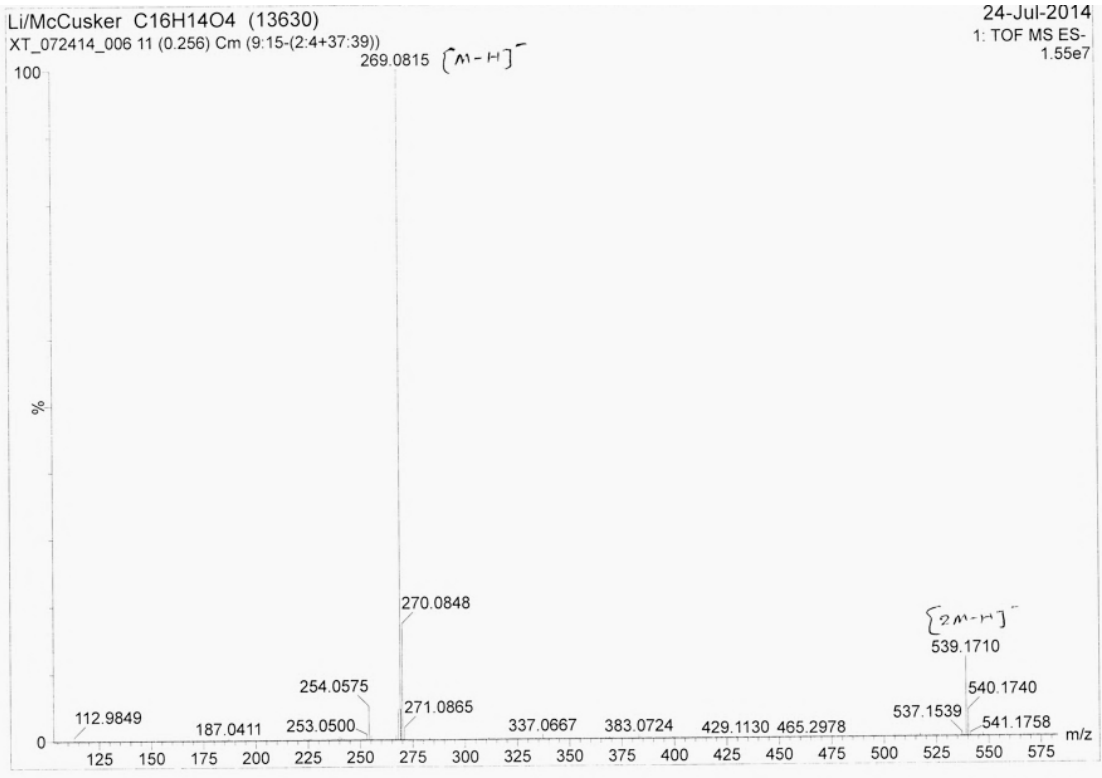

Figure 3.40. ESI-MS of H_4(Me-AnT). Experimental result for $[M-H]^-$ ($C_{12}H_{15}O_4$).

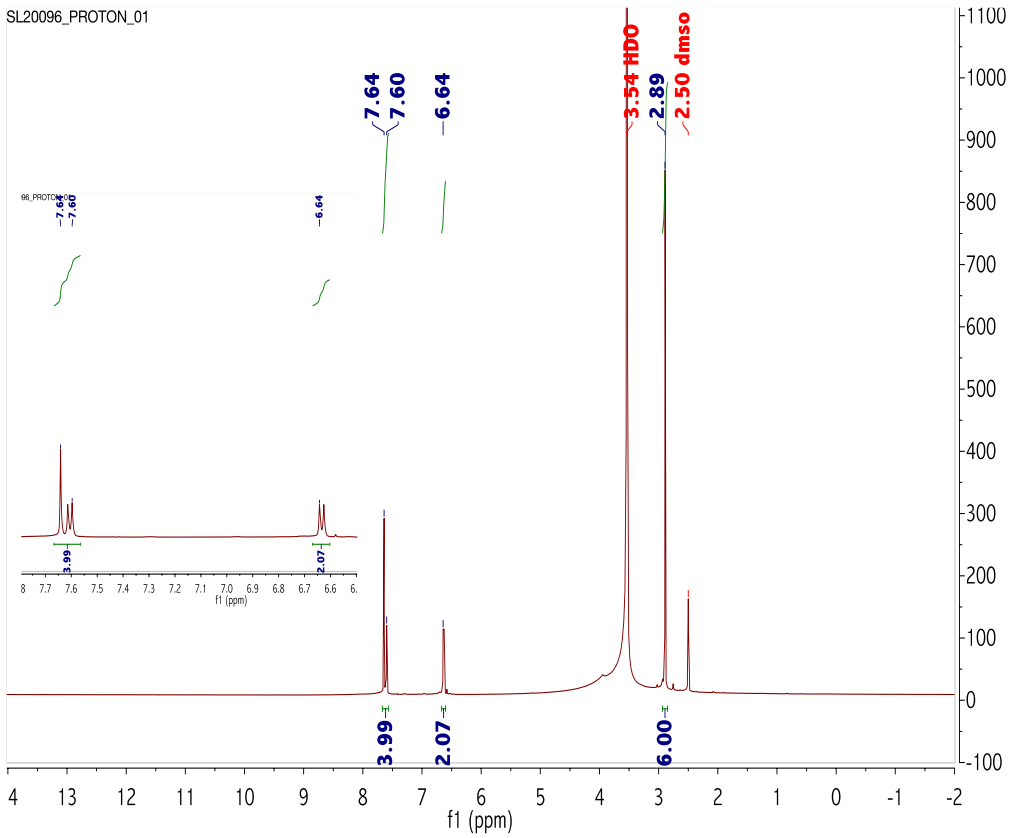

Figure 3.41. ^{1}H NMR of 4-(N,N-Dimethylamino)phenylboronic acid in dmso-d_6.

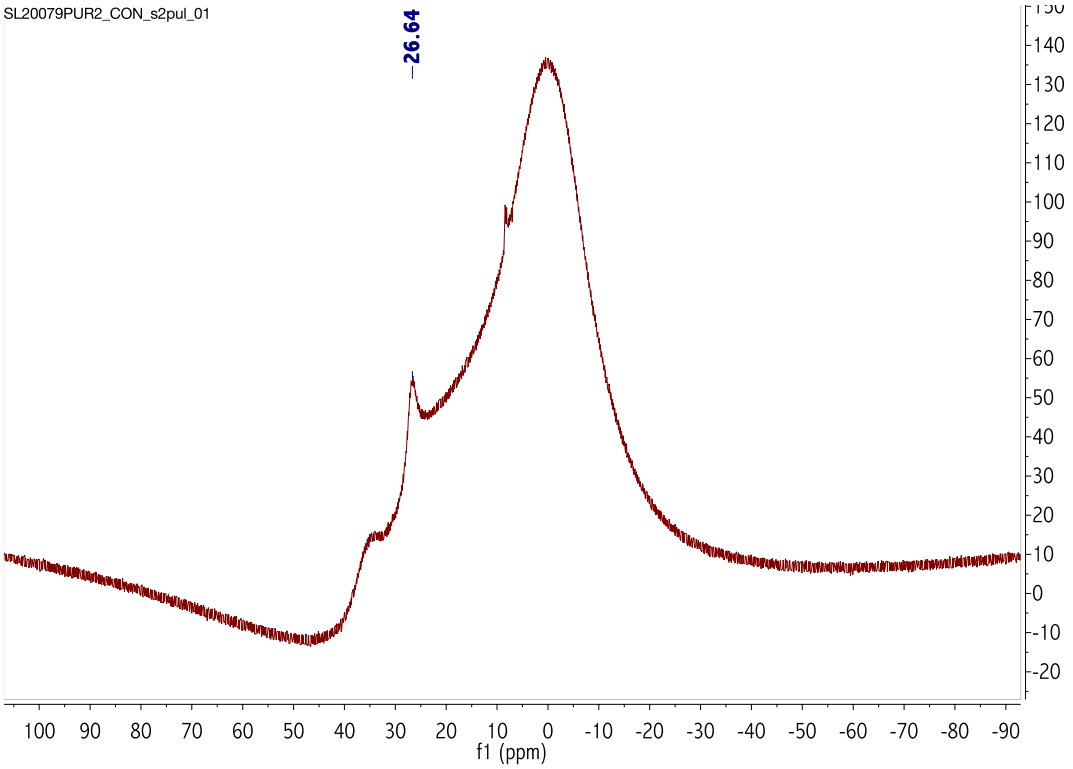

Figure 3.42. ^{11}B NMR of 4-(N,N-Dimethylamino)phenylboronic acid in dmso-d_6.

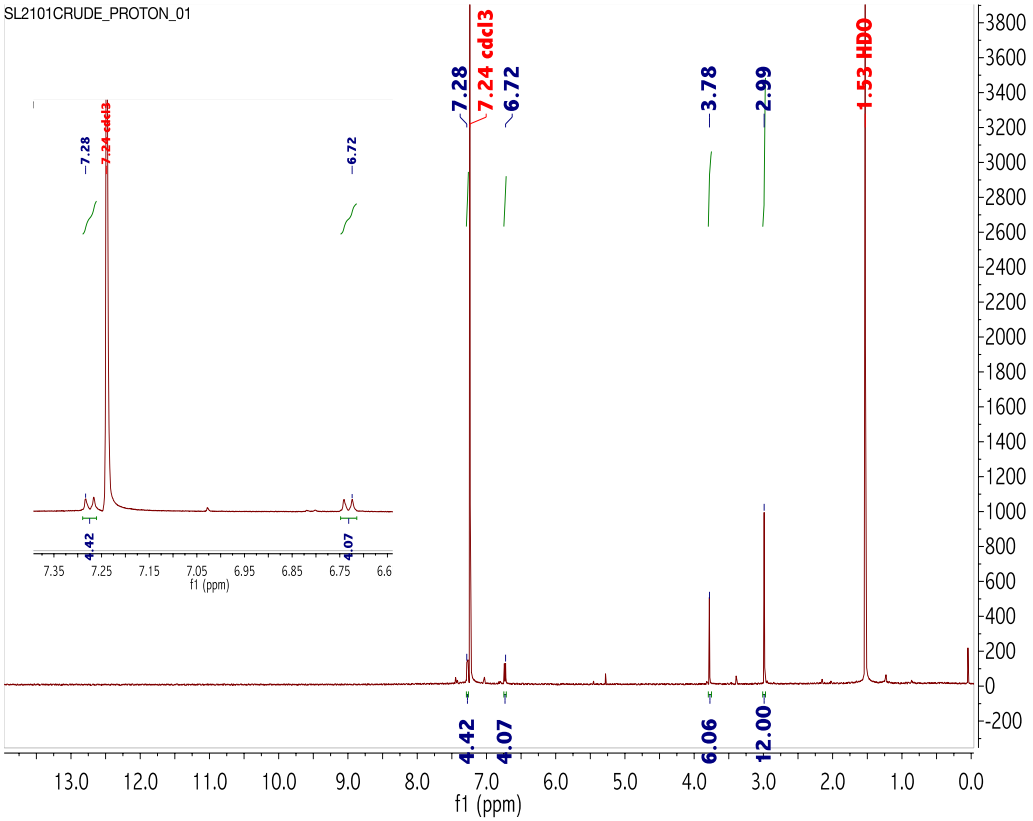

Figure 3.43 ^{1}H NMR of 2,7-dimethoxy-3,6-di(N,N-dimethylaminophenyl)benzoquinone in $CDCl_3$.

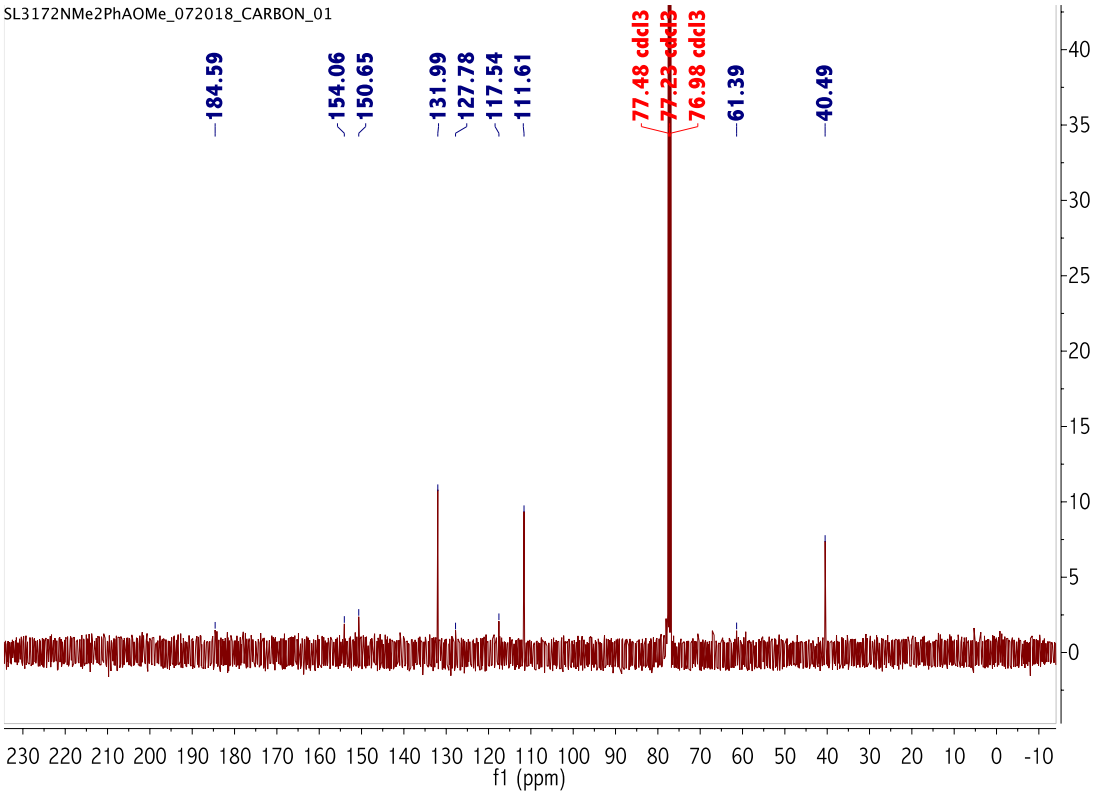

Figure 3.44. ^{13}C NMR of 2,7-dimethoxy-3,6-di(N,N-dimethylaminophenyl)benzoquinone in $CDCl_3$.

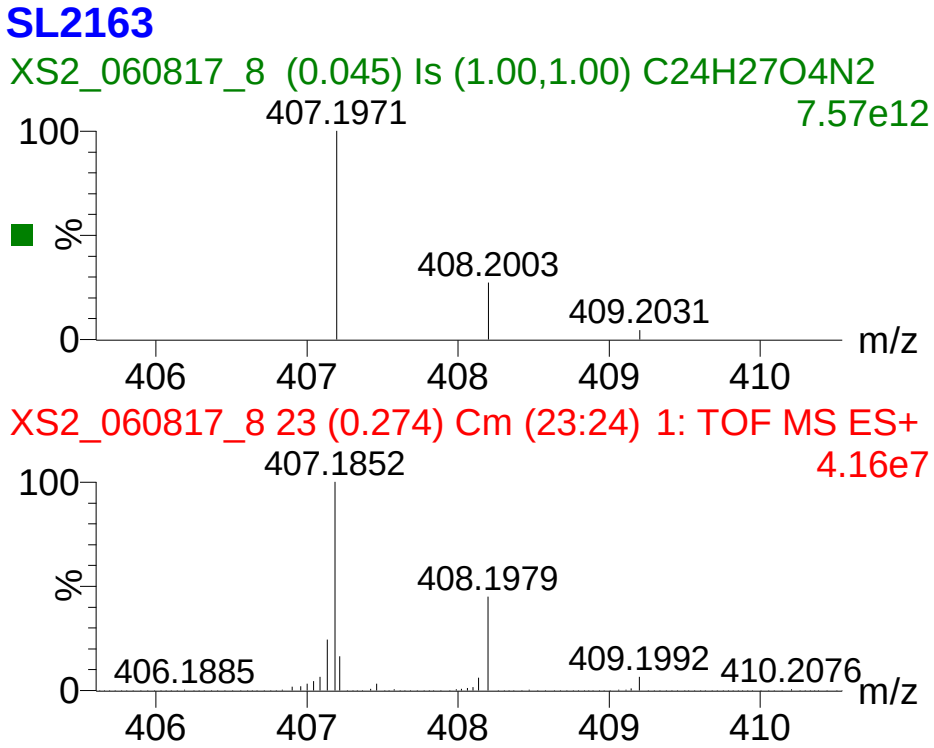

Figure 3.45. ESI-MS of 2,7-dimethoxy-3,6-di(N,N-dimethylaminophenyl)benzoquinone. Top: calculated isotope pattern for $[M+H]^+$ ($C_{24}H_{27}O_4N_2$). Bottom: experimental result.

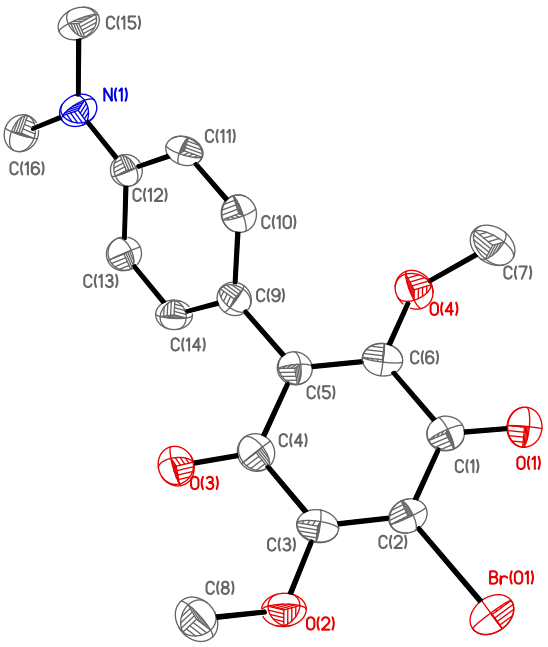

Figure 3.46. ORTEP drawing of 2,7-dimethoxy-3-bromo-6-(N,N-dimethylaminophenyl)benzoquinone from single-crystal x-ray structure determination. Atoms are represented as 50% thermal ellipsoids. Hydrogen atoms are omitted for clarity.

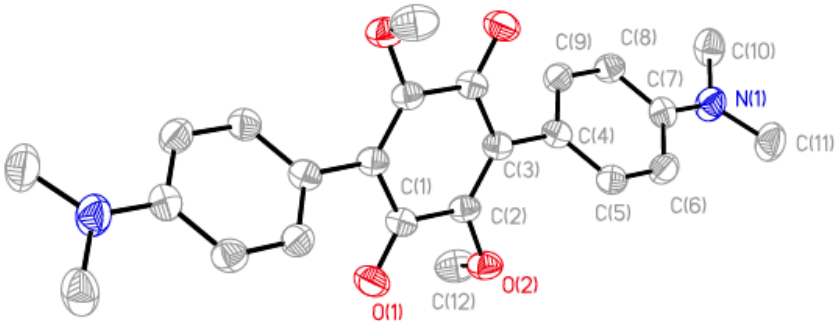

Figure 3.47. ORTEP drawing of 2,7-dimethoxy-3,6-di(N,N-dimethylaminophenyl)benzoquinone from single-crystal x-ray structure determination. Atoms are represented as 50% thermal ellipsoids. Hydrogen atoms are omitted for clarity.

Table 3.7. Crystal data and structural refinement for 2,7-dimethoxy-3,6-di(N,N-dimethylaminophenyl)benzoquinone).

Empirical formula	$C_{12}H_{14}NO_2$
Formula weight (g/mol)	204.24
Temperature (K)	173(2)
Crystal system	Triclinic
Space group	$P\bar{1}$
Cell dimension:	
a (Å)	8.1020(7)
b (Å)	8.3200(7)
c (Å)	8.7689(7)
$\boldsymbol{\alpha}$ (˚)	98.2520 (10)
$\boldsymbol{\beta}$ (˚)	113.4700 (10)
$\boldsymbol{\gamma}$ (˚)	101.4940 (10)
Volume (Å^3)	514.73(7)
Reflections measured	8864
unique reflections	2034
Z	2
μ(MoKσ) (mm^{-1})	0.090
D_{calc} (g cm^{-3})	1.318
R_{int}	0.0272
R_1 (I>2σ(I))[a]	0.0547
wR_2[b]	0.1712

[a] $R_1=\sum\frac{||F_o|-|F_c||}{\Sigma|F_o|}$. [b] $wR_2=[\sum w(F_o^2-F_c^2)^2/\sum w(F_o^2)^2]^{1/2}$, $w=1/[\alpha^2(F_o^2)+(aP)^2+bP]$, where $P=[F_o^2+F_c^2]/3$.

Table 3.8. Bond lengths for 2,7-dimethoxy-3,6-di(N,N-dimethylaminophenyl)benzoquinone).

Atoms	Length/Å	Atoms	Length/Å	Atoms	Length/Å
O1-C1	1.223(2)	C1-C2	1.484(2)	C4-C9	1.394(3)
O2-C2	1.364(2)	C1-C3	1.490(2)	C5-C6	1.378(3)
O2-C12	1.417(3)	C2-C3	1.350(2)	C6-C7	1.409(3)
N1-C7	1.371(2)	C3-C1	1.490(2)	C7-C8	1.405(3)
N1-C10	1.447(2)	C3-C4	1.479(2)	C8-C9	1.382(2)
N1-C11	1.445(3)	C4-C5	1.391(3)		

Table 3.9. Bond angles for 2,7-dimethoxy-3,6-di(N,N-dimethylaminophenyl)benzoquinone).

Atoms	Angle/˚	Atoms	Angle/˚	Atoms	Angle/˚
O2-O2-C12	113.76(15)	C4-C3-C1	118.79(15)	O1-C1-C2	118.93(15)
C7-N1-C10	119.84(16)	C5-C4-C3	121.33(16)	O1-C1-C3	121.79(16)
C7-N1-C11	119.82(17)	C5-C4-C9	117.01(16)	C2-C1-C3	119.27(16)
C11-N1-C10	117.97(16)	C9-C4-C3	121.65(16)	O2-C2-C1	114.29(15)
C3-C2-O2	122.33(15)	C2-C3-C1	117.32(16)	C6-C5-C4	122.01(17)
C3-C2-C1	123.38(15)	C2-C3-C4	123.88(15)	C5-C6-C7	121.09(17)
N1-C7-C6	121.48(17)	N1-C7-C8	121.56(17)	C8-C7-C6	116.95(16)
C9-C8-C7	120.97(17)	C8-C9-C4	121.95(17)		

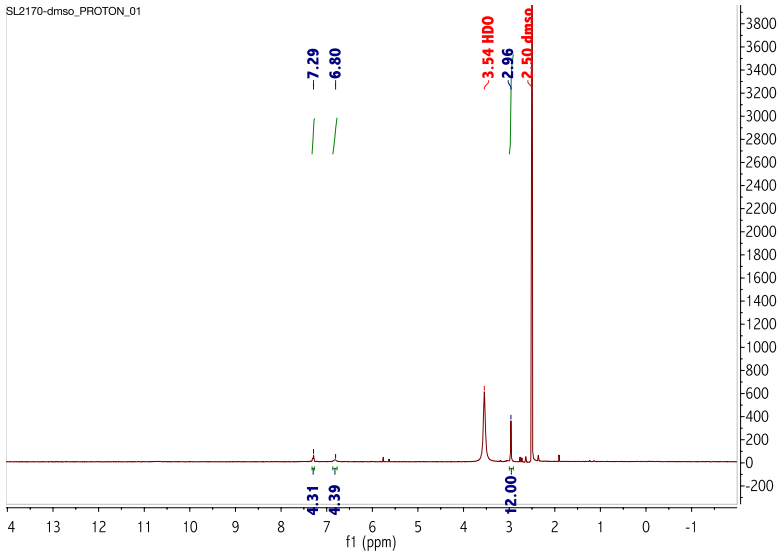

Figure 3.48. ^{1}H NMR of H_2NMe_2-PhA in dmso-d_6.

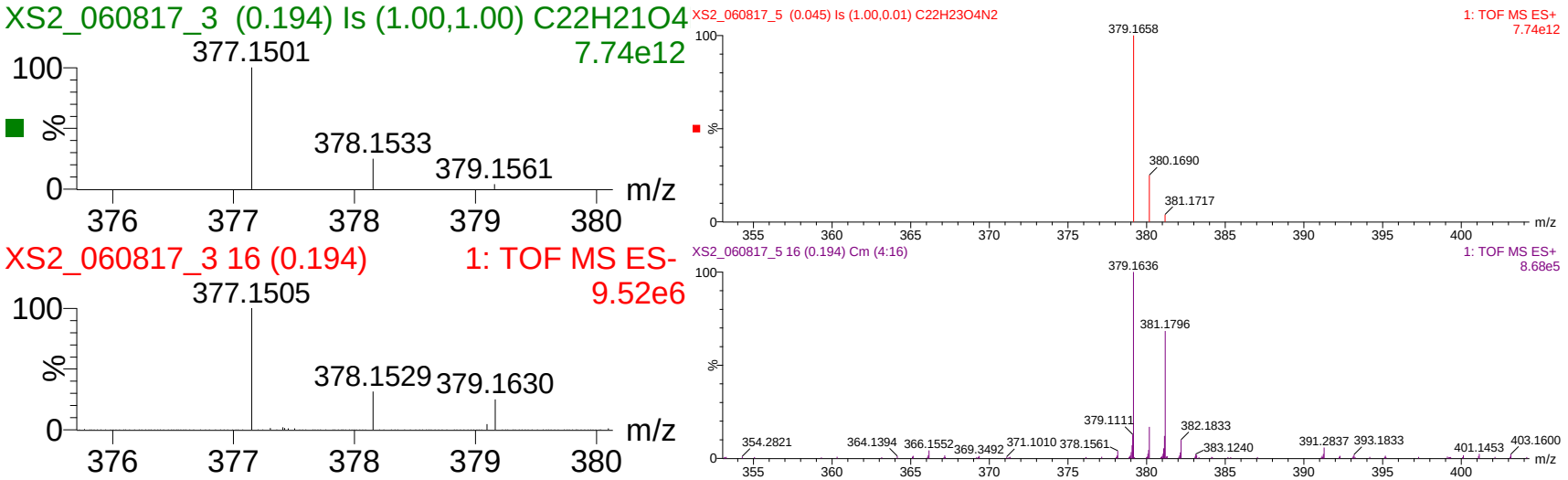

Figure 3.49. ESI-MS of H_2NMe_2-PhA. Left: top, calculated isotope pattern for $[M-H]^-$ ($C_{22}H_{21}O_4N_2$); bottom: experimental result. Right: top, calculated isotope pattern for $[M+H]^+$ ($C_{22}H_{23}O_4N_2$); bottom: experimental result.

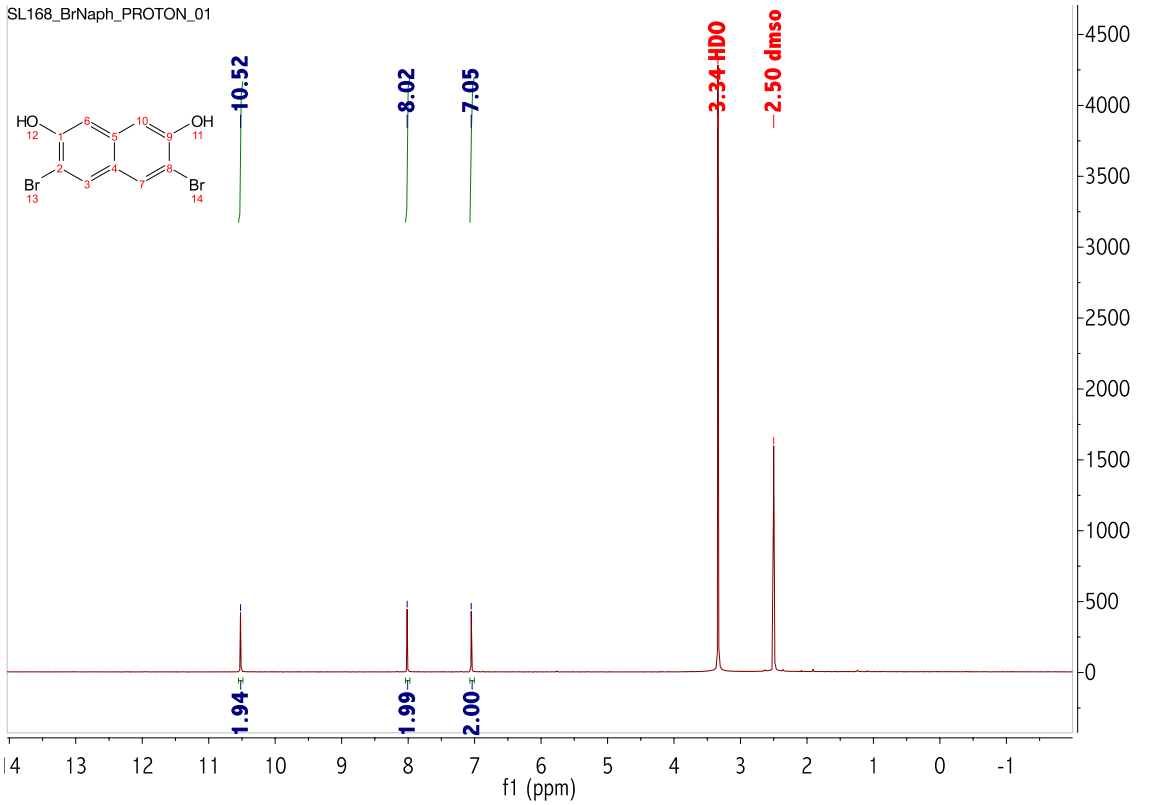

Figure 3.50. ^{1}H NMR of 3,6-dibromo-2,7-dihydroxynaphthalene in DMSO-d_6.

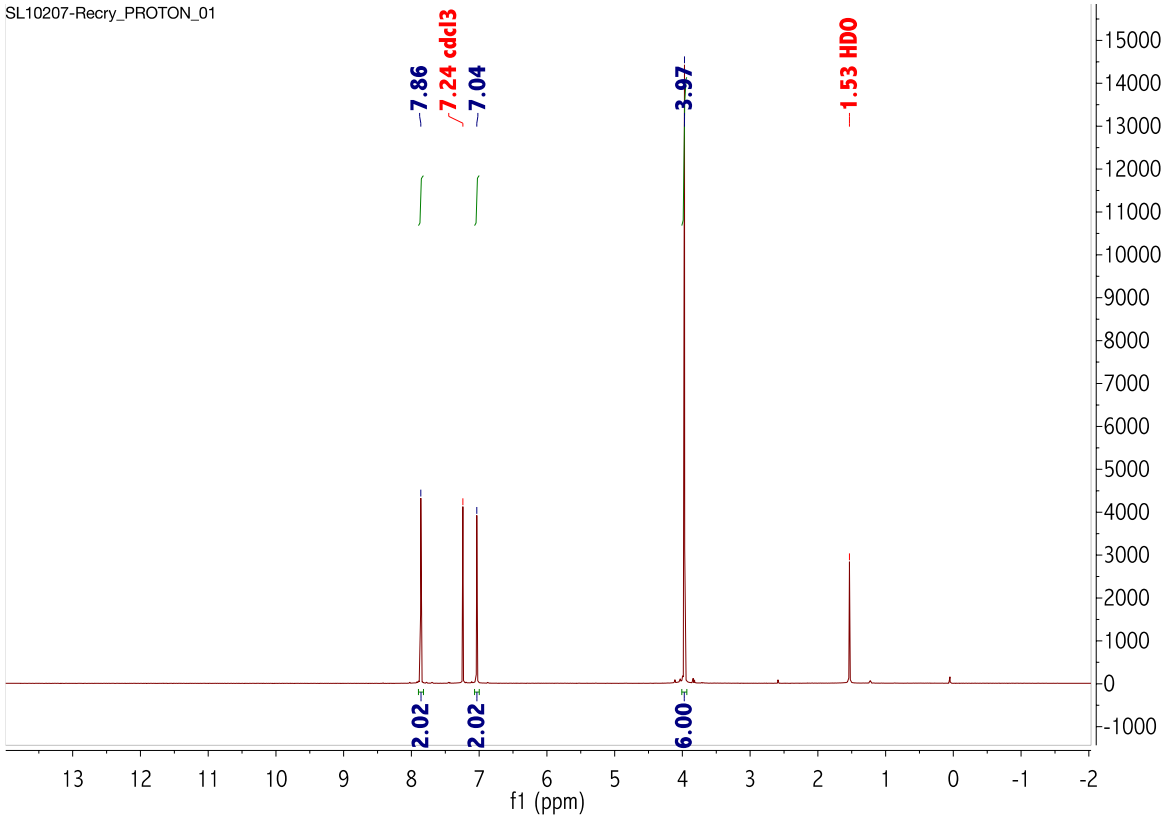

Figure 3.51. ^{1}H NMR of 3,6-dibromo-2,7-dimethoxynaphthalene in $CDCl_3$.

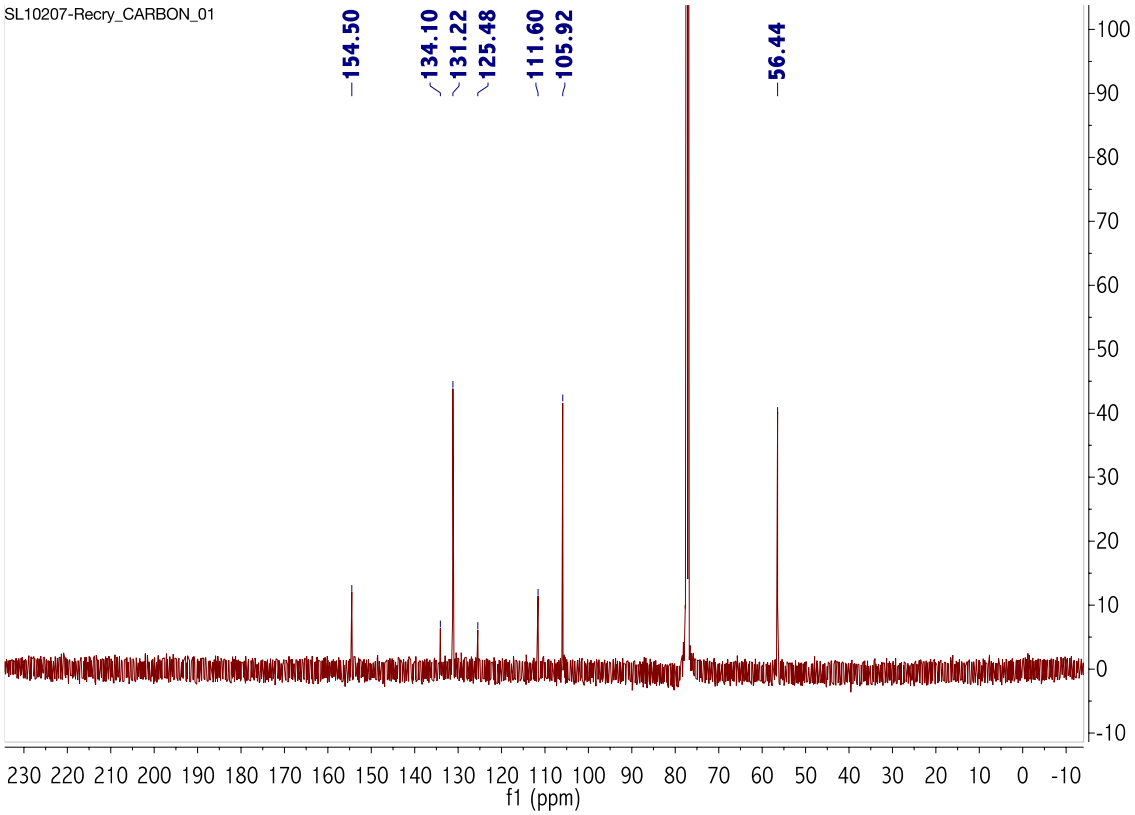

Figure 3.52. ^{13}C NMR of 3,6-dibromo-2,7-dimethoxynaphthalene in $CDCl_3$.

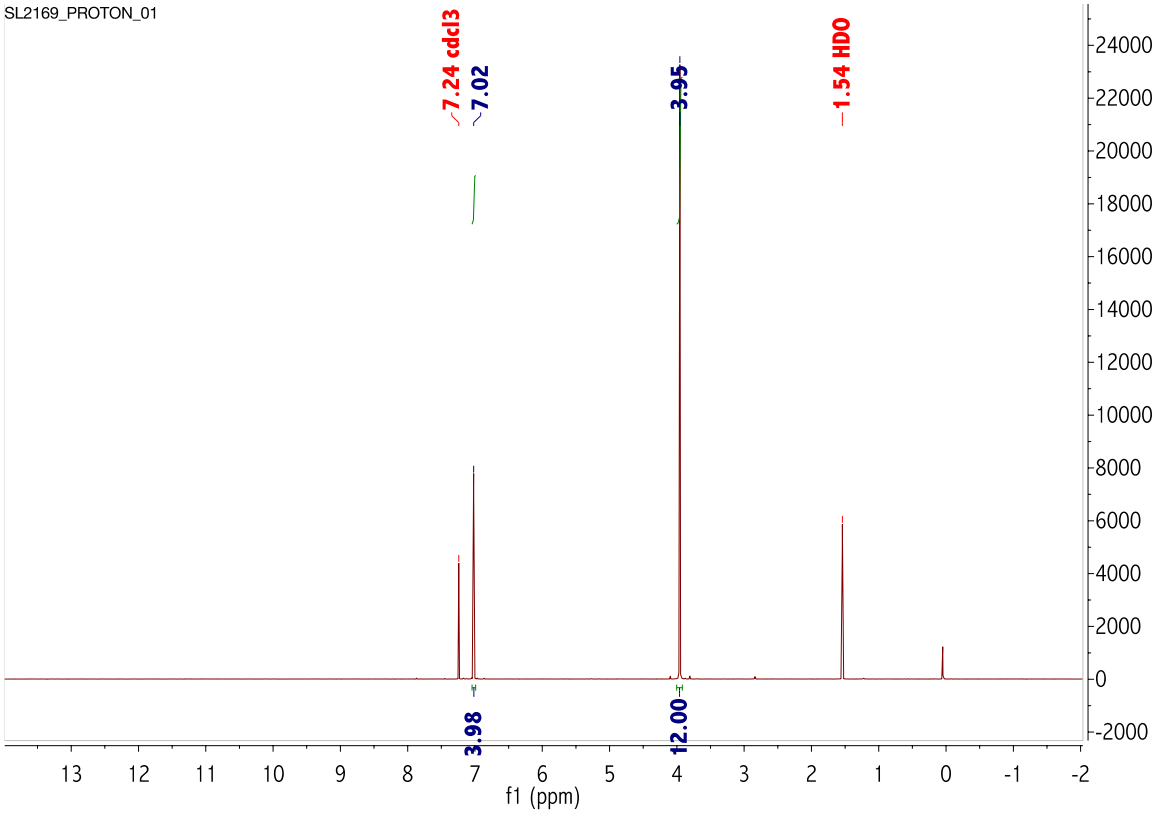

Figure 3.53. ^{1}H NMR of 2,3,6,7-tetramethoxynaphthalene in $CDCl_3$.

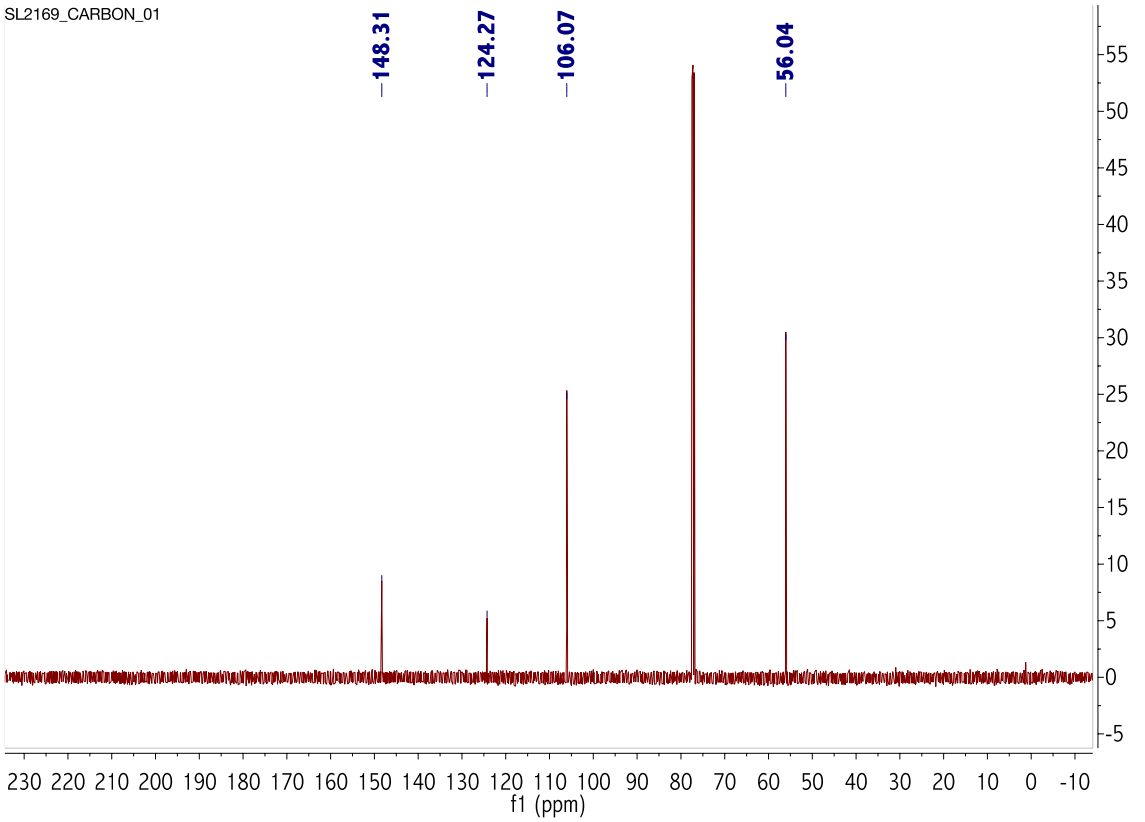

Figure 3.54. ^{13}C NMR of 2,3,6,7-tetramethoxynaphthalene in $CDCl_3$.

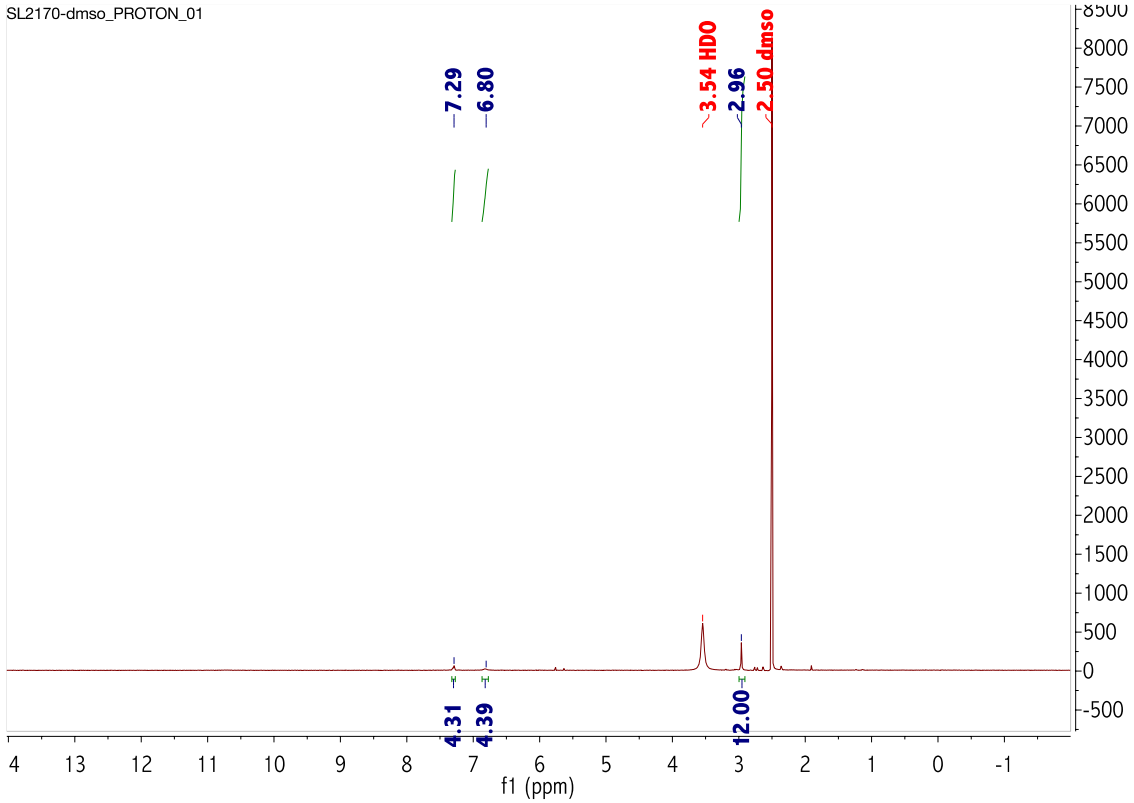

Figure 3.55. ^{1}H NMR of H_4NAT in dmso-d_6.

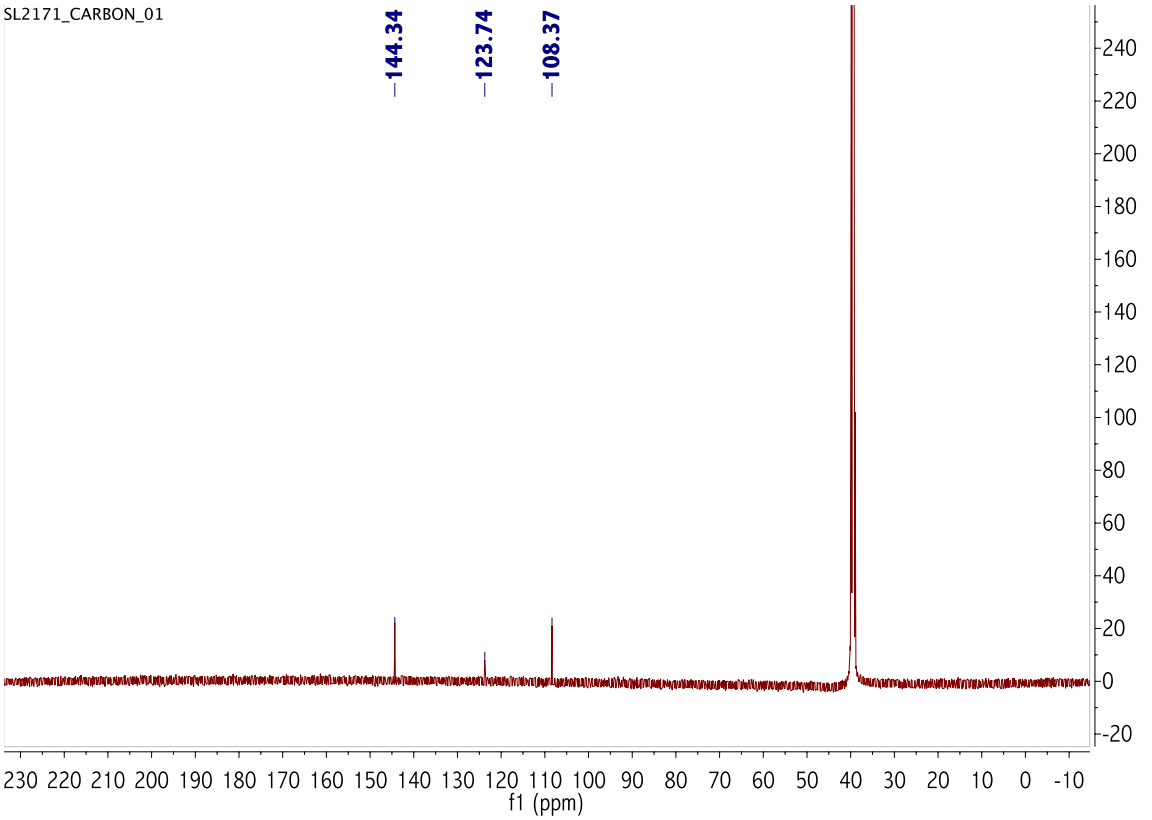

Figure 3.56. ^{13}C NMR of H_4NAT in dmso-d_6.

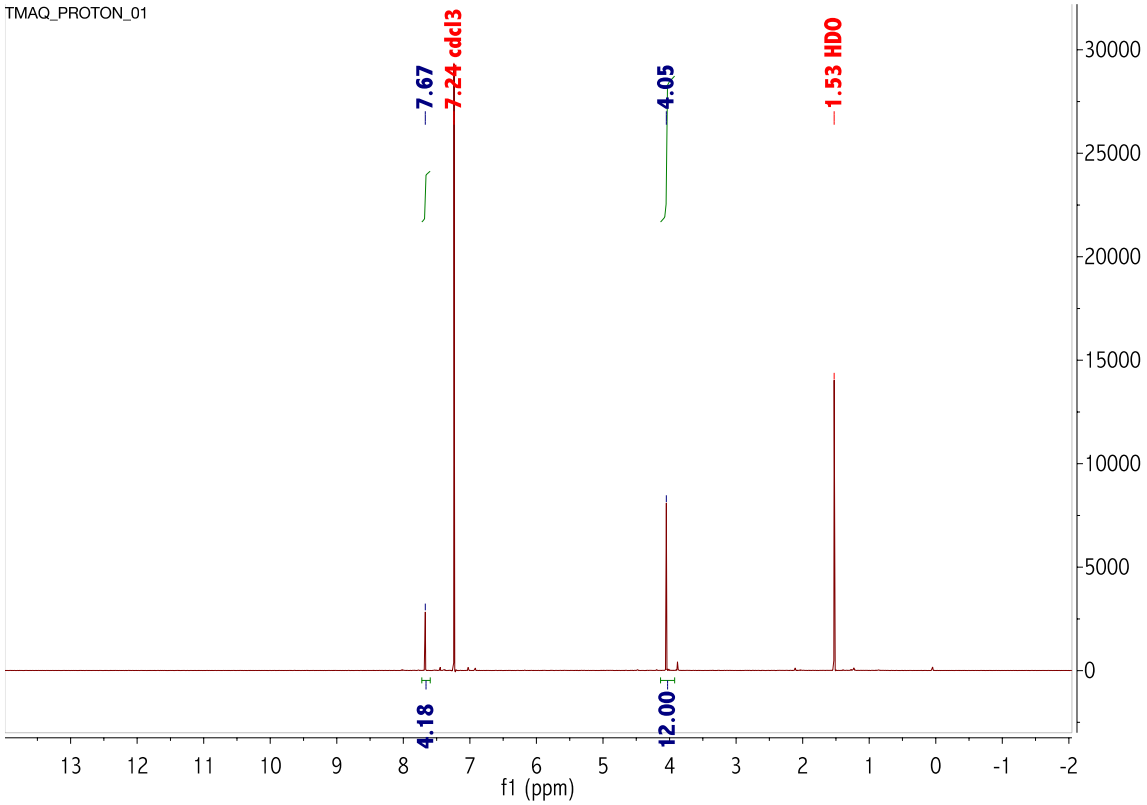

Figure 3.57. ^{1}H NMR of 2,3,6,7-Tetramethoxyanthraquinone in $CDCl_3$.

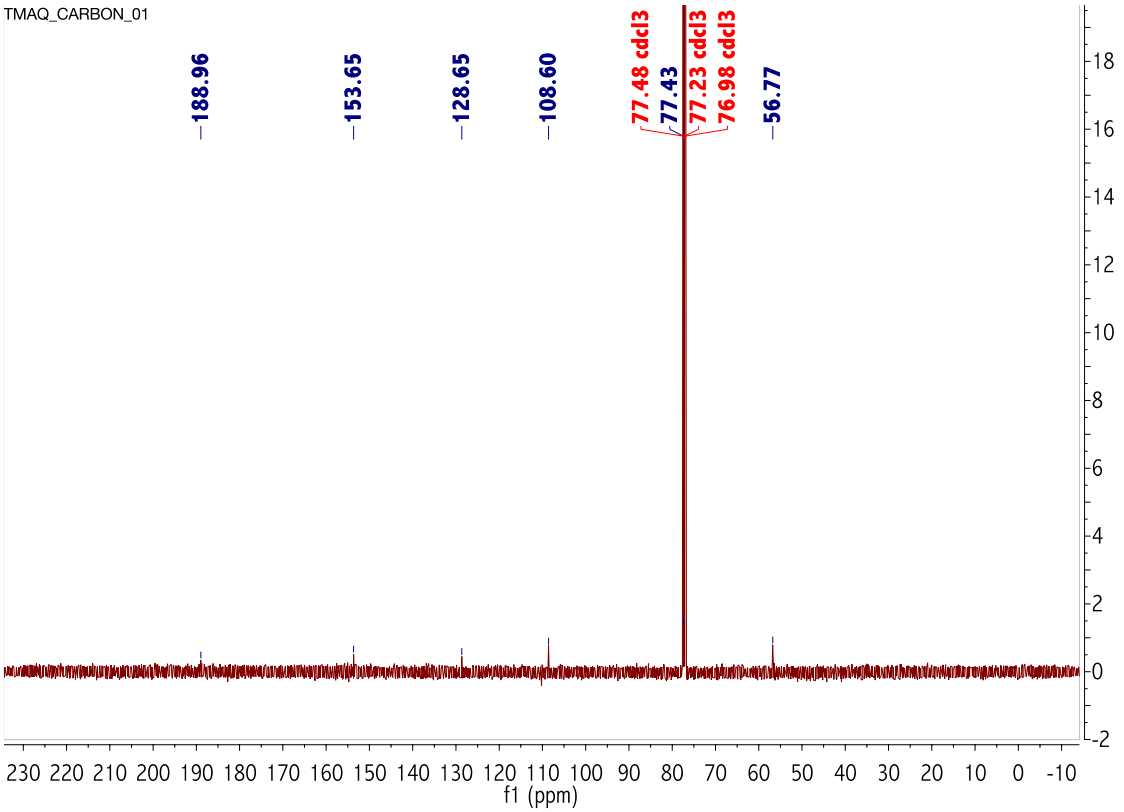

Figure 3.58. ^{13}C NMR of 2,3,6,7-Tetramethoxyanthraquinone in $CDCl_3$.

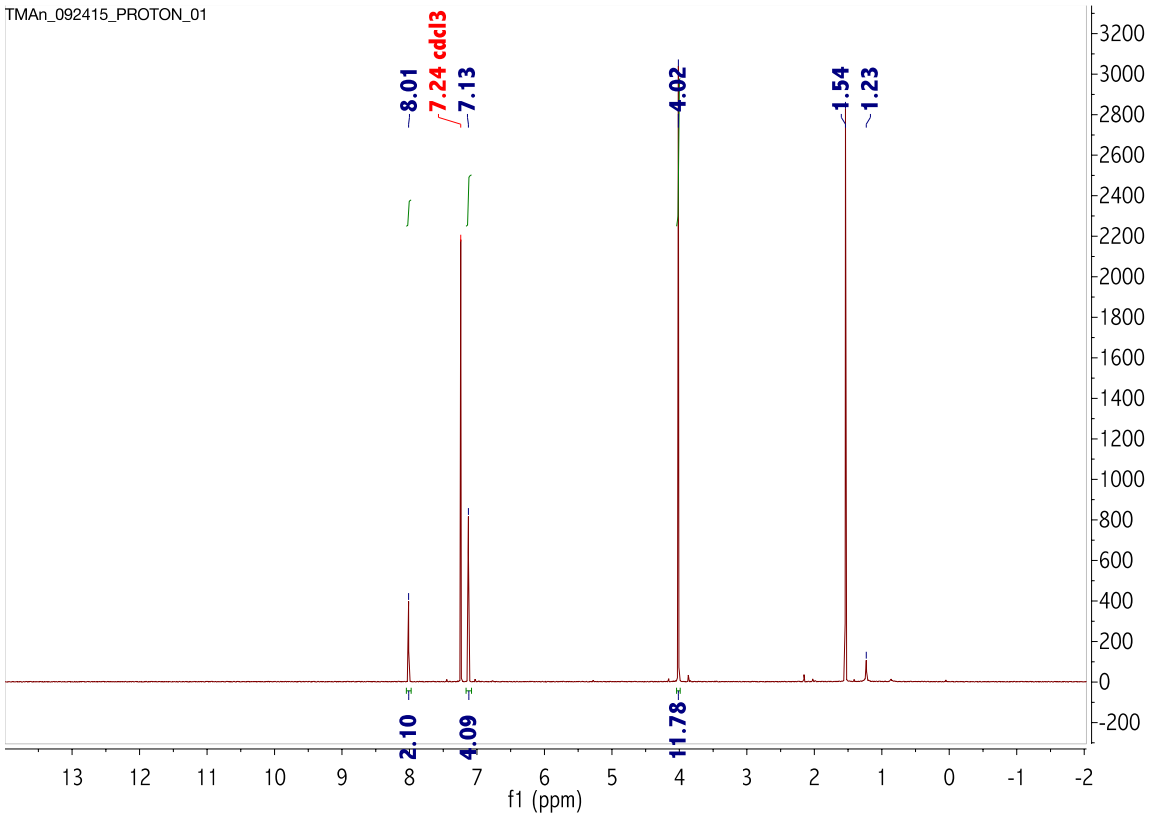

Figure 3.59. ^{1}H NMR of 2,3,6,7-tetramethoxyanthracene in $CDCl_3$.

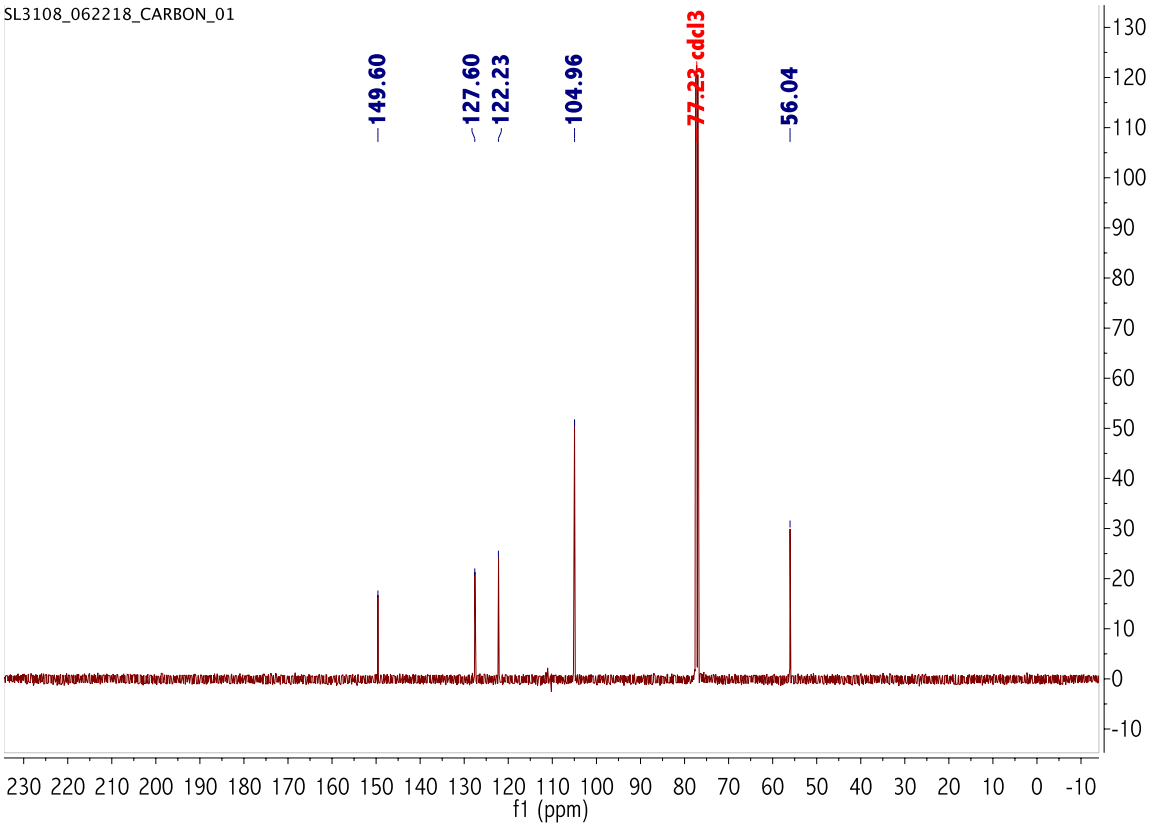

Figure 3.60. ^{13}C NMR of 2,3,6,7-tetramethoxyanthracene in $CDCl_3$.

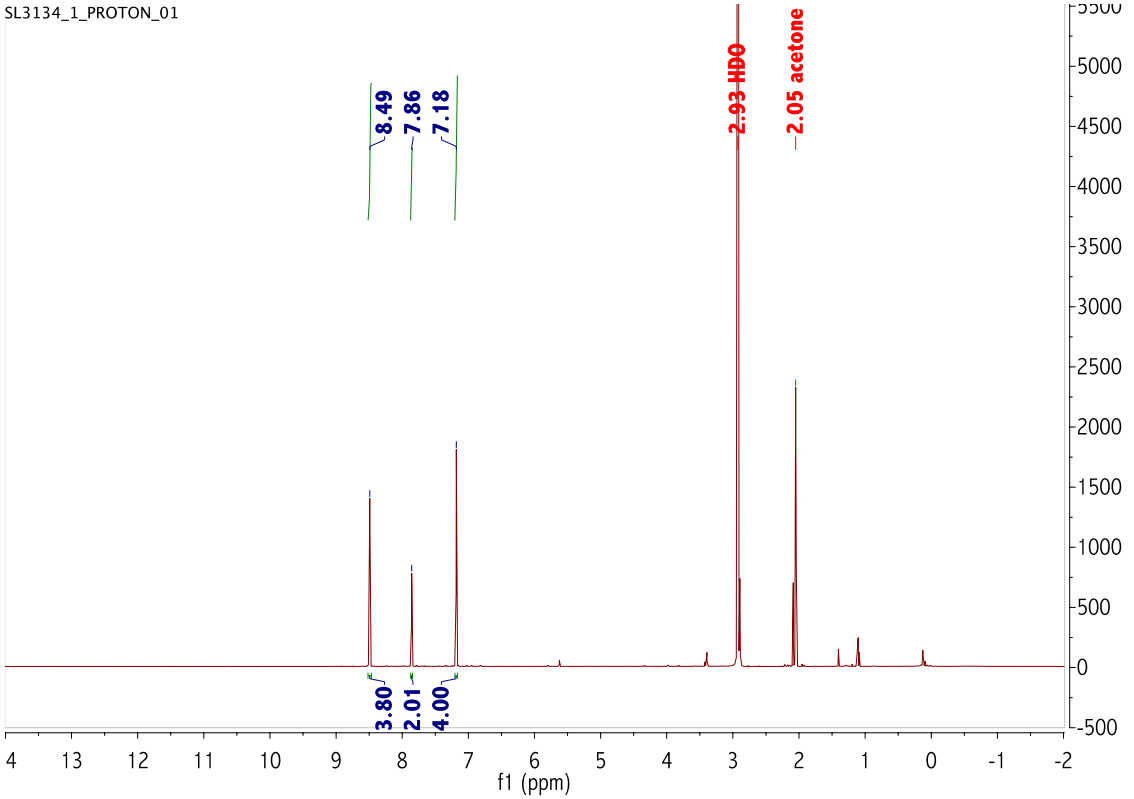

Figure 3.61. ^{1}H NMR of H_4AnT in acetone-d_6.

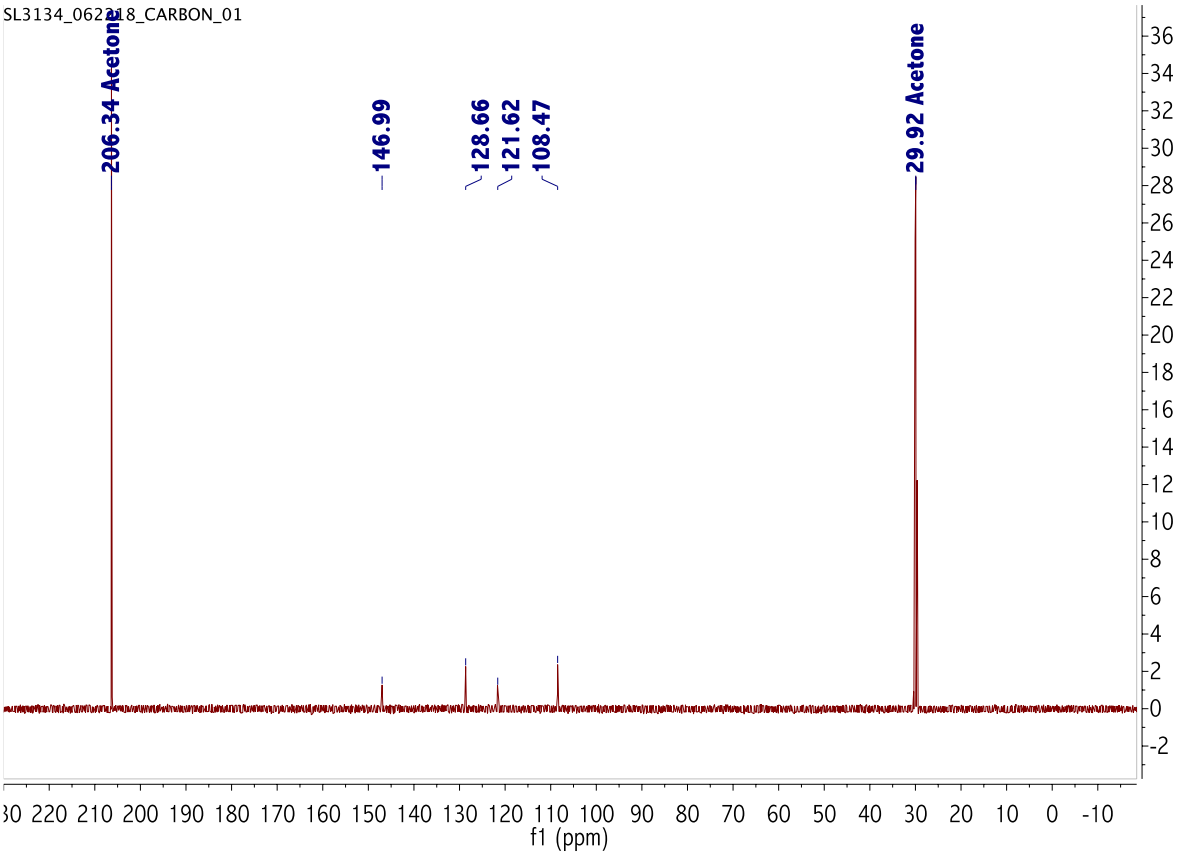

Figure 3.62. ^{13}C NMR of H_4AnT in acetone-d_6.

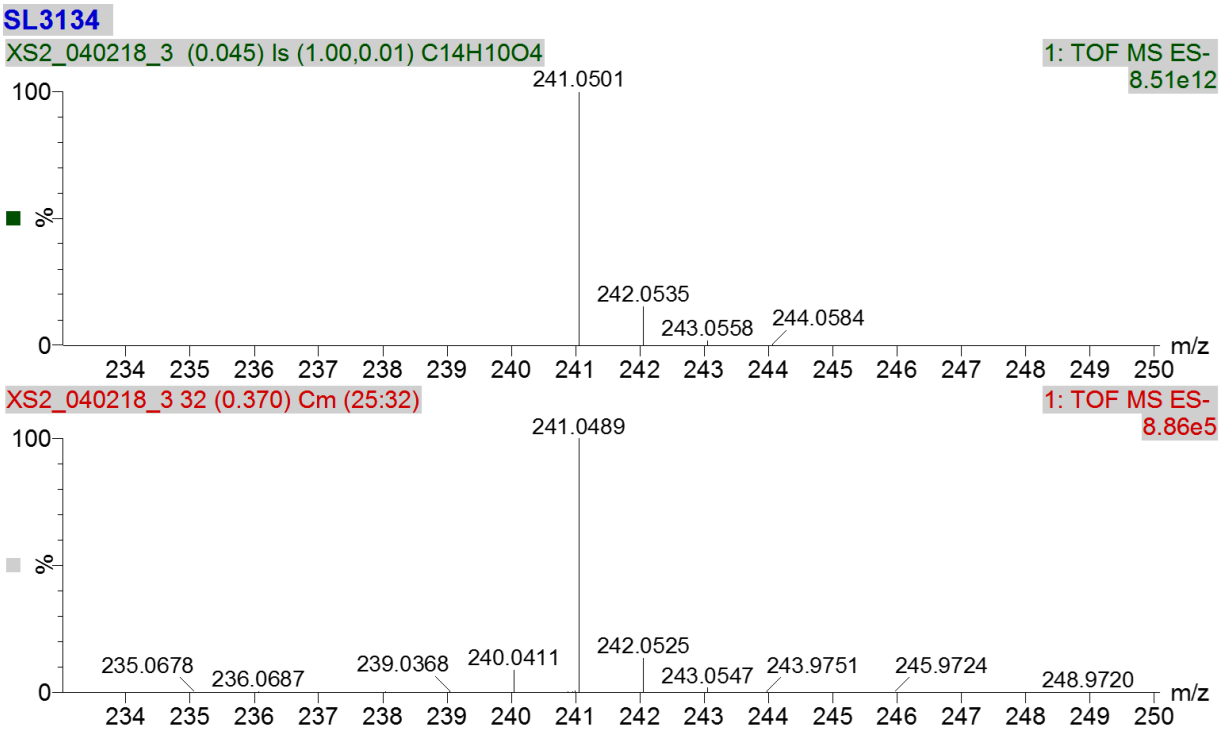

Figure 3.63. ESI-MS of H_4AnT. Top: calculated isotope pattern for $[M-H]^-$ ($C_{14}H_9O_4$). Bottom: experimental result.

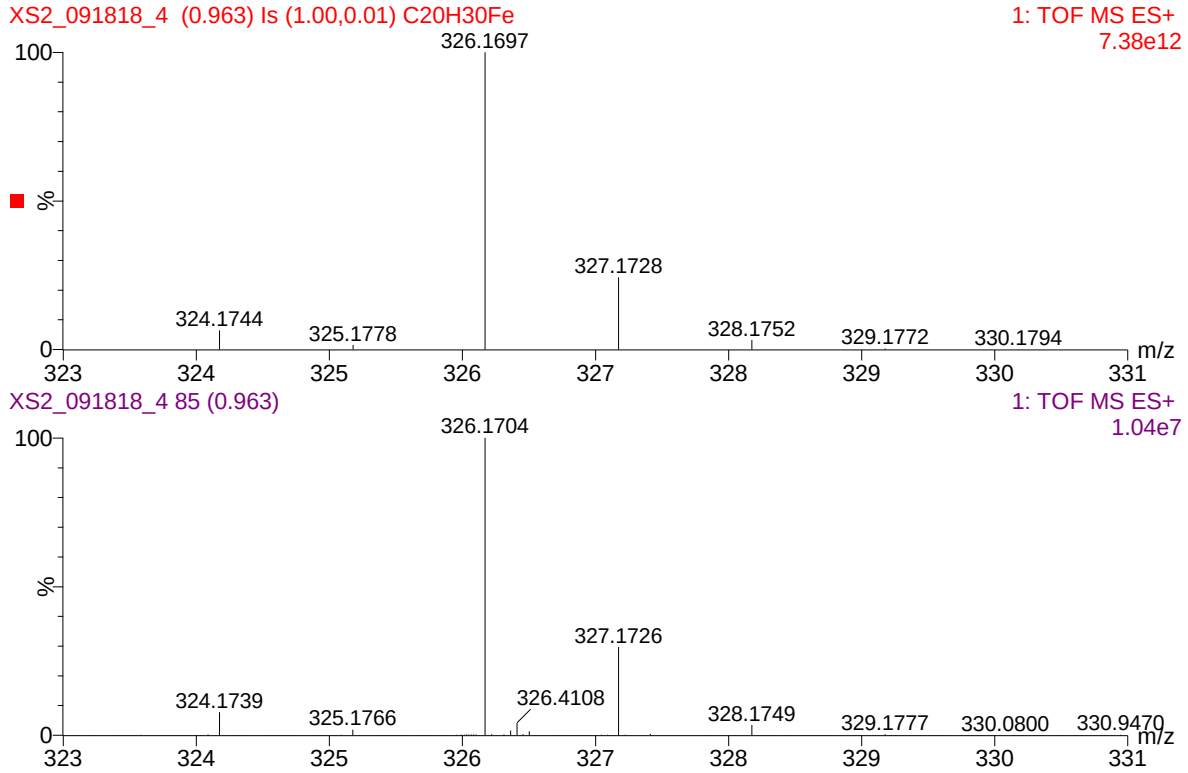

Figure 3.64. ESI-MS of $[FeCp^*_2](BF_4)$. Top: calculated isotope pattern for $[M]^+$ ($C_{20}H_{30}Fe_2$). Bottom: experimental result.

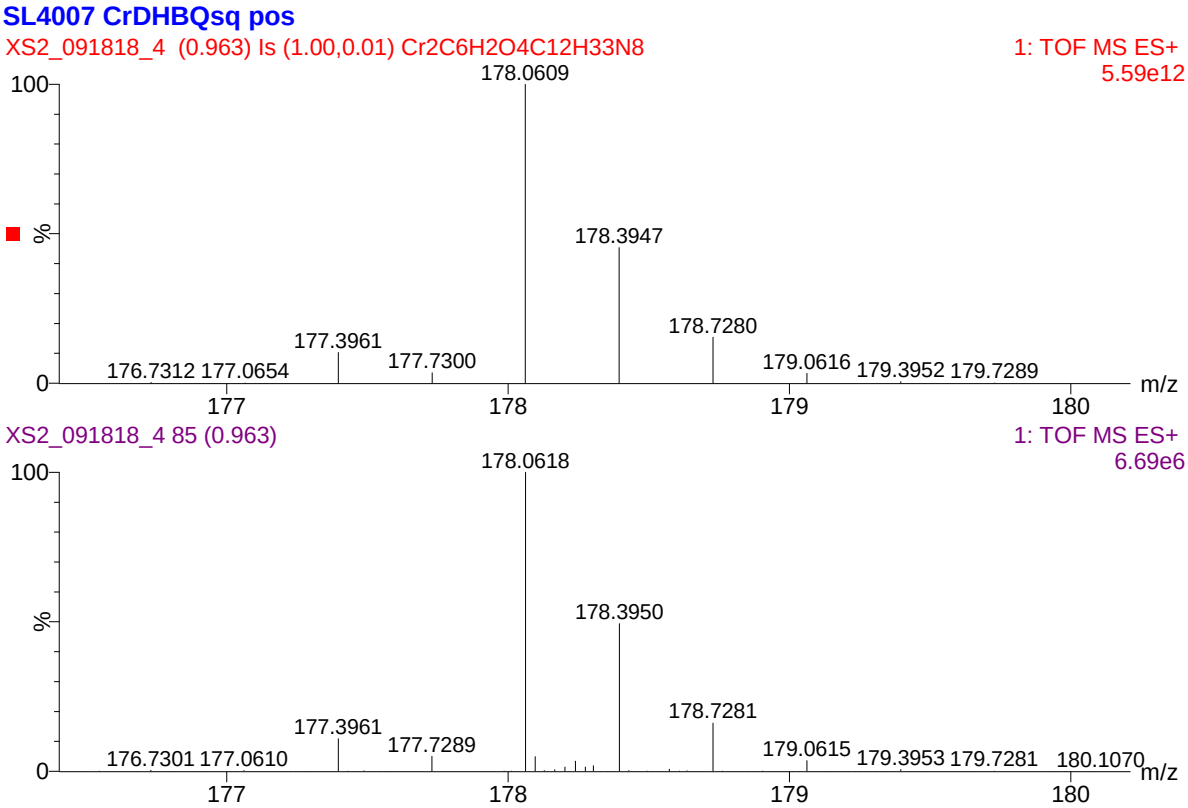

Figure 3.65. ESI-MS of Complex **11**. Top: calculated isotope pattern for $[M]^{3+}$ ($Cr_2C_{18}H_{38}O_4N_8$). Bottom: experimental result.

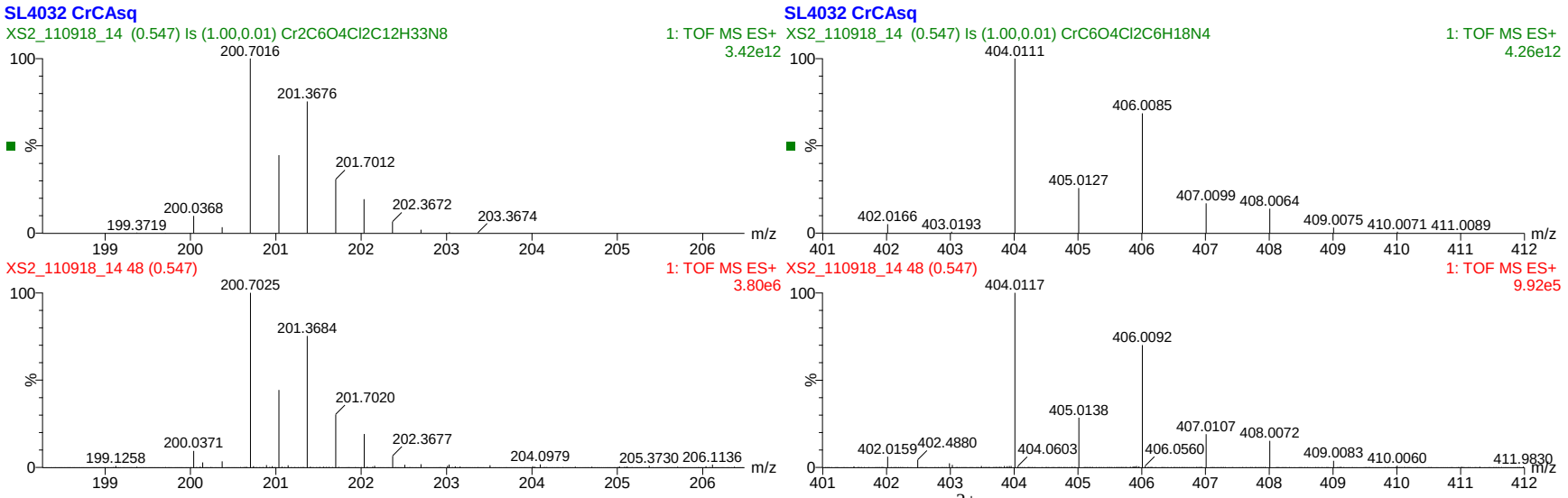

Figure 3.66. ESI-MS of Complex **13**. Left: top, calculated isotope pattern for $[M]^{3+}$ ($Cr_2C_{18}Cl_2H_{36}O_4N_8$); bottom, experimental result. Right: top, calculated isotope pattern for $[Cr(tren)(C_6Cl_2O_4)]^+$ ($CrC_{12}H_{18}O_4N_4Cl_2$); bottom, experimental result.

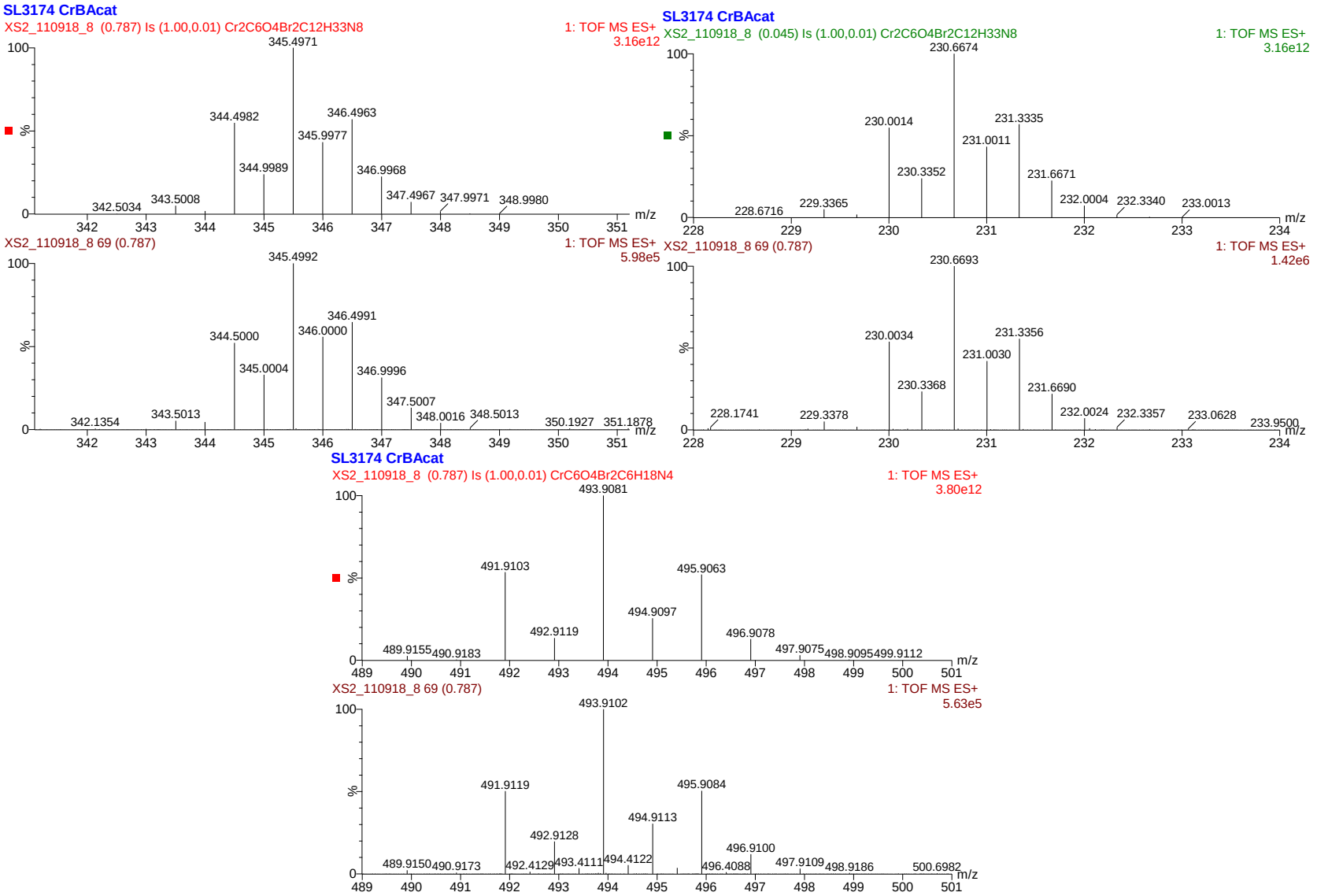

Figure 3.67. ESI-MS of Complex **4**. Upper left: top, calculated isotope pattern for $[M]^{2+}$ ($Cr_2C_{18}O_4Br_2H_{35}N_8$); bottom: experimental result. Upper right: top, calculated isotope pattern for $[M]^{3+}$ ($Cr_2C_{18}O_4Br_2H_{36}N_8$); bottom: experimental result. Lower: top, calculated isotope pattern for $[Cr(tren)(C_6O_4Br_2)]^{+}$ ($CrC_{12}H_{18}O_4N_4Br_2$); bottom, experimental result.

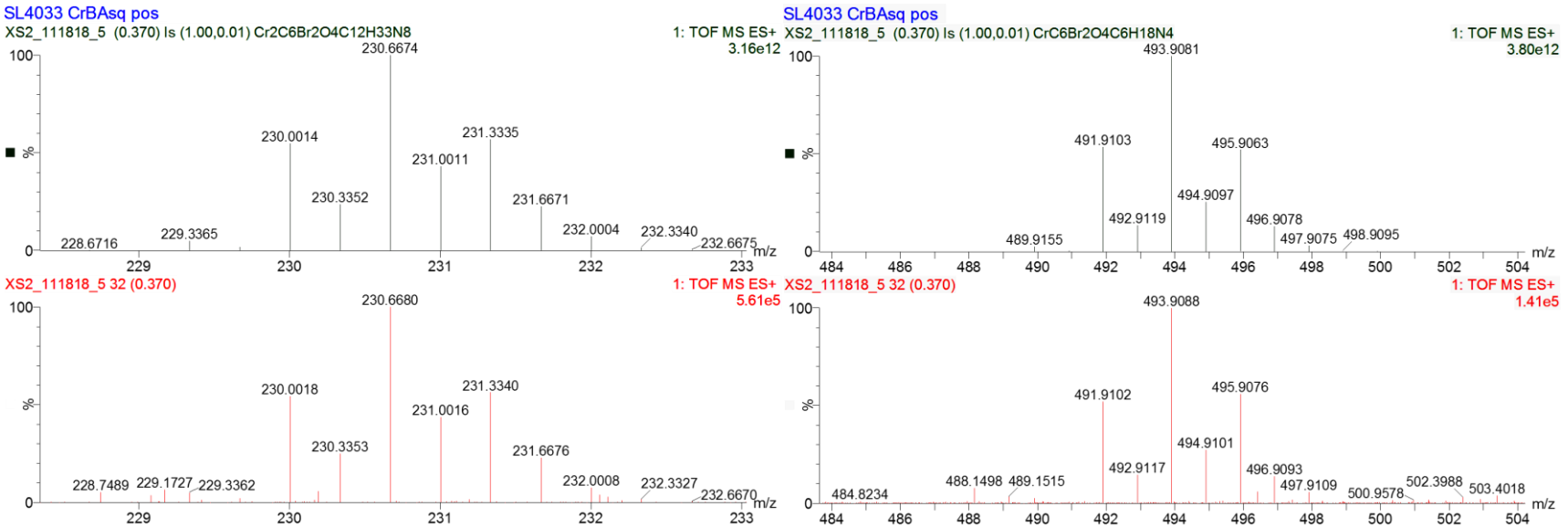

Figure 3.68. ESI-MS of Complex **14**. Left: top, calculated isotope pattern for $[M]^{3+}$ ($Cr_2C_{18}H_{36}O_4N_8Br_2$); bottom, experimental result. Right: top, calculated isotope pattern for $[Cr(tren)(C_6O_4Br_2)]^+$ ($CrC_{12}H_{18}O_4N_4Br_2$); bottom, experimental result.

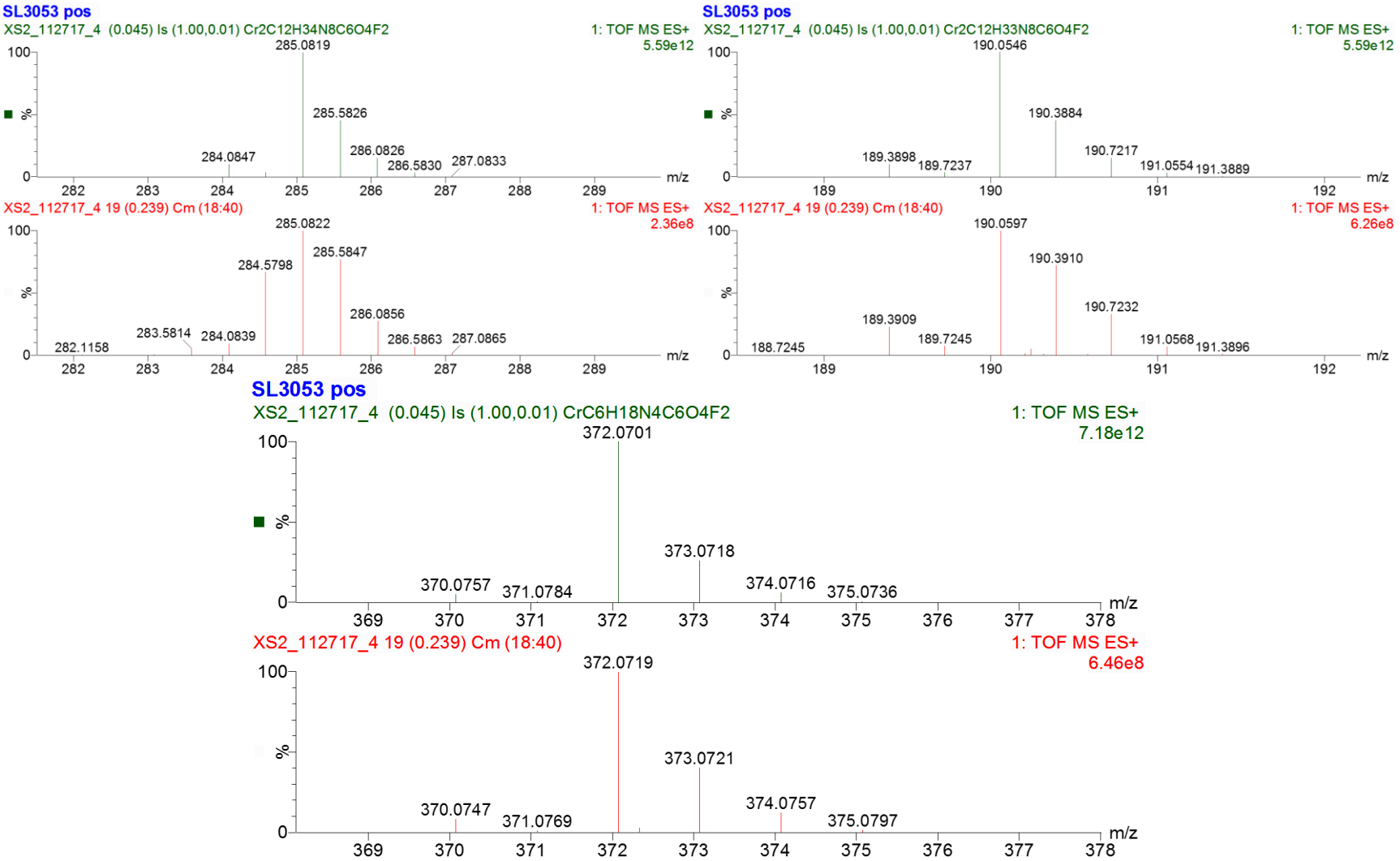

Figure 3.69. ESI-MS of Complex **2**. Upper left: top, calculated isotope pattern for $[M]^{2+}$ ($Cr_2C_{18}H_{36}O_4N_8F_2$); bottom, experimental result. Upper right: top, calculated isotope pattern for $[M]^{3+}$ ($Cr_2C_{18}H_{36}O_4N_8F_2$); bottom, experimental result. Lower: top, calculated isotope pattern for $[Cr(tren)(C_6F_2O_4)]^+$ ($CrC_{12}H_{18}O_4N_4F_2$); bottom, experimental result.

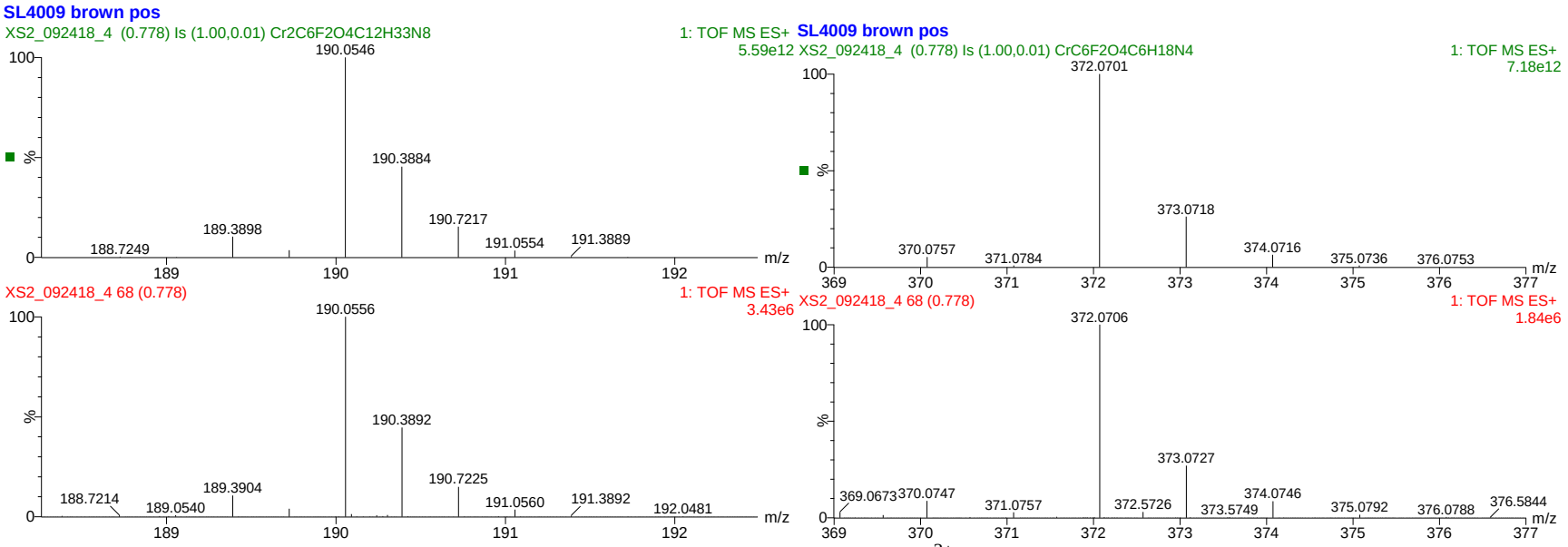

Figure 3.70. ESI-MS of Complex **12**. Top: calculated isotope pattern for $[M]^{3+}$ ($Cr_2C_{18}H_{36}O_4N_8F_2$). Bottom: experimental result. $[Cr(tren)(C_6O_4F_2)]^+$ ($CrC_{12}H_{18}O_4N_4F_2$).

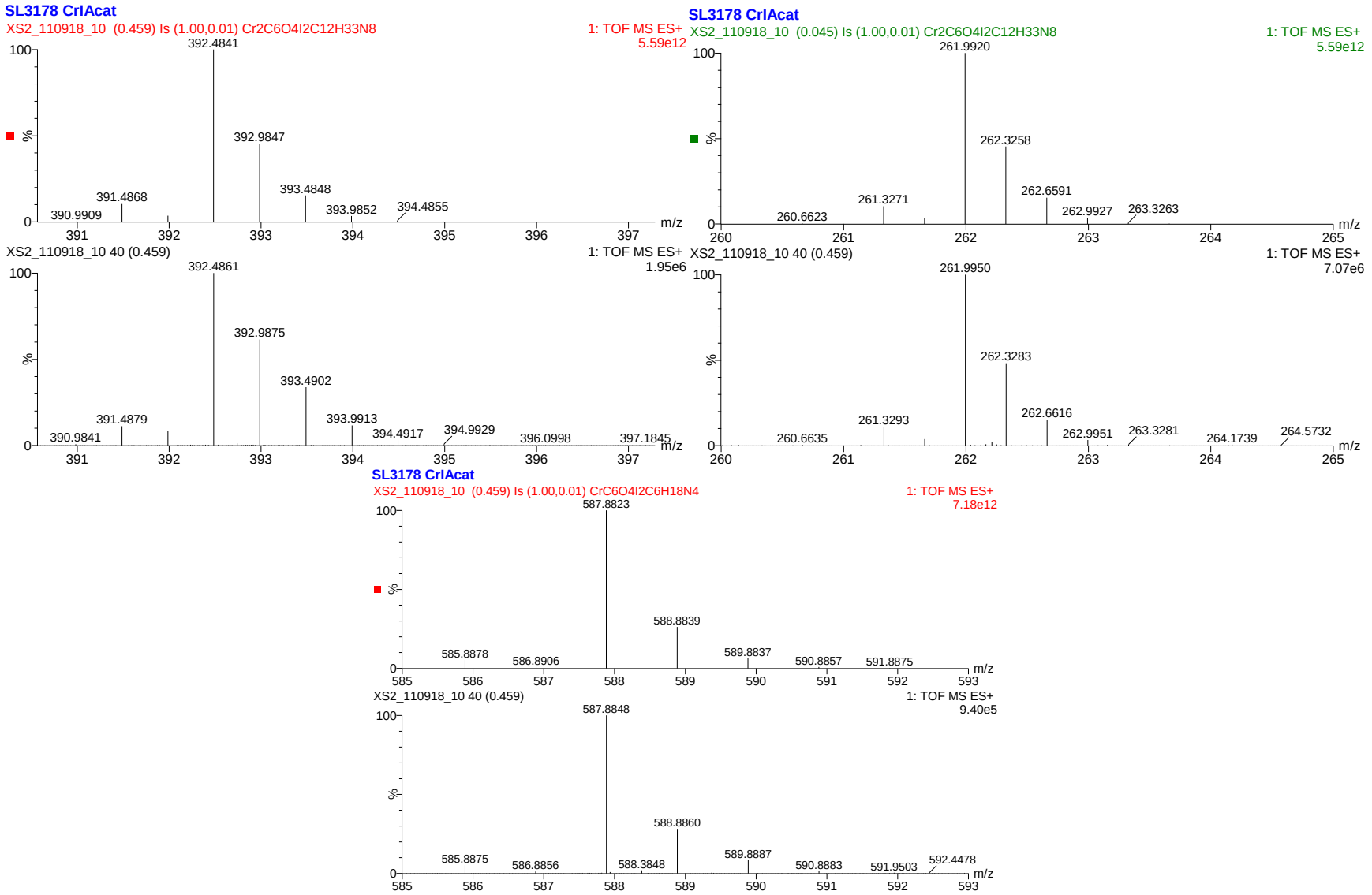

Figure 3.71. ESI-MS of Complex **5**. Upper left: top, calculated isotope pattern for $[M]^{2+}$ ($Cr_2C_{18}H_{36}O_4N_8I_2$); bottom, experimental result. Upper right: top, calculated isotope pattern for $[M]^{3+}$ ($Cr_2C_{18}H_{36}O_4N_8I_2$); bottom, experimental result. Lower: top, calculated isotope pattern for $[Cr(tren)(C_6O_4I_2)]^{+}$ ($CrC_{12}H_{18}O_4N_4I_2$); bottom, experimental result.

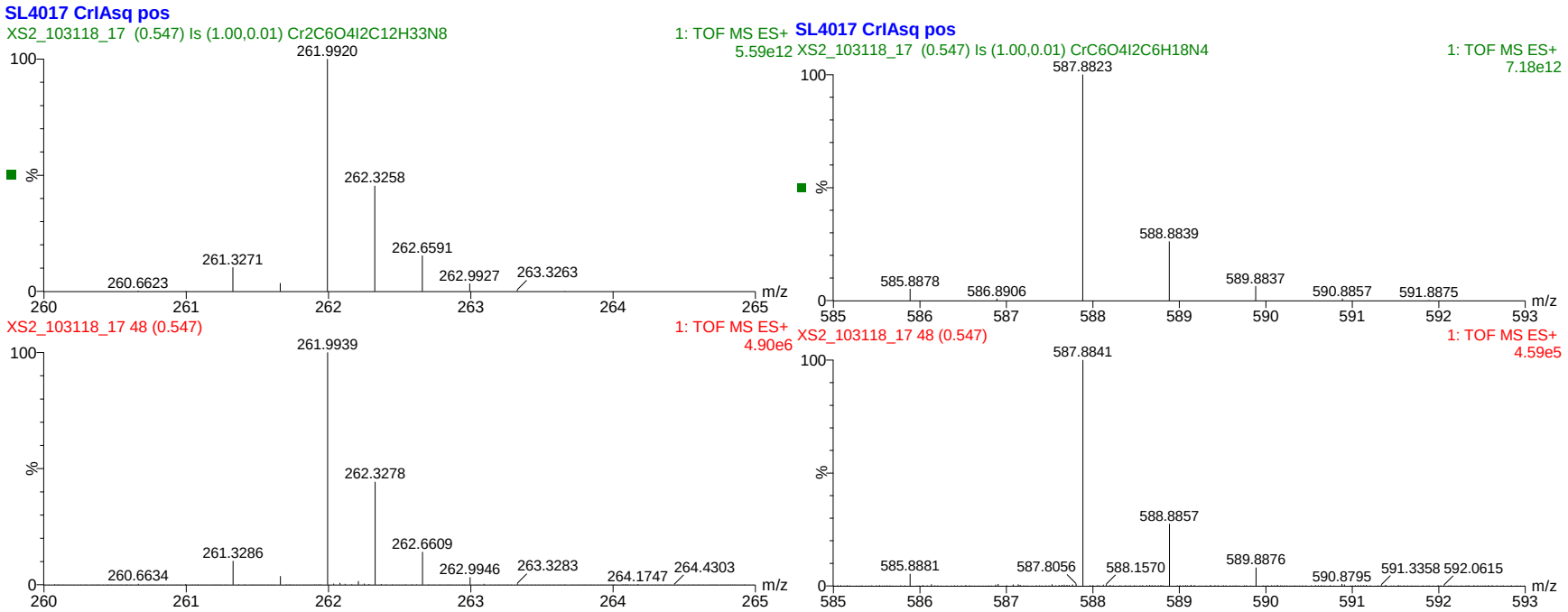

Figure 3.72. ESI-MS of Complex **15**. Left: top, calculated isotope pattern for $[M]^{3+}$ ($Cr_2C_{18}H_{36}O_4N_8I_2$); bottom, experimental result. Right: top, calculated isotope pattern for $[Cr(tren)(C_6O_4I_2)]^+$ ($CrC_{12}H_{18}O_4N_4I_2$); bottom, experimental result.

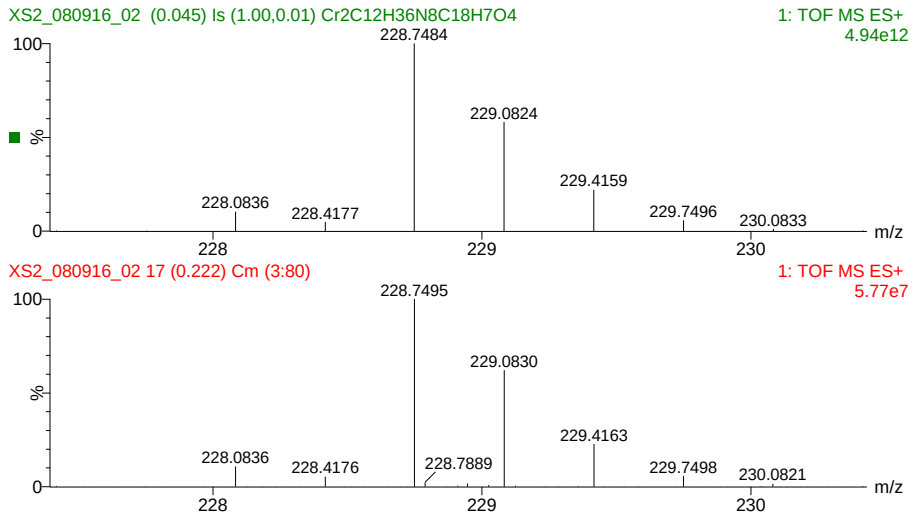

Figure 3.73. ESI-MS of Complex **6**. Top: calculated isotope pattern for $[M]^{2+}$ ($Cr_2C_{30}H_{46}O_4N_8$). Bottom: experimental result.

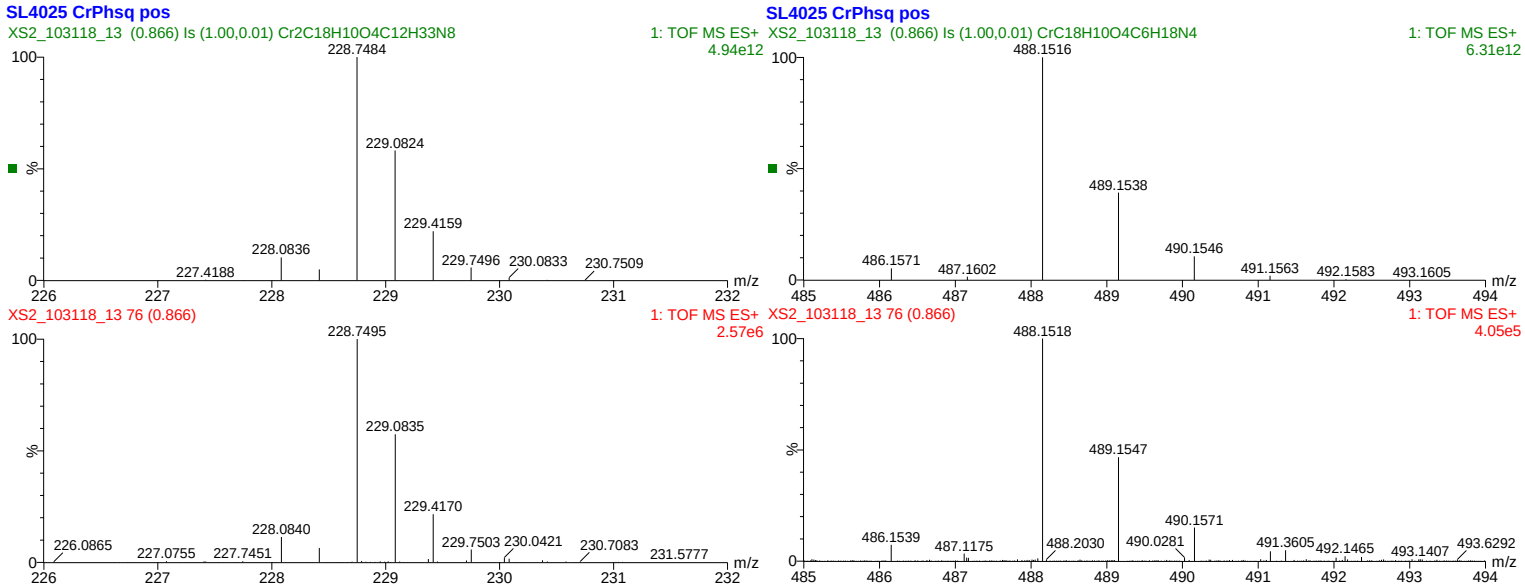

Figure 3.74. ESI-MS of Complex **16**. Left: top, calculated isotope pattern for $[M]^{3+}$ ($Cr_2C_{30}H_{46}O_4N_8$); bottom, experimental result. Right: top, calculated isotope pattern for $[Cr(tren)(C_{18}O_4H_{10})]^{+}$ ($CrC_{24}H_{28}O_4N_4$); bottom, experimental result.

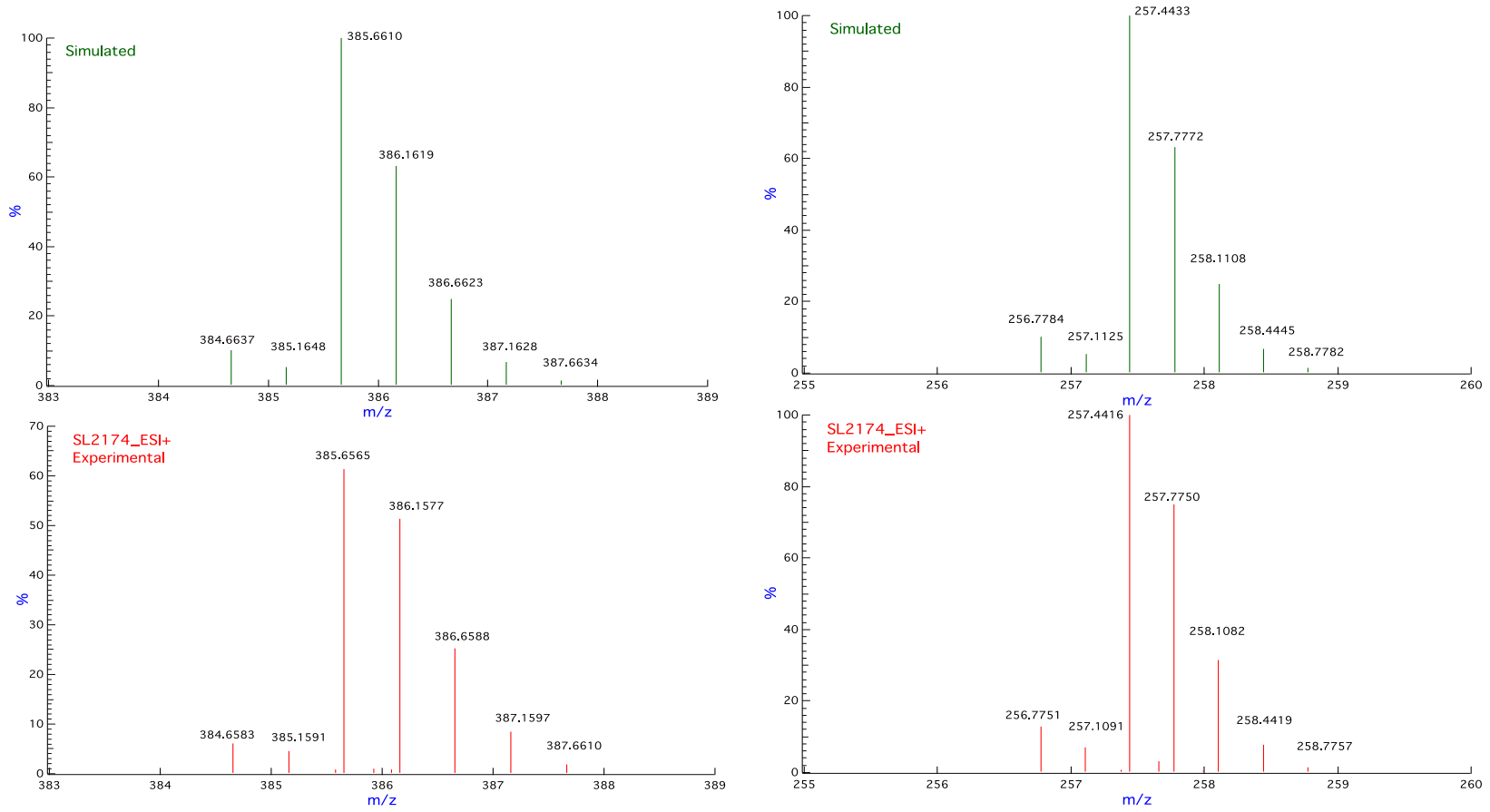

Figure 3.75. ESI-MS of Complex **7**. Left: top, calculated isotope pattern for $[M]^{2+}$ ($Cr_2C_{18}O_4Br_2H_{36}N_8$); bottom, experimental result. Right: top, calculated isotope pattern for $[M]^{+}$ ($Cr_2C_{18}O_4Br_2H_{36}N_8$); bottom, experimental result.

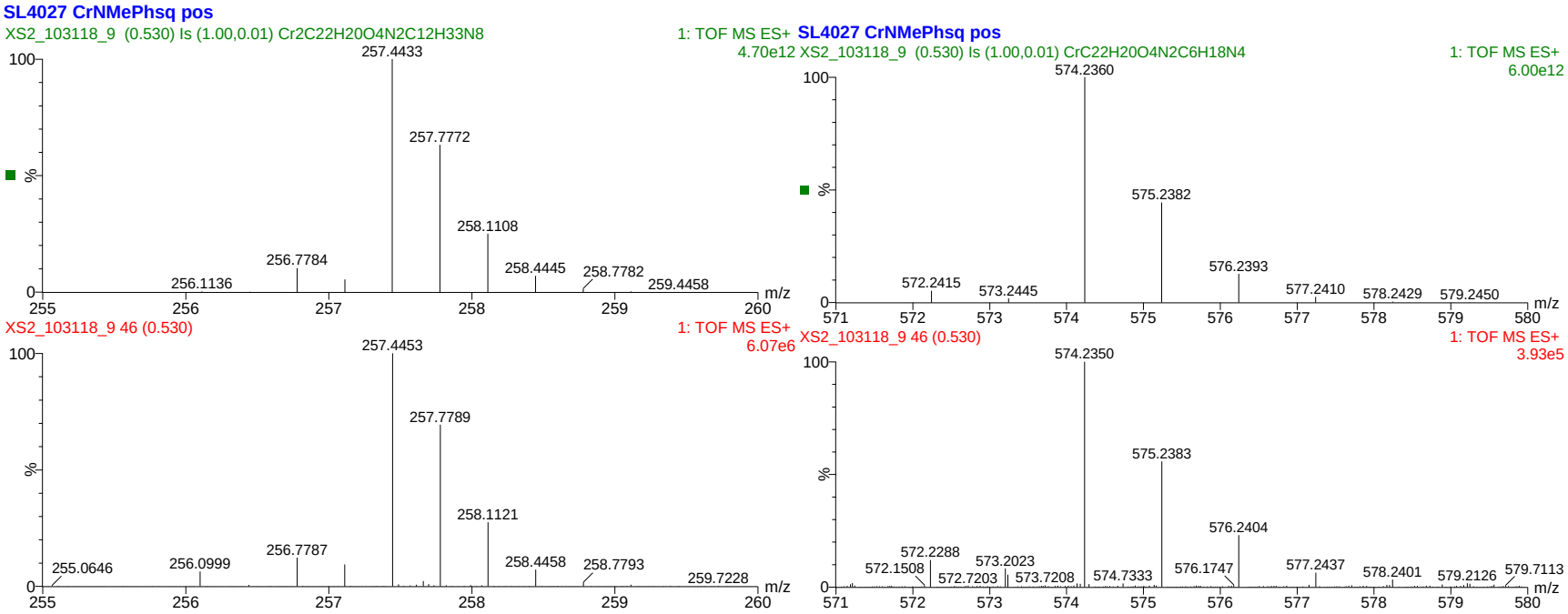

Figure 3.76. ESI-MS of Complex **17**. Left: top, calculated isotope pattern for $[M]^{3+}$ ($Cr_2C_{34}H_{54}O_4N_{10}$); bottom, experimental result. Right: top, calculated isotope pattern for $[Cr(tren)(C_{22}H_{20}O_4N_2)]^+$ ($CrC_{28}H_{38}O_4N_6$); bottom, experimental result.

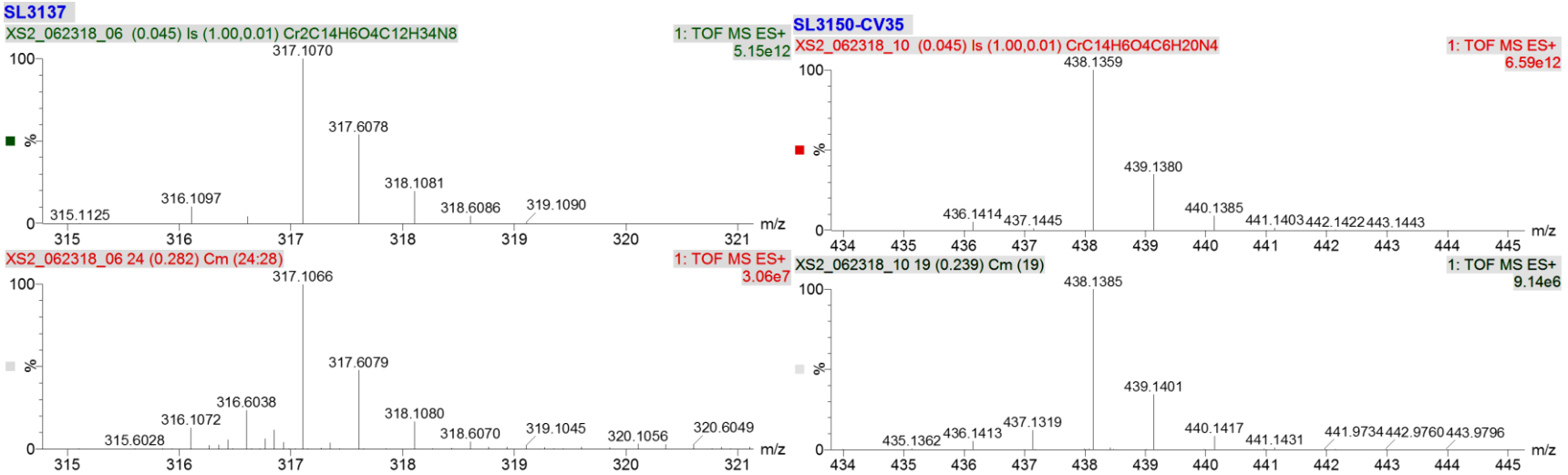

Figure 3.77. ESI-MS of Complex **10**. Left: top, calculated isotope pattern for $[M]^{2+}$ ($Cr_2C_{18}H_{14}O_4N_8$); bottom, experimental result. Right: top, calculated isotope pattern for $[Cr(tren)(C_{14}H_8O_4)]^+$ ($CrC_{22}H_{30}O_4N_4$); bottom, experimental result.

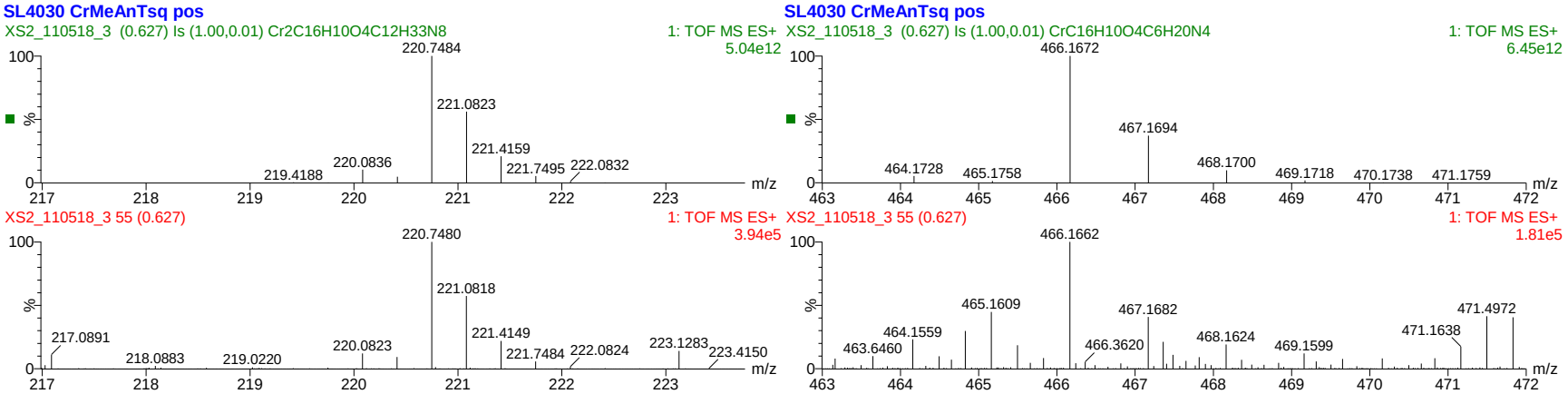

Figure 3.78. ESI-MS of Complex **19.** Left: top, calculated isotope pattern for $[M]^{3+}$ ($Cr_2C_{18}H_{14}O_4N_8$); bottom, experimental result. Right: top, calculated isotope pattern for $[Cr(tren)(C_{14}H_8O_4)]^+$ ($CrC_{22}H_{30}O_4N_4$); bottom, experimental result.

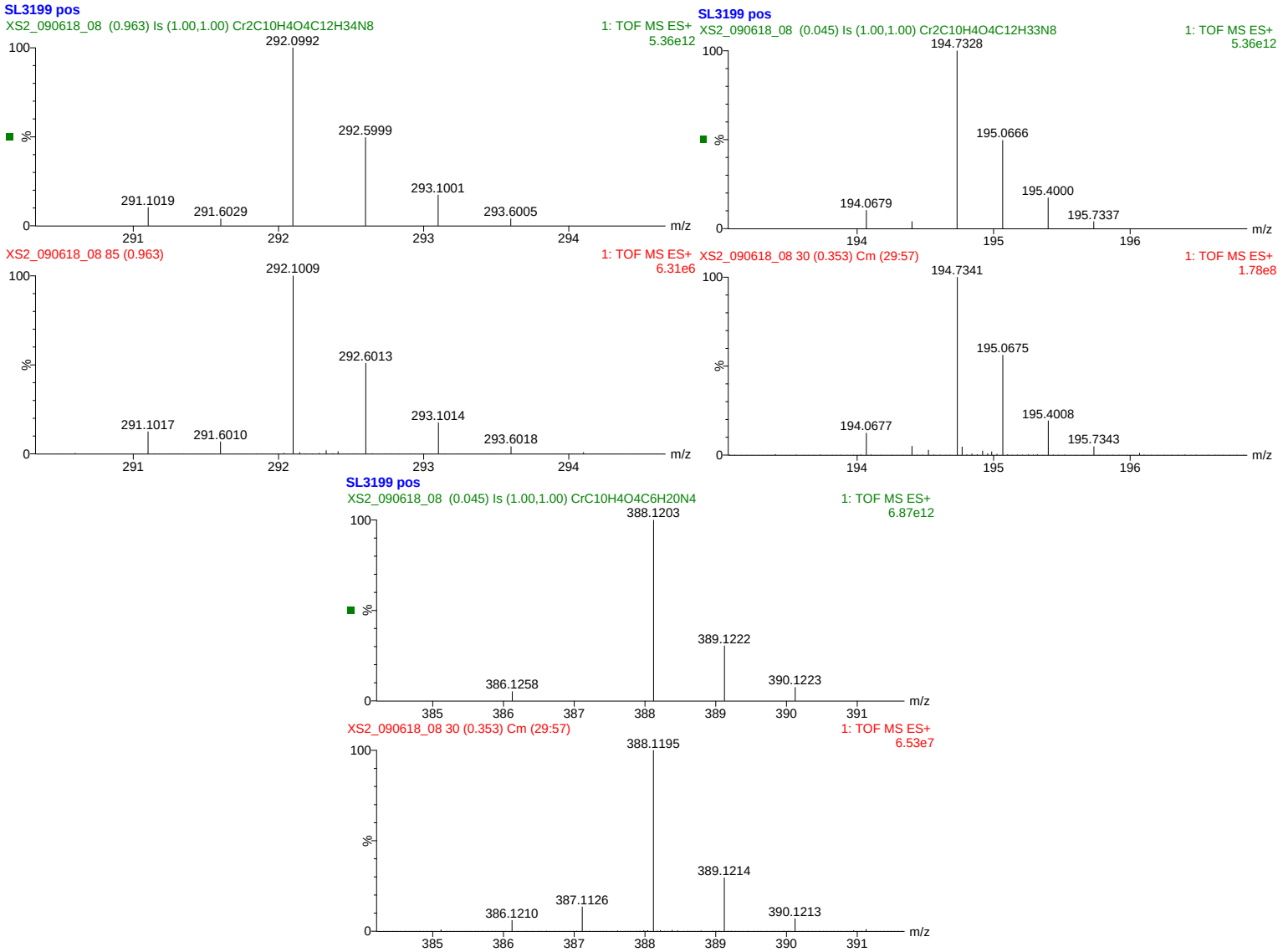

Figure 3.79. ESI-MS of Complex **8**. Upper left: top, calculated isotope pattern for $[M]^{2+}$ ($Cr_2C_{22}H_{40}O_4N_8$); bottom, experimental result. Upper right: top, calculated isotope pattern for $[M]^{3+}$ ($Cr_2C_{22}H_{40}O_4N_8$); bottom, experimental result. Bottom: top, calculated isotope pattern for $[Cr(tren)(C_{10}H_6O_4)]^{+}$ ($CrC_{16}H_{24}O_4N_4$); bottom, experimental result.

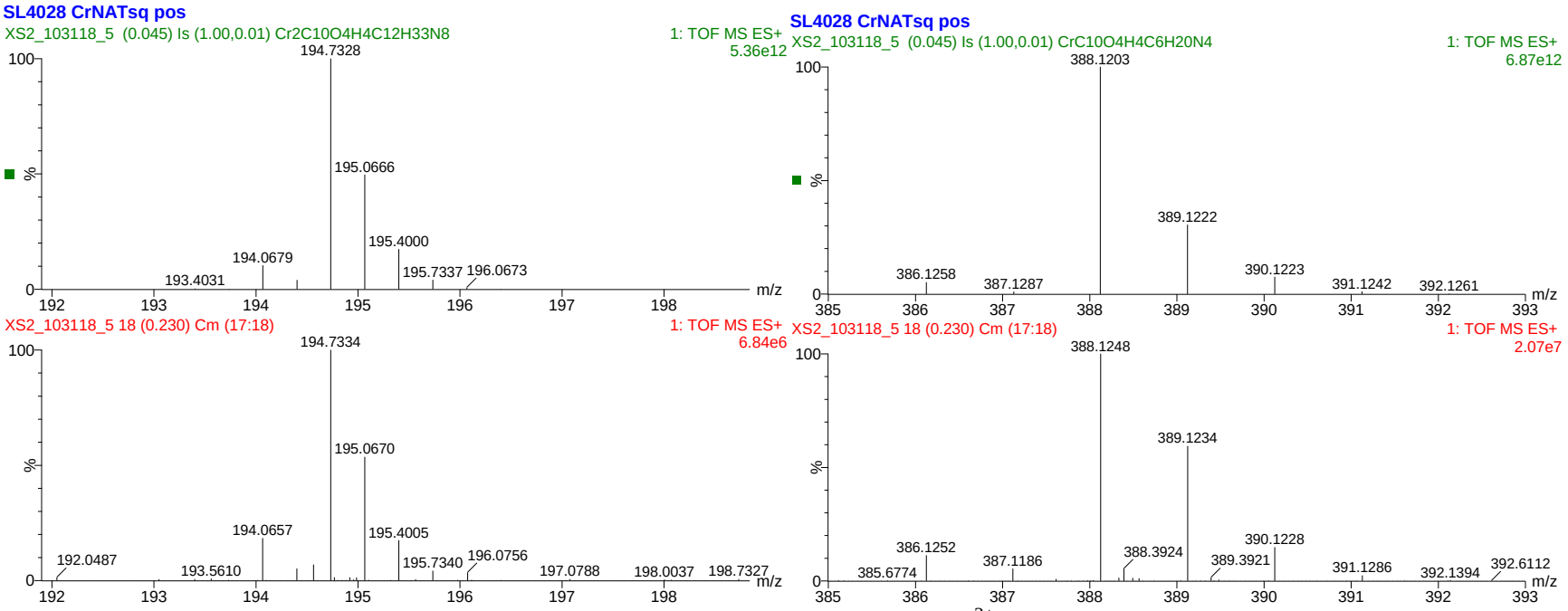

Figure 3.80. ESI-MS of Complex **18**. Left: top, calculated isotope pattern for $[M]^{3+}$ ($Cr_2C_{22}H_{40}O_4N_8$); bottom: experimental result. Right: top, calculated isotope pattern for $[Cr(tren)(C_{10}H_6O_4)]^+$ ($CrC_{16}H_{24}O_4N_4$); bottom: experimental result.

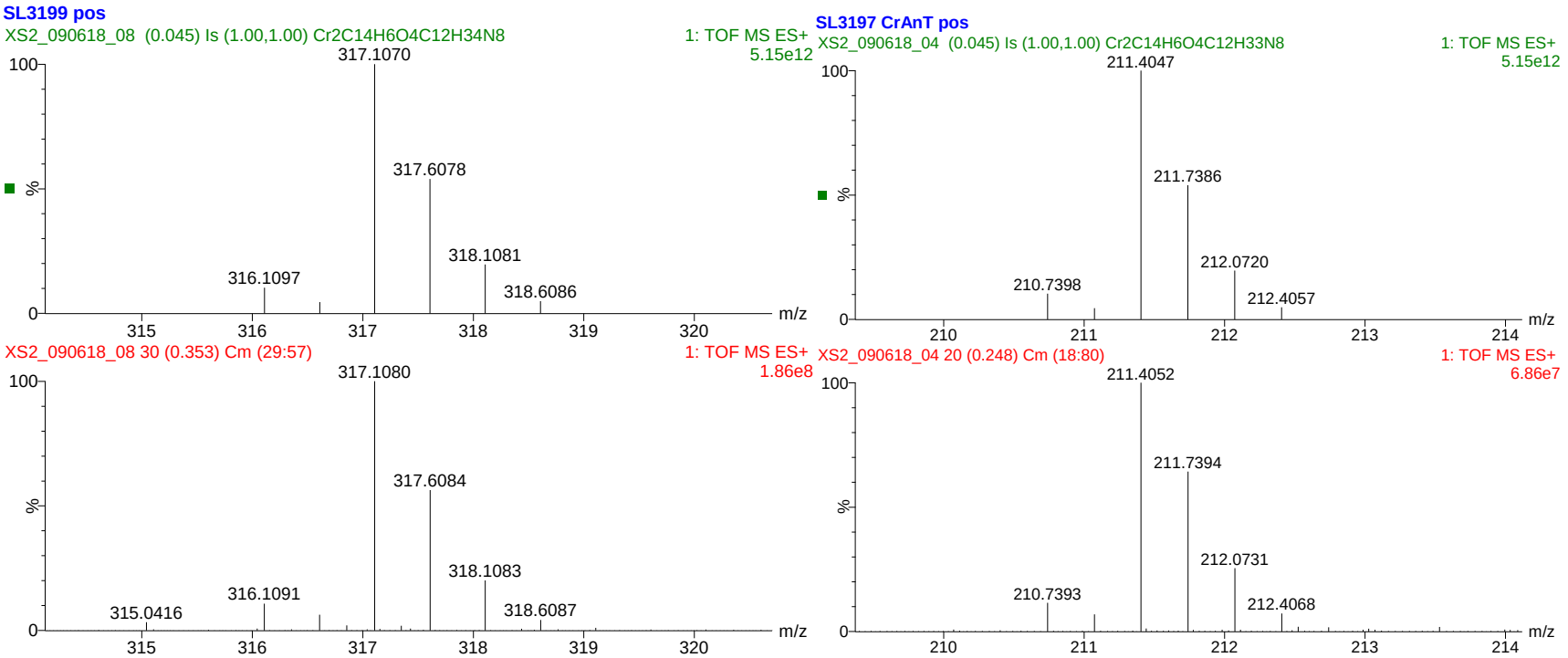

Figure 3.81. ESI-MS of Complex **9**. Left: top, calculated isotope pattern for $[M]^{2+}$ ($Cr_2C_{18}H_{14}O_4N_8$); bottom, experimental result. Right: top, calculated isotope pattern for $[M]^{3+}$ ($Cr_2C_{18}H_{14}O_4N_8$); bottom, experimental result.

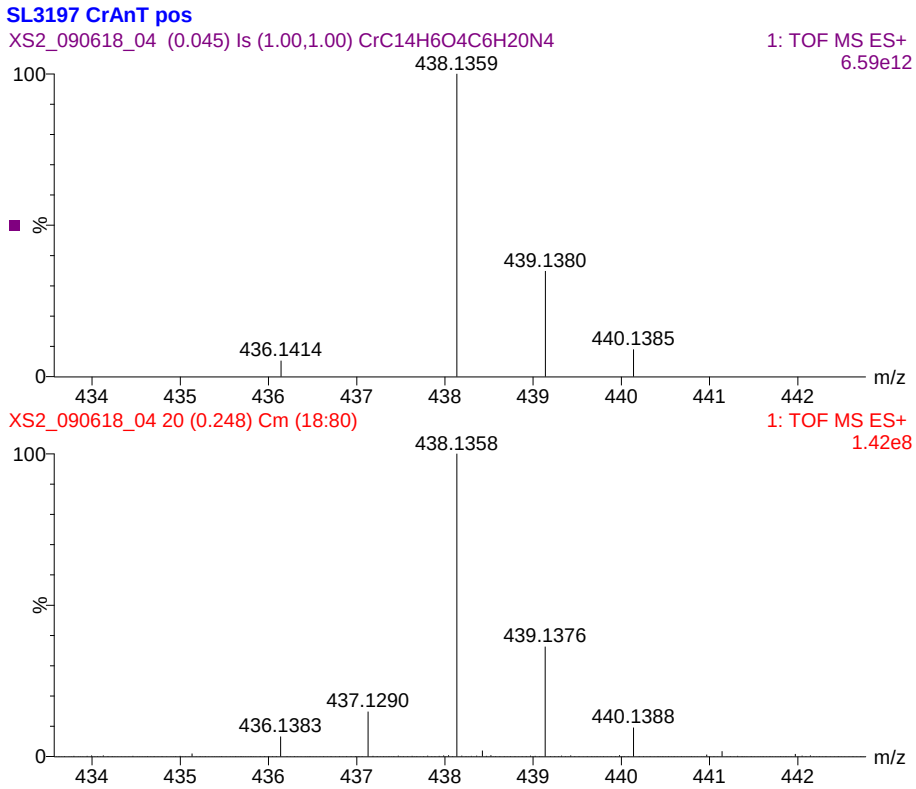

Figure 3.82. ESI-MS of Complex **9**. Top, calculated isotope pattern for $[Cr(tren)(C_{14}H_8O_4)]^+$ ($CrC_{20}H_{26}O_4N_4$); bottom, experimental result.

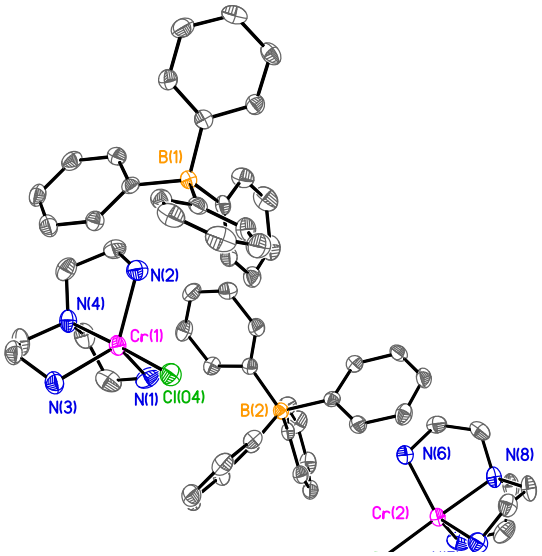

Figure 3.83. ORTEP drawing of [Cr(tren)Cl](BPh$_4$) from single-crystal x-ray structure determination. Atoms are represented as 50% thermal ellipsoids. Hydrogen atoms are omitted for clarity.

Table 3.10. Crystal data and structural refinement for [Cr(II)(tren)Cl](BPh$_4$).

Empirical formula	$C_{102}H_{152}B_4Cl_4Cr_4N_{16}$
Formula weight	2211.62
Temperature (K)	173(2)
Crystal system	Triclinic
Space group	$P\bar{1}$
a (Å)	13.7322(9)
b (Å)	10.3019(7)
c (Å)	20.2201(13)
$\boldsymbol{\beta}$ (˚)	94.3310(10)
Volume (Å^3)	2852.3(3)
Z	1
Radiation	MoKσ
D_{calc} (g cm^{-3})	1.288
Goodness of fit (F^2)	1.017
R_1 (I>2σ(I))[a]	0.0405
wR_2 (I>2σ(I))[b]	0.1042

[a]$R_1=\sum\frac{||F_o|-|F_c||}{\sum|F_o|}$. [b]$wR_2=[\sum w(F_o^2-F_c^2)^2/\sum w(F_o^2)^2]^{1/2}$, $w=1/[\alpha^2(F_o^2)+(aP)^2+bP]$, where $P=[F_o^2+F_c^2]/3$.

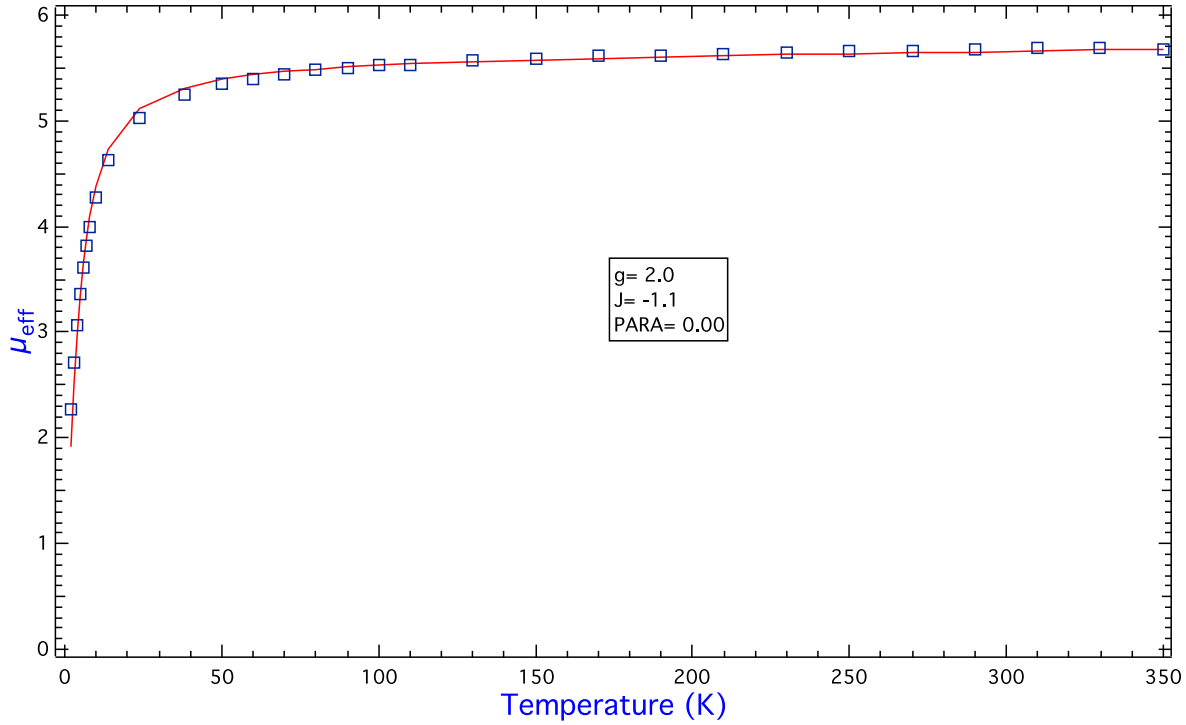

Figure 3.84. The effective magnetic moment of Complex **2** (blue square), and the solid line represents a fit to the data using MagFit.[46]

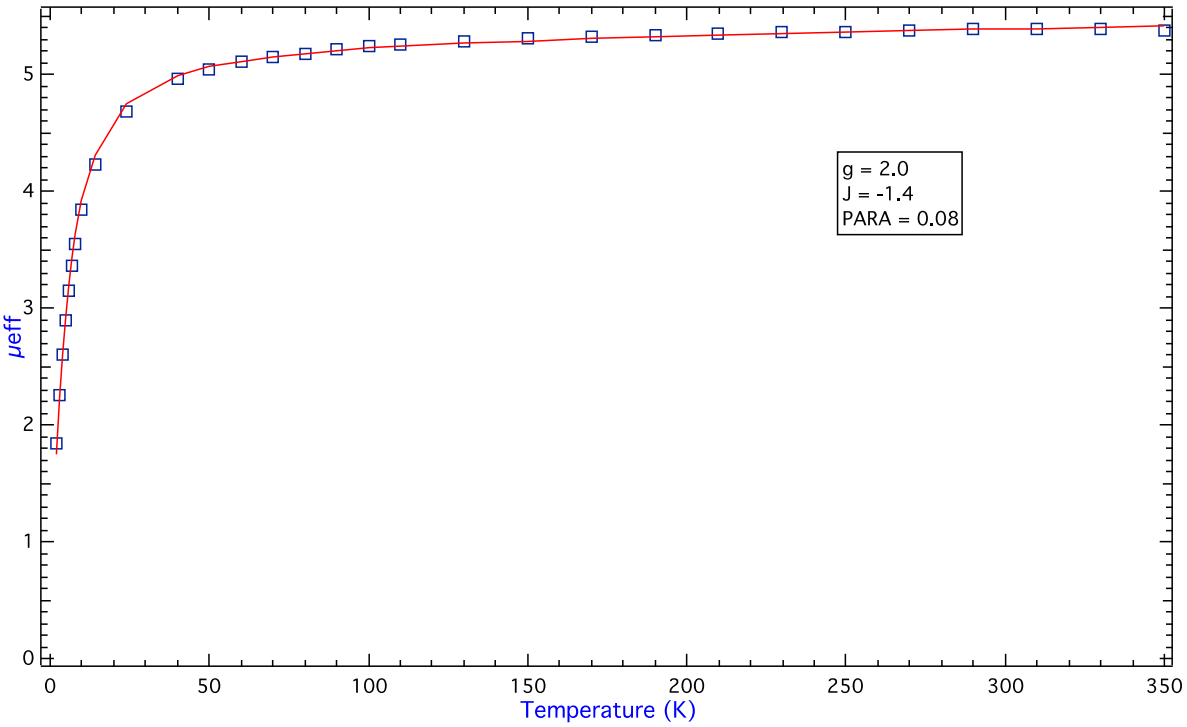

Figure 3.85. The effective magnetic moment of Complex **3** (blue square), and the solid line represents a fit to the data using MagFit.[46]

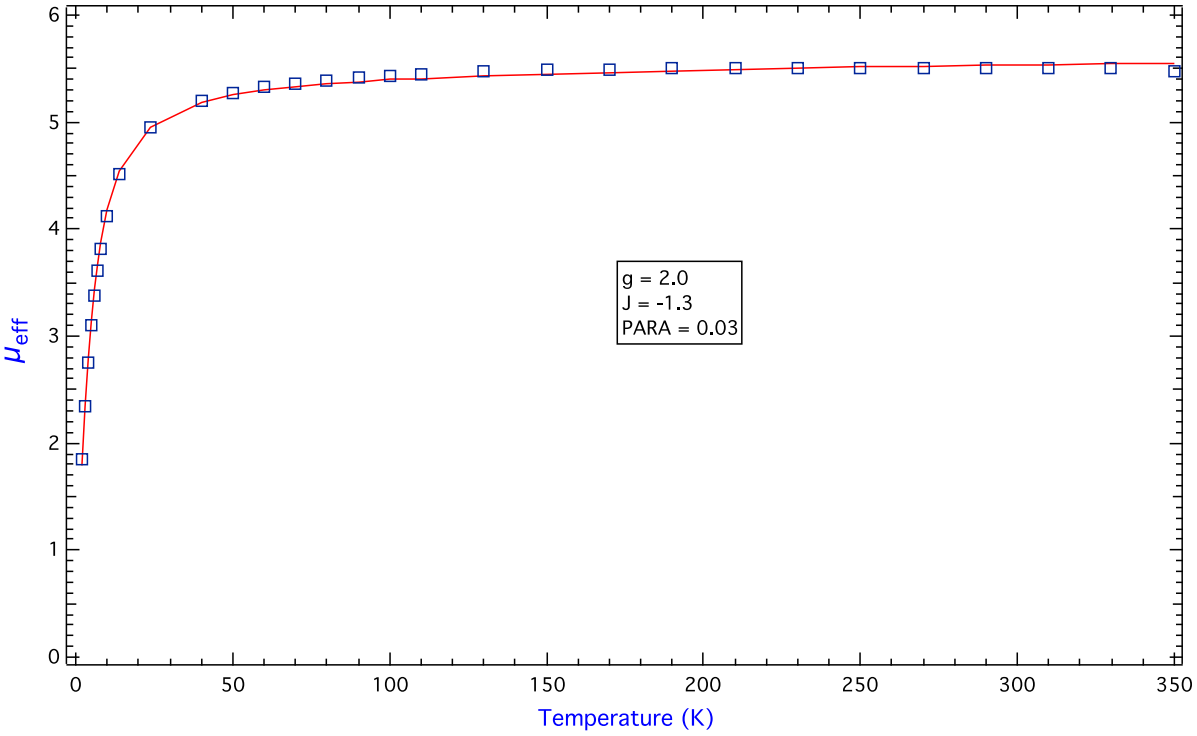

Figure 3.86. The effective magnetic moment of Complex **4** (blue square), and the solid line represents a fit to the data using MagFit.[46]

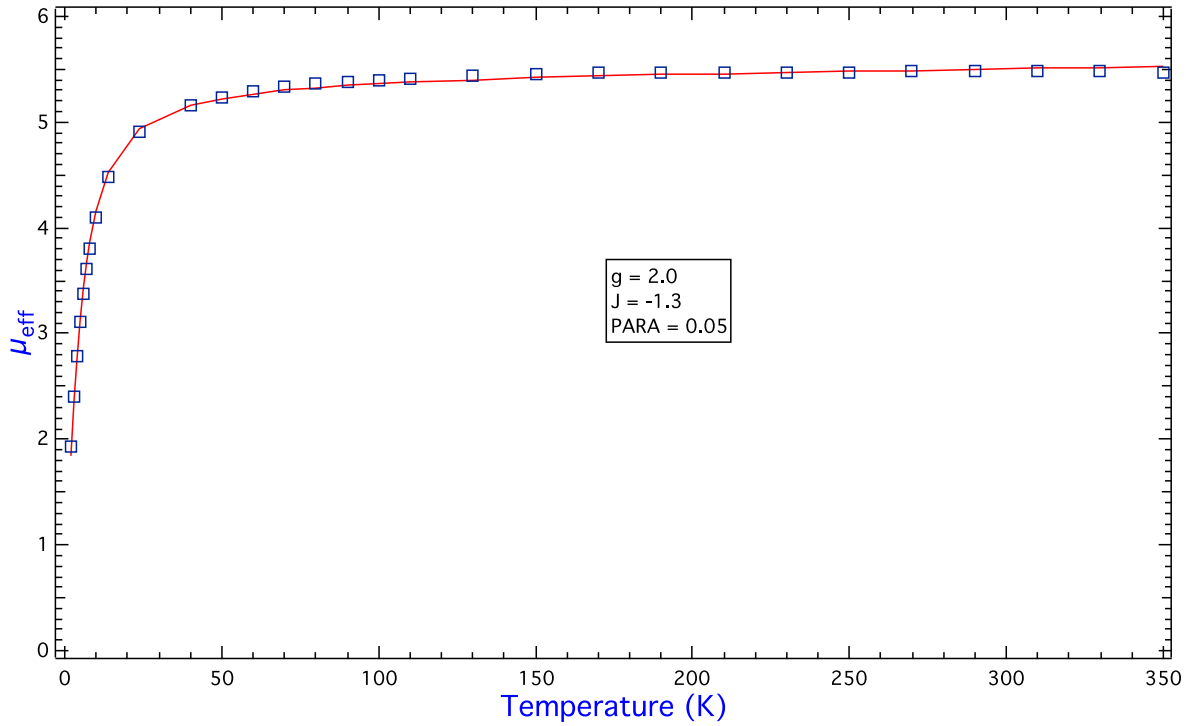

Figure 3.87. The effective magnetic moment of Complex **5** (blue square), and the solid line represents a fit to the data using MagFit.[46]

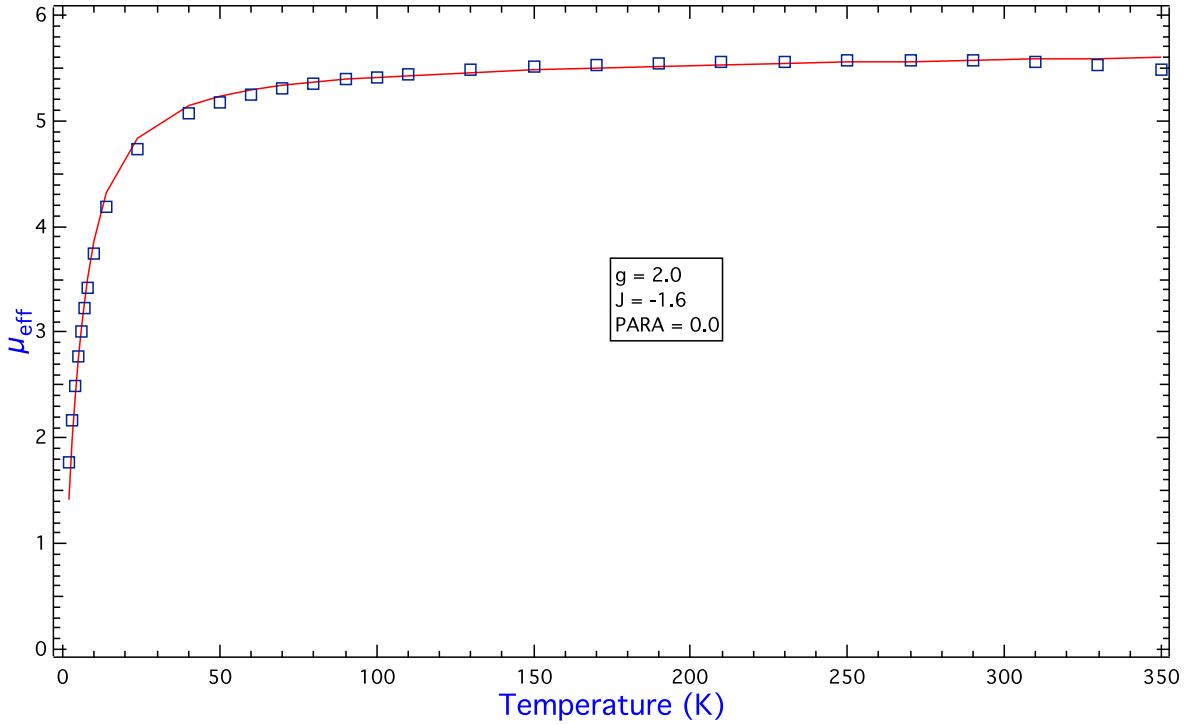

Figure 3.88. The effective magnetic moment of Complex **6** (blue square), and the solid line represents a fit to the data using MagFit.[46]

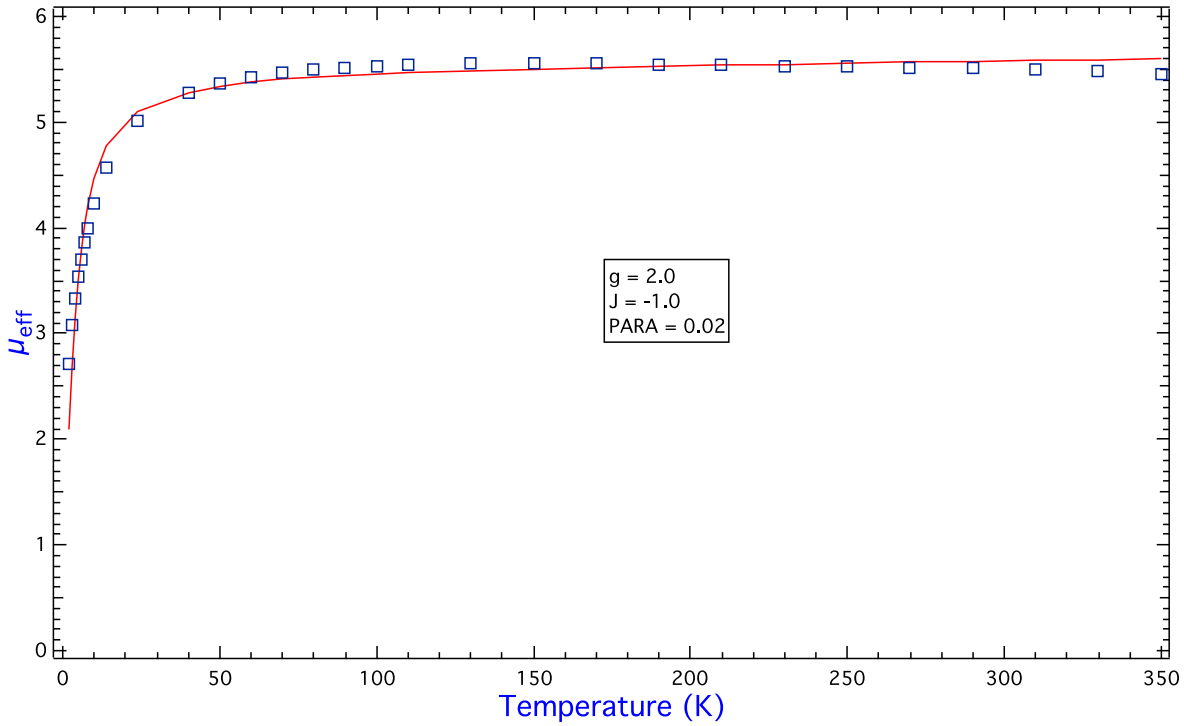

Figure 3.89. The effective magnetic moment of Complex **7** (blue square), and the solid line represents a fit to the data using MagFit.[46]

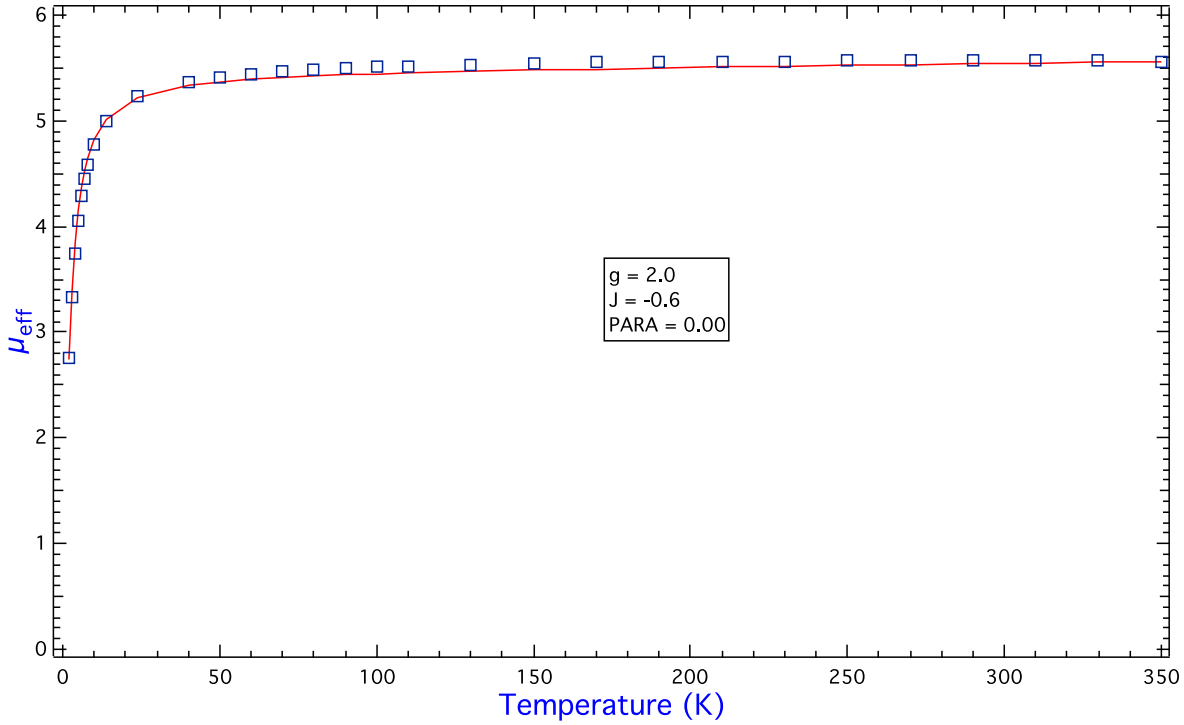

Figure 3.90. The effective magnetic moment of Complex **8** (blue square), and the solid line represents a fit to the data using MagFit.[46]

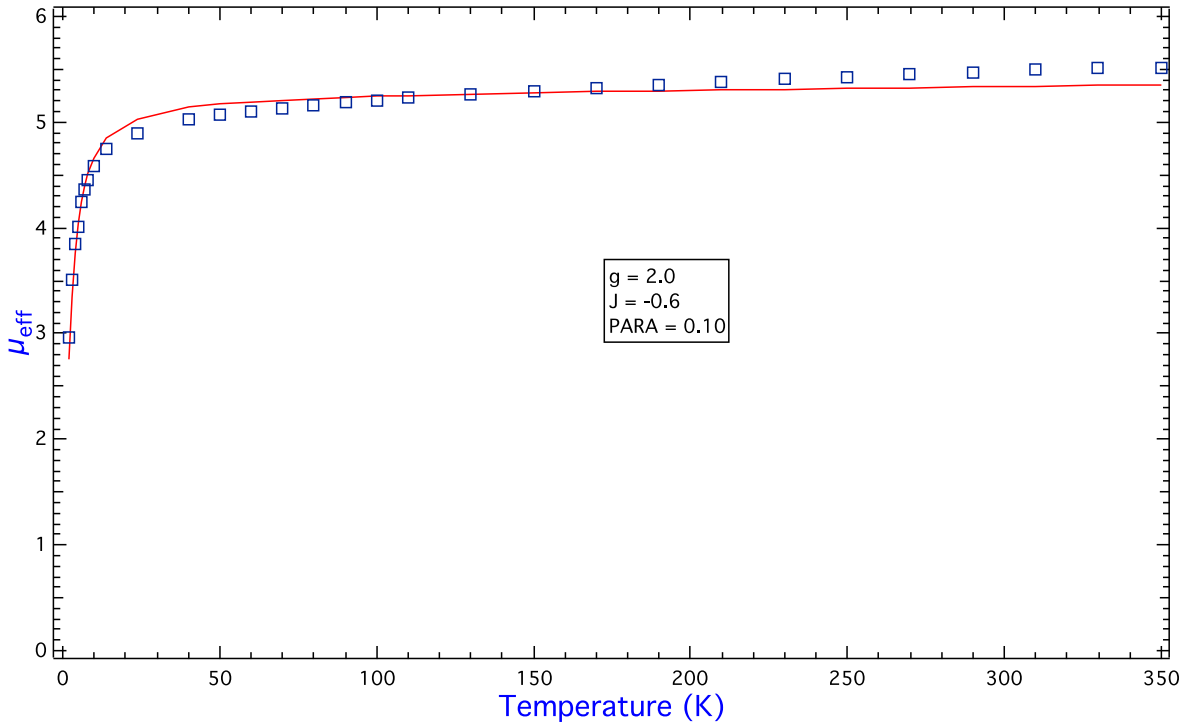

Figure 3.91. The effective magnetic moment of Complex **9** (blue square), and the solid line represents a fit to the data using MagFit.[46]

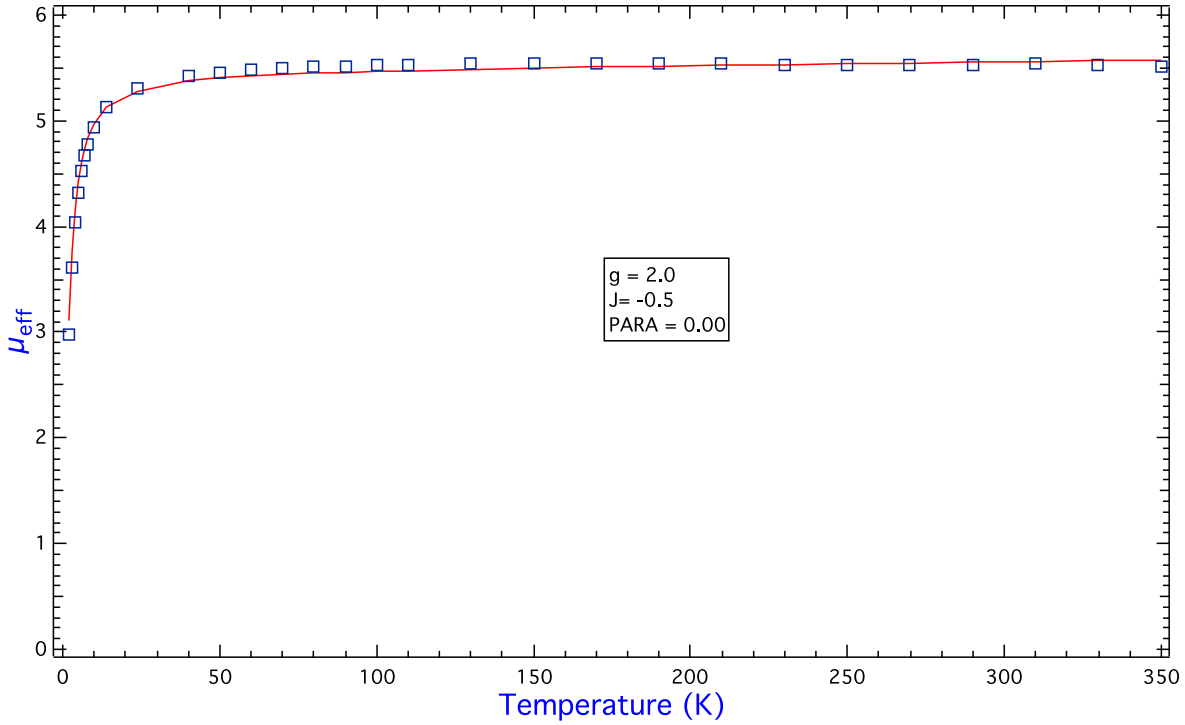

Figure 3.92. The effective magnetic moment of Complex **10** (blue square), and the solid line represents a fit to the data using MagFit.[46]

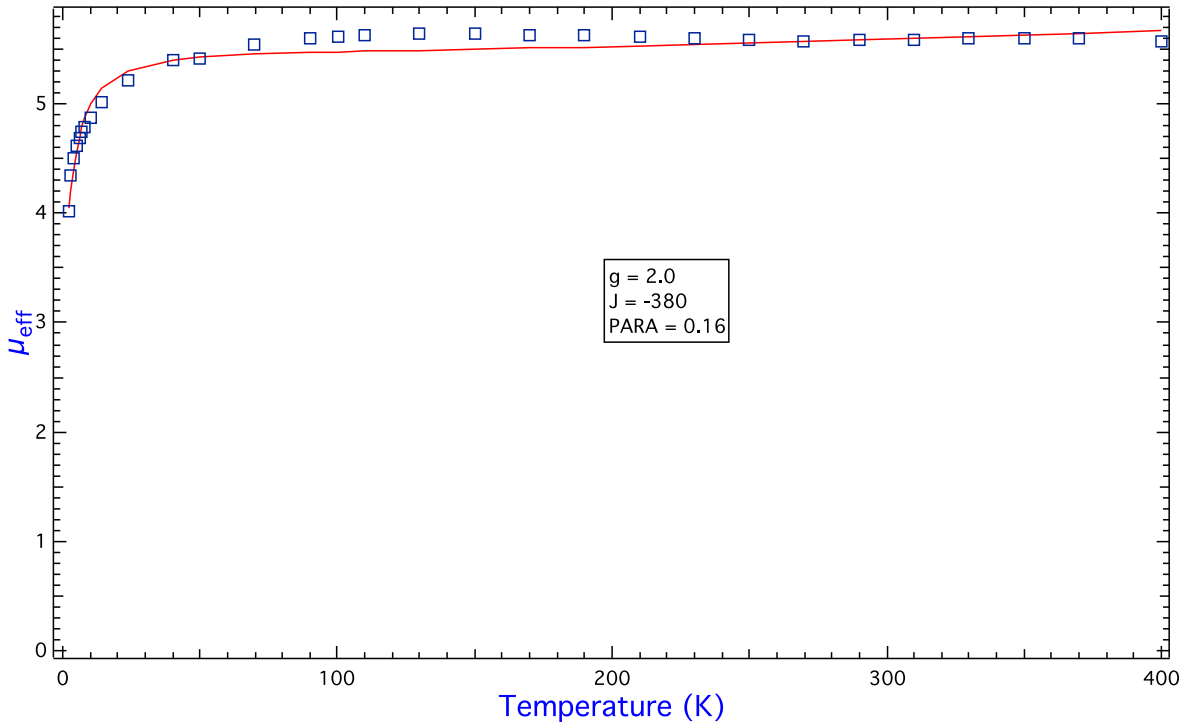

Figure 3.93. The effective magnetic moment of Complex **11** (blue square), and the solid line represents a fit to the data using MagFit.[46]

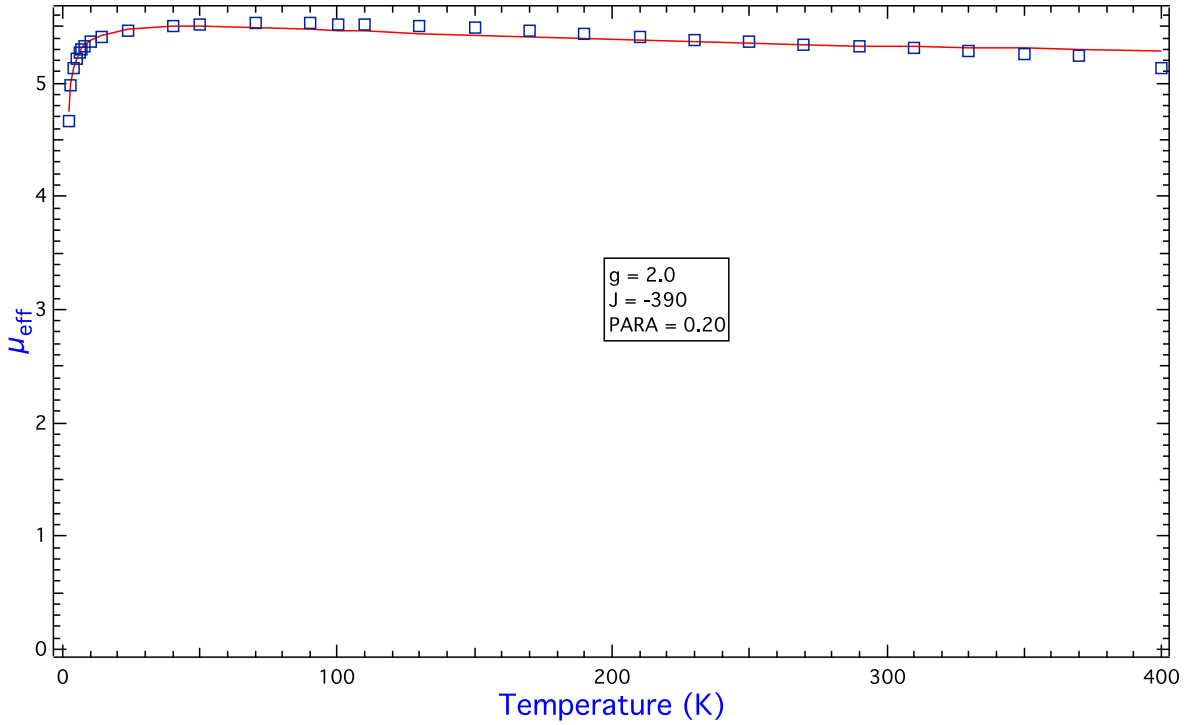

Figure 3.94. The effective magnetic moment of Complex **13** (blue square), and the solid line represents a fit to the data using MagFit.[46]

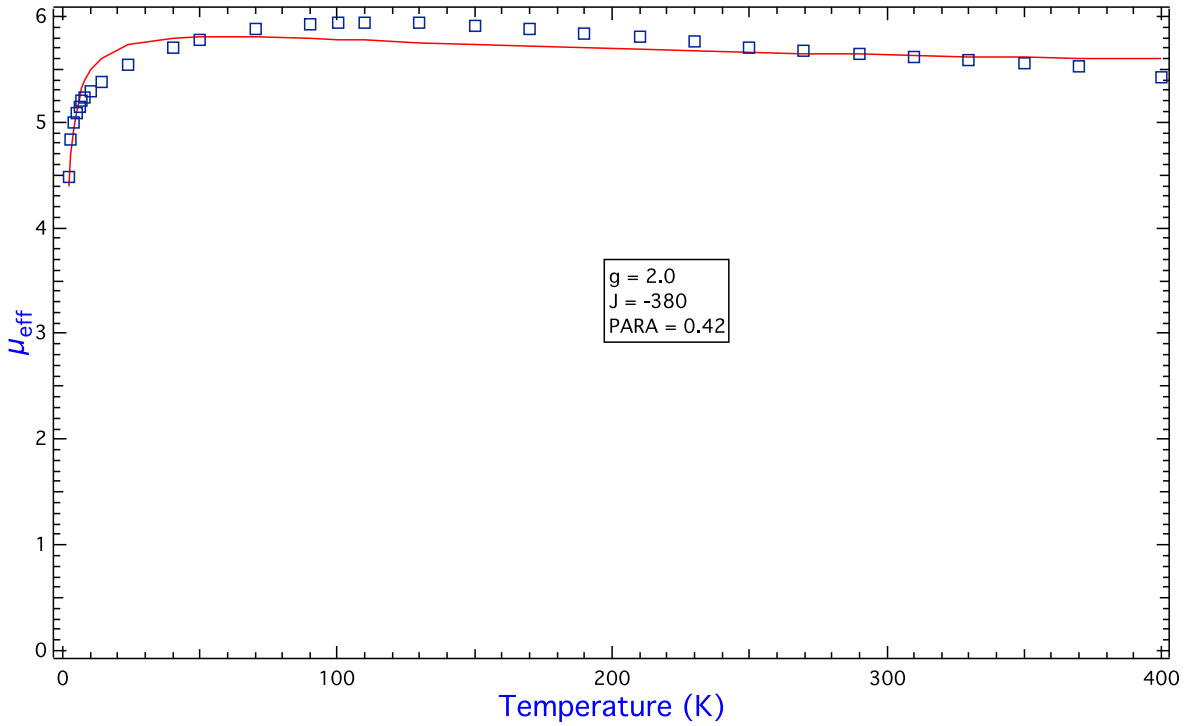

Figure 3.95. The effective magnetic moment of Complex **14** (blue square), and the solid line represents a fit to the data using MagFit.[46]

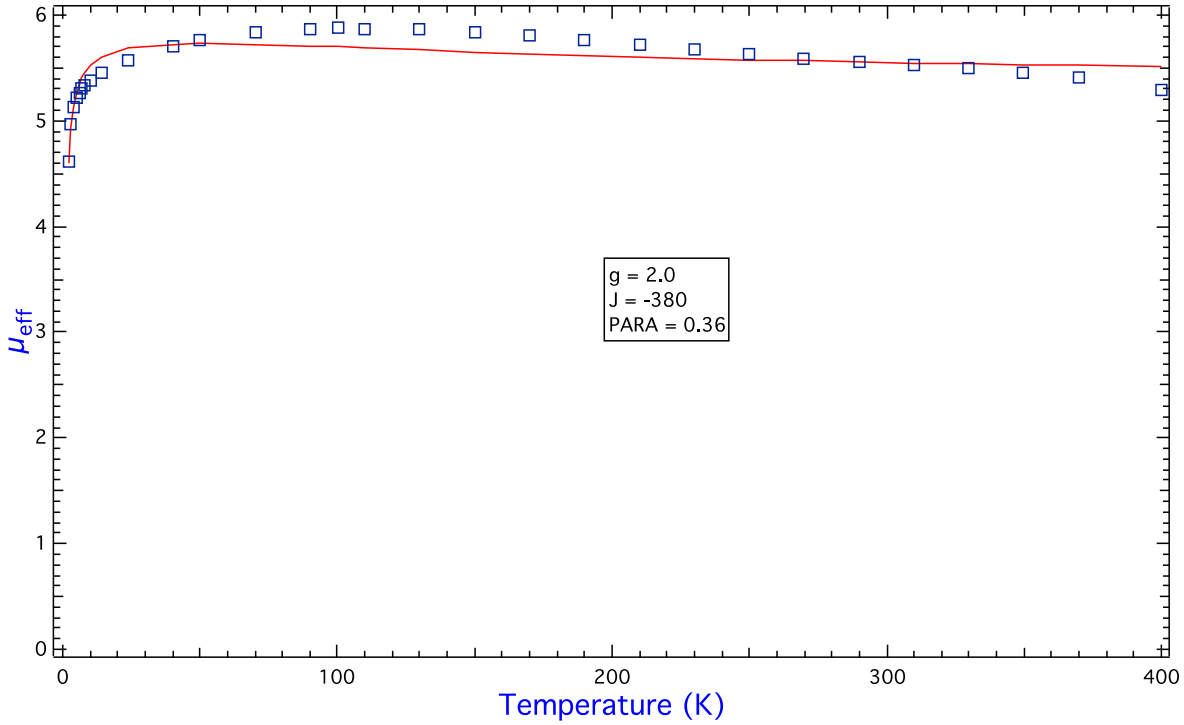

Figure 3.96. The effective magnetic moment of Complex **15** (blue square), and the solid line represents a fit to the data using MagFit.[46]

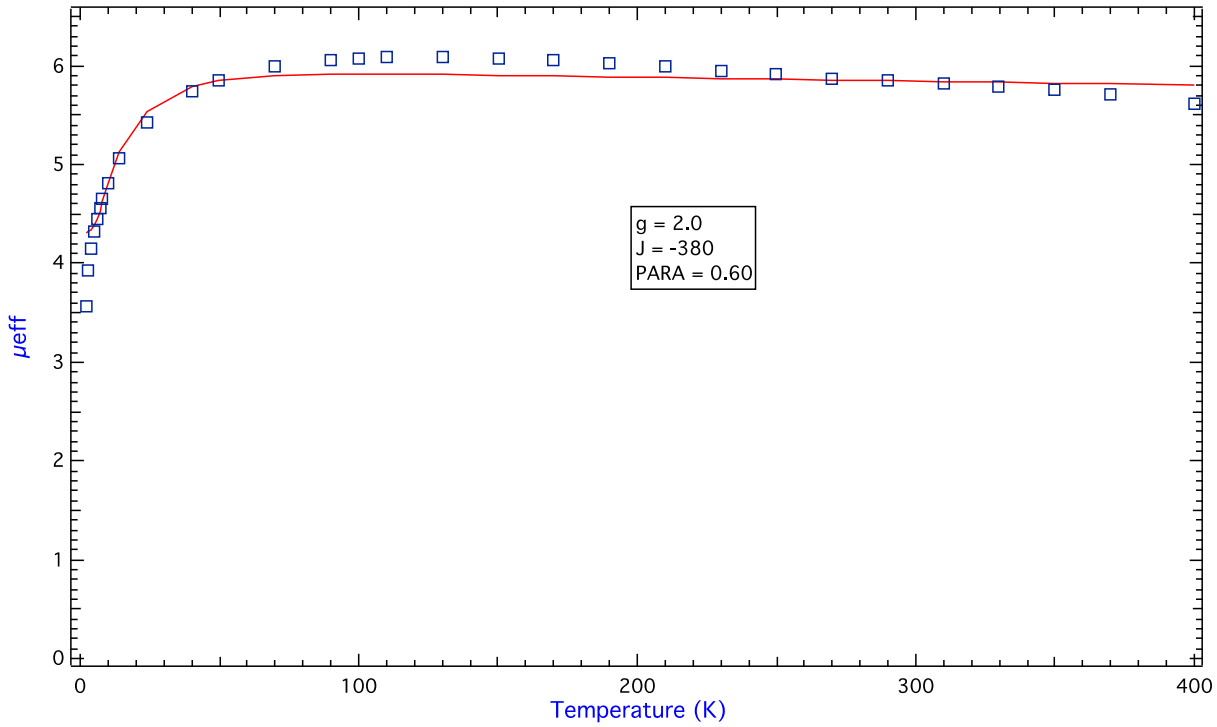

Figure 3.97. The effective magnetic moment of Complex **16** (blue square), and the solid line represents a fit to the data using MagFit.[46]

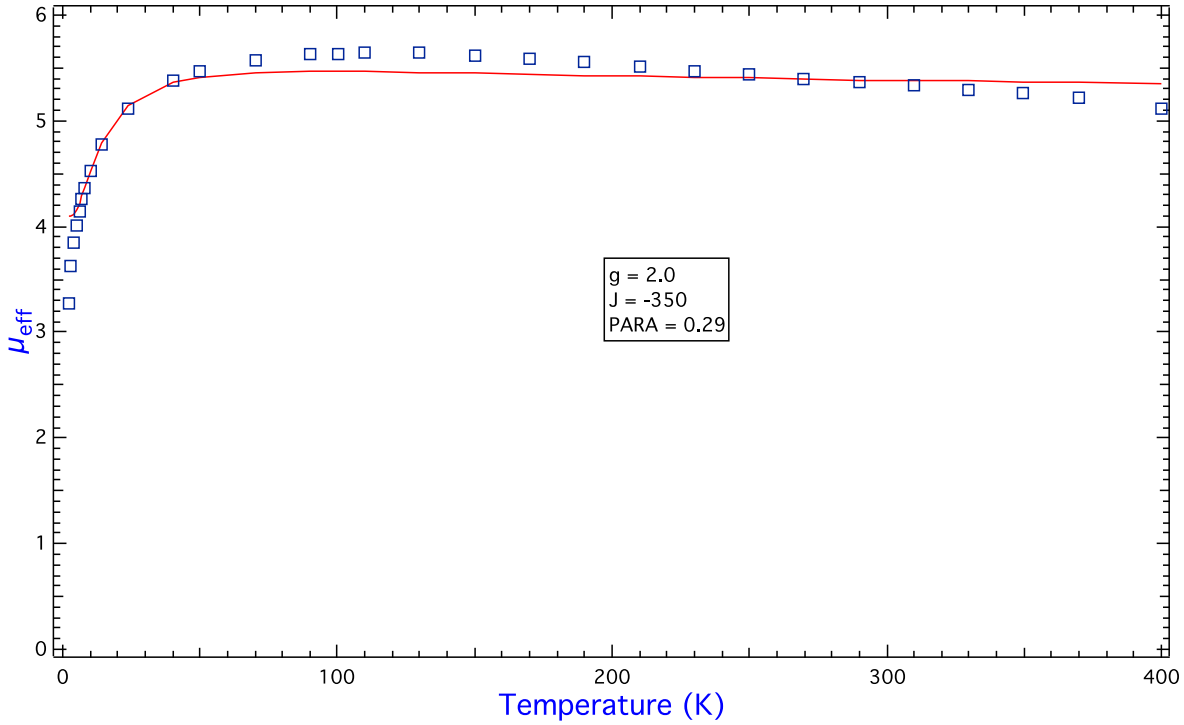

Figure 3.98. The effective magnetic moment of Complex **17** (blue square), and the solid line represents a fit to the data using MagFit.[46]

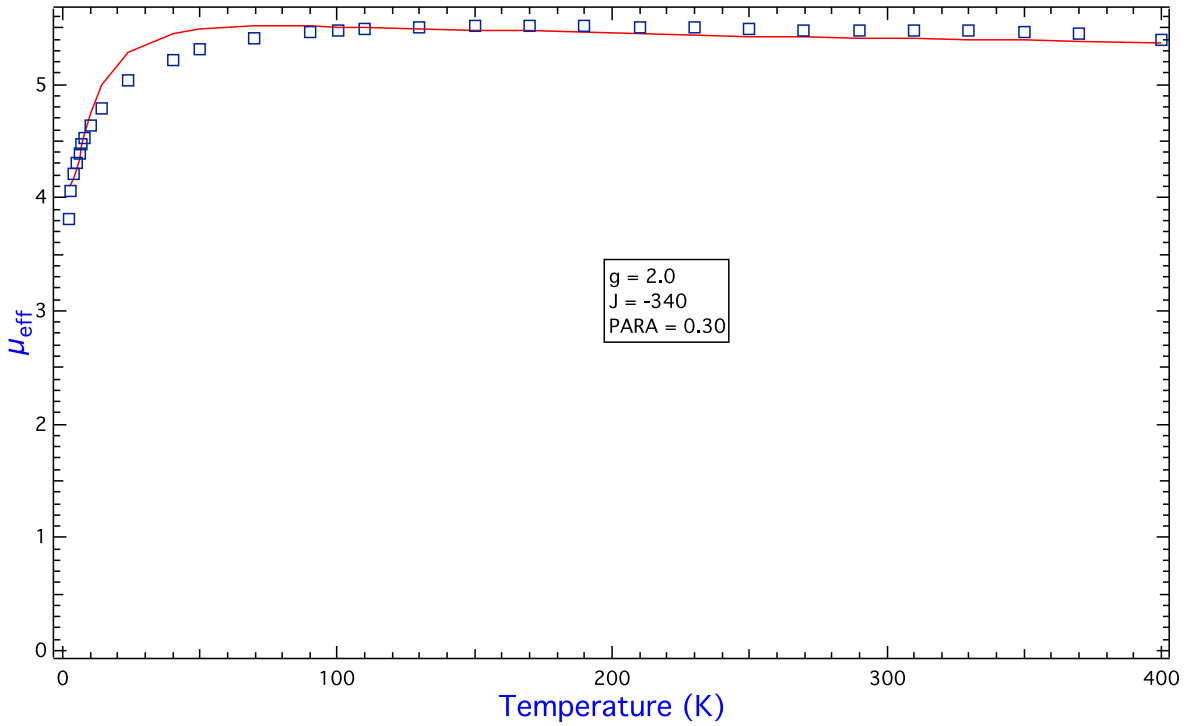

Figure 3.99. The effective magnetic moment of Complex **18** (blue square), and the solid line represents a fit to the data using MagFit.[46]

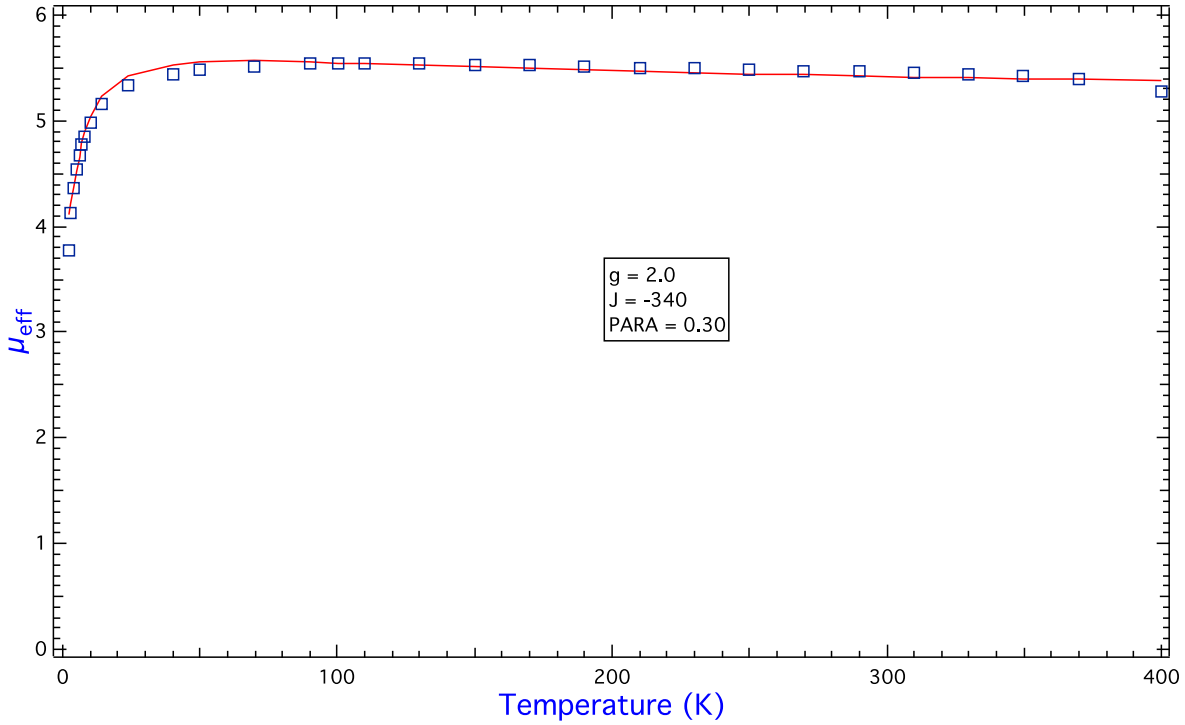

Figure 3.100. The effective magnetic moment of Complex **19** (blue square), and the solid line represents a fit to the data using MagFit.[46]

REFERENCES

REFERENCES

(1) Bertrand, P.; Guigliarellia, B.; Gayda, J. -P.; Beardwood, P.; Gibson, J. F. *Biochim. Biophys. Acta.* **1985**, *831*, 261.

(2) Luneau, D. *Curr. Opin. Solid State Mater. Sci.* **2001**, *5*, 123.

(3) Öhrstrom, L. *C. R. Chimie* **2005**, *8*, 1374.

(4) Shultz, D. A. *Polyhedron* **2001**, *20*, 1627.

(5) Caneschi, A.; Gatteschi, D.; Sessoli, R.; Rey, P. *Acc. Chem. Res.* **1989**, *22*, 392.

(6) Vostrikova, K. E. *Coord. Chem. Rev.* **2008**, *252*, 1409.

(7) Kahn, O.; Martinez, C. *J. Science* **1998**, *279*, 44.

(8) Guo, D.; McCusker, J. K. *Inorg. Chem.* **2007**, *46*, 3257-3274.

(9) Kirk, A. D. *Chem. Rev.* **1999**, *99*, 1607-1640.

(10) Forster, L. S. *Chem. Rev.* **1990**, *90*, 331.

(11) Mishustin, A. I. Russ. J. *Inorg. Chem.* **2008**, *53*, 1376.

(12) Osanai, K.; Okazawa, A.; Nogami, T.; Ishida, T. *J. Am. Chem. Soc.* **2006**, *128*, 14008.

(13) McConnell, H., M, *J. Chem. Phys.* **1963**, *39*, 1910.

(14) Hicks, R. G.; Lemaire, M. T.; Thompson, L. K.; Barclay, T. M. *J. Am. Chem. Soc.* **2000**, *122*, 8077.

(15) Shultz, D. A.; Sloop, J. C.; Washington, G. *J. Org. Chem.* **2006**, *71*, 9104.

(16) Shultz, D. A.; Sloop, J. C.; Coote, T.-A.; Beikmohammadi, M.; Kampf, J.; Boyle, P. D. *Inorg. Chem.* **2007**, *46*, 273.

(17) Chaudhuri, P.; Wagner, R.; Pieper, U.; Biswar, B.; Weyhermüller, T. *Dalton Trans.* **2008**, 1286-1288.

(18) Dei, A.; Gatteschi, D.; Pardi, L.; Russo, U. *Inorg. Chem.* **1991**, *30*, 2589-2594.

(19) Wheeler, D. E.; McCusker, J. K. *Inorg. Chem.* **1998**, *37*, 2296-2307.

(20) Gan, X.; Jiang, W.; Wang, W.; Hu, L. *Org. Lett.*, **2009**, *11*, 589-592.

(21) Kasahara, T.; Kondo, T. *Chem. Commun.*, **2006**, 891- 893.

(22) Tsuji, Y.; Morisaki, Y.; Chujo, Y. *Polym. Chem.* **2013**, *4*, 5361-5367.

(23) Torrey, H. A.; Hunter, W. H. *J. Am. Chem. Soc.*, **1912**, *34*, 702.

(24) Kiral, R. M. Ph.D. Dissertation, University of Notre Dame, Notre Dame, IN, **1980**.

(25) Viault, G.; Grée, D.; Das, S.; Yadav, J. S.; Grée, R. *Eur. J. Org. Chem.*, **2011**, 1233-1241.

(26) Boldt, P. *Chem. Ber.*, **1967**, *100*, 1270-1280.

(27) Chung, Y.; Duerr, B. F.; McKelvey, T. A.; Nanjappan, P.; Czarnik, A. W. *J. Org. Chem.*, **1989**, *54*, 1018-1032.

(28) Leermann, T.; Leroux, F. R.; Colobert, F. *Org. Lett.*, **2011**, *13*, 4479-4481.

(29) Tate, D. J.; Abdelbasit, M.; Kilner, C. A.; Shepherd, H. J.; Warriner, S. L.; Bushby, R. J. *Tetrahedron*, **2014**, *70*, 67-74.

(30) Gan, X.; Jiang, W.; Wang, W.; Hu, L. *Org. Lett.*, **2009**, *11*, 589-592.

(31) Storch, J.; Bernard, M.; Sykora, J.; Karban, J.; Čermák, J. *Eur. J. Org. Chem.*, **2013**, 260.

(32) Hellberg, J.; Dahlstedt, E.; Pelcman, M. E. *Tetrahedron*, **2004**, *60*, 8899-8912.

(33) Rabideau, P. W. *J. Org. Chem.*, **1971**, *36*, 2723-2724.

(34) Wang, R.; Zhang, M.; Liu, X.; Zhang, L.; Kang, Z.; Wang, W.; Wang, X.; Dai, F.; Sun, D. *Inorg. Chem.*, **2015**, *54*, 6084.

(35) Miller, J. S.; Calabrese, J. C.; Rommelmann, H.; Chittipeddi, S. R.; Zhang, J. H.; Reiff, W. M.; Epstein, A. J. *J. Am. Chem. Soc.* **1987**, *109*, 769-781.

(36) Huang, N.; Ding, X.; Kim, J.; Ihee, H.; Jiang, D. *Angew. Chem. Int. Ed.* **2015**, *54*, 8704.

(37) Schrauben, J. N.; Guo, D.; McCracken, J. L.; McCusker, J. K. *Inorganica Chimica Acta*, **2008**, *361*, 3539-3547.

(38) COSMO-V1.61- software for the CCD Detector Systems for Determining Data Collection Parameters, Bruker axs, Madison, WI, 2000.

(39) Software for the Integration of CCD Detector System Bruker Analytical X-ray Systems, Bruker axs, Madison, WI (after 2013).

(40) Krause, L.; Hersbt-Irmer, R.; Sheldrick, G. M.; Stalke, D., *J. Appl. Cryst.*, **2015**, *48*.

(41) Sheldrick, G. M., *Acta. Cryst.* **2015**, *A71*, 3-8.

(42) Sheldrick, G. M., *Acta. Cryst.* **2008**, *A64*, 339-341.

(43) Dolomanov, O. V.; Bourhis, L. J.; Gildea, R. J.; Howard, J. A. K.; Puschmann, H., *J. Appl. Cryst.*, **2008**, *42*, 339-341.

(44) Brown, D. S.; Crawford, V. H.; Hall, J. H.; HatField, W. E. *J. Phys. Chem.* **1977**, *81*, 1303.

(45) Bain, G. A.; Berry, J. F. *J. Chem. Educ.* **2008**, *85*, 532-536.

(46) Schmitt, E. Ph.D Dissertation. Department of Chemistry, University of Illinois, Urbana-Champaign, IL, 1996.

(47) McElfresh, M. Fundamentals of Magnetism and Magnetic Measurements Featuring Quantum Design's Magnetic Property Measurement System, Quantum Design. Purdue University, West Lafayette, IN, 1994.

(48) Quantum Design. Using Straw Sample Holder with DC Scan Mode. *MPMS 3 Application Note 1500-018, Rev. A0*. October 17, 2013.

(49) Bore, M; Luz, Z. *J. Phys. Chem.* **1967**, *71*, 3690.

(50) Kane-McGuire, N. A. P. *Top. Curr. Chem.* **2007**, *280*, 37.

(51) Labinger, J. A.; Bercaw, J. E. *Nature*, **2002**, *417*, 507-514.

(52) Godula, K.; Sames, D. *Science*, **2006**, *312*, 67-72.

(53) Ponduru, T. T.; Qiu, C.; Mao, J. X.; Leghissa, A.; Smuts, J.; Schug, K. A.; Dias, H. V. R. *New J. Chem.* **2018**, *Advance Article*.

(54) Connelly, N. G.; Geiger, W. E. *Chem. Rev.* **1996**, *96*, 887-910.

(55) Rodriguez, J. H.; Wheeler, D. E.; McCusker, J. K. *J. Am. Chem. Soc.* **1998**, *120*, 12051.

(56) Pierpont, C. G.; Attia, A. S. *Collect. Czech. Chem. Commun.* **2001**, *66*, 33.

(57) Pierpont, C. G.; Lange, C. W. *Prog. Inorg. Chem.* **1994**, *41*, 331.

(58) Pierpont, C. G.; Buchanan, R. M. *Coord. Chem. Rev.* **1981**, *38*, 45.

(59) Coulson, F. R. S., C. A.; Daudel, R.; Robertson, F. R. S., J. M. *Proc. R. Soc. Lond. A.* **1951**, *207*, 306-320.

(60) Kalescky, R.; Kraka, E.; Cremer, D. *J. Phys. Chem. A.* **2014**, *118*, 223-237.

(61) Damrauer, N. H.; Weldon, B. T.; McCusker, J. K. *J. Phys. Chem. A* **1998**, *102*, 3382.

(62) Damrauer, N. H.; McCusker, J. K. *J. Phys. Chem. A* **1999**, *103*, 8440-8446.

(63) Fehir, Jr., R. J. Ph. D. Dissertation. Department of Chemistry, Michigan State University, East Lansing, MI, 2009.

(64) Kahn, O. Molecular Magnetism; VCH Publishers: New York, 1993.

(65) Kambe, K. *J. Phys. Soc. Japan* **1950**, *5*, 48-51.

(66) Fryzuk, M. D.; Leznoff, D. B.; Rettig, S. J.; Thompson, R. C. *Inorg. Chem.* **1994**, *33*, 4428-4434.

(67) Vučinić, M.; Mitirć, M.; Kusigerski, V.; Kapor, A.; Szytula, A. *J. Res. Phys.* **2002**, *29*, 79.

(68) Fleischer, U.; Schindler, M. *Chem. Phys.* **1988**, *120*, 103-121.

(69) Carroll, T. X.; Thomas, T. D.; Bergersen, H.; Børve, K. J.; Sæthre, L. J. *J. Org. Chem.* **2006**, *71*, 1961-1968.

(70) Mukherjee, S.; Torres, D. E.; Jakubikova, E. *Chem. Sci.* **2017**, *8*, 8115.

(71) Wieser, M. E.; Coplen, T. B. *Pure Appl. Chem.* **2011,** *83*, 359.

(72) Anderson, P. W. *Phys. Rev.* **1950**, *79*, 350-356.

(73) White, R. M. *Quantum Theory of Magnetism.* Springer-Verlag: Berlin, Germany, 1996.

(74) Goodenough, J. B. *Phys. Rev.* **1955**, *100*, 564.

(75) Kanamori, J. *J. Phys. Chem. Solid.* **1959**, *10*, 87.

(76) Goodenough, J. B. *Magnetism and the Chemical Bond.* Interscience Publisher: New York, NY, 1963.

(77) Carey, F. A.; Sundberg, R. J. *Advanced Organic Chemistry Part A: Structure and Mechanisms.* 5th Ed.; Springer: New York, NY, 2008.

(78) Hansch, C.; Leo, A.; Taft, R. W. *Chem. Rev.* **1991**, *91*, 165-195.

(79) James, B. R.; Williams, R. J. P. *J. Chem. Soc.* **1961**, *0*, 2007-2019.

(80) Damrauer, N. H.; Boussie, T. R.; Devenney, M.; McCusker, J. K. *J. Chem. Soc.* **1997**, *119*, 8253.

(81) Scalettar, R. T. *An Introduction to the Hubbard Hamiltonian.* Edicted by Pavarini, E.; Koch, E.; van den Brink, J.; Sawatzky, G. *Quantum Materials: Experimentals and Theory*. Vol. 6; Forschungszentrum Jülich: Jülich, Germany, 2016.

Chapter 4. Magnetic Properties and Substituent Effects of Gallium (III) Tetraoxo-Dimeric Complexes

4.1 Introduction

The substituent effects of spin delocalization on free radicals were discussed in Chapter 2, and transition metal radical complexes should be the next models for the examination of whether the same principles apply. When a radical is incorporated to a Lewis acidic metal ion, the empty metal orbitals can accommodate lone electrons from the ligand to form a coordination compound. The formation of coordination compound alters the overall electronic structure through linear combination of metal and ligand atomic orbitals.[1] Upon formation, reduction in interelectronic repulsion and spin-orbit coupling can be observed experimentally due to the expansion of valence electron cloud around the metal centers.[2-4] This similar situation manifests on the magnetic moment of transition metal complexes because the orbital contribution is decreased by covalency.[5] This predicts that the magnetic behaviors may be very different from that of a free radical ligand, and the Lewis acidity of metal ion and orbital overlaps between metal and ligands may change the spin distribution. Therefore, it will be unreasonable to employ the computational information of free ligands for transition metal complexes even though the ligands remain the same.

The coordination of such quinoidal ligands with relatively redox-inert metal ions allows the systematical study of the substituent effects on the physical properties without changing the overall elemental composition or drastically altering the structures upon oxidation. Ga(III) complexes are goods model for the study of paramagnetic metal complexes due to their diamagnetic d^{10} electronic configuration with no Heisenberg exchange interaction. Ga(III) has been widely employed in literature for the study of bound-semiquinone ligands.[6-12]

In addition, Ga (III) -quinoidal complexes are treated as a reference to the Cr (III) analogues, because of Ga (III) nearly identical charge-to-radius ratio to Cr (III) and its spectroscopic silent property. In order to understand changes in spin polarization of substituted semiquinone radical when coordinating to a metal center, and establish the thermodynamic correlation between electrochemical and magnetic behavior induced by spin exchange interaction, Ga (III) -semiquinone complexes are synthesized and reported here.

4.1.1 Previous Studies on Similar Systems: An EPR, ENDOR, and Density Functional Study on Ga (III) Phenanthrenesemiquinone Complexes, $[Ga_2(tren)_2(CA^{sq,cat})]^{3+}$ and $[Ga_2(tren)_2(DHBQ^{sq,cat})]^{3+}$

Electron Paramagnetic Resonance (EPR) spectroscopy is a powerful tool to study the electronic structure of radicals by detecting unpaired electrons. It can help identify paramagnetic species and short-lived reactive free radicals under applied field, so it has been widely used in the field of biomedical engineering, pathologies, and other life science related studies. Electron nuclear double resonance (ENDOR) and electron spin echo envelope modulation (ESEEM) are two methods to measure the interactions between unpaired electrons and the surrounding nuclei.[42-44] Previous studies in our group conducted DFT computational and EPR studies on Ga (III) Phenanthrenesemiquinone Complexes,[36] $[Ga_2(tren)_2(CA^{sq,cat})]^{3+}$ and $[Ga_2(tren)_2(DHBQ^{sq,cat})]^{3+}$.[36] DFT calculations were conducted to interpret the overall mechanism of spin delocalization of these Ga (III) complexes, and EPR spectroscopy was employed to experimentally examine the validity of the computational results.[36,37]

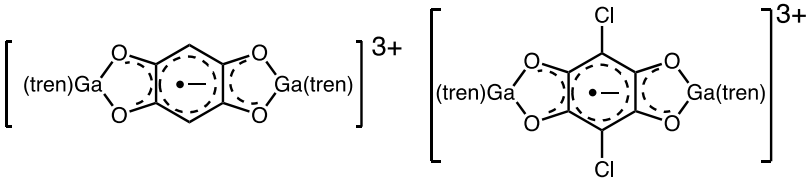

Figure 4.1. Chemical structures of $[Ga_2(tren)_2(DHBQ^{sq,cat})]^{3+}$ (left) and $[Ga_2(tren)_2(CA^{sq,cat})]^{3+}$ (right).

In the studies of $[Ga_2(tren)_2(CA^{sq,cat})]^{3+}$ and $[Ga_2(tren)_2(DHBQ^{sq,cat})]^{3+}$ (Fig. 4.1), EPR spectroscopy was used experimentally for the spatial disposition of the unpaired electrons on the bridging ligands, and DFT calculations were incorporated to provide guidance for the simulated and experimental EPR spectra.[37] The DFT calculation predicted that excess α spin on the four interacting oxygens, the ones directly coordinate to Ga (III), which is consistent with experimental observation from EPR spectra.[37] The β spin character within the ligand gives rise to negative hyperfine coupling constants, and the number of signal obtained experimentally agrees with the prediction of the number of signals from DFT.[37] This study also suggests that the presence of triplet state in EPR spectra could be the consequence of comproportionation of $[Ga_2(tren)_2(CA^{sq,cat})]^{3+}$ (Eq. 4.1) in solution.[37] The β spin density spreading over to two chlorines is possible residual effect caused by the α-SOMO, because Cl effectively induces spin delocalization in the system.[36]

$$\mathbf{[(tren)_2M^{III}_2\text{-}CA^{cat,cat}]^{2+} + [(tren)_2M^{III}_2\text{-}CA^{sq,sq}]^{4+} \underset{}{\overset{K_C}{\rightleftharpoons}} 2[(tren)_2M^{III}_2\text{-}CA^{sq,cat}]^{3+}} \quad (4.1)$$

$$\mathbf{K_c = \frac{[(tren)_2M^{III}_2\text{-}CA^{sq,cat}]^2}{[(tren)_2M^{III}_2\text{-}CA^{cat,cat}]\,[(tren)_2M^{III}_2\text{-}CA^{sq,sq}]}} \quad (4.2)$$

Although EPR spectroscopy is not utilized as a characterization technique in this project, similar DFT natural population analysis (NPA) was performed on various substituted $[Ga_2(tren)_2(L^{sq,cat})]^{3+}$ to better understanding the substituent effect on spin polarization and used as a tool to help interpret experimental results.

4.2 Computational Details of DFT Calculations

General Methods. All electronic structure calculations of $[Ga_2(tren)_2(L^{sq,cat})]^{3+}$ cations were carried out using density functional theory implemented in Gaussian 09[13] on HPCC at

Institute for Cyber-Enabled Research at Michigan State University. The B3LYP functional with open shelled was used in the calculation.[14-18] The calculation was performed using the default tight convergence criteria with ultrafine integration grid. Analysis of atomic charge and spin densities were performed using natural population analysis (NPA) framework developed by Weinhold et al.[19]

4.2.1 Geometry Optimization and Single Point Energy Calculations

The initial geometries of $[Ga_2(tren)_2(DHBQ^{sq,cat})]^{3+}$ (**20**), $[Ga_2(tren)_2(FA^{sq,cat})]^{3+}$ (**21**), $[Ga_2(tren)_2(CA^{sq,cat})]^{3+}$ (**22**), $[Ga_2(tren)_2(BA^{sq,cat})]^{3+}$ (**23**), and $[Ga_2(tren)_2(IA^{sq,cat})]^{3+}$ (**24**) were modified from the crystal structure of their catecholate derivatives, and subsequently optimized using the UB3LYP functional and a 6-31G basis set with imposed symmetries of C_i. The initial geometries of other Gallium (III) dimeric derivatives were generated using GaussView[20] with subsequently optimized using the UB3LYP functional and a 6-31G basis set with imposed symmetries of C_i. Final geometries were checked with frequency calculations at the UB3LYP/6-31G level. Imaginary frequencies were obtained for some sterically bulky structures or structures with extended aromatic conjugation. Those structures were reoptimized with increased convergence cycles (default maxcycle = 64) and the exact computed Hessian matrix for frequency calculations with CalcFC or CalcAll command. Heissian matrix is the matrix of second derivatives of the energy in regard to displacement of atoms.[21] Frequency calculations generally are based on an estimated Hessian from geometry optimization.[22] Geometry optimizations were then re-run for all structures with UltraFine grid to help obtain smoother convergence to the stationary point. Structures were reoptimized with subsequent frequency calculations until no imaginary frequencies, which indicates that the final structures have reached

the global minima. The final optimized structures were then used for single-point energy calculations.

Single-point energy calculations were performed using the unrestricted open shelled density function UB3LYP with the 6-311G basis set with natural population analysis assuming the doublet ground state and a molecular charge of 3+.

4.3 Experimental Section

General. All chemicals were of reagent grade, purchased from Alfa Aesar, Sigma-Aldrich, Acros Organics, TCI Chemicals, Oakwood Chemicals, Strem Chemicals, or Matrix Chemicals, and used as received unless otherwise noted. Solvents were purchased from Sigma-Aldrich, Jade Scientific, Alfa Aesar, Fisher Scientific, EMD Chemicals, Mallinckrodt, or CCI and were purified using standard purification techniques. All air-sensitive and water-sensitive reactions were carried out under inert atmosphere either by standard Schlenk techniques or in dryboxes. The solvents utilizing for these reactions were thoroughly dried by being stored over 4 Å molecular sieve and deoxygenated by the freeze-pump-thaw method. The ligand tris(2-aminoethyl)amine (tren) was purchased from either Sigma-Aldrich or Alfa Aesar, vacuum-distilled, and degassed by the freeze-pump-thaw method prior to use. ^{1}H NMR and ^{13}C NMR were collected on Agilent DDR2 500 MHz NMR spectrometers equipped with 7600AS 96-sample autosamplers. Electrospray mass spectra (ESI-MS) were obtained on Waters Xevo G2-XS QTof Quadruple UPLC/MS/MS at Michigan State University Mass Spectrometry and Metabolomics Core. CHN elemental analyses were obtained on a Perkin-Elmer 2400 Series II CHNS/O Analyzer through the analytical facilities at Chemistry of Michigan State University.

4.3.1 Synthetic Procedures of Substituted Tetrahydroxy-Ligands.

2,3,5,6-Tetrahydroxybenzene (THB).[23,24] DHBQ (2.0 g, 14.3 mmol) and 37% (w/v) HCl (50 mL) were mixed together and stirred for 10 min. After addition of Sn metal (4.0 g, 33.7 mmol), the reaction was refluxed under N_2 until the solution turned colorless. The hot solution was filtered under N_2 and cooled to RT, resulting in white microcrystalline. The product was washed with cooled degassed H_2O under N_2, and dried under vacuum overnight. The product is air-sensitive, and needs to be stored under inert-gas environment. Yield: 1.03 g (51%). ^{1}H NMR (CD_3CN, 500 MHz) δ (ppm): 6.04 (s, 4 H, OH), 6.35 (s, 2 H, ArH). ^{13}C NMR (CD_3CN, 500 MHz) δ (ppm): 105.08, 138.58.

Tetrahydroxy-1,4-dichlorobenzene (H_4CA).[24] The synthetic procedure was similar to that of THB. Instead, H_2CA (2.0 g, 9.6 mmol), 37% (w/v) HCl (50 mL), and Sn (4.0 g, 34 mmol) were used for the reaction. Yield: 0.8 g (40%). HRMS [ESI-TOF, *m/z* (rel. int.)]: $[M-H]^-$ Calcd for $[C_6O_4H_3Cl_2]^-$, 208.9408; Found, 208.9406.

Tetrahydroxy-1,4-dibromobenzene (H_4BA).[25-27] H_2BA (1.04 g, 3.5 mmol) was dissolved in degassed EtOAc under N_2. 0.5 M aq. $Na_2S_2O_4$ solution (25 mL) was added dropwise into the solution above while stirring. The reaction was allowed to react overnight. The work-up procedure was performed in N_2-inflated glove bag due to the sensitivity of the fully reduced product. The product was extracted with EtOAc (3 x 30 mL), washed by 1 M HCl (2 x 30 mL), H_2O (2 x 20 mL), and dried over Na_2SO_4. Beige product was obtained after the solvent was completely evaporated under vacuum. Yield: 0.85 g (82%). HRMS [ESI-TOF, *m/z* (rel. int.)]: $[M-H]^-$ Calcd for $[C_6O_4H_3Br_2]^-$, 298.8378; Found, 298.8354.

Tetrahydroxy-1,4-difluorobenzene (H_4FA). The synthetic procedure is similar to that of H_4BA. 0.5 M aq. $Na_2S_2O_4$ solution (20 mL) was added dropwise to a solution of H_2FA (0.36

g, 2.0 mmol) in EtOAc (20 mL). Yield: 0.28 g (78%). HRMS [ESI-TOF, *m/z* (rel. int.)]: $[M-H]^-$ Calcd for $[C_6O_4H_3F_2]^-$, 176.9999; Found, 177.0058.

Tetrahydroxy-1,4-diiodobenzene (H_4IA). The synthetic procedure is similar to that of H_4BA. Due to the light sensitivity of iodo compounds, this reaction needs to be carried out in the dark. An aq. solution of $Na_2S_2O_4$ (0.12 g, 1.2 mmol) in H_2O (5 mL) was added dropwise to a solution of H_2IA (0.12 g, 0.3 mmol) in EtOAc (5 mL). Light yellow/brown oil was obtained; however, the product is unstable even under inert gas environment. It has to be freshly prepared prior use, and the next reaction with H_4IA as starting material needs to be carried out immediately after due to its instability. Yield: 0.11 g (92%). HRMS [ESI-TOF, *m/z* (rel. int.)]: $[M-H]^-$ Calcd for $[C_6O_4H_3I_2]^-$, 392.8121; Found, 392.8141.

4.3.2 Synthetic Procedures of Gallium(III) Dimeric Complexes

Ga(tren)$(NO_3)_3$.[23] A solution of $Ga(NO_3)_3$ (0.76 g, 3.0 mmol) in EtOH (10 mL) was added dropwise into a stirring solution of tren (0.52 mL, 3.3 mmol) in 5 mL of EtOH under N_2. White precipitates formed upon addition. The solids were filtered, washed by EtOH (3 x 10 mL), and Et_2O (1 x 10 mL). The product is extremely hygroscopic, and needs to be stored under inert-gas environment. Yield: 1.0 g (85%).

(20) [Ga_2(tren)$_2$(DHBQ^{cat,cat})]$(BPh_4)_2$. THB (0.042 g, 0.2 mmol) was deprotonated by Et_3N (0.11 mL, 0.8 mmol) in 5 mL of MeOH. After 5 min, the deprotonated THB solution was added dropwise into a solution of Ga(tren)$(NO_3)_3$ (0.16 g, 0.4 mmol) in MeOH (40 mL) resulting in a cloudy yellow mixture. The mixture was filtered through a pad of Celite. A solution of $NaBPh_4$ (0.34 g, 1.0 mmol) in MeOH (40 mL) was layered carefully on top of the filtrate, and allowed to stand overnight without being disturbed. Yellow crystals, suitable for x-ray

diffraction, were obtained, if the solution was allowed to stand for over one week without disturbance. Yield: 0.2 g (83%). HRMS [ESI-TOF, *m/z* (rel. int.)]: $[M]^{2+}$ Calcd for $[Ga_2C_{18}H_{38}O_4N_8]^{2+}$, 282.0760; Found, 282.0767. $[M]^{3+}$ Calcd for $[Ga_2C_{18}H_{38}O_4N_8]^{3+}$, 190.0507; Found, 190.0516. $[Ga(tren)(C_6H_2O_4)]^+$ Calcd for $[GaC_{12}H_{20}O_4N_4]^+$, 353.0740; Found, 353.0744.

(25) $[Ga_2(tren)_2(DHBQ^{sq,cat})](BPh_4)_2(BF_4)$. Under N_2, a solution of $(FeCp^*_2)(BF_4)$ (g, mmol) in MeCN (10 mL) was added dropwise into a stirring solution of $[Ga_2(tren)_2(DHBQ^{cat,cat})](BPh_4)_2$ (0.20 g, 0.166 mmol) in MeCN (10 mL). The solution was stirred for 6 h, which turned yellow-green. After filtration, the solvent volume of the filtrate was reduced under vacuum to 10 mL. 30 mL of DCM was added, and the mixture was filtered to eliminate excess $[FeCp^*_2](BF_4)$ salt. The filtrate was reduced in volume under vacuum again to 10 mL, and 30 mL of Et_2O was added to yield yellow brown solids. The product was filtered, washed by DCM (3 x 10 mL), and Et_2O (3 x 10 mL). Yield: 0.1 g (47%). HRMS [ESI-TOF, *m/z* (rel. int.)]: $[M]^{3+}$ Calcd for $[Ga_2C_{18}H_{38}O_4N_8]^{3+}$, 190.0507; Found, 190.0510. $[Ga(tren)(C_6H_2O_4)]^+$ Calcd for $[GaC_{12}H_{20}O_4N_4]^+$, 353.0740; Found, 353.0736.

(21) $[Ga_2(tren)_2(CA^{cat,cat})](BPh_4)_2$.[24] The synthesis of this compound is similar to that of $[Ga_2(tren)_2(DHBQ^{cat,cat})](BPh_4)_2$. H_4CA (0.042 g, 0.2 mmol) was deprotonated by Et_3N (0.11 mL, 0.8 mmol) in 3 mL of MeOH. A solution of $Ga(tren)(NO_3)_3$ (0.162 g, 0.4 mmol) in MeOH (80 mL) was added into the reaction mixture. Crystals suitable for x-ray diffraction were obtained by carefully layering a solution of $NaBPh_4$ (0.34 g, 1.0 mmol) in MeOH (10 mL). Yield: 0.19 g (75%). HRMS [ESI-TOF, *m/z* (rel. int.)]: $[M]^{2+}$ Calcd for $[Ga_2C_{18}H_{36}O_4N_8Cl_2]^{2+}$, 319.0367; Found, 319.0361. $[Ga(tren)(C_6H_2O_4)]^+$ Calcd for $[GaC_{12}H_{18}O_4N_4Cl_2]^+$, 442.9943; Found, 442.9969.

(26) [$Ga_2(tren)_2(CA^{sq,cat})](BPh_4)_2(BF_4)$.[24] The synthesis of this compound is similar to that of $[Ga_2(tren)_2(DHBQ^{cat,cat})](BPh_4)_2$. A solution of $[FeCp^*_2](BF_4)$ in MeCN (20 mL) was added dropwise to $[Ga_2(tren)_2(CA^{cat,cat})](BPh_4)_2(BF_4)$ (0.16 g, 0.12 mmol) in 25 mL of MeCN while stirring. After 30 min, the solution was filtered. Et_2O (100 mL) was added to the filtrate, and yellow precipitates were formed. The product was filtered and washed by Et_2O (3 x 20 mL). Yield: 0.11 g (66%). HRMS [ESI-TOF, *m/z* (rel. int.)]: $[M]^{3+}$ Calcd for $[Ga_2C_{16}H_{38}O_4N_8Cl_2]^{3+}$, 212.6902; Found, 212.6905. $[Ga(tren)(C_6H_2O_4)]^+$ Calcd for $[GaC_{12}H_{18}O_4N_4Cl_2]^+$, 442.9943; Found, 442.9966.

(22) [$Ga_2(tren)_2(FA^{cat,cat})](BPh_4)_2$. The synthesis of this compound is similar to that of $[Ga_2(tren)_2(DHBQ^{cat,cat})](BPh_4)_2$. H_4FA (0.018 g, 0.1 mmol) was deprotonated by Et_3N (0.13 mL, 0.8 mmol) in 3 mL of MeOH. A solution of $Ga(tren)(NO_3)_3$ (0.081 g, 0.2 mmol) in MeOH (60 mL) was added into the reaction mixture. Crystals suitable for x-ray diffraction were obtained by carefully layering a solution of $NaBPh_4$ (0.34 g, 1.0 mmol) in MeOH (20 mL). Yield: 0.88 g (71%). HRMS [ESI-TOF, *m/z* (rel. int.)]: $[M]^{2+}$ Calcd for $[Ga_2C_{18}H_{36}O_4N_8F_2]^{2+}$, 303.0666; Found, 303.0664. $[Ga(tren)(C_6F_2O_4)]^+$ Calcd for $[Ga_2C_{12}H_{18}O_4N_4F_2]^+$, 389.0552; Found, 389.0537.

(27) [$Ga_2(tren)_2(FA^{sq,cat})](BPh_4)_2(BF_4)$. The synthesis of this compound is similar to that of $[Ga_2(tren)_2(DHBQ^{cat,cat})](BPh_4)_2$. Instead, $[FeCp^*_2](BF_4)$ (0.08 g, 0.19 mmol) was used to react with $[Ga_2(tren)_2(FA^{cat,cat})](BPh_4)_2$ (0.15 g, 0.12 mmol), and the reaction mixture was stirred for 2 h. Yield: 0.085 g (53%). [ESI-TOF, *m/z* (rel. int.)]: $[M]^{3+}$ Calcd for $[Ga_2C_{16}H_{38}O_4N_8F_2]^{3+}$, 202.0444; Found, 202.0448. $[Ga(tren)(C_6F_2O_4)]^+$ Calcd for $[Ga_2C_{12}H_{18}O_4N_4F_2]^+$, 389.0552; Found, 389.0538.

(23) $[Ga_2(tren)_2(BA^{cat,cat})](BPh_4)_2$. The synthesis of this compound is similar to that of $[Ga_2(tren)_2(DHBQ^{cat,cat})](BPh_4)_2$. H_4BA (0.85 g, 2.8 mmol) was deprotonated by Et_3N (1.6 mL, 11.5 mmol) in 10 mL of MeOH. A solution of $Ga(tren)(NO_3)_3$ (2.24 g, 5.6 mmol) in MeOH (60 mL) was added into the reaction mixture. Crystals suitable for x-ray diffraction were obtained by carefully layering a solution of $NaBPh_4$ in MeOH. Yield:2.0 g (54%). HRMS [ESI-TOF, *m/z* (rel. int.)]: $[M]^{2+}$ Calcd for $[Ga_2C_{18}H_{36}O_4N_8Br_2]^{2+}$, 363.9854; Found, 363.9865. $[M]^{3+}$ Calcd for $[Ga_2C_{18}H_{36}O_4N_8Br_2]^{3+}$, 242.6570; Found, 242.6592. $[Ga(tren)(C_6Br_2O_4)]^+$ Calcd for $[Cr_2C_{18}H_{18}O_4N_4]^+$, 510.8934; Found, 510.8938.

(28) $[Ga_2(tren)_2(BA^{sq,cat})](BPh_4)_2(BF_4)$. The synthesis of this compound is similar to that of $[Ga_2(tren)_2(DHBQ^{cat,cat})](BPh_4)_2$. Instead, $[FeCp^*_2](BF_4)$ (0.14 g, 0.34 mmol) was used to react with $[Ga_2(tren)_2(BA^{cat,cat})](BPh_4)_2$ (0.23 g, 0.17 mmol). Yield: 0.138 g (57%). [ESI-TOF, *m/z* (rel. int.)]: $[M]^{3+}$ Calcd for $[Ga_2C_{16}H_{38}O_4N_8Br_2]^{3+}$, 242.6570; Found, 242.6578. $[Ga(tren)(C_6Br_2O_4)]^+$ Calcd for $[Cr_2C_{18}H_{18}O_4N_4]^+$, 510.8934; Found, 510.8962.

(24) $[Ga_2(tren)_2(IA^{cat,cat})](BPh_4)_2$. The synthesis of this compound is similar to that of $[Ga_2(tren)_2(DHBQ^{cat,cat})](BPh_4)_2$, except that H_4IA has to be prepared freshly due to its instability. H_4IA (0.11 g, 0.28 mmol) was deprotonated by Et_3N (0.16 mL, 1.1 mmol) in 6 mL of MeOH. A solution of $Ga(tren)(NO_3)_3$ (0.227 g, 0.56 mmol) in MeOH (60 mL) was added into the reaction mixture. The product is stable under inert-gas environment after H_4IA bind to Ga^{3+}. Light yellow crystals suitable for x-ray diffraction were obtained by carefully layering a solution of $NaBPh_4$ in MeOH. The product slowly degrades even being stored under inert atmosphere, color change to brown indicates the decomposition. No $[M]^{2+}$ species was observed in HRMS. Yield: 0.12 g (60%). HRMS [ESI-TOF, *m/z* (rel. int.)]: $[M]^{3+}$ Calcd for $[Ga_2C_{18}H_{34}O_4N_8I_2]^{3+}$,

273.9818; Found, 273.9857. $[Ga(tren)(C_6I_2O_4)]^+$ Calcd for $[Cr_2C_{18}H_{18}O_4N_4]^+$, 604.8673; Found, 604.8649.

(29) $[Ga_2(tren)_2(IA^{sq,cat})](BPh_4)_2(BF_4)$. The synthesis of this compound is similar to that of $[Ga_2(tren)_2(DHBQ^{cat,cat})](BPh_4)_2$. Instead, $[FeCp^*_2](BF_4)$ (0.04 g, 0.11 mmol) was used to react with $[Ga_2(tren)_2(IA^{cat,cat})](BPh_4)_2$ (0.08 g, 0.055 mmol). Yield: 0.036 g (42%). [ESI-TOF, *m/z* (rel. int.)]: $[M]^{3+}$ Calcd for $[Ga_2C_{18}H_{34}O_4N_8I_2]^{3+}$, 273.9818; Found, 273.9857. $[Ga(tren)(C_6I_2O_4)]^+$ Calcd for $[Cr_2C_{18}H_{18}O_4N_4]^+$, 604.8673; Found, 604.8649.

$[Ga_2(tren)_2(PhA^{cat,cat})](BPh_4)_2$. The synthesis of this compound is similar to that of $[Ga_2(tren)_2(DHBQ^{cat,cat})](BPh_4)_2$. H_4PhA (0.03 g, 0.1 mmol) was deprotonated by Et_3N (0.06 mL, 0.4 mmol) in 3 mL of MeOH. A solution of $Ga(tren)(NO_3)_3$ (0.08 g, 0.2 mmol) in MeOH (50 mL) was added into the reaction mixture. Pink product was obtained; however, no $[M]^{2+}$ was observed from ESI+ spectrum. Several attempts of recrystallization for x-ray diffraction were unsuccessful. HRMS [ESI-TOF, *m/z* (rel. int.)]: $[M]^{3+}$ Calcd for $[Ga_2C_{30}H_{46}O_4N_8]^{3+}$, 240.7383; Found, 240.7348. $[Ga(tren)(C_{18}H_{10}O_4)]^+$ Calcd for $[GaC_{24}H_{28}O_4N_4]^+$, 505.1366; Found, 505.1329.

4.3.3 Physical Measurements

X-Ray Single-Crystal Structure Determinations. Single-crystal structure measurement for all Cr (III) dimeric complexes was acquired at the center for crystallographic research of Michigan State University. The crystals were mounted on nylon loops using small amount of paratone oil. X-ray diffraction data were collected at 173 K on Bruker SMART APEX II CCDs (charge coupled device) either with molybdenum radiation using a 3-axis goniometer with Oxford 600 low-temperature device or with copper radiation using a 3-axis goniometer APEX II

diffraction system with Oxford Cyrosystream 700 low-temperature device. Each system is equipped with a camera for viewing the crystals and a Pentium PC to control the diffractometer. The total number of runs and images was based on results from the program **COSMO**,[27] of which redundancy was expected to be 4.0 and completeness of 100% out to 0.83 Å for the Mo Kα radiation diffractometer or 0.81 Å for the Cu Kα radiation diffractometer. Cell parameters were retrieved and refined using the **SAINT** software.[28] Scaling and absorption corrections were applied by the **SAINT**[29] for Lorentz and polarization factors. A multi-scan absorption correction was performed by **SADABS**-2014/5.[30] The structures were solved by intrinsic phasing using **ShelXT**[31] structure solution program. The structures were refined by least squares using **XL**-2014/6[31] with **Olex2**[32] incorporated. All non-hydrogen atoms were refined anisotropically. The positions of hydrogen atom were calculated geometrically and refined using the riding model, except for the hydrogen atoms on the non-carbon atoms, which was found by difference Fourier methods and refined isotropically.

Table 4.1. Crystallographic data for Complex **20**, **21**, **23**, and **24**.

	20	**21**	**23**	**24**
Empirical Formula	$C_{68}H_{86}B_2Ga_2N_8O_6$	$C_{47}H_{67}BGa_2F_2N_9O_9$	$C_{68}H_{84}B_2Ga_2Br_2N_8O_6$	$C_{68}H_{84}B_2Ga_2I_2N_8O_6$
Formula Weight (g/mol)	1272.51	1090.35	1430.31	1524.29
Temperature (K)	173(2)	173(2)	173(2)	173(2)
Crystal System	Monoclinic	monoclinic	Monoclinic	monoclinic
Space Group	$P2_1/c$	$P2_1/n$	$P2_1/n$	$P2_1/n$
a (Å)	9.5971(6)	9.34520(10)	13.5579(2)	13.4607(8)
b (Å)	14.9395(10)	17.4847(2)	9.72430(10)	9.8773(6)
c (Å)	22.1237(14)	30.8815(3)	25.0744(4)	25.1172(15)
β (˚)	97.9990(10)	93.8800(10)	96.4290(10)	96.6560(10)
Volume (Å^3)	3141.1(3)	5034.41(9)	3285.05(8)	3317.0(3)
Z	2	4	2	2
D_{calc} (g/cm^3)	1.345	1.439	1.446	1.526
Radiation	MoKσ	CuKσ	CuKσ	MoKσ
Goodness of Fit (F^2)	1.048	1.015	1.052	1.052
R_1 ($I \geq 2\sigma(I)$)[a]	0.0462	0.0465	0.0420	0.0573
wR_2 ($I \geq 2\sigma(I)$)[b]	0.1070	0.1124	0.1244	0.1728

[a] $R_1 = \sum \frac{||F_o| - |F_c||}{\sum |F_o|}$. [b] $wR_2 = [\sum w(F_o^2 - F_c^2)^2 / \sum w(F_o^2)^2]^{1/2}$, $w = 1/[\alpha^2(F_o^2) + (aP)^2 + bP]$, where $P = [F_o^2 + F_c^2]/3$.

4.4 SQUID Variable-Temperature Magnetic Susceptibility Measurement on $[Ga_2(tren)_2(L^{sq,cat})]^{3+}$

General. Magnetic susceptibility measurement was collected using a Quantum Desgien MPMS® 3 SQUID magnetometer Cryogen Free with EverCool® He gas regulator interfaced to a Dell PC. Data were collected in an applied field of 1 T. Temperature was ramped up with small temperature increments to ensure the samples were thermally equilibrated. Data were corrected for diamagnetism of the sample using Pascals' constants,[34] and the measured susceptibility of the sample holder, including a plastic straw and a plastic sealed bag. and were reported as effective magnetic moment (μ_{eff}). Paramagnetic impurity (5 mol % of an S = ½ compound) and temperature-independent paramagnetism (200 x 10^{-6} cgsu for each Ga (III) center) were included in fitting. Sample preparation has been discussed in Chapter 3.

4.5 Results and Discussion

4.5.1 Synthesis and Characterization

Gallium (III) ion was incorporated in our binuclear motif as a reference to chromium (III) dimeric system because of its spectroscopically silent and diamagnetic d^{10} electronic configuration and its nearly identical charge-to-radius ratio to that of Cr (III). Complex **22** and **27** were previously prepared and reported by Dr. Dong Guo,[24] a former group member in the McCusker group.

Synthesis of Ga (III) analogues starts with $Ga(tren)(NO_3)_3$, and H_4L. $Ga(tren)(NO_3)_3$ is extremely hygroscopic, and H_4L is air-sensitive, so all synthetic procedures were performed under inert atmosphere. Then, $[Ga_2(tren)_2(L^{cat,cat})]^{2+}$ was oxidized with $[FeCp^*_2](BF_4)$ to result in $[Ga_2(tren)_2(L^{sq,cat})]^{3+}$, where $[FeCp^*_2](BF_4)$ was prepared following a literature method,[25] and detailed procedure was reported in Chapter 3.

THB and H_4CA were synthesized according to a procedure modified from literature methods[23-24] with Sn and 37% HCl under reflux. However, this condition is too harsh for the other halogenated tetrahydroxyanilate, and no desired product was detected for H_4BA when following this reaction condition. The hypothesis of why this reaction condition has failed for reducing H_2BA to H_4BA is that bromine is a much better leaving group than H and Cl. Under reflux with such an acidic condition, C-Br bond may break resulting from the decomposition of H_2BA before the reduction. Therefore, a much milder condition was employed,[26,27] where H_2BA reacted with a reductant, $Na_2S_2O_4$, at room temperature. Since $Na_2S_2O_4$ is insoluble in most of the common organic solvent, this reaction cannot be conducted inside an air-free and water-free drybox, where most of the air-sensitive reactions in this project were performed in. The reaction was conducted with Schlenk line technique. Due to the extreme air-sensitivity of the product, reaction workup has to be done under an inert atmosphere, so it was performed in a N_2-filled glovebag. The colors of these halogenated-anilates are very vibrant (e.g. H_2CA is orange), and the solution changed to white upon reduction, which were observed for most of these compounds. After the formation of the reduced H_4L, it was dried under vacuum and pumped into a drybox to react with Ga(III) source.

Most of these H_4L compounds can be stored under N_2 without decomposition, but H_4IA. Upon reduction, the H_4IA product was yellow beige color, and $[H_3IA]^-$ was detected by ESI-mass spectrometry. Color change was observed over a one-hour period even under N_2. Eventually, the product turned completely dark purple brown, and no product was detected with ESI-. Thus, H_4IA is suspected to be extremely sensitive, and iodine is too nucleophilic to result in a very weak C-I bond. The dark purple brown color is suspected to be I_2, which is coincide with its purple color in solid state. Therefore, H_4IA has to be freshly prepared each time before

the reaction of $[Ga_2(tren)_2(IA^{cat,cat})]^{2+}$. After binding to Ga (III), the compound can be stored stably under N_2 for c.a. one month, then it slowly decomposes over time even under inert atmosphere. The color of Complex **24** is yellow beige, and its color change to brown indicate the degradation of the product.

The synthesis of tetrahydroxy-1,4-diphenylbenzene (H_4PhA) was attempted with 0.5 M aq. $Na_2S_2O_4$ solution (5 mL) added dropwise in EtOAc (15 mL). However, ESI- spectra indicate that only the starting material, H_2PhA, was observed after the reaction. It is unknown whether the negative charge species was re-oxidized under high voltage inside the Taylor cone in the ESI mass spectrometer or simply no reduction happens. DFT calculations results obtained on a series of phenyl-substituted pyridine previously in our group[45] indicates that no intraligand electron delocalization at θ=90˚ due to the orthogonality of the phenyl and pyridyl π systems, whereas these systems are stabilized by electron delocalization at θ=0˚. Therefore, it requires significant driving force in order to achieve a coplanar delocalized structure.[46] The reaction of H_4PhA is a two-electron reduction involving (1) a reduction to a coplanar delocalized form (Fig. 4.2 form (2) and (3)), (2) a further reduction to a twist angle fully reduced form (Fig. 4.2 form(4), (5) and (6)). This means the reduction will first need to overcome a huge thermodynamic energy barrier, and this reaction is possibly too thermodynamically unfavorable to happen.

Ga(III) coordination reaction was then proceeded in the presence of $Na_2S_2O_4$. Nude pink product was collected after the reaction, and ESI+ spectra were collected for the characterization of this product. $[Ga(tren)(PhA^{q,cat})]^+$ and $[Ga_2(tren)_2(PhA^{sq,cat})]^{3+}$ were detected with matching isotope patterns. However, no $[Ga_2(tren)_2(PhA^{cat,cat})]^{2+}$ species was observed. It is hard to conclude whether all $[M]^{2+}$ species was oxidized to $[M]^{3+}$ inside the mass spectrometer, or $[M]^{2+}$ product was never formed during the reaction. We incline to propose the former hypothesis,

because there will not be $[M]^{3+}$ without the initial formation of $[M]^{2+}$. However, it is still too early to conclude anything until more experimental evidence are presented. Discussion will be continued in Chapter 5 along with the electrochemical data.

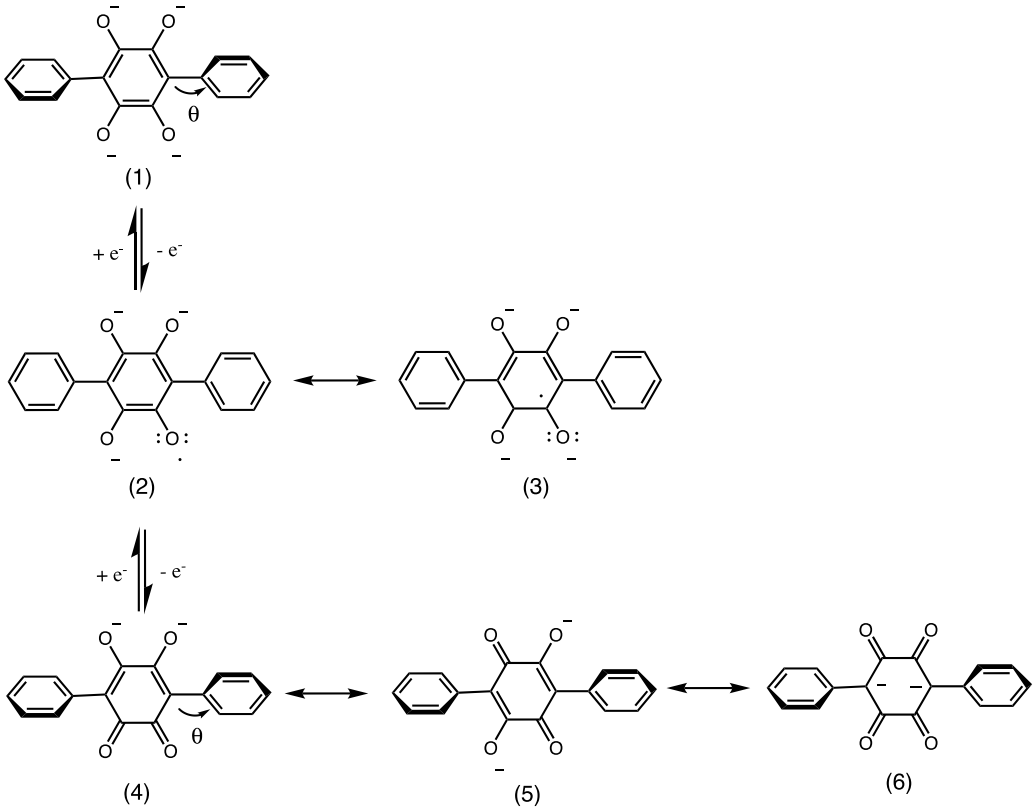

Figure. 4.2. 3,6-diphenyl-tetraoxoanilate undergoing one-electron redox reactions.

The synthesis of $[Ga_2(tren)_2(Me\text{-}AnT^{cat,cat})]^{2+}$ was attempted many times in the past. Even though NO_3^- has very low coordination ability,[35] it may not be the best leaving group. The reaction has been conducted with $Ga(tren)I_3$. They have all failed without the observation of the product with various characterization techniques, including ESI mass spectrometry and NMR spectra. One problem is the solubility of the starting materials. Both $H_4(Me\text{-}AnT)$ and $Ga(tren)(NO_3)_2$ was insoluble in MeOH. For the reaction of $[Cr_2(tren)_2(Me\text{-}AnT^{cat,cat})]^{2+}$, $[Cr(tren)Cl](Cl)_2$ is soluble in MeOH/H_2O mixed solvent system even though the other one is not. As the reaction proceeds, the equilibrium is shifted to the product side as more product

formed. In addition, heat can be applied to increase the solubility of all starting materials. The next modification of the reaction is to apply heat, and monitor the reaction with ESI for product formation. Another option is to change the solvent system to make the starting materials more soluble. The biggest concern is that the formation of $[Cr_2(tren)_2(Me\text{-}AnT^{cat,cat})]^{2+}$ is unfavorable, since Ga (III) is a much weaker Lewis acid compared with Cr (III), and H_2Me-AnT is a weak Lewis base due to its highly conjugated structure. If this is the main reason why the synthesis of this complex is challenging, it will not be stable even if it can form after all attempts eventually.

4.5.2 Single Crystal X-Ray Structures

X-ray diffraction quality crystal structures were collected for Complex **20**, **21**, **23** and **24**. The crystal structure of Complex **22** has been reported by Dr. Guo in our group.[24] The crystals of H, F, Br, and I were grown via metathesis by carefully layering $NaBPh_4$ MeOH solution on top of its product MeOH solution in a N_2-filled drybox. The crystals were grown in dark after 2 weeks. The challenging parts of growing crystals are similar as those for $[Cr_2(tren)_2(L^{cat,cat})](BPh_4)_2$, i.e. concentration of mother solution and air-sensitivity. The benefit of incorporating Ga(III) in complexes for x-ray structure determination is that Ga(III) has high diffraction rate. However, some crystals were not packed as large to diffract well even under Cu Kσ radiation when following our conventional approach. In order to grow larger crystals for $[Ga_2(tren)_2(FA^{cat,cat})]^{2+}$, a few drops of benzene were added into the MeOH mother solution before layering $NaBPh_4$ MeOH solution. The addition of benzene was thought to facilitate the packing of crystals in the lattice by π-stacking.

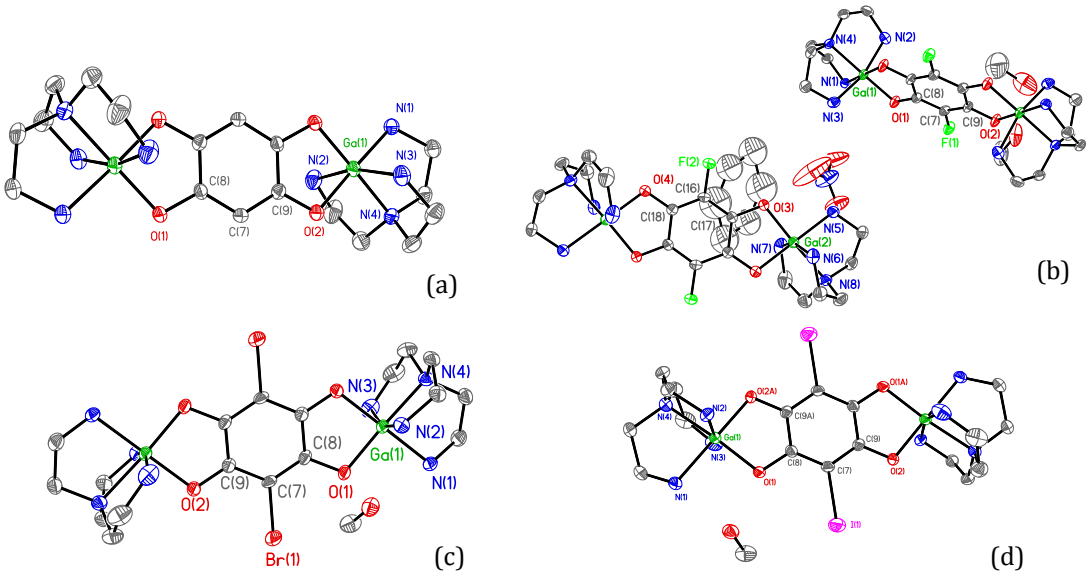

Figure 4.3. ORTEP drawing of Complex **20** (a), **21** (b), **23** (c), and **24** (d) obtain from single crystal x-ray structure determination. Atoms are represented as 50% probability thermal ellipsoids. Hydrogen atoms are omitted for clarity.

Complex **20**, **23**, and **24** contained two MeOH solvent molecules in their crystal lattice. The crystal of $[Ga_2(tren)_2(FA^{cat,cat})]^{2+}$ is a mixed counteranionic salt with BPh_4^- and NO_3^-. The lattice was confined with two MeOH solvent molecules and one disordered benzene. Benzene was added to facilitate the packing of a bigger crystal. More efforts were made to grow purely BPh_4^- salt, but those attempts were unsuccessful. When increasing the equivalent of $NaBPh_4$ for metathesis, the product crashed out from the solution too quickly resulting in small crystals. Modulation of solution concentration was attempted, but the optimized concentration has not been configurated thus far. Since BPh_4^- and NO_3^- are both considered very weakly coordinating counteranions for different reason, they are unlikely to alter the overall structure of this compound. We believe that its bond lengths and bond angles will still be comparable with other Ga (III) complexes with BPh_4^- as their only counteranion. BPh_4^- has low coordinating ability because of the bulky structure and increased charge delocalization, and the low coordinating

ability of NO_3^- is caused by its high electronegative external atoms.[35] Thus, the structure of mixed counteranionic complex F is reported and compared here.

Table 4.2. Selected Bond Length (Å) and Angle (˚) for Complex **20**, **21**, **23**, and **24**.

	20 (H)	**21 (F)**	**23 (Br)**	**24 (I)**
	Bond Length (Å)			
Ga(1) – O(1)	1.9185(17)	1.9120(19)	1.928(2)	1.928(3)
Ga(1) – O(2)	1.9131(17)	1.986(2)	1.921(2)	1.920(3)
Ga(1) – N(1)	2.082(2)	2.072(2)	2.070(3)	2.065(4)
Ga(1) – N(2)	2.152(2)	2.095(3)	2.086(3)	2.083(4)
Ga(1) – N(3)	2.096(2)	2.076(3)	2.182(3)	2.190(4)
Ga(1) – N(4)	2.083(2)	2.102(2)	2.097(2)	2.099(4)
O(1) – C(8)	1.387(3)	1.362(4)	1.370(4)	1.366(5)
O(2) – C(9)	1.356(3)	1.361(3)	1.342(3)	1.343(5)
C(7) – C(8)	1.387(3)	1.386(4)	1.382(4)	1.390(6)
C(8) – C(9)	1.400(3)	1.407(5)	1.407(4)	1.409(6)
C(7) – C(9)	1.386(3)	1.377(4)	1.397(4)	1.398(6)
Ga ··· Ga[a]	7.551	7.643	7.595	7.594
	Bond Angles (˚)			
O(1) – Ga(1) – N(1)	94.69(7)	92.41(9)	91.38(9)	93.38(15)
O(1) – Ga(1) – N(2)	93.23(8)	96.00(10)	101.71(10)	101.87(15)
O(1) – Ga(1) – N(3)	100.95(8)	99.66(10)	94.76(11)	94.64(17)
O(1) – Ga(1) – N(4)	175.70(8)	176.13(9)	173.27(10)	175.53(15)
O(2) – Ga(1) – O(1)	88.48(7)	86.96(8)	88.18(9)	88.13(14)
O(2) – Ga(1) – N(1)	175.68(8)	178.91(10)	177.30(10)	177.05(17)
O(2) – Ga(1) – N(2)	86.40(9)	88.33(10)	87.41(10)	87.87(16)
O(2) – Ga(1) – N(3)	87.81(8)	88.21(10)	86.18(11)	91.63(17)
O(2) – Ga(1) – N(4)	92.69(7)	96.10(9)	95.93(10)	94.78(15)
N(1) – Ga(1) – N(2)	90.48(9)	90.85(10)	95.29(11)	94.90(17)
N(1) – Ga(1) – N(3)	94.45(9)	92.78(10)	91.20(11)	91.63(17)
N(1) – Ga(1) – N(4)	83.94(8)	84.49(10)	84.26(10)	84.53(16)
N(2) – Ga(1) – N(3)	165.53(9)	163.75(10)	162.12(11)	161.96(17)
N(2) – Ga(1) – N(4)	82.72(9)	81.76(10)	83.84(10)	84.03(15)
N(3) – Ga(1) – N(4)	83.23(9)	82.83(10)	80.25(11)	79.86(17)

[a]Nonbonding metal-to-metal distance.

The halogenated Ga (III) complexes are isostructural in monoclinic space group *P2₁/n* (a more orthogonal cell), and crystallographic details are shown in Table 4.1. with selected bond lengths and angle given in Table 4.2. $[Ga_2(tren)_2(DHBQ^{cat,cat})](BPh_4)_2$ (**20**) and $[Cr_2(tren)_2(DHBQ^{cat,cat})](BPh_4)_2$ (**1**) are isostructural in monoclinic space group *P2₁/c*, a more oblique cell compared with *P2₁/n*. These complexes are all structurally similar with centrosymmetric monoclinic space groups, and complexes **20**, **21**, **22**,[1] **23**, and **24** are situated on

inversion centers making only half of a dimer unique in a cell. The ORTEP drawings of the cations are shown in Figure 4.3.

The gallium center is also coordinated tripodally with four aliphatic nitrogens from the tren capping ligand and two oxygens to form a distorted octahedral environment. The bite angles around the chromium coordination site for a given complex are c.a. 90˚, 100˚ and 180˚, which are larger than those observed in the Cr (III) analogues reported in Chapter 3. The Ga-N bond lengths are ranging from 2.087 to 2.101 Å, which are slightly longer than those collected for the Cr (III) analogues. The Ga-O bond distances are nearly identical (Table 4.2), except for the Cl derivative; for example, the bond distances are 1.913 Å and 1.919 Å respectively in complex H, and 1.944 and 1.918 Å in the Cl analogue. These bond distances are much shorted than those seen in $[Ga(Cat)_3]^{3-}$, 1.983 Å.[32] No discrepancy in Ga-O bond distances were observed except in $[Ga_2(tren)_2(CA^{cat,cat})](BPh_4)_2$. This is not consistent with those observed in the Cr (III) dimers.

The C-C bond length within the ring can indicate the oxidation state of the quinoidal ligand.[31-33] In fully reduced catecholate ligand, the difference of C-C bond distances is statistically negligible indicating the aromatic nature of the ligand: $[Ga(Cat)_3]^{3-}$ shows C-C bond lengths of 1.366, 1.382, 1.391, 1.397, 1.398, and 1.411 Å.[37] The ring shows alternating single and double C-C bond feature in semiquinone, because the electrons are more localized in the C=C bond. This generally exhibit on the short and long C-C bond lengths seen in x-ray crystal structure: the C-C bonds are 1.494, 1.430, 1.327, 1.437, 1.355, and 1.402 Å in $[Ga(3,6\text{-}DTBSQ)_3]$.[40] The C-C bond lengths within the bridging ring show a various range (Table 4.2.): 1.382 – 1.400 Å in complex H; 1.382 – 1.414 Å in complex F; 1.393 – 1.401 Å in Complex **22**[1]; 1.382 – 1.407 Å in Complex **23**; 1.390 – 1.409 Å in Complex **24**. More physical evidence and characterization are needed to interpret the bond information, and will be further discussed in Chapter 5.

The C-O bonds in quinoidal ligands can also provide information about the oxidation state of the ligands. [36-38] The C-O bond lengths are close in values in semiquinoidal complexes, e.g. 1.271 Å and 1.262 Å in [Ga(3,6-DTBSQ)$_3$].[37] The C-O bond distances exhibit similar difference in catecholate complexes compared with the semiquinoidal analogue, e.g. 1.337 and 1.351 Å in [Ga(Cat)$_3$]$^{3-}$.[30] However, C-O bond distances cannot be a valid indication for the oxidation state in these gallium complexes reported here, since their differences are not negligible (Table 4.1 and 4.2). Even though the C-O bond lengths are not identical, they are all much longer than the reported C-O bond length in chromium-semiquinoidal complexes.[38]

The information obtained from the crystal structure determination of these gallium systems are preliminary. There are not enough similar structures reported in literature for a fair comparison, although the ones cited here are Ga(L)$_3$ complexes instead of Ga(tren)(L). The development of [Ga(tren)(3,6-DTBCat)]$^+$ and [Ga(tren)(3,6-DTBSQ)]$^{2+}$ can be useful and informative to better understand how C-C and C-O bond distances manifest on the oxidation states on both chromium and gallium complexes, since our group already develop a mechanism for the synthesis and recrystallization of their chromium analogues. It will still be highly desirable to structurally compare [Ga$_2$(tren)$_2$(L^{cat,cat})]$^{2+}$ and [Ga$_2$(tren)$_2$(L^{sq,cat})]$^{3+}$ so that more evidence of how the oxidation state impact the various bond distance can be discussed. The similar challenge is faced for the recrystallization of x-ray quality crystal for [Cr$_2$(tren)$_2$(L^{sq,cat})]$^{3+}$, and they have thus far been unsuccessful.

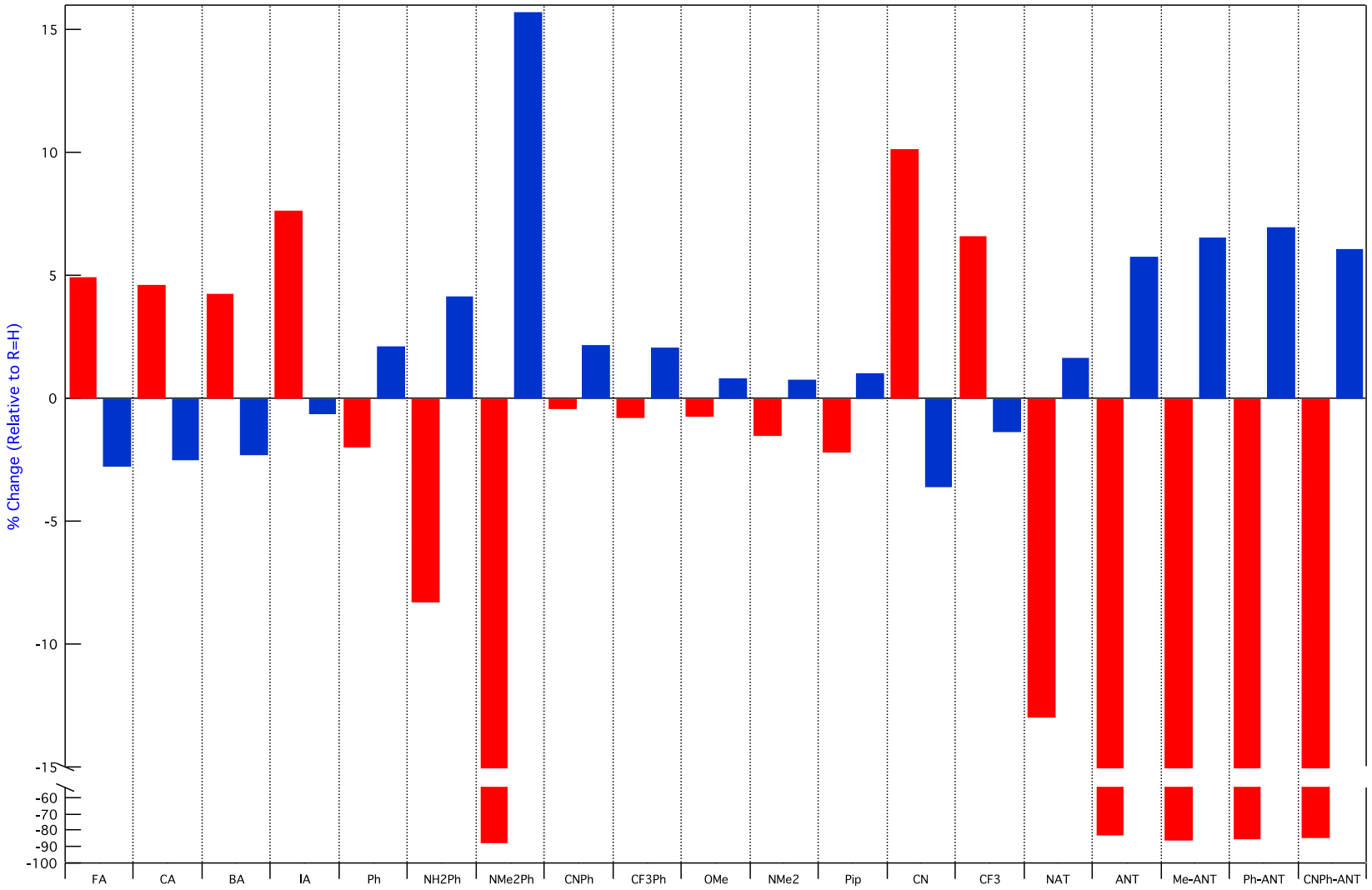

Figure 4.4. Shift in spin (red) and charge (blue) density at the oxygen atom for a series of substituted-anilate, naphthalene, and anthracene bridging radicals. The % change is referenced to the parameters obtained for $[Ga_2(tren)_2(DHBQ^{sq,cat})]^{3+}$ (i.e. R = H, where spin = 0.102 σ-electron and charge = -0.558 electron).

4.5.3 DFT Calculations

The same substituents and derivatives calculated for the deprotonated trianionic ligand radicals in Chapter 2 were performed on the Ga(III) dimeric systems to further examine the spin and charge delocalization effects when these radical ligands are coordinated to two Lewis acid Ga(III) ions. The spin and charge density of Ga(III) paramagnetic complexes show slight discrepancy compared with the computational results of deprotonated trianionic free ligands in Chapter 2.

Among the halogen series, the DFT results predict spin delocalization corresponding a decrease of spin density on the interacting oxygens. The spin delocalization effect is the most significant in I-substituted Ga(III) complex. Excess σ-spin on the four oxygen and the adjacent carbon atoms of $L^{sq,cat}$ bridge is shown in Fig. 4.4, and this essentially reflect on the molecular orbital picture of the SOMO of the complexes (see figures in Appendix). The σ-spin induces β-spin at adjacent positions, i.e. the middle two carbons and the substituents, is a result of the spin-polarization mechanism.[41] σ-spin density is sparse on the oxygens in the Br and I-substituted Ga (III) complexes, and this shows that as the electronegativity of the halogenated substituents decreases. The spin moving away from the oxygen atoms is indicative of spin delocalization. β-spin density on F and Cl indicates they effectively induce spin delocalization, whereas no such an effect is observed on the protio, Br, and I-substituted systems (Fig. 4.5). Charge density is the smallest in $[Ga_2(tren)_2(IA^{sq,cat})]^{3+}$, which suggests the formation of this complex is unfavorable. Both Complex **24** and **29** are proved to be unstable even being stored in the dark under inert atmosphere. The instability of these complexes matches the DFT results.

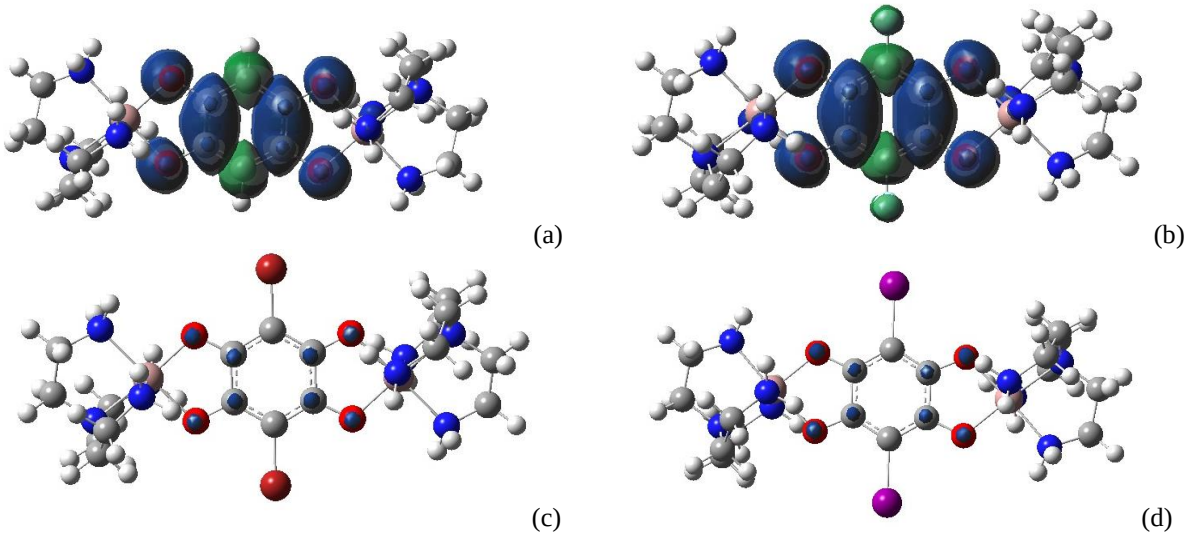

Figure 4.5. Excess spin density associated with the highest energy, singly-occupied molecular orbital of Complex **25** (a), **26** (b), **28** (c) and **29** (d).

According to *J* coupling constants obtained for dichromium(III) analogues, no significant change of *J* was caused by substituting F, Br, and I, except the Cl-substituted moiety. A drastic increase of *J* is observed for both Complex **3** and **13**. The experimental results of the halogenated Cr(III) dimers disagree with the trend predicted by NPA analysis. However, it will be insufficient to equate Cr(III) with Ga(III). Ga(III) is a much weaker Lewis acid and it does not have a partially filled metal *d* orbital for orbital overlap between the metal and ligand. F is a special halogen with extremely large electronegativity, and it has almost no effect when substituting on aromatic rings. Iodine is less electronegative with extreme large electron cloud and weaker electron withdrawing effect. In general, DFT calculation fails to correctly calculate spin density trend for halide.

In order to evaluate how well DFT predicts spin delocalization in both vertical and horizontal extended conjugated system, the Cr(III) series is used as reference due in fact that the Ga(III) analogues have not been successfully synthesized. In general, reduction of *J* caused by spin delocalization is observed both experimentally and computationally in naphthalene and

anthracene dichromium(III) assemblies (Fig. 4.2). With NMe_2 electron donating group substituting on the phenyl group, more metal and ligand orbital mixing is promoted to delocalize spins. The diminishing of *J* is observed, which is consistent with the computational result.

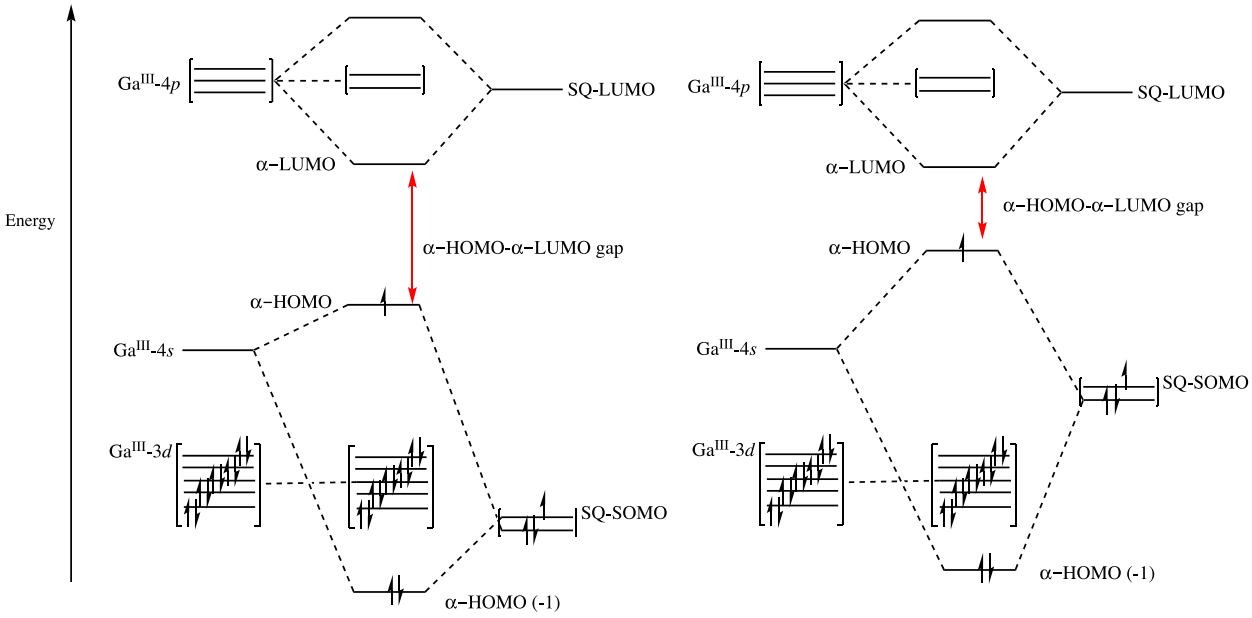

Figure 4.6. Weak bonding interaction between the Ga(III) *3d*, *4s*, *4p* orbitals and two energetically different SQ-SOMO orbitals, where the α-HOMO-α-LUMO gap is labeled in red.

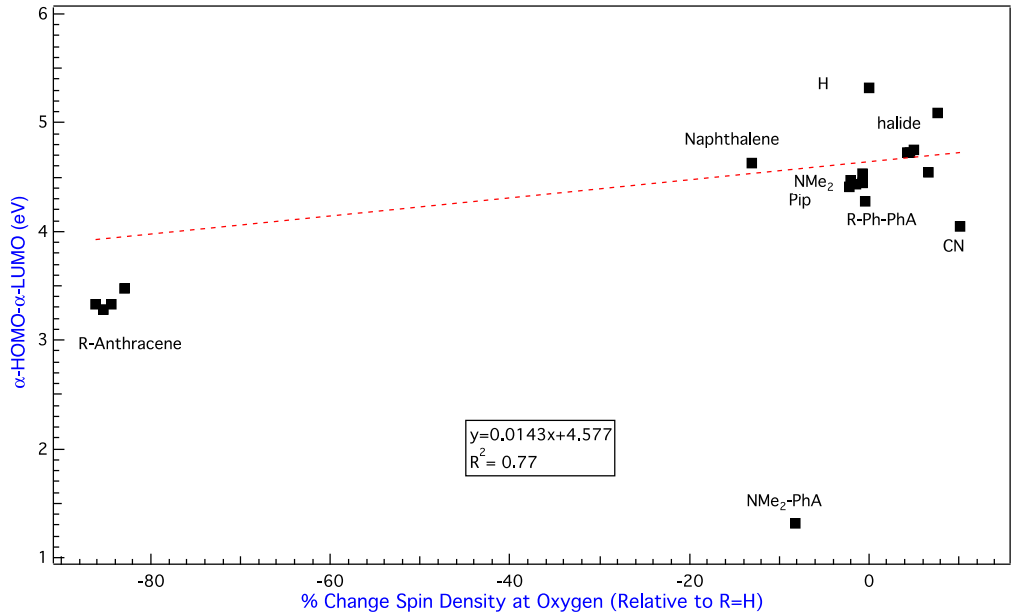

Figure 4.7. % Change spin density vs. σ-HOMO- σ-LUMO gap (eV) parameters for digallium (III)-tetraoxosemiquinones complexes.

Orbital mixing is considered as the major reason of spin delocalization caused by substituents or ligands with extended conjugated structures. When a substituent is strongly electron withdrawing (left in Fig. 4.6), the ligand SOMO is lower in energy with less mixing between Ga(III) *4s* orbital and ligand LUMO to stabilize σ-HOMO. This results in a larger σ-HOMO- σ-LUMO gap. If a substituent is strongly electron donating (right in Fig. 4.6), the ligand SOMO is higher in energy with more mixing between Ga(III) *4s* orbital and ligand SOMO to destabilize σ-HOMO, and a smaller σ-HOMO- σ-LUMO gap is resulted. Therefore, spin density should increase as a function of σ-HOMO- σ-LUMO gap. A correlation (r = 0.88) between the change of spin density and the frontier molecular orbital gap is plotted based on the result obtained computationally (Fig. 4.7). This correlation is not very strong with NMe_2-PhA as an outliner, so it is inconclusive to based off computational results for the prediction of spin polarization by the cause of σ-HOMO- σ-LUMO gap. A better understanding of the electronic structures is required for a more complete orbital picture, and EPR spectroscopy of this substituted Ga (III) series will be useful.

The *J* values extrapolated from the magnetic data of both $[Cr_2(tren)_2(NMe_2\text{-}PhA^{cat,cat})](BPh_4)_2$ (**7**) and $[Cr_2(tren)_2(NMe_2\text{-}PhA^{sq,cat})](BPh_4)_2(BF_4)$ (**17**) show a slight weakening effect of spin exchange. The spin density plot (Fig. 4.8) shows that β-spin density spreading from the two Cs in the middle to the NMe_2 substituted phenyl ring as an indication of spin delocalization induced by the substituted phenyl ring.

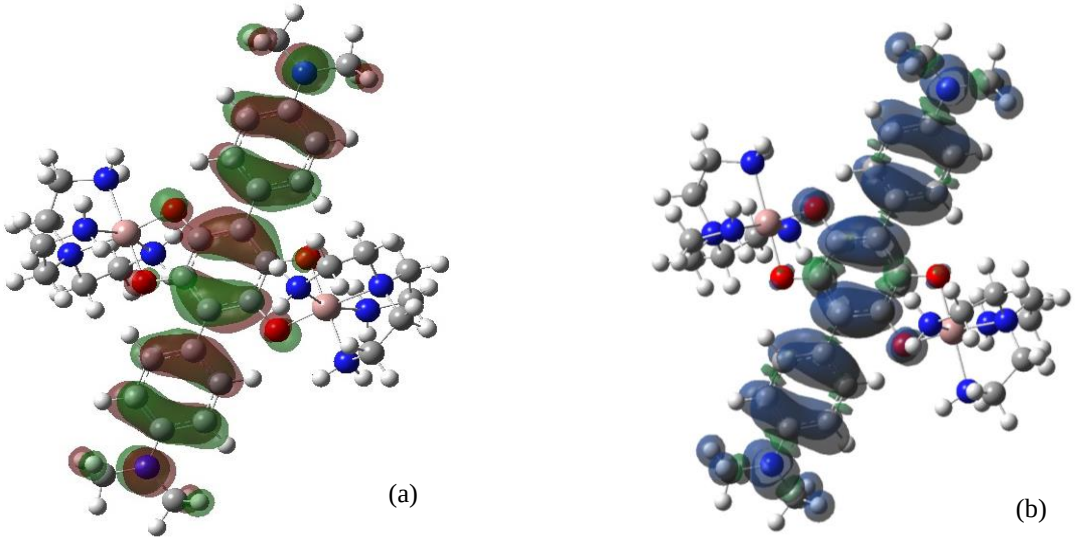

Figure 4.8. The SOMO (a) orbital picture and total spin density (b) distribution plot of $[Ga_2(tren)_2(NMe_2\text{-}PhA^{sq,cat})]^{3+}$ based on NPA of single point energy calculations.

As reported previously in our group,[45] electron polarization in complexes with inter-ring structure reflects mostly as a function of *2p-2p* orbital overlap between the inter-ring C-C. Better overbital overlap with coplanar geometry facilitates electron delocalization. Orbital overlap can be quantified with overlap intergral *S* as a function of distance r (Eq. 4.1) and dihedral angles θ (Eq. 4.2) between orbitals.[45,47]

$$S(\theta) = \cos\theta \tag{4.1}$$

$$S(r) = (1 + s + \frac{s^2}{5} + \frac{s^3}{15})e^{-s} \tag{4.2}$$

where $s = \frac{Z^* r}{n a_o}$, Z* is the effective atomic number, n is the principle quantum number, and a_o is the Bohr radius.[47]

Unfortunaly, no x-ray quality crystal was collected for $[Ga_2(tren)_2(PhA^{cat,cat})](BPh_4)_2$, and $[Ga_2(tren)_2(Me\text{-}AnT^{cat,cat})](BPh_4)_2$ has not been synthesized. These two systems are essential for a better understanding on how substituent affect the electronic structure of paramagnetic

species. Therefore, the syntheses of these two Ga(III) complexes need to be continuously pursued to illustrate this effect.

Both $[Cr_2(tren)_2(Me\text{-}AnT^{cat,cat})](BPh_4)_2$ (**10**) and $[Cr_2(tren)_2(Me\text{-}AnT^{sq,cat})](BPh_4)_2(BF_4)$ (**19**) were synthesized, quasi-reversible and reversible redox potential were observed electrochemically (detail discussion see Chapter 5). However, only $[Cr_2(tren)_2(AnT^{cat,cat})](BPh_4)_2$ was detected by ESI-MS, and the electrochemical data indicate this system is not chemically reversible. This implies $[AnT^{sq,cat}]^{3-}$ is a weaker Lewis base compared with $[Me\text{-}AnT^{sq,cat}]^{3-}$. The larger charge density in $[Ga_2(tren)_2(Me\text{-}AnT^{sq,cat})]^{3+}$ (Fig. 4.2) is indicative of better stability compared with $[Ga_2(tren)_2(AnT^{sq,cat})]^{3+}$.

4.5.4 Magnetic Properties of $[Ga_2(tren)_2(L^{sq,cat})](BPh_4)_2(BF_4)$

Variable-temperature magnetic susceptibility data were collected for $[Ga_2(tren)_2(L^{sq,cat})](BPh_4)_2(BF_4)$ in solid state in a temperature range of 2 – 350 K at applied field of 1.00 T.

$[Ga_2(tren)_2(L^{sq,cat})](BPh_4)_2(BF_4)$ is a paramagnetic complex without exchange coupling taken, because it only contains one paramagnetic center, the bridge radical (**S** = ½). The spin of ground state for these systems can be calculated from the effective magnetic moment (Eq. 4.1). While the plot shows the magnetic moment of Complex **27** was constant while temperature increased. The constant experimental magnetic moment, μ_{eff} =1.64 μ_B, reflected in the data indicates S = ½ (i.e. $\mu_{s.o.}$=1.73 μ_B), as expected for the semiquinone form of the bridge.

$$\mu_{eff} = \sqrt{4S(S+1)} \tag{4.1}$$

However, the magnetic data of Complex **25** and **28** show temperature dependence, which should not be observed for a paramagnetic sample (Fig. 4.9). Magnetic defect was also observed

in Complex **26** with a huge increase of magnetic moment when temperature increases. It is suspected that these samples are not pure, because temperature independent paramagnetism (TIP) contribution will not be as significant. This set of data need to be recollected with pure complexes.

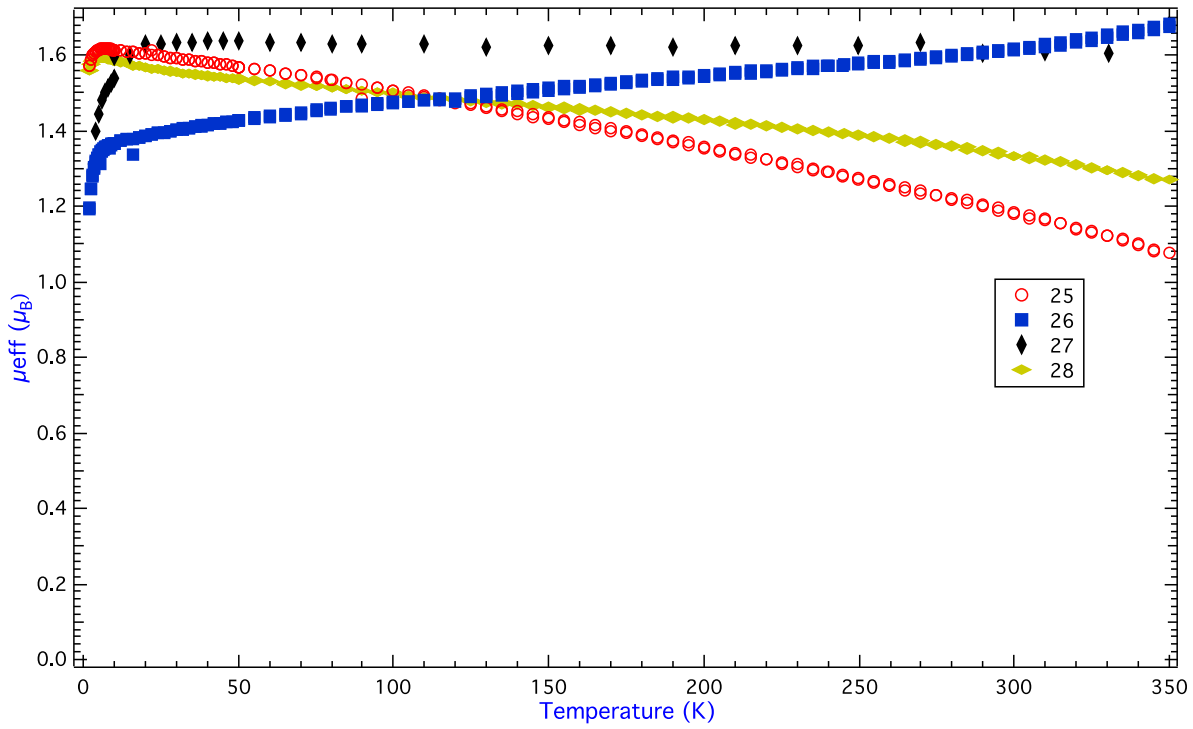

Figure 4.9. Plots of the effective magnetic moment versus temperature for all samples in solid states, Complex **25**, **26**, **27** and **28**.

Magnetic susceptibility measurement cannot be performed on $[Ga_2(tren)_2(IA^{sq,cat})](BPh_4)_2(BF_4)$, because this compound slowly decomposes even under inert atmosphere. Therefore, $[Ga_2(tren)_2(IA^{cat,cat})](BPh_4)_2$ needs to be freshly prepared and immediately oxidized to $[Ga_2(tren)_2(IA^{sq,cat})](BPh_4)_2(BF_4)$ for measurement.

4.6 Concluding Comments

This chapter illustrated the development of digallium(III)-semiquinone complexes. This series is developed initially for the study of ground state electronic structure due to d^{10} spectroscopic silent characteristic of gallium(III). Ga(III) is chosen also due to it similar charge-over-radius ratio to Cr(III).

DFT calculation has continuously be proven as effective tool to provide insight about spin delocalization effects. The spin polarization calculated computationally on the digallium(III) semiquinone complexes manifest on the experimental of the corresponding Cr(III) analogues, and the trend of spin polarization predicted computationally matches the experimental observation.

One of the biggest obstacles is the synthesis of the fully reduced anilate, because they are extremely air-sensitive. Their syntheses and purification procedures need to be performed under inert atmosphere with Schlenk line technique, and the purification steps have to proceed in an inert gas-filled glovebag for product extraction. In addition, the fully reduced iodoanilate is extremely unstable even stored in dark under inert atmosphere. It has to be coordinated to Ga(III) immediately; otherwise, the ligand will decompose within one hour. Even with the difficulties, a complete series of the halogenated digallium(III) complexes was synthetized usefully, and x-ray quality structure of the catecholate derivatives were determined. $[Ga_2(tren)_2(IA^{cat,cat})](BPh_4)_2$ is light sensitive and unstable even stored under inert atmosphere. This complex is stable for about a week upon coordination with Ga(III); however, it slowly starts to decompose over 1 month. In order to study the photophysical and magnetic properties of this iodo analogue, it needs to be freshly prepared. Similar instability was observed for $[Ga_2(tren)_2(IA^{cat,cat})](BPh_4)_2(BF_4)$.

In general, the synthesis of the digallium(III) assemblies is harder than their dichromium(III) analogues, since Ga(III) is a weaker Lewis acid. For the reaction of the Ga(III) phenylanilate compound, $[M]^{3+}$ species was observed by ESI-MS with no detection of $[M]^{2+}$ species. it is hard to conclude the identity of the product solely based on the result from mass spectrometry. DFT calculations conducted on this free ligand suggests it is a very weak Lewis base with significant decrease of charge density in Chapter 2, so this complex is likely to be synthetically unfavorable with small formation constant. The identification of this compound will be continuously discussed along with its electrochemical data in Chapter 5.

As a paramagnetic compound with **S** = ½, the magnetic data should show temperature independence at high temperature with μ_{eff} close to 1.73 μ_B. All of the data collected for these halogenated series (Fig. 4.6) have effective magnetic moment around 1.6 μ_B. However, significant temperature dependence trend was observed in Complex **26**, **27**, and **28**. The products may contain impurity contribute to this feature. Due to the instability of Complex **29**, there was not enough sample for magnetic measurement. Therefore, variable-temperature magnetic susceptibility measurement should be conducted on the halogenated digallium(III) complexes again, even though the absence of these data does not affect the discussion in this project.

APPENDIX

APPENDIX

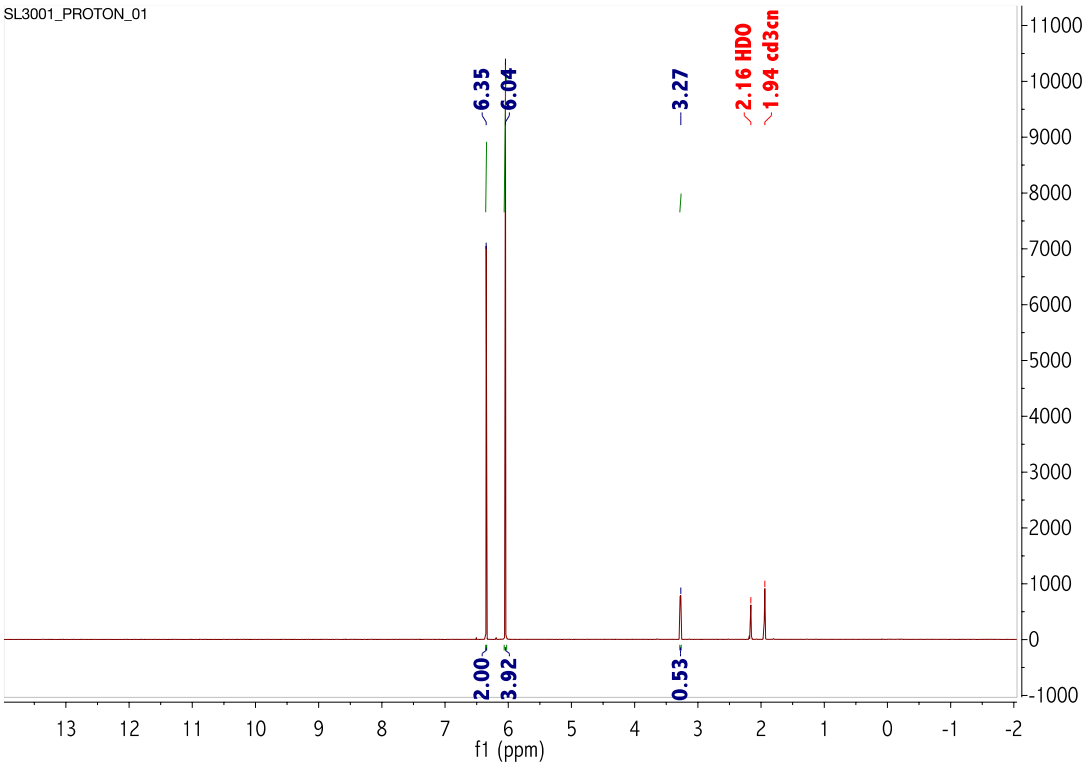

Figure 4.10. ^{1}H NMR of THB in CD_3CN.

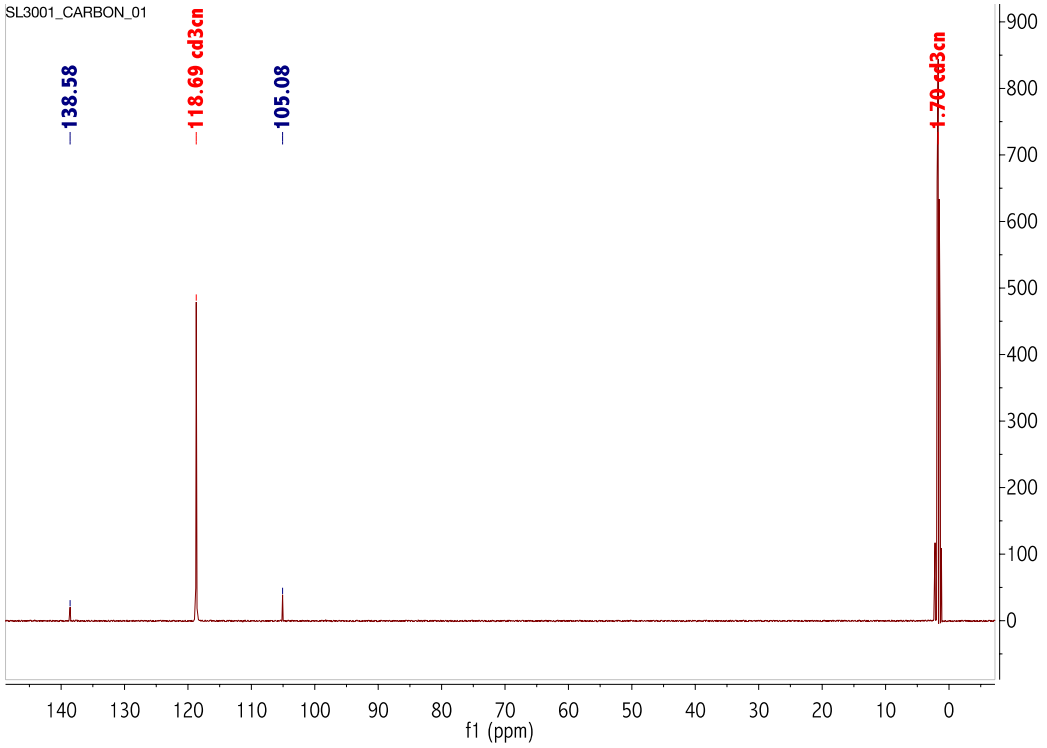

Figure 4.11. ^{13}C NMR of THB in CD_3CN.

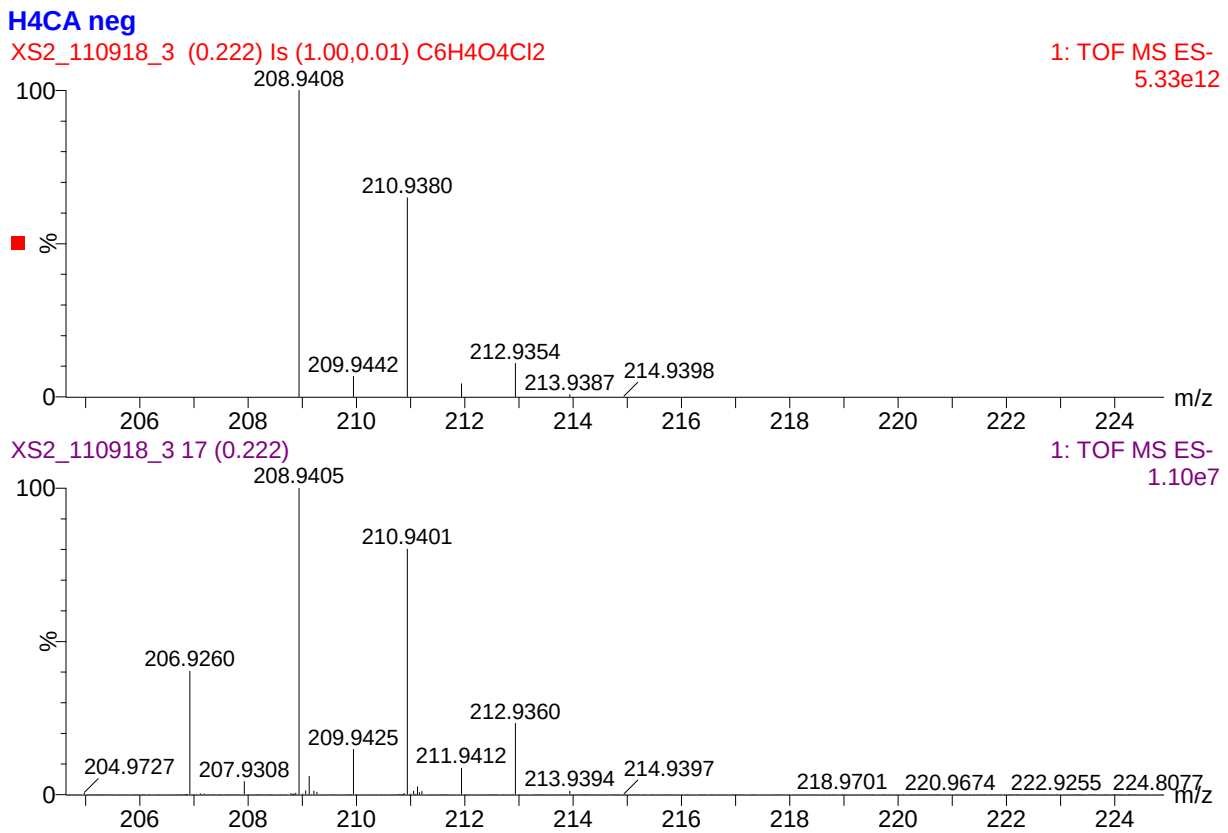

Figure 4.12. ESI-MS of H_4CA. Top: calculated isotope pattern for $[M-H]^-$ ($C_6O_4H_3Cl_2$). Bottom: experimental result.

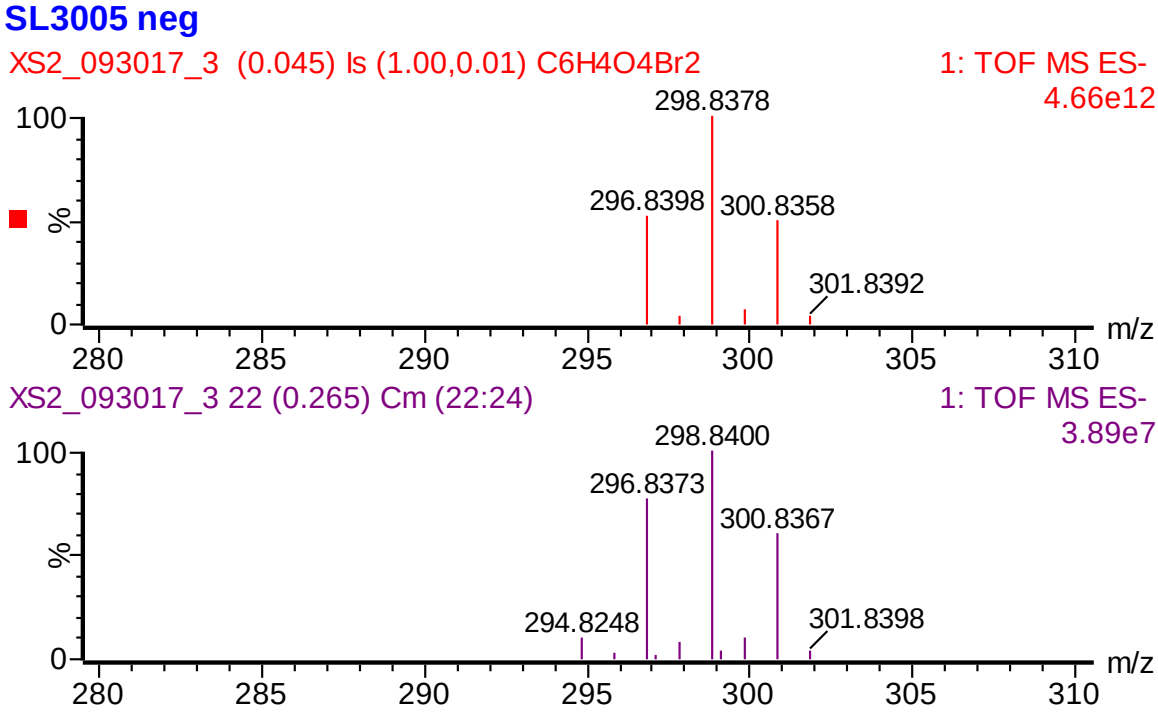

Figure 4.13. ESI-MS of H_4BA. Top: calculated isotope pattern for $[M-H]^-$ ($C_6O_4H_3Br_2$). Bottom: experimental result.

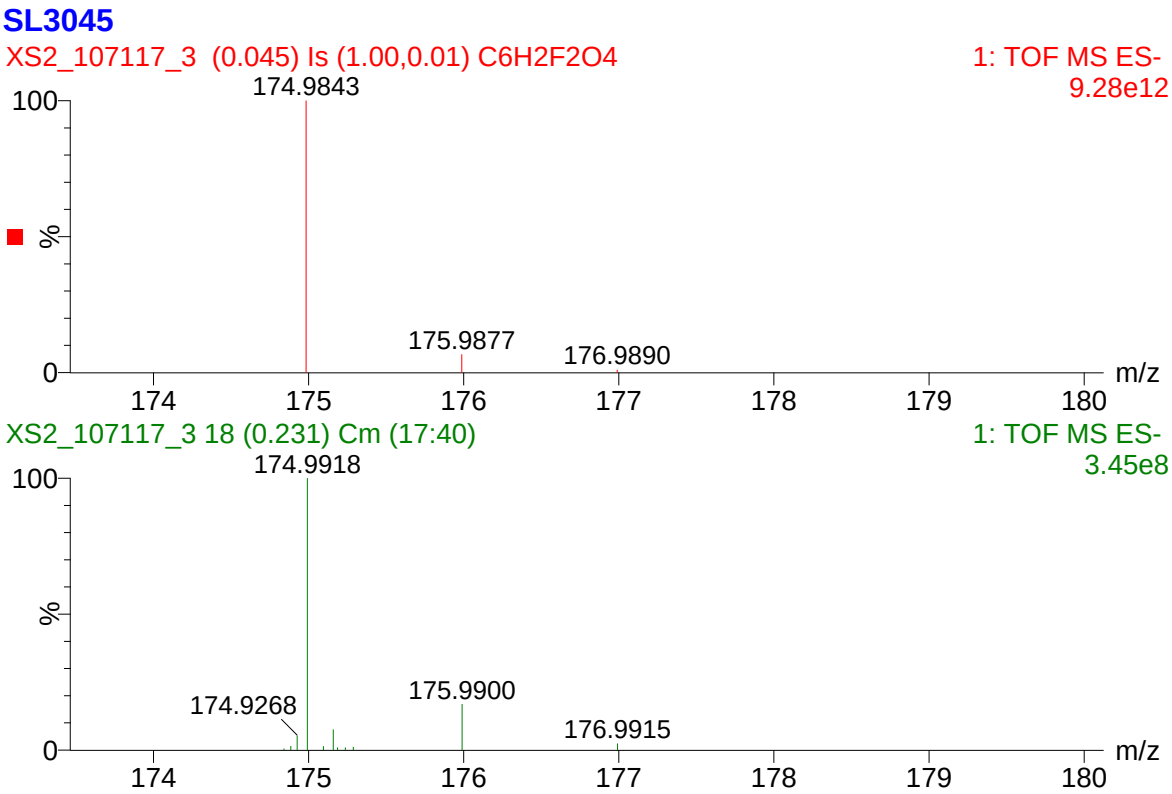

Figure 4.14. ESI-MS of H_4FA. Top: calculated isotope pattern for $[M-H]^-$ ($C_6O_4H_3F_2$). Bottom: experimental result.

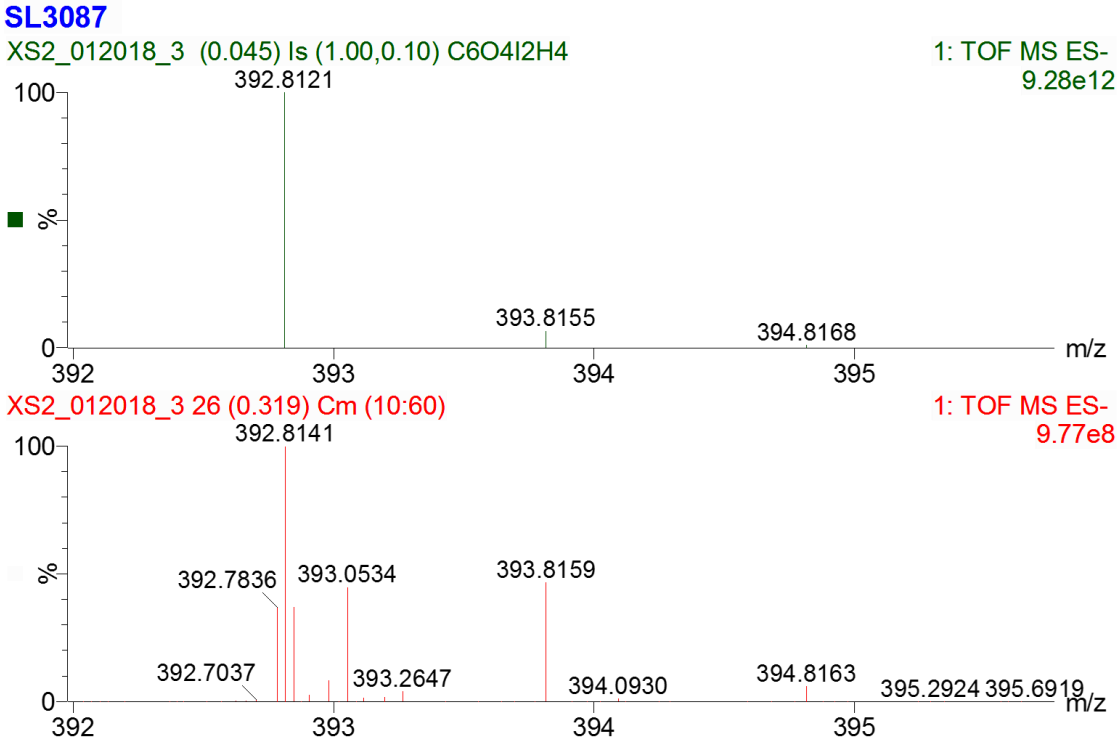

Figure 4.15. ESI-MS of H_4IA. Top: calculated isotope pattern for $[M-H]^-$ ($C_6O_4H_3I_2$). Bottom: experimental result.

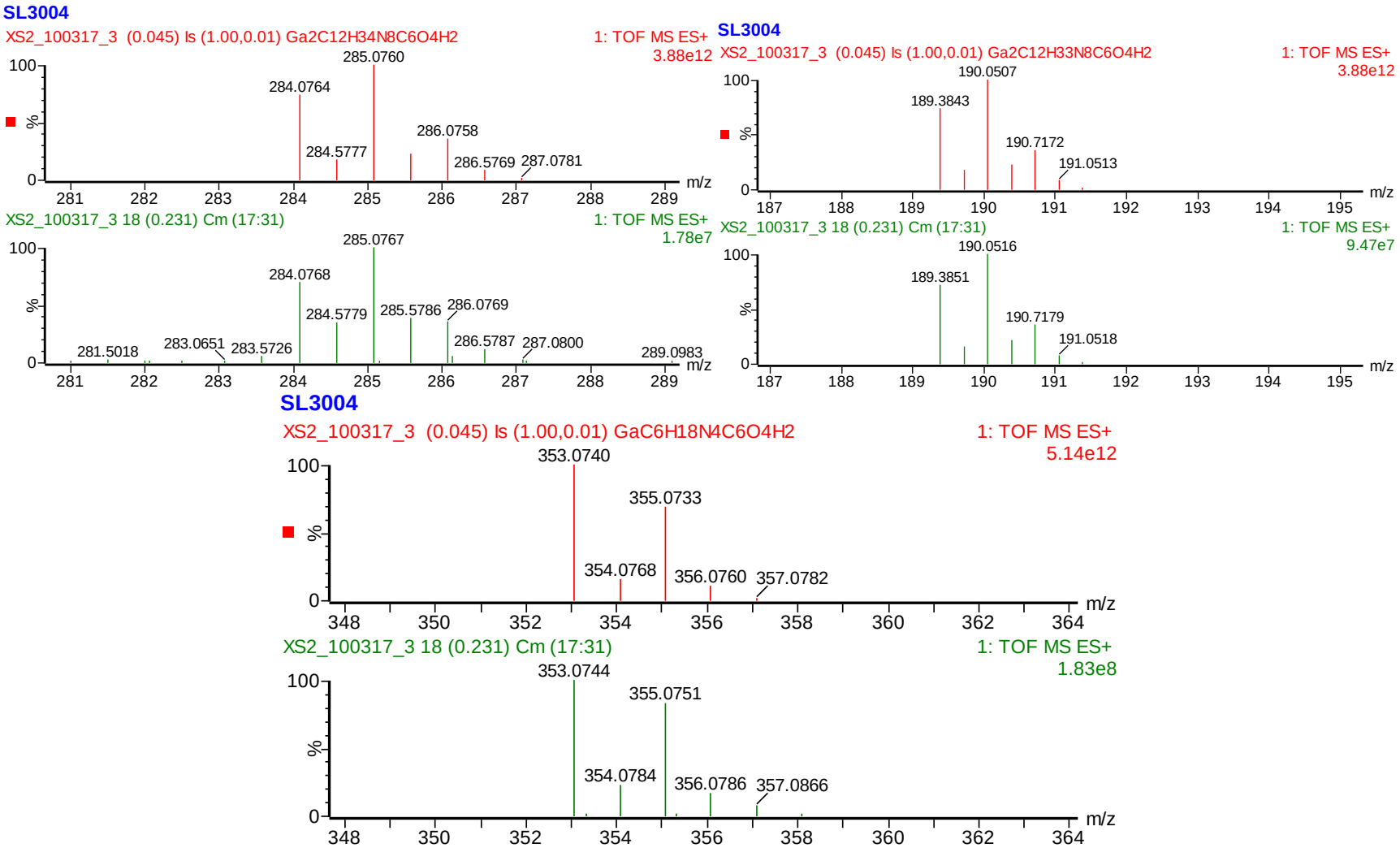

Figure 4.16. ESI-MS of Complex **20**. Upper left: top, calculated isotope pattern for $[M]^{2+}$ ($Ga_2C_{18}O_4H_{38}N_8$); bottom, experimental result. Upper right: top, calculated isotope pattern for $[M]^{3+}$ ($Ga_2C_{18}O_4H_{38}N_8$); bottom, experimental result. Lower: top, calculated isotope pattern for $[Ga(tren)(C_6H_2O_4)]^{+}$ ($GaC_{12}H_{20}O_4N_4$); bottom, experimental result.

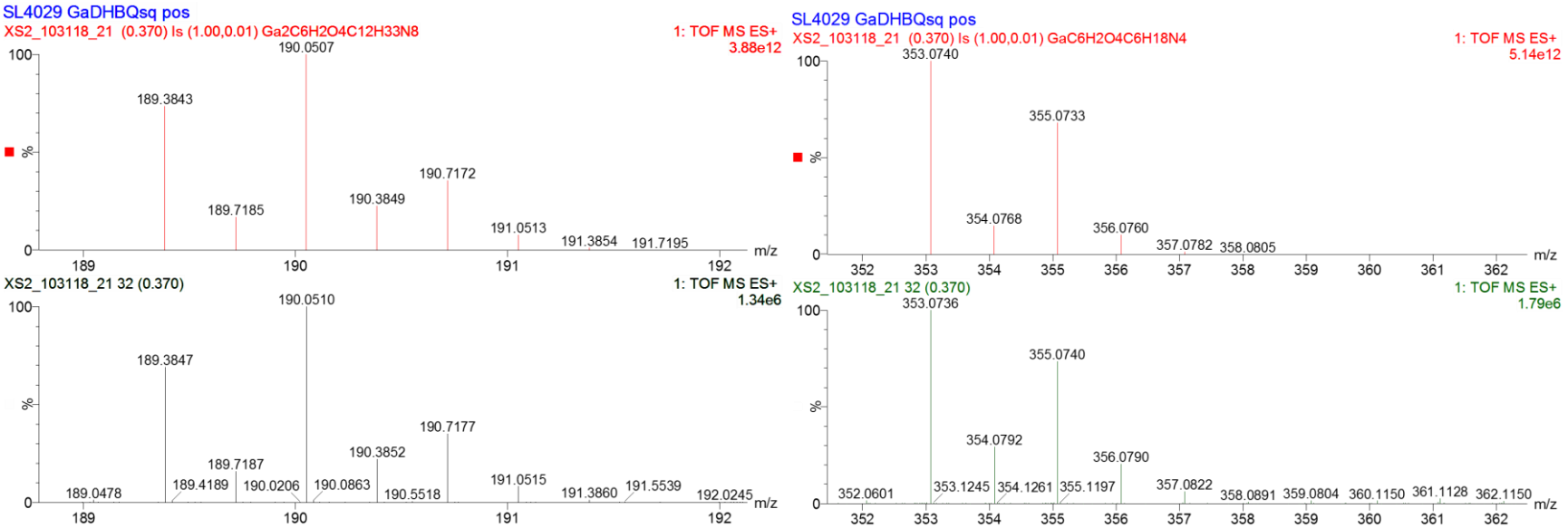

Figure 4.17. ESI-MS of Complex **25**. Left: top, calculated isotope pattern for $[M]^{3+}$ ($Ga_2C_{18}O_4H_{38}N_8$); bottom, experimental result. Right: top, calculated isotope pattern for $[Ga(tren)(C_6H_2O_4)]^+$ ($GaC_{12}H_{20}O_4N_4$); bottom, experimental result.

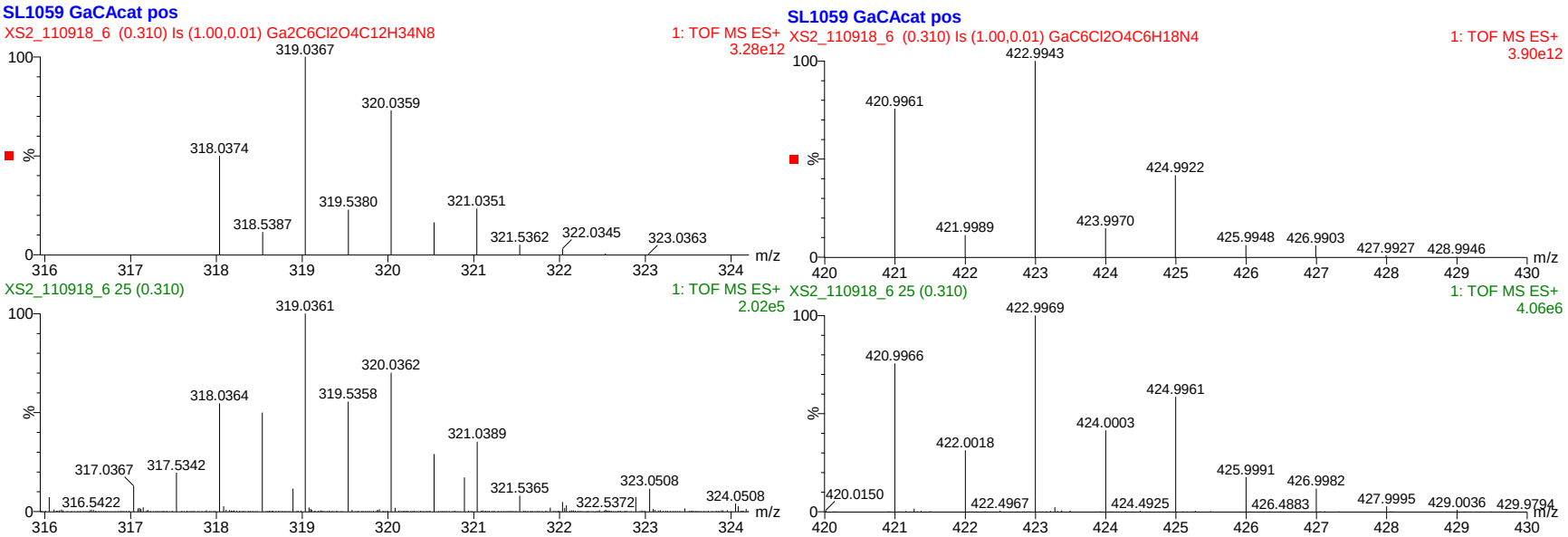

Figure 4.18. ESI-MS of Complex **22**. Left: top, calculated isotope pattern for $[M]^{2+}$ ($Ga_2C_{18}H_{36}O_4N_8Cl_2$); bottom, experimental result. Right: top, calculated isotope pattern for $[Ga(tren)(C_6Cl_2O_4)]^+$ ($GaC_{12}H_{18}O_4N_4Cl_2$); bottom, experimental result.

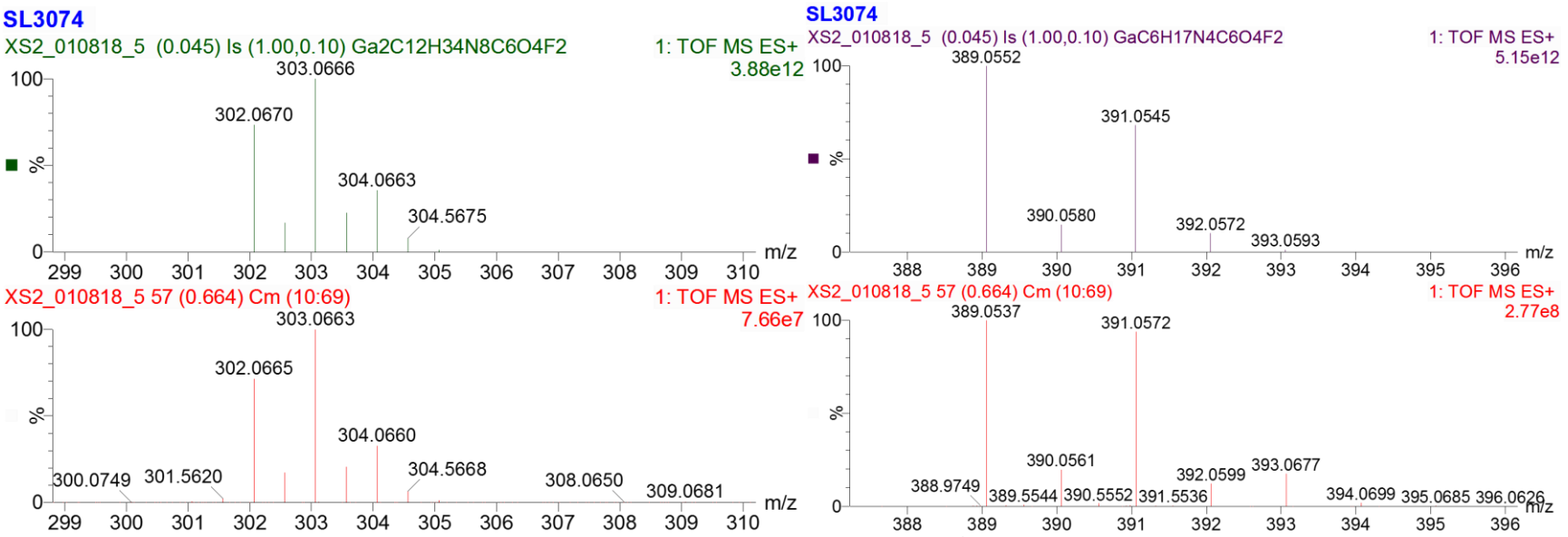

Figure 4.19. ESI-MS of Complex **21**. Left: top, calculated isotope pattern for $[M]^{2+}$ ($Ga_2C_{18}H_{36}O_4N_8F_2$); bottom, experimental result. Right: top, calculated isotope pattern for $[Ga(tren)(C_6F_2O_4)]^+$ ($GaC_{12}H_{18}O_4N_4F_2$); bottom, experimental result.

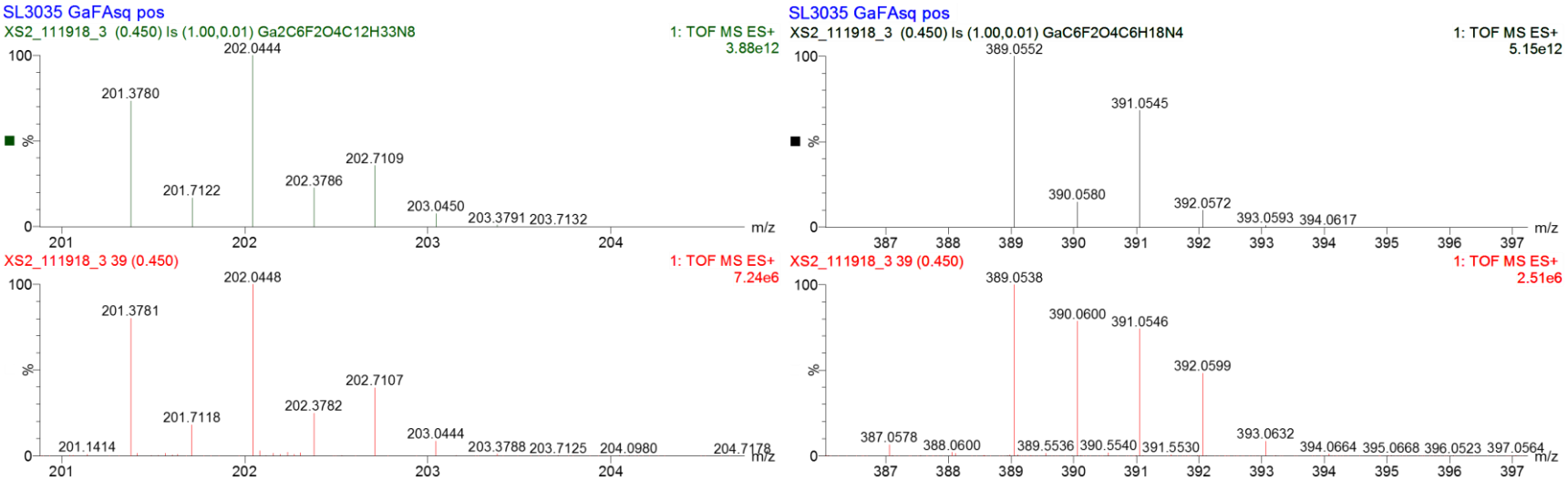

Figure 4.20. ESI-MS of Complex **26**. Left: top, calculated isotope pattern for $[M]^{3+}$ ($Ga_2C_{18}H_{36}O_4N_8F_2$); bottom, experimental result. Right: top, calculated isotope pattern for $[Ga(tren)(C_6F_2O_4)]^+$ ($GaC_{12}H_{18}O_4N_4F_2$); bottom, experimental result.

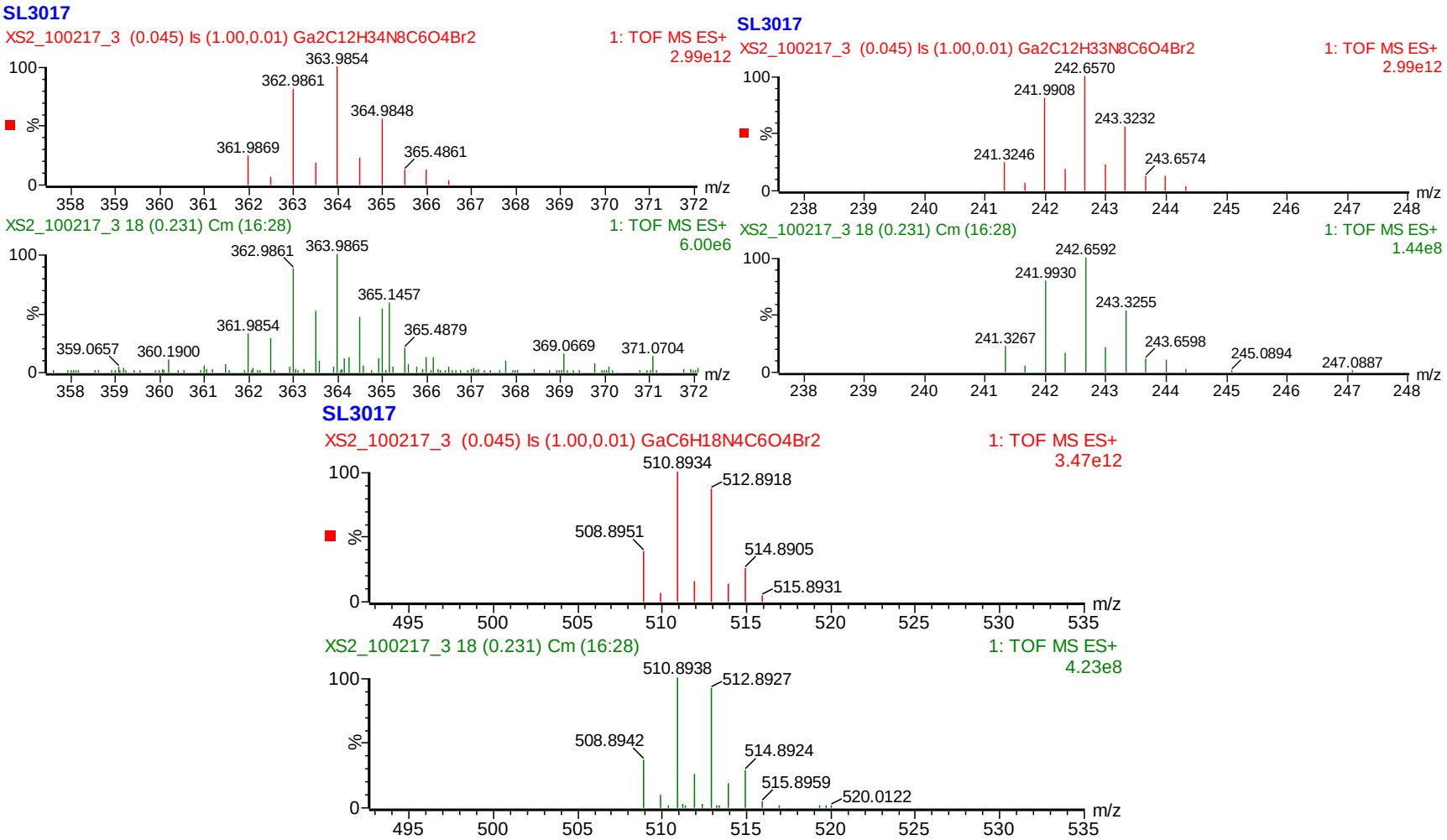

Figure 4.21. ESI-MS of Complex **23**. Upper left: top, calculated isotope pattern for $[M]^{2+}$ ($Ga_2C_{18}H_{36}O_4N_8Br_2$); bottom, experimental result. Upper right: top, calculated isotope pattern for $[M]^{3+}$ ($Ga_2C_{18}H_{36}O_4N_8Br_2$); bottom, experimental result. Lower: top, calculated isotope pattern for $[Ga(tren)(C_6Br_2O_4)]^+$ ($GaC_{12}H_{18}O_4N_4Br_2$); bottom, experimental result.

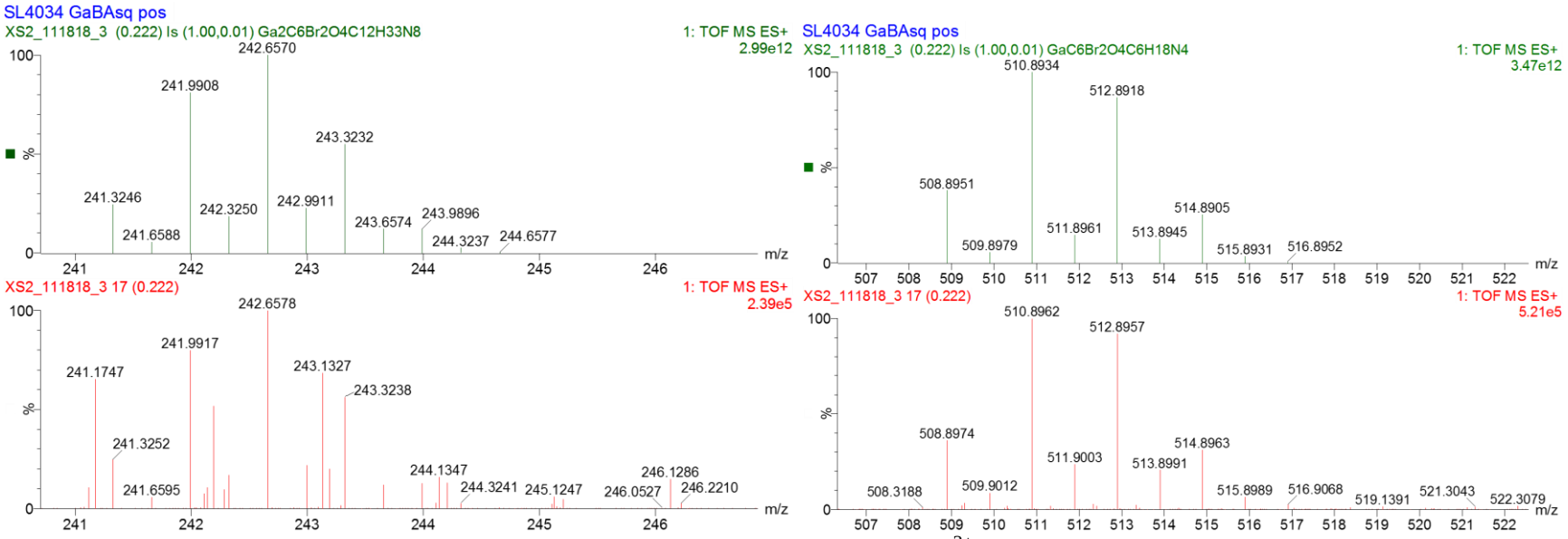

Figure 4.22. ESI-MS of Complex **28**. Left: top, calculated isotope pattern for $[M]^{3+}$ ($Ga_2C_{18}H_{36}O_4N_8Br_2$); bottom, experimental result. Right: top, calculated isotope pattern for $[Ga(tren)(C_6Br_2O_4)]^+$ ($GaC_{12}H_{18}O_4N_4Br_2$); bottom, experimental result.

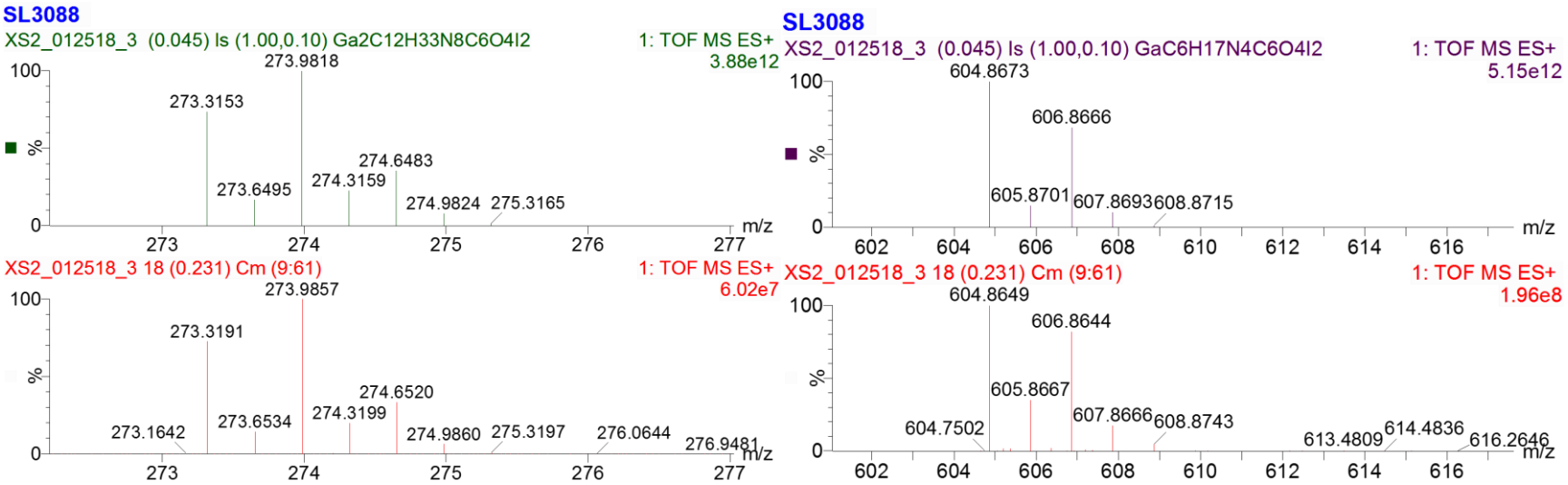

Figure 4.23. ESI-MS of Complex **24**. Left: top, calculated isotope pattern for $[M]^{3+}$ ($Ga_2C_{18}H_{36}O_4N_8I_2$); bottom, experimental result. Right: top, calculated isotope pattern for $[Ga(tren)(C_6Br_2O_4)]^+$ ($GaC_{12}H_{18}O_4N_4I_2$); bottom, experimental result.

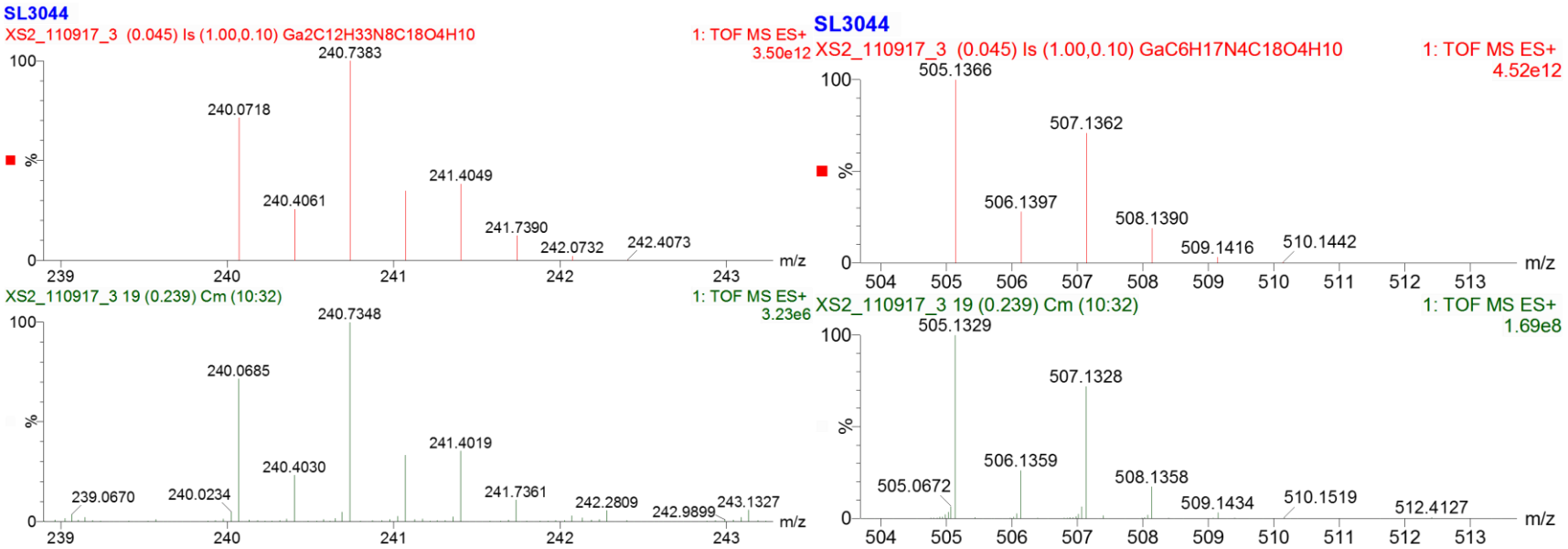

Figure 4.24. ESI-MS of $[Ga_2(tren)_2(PhA^{cat,cat})](BPh_4)_2$. Left: top, calculated isotope pattern for $[M]^{2+}$ ($Ga_2C_{30}H_{46}O_4N_8$); bottom, experimental result. Right: top, calculated isotope pattern for $[Ga(tren)(C_{18}H_{10}O_4)]^+$ ($GaC_{24}H_{28}O_4N_4$); bottom, experimental result.

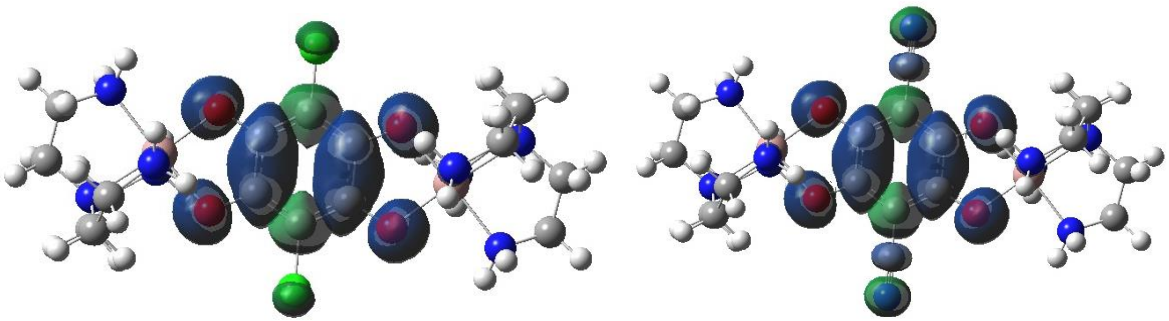

Figure 4.25. Total spin density associated with the highest energy, singly-occupied molecular orbital of $[Ga_2(tren)_2(CA^{sq,cat})]^{3+}$ (left), and $[Ga_2(tren)_2(CNA^{sq,cat})]^{3+}$ (right).

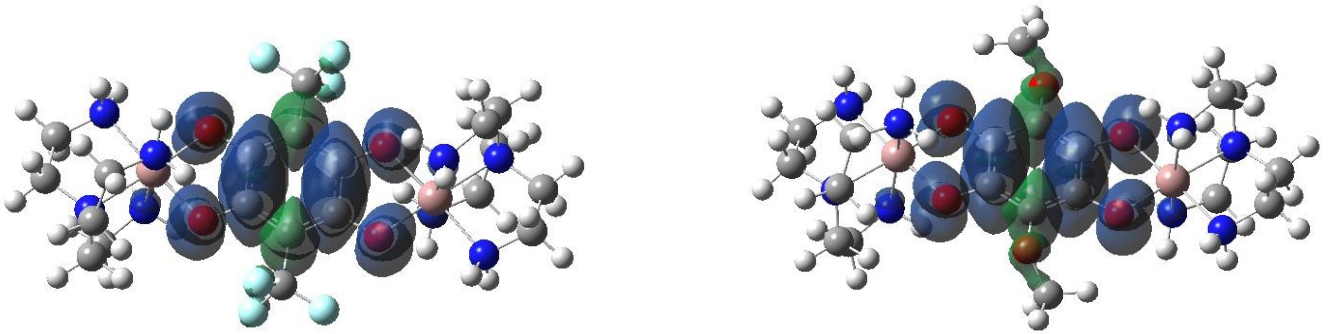

Figure 4.26. Total spin density associated with the highest energy, singly-occupied molecular orbital of $[Ga_2(tren)_2(CF_3A^{sq,cat})]^{3+}$ (left), and $[Ga_2(tren)_2(OMeA^{sq,cat})]^{3+}$ (right).

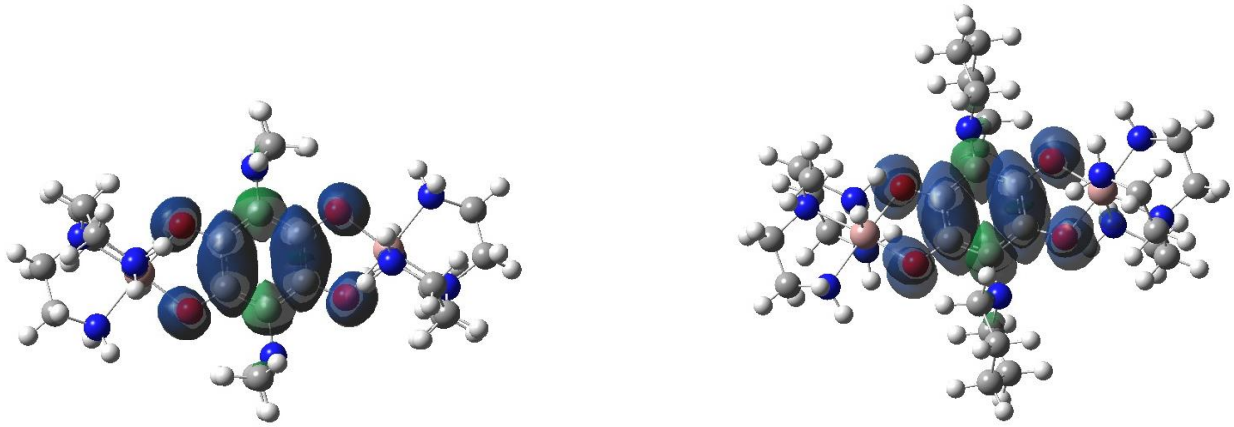

Figure 4.27. Total spin density associated with the highest energy, singly-occupied molecular orbital of $[Ga_2(tren)_2(NMe_2A^{sq,cat})]^{3+}$ (left), and $[Ga_2(tren)_2(PipA^{sq,cat})]^{3+}$ (right).

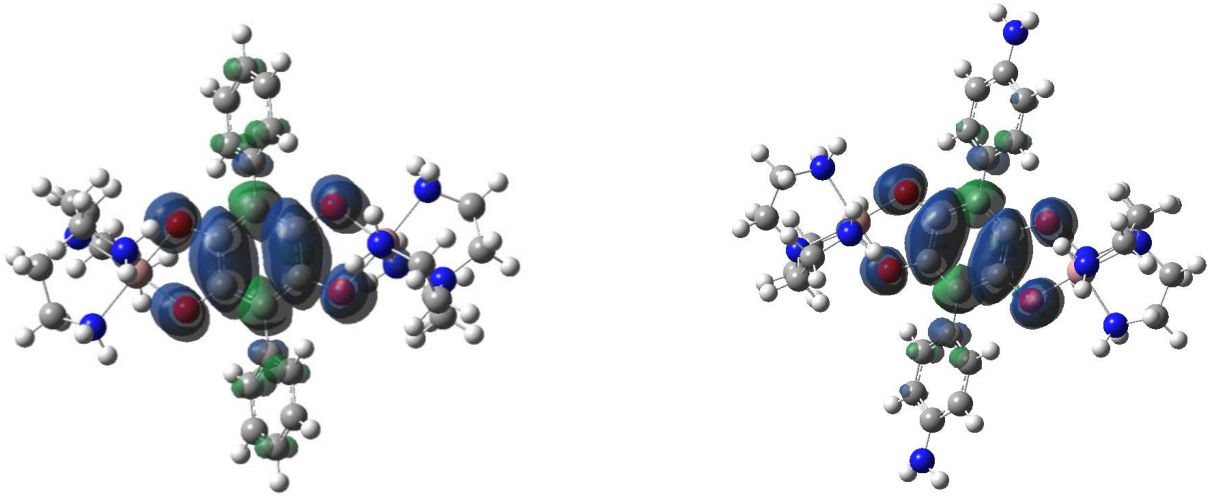

Figure 4.28. Total spin density associated with the highest energy, singly-occupied molecular orbital of $[Ga_2(tren)_2(PhA^{sq,cat})]^{3+}$ (left), and $[Ga_2(tren)_2(NMe_2\text{-}PhA^{sq,cat})]^{3+}$ (right).

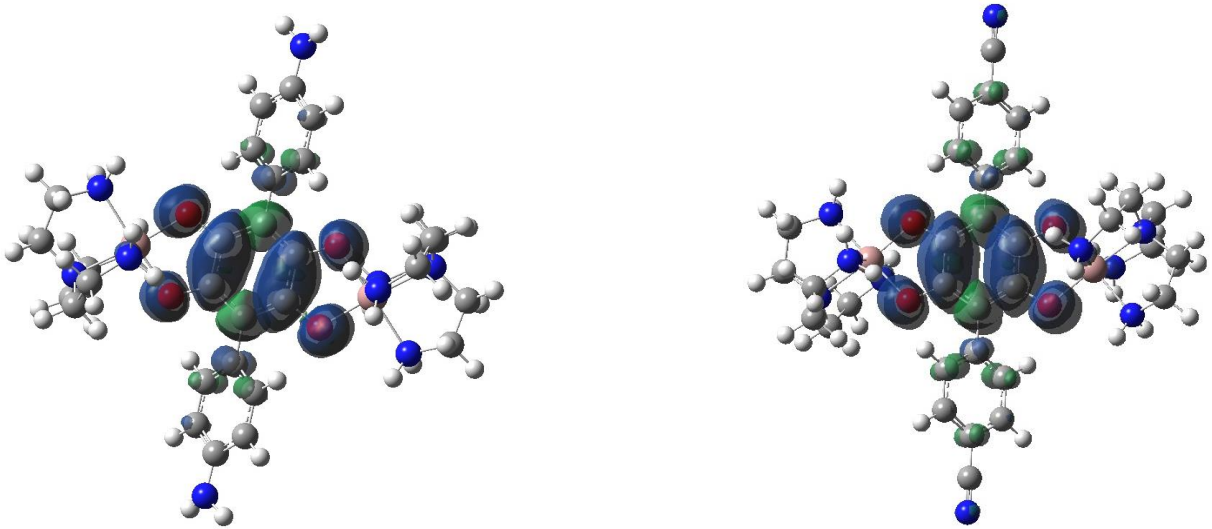

Figure 4.29. Total spin density associated with the highest energy, singly-occupied molecular orbital of $[Ga_2(tren)_2(NH_2\text{-}PhA^{sq,cat})]^{3+}$ (left), and $[Ga_2(tren)_2(CN\text{-}PhA^{sq,cat})]^{3+}$ (right).

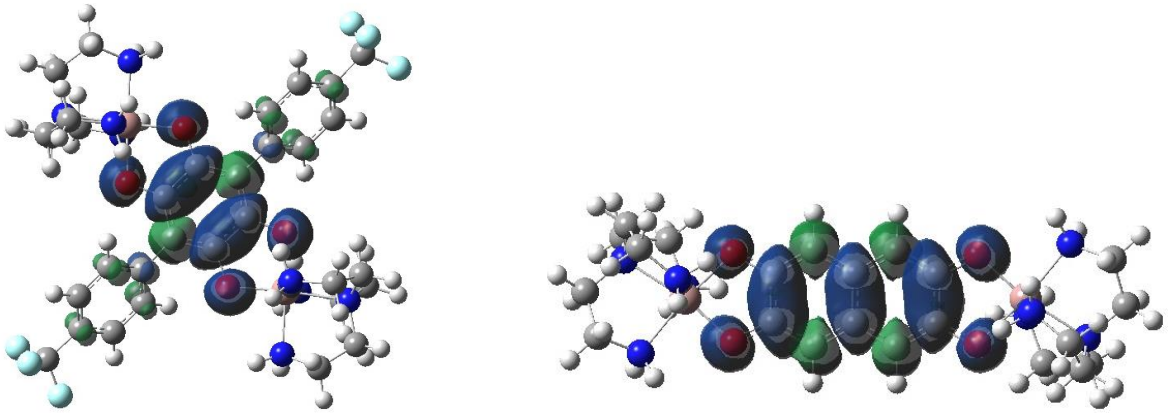

Figure 4.30. Total spin density associated with the highest energy, singly-occupied molecular orbital of $[Ga_2(tren)_2(CF_3\text{-}PhA^{sq,cat})]^{3+}$ (left), and $[Ga_2(tren)_2(NAT^{sq,cat})]^{3+}$ (right).

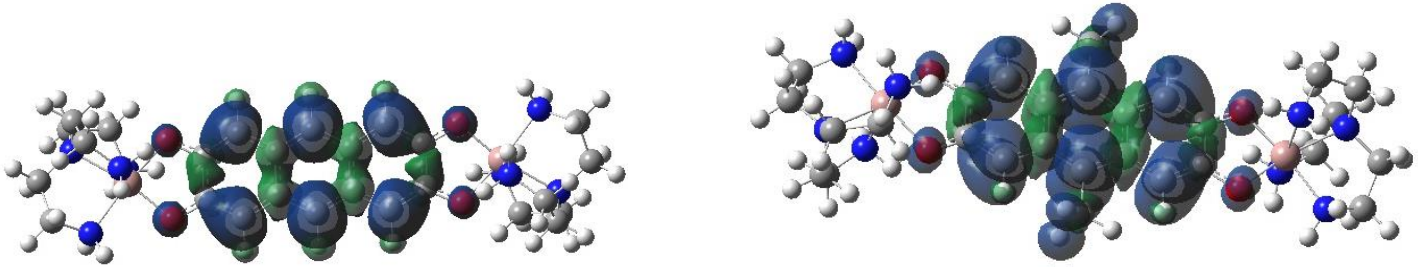

Figure 4.31. Total spin density associated with the highest energy, singly-occupied molecular orbital $[Ga_2(tren)_2(AnT^{sq,cat})]^{3+}$ (left), and of $[Ga_2(tren)_2(Me\text{-}AnT^{sq,cat})]^{3+}$ (right).

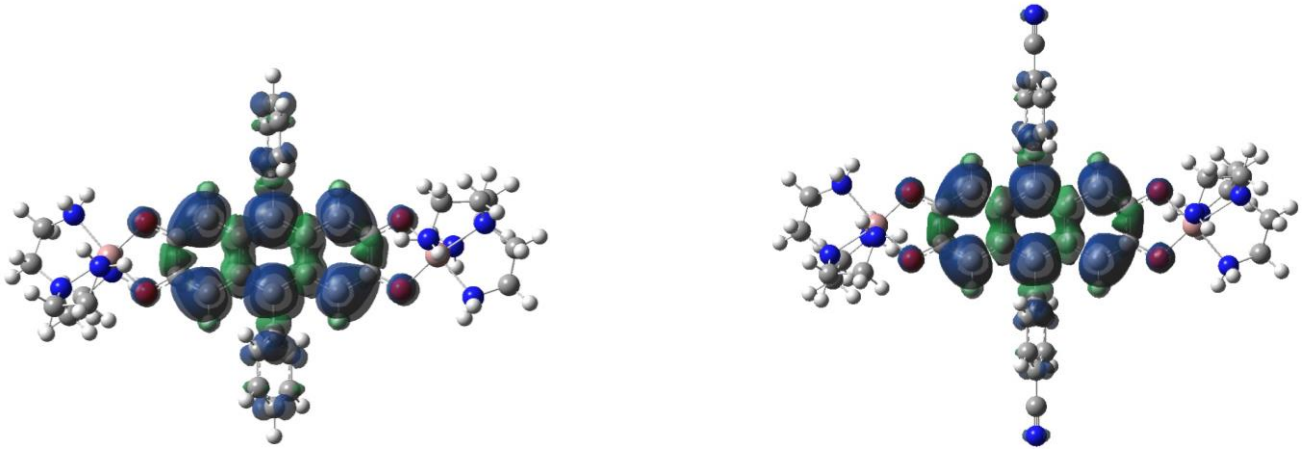

Figure 4.32. Total spin density associated with the highest energy, singly-occupied molecular orbital of $[Ga_2(tren)_2(Ph\text{-}AnT^{sq,cat})]^{3+}$ (left), and $[Ga_2(tren)_2(CNPh\text{-}AnT^{sq,cat})]^{3+}$ (right).

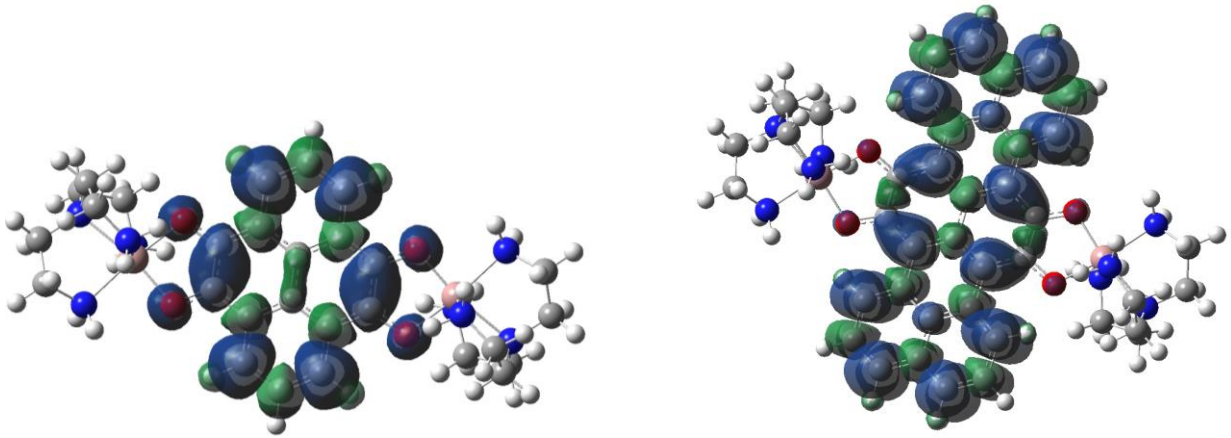

Figure 4.33. Total spin density associated with the highest energy, singly-occupied molecular orbital of $[Ga_2(tren)_2(Pyrene^{sq,cat})]^{3+}$ (left) and $[Ga_2(tren)_2(Terrylene^{sq,cat})]^{3+}$ (right).

REFERENCES

REFERENCES

(1) Gary, H. B. *J. Chem. Educ.* **1964**, *41*, 2-12.

(2) Orgel, L. E. *An Introduction to Transition-Element Chemistry: Ligand Field Theory.* Methuen: London, U.K., 1960.

(3) Owen, J. *Proc. Roy. Soc.,* **1955**, *A227*, 183.

(4) Dunn, T. M. *J. Chem. Soc.,* **1959**, 623.

(5) Owen, J. *Discussions Faraday Soc.*, **1955**, *19*, 127.

(6) Beckmann, U.; Bill, E.; Weyhermüller, T.; Wieghardt, K. *Eur. J. Inorg. Chem.* **2003**, 1768.

(7) McCracken, J.; Pember, S.; Benkovic, S. J.; Villafranca, J. J.; Miller, R. J.; Peisach, J. *J. Am. Chem. Soc.* **1988**, *110*, 1069.

(8) Brown, M. A.; El-Hadad, A. A.; McGarvey, B. R.; Sung, R. C. W.; Trikha, A. K.; Tuck, D. G. *Inorg. Chim. Acta* **2000**, *300*, 613-621.

(9) Figuet, M.; Averbuch-Pouchot, M. T.; d'Hardemare, A. d. M.; Jarjayes, O. *Eur. J. Inorg. Chem.* **2001**, 2089-2096.

(10) Lanznaster, M.; Hratchian, H. P.; Heeg, M. J.; Hryhorczuk, L. M.; McGarvey, B. R.; Schlegel, H. B.; Verani, C. N. *Inorg. Chem.* **2006**, *45*, 955-957.

(11) Gaussian 09, Revision A.02, M. J. Frisch, G. W. Trucks, H. B. Schlegel, G. E. Scuseria, M. A. Robb, J. R. Cheeseman, G. Scalmani, V. Barone, G. A. Petersson, H. Nakatsuji, X. Li, M. Caricato, A. Marenich, J. Bloino, B. G. Janesko, R. Gomperts, B. Mennucci, H. P. Hratchian, J. V. Ortiz, A. F. Izmaylov, J. L. Sonnenberg, D. Williams-Young, F. Ding, F. Lipparini, F. Egidi, J. Goings, B. Peng, A. Petrone, T. Henderson, D. Ranasinghe, V. G. Zakrzewski, J. Gao, N. Rega, G. Zheng, W. Liang, M. Hada, M. Ehara, K. Toyota, R. Fukuda, J. Hasegawa, M. Ishida, T. Nakajima, Y. Honda, O. Kitao, H. Nakai, T. Vreven, K. Throssell, J. A. Montgomery, Jr., J. E. Peralta, F. Ogliaro, M. Bearpark, J. J. Heyd, E. Brothers, K. N. Kudin, V. N. Staroverov, T. Keith, R. Kobayashi, J. Normand, K. Raghavachari, A. Rendell, J. C. Burant, S. S. Iyengar, J. Tomasi, M. Cossi, J. M. Millam, M. Klene, C. Adamo, R. Cammi, J. W. Ochterski, R. L. Martin, K. Morokuma, O. Farkas, J. B. Foresman, and D. J. Fox, Gaussian, Inc., Wallingford CT, 2016.

(12) Vosko, S. H.; Wilk, L.; Nusair, M. *Can. J. Phys.* **1980**, *58*, 1200-1211.

(13) Lee, C.; Yang, W.; Parr, R.G. *Phys. Rev. B* **1988**, *37*, 785-789.

(14) Becke, A. D. *J. Chem. Phys.* **1993**, *98*, 5648-5652.

(15) Stephens, P. J.; Devlin, F. J.; Chabalowski, C. F.; Frisch, M. J. *J. Phys. Chem.* **1994**, *98*, 11623-11629.

(16) Tirado-Rives, J.; Jorgensen, W. *J. Chem. Theory Comput.* **2008**, *4*, 297-306.

(17) Glendening, E. D.; Reed, A. E.; Carpenter, J. E.; Weinhold, F. NBO 3.1; Theoretical Chemistry Institute, University of Wisconsin: Madison, WI, 1994.

(18) GaussView, Version 5, Dennington, R.; Keith, T. A.; Millam, J. M. Semichem Inc., Shawnee Mission, KS, 2009.

(19) Ochterski, J. W. Vibrational Analysis in *Gaussian.* http://gaussian.com/wp-content/uploads/dl/vib.pdf. June 14, 2018.

(20) Graebe *Justus Liebigs Ann. Chem.* **1868**, 1*46*, 31.

(21) Weider, P. R.; Hegedus, L. S.; Asada, H.; D'Andreq, S. V. *J. Org. Chem.*, **1985**, *50*, 4276.

(22) Guo, D.; McCusker, J. K. *Inorg. Chem.* **2007**, *46*, 3257-3274.

(23) Abrahams, B. F.; Hudson, T. A.; McCormick, L. J.; Robson, R. *Cryst. Growth Des.* **2011**, *11*, 2717-2720.

(24) Ye, Y. Q.; Koshino, H.; Onose, J.; Yoshikawa, K.; Abe, N.; Takahashi, S. *Org. Lett.*, **2007**, *9*, 4131-4134.

(25) Tsuji, Y.; Morisaki, Y.; Chujo, Y. *Polym. Chem.*, **2013**, *4*, 5361-5367.

(26) COSMO-V1.61- software for the CCD Detector Systems for Determining Data Collection Parameters, Bruker axs, Madison, WI, 2000.

(27) Software for the Integration of CCD Detector System Bruker Analytical X-ray Systems, Bruker axs, Madison, WI (after 2013).

(28) Krause, L.; Hersbt-Irmer, R.; Sheldrick, G. M.; Stalke, D., *J. Appl. Cryst.*, **2015**, *48*.

(29) Sheldrick, G. M., *Acta. Cryst.* **2015**, *A71*, 3-8.

(30) Sheldrick, G. M., *Acta. Cryst.* **2008**, *A64*, 339-341.

(31) Dolomanov, O. V.; Bourhis, L. J.; Gildea, R. J.; Howard, J. A. K.; Puschmann, H., *J. Appl. Cryst.*, **2008**, *42*, 339-341.

(32) Bain, G. A.; Berry, J. F. *J. Chem. Educ.* **2008**, *85*, 532-536.

(33) Díaz-Torres, R.; Alvarez, S. *Dalton Trans.*, **2011**, *40*, 10742.

(34) Huang, N.; Ding, X.; Kim, J.; Ihee, H.; Jiang, D. *Angew. Chem. Int. Ed.* **2015**, *54*, 8704.

(35) Borgias, B. A.; Barclay, S. J.; Raymond, K. N. *J. Coord. Chem.* **1986**, *15*, 109.

(36) Pierpont, C. G.; Attia, A. S. *Collect. Czech. Chem. Commun.* **2001**, *66*, 33.

(37) Pierpont, C. G.; Lange, C. W. *Prog. Inorg. Chem.* **1994**, *41*, 331.

(38) Pierpont, C. G.; Buchanan, R. M. *Coord. Chem. Rev.* **1981**, *38*, 45.

(39) Lange, C. W.; Conklin, B. J.; Pierpont, C. G. *Inorg. Chem.* **1994**, *33*, 1276-1283.

(40) Fehir, Jr., R. J. Ph. D. Dissertation. Department of Chemistry, Michigan State University, East Lansing, MI, 2009.

(41) Schrauben, J. N.; Guo, D.; McCracken, J. L.; McCusker, J. K. *Inorganica Chimica Acta*, **2008**, *361*, 3539-3547.

(42) Deligiannakis, Y.; Louloudi, M.; Hadjiliadis, N. *Coord. Chem. Rev.* **2000**, *204*, 1.

(43) McCracken, J. L. In *Handbook of Electron Spin Resonance*; Poole, J., C. P., Farach, H. A., Eds.; Springer-Verlag: New York, 1999; Vol. 2, p 69.

(44) Piekara-Sady, L.; Kispert, L. D. *Handbook of Electron Spin Resonance.* AIP Press: New York, 1994; Vol. 1, p 311-357.

(45) Damrauer, N. H.; Weldon, B. T.; McCusker, J. K. *J. Phys. Chem. A* **1998**, *102*, 3382.

(46) Damrauer, N. H.; Boussie, T. R.; Devenney, M.; McCusker, J. K. *J. Chem. Soc.* **1997**, *119*, 8253.

(47) Atkins, P. W. *Molecular Quantum Mechanics*; Oxford University Press: New York, NY, 1988; pp 285.

Chapter 5. Thermodynamics of Heisenberg Spin Exchange Coupling Reflected on Electrochemical Properties: Comparison of Chromium (III) and Gallium (III) Dimeric Complexes

5.1 Introduction

Metalloproteins have been intensively researched for decades on the spectroscopic and magnetic properties on how exchange coupling affects the electronic structures, chemical reactivity, and biological functions.[1-6] Many metalloproteins contain one or more paramagnetic metal ions in their active sites. For those systems with two or more paramagnetic center, the spin exchange interaction can be an important phenomenon to affect their electronic structure, optical, electrochemical properties, and even biological function.

The studies by Bertrand and Gayda[7] on rubredoxin and ferredoxin show a shift of the redox potential of $Fe^{2+/3+}$ in superexchange-coupled ferredoxin [2Fe-2S] is generally c.a. 100 mV more negative than the non-coupled rubredoxin (Fig. 5.1). Bertrand and Gayda's studies are the first experimental evidence proposing the hypothesis of Heisenberg spin exchange affecting the electrochemical properties of a biological system. Similar phenomenon was observed on the electrochemical properties of $[Cr_2(tren)_2(CA)]^{n+}$ reported by Dr. Guo in our group.[8] Spin exchange-coupled $[Cr_2(tren)_2(CA)]^{n+}$ shows a larger potential separation, ΔE_{echem}, compared with the non-coupled $[Ga_2(tren)_2(CA)]^{n+}$. The larger ΔE_{echem} reflects the greater stability of $[Cr_2(tren)_2(CA)]^{n+}$, which suggests the spin exchange interaction introduces an added thermodynamic stabilization.

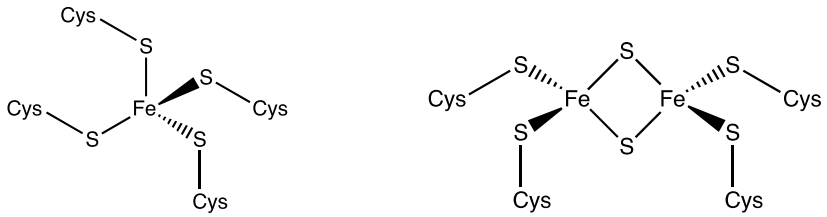

Figure 5.1. The structural representation of protein cluster rubredoxin (left) and ferredoxin (right) active sites.

To further examine the effect of the thermodynamic stabilization by spin exchange interaction and establish the correlation between electrochemical and magnetic behaviors, cyclic voltammetry measurements were performed on Cr(III)-Cr(III) and Ga(III)-Ga(III) semiquinoidal complexes.

5.2 Electronic Absorption Spectroscopy of Chromium(III) and Gallium(III) Dimeric Complexes

General. Electronic absorption spectra were measured using a Varian Cary 50 UV-vis spectrophotometer for all $[Ga_2(tren)_2(L^{cat,cat})](BPh_4)_2$ at a spectral resolution of ≤ 1.5 nm. The high-resolution spectra of $[Ga_2(tren)_2(L^{sq,cat})](BPh_4)(BF_4)$ were recorded on a Perkin-Elmer Lambda 1050 UV-vis/NIR spectrophotometer at a spectral resolution of 0.2 nm. Data were obtained on samples dissolved in MeCN, which had been degassed, dried over neutral alumina, and stored under inert atmosphere. All solutions were prepared in a N_2-flushed drybox in 1 cm pathlength air-tight optical cells.

5.3 Electrochemistry Studies of Chromium(III) and Gallium(III) Dimeric Complexes

5.3.1 Experimental Sections

Electrochemical measurements were collected using CH Instruments CH620D electrochemical analyzer to determine the $E_{1/2}$ for the redox properties of $[M_2(tren)_2(L^{cat,cat})](BPh_4)_2$, M = Cr(III) or Ga(III), in an argon-filled drybox. Solutions of the compounds were prepared in degassed and distilled CH_3CN or DMF containing NBu_4PF_6 (ca. 0.1 M) as the supporting electrolyte. The NBu_4PF_6 salts were crystallized twice in hot EtOH before use.

A standard three-electrode setup[9] was used with a platinum or glassy carbon working electrode, a platinum wire counter electrode, and an Ag wire pseudo-reference electrode.[10] All measurements were conducted inside an Ar-purged glovebox. Data were acquired by cyclic voltammetry (CV) at a scan rate of 100 mV/s, and the differential pulse voltammetry (DPV) data were collected at a scan rate of 20 mV/s with a pulse width of 50 mV. After data collection, ferrocene ($Fc^{+/0}$)[11,12] or decamethylferrocene ($DmFc^{+/0}$),[13,14] depending on where the redox potentials lie for the specific compounds, was added to subsequent solution as internal reference for reported potentials and the reversibility of the compounds. $E_{1/2}$ values obtained both from CV and DPV (Fig. 5.2) are comparable: the reversibility of the redox couples was based on the data from CV, and the reported redox potentials were obtained from the DPV peak values.[15]

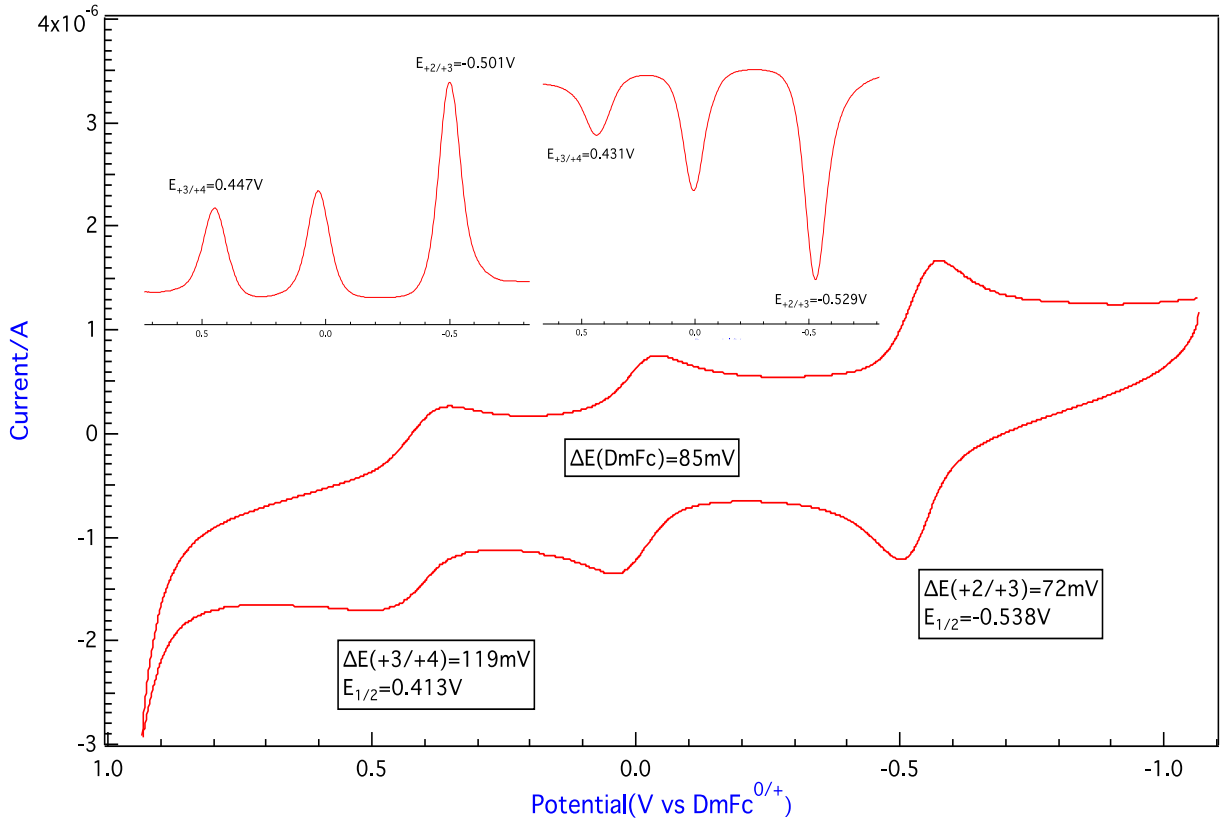

Figure 5.2. The cyclic voltammogram of $[Cr_2(tren)_2(DHBQ^{cat,cat})](BPh_4)_2$ in MeCN with 1.0 M $TBAPF_6$ as supporting electrolyte. All potentials are referenced to the $DmFc^{+/0}$ couple ($E_{1/2}$ =0 V in MeCN), and the inserts show the DPV traces.

5.3.2 Electrochemical Properties of $[M_2(tren)_2(L)]^{n+}$ ($M = Ga^{3+}$ or Cr^{3+}).

In order to examine the thermodynamic stabilization induced by spin exchange interaction, the cyclic voltammetry electrochemical data of $[Cr_2(tren)_2(L)]^{n+}$ and $[Ga_2(tren)_2(L)]^{n+}$ were collected and compared for the effects of thermodynamic stabilization induced by spin exchange interaction. Decamethylferrocene was used as internal reference for most of our bimetallic complexes, because the potential window of ferrocene, the most commonly used internal reference, overlaps with one of the redox traces in all dichromium (III)-quinoidal complexes, and the halogenated digallium (III) analogues, except for $[Ga_2(tren)_2(PhA)]^{n+}$ and $[Cr_2(tren)_2(NAT)]^{n+}$. Thus, data are reported as potential vs the $DmFc^{+/0}$ coupled.

The potential window of DmFc slightly interferes with the redox trace in $[Ga_2(tren)_2(PhA)]^{n+}$, and two separate CVs were collected with $DmFc^{+/0}$ (see Fig. 5.24 in Appendix) and $Fc^{+/0}$ (Fig. 5.3), respectively, for accurate determination of redox reversibility. The electrochemical data is still reported as V vs $DmFc^{+/0}$ in order to compare data among the entire series of complexes. To ensure the validity and consistency of reported potential with internal references, another CV was collected with the presence of both DmFc and Fc (see Fig. 5.25 in Appendix).

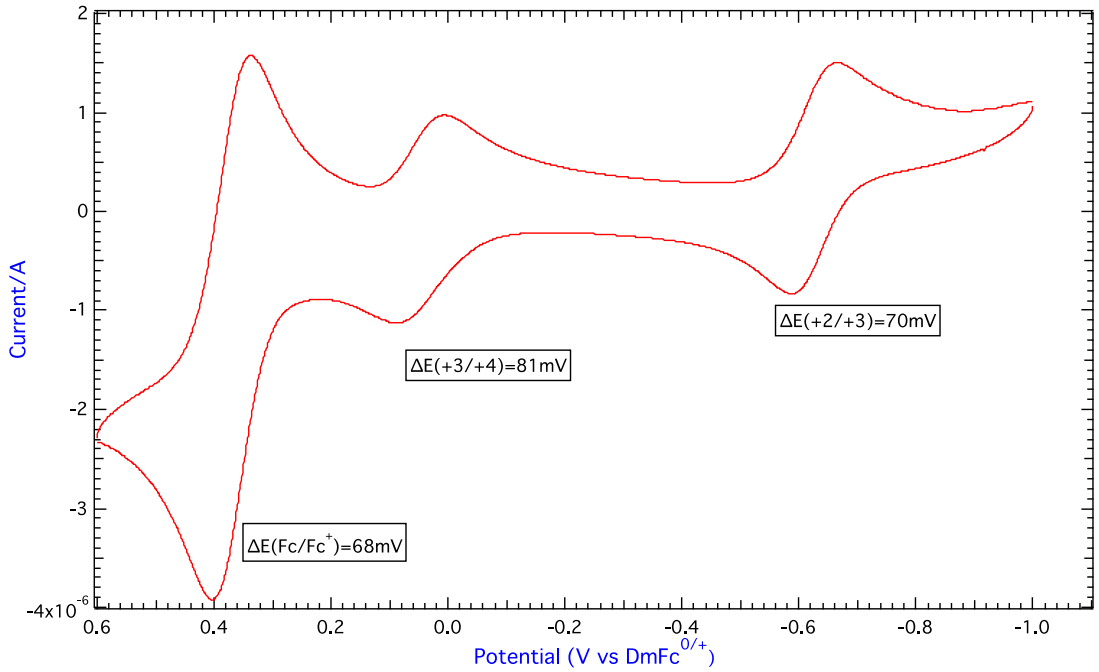

Figure 5.3. The cyclic voltammogram of $[Ga_2(tren)_2(PhA^{cat,cat})](BPh_4)_2$ in MeCN with 1.0 M $TBAPF_6$ as supporting electrolyte. The redox potential of ferrocene is at 0.324V.

Pt working electrodes were generally employed for most of the CV measurements, but a glassy carbon was used for the data collection of $[Cr_2(tren)_2(NMe_2\text{-}PhA)]^{n+}$. Some weird features were observed for the CV of $[Cr_2(tren)_2(NMe_2\text{-}PhA)]^{n+}$ (Fig. 5.4) with a Pt working electrode at more oxidative potential, > 0.5 V vs $DmFc^{+/0}$, and these features may correspond to the formation of solvento species. Pt is a catalytic and electrocatalytic material, so it might have a more reactive surface.[17] It has been reported that N,N-dimethylaniline can react with tetracyanoethylene to produce N,N-dimethyl-4-tricyanovinylaniline and HCN.[16] Since the measurement was conducted in MeCN to ensure consistency for data comparison, similar reaction is predicted to happen, and one of the possible reactions is shown in Fig. 5.6. The CV data was recollected for this system with a glassy carbon working electrode, because glassy carbon has slower electron transfer kinetics for most inner sphere processes,[18] so it can prevent overpotential and electrochemical side product deposit on the surface. As shown in Fig. 5.5,

weird electrochemistry happened at more positive potential and potentially appeared as solution impurities, so the use of glassy carbon may prevent the side products electrochemical features from reflecting on the CV traces.

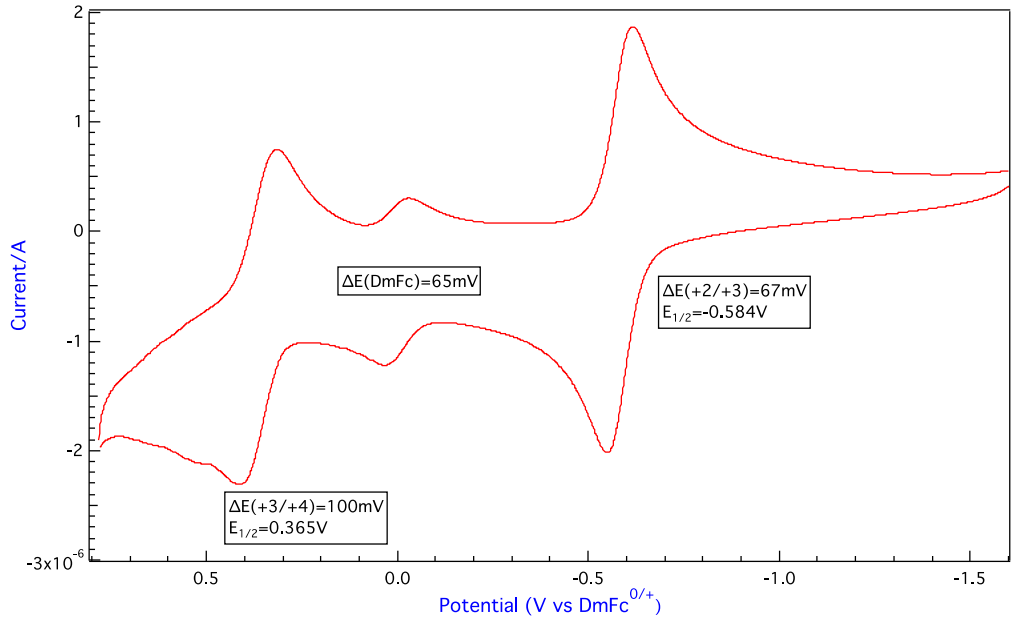

Figure 5.4. The cyclic voltammogram of $[Cr_2(tren)_2(NMe_2PhA^{cat,cat})](BPh_4)_2$ in MeCN with 1.0 M $TBAPF_6$ as supporting electrolyte and Pt working electrode.

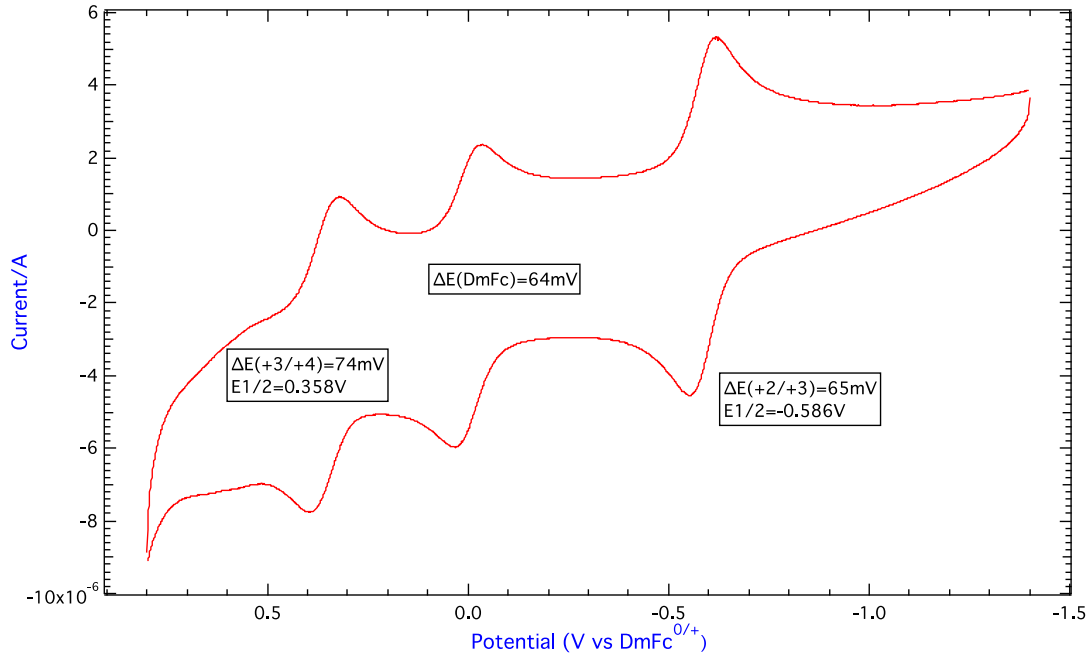

Figure 5.5. The cyclic voltammogram of $[Cr_2(tren)_2(NMe_2\text{-}PhA^{cat,cat})](BPh_4)_2$ in MeCN with 1.0 M $TBAPF_6$ as supporting electrolyte and glassy carbon working electrode.

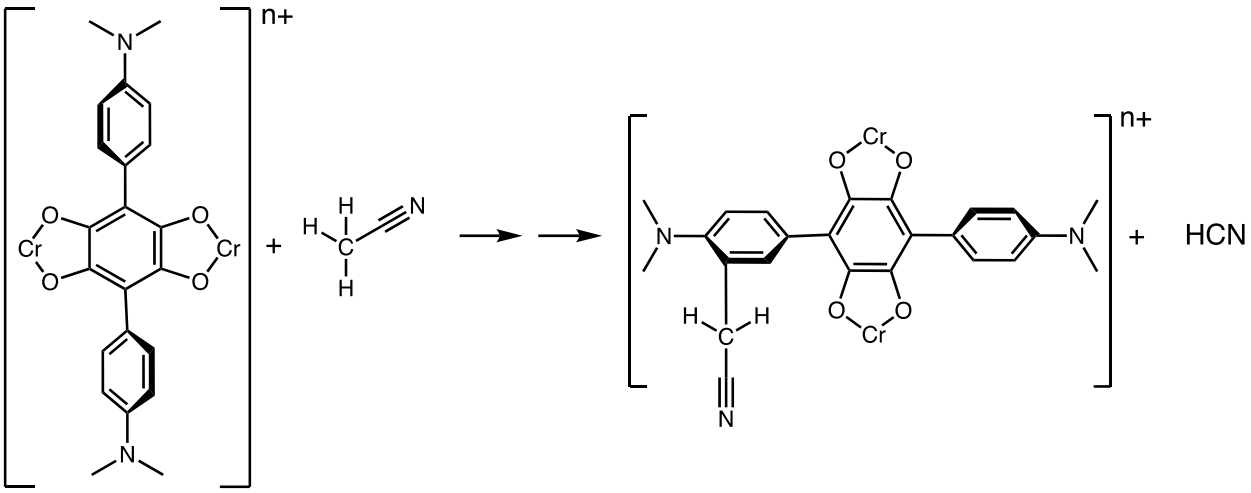

Figure 5.6. Possible reaction of $[Cr_2(tren)_2(NMe_2\text{-}PhA)]^{n+}$ with MeCN to produce HCN and an acetonitrilo-coordinated complex.

The cyclic voltammogram (Fig. 5.5) collected in a set-up with a glassy carbon working electrode exhibits less electrochemical features of side products beyond 0.5 V vs $DmFc^{+/0}$. It might be not possible to completely eliminate the electrochemical feature if it is caused by the solvento-species. Inert solvents, e.g. dichloromethane, can be used to see if it can eliminate the production of side product; however, the solubility of the complex raises a concern of switching solvent to DCM.

The quasi-reversible process is indicative of the instability of $[M_2(tren)_2(L^{sq,sq})]^{4+}$. Upon oxidation, the preferred resonance of the bridging ligand is $(L^{cat,q})^{2-}$ instead of $(L^{sq,q})^{2-}$ (Fig. 5.7). This leads to the decomposition of the bimetallic dimer resulting in a monomer, which is detected by ESI-MS as a major byproduct shown in Chapter 3 and 4. CVs were collected with various scan rate ranging from 50 mV/s to 400 mV/s (Fig. 5.25 in Appendix). At fast scan rate, it showed better reversibility of $[M_2(tren)_2(L)]^{3+/4+}$; at slow scan rate, the intensity of the peak on the reverse scan diminished. The reason could be that the slow scan rate allowed sufficient time for the formation of the monomer. Once the production of the monomer happens, this is a direct

result of the dimeric complex decomposition. The deformation of the peak on the reverse scan at slow scan rate indicates this redox process is chemically irreversible.

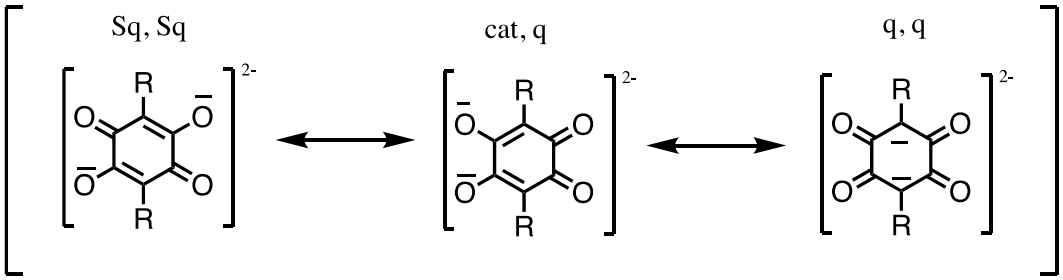

Figure 5.7. Resonance structures of dianionic anilate bridging ligand.

In $[Cr_2(tren)_2(NAT)]^{n+}$, only one redox potential with $E_{1/2}$ = 0.057 V vs $DmFc^{+/0}$ was observed (Fig. 5.8), which suggests only one electron redox reaction occured under applied potential. Two possible rationales are rised about the identity of this complex: (1) this is the redox reaction of the monomeric version, 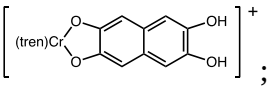

; (2) $[Cr_2(tren)_2(NAT^{sq,cat})]^{3+}$ does not exhibit electrochemical properties at more positive potential. Compared with the other Cr(III) and Ga(III) complexes in the series, $E_{1/2}^{+2/+3}$ generally occur at more negative potentials, but the redox potential observed here is more positive. The change of molecular composition may reflect on its electrochemical properties. Thus, the directionality of potential energy required is not enough to predict the identity of this complex. All three charged species, i.e. $[M]^{2+}$, $[M]^{3+}$, and [monomer]$^{+}$, were detected by ESI-MS and reported in Chapter 3. Unfortunately, the experimental evidence we have is inconclusive. To rationalize the CV data observed here, a better understanding of the redox and resonance properties of the deprotonated 2,3,6,7-tetraoxonaphthalene is necessary.

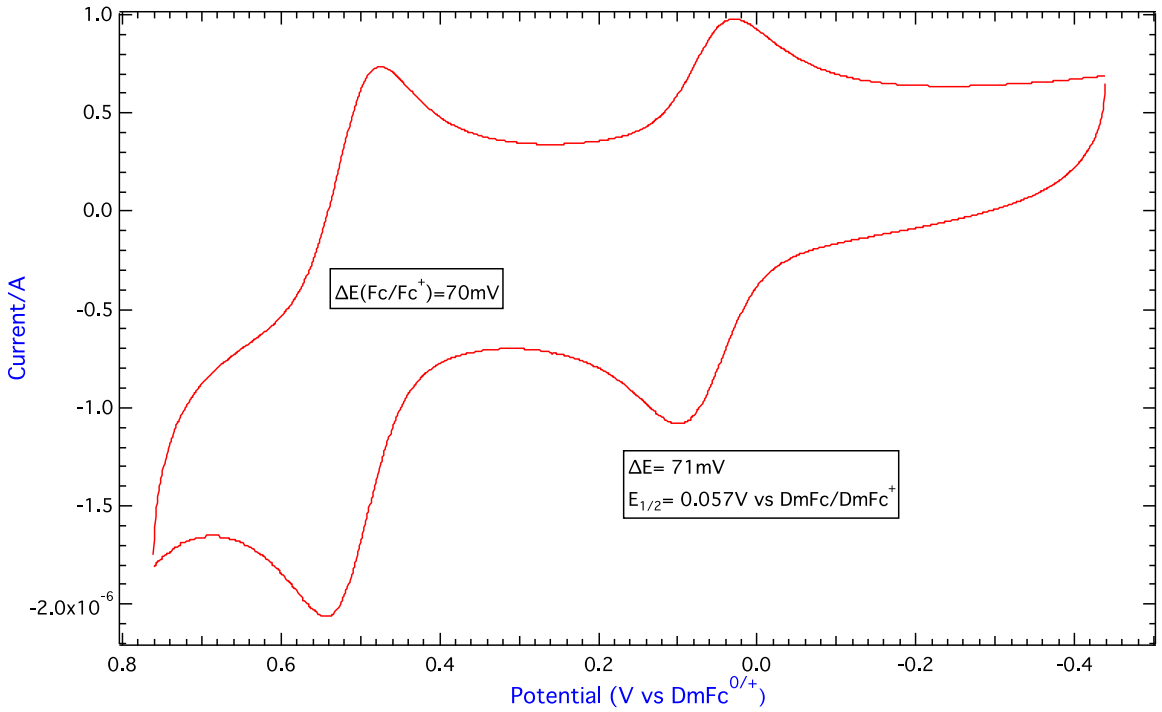

Figure 5.8. The cyclic voltammogram of $[Cr_2(tren)_2(NAT^{cat,cat})](BPh_4)_2$ in MeCN with 1.0 M $TBAPF_6$ as supporting electrolyte with $Fc^{+/0}$ as internal reference. The reported potential is referenced to DmFc couple at 0V vs $DmFc^{+/0}$.

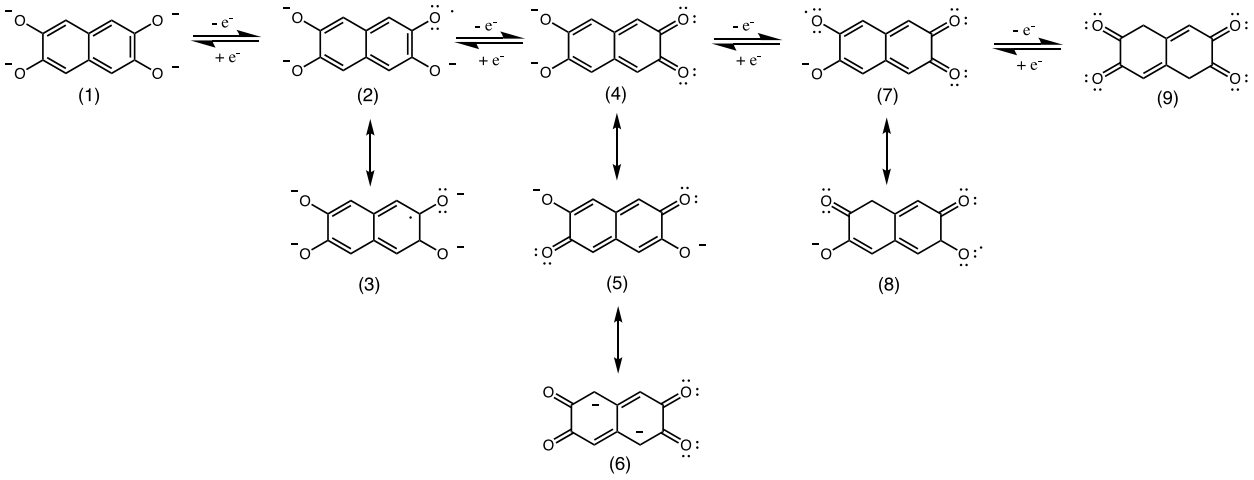

Figure 5.9. Multiple possible chelating forms of deprotonated 2,3,6,7-tetraoxonaphthalene undergoing one-electron redox reactions.

As a highly conjugated system, electrons are more delocalized within the naphthalene rings (Fig. 5.9) with decreased charge density on the interacting oxygens, so it makes 2,3,6,7-

tetraoxonaphthalene a weaker Lewis base. This implies that the formation of dichromium complex is not as favorable resulting in a less stable system. Upon oxidation, $[Cr_2(tren)_2(NAT^{sq,cat})]^{3+}$ may quickly decompose into the monomer without the formation of $[Cr_2(tren)_2(NAT^{sq,sq})]^{4+}$ intermediate. The detection of both $[M]^{2+}$ and $[M]^{3+}$ also proves the possible occurrence of the redox potential between them. At this point, we cannot assert the mechanism of this redox reaction, but we incline to proposed the redox trace is indicative of $[Cr_2(tren)_2(NAT)]^{2+/3+}$ process.

No reversible redox process was observed for $[Cr_2(tren)_2(AnT)]^{n+}$, and the redox potential in DPV traces move as the number of sweep increases (Fig. 5.10). The unsuccessful synthesis of $[Cr_2(tren)_2(AnT^{sq,cat})](BPh_4)_2(BF_4)$ agrees with the electrochemical data collected experimentally, that the formation of $[M]^{3+}$ is unfavorable due to the preferred resonance structure of $[AnT]^{3-}$.

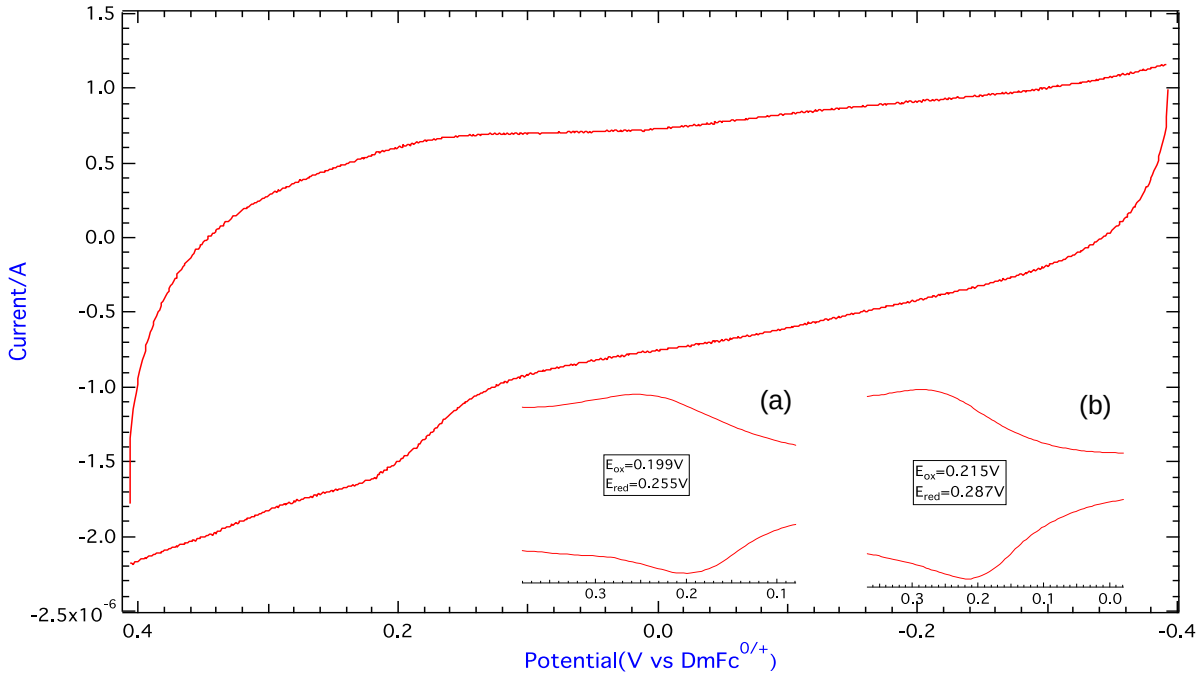

Figure 5.10. The cyclic voltammogram of $[Cr_2(tren)_2(AnT^{cat,cat})](BPh_4)_2$ in MeCN with 1.0 M $TBAPF_6$ as supporting electrolyte with $Fc^{+/0}$ as internal reference. The reported potential is referenced to DmFc couple at 0V vs $DmFc^{+/0}$. DPV shows in the inserts collected at the 1st sweep (a), and 2nd sweep (b).

Electrochemical reversibility describes the rate of electron transfer, and a reversible electrochemical reaction needs to meet four requirements.[19] According to the Nernst equation (Eq. 5.1) and the Gibbs Free Energy equilibrium constant, (1) the voltage separation between the current peak is $\Delta E = E_p^a - E_p^c = \frac{59\,mV}{n}$ in aqueous solution at 25 ˚C, where E_p^a is the anodic peak potential, E_p^c is the cathodic peak potential, and n is the number of electrons, and (2) the position of peak potential, E_p^a and E_p^c, will not change as a function of scan rate; (3) the ratio of peak current is $\left|\frac{i_p^a}{i_p^c}\right| = 1$, where i_p^a is the andodic peak current, and i_p^c is the cathodic peak current; (4) the peak current is proportional to the square root of scan rate.[19]

$$E = E^\circ - \frac{0.059V}{n}\log_{10}Q = E^\circ - \frac{0.059V}{n}\log_{10}\frac{[Ox]}{[Red]}, \text{ at } 25^\circ\text{C} \qquad (5.1)$$

where E is the applied potential, E˚ is the standard cell potential, and Q is the reaction quotation between the concentration of oxidized and reduced species at the electrode surface. Since the electrochemical measurements were performed in nonaqueous solution, ΔE will not be equal to 59 mV in organic solvent with lower dielectric constants. Therefore, $Fc^{+/0}$ and $DmFc^{+/0}$ couples are also used as a reference for electrochemical reversibility because of their well-studied electrochemical reversible properties. In reversible reactions, the electron transfer rate is greater than the mass transfer rate, so the peak potential is independent of the applied scan rate during CV measurement.[20] In quasireversible reactions, the electron transfer rate and mass transfer rate are similar; therefore, the peak potential increases as the scan rate increases.[20]

The total current of quasireversible redox processes is relatively lower than the one of reversible processes because of the thickness of the diffusion layer in solution. The diffusion layer is thick at fast scan rate, and thinner at slow scan rate. As illustrated above, the reversibility of an electrochemical process reflects the competition between the electrode

kinetics and mass transport, so faster scan rate will encourage electrochemical irreversibility. However, the $[Cr_2(tren)_2(CA)]^{3+/4+}$ redox trace (Fig. 5.11) shows more electrochemical reversibility with ΔE closer to ΔE ($DmFc^{0/+}$) at higher scan rate, which implies the formation of $[Cr(tren)(CA^{cat,q})]^{+}$ at more positive potentials and the decomposition of the dichromium(III) dimer.

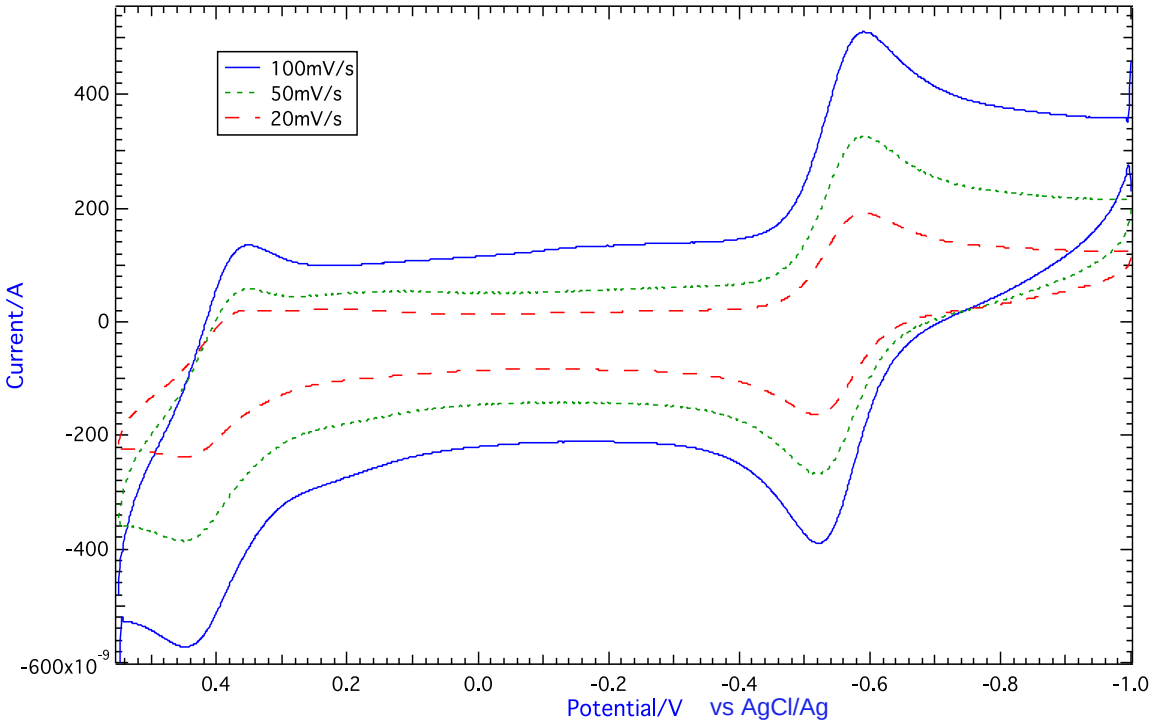

Figure 5.11. Cyclic voltammograms of the $[Cr_2(tren)_2(CA^{cat,cat})](BPh_4)_2$ in MeCN with 1.0 M $TBAPF_6$ collected at 20 mV/s (red dash), 50 mV/s (green dash), and 100 mV/s (blue solid).

The redox trace of $[M_2(tren)_2(L)]^{2+/3+}$ observed at negative potentials matches the characteristics of reversibility, whereas the trace of $[M_2(tren)_2(L)]^{3+/4+}$ shows quasireversible characteristics as shown in the following Eq. 5.2 and 5.3:

$$[M_2(tren)_2(L^{cat,cat})]^{2+} \underset{+\,e^-}{\overset{-\,e^-}{\rightleftharpoons}} [M_2(tren)_2(L^{sq,cat})]^{3+} \qquad E_{1/2}{}^{+2/+3} \quad (5.2)$$

$$[M_2(tren)_2(L^{sq,cat})]^{3+} \underset{+\,e^-}{\overset{-\,e^-}{\rightleftharpoons}} [M_2(tren)_2(L^{sq,sq})]^{4+} \qquad E_{1/2}{}^{+3/+4} \quad (5.3)$$

As shown in Fig 5.12, ΔE_{echem} (Eq. 5.4) of $[Cr_2(tren)_2(IA)]^{n+}$ is smaller than the one of $[Ga_2(tren)_2(IA)]^{n+}$. ΔE_{echem} of the Me_2AnT-Cr(III) complex is the smallest among all the other Cr(III) analogues.

$$\Delta E_{echem} = E_{1/2}{}^{+3/+4} - E_{1/2}{}^{+2/+3} \quad (5.4)$$

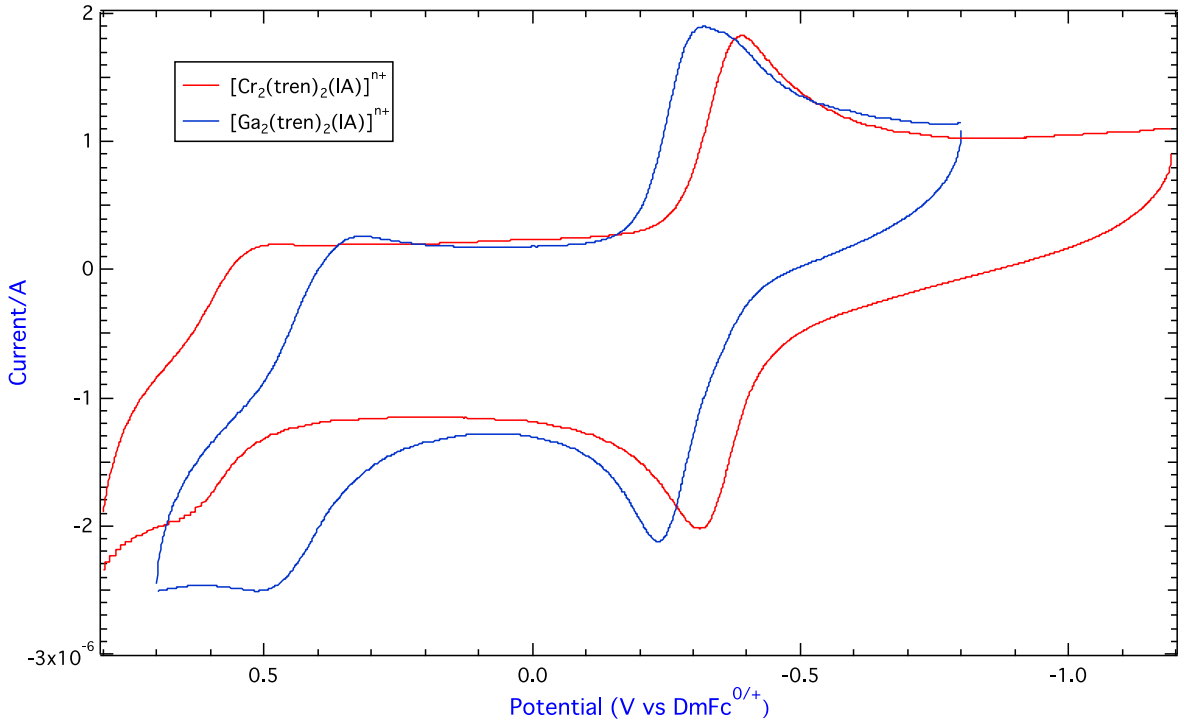

Figure 5.12. Cyclic voltammograms of $[Cr_2(tren)_2(IA^{cat,cat})](BPh_4)_2$ (red) and $[Ga_2(tren)_2(IA)]^{n+}$ (blue) in MeCN with 1.0 M $TBAPF_6$ as supporting electrolyte. All potentials are referenced to the $DmFc^{+/0}$ couple ($E_{1/2}$ =0 V in MeCN), and Ag wire is the pseudoreference electrode.

The Heisenberg exchange interaction occurs within $[Cr_2(tren)_2(IA)]^{n+}$, whereas no intramolecular exchange coupling exists in $[Ga_2(tren)_2(IA)]^{n+}$. The larger ΔE_{echem} in the Cr analogue may be the prediction of thermodynamic stabilization induced by the exchange interaction, which will be further elaborated below along with comproportionation constant. This trend is generally observed throughout the entire series (Table 5.1), so it will be reasonable to believe this as a thermodynamic consequence of exchange interaction.

Table 5.1. Electrochemical Properties of $[M_2(tren)_2(L)]^{n+}$ (M = Ga^{3+} or Cr^{3+}).[a]

Bridging Ligand	M	+2/+3		+3/+4		ΔE_{echem} (V)[c]	ΔE(DmFc) (mV)[b]
		$E_{1/2}$ (V)	ΔE (mV)[b]	$E_{1/2}$ (V)	ΔE (mV)[b]		
H	Cr^{III}	-0.515	72	0.439	119	0.954	85
	Ga^{III}	-0.491	78	0.241	128	0.732	72
F	Cr^{III}	-0.253	68	0.705	112	0.958	65
	Ga^{III}	-0.206	80	0.402	184	0.608	74
Cl	Cr^{III}	-0.316	69	0.644	136	0.960	66
	Ga^{III}	-0.272	84	0.332	130	0.604	66
Br	Cr^{III}	-0.333	72	0.617	137	0.950	79
	Ga^{III}	-0.276	80	0.450	124	0.726	68
I	Cr^{III}	-0.348	80	0.594	115	0.942	74
	Ga^{III}	-0.308	86	0.396	140	0.704	78
Ph	Cr^{III}	-0.568	77	0.394	117	0.962	80
	Ga^{III}	-0.508	77	0.176	84	0.684	74
$N(Me)_2Ph$	Cr^{III}	-0.586	66	0.358	100	0.944	66
	Ga^{III}	n.a.	n.a.	n.a.	n.a.	n.a.	n.a.
NAT	Cr^{III}	0.057	71	n.a.	n.a.	n.a.	70 (vs $Fc^{0/+}$)[e]
	Ga^{III}	n.a.	n.a.	n.a.	n.a.	n.a.	n.a.
Me_2AnT	Cr^{III}	-0.19	60	0.503	103	0.693	63
	Ga^{III}	n.a.	n.a.	n.a.	n.a.	n.a.	n.a.

[a] All potentials are referenced to the decamethylferrocenium/decamethylferrocene couple ($E_{1/2}$ = 0V).
[b] $\Delta E = E_p^{anodic} - E_p^{cathodic}$. [c] $\Delta E_{echem} = E_{1/2}^{+3/+4} - E_{1/2}^{+2/+3}$. [d] n.a. indicates the complexes has either not been synthesized, or the redox potential was not detected. [e] electrochemical reversibility is referenced to $Fc^{0/+}$ because of the overlap potential window between the product and $DmFc^{0/+}$.

Due to the quasireversibility and the highly variable oxidative electrochemistry of $[M_2(tren)_2(L)]^{3+/4+}$, $\Delta E_{1/2}^{3+/4+}$ is only an estimation, so ΔE_{echem} calculated is also an estimation. Although the values of ΔE_{echem} is only an estimation of the thermodynamic stabilization, it can still be useful for analytical comparison among the substituted complexes to gauge the substituent effect on the electron delocalization. ΔE_{echem} of the $[Cr_2(tren)_2(Me_2\text{-}AnT)]^{n+}$ complex is the smallest among all the other Cr(III) analogues. This provides further experimental evidence to rationalize our hypothesis about the attenuation of exchange coupling by spin delocalization reflected both magnetically and computationally, since $[Cr_2(tren)_2(Me_2\text{-}AnT)]^{n+}$ complex should possess the weakest *J* (Fig. 5.13). Some may agree the slight shift of redox potentials may be the cause by the different metal centers. Ga(III) is a weaker Lewis acid than Cr(III), so its ability to attract electrons will be stronger, which may cause the redox potential of Ga(III) complexes more positive and easier to be reduced. If this is true for the prediction of metal redox potentials,

this trend should be applied for both redox traces in a complex. More positive potential is observed in the redox trace of $[Ga_2(tren)_2(L)]^{2+/3+}$, but the potential of $[Ga_2(tren)_2(L)]^{3+/4+}$ is more negative, which implies it is harder to be reduced. Thus, we predict that the larger potential separation of both redox potentials in the Cr(III) analogues are not a reflection of different metal centers.

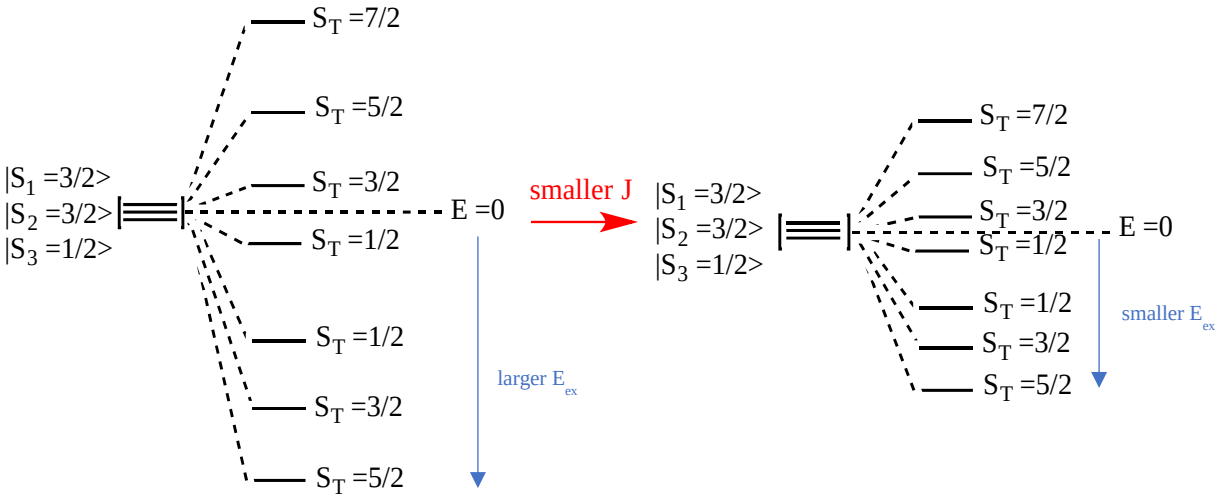

Figure 5.13. Energy level diagram for $[Cr_2(tren)_2(L^{sq,cat})]^{3+}$ with (left) stronger spin exchange interaction, larger *J*; (right) weaker spin exchange interaction, smaller *J*. The energy of the lowest energy spin state relative to the spin barycenter, E = 0 (i.e., the energy in the limit of no spin coupling) reflects the thermodynamic influence of spin exchange.

5.3.3 Thermodynamic Stabilization of Spin Exchange Interactions

As it has been previously discussed, the Heisenberg model predicts that the introduction of spin exchange results in the spin state with preferred orientation being stabilized, as illustrated in Fig. 5.14.[21,22] A net stabilization energy, ΔE_{ex}, is a thermodynamic consequence of spin exchange interaction.

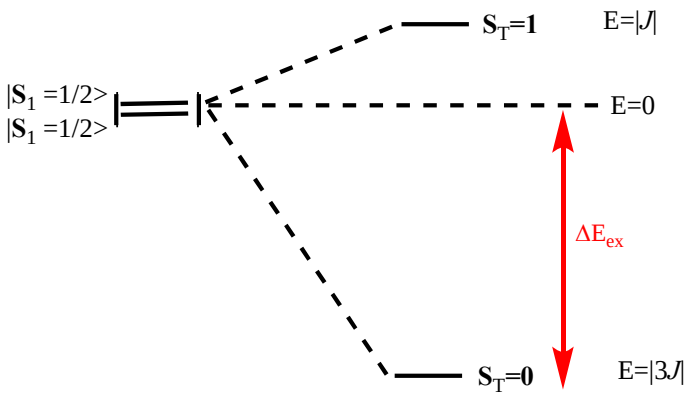

Figure 5.14. The spin ladder of a molecule with $\mathbf{S}_1 = \mathbf{S}_2 = ½$ based on the Heisenberg exchange Hamitonian. The red arrow indicates a net thermodynamic stabilization resulted from spin exchange coupling.

J values can be extrapolated with the Heisenberg exchange Hamiltonian from variable-temperature magnetic susceptibility measurements. This experimental method reflects the Boltzmann distribution across the spin states of the spin ladder of a magnetic system. Thus, it only provides information concerning the energy separations between the spin states relative to each other (Fig. 5.14).[23] The relative magnitude of ΔE_{ex} can be calculated by the eigenvalues generated from the Heisenberg Hamiltonian with *J* extrapolated from magnetic data. A measurement of the absolute energy of each spin-coupled state is necessary to quantify the thermodynamic consequence induced by the spin exchange interaction. In order to validate the net thermodynamic stabilization energy calculated from magnetic data, an independent experimental analysis is necessary. Electrochemical measurement may be a good choice in accordant to the phenomena observed in our series of dichromium(III) and digallium(III) complexes.

5.3.3.1 Comproportionation Free Energy

Comproportionation is a chemical reaction between two reactants with the same composition of elements with different oxidation states to form a product of another oxidation

state, which is commonly used to meausre the stability and charge transfer of mixed valence complexes.[21,22,24] Cyclic voltammetry has been developed and widely employed to evaluate the thermodynamic stability of mixed-valence (MV) complexes (Eq. 5.5).[25-27] The comproportionation constant, K_C, (Eq. 5.6) and the free energy of comproportionation constant, ΔG_C°, provide alternative means to determine the degree of electronic delocalization.

$$M^{(n-1)+}M^{(n-1)+} + M^{n+}M^{n+} \underset{}{\overset{K_c}{\rightleftharpoons}} 2\ M^{(n-1)+}M^{n} \tag{5.5}$$

$$\text{where } K_c = \frac{[M^{(n-1)}M^{n}]^2}{[M^{(n-1)}M^{(n-1)}][M^{n}M^{n}]} \tag{5.6}$$

In the studies of MV complexes, K_C reflects the stability of the mixed-valence form of the system relative to the other two isovalent species.

The bimetallic systems studied in this project are analogous to the MV complexes (Eq. 5.7). According to the EPR studies conducted previously in our group on $[Ga_2(tren)_2(CA^{sq,cat})](BPh_4)_2(BF_4)$, the observation of the triplet state suggests the presence of $[Ga_2(tren)_2(CA^{cat,cat})]^{2+}$ and $[Ga_2(tren)_2(CA^{sq,sq})]^{4+}$ formed by comproportionation.[28] The magnitude of K_C represents how strongly coupled the metal ion and the bridging ligand are (Eq. 5.8). Therefore, we attempt to use comproportionation constant, K_C, to analyze the electrochemical data and the free energy of our systems, since its magnitude reflects a thermodynamic stabilization inherent to the system.

$$M^{III}\text{-}L^{4-}\text{-}M^{III} + M^{III}\text{-}L^{2-}\text{-}M^{III} \underset{}{\overset{K_C}{\rightleftharpoons}} 2[M^{III}\text{-}L^{3-}\text{-}M^{III}] \tag{5.7}$$

$$\text{where } K_c = \frac{[M^{III}-L^{3-}M^{III}]^2}{[M^{III}-L^{2-}-M^{III}][M^{III}-L^{4-}-M^{III}]} \tag{5.8}$$

$$M^{III}\text{-}L^{2-}\text{-}M^{III} \underset{-\ e^-}{\overset{+\ e^-}{\rightleftharpoons}} M^{III}\text{-}L^{3-}\text{-}M^{III} \underset{-\ e^-}{\overset{+\ e^-}{\rightleftharpoons}} M^{III}\text{-}L^{4-}\text{-}M^{III} \qquad \Delta E_1,\ \Delta E_2 \tag{5.9}$$

The potential difference, $\Delta E = |\Delta E_1 - \Delta E_2|$, (Eq. 5.9) between the electrodes of a cell is a measure of the tendency for a reaction to occur. According to the van't Hoff equation and Gibb Free energy, ΔE correlates to the free energy of comproportionation (Eq. 5.10), ΔG_C, which also evaluates the strength of the exchange coupling between redox centers through the ligand bridge.[25] In this case, ΔG_C can be considered equivalent to ΔE_{ex}. In this regard, an electrochemical measurement for ΔE offers an experimental mean to determine the thermodynamic stabilization of a system.

$$\Delta G_C = -nF\Delta E = -2.303RT \log (K_C) \quad (5.10)$$

Between the two electrochemical waves in Fig. 5.12, the potential difference of $[Cr_2(tren)_2(IA)]^{n+}$ is larger than $[Ga_2(tren)_2(IA)]^{n+}$. Compared with $[Ga_2(tren)_2(IA)]^{n+}$, the redox potential of $[Cr_2(tren)_2(IA)]^{2+/3+}$ is more negative, and the one of $[Cr_2(tren)_2(IA)]^{3+/4+}$ is more positive. In other words, $[Cr_2(tren)_2(IA^{sq,cat})]^{3+}$ is harder to be oxidized and reduced at the same time. This observation reveals that there should be an intrinsic factor cause$[Cr_2(tren)_2(IA^{sq,cat})]^{3+}$ to be more stable than the Ga(III) analogue. This intrinsic factor is thought to be spin exchange interaction, because no exchange interaction presents within the noncoupled $[Ga_2(tren)_2(CA^{sq,cat})]^{3+}$ system.

Based on the electrochemical data for $[Cr_2(tren)_2(CA^{cat,cat})]^{2+}$, a net thermodynamic stabilization larger in magnitude is suggested to be induced by the direct exchange interaction between the Cr(III) ions and the $CA^{sq,cat}$ ligand. As mentioned above, ΔG_C can be calculated from redox potential difference (Eq. 5.7),[29] and it corresponds to the comproportionation constant, K_C, in accordance to van't Hoff equation in aqueous solution at 298 K (Eq. 5.10 and 5.11).[26]

$$K_C = 10^{\frac{|E_1 - E_2|}{0.059\,V}} = 10^{\frac{\Delta E}{0.059\,V}} \quad (5.11)$$

K_C >1 reflects higher stability of the semiquinone form of the system relative to the other two states as illustrated in Eq. 5.8. Exchange coupling inherent in $[Cr_2(tren)_2(CA^{sq,cat})]^{3+}$ is considered to be the contribution of the thermodynamic stabilization,[30] since the $CA^{sq,cat}$ species is subject to significant direct exchange interaction rather than the $CA^{sq,sq}$ and $CA^{cat,cat}$ forms of the diamagnetic bridge.

5.4 Extrapolation of Thermodynamic Stabilization Energies of Cr(III) Dimers from Magnetic Susceptibility Data by Referencing Ga(III) Analogues

The other intrinsic effects associated with the redox chemistry of the bridge must also be considered. This concept was also introduced for the study of mixed-valence (MV) complexes stating that ΔG_C could be divided into five intrinsic energetic components of the system.[25,31] In Eq. 5.9, ΔG_s is an entropic factor dealing with statistic distribution of comproportionation equilibrium, implying $K_c = 4$ for a symmetric system; [22,24] ΔG_e is the electrostatic force arising from the repulsion of two metal ions bridged by a ligand;[32] ΔG_i is an inductive factor dealing with bonding coordination due to metal-ligand interaction;[32] ΔG_r is the stabilziation energy of resonance exchange due to electron delocalization.[29] ΔG_{ex} term was added later for measuring a stabilizing influence introduced by exchange coupling, e.g. superexchange coupling in a MV complex.[25,26]

$$\Delta G_c = (\Delta G_s + \Delta G_e + \Delta G_i + \Delta G_r) + \Delta G_{ex} \qquad (5.9)$$

The breakdown of ΔG_c in MV complexes is modified and adopted into our systems. ΔG_C will be used to evaluate the thermodynamic stabilization arise from exchange interaction for all Cr(III) dimeric systems, the Ga(III) analogues will be used as a reference point for the electrochemical data acquired on the Cr(III) complex to eliminate other energetic factors. With the same oxidation state of the ligand and metal ion, ΔG_s and ΔG_e may be negligible. Since the

overall composition of these tetraoxolene bimetallic compounds are similar with ionic metal-ligand interaction, ΔG_r can also be canceled. Cr^{3+} and Ga^{3+} have similar charge-to-radius ratio and are both relatively redox-inert, and ΔG_i is considered to be eliminated by referencing the gallium complex. In this case, $\Delta K_{c,echem}$ (defined in Eq. 5.12) larger than 1 will reflects the added stabilization associated with the introduction of spin exchange upon substitution of Ga(III) by Cr(III) (the data is shown in Table 5.1 and 5.2).

$$\Delta K_C^{echem} = K_C/K_C^{Ga(III)Ga(III)} \quad (5.12)$$

ΔG_i relates to the bonding interaction and coordination between metal centers and the bridging ligand. Ga(III) is a d^{10} metal ion with fully occupied d-orbitals, but Cr(III) has only half-filled t_{2g} orbitals.

Table 5.2. Electrochemical and Magnetic Data for $[M_2(tren)_2(L)]^{n+}$ (M = Ga^{3+} or Cr^{3+}).[a]

Bridging Ligand	M	ΔE_{echem} (V)[a]	K_c[b] (x 10^{12})	$\Delta K_{c,echem}$[c] (x 10^3)	*J* (cm^{-1})	$\Delta K_{c,mag}$[d]
H	Cr^{3+}	0.954 ± 0.01	14800	5.8	-380	1486
	Ga^{3+}	0.732 ± 0.01	2.55	1	n.a.	n.a.
F	Cr^{3+}	0.958 ± 0.01	17300	856	-380	1486
	Ga^{3+}	0.608 ± 0.01	0.202	1	n.a.	n.a.
Cl	Cr^{3+}	0.960 ± 0.01	18800	1081	-430	3884
	Ga^{3+}	0.604 ± 0.01	0.173	1	n.a.	n.a.
Br	Cr^{3+}	0.950 ± 0.01	12600	6.3	-380	1486
	Ga^{3+}	0.726 ± 0.01	2.02	1	n.a.	n.a.
I	Cr^{3+}	0.942 ± 0.01	9250	10.8	-380	1486
	Ga^{3+}	0.704 ± 0.01	0.855	1	n.a.	n.a.
Ph	Cr^{3+}	0.962 ± 0.01	20200	51.5	-380	1486
	Ga^{3+}	0.684 ± 0.01	0.392	1	n.a.	n.a.

[a] $\Delta E_{echem} = E_{1/2}^{+3/+4} - E_{1/2}^{+2/+3}$. [b] see Eq. 5.8. [c] see Eq. 5.10. [d] see Eq. 5.11.

Electrochemical and K_C data obtained for Ga(III)-Ga(III) and Cr(III)-Cr(III) complexes are summarized in Table 5.2. There is an increase of 600-fold or more in the magnitude of K_C upon replacing Ga(III) for Cr(III) depending on the substituents. Therefore, a significant thermodynamic stabilization is seen for the exchange-coupled complex compared with the non-

coupled one. The various elevation of $\Delta K_{c,echem}$ also implies the substituent effect on the strength of spin exchange.

Variable-temperature magnetic susceptibility measurements have been performed on these compounds (detail discussion see Chapter 3). ΔE_{ex}, a net thermodynamic stabilization energy, is treated as free energy change caused by intramolecular exchange interaction at room temperature. Then, the equilibrium constant can be calculated with the estimated *J* value for the calculation of $\Delta K_{c,mag}$ (Eq. 5.11).

$$\Delta K_{c,mag} = \exp(-\Delta E_{ex}/RT) \tag{5.11}$$

where ΔE_{ex} corresponds to the ground spin state $|5/2, 3>$, $4J$, generated by the Heisenberg spin Hamiltonian (Fig. 5.14). If the $\Delta K_{c,mag}$ with $\Delta K_{c,echem}$ obtained for a particular system agree with each other, a thermodynamic stabilization of spin states is likely to be induced by exchange coupling, which will be proved to be effectively measured by cyclic voltammetry.

The magnitude of $\Delta K_{c,echem}$ is much larger than $\Delta K_{c,mag}$ even after error propagations. As discussed above, the thermodynamic stabilization observed in electrochemical data reflects thermodynamic free energy, which is a sum of various intrinsic energetic contributions within a spin-coupled system mentioned above. Nevertheless, the thermodynamic stabilization observed in magnetic data is solely contributed from the magnetic spin exchange. Therefore, simply using the Ga(III)-Ga(III) compound as reference may not be able to eliminate both ΔG_i and ΔG_s terms as illustrated in Eq. 5.9. With ΔG_i remaining in ΔG_C, the free energy of comproportionation cannot be directly used to evaluate the thermodynamic consequence of exchange interaction.

There are two possible way to determine and evaluate the strength of ligands and metal ions coordination in Cr(III)-Cr(III) dimer. One way is to conduct infrared or Raman spectroscopy and compare the stretching mode of the metal-oxygen interaction; the other way is to determine

the metal-oxygen bond length by x-ray crystallography subject to metal ion radius to eliminate the uncertainty. The latter option is more challenging because all attempts of growing single x-ray crystal structure of $[M_2(tren)_2(L^{sq,cat})](BPh_4)_2(BF_4)$ have failed. Since x-ray structures were determined for various assemblies of $[M_2(tren)_2(L^{cat,cat})](BPh_4)_2$, the M-O bond distances can be treated as a reference to provide some insight about the differences between Cr-O and Ga-O bonding nature (see Chapter 3 Table 3.3 and 3.4, and Chapter 4 Table 4.2). The range of Ga-O bond length is 1.91 – 1.92 Å, while Cr-O can range from 1.90 – 1.95 Å. This implies their metal-ligand interactions are different with Cr (III) being a stronger Lewis acid.

Even though the entropic term, ΔG_s, was initially considered as negligible, the entropic contribution of Cr (III) and Ga (III), d^3 vs d^{10}, may not be comparable. For a d^5 spin-crossover system, there are less entropic contributions in the high spin state,[33] so it is more stabilized than the low spin state and it undergoes a spin-transition at lower temperature.[34] If the similar principle is applied to compare the entropy of d^3 and d^{10}, d^3 is more entropically favorable with less electron-electron repulsion. Unfortunately, various contradictory theories about the entropy of d^{10} electron configuration are reported in literature, it is not certain either d^3 or d^{10} has more entropic contribution.

In addition to that, the magnetic data were all collected in solid state, and the electrochemical measurements were performed in solution. Interaction between solvent molecules and the spin-exchanged compounds were not considered based on our comparison. Liquid SQUID variable-temperature magnetic susceptibility should be measured to obtain magnetic data that is comparable with the electrochemical data.

5.5 Concluding Comments

In this chapter, our main motive is to seek for analytical methodology to establish the thermodynamic correlation seen in both electrochemical and magnetic behaviors. UV-vis spectroscopy is useful tool to facilitate our understanding of electronic transitions arising by spin exchange interaction. The absorption features observed in our systems match the one reported by Dr. Dong Guo, who previously reported a thorough study and interpretation on $[MM'(tren)_2(CA)]^{n+}$.[8]

The comparison of electrochemical data collected for both Cr (III) and Ga (III) dimers reveals thermodynamic stabilization induced by spin exchange interaction, since Cr (III) complexes generally exhibit larger ΔE_{echem}. Spin delocalization effects also reflect on the electrochemical data with $[Cr_2(tren)_2(Me_2\text{-}AnT)]^{n+}$ possessing the smallest ΔE_{echem}. The spin polarization effect is not pronounced within the halogen series, no drastic difference is observed. Unfortunately, the CV trace of $[Cr_2(tren)_2(NAT^{cat,cat})](BPh_4)_2$ only show one-electron redox reaction, so ΔE_{echem} can be calculated for comparison. Similar situation is observed in $[Cr_2(tren)_2(AnT^{cat,cat})](BPh_4)_2$. If we want to continue use the horizontal extension of conjugated series as an avenue for the study of substituent effects, EDG need to be installed on the 2,3,6,7-tetrahydroxynaphthalene to stabilized the system. ΔE_{echem} calculated is only an estimation due to the quasireversibility of $[M_2(tren)_2(L)]^{3+/4+}$, fast-scan cyclic voltammetry measurements with microelectrodes will be useful to learn about the nature of this quasireversible redox process in the future.

The concept of comproportionation free energy and constant can be modified and applied in our systems as an analytical method to compare electrochemical and magnetic data for evaluating thermodynamic stabilization. However, the K_c extracted from electrochemical data

contains energetic components arising from various terms not just from spin exchange contribution. A more effective way needs to be developed to eliminate the other intrinsic components for a valid comparison. The data comparison also ignores the solvent-molecule interaction in solution by simply comparing solution-phase electrochemical data and solid-state magnetic data. Therefore, liquid SQUID measurement should be performed to account for the solvent effect.

Overall, we have established a rough thermodynamic correlation between electrochemical and magnetic behaviors. In order to use electrochemical measurement as a quantitative analysis to assess thermodynamic consequence induced by spin exchange interaction, more unknown properties need to be understood with more experimental procedures.

APPENDIX

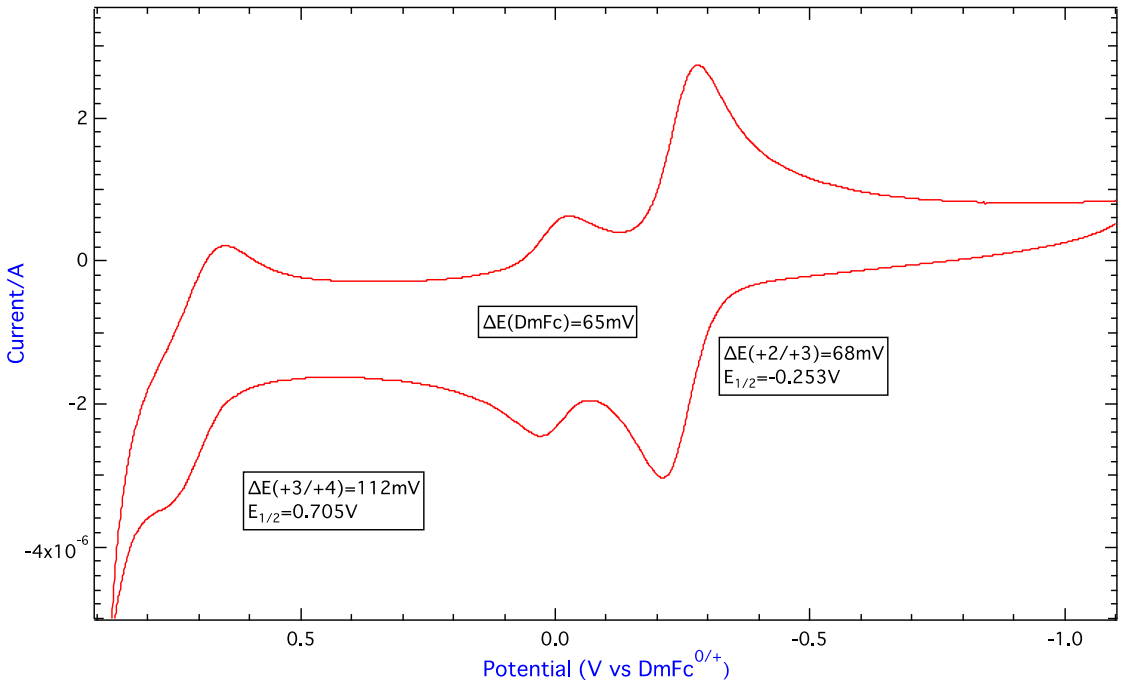

Figure 5.15. CV of $[Cr_2(tren)_2(FA)](BPh_4)_2$ in MeCN with 1.0 M $TBAPF_6$ as supporting electrolyte. All potentials are referenced to the $DmFc^{+/0}$ couple.

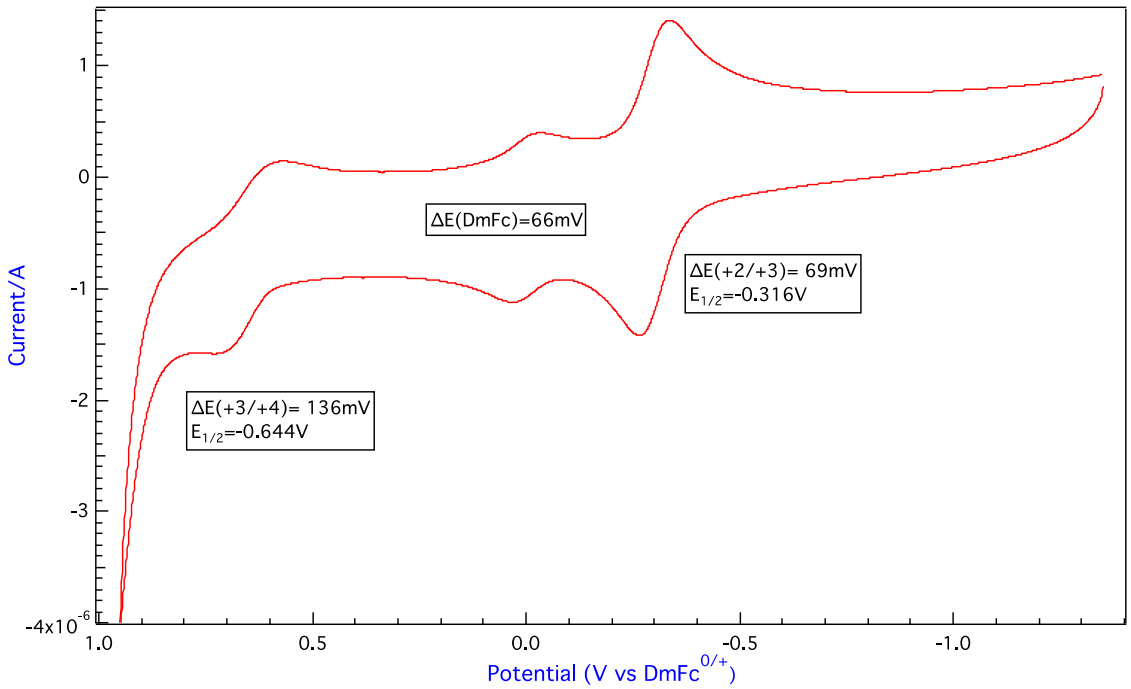

Figure 5.16. CV of $[Cr_2(tren)_2(CA)](BPh_4)_2$ in MeCN with 1.0 M $TBAPF_6$ as supporting electrolyte. All potentials are referenced to the $DmFc^{+/0}$ couple.

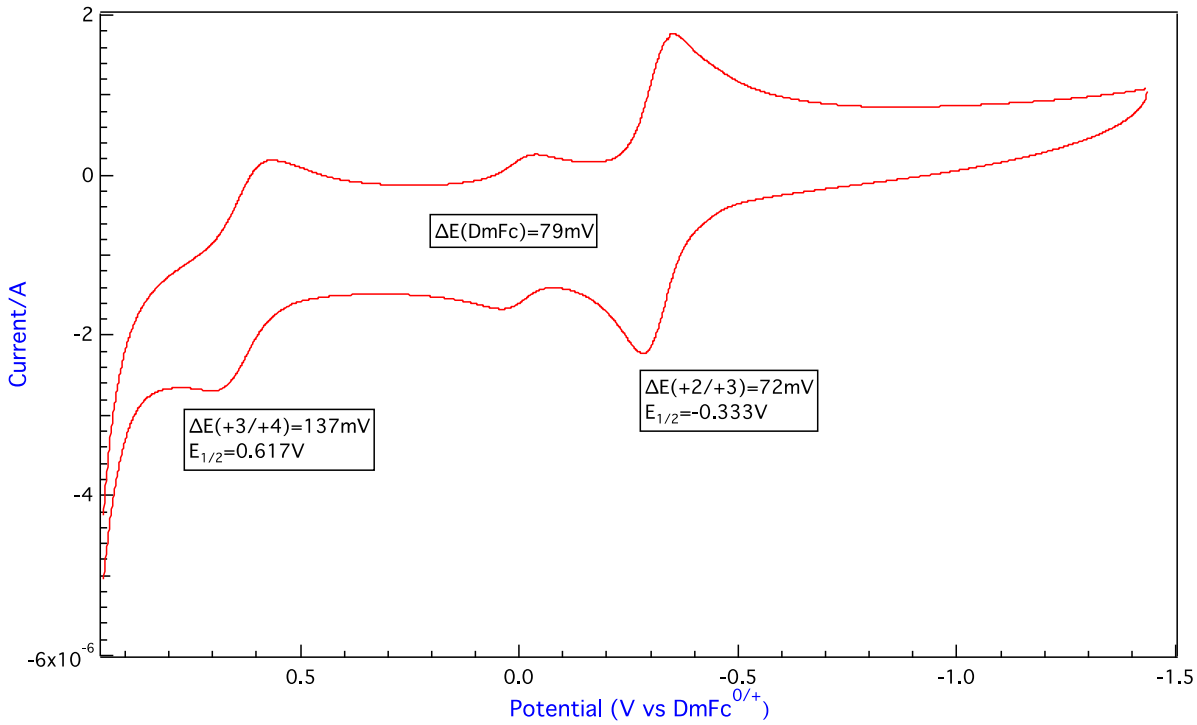

Figure 5.17. CV of $[Cr_2(tren)_2(BA)](BPh_4)_2$ in MeCN with 1.0 M $TBAPF_6$ as supporting electrolyte. All potentials are referenced to the $DmFc^{+/0}$ couple.

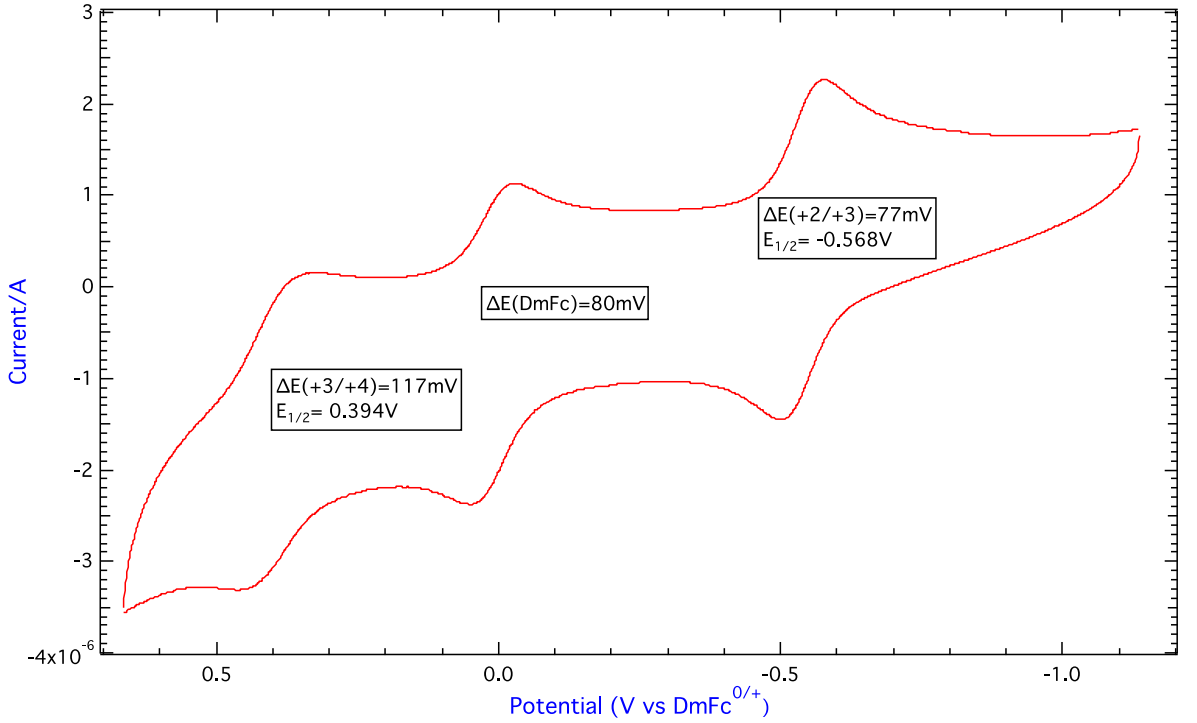

Figure 5.18. CV of $[Cr_2(tren)_2(PhA)](BPh_4)_2$ in MeCN with 1.0 M $TBAPF_6$ as supporting electrolyte. All potentials are referenced to the $DmFc^{+/0}$ couple.

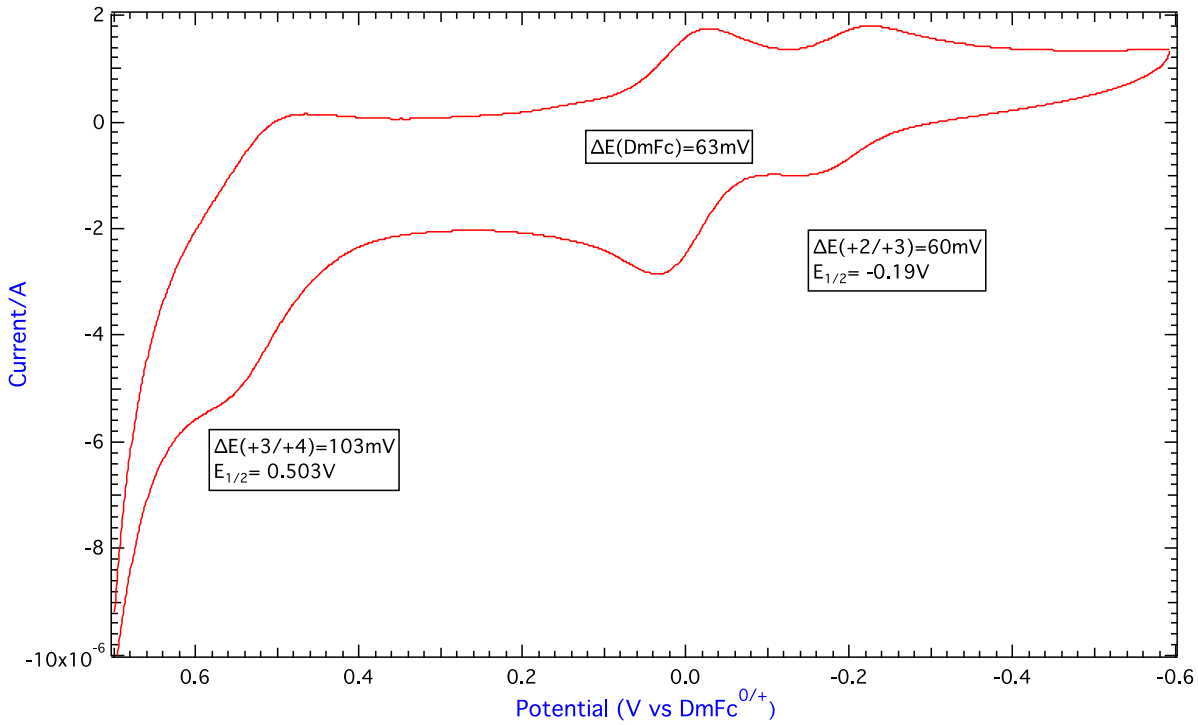

Figure 5.19. CV of $[Cr_2(tren)_2(Me_2\text{-}AnT)](BPh_4)_2$ in MeCN with 1.0 M $TBAPF_6$ as supporting electrolyte. All potentials are referenced to the $DmFc^{+/0}$ couple.

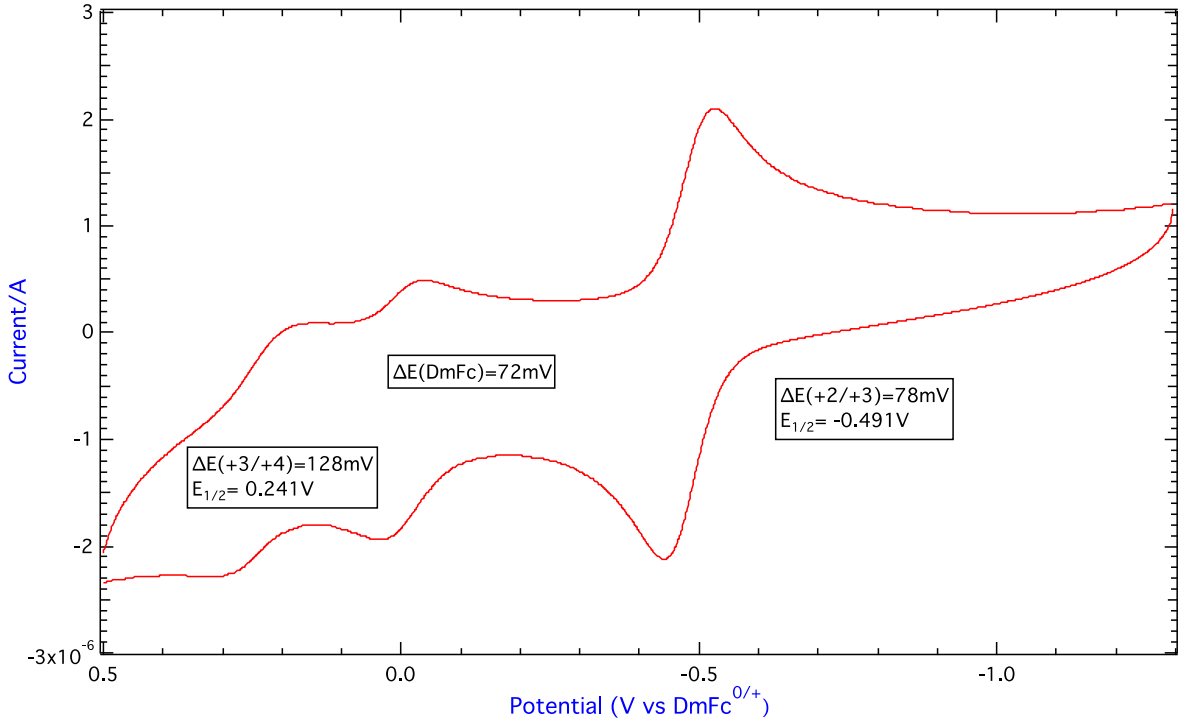

Figure 5.20. CV of $[Ga_2(tren)_2(DHBQ)](BPh_4)_2$ in MeCN with 1.0 M $TBAPF_6$ as supporting electrolyte. All potentials are referenced to the $DmFc^{+/0}$ couple.

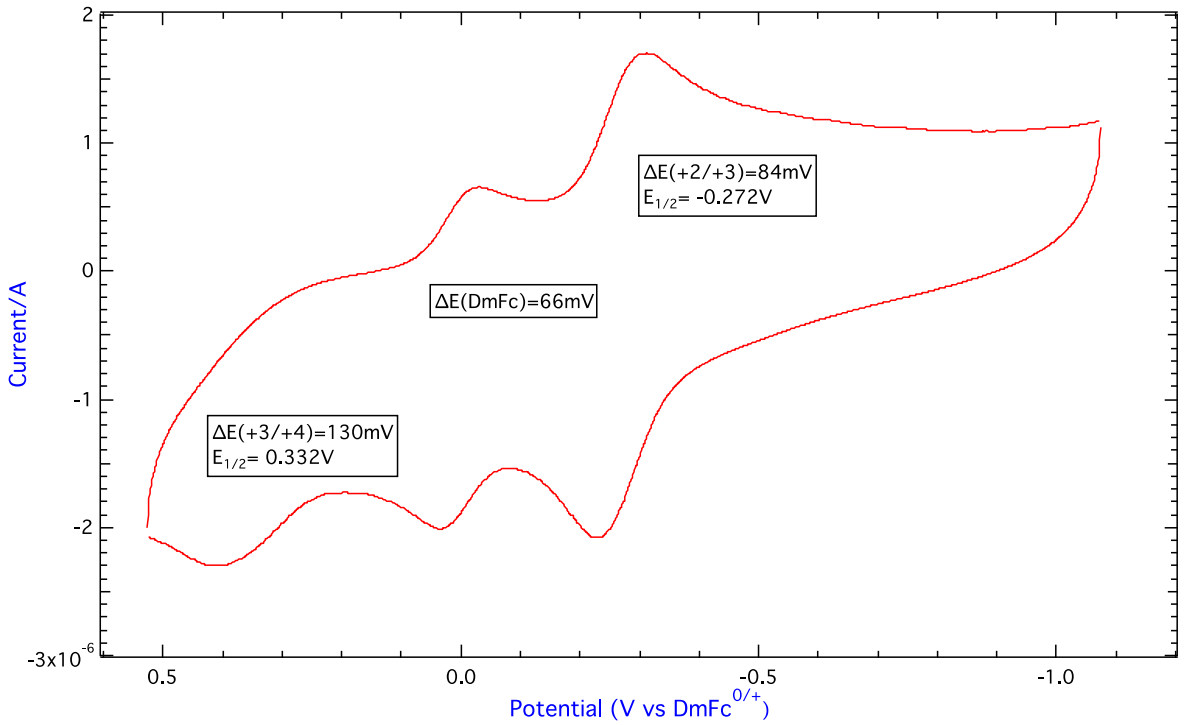

Figure 5.21. CV of $[Ga_2(tren)_2(CA)](BPh_4)_2$ in MeCN with 1.0 M $TBAPF_6$ as supporting electrolyte. All potentials are referenced to the $DmFc^{+/0}$ couple.

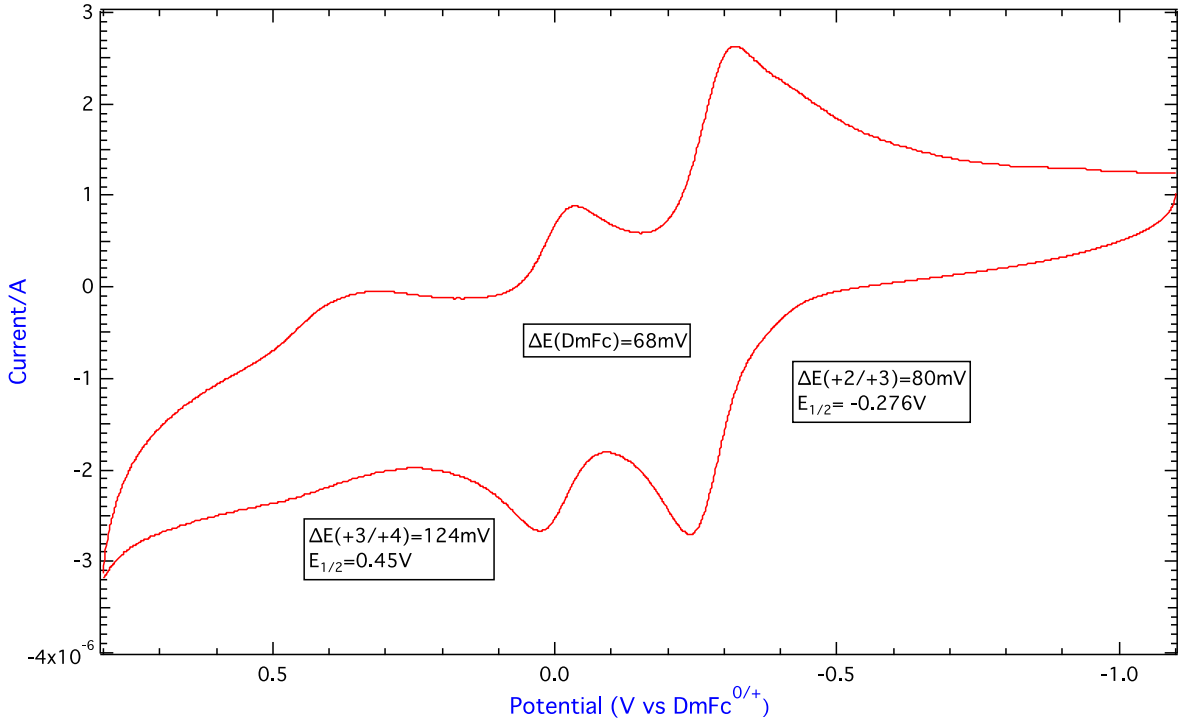

Figure 5.22. CV of $[Ga_2(tren)_2(BA)](BPh_4)_2$ in MeCN with 1.0 M $TBAPF_6$ as supporting electrolyte. All potentials are referenced to the $DmFc^{+/0}$ couple.

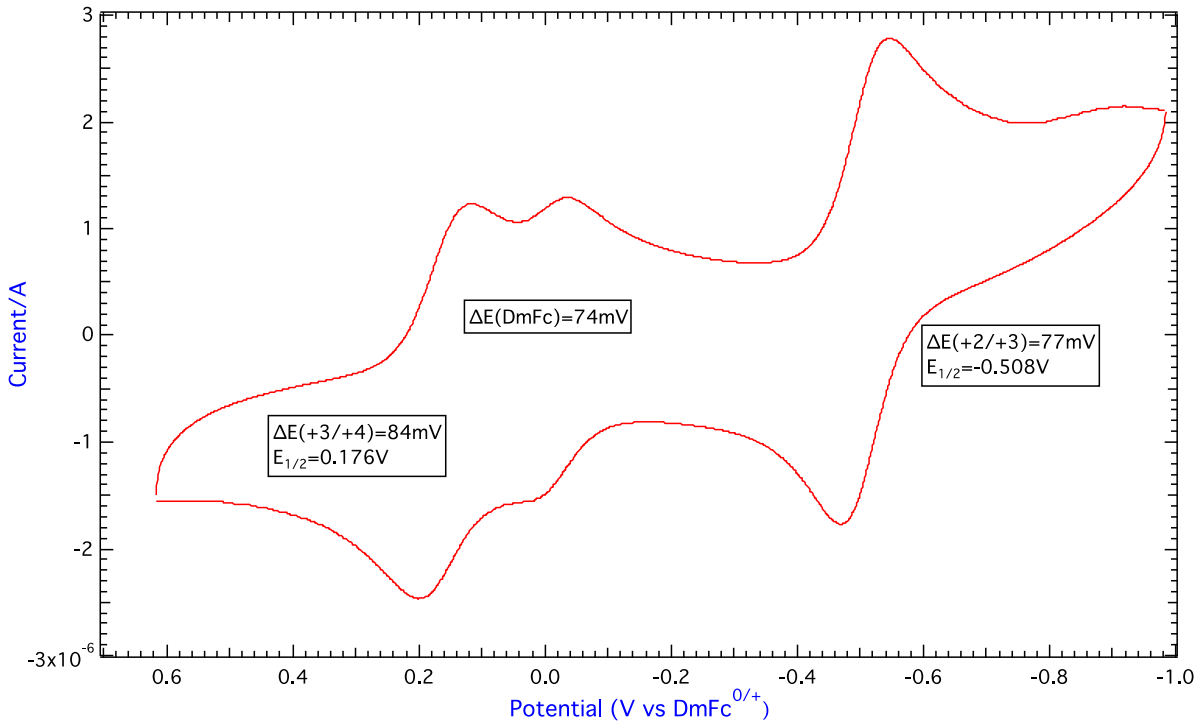

Figure 5.23. CV of $[Ga_2(tren)_2(PhA)](BPh_4)_2$ in MeCN with 1.0 M $TBAPF_6$ as supporting electrolyte. All potentials are referenced to the $DmFc^{+/0}$ couple.

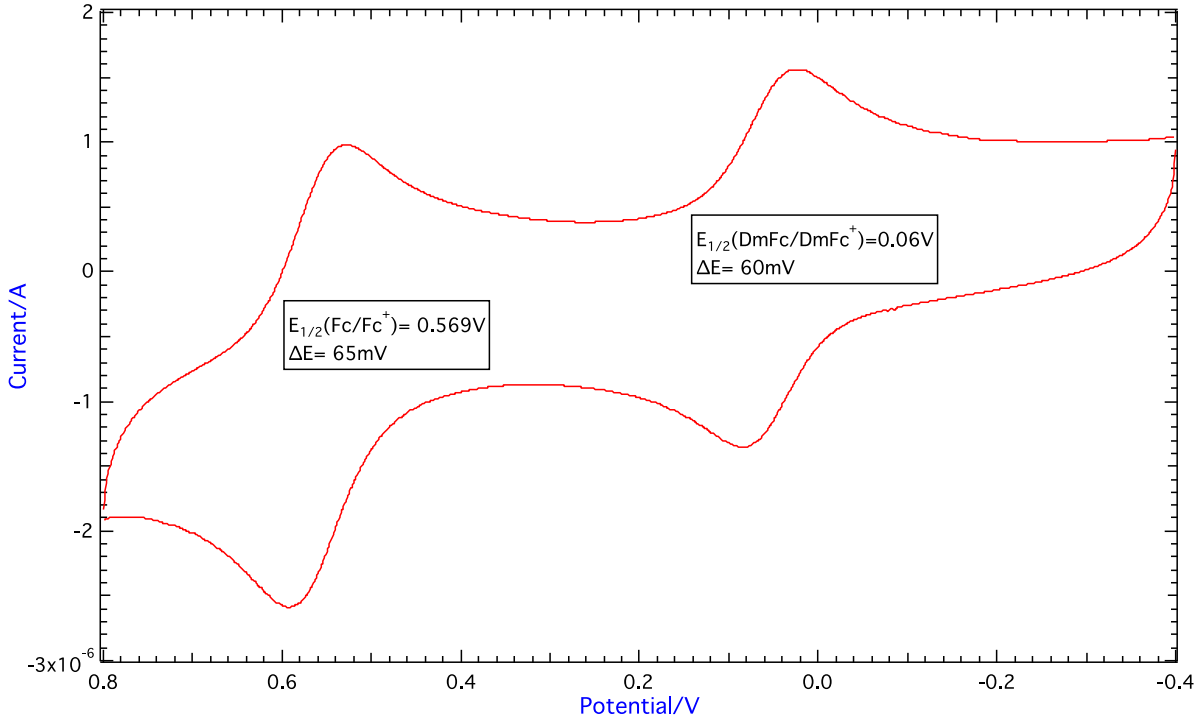

Figure 5.24. CV of ferrocene (at 0.569V) and decamethylferrocene (at 0.06V) in MeCN with 1.0 M $TBAPF_6$ as supporting electrolyte.

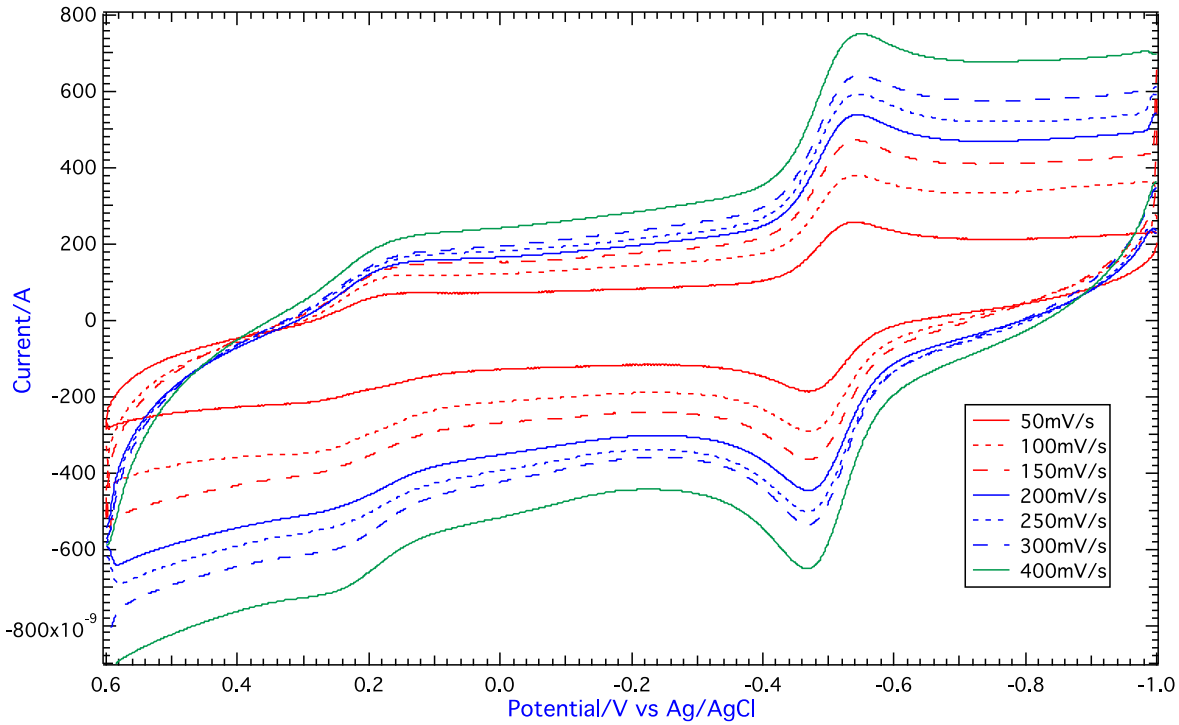

Figure 5.25. Cyclic voltammograms of the $[Cr_2(tren)_2(CA^{cat,cat})](BPh_4)_2$ in MeCN with 1.0 M $TBAPF_6$ collected from 50 mV/s to 400 mV/s.

REFERENCES

REFERENCES

(1) Picraux, L. B.; Smeigh, A. L.; Guo, D.; McCusker, J. K. *Inorg. Chem.* **2005**, *44*, 7846.

(2) Picraux, L. B.; Weldon, B. T.; McCusker, J. K. *Inorg. Chem.* **2003**, *42*, 273.

(3) Blondin, G.; Girerd, J.-J. *Chem. Rev.* **1990**, *90*, 1359.

(4) Wei, P. P.; Skulan, A. J.; Wade, H.; DeGrado, W. F.; Solomon, E. I. *J. Am. Chem. Soc.* **2005**, *127*, 16098.

(5) Chen, P.; Solomon, E. I. *J. Am. Chem. Soc.* **2004**, *126*, 4991.

(6) Holm, R. H.; Kennepohl, P.; Solomon, E. I. *Chem. Rev.* **1996**, *96*, 2239–2314.

(7) Bertrand, P.; Gayda, J. *Biochim. Biophys. Acta*. **1982**, *680*, 331-335.

(8) Guo, D.; McCusker, J. K. *Inorg. Chem.* **2007**, *46*, 3257-3274.

(9) Elgrishi, N.; Rountree, K. J.; McCarthy, B. D.; Rountree, E. S.; Eisenhart, T. T.; Dempsey, J. L. *J. Chem. Educ.* **2018**, *95*, 197-206.

(10) McCarthy, B. D.; Martin, D. J.; Rountree, E. S.; Ullman, A. C.; Dempsey, J. L. *Inorg. Chem.* **2014**, *53*, 8350−8361.

(11) Gagne, R. R.; Koval, C. A.; Lisensky, G. C. *Inorg. Chem.* **1980**, *19*, 2854.

(12) Trasatti, S. *Pure Appl. Chem.* **1986**, *58*, 955−966.

(13) Noviandri, I.; Brown, K. N.; Fleming, D. S.; Gulyas, P. T.; Lay, P. A.; Masters, A. F.; Phillips, L. *J. Phys. Chem. B* **1999**, *103*, 7613-6722.

(14) Aranzaes, J. R.; Daniel, M.-C.; Astruc, D. *Can. J. Chem.* **2006**, *84*, 288−299.

(15) Richardson, D. E.; Taube, H. *Inorg. Chem.* **1981**, *20*, 1278-1285.

(16) Zweig, A.; Lancaster, J. E.; Neglia, M. T.; Jura, W. H. *J. Am. Chem. Soc.* **1964**, *86*, 4130-3146, and reference herein.

(17) Valenti, G.; Boni, A.; Melchionna M.; Cargnello, M.; Nasi, L.; Bertoni, G.; Gorte, R. J.; Marcaccio, M.; Rapino, S.; Bonchio, M.; Fornasiero, P.; Prato, M; Paolucci, F. *Nature Communications*, **2016**, *7*, 13549.

(18) Chen, P.; McCreery, R. L. *Anal. Chem.* **1996**, *68*, 3958-3965, and reference herein.

(19) Bard, A. J.; Faulkner, L. R. *Electrocthhemical Methods: Fundamentals and Application,* 2nd Ed. John Wiley & Sons: New York, NY, 2000.

(20) Matsuda, H.; Ayabe, Y. *Z. Elektrochem.* **1955**, *59,* 494–503.

(21) Gogolin, A. O.; Nersesyan, A. A.; Tsvelik, A. M. *Nucl. Phys. B.* **1999,** *540,* 705.

(22) Lapinte, C. *J. Organomet. Chem.* **2008,** *693,* 793.

(23) Mabbs, F. E.; Machin, D. J. *Magnetism and Transition Metal Complexes.* Dover Publication: Mineola, NY, 2008.

(24) Sutton, J. E.; Sutton, P. M.; Taube, H. *Inorg. Chem.* **1979**, *18*, 1017.

(25) Gagné, R. R.; Spiro, C. L.; Smith, T. J.; Hamann, C. A.; Thies, W. R.; Shiemke, A. K. *J. Am. Chem. Soc.* **1981**, *103*, 4073.

(26) Aquino, M. A. S.; Lee, F. L.; Gabe, E. J.; Bensimon, C.; Greedan, J. E.; Crutchley, R. J. *J. Am. Chem. Soc.* **1992**, *114,* 5130.

(27) Astruc, D. *Electron Transfer and Radical Processes in Transition-Metal Chemistry,* VCH, New York, 1995.

(28) Schrauben, J. N.; Guo, D.; McCracken, J. L.; McCusker, J. K. *Inorganica Chimica Acta*, **2008**, *361*, 3539-3547.

(29) Kaim, W.; Klein, A.; Glöckle, M. *Acc. Chem. Res.* **2000,** *33,* 755.

(30) Palaniappan, V.; Singru, R. M.; Agarwala, U. C. *Inorg. Chem.* **1988,** *27,* 181.

(31) McCleverty, J. A.; Meyer, T. J. *Comprehensive Coordination Chemistry II,* 2nd Ed. Elsevier: Amsterdam, 2003.

(32) D'Alessandro, D. M.; Keene, F. R. *Chem. Soc. Rev.* **2006**, *35*, 424-440.

(33) G¨utlich, P.; Hauser, A.; Spiering, H. *Angew. Chem. Int. Ed.*, **1994**, *33*, 2024–2054.

(34) Berry, J. F., Cotton, F. A., Lu, T., Murillo, C. A. *Inorg. Chem.* **2003**, *42*, 4425–4430.

(35) Brownson, D. A. E.; Banks, C. E. *The Handbook of Graphene Electrochemistry.* Springer-Verlag London: London, the U. K., 2014, pp 126.

(36) Shorter, J. *Correlation analysis in organic chemistry: an introduction to linear free-energy relationships.* Oxford University Press: Oxford, 1973.

Chapter 6. Conclusion and Future Directions

6.1 Future Works

Proper substituents need to be chosen with dramatic electron withdrawing, donating, or delicalization effect to systematically modify the strength of the spin exchange interaction. As we observed in Chapter 3, the magnitude of the *J* constants of the halogenated Complex **2**, **3**, **4**, **5**, **12**, **13**, **14** and **15** falls in the same scale within analytical error, and Complex **8**, **9**, **10**, **18** and **19** with polyaromatic hydrocarbon bridging ligands present more pronounced difference in the magnitude of the *J* values. Thus, it is important to explore the spin polarization effects on more substituents in order to provide more insightful guide on the choice of substituents. The series of dichromium (III) and digallium (III) complexes in this project are still lacking a π-donor and π-acceptor to show all possible variations to modulate spin polarization. The syntheses of all substituted ligands are quite challenging because they do not follow similar synthetic schemes. Their synthetic routes are still under development, and they will be discussed below along with some suggestions.

6.1.1 DFT Calculations

General Methods. All electronic structure calculations of deprotonated $(L^{sq,cat})^{3-}$ anions and $[Ga_2(tren)_2(L^{sq,cat})]^{3+}$ cations were carried out using density functional theory implemented in Gaussian 09[20] on HPCC at Institute for Cyber-Enabled Research at Michigan State University. The B3LYP functional with open shelled was used in the calculation.[21-25] The calculation was performed using the default tight convergence criteria with ultrafine integration grid. Analysis of atomic charge and spin densities were performed using natural population analysis (NPA) framework developed by Weinhold et al.[26]

6.1.1.1 Geometry Optimization and Single Point Energy Calculations

The initial geometries of the deprotonated free ligands and Gallium (III) dimeric derivatives were generated using GaussView[27] with subsequently optimized using the UB3LYP functional and a 6-31G basis set with imposed symmetries of C_i. Final geometries were checked with frequency calculations at the UB3LYP/6-31G level. Imaginary frequencies were obtained for some sterically bulky Ga (III) structures or structures with extended aromatic conjugation. Those structures were reoptimized with increased convergence cycles (default maxcycle = 64) and the exact computed Hessian matrix for frequency calculations with CalcFC or CalcAll command. Heissian matrix is the matrix of second derivatives of the energy in regard to displacement of atoms.[28] Frequency calculations generally are based on an estimated Hessian from geometry optimization.[29] Geometry optimizations were then re-run for the Ga (III)structures with UltraFine grid to help obtain smoother convergence to the stationary point. Structures were reoptimized with subsequent frequency calculations until no imaginary frequencies, which indicates that the final structures have reached the global minima. The final optimized structures were then used for single-point energy calculations.

Single-point energy calculations were performed using the unrestricted open shelled density function UB3LYP with the 6-311G basis set with natural population analysis (NPA) assuming the doublet ground state and a molecular charge of 3+.

6.1.2 Finish the Other Derivatives of the Substituted Anilate and Anthracene Bridging Systems

A few other substituents are chosen due to their electron withdrawing and donating ability to complete the series in this project, so we can target and study more thoroughly on substituent effect on the thermodynamics of the spin exchange interactions. The syntheses of these

substituted derivatives have been attempted; however, some of the multi-step synthetic routes are slightly more challenging. These synthetic procedures and purification are still under development, which include -CN, -piperidino, and -cyanophenyl. The developed steps are listed below with some suggestions for improvement in the future.

6.1.2.1 Synthesis

Potassium 2-hydroxy-3-chloro-6-cyanoanilate.[1,2] 2,3-Dichloro-5,6-dicyano-1,4-benzoquinone (DDQ) (1.44 g, 6.34 mmol) was suspended in 40 mL of H_2O, and the yellow orange suspension was stirred at 60˚C for 30 min. 6M KOH aqueous solution (8.7 mL) was added dropwise into the DDQ suspension, and the suspension slowly turned dark red. It was continuously heated at 60˚C for 1 h until everything was completely dissolved. After the solution was cooled down to RT, the volume of the solution was reduced to one half of its original volume under vacuum, and then it was kept in the fridge overnight for recrystallization. Red crystals formed, which is suitable for x-ray diffraction. The product was filtered, washed with 3M KOH (3 x 30 mL), acetone (3 x 20 mL), and dried in air. Yield: 0.4 g (26%). HRMS [ESI-TOF, *m/z* (rel. int.)]: $[M-K]^-$ Calcd for $[C_7O_4HNCl]^-$, 197.9594; Found, 197.9602. $[M-K-H-Cl]^-$ Calcd for $[C_7O_4N]^-$, 161.9827; Found, 161.9832.

2,5-Dichloro-3,6-dipiperidino-1,4-benzoquinone.[5] Unscented laundry detergent (0.5% mol LD) was added in H_2O (50 mL) to serve as a surfactant to facilitate the dissolution of all reactants. Following by the addition of piperidine (4 mL, 40 mmol), chloranil (2.46g, 10 mmol) and K_2CO_3 (5.53g, 40 mmol) were added into the suspension while stirring. The suspension turned from yellow to brown. After overnight stirring, brown products were filtered and washed by H_2O and Et_2O. Purple crystals, suitable for x-ray diffraction, were obtained from

recrystallization from EtOAc/hexane (4:1). Yield: 1.2 g (35%). ^{1}H NMR ($CDCl_3$, 500 MHz) δ (ppm): 1.6-1.7 (d, 12 H, CH_2), 3.48 (d, 8 H, NCH_2). ^{13}C NMR ($CDCl_3$, 500 MHz) δ (ppm): 24.48, 27.12, 53.49, 115.52, 149.55, 176.24. HRMS [ESI-TOF, *m/z* (rel. int.)]: $[M+H]^+$ Calcd for $[C_{16}O_2H_{21}N_2Cl_2]^+$, 343.0965; Found, 343.1077.

2,7-Dimethoxy-3,6-di-(4-cyanophenyl)benzoquinone. A mixture of Cs_2CO_3 (1.6 g, 5.0 mmol), 4-cyanophenylboronic acid (0.147 g, 4.0 mmol), and $Pd(PPh_3)_4$ (0.06 g, 5 mol%) in 1,4-dioxane (20 mL) was stirred at 90˚C for 30 min under N_2. 2,5-Dibromo-3,6-dimethoxy-1,4-benzoquinone (0.326 g, 1.0 mmol) and Ag_2O (0.58 g, 2.5 mmol) were added into the mixture, and the reaction was stirred at 110 ˚C for 18 h. 30 mL of DCM was added to the solution at RT, and it was filtered through a pad of Celite. Purification of flash silica column with DCM/n-pentane (6:4) and hexane/DCM/EtOAc (8:1:1) was attempted; however, impurity was still present. The yield of this reaction is too low to be reported. The product was detected by HRMS. HRMS [ESI-TOF, *m/z* (rel. int.)]: $[M+H]^+$ Calcd for $[C_{20}O_4H_{15}N_2]^+$, 371.1032; Found, 371.1012.

6.1.2.2 Discussion

3,6-cyananilic acid, $H_2(CN)_2An$, and 3,6-piperidinoanilic acid, $H_2(Pip)_2An$, are chosen to examine the electron-withdrawing (EW) and electron-donating (ED) effects respectively on the spin exchange coupling effect, when these substituents directly bind to the benzoquinoidal bridging ligand. Phenyl and 4-(N,N-dimethylamino)-phenyl substituted Cr(III) dimers have been successfully synthesized to investigate the effects of intraligand electron delocalization, while EWG and EDG are indirectly connected through a phenyl group on the bridging ligand. Therefore, the synthesis and study of 4-cyanophenyl substituted moiety will provide another piece of useful information for our studies on intraligand electron delocalization. In addition,

9,10-diphenylanthracene substituted Cr(III) analogues will serve as an important role for our studies on the effects of horizontal electron delocalization, and whether they will possess added effect on decreasing the strength of spin exchange coupling.

Some of these products have been successfully synthesized, but the reaction yield is too low to be proceeded further. The intermediates of other products have been synthesized; however, some difficulties are encountered for the remaining steps due to the reactivity of the intermediate products.

H_2(Pip)$_2$An. 2,5-Dichloro-3,6-dipiperidino-1,4-benzoquinone has been synthesized,[5] and the crystal suitable for x-ray diffraction was collected. However, the hydroxylation of this compound with NaOH following by protonation with HCl was unsuccessful, which can be due to the fact that chlorine is not acting as a better leaving group with such a strong EWG, piperidino, binding on the 3,6-positions. The suggestion is to make 2,5-dibromo-3,6-dipieridino-1,4-benzoquinone with bromanil as reactant, since bromine is a better leaving group than chlorine, and bromanil is commercially available. The resulting product can then be hydroxylated with NaOH, and acidified with H_2SO_4, which has the similar procedure with H_2IA.[6,7] If 2,5-Diamino-3,6-dihydroxy-1,4-benzoquinone ($H_2(NH_2)_2$An) can be synthesized, it serves the same purpose as H_2(Pip)$_2$An, which is also an EDG derivative. However, the literature reported methods[8,9] are not clear, and the success of synthesis for 2,5-Dichloro-3,6-dipiperidino-1,4-benzoquinone lead us to continue pursue piperidino as the chosen EDG.

H_2(CN)$_2$An.[1,2] Potassium 2-hydroxy-3-chloro-6-cyanoanilate (HKCNAn) was synthesized and obtained as red crystals.[10,11] In order to substitute the chloro on the 3-position, this potassium salt was reacted with 2 eq. of KCN in MeOH/H_2O (1:1).[12] The reaction was refluxed for 2 h. No product was detected by ESI+ mass spectrometry, and HKCNA was fully recovered. The failure

of this reaction can be due to the fact that chloro becomes a worse leaving when being *para*-substituted with the cyano group. My suggestion is to react either chloranil or bromanil with 4 eq. of KCN under refluxing temperature.

H_2(CN-Ph)$_2$An. 2,7-Dimethoxy-3,6-di-(4-cyanophenyl)benzoquinone was synthesized by Suzuki coupling with commercially available 4-cyanophenylboronic acid reported in Chapter 3 with a very low yield. Several different column chromatography, including flash or gravitational columns with silica gel or neutral alumina with various eluents, were attempted, and the purification was unsuccessful. In order to improve the yield of this step, the first thing is to investigate the most effective and optimal route of the reaction with various Pd catalysts, solvents, reaction time, and temperature based on the work reported by Hu et al[13] and Langer et al.[14] After finding the most effective Pd catalyst, eluent combination needs to be optimized for column chromatography purification process. Pet. Et_2O/EtOAc (4:1) is recommended as the first combination to be tested out.[15] Another route is to synthesize 2,7-Dimethoxy-3,6-di-(4-bromophenyl)benzoquinone as an intermediate; this intermediate can then react with ZnCN with $Pd_2(dba)_3$ as a catalyst[16] to possibly form 2,7-Dimethoxy-3,6-di-(4-cyanophenyl)benzoquinone. The latter route is not my primary option, because it involves more steps, which can potentially lead to even lower yield.

6.1.3 Expand the Conjugation of Tetraoxo-Bridging Ligands with 9,10-Diphenylanthracene, Terrylene, and Pyrene

Polyaromatic aromatic hydrocarbon consists of a large communicative π-system in order to reduce electron repulsion within the rings for its planarity.[18] The intense π-stacking in the extended conjugated network allows these ligands to effectively delocalized electrons. The use of naphthalene and anthracene as bridging ligands discussed in Chapter 3 proves that they can

effectively delocalize electrons within the systems to exhibit the most significant decrease on the strength of the spin exchange interaction. Pyrene and terrylene (Fig. 6.1) will be the next targets for our study of spin polarization in spin exchange coupled systems.

Density functional calculations were performed on the PAHs free ligands, the change in spin and charge density generated computationally match computational results reported in literature, which suggest that PAHs show bond length alternation with more localized bond and aromatic dilution.[19] Due to their highly π-delocalized conjugation, the Lewis basicity of PAHs can be very weak. If they are too weak, the coordination chemistry between the transition metal ions and the deprotonated PAHs may not be thermodynamically favorable. The computational results indicate the decrease of charge density on tetraoxo-phenylanthracene, pyrene and terrylene (Fig. 6.2), so they are proved to be weaker Lewis base computationally. It will be hard to determine if the formation of bimetallic terrylene is feasible due to the drastic decrease shown in its charge density. The charge density of pyrene is comparable with 9,10-dimethyltetraoxoanthracene, and both $[Cr_2(tren)_2(Me\text{-}AnT^{cat,cat})](BPh_4)_2$ and $[Cr_2(tren)_2(Me\text{-}AnT^{cat,cat})](BPh_4)_2(BF_4)$ were successfully synthesized. Thus, the synthesis of bimetallic pyrene seems to be thermodynamically viable. However, it will be hard to determine if the formation of bimetallic terrylene is feasible due to the drastic decrease of the charge density shown computationally.

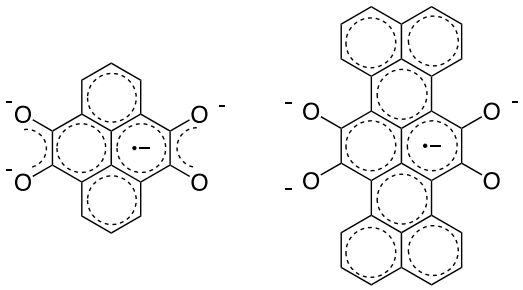

Figure 6.1. The calculated structures of 4,5,9,10-tetraoxopyrene (left), and 4,5,12,13-tetraoxoterrylene (right).

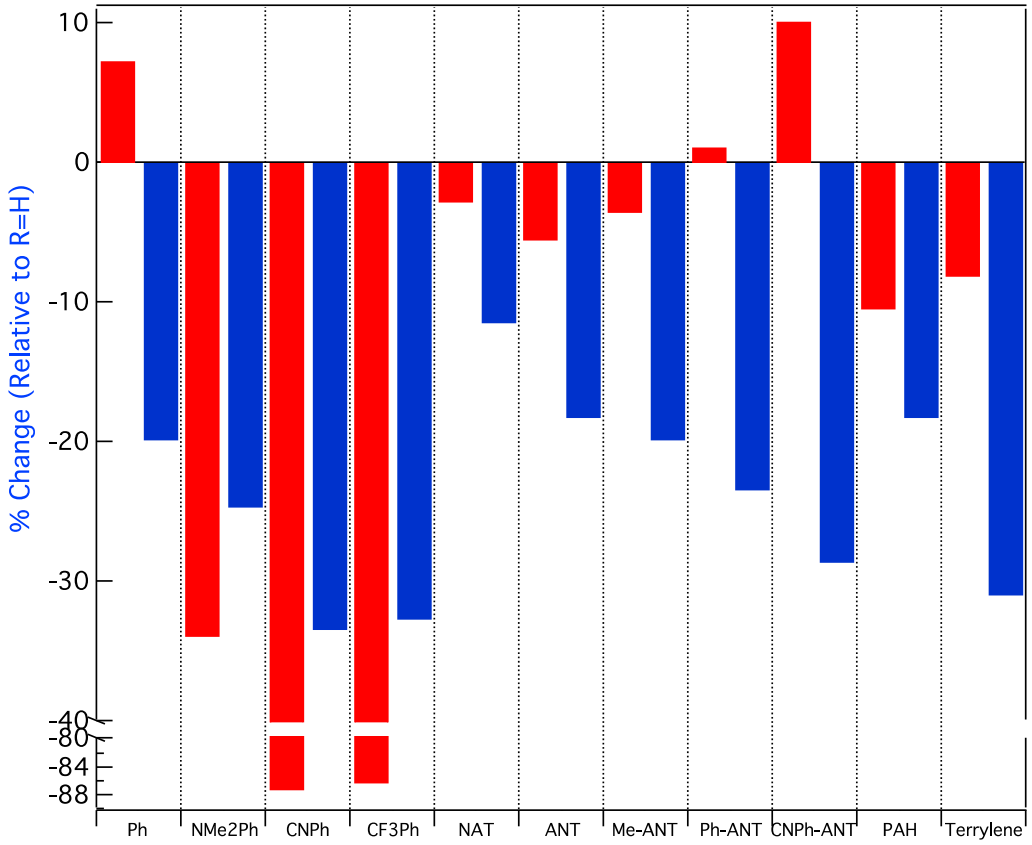

Figure 6.2. Shift in spin (red) and charge (blue) density at the oxygen atom for a series of deprotonated trianionic tetraoxo-substituted phenylanilate, naphthalene, anthracene, pyrene (PAH), and terrylene bridging radicals.

A considerable decrease of charge density was also observed computationally in 9,10-diphenyl-tetraoxoanthracene (Ph-ANT), and 9,10-di(cyano)phenyl-tetraoxoanthracene (CNPh-ANT) (Fig. 6.2) to show their diminishing Lewis basicity. Thus, the DFT calculations suggest the coordination between these bridging ligands and the transitional metal ions may not be thermodynamically favorable. Since the synthesis of H_4(Ph-AnT) has been developed, characterization and transition metal coordination should be reasonably easy to examine the computational prediction. My suggestion is to coordinate the deprotonated H_4(Ph-AnT) with [Cr(tren)Cl_2]Cl. If the synthesis is successful, CNPh-ANT should be synthesized after that, because the DFT result shows a drastic increase on spin density. However, if the synthesis

between H_4(Ph-AnT) and [Cr(tren)Cl_2]Cl is unsuccessful, then the synthesis of CNPh-ANT might be as meaningful. Bimetallic 9,10-di(cyano)phenyl-tetraoxoanthracene complex may not worth the attempt because its formation does not seem thermodynamically viable based on the change of charge density shown in DFT calculations.

6.1.3.1 Synthesis

2,3,6,7-Tetramethoxy-9,10-diphenylanthracene.[3,4] Benzaldehyde (12.5 mL, 122.5 mmol) in MeOH (10 mL) was added dropwise in a stirring solution of veratrole (16 mL, 128.7 mmol) in AcOH (60 mL) at 0˚C for 1 h. 90% aq. H_2SO_4 (62 mL) solution was added over 1-hour period into the solution above at 0˚C for 24 h, and the mixture was vigorously stirred. As more H_2SO_4 solution was added, the reaction mixture became viscous. The dark purple mixture was poured into 500 mL of ice H_2O, and precipitation happen over time. The solvent was decanted, and the viscous tacky products were triturated and washed with EtOH. Beige products were dissolved in $CHCl_3$, and filtered to eliminate impurity. The solvent was evaporated under reduced pressure. The solids were washed by MeOH. Light pink products were recrystallized from acetone. However, impurity was shown in the ^{1}H NMR spectrum. Purification with silica flash column (DCM) was attempted; however, it was unsuccessful. The impurity is 2,3,6,7-tetramethoxy-9,10-diphenyl-9,10-dihydroanthracene, which is the reduced version of the product. ^{1}H NMR ($CDCl_3$, 500 MHz) δ (ppm): [Product] 3.71 (s, 12 H, OCH_3), 6.80 (s, 4 H, ArH), 7.47 (d, 4 H, phenyl-H), 7.52 (t, 2 H, phenyl-H), 7.59 (t, 4 H, phenyl-H). [Reduced form] 3.68 (s, 12 H, OCH_3), 5.15 (s, 2 H, 9,10-dihydro), 6.52 (s, 4 H, ArH), 7.14 (d, 4 H, phenyl-H), 7.20 (t, 2 H, phenyl-H), 7.28 (t, 4 H, phenyl-H).

6.1.3.2 Discussion

H_4(Ph-AnT). [3,17] 2,3,6,7-Tetramethoxy-9,10-diphenylanthracenewas successfully synthesized; however, a byproduct, 2,3,6,7-tetramethoxy-9,10-diphenyl-9,10-dihydroanthracene, which is the reduced form of the product, was also produced. Due to the similarity of size and polarity of this byproduct with the desired product, purification becomes extra difficult. To prevent the reduction of the product, O_2 can be bubbled through the reaction, or small amount of Ag_2O can be added at the next attempt.

6.1.4 Fast-Scan Cyclic Voltammetry Measurements

As discussed in Chapter 5, $[M_2(tren)_2(L)]^{3+/4+}$ is a quasi-reversible redox process, which indicates highly variable oxidative chemistry of $[M_2(tren)_2(L^{sq,cat})]^{3+}$, so the $\Delta E_{1/2}$ extrapolated from the electrochemical data is only an estimation. This implies the $\Delta E_{c,echem}$ may not accurately reflect the degree of thermodynamic stabilization, and this certainly introduces analytical error to the comparison between $\Delta E_{c,echem}$ and $\Delta E_{c,mag}$. The cyclic voltammetry measurement of both Cr(III) and Ga(III) shows better reversibility of $[M_2(tren)_2(L)]^{3+/4+}$ at a faster scan rate compared with the data collected at a slow scan rate. In order to establish a qualitative or even a quantitative relationship between the electrochemical and magnetic properties for the explanation of the thermodynamic consequence induced by the spin exchange interaction, an accurate determination of $\Delta E_{c,echem}$ is necessary.

The fast-scan cyclic voltammetry measurement employing microelectrode methods with a scan rate up to 1×10^6 V/s will allow us to investigate if this is a kinetic phenomenon, since increased reversibility of $[M_2(tren)_2(L)]^{3+/4+}$ was observed at higher scan rate. Unfortunately, this kind of measurement was not done due to the instrumental limitation in our lab. The fast-scan

cyclic voltammetry measurement should be researched and conducted for my samples in the future for a more accurate determination of $\Delta E_{1/2}$ on the $[M_2(tren)_2(L)]^{3+/4+}$ redox trace.

6.1.5 Electron Paramagnetic Resonance and DFT Studies of the Electronic Structures of the Semiquinoidal Gallium(III) Dimeric Systems

Electron paramagnetic resonance (EPR) spectroscopy can be used to develop a more comprehensive electronic structures of all digallium(III) semiquinone complexes studied in this project, and it has been proved to be an effective tool to characterize the ground states of $[Ga_2(tren)_2(CA^{sq,cat})](BPh_4)_2(BF_4)$ and $[Ga_2(tren)_2(DHBQ^{sq,cat})](BPh_4)_2(BF_4)$ in a previous study reported by our group.[30] Meanwhile, DFT calculations effectively predict spin densities of these paramagnetic systems.[30]

DFT calculations were performed on the digallium(III) phenylanthracene, pyrene, and terrylene complexes to provide some insights about their spin density to verify if their syntheses are necessary (Fig. 6.3). Spin delocalization effects of phenylanthracene, cyanophenylanthracene, and pyrene are predicted to be similar, and decrease of spin density is generally seen in all these three Ga(III) complexes in accordance to the DFT results. The resonance effect makes the most impact on terrylene, but the decrease is similar to the one of Me-AnT. The substituent effects were not making a huge impact on the strength of spin exchange for the halogenated Cr(III) complexes, even though the computational results indicate a change in spin density. There might not be significant change of the exchange coupling constants observed experimentally in bimetallic terrylene complexes. Thus, only the synthesis of bimetallic pyrene complex is necessary. DFT calculations should be employed to evaluate spin polarization in the future work of this project, since it was able to predict the synthetic difficulty of $[Ga_2(tren)_2(IA^{sq,cat})]^{3+}$ elaborated in Chapter 4.

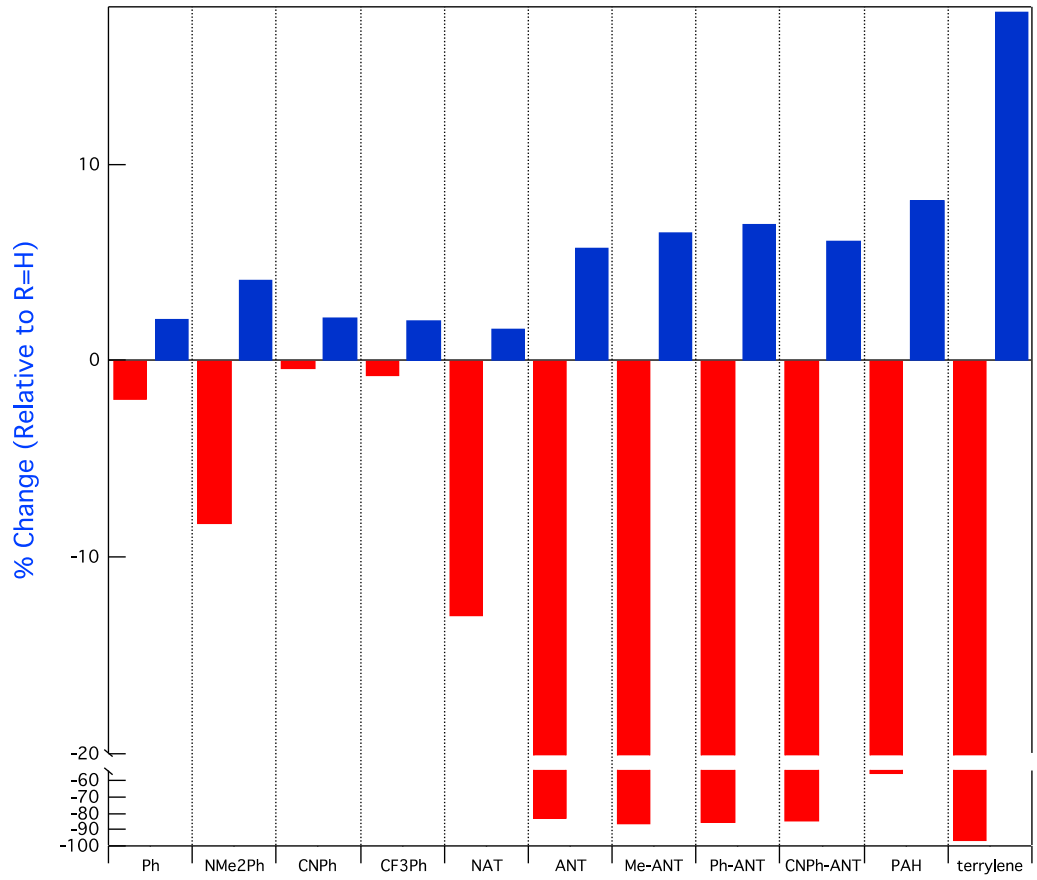

Figure 6.3. Shift in spin (red) and charge (blue) density at the oxygen atom for a series of tetraoxo-substituted phenylanilate, naphthalene, anthracene, pyrene (PAH), and terrylene Ga (III) complexes.

6.1.6 A Broken Symmetry DFT Study for the Spin Exchange Coupling Constants of the Semiquinoidal Cr(III) Dimeric Systems

For multiple paramagnetic centered systems, broken symmetry DFT calculations can be conducted on $[Cr_2(tren)_2(L^{cat,cat})]^{2+}$ and $[Cr_2(tren)_2(L^{sq,cat})]^{3+}$, so they can provide information about orbitals involving in the spin exchange interaction and computationally calculate their *J* values. *J* values were not accurately determined for neither $[Cr_2(tren)_2(L^{cat,cat})]^{2+}$ nor $[Cr_2(tren)_2(L^{sq,cat})]^{3+}$, due in fact that the superexchange coupling strength resulted from $[Cr_2(tren)_2(L^{cat,cat})]^{2+}$ is too small and the MagFit program fails accurately extrapolate *J*s. The

magnitude of *J* constants obtained from the halogenated $[Cr_2(tren)_2(L^{sq,cat})]^{3+}$ are too close to show any variation due to the substituent effect. In this case, computational results may provide useful information about whether the estimation of *J* extrapolated from the least square fit falls in a right direction.

6.1.7 Solution-Phase SQUID Magnetic Susceptibility Measurements

Although the $\Delta K_{c,echem}$ and $\Delta K_{c,mag}$ reported in Chapter 5 track each other, no trend can be observed to conclude substituent effects caused by electron localization/delocalization within the Cr(III) bimetallic series. One of the hypotheses is that the magnetic data collected in solid state of these samples do not account for the solvent effect, since the electrochemical measurements were performed in solution. The comparison of thermodynamic energy extrapolated from electrochemical and magnetic data will not be valid by disregarding the solvent interaction. Liquid SQUID variable-temperature magnetic susceptibility should be measured to obtain magnetic data that is comparable with the electrochemical data. MeCN and DMF can be used to dissolve the samples for the magnetic measurement due to the solubility of the Cr(III) dimeric complexes in these two solvents. The temperature range suggested for the measurement in MeCN is 230 – 350 K, and the measurement in DMF is 220 – 400 K.

Liquid SQUID measurement is challenging because of its complicated sample preparation. Former group member, Rich Fehir, attempted to conduct the experiment in a flame sealed Quartz tube.[31] Concentration of the samples is one of the biggest challenges in his measurement. Since Quartz contributes significantly large diamagnetic background signal, the magnetization of a less concentrated sample can be convoluted by the background signal. Therefore, the concentration of the sample is crucial for liquid SQUID measurements. Regarding

the background signal of a Quartz cell, Dr. Rodolphe Clérac from University of Bordeaux was consulted. His research group focusing on molecular material and magnetism is experienced with various types SQUID measurements and have been employing a sealed plastic straw as a sample holder, which is a similar holder material used for the solid-state SQUID measurement. The background signal of plastic straw is relatively low. Sara Adelman in our group has success with variable-temperature magnetic susceptibility measurement of liquid samples with this kind of sample holder. The challenging part is how to seal the straw to prevent leaking, and it will be beneficial for students who fallow up this project to talk to Sara about this type of measurement before proceeding.

6.2 Concluding Comments

This chapter described the developed synthetic routes for substituted briding ligands in pursuit of a more complete series of Cr (III) and Ga (III) complexes to fulfil our understanding of substituent effects on spin polarization of spin exchange interactions. A few more choices of substituents, i.e. $H_2(CN)_2An$, $H_2(Pip)_2An$, and $H_2(CN\text{-}Ph)_2An$, $H_4(Ph\text{-}AnT)$, and H_4pyrene, are proposed along with synthetic modification/sugguestion and computation results. The viability of the synthesis was discussed to avoid unnecessary synthetic difficulties. The syntheses of these ligands are not without obstacles; however, $H_4(Ph\text{-}AnT)$ has been successfully synthesized and its purification requires more work. The synthetic routes of $H_2(CN)_2An$, $H_2(Pip)An$, and $H_2(CN\text{-}Ph)_2An$ are half-developed, and the most challenging parts are the reactivity on the *ortho*-substituting positions and the development of column chromatography for purification purposes.

DFT calculation continuously proves as an effective tool for the prediction of charge and spin polarization on both paramagnetic deprotonated free ligand and digallium (III) complexes. It

provides useful synthetic direction of PAHs, e.g. the spin polarization effect of bimetallic pyrene does not show drastic impact. Although the spin polarization effect is non-zero, the necessity of the synthesis is low.

There are still many unknown properties of these bimetallic-semiquinone complexes. Without better understanding of their electronic structures, the interpretation of certain experimental features will be difficult. EPR spectroscopy is a powerful tool for the study of paramagnetic compounds, and it can hopefully provide more insight to facilitate our understanding of the substituent effect on the spin polarization and the spin exchange interaction.

The analysis to correlate comproportionation constant from electrochemical data and equilibrium constant magnetic data were demonstrated. Unfortunately, a few missing pieces of information prevented this analysis from quantifying the thermodynamic consequence of Heisenberg spin exchange. One of them is the disregard of solvent interaction in solid-state variable-temperature magnetic measurement. Herein, liquid SQUID measurement was proposed to consider the solvent effects.

Overall, a rough relationship is established between electrochemical and magnetic properties of the molecular systems developed in this project. In the future, there are many advantageous and plausible avenues in theoretical chemistry, SQUID magnetic susceptibility, EPR spectroscopy, and synthetic chemistry to continuously pursue the goal of this project.

APPENDIX

APPENDIX

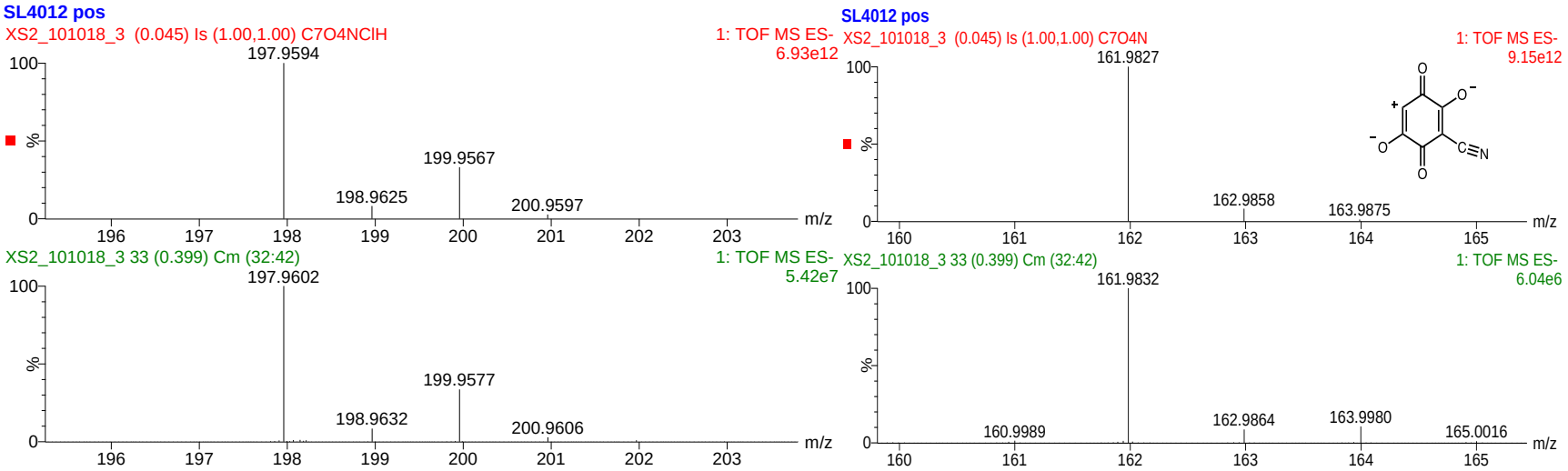

Figure 6.4. ESI-MS of potassium 2-hydroxy-3-chloro-6-cyanoanilate. Right: top, calculated isotope pattern for $[M-K]^-$ (C_7O_4HNCl); bottom, experimental result. Left: top, calculated isotope pattern for $[M-K-H-Cl]^-$ (C_7O_4N); bottom, experimental result.

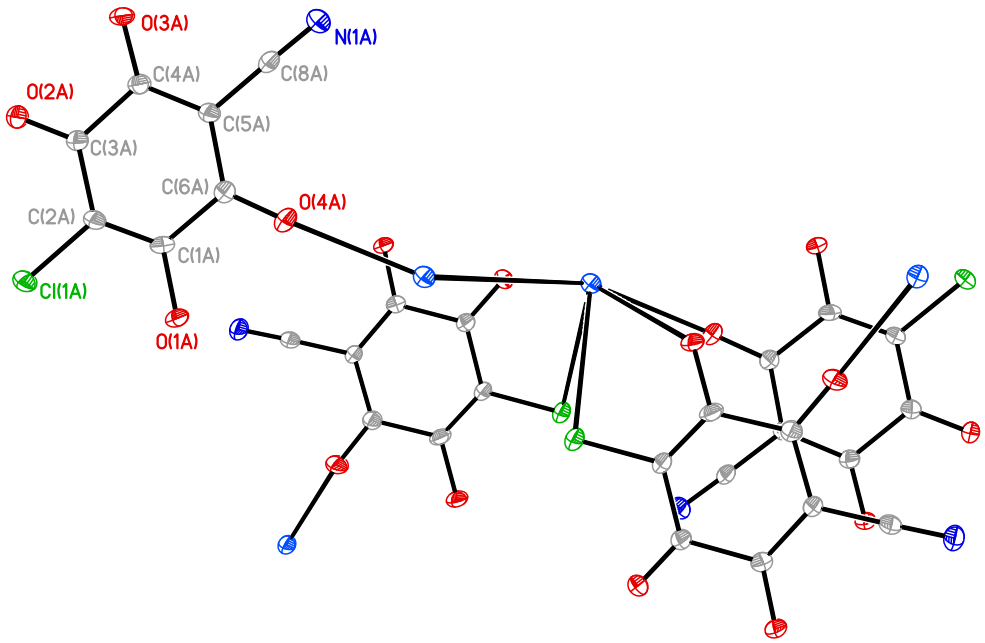

Figure 6.5. ORTEP drawing of potassium 2-hydroxy-3-chloro-6-cyanoanilate from single-crystal x-ray structure determination. Atoms are represented as 50% thermal ellipsoids. Hydrogen atoms are omitted for clarity.

Table 6.1. Crystallographic data of potassium 2-hydroxy-3-chloro-6-cyanoanilate.

Empirical formula	$C_7HClKNO_4$
Formula weight	237.64
Temperature (K)	173(2)
Crystal system	monoclinic
Space group	$P2_1/c$
a (Å)	7.08810(10)
b (Å)	16.9447(3)
c (Å)	6.95160(10)
β (˚)	102.3740(10)
Volume (Å^3)	815.53(2)
Z	4
Radiation	CuKσ
D_{calc} (g cm^{-3})	1.935
Goodness of fit (F^2)	1.201
R_1 (I>2σ(I))[a]	0.0472
wR_2 (I>2σ(I))[b]	0.1792

[a] $R_1=\sum\frac{||F_o|-|F_c||}{\sum|F_o|}$. [b] $wR_2=[\sum w(F_o^2-F_c^2)^2/\sum w(F_o^2)^2]^{1/2}$, w=1/$[\alpha^2(F_o^2)+(aP)^2+bP]$, where P=$[F_o^2+F_c^2]/3$.

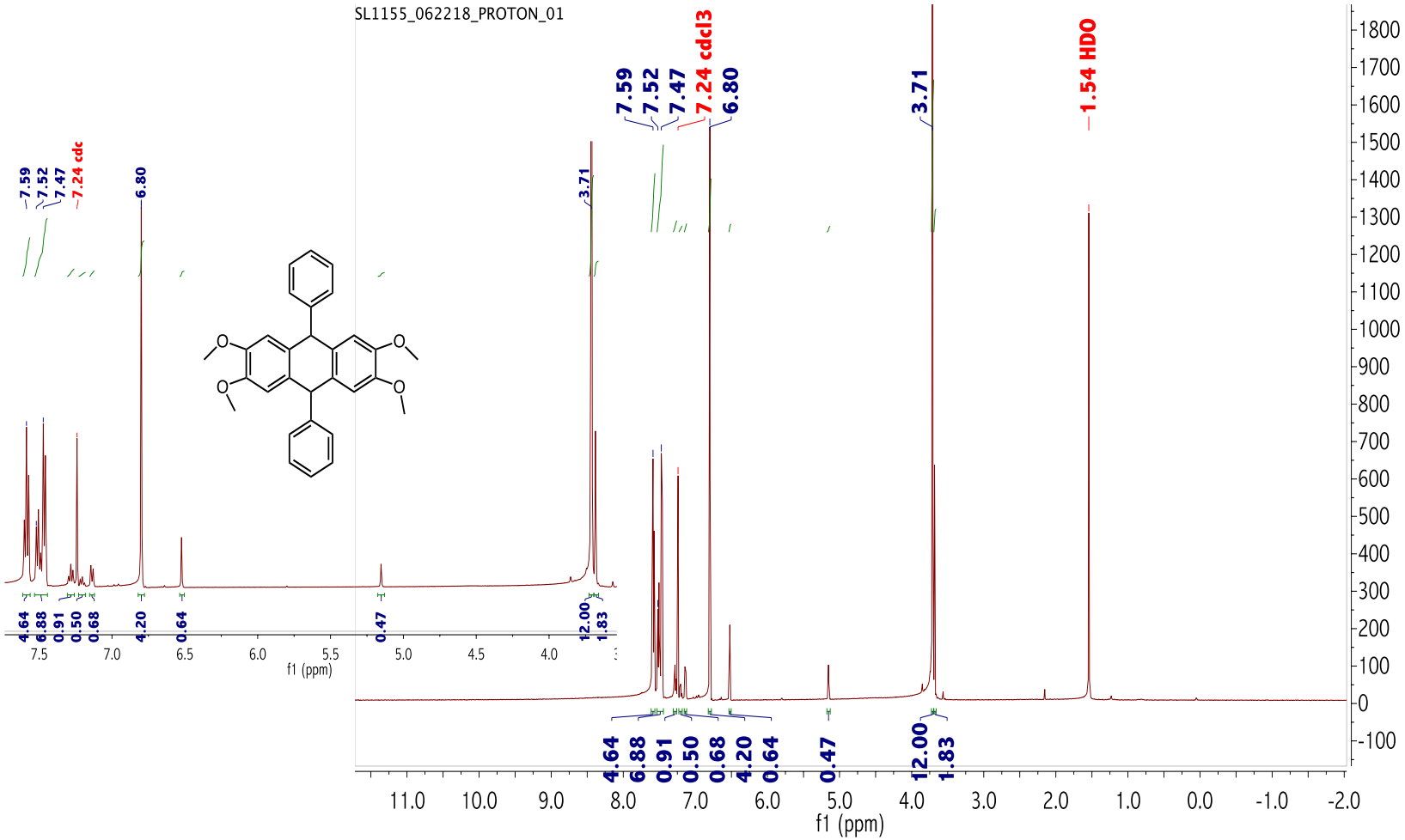

Figure 6.6. ^{1}H NMR of 2,3,6,7-tetramethoxy-9,10-diphenylanthracene in $CDCl_3$. The insert showed the formation of 2,3,6,7-tetramethoxy-9,10-diphenyl-9,10-dihydroanthracene, the reduced form of the product.

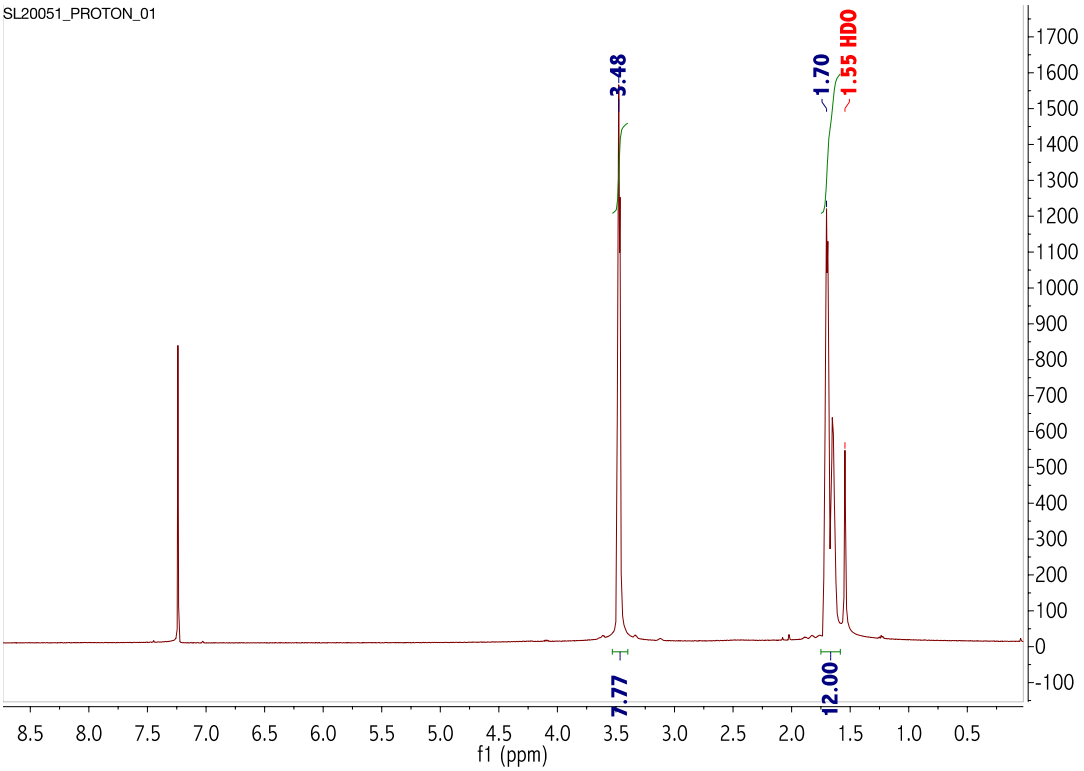

Figure 6.7. ^{1}H NMR of 2,5-dichloro-3,6-dipiperidino-1,4-benzoquinone in $CDCl_3$.

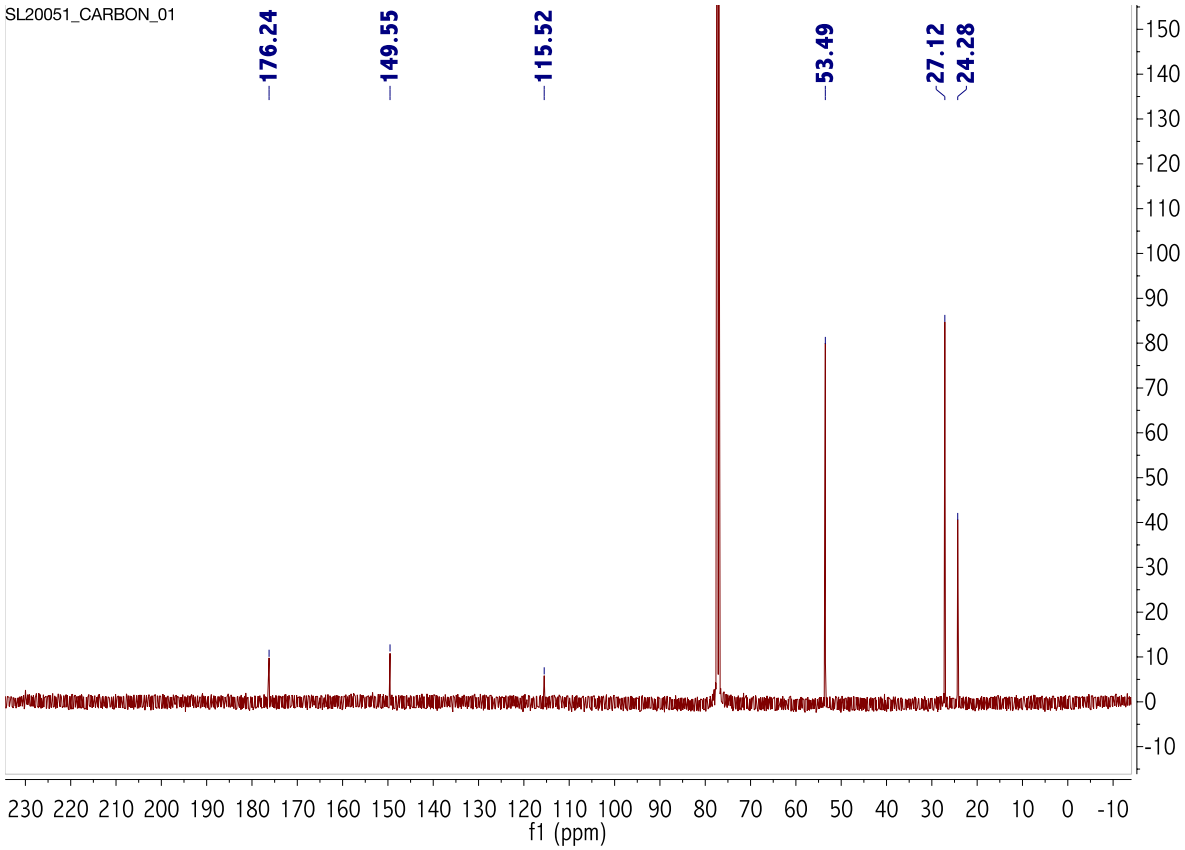

Figure 6.8. ^{13}C NMR of 2,5-dichloro-3,6-dipiperidino-1,4-benzoquinone in $CDCl_3$.

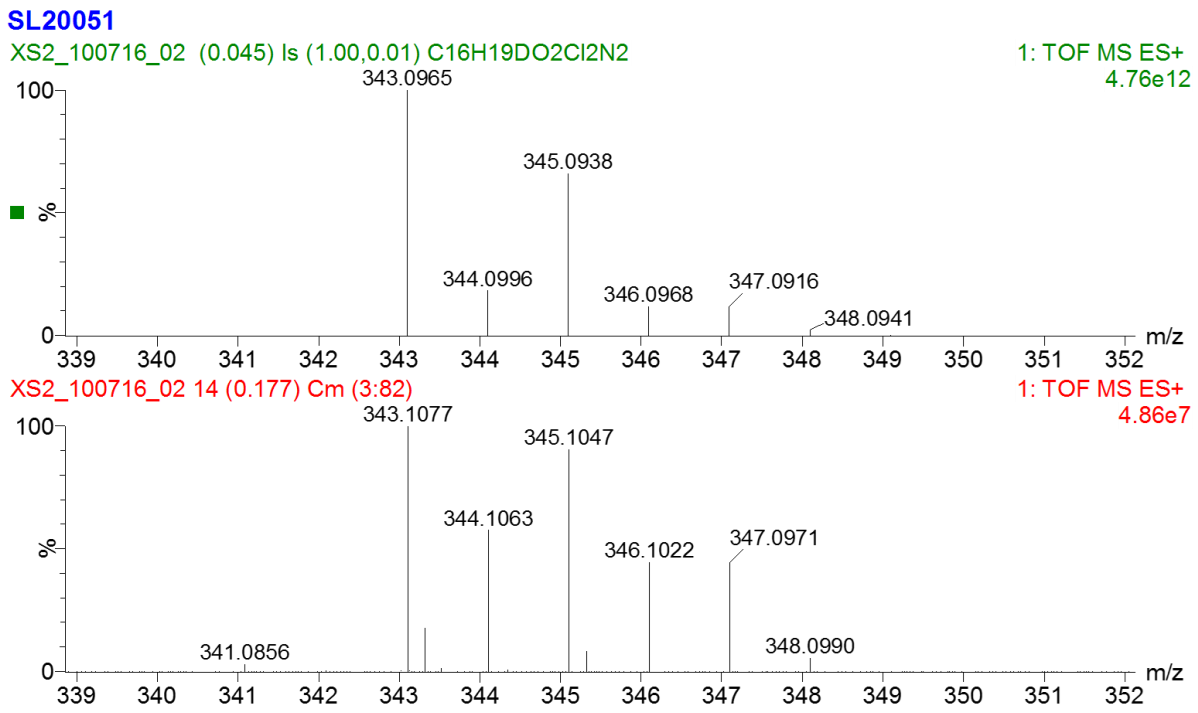

Figure 6.9. ESI-MS of 2,5-dichloro-3,6-dipiperidino-1,4-benzoquinone. Top: calculated isotope pattern for $[M+H]^+$ ($C_{16}H_{21}O_2N_2Cl_2$). Bottom: experimental result.

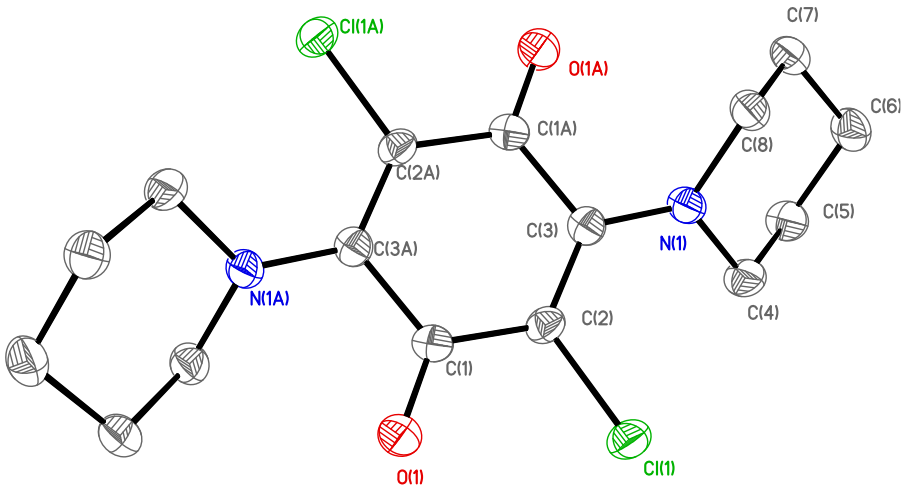

Figure 6.10. ORTEP drawing of 2,5-dichloro-3,6-dipiperidino-1,4-benzoquinone from single-crystal x-ray structure determination. Atoms are represented as 50% thermal ellipsoids. Hydrogen atoms are omitted for clarity.

Table 6.2. Crystallographic data of 2,5-dichloro-3,6-dipiperidino-1,4-benzoquinone.

Empirical formula	$C_{16}H_{20}Cl_2N_2O_4$
Formula weight	323.24
Temperature (K)	173(2)
Crystal system	monoclinic
Space group	$P2_1/c$
a (Å)	6.3855(6)
b (Å)	8.9434(9)
c (Å)	13.7532(13)
β (˚)	99.9310(10)
Volume (Å^3)	773.65(13)
Z	2
Radiation	MoKσ
D_{calc} (g cm^{-3})	1.473
Goodness of fit (F^2)	1.049
R_1 ($I>2\sigma(I)$)[a]	0.0381
wR_2 ($I>2\sigma(I)$)[b]	0.0953

[a] $R_1=\sum\frac{||F_o|-|F_c||}{\Sigma|F_o|}$. [b] $wR_2=[\sum w(F_o^2-F_c^2)^2/\sum w(F_o^2)^2]^{1/2}$, $w=1/[\alpha^2(F_o^2)+(aP)^2+bP]$, where $P=[F_o^2+F_c^2]/3$.

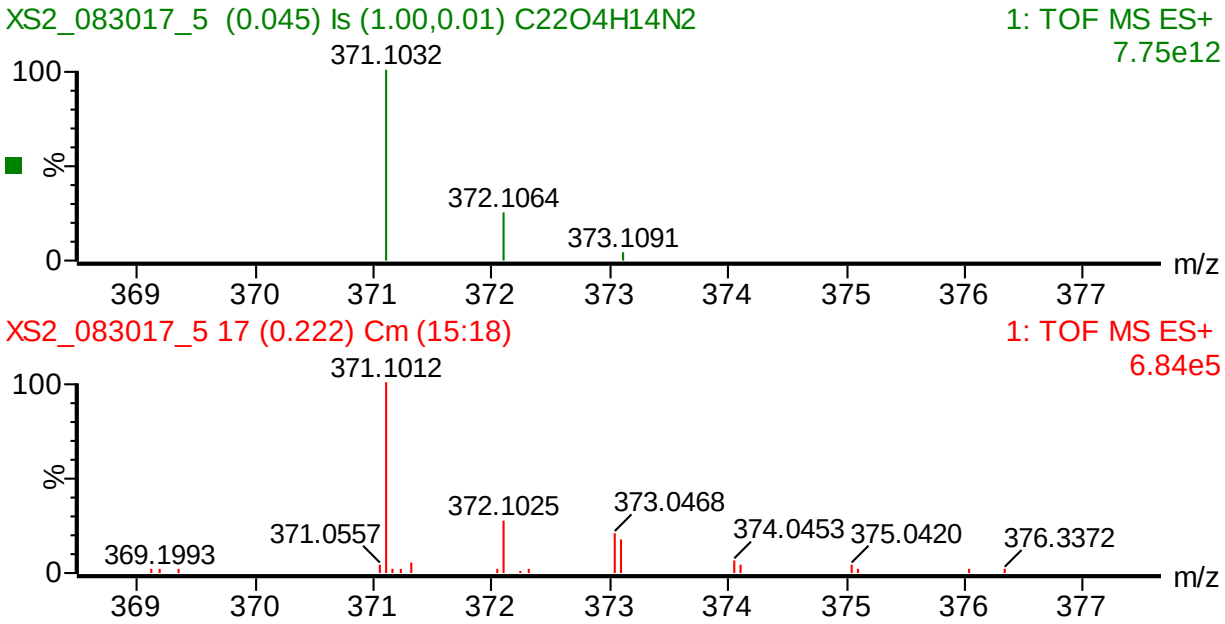

Figure 6.11. ESI-MS of 2,7-dimethoxy-3,6-di-(4-cyanophenyl)benzoquinone. Top: calculated isotope pattern for $[M+H]^+$ ($C_{20}O_4H_{15}N_2$). Bottom: experimental result.

REFERENCES

REFERENCES

(1) Atzori, M. Ph.D. Dissertation, University of Cagliari, Cagliari, CA, Italy, **2015**.

(2) Atzori, M.; Artizzu, F.; Marchiò, L.; Loche, D.; Caneschi, A.; Serpe, A.; Deplano, P.; Avavari, N.; Mercuri, M. L. *Dalton Trans.* **2015**, *44*, 15786-15802.

(3) Aubry, J. M.; Schmitz, C.; Rigaudy, J.; Cuong, N. K. *Tetrahedron*, **1983**, *39*, 623-627.

(4) McKelvey, T. Ph.D. Dissertation, Ohio State University, Columbus, OH, **1987**.

(5) Tandon, V. K.; Kumar, S.; Mishra, N. N.; Shukla, P. K. *Eur. J. Med. Chem.*, **2012**, *56*, 375.

(6) Torrey, H. A.; Hunter, W. H. *J. Am. Chem. Soc.*, **1912**, *34*, 702.

(7) Kiral, R. M. Ph.D. Dissertation, University of Notre Dame, Notre Dame, IN, **1980**.

(8) Winkelmann, E. *Tetrahedron* **1969**, *25*, 2427.

(9) Akutagawa, T.; Nakamura, T. *Cryst. Growth Des.* **2006**, *6*, 70-74.

(10) Zaman, B. M.; Morita, Y.; Toyoda, J.; Yamochi, H.; Sekizaki, S.; Nakasuji, K. *Mol. Cryst. Liq. Cryst. Sci. Technol. Section A Mol. Cryst. Liq. Cryst.* **1996**, *287*, 249-254.

(11) Wallenfels, K.; Bachmann, G.; Hofmann, D.; Kern, R. *Tetrahedron*, **1965**, *21*, 2239.

(12) Nagata, W.; Yoshioka, M.; Dauben, W. G. (editor). *Organic Reactions.*, **1978**, *25*, 270.

(13) Gan, X.; Jiang, W.; Wang, W.; Hu, L. *Org. Lett.*, **2009**, *11*, 589-592.

(14) Hassan, Z.; Ullah, I.; Ali, I.; Khera, R. A.; Knepper, I.; Ali, A.; Patonay, T.; Villinger, A.; Langer, T. *Tetrahedron*, **2013**, *69*, 460-469.

(15) Walker, S. E.; Jordan-Hore, J. A.; Johnson, D. G.; Macgregor, S. A.; Lee, A. *Angew. Chem. Int. Ed.* **2014**, *53*, 13876-13879.

(16) McCusker, C. E.; McCusker, J. K. *Inorg. Chem.* **2011**, *50*, 1656-1669.

(17) McKelvey, T. Ph.D. Dissertation, Ohio State University, Columbus, OH, **1987**.

(18) Hellberg, J.; Dahlstedt, E.; Pelcman, M. E. *Tetrahedron*, **2004**, *60*, 8899-8912.

(19) Matta, C. F.; Hernández-Trujillo, J. *J. Phys. Chem. A.* **2003**, *107*, 7496-7504.

(20) Gaussian 09, Revision A.02, M. J. Frisch, G. W. Trucks, H. B. Schlegel, G. E. Scuseria, M. A. Robb, J. R. Cheeseman, G. Scalmani, V. Barone, G. A. Petersson, H. Nakatsuji, X. Li, M. Caricato, A. Marenich, J. Bloino, B. G. Janesko, R. Gomperts, B. Mennucci, H. P. Hratchian, J. V. Ortiz, A. F. Izmaylov, J. L. Sonnenberg, D. Williams-Young, F. Ding, F. Lipparini, F. Egidi, J. Goings, B. Peng, A. Petrone, T. Henderson, D. Ranasinghe, V. G. Zakrzewski, J. Gao, N. Rega, G. Zheng, W. Liang, M. Hada, M. Ehara, K. Toyota, R. Fukuda, J. Hasegawa, M. Ishida, T. Nakajima, Y. Honda, O. Kitao, H. Nakai, T. Vreven, K. Throssell, J. A. Montgomery, Jr., J. E. Peralta, F. Ogliaro, M. Bearpark, J. J. Heyd, E. Brothers, K. N. Kudin, V. N. Staroverov, T. Keith, R. Kobayashi, J. Normand, K. Raghavachari, A. Rendell, J. C. Burant, S. S. Iyengar, J. Tomasi, M. Cossi, J. M. Millam, M. Klene, C. Adamo, R. Cammi, J. W. Ochterski, R. L. Martin, K. Morokuma, O. Farkas, J. B. Foresman, and D. J. Fox, Gaussian, Inc., Wallingford CT, 2016.

(21) Vosko, S. H.; Wilk, L.; Nusair, M. *Can. J. Phys.* **1980**, *58*, 1200-1211.

(22) Lee, C.; Yang, W.; Parr, R.G. *Phys. Rev. B* **1988**, *37*, 785-789.

(23) Becke, A. D. *J. Chem. Phys.* **1993**, *98*, 5648-5652.

(24) Stephens, P. J.; Devlin, F. J.; Chabalowski, C. F.; Frisch, M. J. *J. Phys. Chem.* **1994**, *98*, 11623-11629.

(25) Tirado-Rives, J.; Jorgensen, W. *J. Chem. Theory Comput.* **2008**, *4*, 297-306.

(26) Glendening, E. D.; Reed, A. E.; Carpenter, J. E.; Weinhold, F. NBO 3.1; Theoretical Chemistry Institute, University of Wisconsin: Madison, WI, 1994.

(27) GaussView, Version 5, Dennington, R.; Keith, T. A.; Millam, J. M. Semichem Inc., Shawnee Mission, KS, 2009.

(28) Ochterski, J. W. Vibrational Analysis in *Gaussian.* http://gaussian.com/wp-content/uploads/dl/vib.pdf. June 14, 2018.

(29) Graebe *Justus Liebigs Ann. Chem.* **1868**, 1*46*, 31.

(30) Schrauben, J. N.; Guo, D.; McCracken, J. L.; McCusker, J. K. *Inorganica Chimica Acta*, **2008**, *361*, 3539-3547.

(31) Fehir, Jr., R. J. Ph. D. Dissertation. Department of Chemistry, Michigan State University, East Lansing, MI, 2009.